Faculty of Science and Engineering
Department of Applied Geology

A Petrochronological Investigation of Metamorphic, Melt and Fluid Related Processes in Lower Crustal Rocks from Southwestern Norway and Southern India

Eleanore Renee Blereau

This thesis is presented for the Degree of
Doctor of Philosophy
of
Curtin University

July 2017

DECLARATION

To the best of my knowledge and belief this thesis contains no material previously published by any other person except where due acknowledgement has been made. This thesis contains no material which has been accepted for the award of any other degree or diploma in any university.

The author acknowledges that copyright of published works contained within this thesis resides with the copyright holder(s) of those works. I warrant that I have obtained, where necessary, permission from the copyright owners to use any of my own published work (e.g. journal articles) in which the copyright is held by another party (e.g. publisher).

18 / 7 / 2017

Eleanore Renee Blereau

Date

ABSTRACT

Long-lived high temperature terranes can be difficult to quantify as a consequence of containing complex and potentially perturbed data sets. Increased rates of diffusion, partial melting and fluid interaction can modify geochronological and geochemical data, obscuring the exact timing of discrete events. By applying a multidisciplinary petrochronological approach two prolonged high-*T* terranes are investigated to provide new constraints on the duration of high-*T* conditions. The effect of prolonged high-*T* on the common geochronometers zircon and monazite is examined and new petrochronological tools for future studies are presented.

Orthopyroxene, the foundation of the charnockite assemblage, is shown to potentially grow during high-*T* metamorphism at *ca* 590–540 Ma (reaching 830–925°C and 6–9 kbar) at Kakkod, Southern India based on the three key lithologies recording overlapping *P–T* conditions and mineral textures. Contrasting with previous interpretations of charnockite formation being an exclusively post-peak fluid-related process. The crystallisation of the local melt system (*ca* 540–510 Ma) is interpreted to be the source of a later localised fluid event (*ca* 525–490 Ma), that altered the already existing orthopyroxene and caused coupled dissolution-reprecipitation of monazite. Charnockite formation likely occurs on a localised scale due to differences in fluid composition and event ages with a similar nearby locality.

A petrochronological approach shows that the Rogaland–Vest Agder Sector followed a high-*T* polymetamorphic evolution, with regional metamorphism between *ca* 1070–955 Ma (peaking at 850–900°C and 7–8 kbar between *ca* 1035–995 Ma). Samples closer to the Rogaland Igneous Complex (RIC) also experienced later contact metamorphism (at 3–6 kbar and 900°C (2 km) to ~1100°C (at contact)) and display a continuum of ages (from regional to younger), with no clear melt crystallisation until *ca* 900 Ma, 30 Myr after the emplacement of the RIC. High temperature conditions were prolonged, extending previous estimates, remaining at elevated geothermal conditions for at least 100 Myr to ~150 Myr, with implications for the stability of high-grade crust. Based on the results of this study and an assessment of current literature the earlier continent-continent collisional model cannot satisfactorily explain the metamorphic and magmatic evolution of the Sveconorwegian Belt. A long-lived subduction-accretionary model better explains the distribution of magmatism and metamorphism.

Osumilite is successfully dated using the $^{40}Ar/^{39}Ar$ method for the first time with a measured closure temperature of ~770°C for a grain radius of 175 µm and a cooling rate of 10°C/Myr. Osumilite presents an opportunity to directly date portions of a high-*T P–T* path by being a datable mineral with quantified thermodynamic activity models, a feat zircon is currently unable to do directly. Diffusion modelling of the age distribution preserved in osumilite provided additional constraints on the maximum temperatures experienced by the sample.

REE-in-zircon diffusion modelling can provide additional constraints on the duration and conditions of high-temperature metamorphism in rocks dominated by recrystallisation and shows,

under appropriate conditions and time-scales, REE in zircon are not immobile and can be potentially modified or equilibrated. This modelling also provided constraints on the method of emplacement of the RIC, requiring a rapid assembly as a series of pulses over 1–5 Myr to achieve appropriate temperatures, differing to previous two pulse models.

Whilst both case studies produced geochronological data sets that initially appear similar, the generation of these data sets resulted from unique combinations of processes. The combination of processes generating the resulting data set were resolvable by careful petrochronological analysis. Zircon at Kakkod was controlled by the presence of melt and neocrystallisation whereas in Rogaland zircon was primarily modified by recrystallisation. Monazite recorded the fluid processes at Kakkod whereas high-*T* fluid-absent conditions were recorded by monazite in Rogaland. Combining a number of techniques and multiple geochronometers was highly beneficial in unravelling high temperature systems due to variable responses to different geodynamic and geochemical factors by each mineral, providing new constraints on high-*T* processes. Zircon and monazite are not impervious to modification by high-grade processes but the resultant effects can be recognised in a number of ways and may also be used to provide additional constraints.

‘Science is nothing but storytelling under rigorous circumstances’

–Adam Savage

“In the beginning the Universe was created. This has made many people very angry and has been widely regarded as a bad move.”

“The Hitchhiker’s Guide to the Galaxy is an indispensible companion to all those who are keen to make sense of life in an infinitely complex and confusing Universe, for though it cannot hope to be useful or informative on all matters, it does at least make the reassuring claim, that where it is inaccurate it is atleast definitively inaccurate.”

“Forty-two!... Is that all you’ve got to show for seven and a half million years’ work? I checked it very thoroughly, said the computer, and that quite definitely is the answer. I think the problem, to be quite honest with you, is that you’ve never actually known what the question is.”

“Don’t Panic. It’s the first helpful or intelligible thing anybody’s said to me all day.”

“Life... is like a grapefruit. It’s orange and squishy, and has a few pips in it, and some folks have half a one for breakfast.”

“I only know as much about myself as my mind can work out under its current conditions. And its current conditions are not good.”

“We’ll be saying a big hello to all intelligent life forms everywhere.. and to everyone else out there, the secret is to bang the rocks together, guys.”

– Douglas Adams “The Hitchhikers Guide to the Galaxy

“Mischeif Managed.”

– J. K. Rowling

ACKNOWLEDGEMENTS

This PhD has been a tumultuous experience of highs, lows, laughter, stress, frustration and confusion with bright points of joy, success and achievement. All of which, especially lately, were experienced in a coffee fueled haze. It's an experience I am grateful for and it's made me appreciate a real weekend, the joys of a nice glass of wine or cider at the end of the day, making time for the things that I enjoy in life, traveling to new places, trying new things and the thrill of scientific discovery. It has also introduced me to an inordinate amount of people and if you are inheretly absent from the thanks below, I apologise and thank you muchly.

Firstly, many thanks to my supervisors Chris Clark, Tim Johnson, Rich Taylor and Pete Kinny for your guidance and answering my many many questions. You made me want to work hard to impress you all and helped me grow so I could achieve my goals. I hope we can continue to work together in the future. I know you will miss my enthusiasm, my over use of air quotations and the all time favourite: yes, osumilite is isostructural with millerite.

Thanks also to Martin Hand for interesting and enlightening chats and for helping me the time we went down the 'wrong' side of that mountain in Norway. Many thanks also to Fred Jourdan, Ian Fitzsimons and M. Santosh for working with me, answering my many questions and all the great feedback. Thanks to all the technicians in the SHRIMP, LA–ICP–MS, SEM and Argon labs for all your assistance. Thanks to Luke Hersey for helping me out in the field, sharing my frozen delirium, nonsensical Norwegian store hours, mapping fever and the discovery of the magical cabinet. Thanks also to Mehrooz Aspandiar for all your support and guidance over the years.

A huge amount of hugs and thanks to all my PhD friends, for making me laugh, keeping me positive and looking after me when times were hard. Thanks to you all for listening to my chatty babble, keeping me company during my many coffee runs and supporting my occasional couch surfing. Special thanks to Lucy for your positivity, many laughs and company during all those late night and weekend work days. Also heaps of thanks to Ellie for saving me from MATLAB and calculus hell! To my friends outside of uni, thanks for giving me a taste of the real world now and then, for always being free to talk and for always looking after me. I know you were all quizzical when you found out I liked rocks, but I made you see that they were interesting in the end!

Thank you to the QWERTY keyboard for placing G so close to F, making 'buffered' very easily becomes 'buggered' during tired and furious typing.

Last but not least, to my parents and my family for putting up with my crazy, stress-filled, occasionally grumpy and sleep-deprived self. For keeping me fed and watered and for listening to my occasional rants about geology (life), the universe and everything. If only the answer to my thesis was 42! It was fun surprising you with how technical my work is, and showing you that geology is much more than smashing two rocks together.

I'm happy to now say so long to my thesis and thanks for all the schist (fish).

LIST OF PUBLICATIONS INCLUDED AS PART OF THIS THESIS

This thesis is a compilation of a number of research papers that were either published, submitted or in preparation at the time of writing this document. All papers have a statement of co-authorship in Appendix A and published papers 1 and 2 are reprinted in their published form in Appendix A at the end of this thesis.

Paper 1:

Blereau, E., Clark, C., Taylor, R. J. M., Johnson, T. E., Fitzsimons, I. C. W., and Santosh M., 2016. Constraints on the timing and conditions of high-grade metamorphism, charnockite formation and fluid-rock interaction in the Trivandrum Block, southern India. *Journal of Metamorphic Geology*, 34, 527–549.
doi:10.1111/jmg.12192.

Paper 2:

Blereau, E., Johnson, T. E., Clark, C., Taylor, R. J. M., Kinny, P. D., and Hand, M., 2017. Reappraising the P–T evolution of the Rogaland–Vest Agder Sector, southwestern Norway. *Geoscience Frontiers*, 8, 1–14.
doi: http://dx.doi.org/10.1016/j.gsf.2016.07.003

Paper 3:

Blereau, E., Clark, C., Jourdan, F., Johnson, T. E., Taylor, R. J. M., Kinny, P. D., Hand, M. and Eroglu, E. Constraining the timing of prograde metamorphism in long-lived hot orogens.
(Under review in *Geology* since 7/6/2017)

Paper 4:

Blereau, E., Clark, C., Taylor, R. J. M., Kinny, P. D., Johnson, T. E., Sansom, E., Hand, M. Using accessory minerals to unravel thermal histories in polymetamorphic terranes: an example from Rogaland, SW Norway.
(Under review in the *Journal of Metamorphic Geology* since 23/6/2017)

TABLE OF CONTENTS

THESIS AIMS

Petrochronology is a relatively young research field, integrating geochemistry, geochronology and petrography to create a firm connection between age constraints and phase equilibria modelling, with the aim of unravelling complex terranes and geological problems. High temperature terranes push the limits of petrochronology and many mineral phases due to the interconnected involvement of fluids, melt and higher rates of diffusion, resulting in complex reaction textures as well as complex geochronological and geochemical information. Southern India and Southwestern Norway are two complex metamorphic regions where the metamorphic evolutions of both regions have been highly debated, with contrasting interpretations on the timing, duration and *P–T* conditions as well as the involvement of melt and fluid processes and factors controlling metamorphism. SW Norway also has two contrasting tectonic models representative of two very different geodynamic settings, with potential implications for the formation of magmatic suites hosted within the region. This thesis will apply current analytical techniques (SHRIMP U–Pb, LA–ICP–MS) and a newly updated thermodynamic modelling dataset ('ds62') to these regions to evaluate previous data and provide new constraints and interpretations.

Using these two regions as case studies, this thesis has three main aims:

- Quantify the timing, conditions and factors controlling high-*T* metamorphic processes in S India and SW Norway through a petrochronological approach.
- Investigate the behaviour of traditional geochronometers during high-*T* conditions.
- Highlight the importance of a petrochronological approach in assessing high-grade terranes.

Additional aims and side projects:

- Tectonic implications for SW Norway based on this study.
- Test osumilite as a new potential thermochronometer.

THESIS STRUCTURE

This thesis has been written as a series of individual manuscripts investigating the aims of this thesis within two case studies: one within southern India (**Chapter 2**) and one within SW Norway (**Chapter 3–5**). These manuscripts are either published in peer review journals, in preparation for submission or under review. The formatting of each chapter within this thesis may vary due to the requirements and formatting guidelines of each individual journal as well as the requirements of this thesis. Due to the composite nature of this thesis there is some repetition in the methodology. Regional geological backgrounds with relevant information for the contents of each manuscript are given within each pertinent chapter. Supplementary information for each manuscript is provided in appendices at the end of this thesis.

Introduction: Chapter 1

This chapter provides a review of U–Pb petrochronological techniques as applied to metamorphic rocks, with a focus on the application of accessory minerals and how various forms of analytical data may be combined and interpreted. This chapter is written in the style of a review paper.

Southern India: Chapter 2

Chapter 2 provides a case study from Kakkod, southern India. Kakkod is a previously unstudied quarry located in the Trivandrum Block (TB) within the Southern Granulite Terrane (SGT). The *P–T–t* history of the TB has been subject to debate for many years. The occurrence and generation of incipient charnockites has also been highly debated, with many key localities within the TB. Kakkod quarry provided an opportunity to evaluate the *P–T* conditions and timing of metamorphism on a local scale, as well as increase understanding of charnockite formation due to the fact that all three of the key rock types of the TB were present within one exposure (unique from other exposures). **Chapter 2** applies the techniques of SHRIMP U–Pb geochronology and LA–ICP–MS REE and trace element geochemistry of zircon and monazite, petrography and phase equilibria modelling ('ds62').

This chapter is published in the *Journal of Metamorphic Geology* as:

Blereau, E., Clark, C., Taylor, R. J. M., Johnson, T. E., Fitzsimons, I. C. W., and Santosh M., 2016. Constraints on the timing and conditions of high-grade metamorphism, charnockite formation and fluid-rock interaction in the Trivandrum Block, southern India. Journal of Metamorphic Geology, 34, 527–549. doi:10.1111/jmg.12192.

Southwestern Norway: Chapter 3–5

Chapters 3–5 provide a case study from the Rogaland–Vest Agder (RVA) Sector of SW Norway. The RVA sector is a high-grade metamorphic province with two contrasting tectonic models (collisional vs. prolonged subduction/accretionary) as well as two different *P–T–t* models (polymetamorphic vs. singular metamorphic evolution) that have been proposed by previous studies. The RVA sector is also host to the ~1000 km^2 Rogaland Igneous Complex (RIC) which has been postulated in some studies to be intrinsically related to the metamorphic evolution in the form of a contact metamorphic event.

Chapter 3 combines detailed petrographic observation with phase equilibria modelling ('ds62') on a suite of samples collected at different distances from the RIC (30 km, 10 km and at the RIC contact). This sampling approach was used to re-evaluate the *P–T* conditions of the RVA on a regional scale and evaluate the temporal affect of the RIC on the metamorphic evolution. An assessment of the two tectonic models based on previous literature and the metamorphic evolution proposed in this paper was also conducted with implications for the tectonic setting of the Sveconorwegian Orogeny.

This chapter is published in *Geoscience Frontiers* as:

Blereau, E., Johnson, T. E., Clark, C., Taylor, R. J. M., Kinny, P. D., and Hand, M., 2017. Reappraising the P–T evolution of the Rogaland–Vest Agder Sector, southwestern Norway. Geoscience Frontiers, 8, 1–14. doi: 10.1016/j.gsf.2016.07.003.

Chapter 4 provides the first attempt of $^{40}Ar/^{39}Ar$ dating on osumilite, a silicate mineral found in HT/UHT metamorphic rocks and volcanic rocks. Comparisons are made between $^{40}Ar/^{39}Ar$ osumilite ages and U–Pb monazite geochronology from a previous study on the same sample. Phase equilibria modelling ('ds55') are compared with *P–T* conditions from **Chapter 3**. The applicability of osumilite as a thermochronometer is accessed and the closure temperature from diffusion experiments is also reported for the first time. The implications and additional constraints on the metamorphic evolution of the RVA are also discussed.

This chapter is under review in *Geology* as:

Blereau, E., Clark, C., Jourdan, F., Johnson, T. E., Taylor, R. J. M., Kinny, P. D., Hand, M. and Eroglu, E. Constraining the timing of prograde metamorphism in long-lived hot orogens. (Since 7/6/2017)

Chapter 5 applies SHRIMP U–Pb geochronology and LA–ICP–MS REE and trace element geochemistry to the samples as in **Chapter 3** as well as two additional samples (at 2 km from the RIC (same sample used in **Chapter 4**) and at the contact of the RIC). The affects of anorthosite emplacement on the country rocks of the RVA are investigated as well as refining the timing of different events. Diffusion modelling was conducted to evaluate and quantify diffusion modification of REE in zircon due to high-grade metamorphism. REE data from Rogaland are interpreted using the aforementioned model, providing additional constraints on the method of emplacement of the RIC.

This chapter is under review in the *Journal of Metamorphic Geology* as:

Blereau, E., Clark, C., Taylor, R. J. M., Kinny, P. D., Johnson, T. E., E. Sansom, Hand, M. Using accessory minerals to unravel thermal histories in polymetamorphic terranes: an example from Rogaland, SW Norway. (Since 23/6/2017)

Conclusions and future research directions: Chapter 6

Chapter 6 summarises the key findings of each case study and future research suggestions.

Bibliography: Chapter 7

Complete bibliography of all references included in this thesis.

Chapter 1

INTRODUCTION

An overview of U–Pb petrochronology and its application in high-grade rock systems

1. INTRODUCTION

The stability of zircon and monazite in most geological settings, the typically low concentrations of common lead (^{204}Pb) in these minerals and their high closure temperatures (T_c) (>900°C: Ashwal et al., 1999; Cherniak and Watson, 2001; Cherniak et al., 2004; Cherniak and Pyle, 2008) have made these accessory minerals the two most commonly used U–Pb geochronometers. As a result of forming from the interplay of a variety of processes, both zircon and monazite have a high degree of inherent complexity in terms of growth zones and geochemical signatures, with individual grains often recording multiple ages. Petrochronology uses this internal complexity, petrography and geochronology to connect accessory minerals like zircon and monazite to the silicate mineral evolution, forming a strong connection between recorded age data and *P–T* conditions. Linking age data to the silicate mineral evolution is crucial for increasing understanding on the time-scales and rates of orogenic processes (e.g. Hermann and Rubatto, 2003; Janots et al., 2009), unravelling complex metamorphic terranes (e.g. Rubatto et al., 2013) and generating quantitative *P–T–t* paths (e.g. Foster et al., 2004). However, the age data recorded by accessory minerals are further complicated in high temperature terranes due to increased rates of diffusion (e.g. Kohn and Penniston-Dorland, 2017), partial melting (e.g. Bea and Montero, 1999) and fluid influx (e.g. Kelly et al., 2012), perturbing recorded age and geochemical data and resulting in complex data sets. Polymetamorphic terranes take this a step further, potentially removing earlier parageneses and overprinting recorded age data. This overview highlights how petrochronology may be used to unravel complex high-grade and polymetamorphic terranes, by providing a resource for interpreting a range of textural, geochemical and partitioning data from accessory minerals. It also provides an overview of the history of petrochronology, a relatively young field of research, including the main high-resolution *in situ* analytical techniques used and their relative advantages and limitations. The range of zoning and geochemical signatures within zircon and monazite and their use in petrochronological studies are characterised in terms of high temperature processes. The importance of rare earth elements (REE) and their partitioning behaviour for petrochronological studies is discussed. Examples of how accessory mineral information can be integrated with forward modelling is demonstrated using synthetic *P–T–t* paths of high-grade lithologies related to natural examples of textures, geochemistry and REE relationships. The current limitations and complications when using accessory minerals in high-grade rocks are also discussed.

2. PETROCHRONOLOGICAL TECHNIQUES

The importance of the petrochronological approach was first put forward by Fraser et al. (1997), shortly after the recognition of complex internal structures in accessory minerals previously described as featureless in transmitted light through the application of BSE and CL imaging (Vavra, 1990; Hanchar and Rudnick, 1995). Previously, analysing these featureless grains using earlier dissolution methods could provide minimal whole grain chemical information. However, as described

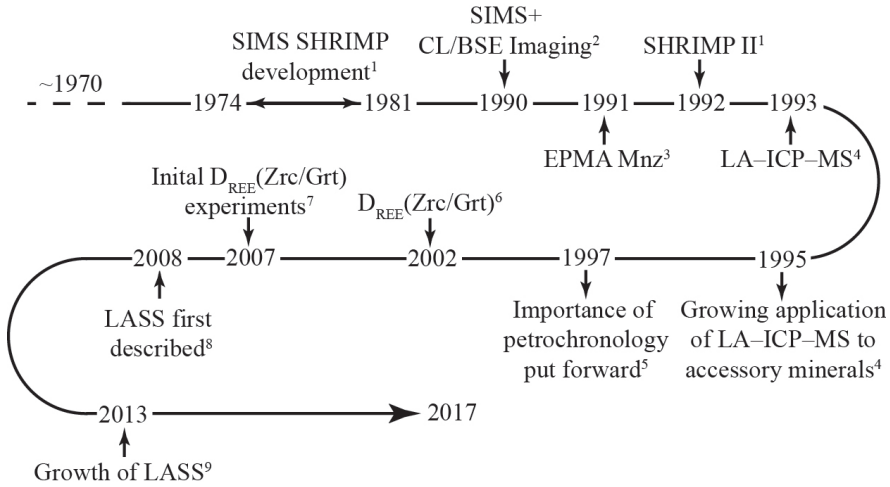

Fig. 1: Timeline of important petrochronological developments from the 1970's till present. 1: Davis et al. (2003), 2: Vavra (1990), 3: Suzuki and Adachi (1991), 4: Jackson et al. (2004), 5: Fraser et al. (1997), 6: Rubatto (2002), 7: Rubatto and Hermann (2007), 8: Yuan et al. (2008), 9: Kylander-Clark et al. (2013)

by Hanchar and Rudnick (1995), the presence of multiple growth zones would make it difficult to date individual events through dissolution and to isolate structures such as thin rims from older cores. The ability to measure an array of major and trace elements by *in situ* targeting was essential in order to properly characterise different domains and avoid age mixing, as this would open up a complex array of geological information within individual grains (Ireland and Williams, 2003). The application of *in situ* Secondary Ion Mass Spectrometry (SIMS) analysis to accessory minerals and later Laser Ablation Inductively Coupled Plasma Mass Spectrometry (LA–ICP–MS) saw these techniques become the most widely used and foundational petrochronological technique(s) due to their high spatial resolution and ability to measure a range of isotopes *in situ* within a small analytical volume. The application and types of interpretations that can be made using these techniques will be covered in the most detail, with the use of SIMS for U–Pb and LA–ICP–MS for REE of particular focus for this thesis. Other techniques such as EPMA and their advantages and disadvantages compared to SIMS and/or LA–ICP–MS will also be discussed.

2.1 The path to petrochronology

Earlier dissolution techniques (e.g. ID–TIMS) provided age information from the dissolution of a single grain, and therefore were unable to resolve useful information from grains with high levels of internal complexity (Ireland et al., 2008; Nemchin et al., 2013). The development of SIMS instruments with high spatial resolution made it possible to study several age domains or growth generations within a single grain, providing an alternative to dissolution methods. The Sensitive High Resolution Ion MicroProbe (SHRIMP I) was developed between 1974–1981 and was the first SIMS instrument fully dedicated to the evaluation of geological materials (Fig. 1), with some of the first U–Pb SHRIMP data published in the early 80's by Compston et al. (1982), Froude et al. (1983) and Williams et al. (1983). The SHRIMP II became operational in 1992, with four times the sensitivity of its predecessor and faster analysis

speeds, increasing the number of grains analysable in one session (Davis et al., 2003; Ireland et al., 2008). Targeting of identified internal textures from cathodoluminescence (CL) and back scattered electron (BSE) imaging in the early 1990's (Vavra, 1990; Hanchar and Miller, 1993) facilitated analysis of different growth zones that are not visible under typical light sources, with the added bonus of reducing mixed analyses and avoiding potential problems such as cracks. These forms of imaging have been combined with all techniques (i.e. LA–ICP–MS, SIMS, EPMA) and have become crucial for interpreting geological processes behind analysed age domains, such as protolith ages (Hanchar and Rudnick, 1995), metamorphism (Rubatto et al., 2001) or fluid infiltration (Taylor et al., 2014). The early 1990's were also important with the development of EPMA dating (Suzuki and Adachi, 1991) as well as the start of LA–ICP–MS in 1993 (Feng et al., 1993; Fryer et al., 1993; Jackson et al., 2004)(Fig. 1). LA–ICP–MS was first used to measure in situ $^{207}Pb/^{206}Pb$ ages (Feng et al., 1993; Fryer et al., 1993; Jackson et al., 2004)(Fig. 1), with increasing applications from the mid 90's for both ages and trace element geochemistry (Hirata and Nesbitt, 1995; Fernández-Suárez et al., 1998; Horn et al., 2000; Ketchum et al., 2001; Li et al., 2001; Košler et al., 2002; Tiepolo, 2003). The use of REE geochemistry to categorise zircon textures and associated formative processes through correlating geochemistry and textures with microstructures was highlighted by Rubatto (2002), and saw the growth of REE in petrochronological applications. In response to the growth in the application of REE geochemistry, experimental studies to provide quantitative constraints on REE partitioning between accessory minerals and other minerals were conducted, e.g. zircon and garnet (Rubatto and Hermann, 2007; Taylor et al., 2015a). These experiments increased understanding on the partitioning of these elements between minerals and provided a framework to interpret REE distributions in natural samples. Until the late 2000's the collection of both REE and age data required the use of multiple analytical spots. Laser Ablation Split Stream (LASS) provided a new tool to analyse both geochemical and geochronological information from the same analytical volume. The premise for LASS was first described in 2008 (Yuan et al., 2008) and was adopted by Xie et al. (2008) and Chen et al. (2010) with improved precision and changes to ablation volume. In 2013, the key paper of Kylander-Clark et al. (2013) underpinned the widespread uptake of LASS, due to its flexibility and wide applicability to a variety of accessory and major minerals as well as its petrochronological applications.

2.2 SIMS & LA–ICP–MS

SIMS (and more specifically the SHRIMP) allows measurement of small domains for isotopic and elemental abundance and has been instrumental to petrochronology as a tool for resolving complicated growth histories of accessory minerals. For the analysis of minerals such as zircon and monazite a primary oxygen ion beam is used to ablate material within a small diameter spot (~5–30 µm), forming a very shallow pit (<5 µm) with ionised positive material accelerated using a charge differential into a multi-collector mass spectrometer (when first designed the SHRIMP II used a single collector). SIMS requires very

high mass resolution to separate between ions of all elements as well as accompanying oxides and hydroxides within the ionised material. Analysis times are long (~20 minutes per spot) in order to achieve the required high resolution without the loss of precision.

LA–ICP–MS applies a more destructive laser instead of an ion beam to ablate the sample, resulting in an ablated aerosol transported by a carrier gas (e.g. Argon) to a mass spectrometer. LA–ICP–MS has high spatial resolution, analysing spot sizes of ~10–30 µm to a depth of ~5–15 µm, which is a larger analytical volume than analysed by SIMS. By ablating a larger analytical volume, shorter analysis times are possible (~1 min) whilst achieving resolution on par with SIMS under ideal conditions. LA–ICP–MS can apply either a quadrapole or a multi-collector mass spectrometer: the quadrapole's ability to analyse a large range of elemental masses with low detection limits is best applied to trace and major elements, and the multi-collector's high precision and narrow mass range is most suited for isotope ratios for age derivation and Hf isotopes.

The derivation of isotopic ages measured by SIMS and LA–ICP–MS require the collection of primary and secondary standards with known ages throughout an analytical session to correct for fractionation in combination with other uncertainties (Schmitt and Vazquez, 2017). SIMS and LA–ICP–MS are capable of measuring U–Pb and REE individually, but there are advantages and disadvantages to this approach which will be discussed below. SIMS and LA–ICP–MS may be integrated with other techniques such as EBSD, EPMA, CL/BSE imaging and can be used to collect data from experiments involving accessory minerals. Within this thesis SIMS is combined with LA–ICP–MS through initial SIMS analysis for U–Pb followed by LA–ICP–MS for trace elements on top of the SIMS analytical spots, with this combination of techniques being widely in a number of other studies (e.g. Rubatto, 2002; Hermann and Rubatto, 2003; Rubatto and Hermann, 2003; Rubatto et al., 2006; Taylor et al., 2014; Johnson et al., 2015). The application of SIMS and LA–ICP–MS provided a foundation for how REE and U–Pb vary in zircon and monazite in different geological and mineralogical environments and the measurement other diagnostic geochemical features.

2.3 Electron Probe geochronology

EPMA dating provides an alternative to SHRIMP and LA–ICP–MS and is applicable to monazite (Suzuki and Adachi, 1991, 1994; Braun et al., 1998; Cocherie et al., 1998; Dahl et al., 2005; Mahan et al., 2006; Williams et al., 2006; Zhou et al., 2008)(also known as CHIME dating), but is rarely applied to zircon (Santosh et al., 2003), generating chemical Th–U–total Pb ages. EPMA offers high spatial resolution as it is capable of analysing features on the micron scale (~1–2 µm) (Cocherie et al., 1998; Williams et al., 2017). This makes the technique very useful for analysing small textural features visible only on high-resolution geochemical maps. This technique is non-destructive as it relies on the application of an electron beam to the sample causing atoms to release characteristic X-rays, as opposed to the destructive ionisation of sample material utilised by previously described techniques. This makes EPMA perferable for use when analysing rare

and important samples where minimal sample destruction is desired. However, by analysing a small analytical volume this technique can only achieve a low compositional resolution (detection limit of a few tens of ppm: Engi et al., 2017). EPMA analysis can be conducted *in situ* as spot analyses, arrays of spots or as maps (e.g. Sanislav, 2011; Williams and Jercinovic, 2012). Using the mapping approach, areas of particular geochemistry can be selected as irregular domains to target with later spot analyses (Williams et al., 1999; Buick et al., 2010; Dumond et al., 2015; Shazia et al., 2015). EPMA dating requires a number of assumptions: that the sample contains no common Pb and that the sample has experienced no Pb loss or modification to U/Th/Pb contents except through radioactive decay. These assumptions are required due to the inability of EPMA to measure individual elemental isotopes, with only total elemental concentrations being measured. This is particularly problematic for non-radiogenic common lead, which is corrected in isotopic studies to determine the amount of radiogenic lead (206, 207, 208). Processing Pb ratios without making this correction will result in overall higher amounts of Pb and anomalously old ages. Whilst EPMA dating may be applicable to some samples, many high-grade metamorphic samples experience partial to complete Pb loss and U and Th concentrations may be modified during the metamorphic evolution by processes such as fluid infiltration (Williams et al., 2011).

2.4 Laser Ablation Split Stream Petrochronology

LASS is the most recent petrochronological technique, becoming available for analytical studies in ~2013 (Kylander-Clark et al., 2013). While LA–ICP–MS applies a single mass spectrometer at a time, LASS splits the ablated aerosole laser stream across two mass spectrometers. One stream is used for collecting isotopes for age information (typically using a multi-collector) and the other is used for collecting many different trace and major elements (typically using a quadrapole detector), with the important point being all data are collected from the same analytical volume. By collecting data from the same analytical volume all data is directly comparable, as opposed to having to apply multiple analytical sites or analytical spots on top of previous analysis sites to collect the same information. LASS has been applied to both monazite (e.g. Holder et al., 2015; Štípská et al., 2015) and zircon (e.g. Gordon et al., 2013; Zhao et al., 2015), simultaneously collecting trace elements and isotopic ratios. LASS was not applied in this study due to the timing of the project research. LASS was in its infancy at the beginning of this project (early 2014) and was not as widely available as SIMS and LA–ICP–MS techniques.

2.5 Advantages and limitations

The small and shallow analysis spots of SIMS cause minimal sample destruction with good spatial resolution in terms of targeting specific textural or chemical domains (Ireland and Williams, 2003). However, in order to maintain high resolution without the loss of precision, SIMS analysis (i.e. SHRIMP) times are slow (~20 mins per spot) limiting the number of analytical spots per session (~50 analytical spots). LA–ICP–MS on the other hand with its fast analysis times thanks

to analysing a larger ablation volume is perfect for evaluating large sample sizes (>100 grains) and, under ideal conditions, can achieve similar levels of precision. U–Pb and REE are both collectable via SIMS or LA–ICP–MS individually, but both techniques require multiple analytical spots adjacent to each other or repolishing in between analytical sessions. As isotopic variations can occur on the micron scale within the sample this limitation can introduce discrepancies between data sets. The combination of SIMS for U–Pb and LA–ICP–MS for REE lessens the effect of different analytical volumes by placing laser spots over previous SHRIMP spots.

EPMA has the best spatial resolution of all techniques, acheiving spots sizes up to 10 times smaller than ion probe and laser ablation spot sizes (Cocherie et al., 1998; Cocherie and Albarede, 2001; Engi et al., 2017). EPMA is less destructive than all the other techniques, is widely available and has shorter analysis times than SIMS (Cocherie and Albarede, 2001; Santosh et al., 2003; Williams et al., 2006). Nevertheless, EPMA dating is limited to monazite as well as samples with (or assumed to have) no common lead due to an inability of measure individual isotopes, with no way to correct for common lead or unusual amount of other Pb isotopes due to parent isotope modification.

The main advantage of LASS is that by splitting the aerosole stream between two mass spectrometers isotope ratios and trace element concentrations may be measured within the same analytical volume. LASS has the same disadvantages as LA–ICP–MS with deeper analytical pits, increasing the risk of mixed analyses due to heterogeneity with depth, but any heterogeneities can be resolved through time-resolved data. LASS, like LA–ICP–MS, is relatively inexpensive per spot compared to SIMS due to faster analysis times, allowing the collection of very large volumes of data within one session (~500 analytical spots).

All of the above limitations and advantages are also dependant on the properties of the sample in question and the aim of the research. Is the desired sample area very small and therefore spot size is the limitation? Are precise trace element concentrations more important than isotopic ratios? Is the sample rich in elements that will cause problems for the instruments collectors? All of the above mentioned techniques and the applicable parameters must be evaluated on a case-by-case basis, in order to determine the most appropriate method that will allow the best results to be achieved.

3. THE CHEMISTRY OF PETROCHRONOLOGY

3.1 Internal textures of metamorphic zircon and monazite

Zircon and monazite have been shown to form from a range of geological processes within different geodynamic environments, with a related empirical catalogue of internal textural features (Corfu et al., 2003; Taylor et al., 2016), allowing processes to be dated based on associated textures. Under CL or BSE imaging internal textures are generated in response to internal variations in chemistry or average atomic number respectively (Corfu et al., 2003). Metamorphic rocks display the widest array of internal textures within

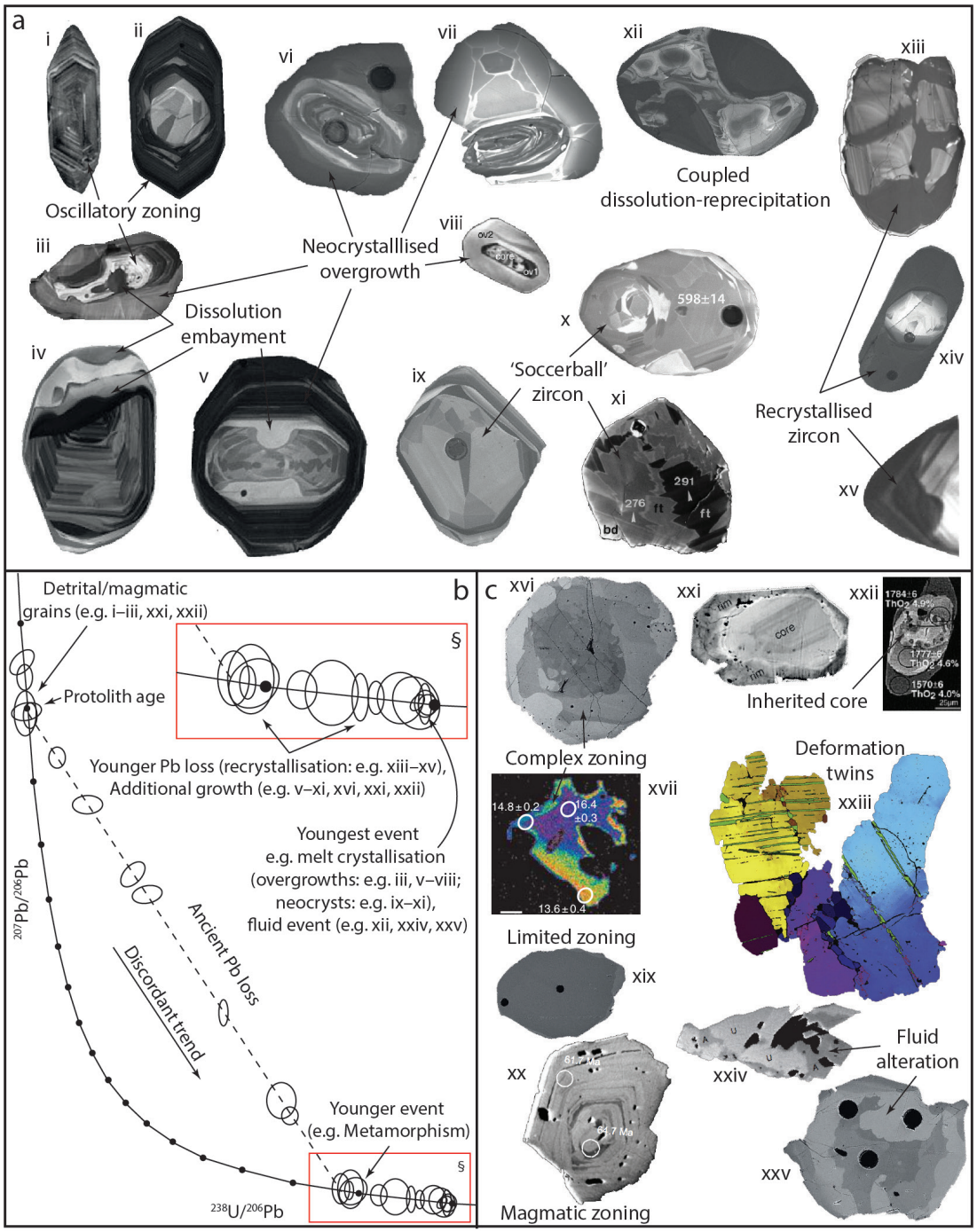

Fig. 2: Catalogue of zircon and monazite textures and a synthetic geochronological data set. a- Zircon textures modified from Corfu et al. (2003) (i, ii, v), Möller et al. (2002) (iii), Nutman et al. (2002) (iv), Johnson et al. (2015) (vi, x), Taylor et al. (2016) (vii, xiii), Hermann and Rubatto (2003) (viii), Taylor et al. (2015b) (ix), Vavra et al. (1996) (xi), Taylor et al. (2014) (xii, xiv) and Hoskin and Black (2000) (xv). b- Synthetic Terra Wasserburg plot with suggestions of potential interpretations based on analysed textures. §- enlarged inset of younger range of ages. c- Monazite textures modified from Taylor et al. (2015b) (xvi), Kohn et al. (2005) (xvii), Johnson et al. (2015) (xix), Ayers et al. (1999) (xx), Rasmussen and Muhling (2007) (xxi), Rubatto et al. (2001) (xxii), Erickson et al. (2015) (xxiii), Williams et al. (2011) (xxiv) and Taylor et al. (2014) (xxv).

accessory minerals due to the large range of possible protoliths as well as numerous processes during metamorphism capable of modifying geologically resilient minerals like zircon.

As a result of their resilient nature, sometimes accessory minerals are the only available source of protolith information, typically in the form of magmatic or detrital zircon with oscillatory zoning (Pidgeon, 1992; Möller et al., 2002; Corfu et al., 2003; Taylor et al., 2016) (Fig 2a i–iii). Following initial crystallisation these grains may be extracted through erosion and incorporated as detrital zircon into sedimentary protoliths (Friend et al., 2003) or metamorphosed as magmatic zircon within an igneous protolith (Hoskin and Black, 2000), recording ages predating metamorphism related to crystallisation or deposition of the protolith (Fig. 2b).

Whilst largely inert during lower grades of metamorphism, the introduction of partial melts at higher temperatures and the compatibility for elements within accessory minerals makes melt crucial for the growth of new material, but can also cause the dissolution of pre-existing phases (Harley et al., 2007). The ability of melt to partially dissolve oscillatory zoned zircon was highlighted by Rubatto et al. (2001), with zircon located within in the leucosome of a metapelite displaying embayments cross cutting original internal zoning that was in-filled by later growth. Irregular shaped relict cores are also associated with melt interaction (Fig. 2a ii–v) (Corfu et al., 2003; Taylor et al., 2016). Within melt bearing rocks most zircon growth is related to post-peak melt crystallisation based on empirical trends (Taylor et al., 2016) and modelling (Roberts and Finger, 1997; Yakymchuk and Brown, 2014a), resulting in overgrowths on pre-existing grains (Taylor et al., 2014) (Fig. 2a v–viii). The occurrence of multiple melt forming reactions during a metamorphic evolution can generate multiple stages of zircon overgrowths as shown by Hermann and Rubatto (2003), who interpreted three periods of zircon growth in relation to two partial melting events separated by cooling. High temperature neocrystallised metamorphic zircon are characterised by sector zoning (aka ‘soccer ball’ zircon) as well as more equant grain shapes compared to igneous zircon (Fig. 2a ix–xi). The formation of ‘soccer ball’ zircon has been shown to occur from prograde anatexis (Vavra et al., 1996) and crystallisation from high-*T* (Schaltegger et al., 1999) to UHT supersolidus melts (Kelly and Harley, 2005).

Melt is very important to zircon growth and modification but the volume of internally or externally derived fluids is just as important. Whilst most melt related zircon growth is related to post-peak crystallisation, Gauthiez-Putallaz et al. (2016) showed that fluids can permit prograde zircon growth in connection to dehydration reactions. The capability of fluids to modify metamict zircon domains was described by Kirkland et al. (2009), leaving altered domains susceptible to further diffusional modification (Cherniak and Watson, 2003). Many studies have noted the importance of fluids in the modification of zircon by coupled dissolution-reprecipitation (e.g. Pidgeon, 1992; Vavra et al., 1996; Williams et al., 1996; Schaltegger et al., 1999; Geisler et al., 2007), creating zircon that may retain original grain shapes but show regions replacing original textures (Fig. 2a xii).

In melt-depleted and fluid-poor areas

increased temperatures during high-grade metamorphism can cause recrystallisation of existing zircon. Recrystallisation is promoted due to increased diffusion rates in connection to high temperatures, causing internal zoning in zircon to become diffuse (Pidgeon, 1992; Vavra et al., 1996; Hoskin and Black, 2000; Hoskin and Schaltegger, 2003), forming 'ghost' zoning as termed by Hoskin and Black (2000) (Fig. 2a xiii–xv). Recrystallisation processes can cause problems in interpreting zircon from high-grade rocks. As shown by Möller et al. (2002), recrystallisation can be incomplete (or partial), resulting in Pb and other trace elements being inherited from the original grain, generating mixed ages. Pb loss during metamorphism associated with recrystallisation can be recognised within a concordia plot, with recrystallised regions typically falling along a discordant trend from older inherited ages towards younger concordant ages dating the Pb loss event (i.e. metamorphism)(Fig. 2b)(Taylor et al., 2014). Currently there is no definitive way to know if a zircon has undergone complete Pb loss other than age trends (recrystallisation towards a younger age intercept or population) and homogenisation of internal textures potentially coupled with variations in chemistry.

Monazite does not have as many textural variations as zircon but can still contain high levels of textural complexity such as five individual monazite generations with unique ages as identified by Kohn et al. (2005) (Fig. 2c xvi, xvii). Monazite has also been reported with limited to no internal structures (e.g. Johnson et al., 2015) (Fig. 2c xix). Zoning in monazite can record both metamorphic (Zhu et al., 1997) or igneous (re)crystallisation events (Ayers et al., 1999) (Fig. 2c xx) depending on the lithologies involved. Textures in monazite should not be the sole basis for interpreting different events, with a study by Martin et al. (2007) reporting monazite where internal textural variations did not correlate at all with age and Tucker et al. (2015) showed that age does not always correlate with internal compositional variations. Monazite can be used to date a range of different processes such as the emplacement of thrust sheets (Kohn et al., 2005), crustal thickening (Cottle et al., 2009b), anatexis (Cottle et al., 2009a) and Walsh et al. (2015) showed monazite can record long periods of growth (e.g. ≥80 Myr) even at UHT conditions. Inherited monazite is possible within metamorphic rocks including those reaching upper greenschist (Rasmussen and Muhling, 2007)(Fig 2c xxi), amphibolite facies (Rubatto et al., 2001)(Fig 2c xxii) as well as high-grade conditions (Cutts et al., 2013), but is less common than inherited zircon due to its more reactive nature (Yakymchuk et al., 2017). In connection to its reactive nature, monazite has been shown to grow during a variety of metamorphic mineral reactions including the appearance of staurolite (Kohn and Malloy, 2004). Pyle and Spear (2003) documented monazite growth in relation to four whole-rock reactions including both xenotime-bearing and absent reactions. This connection to metamorphic reactions makes monazite a great tool in dating petrological evolutions (e.g. Janots et al., 2008; Kelsey et al., 2008; Spear and Pyle, 2010) as well as deformation events in relation to tectonic fabrics (Williams and Jercinovic, 2002), deformation twins and distortion (Erickson et al., 2015)(Fig. 2c xxiii). Monazite is also very adept at recording fluid events, seen as lobate internal

features formed through coupled-dissolution reprecipitation (Vavra and Schaltegger, 1999; Williams et al., 2011; Taylor et al., 2014) (Fig. 2c xxiv, xxv) or irregular alteration textures from hydrothermal alteration (Poitrasson et al., 1996; Poitrasson et al., 2000). Fluids also affect the recorded compositional information (e.g. Taylor et al., 2014) but can also modify U–Pb systematics through Pb loss (Vavra and Schaltegger, 1999; Williams et al., 2011; Kirkland et al., 2016) as well as U and Th loss (Williams et al., 2011) or Th gain (Harlov, 2011). The lobate internal features have been replicated through experiments to gain additional constraints on the types of fluids responsible including alkali-bearing fluids such as $Na_2Si_2O_5 + H_2O$ (Harlov and Hetherington, 2010; Harlov et al., 2011; Williams et al., 2011).

3.2 Within mineral chemical variation

Whilst internal textures alone can provide a lot of information, these textures can be further characterised by chemical variations that may correlate with particular geological processes, growth or breakdown of particular minerals or with respect to age. One of the commonly used chemical variations is the ratio between Th and U. This is routinely measured during dating processes as a means of checking for excess ^{206}Pb in relation to Th decay (Schärer, 1984). The Th/U ratio has mainly been used to classify zircon as either 'metamorphic' or 'magmatic', following initial observations and trends noted in different rock types (Ahrens, 1965; Williams et al., 1996; Hoskin and Ireland, 2000). Zircon is typically classified as 'metamorphic' with a Th/U ratio of <0.1, which has been shown to associate with featureless CL zones associated with metamorphic modification (Williams et al., 1996; Rubatto, 2002). However, the classification of metamorphic zircon based purely on a Th/U ratio of <0.1 is not robust as the ratio has been shown to be strongly affected by other Th-bearing phases such as monazite (Stepanov et al., 2012) and xenotime (Rubatto, 2017), resulting in low Th/U ratios regardless of the growth environment (Möller et al., 2003; Kelly and Harley, 2005). Studies in the Napier Complex have reported Th/U>>0.1 from zircon due to zircon acting as the main sink for Th as a result of no other Th-bearing phases being present (Kelly and Harley, 2005). Kelly and Harley (2005) showed metamorphic zircon with high Th/U ratios can be formed from syn-metamorphic anatectic melts. Metamorphic melts and fluids tend to fractionate U over Th resulting in higher Th/U ratios (Kohn and Kelly, 2017). Another possible interpretation for Th/U>0.1 is presented by Möller et al. (2002) and Harley et al. (2007) where the Th/U ratio of analysed metamorphic zircons was inherited from the original igneous zircon that was recrystallised. Many HT–UHT metamorphic samples also show exception to the <0.1 classification including orthogneisses (Kelly and Harley, 2005), metapelites (Schaltegger et al., 1999; Möller et al., 2003) and metapsammites (Vavra et al., 1996). Th/U ratios have also been used in monazite to differentiate between different age populations. Taylor et al. (2014) related the increase in Th/U with age to fluid modification causing the incorporation of Th + Si and age modification. Monazite in the study by Johnson et al. (2015) showed a continuum of ages, however, these were dividable into two populations based on texture and Th/U ratio (dark BSE response

+ low Th/U = older population, bright BSE response + high Th/U ratio = younger population) corresponding to prograde growth and melt crystallisation. All of these studies highlight the complexity and care that must be taken when classifying and interpreting minerals the Th–U–Pb system.

Yttrium is highly compatible in both monazite and garnet, but garnet with its larger volume exerts greater pressure on the available Y budget (Gibson et al., 2004). This pressure on the available Y budget by garnet has a roll-on effect to monazite due to its sensitivity to available Y. By analysing Y within different age domains, measured ages may be correlated with garnet growth (low Y) or garnet breakdown (high Y) reactions (Bea et al., 1994; Foster et al., 2002; Rubatto, 2002; Foster et al., 2004).

By quantifying the variation of internal chemistry with temperature, minerals may be used to estimate temperature conditions (i.e. geothermometers). Zircon has become a valuable high-temperature (mineral pair) thermometer related to the integration of titanium into zircon at high–*T* accompanied by zirconium substitution in rutile (Zack et al., 2004; Watson and Harrison, 2005; Watson et al., 2006; Ferry and Watson, 2007). However, this technique requires the presence of both of these minerals in a sample otherwise only a minimum temperature may be estimated (Watson and Harrison, 2005). This thermometer can also suffer from temperature overestimates when used in rocks experiencing low-pressure conditions (<5 kbar)(Rubatto, 2017). For samples that are zircon free, monazite can be used within two thermometers. The behaviour of yttrium at different temperatures within garnet-bearing lithologies has been calibrated as the garnet-monazite-xenotime thermometer and is applicable to rocks with only monazite or xenotime as well as rocks containing both (Pyle and Spear, 1999, 2000; Pyle et al., 2001; McFarlane et al., 2005; Tomkins and Pattison, 2007). For garnet-free assemblages monazite-xenotime thermometry may be used, but if no xenotime is present only a minimum temperature estimate may be derived (Gratz and Heinrich, 1997; Andrehs and Heinrich, 1998).

3.3 REE partitioning between minerals

With the aim of unifying zircon with the mineralogical evolution and in-turn metamorphic conditions Rubatto (2002) categorised trace element variations in zircon and accompanying minerals from different textural settings, showing geochemical relationships between REE bearing minerals such as zircon and garnet. This work built a foundation for the petrochronological approach and the usefulness of integrating REE and U–Pb data from accessory minerals. This was achieved by characterising the geochemical response of REE minerals to each other and to metamorphic processes, tying accompanying geochronology to different processes. Once quantified, the distribution of REE between two minerals (i.e. elemental partitioning) can be used to infer the progression of mineral growth, the state of equilibrium between two phases, as well as the presence or absence of a particular phase during a portion of the metamorphic evolution. Partitioning of REE between two minerals is controlled by the degree of fit of the pertinent element, with one mineral more readily accepting that element

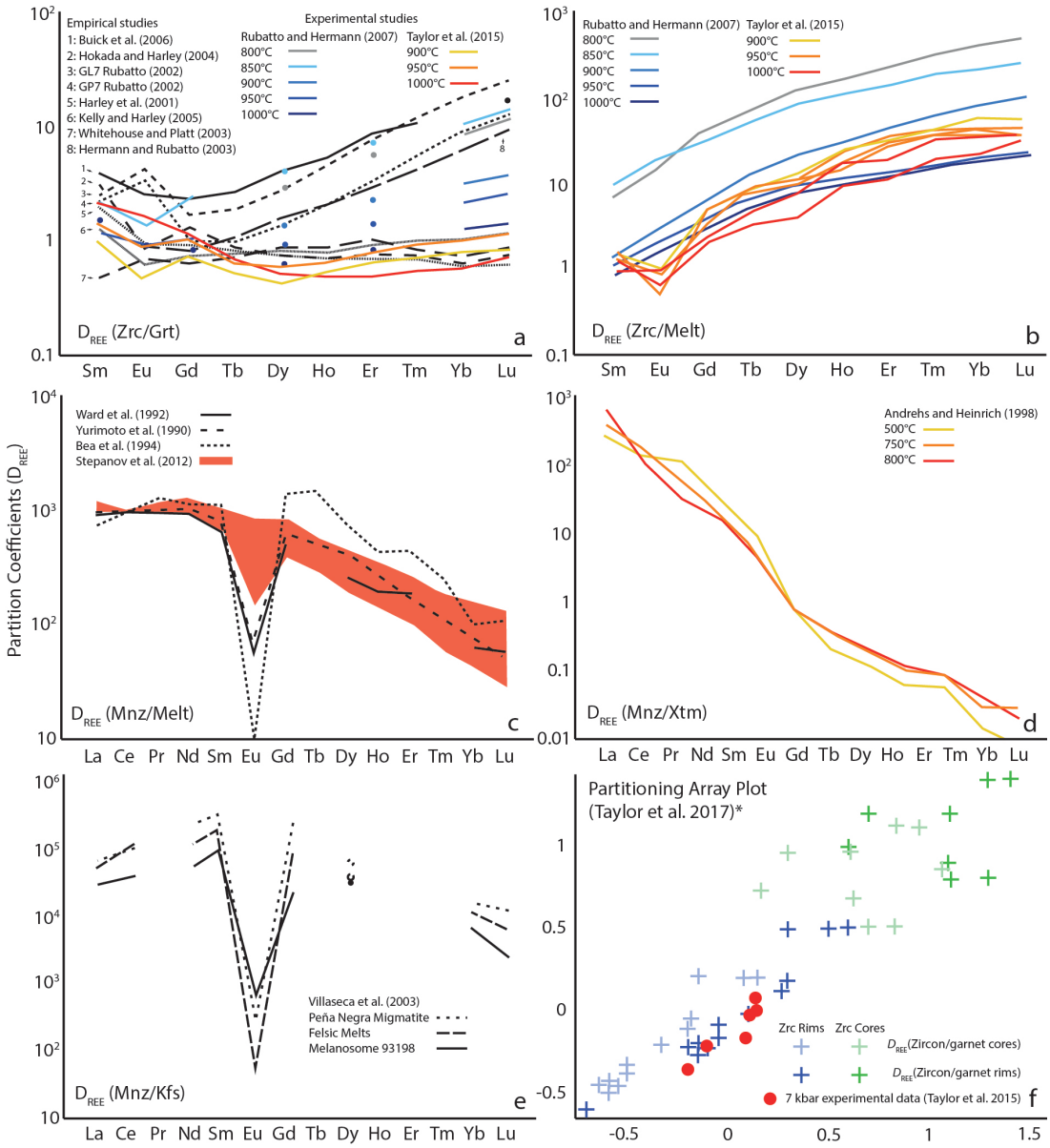

Fig. 3: Partition coefficient plots of experimental (colour) and empirical data (black) (references within figure). a- Partitioning between zircon and garnet (Modified after Taylor et al., 2016). b- Partitioning between zircon and melt (Modified after Taylor et al., 2015a). c- Partitioning between monazite and melt (Modified after Stepanov et al., 2012). d- Partitioning between monazite and xenotime (Modified after Andrehs and Heinrich, 1998). e- Partitioning between monazite and K-feldspar (Modified after Villaseca et al., 2003). f- Partitioning array plot of zircon/garnet compared to the experimental data of Taylor et al., 2015a, *- The axis of this plot are: x: log(D_{Yb}), y: log(D_{slope})= log(D_{Yb}/D_{Gd}) (Modified after Taylor et al., 2017).

into its lattice based on ionic radius, charge and substitution mechanisms. The partitioning of REE (D_{REE}) between different minerals has been quantified through the analysis and observation of natural lithologies such as eclogites (Rubatto, 2002), paragneisses (Hokada and Harley, 2004; Kelly and Harley, 2005) and orthogneisses (Villaseca et al., 2003) as well as experimental studies to quantify relationships such as zircon/garnet, zircon/melt (Rubatto and Hermann, 2007;

Taylor et al., 2015a), monazite/melt (Stepanov et al., 2012) and monazite/xenotime (Andrehs and Heinrich, 1998).

The partitioning of REE between zircon and garnet (D_{REE} (Zrc/Grt))(Fig. 3a) is widely used in high-grade metamorphic rocks such as pelitic granulites (Rubatto, 2002; Whitehouse and Platt, 2003; Clark et al., 2009), associated leucosomes (Hokada and Harley, 2004; Harley and Nandakumar, 2014) and granulites reaching UHT conditions (Baldwin and Brown, 2008). As this technique is reliant on zircon and garnet, this technique is not applicable to rocks that are completely garnet- or zircon-absent; potential alternatives are discussed below. By characterising the REE distribution of certain zircon textures as well as texturally different garnet populations, the REE profiles of each mineral can be compared in terms of relative chondrite normalised abundances or as a ratio of each element (e.g. Yb_{Zrc}/Yb_{Grt}). As both garnet and zircon are minerals rich in mid-to-heavy REE (M–HREE) over light REE (LREE), they compete for the same elements when equilibrating within the same system, resulting in similar REE patterns if equilibrium is reached. By comparing the REE patterns between zircon and garnet, zircon ages can be attributed to a particular stage of the metamorphic evolution based on the presence or absence of equilibrium with garnet (i.e. pre-dating or post-dating garnet growth). The partitioning of REE between zircon and garnet is largely controlled by garnet, an important sink for trace elements (Bea et al., 1994; Hermann and Rubatto, 2003). Although both garnet and zircon compete for M–HREE, garnet preferentially incorporates M–HREE easier than zircon into its structure. This relationship has been empirically observed in rocks (e.g. granulite to UHT/UHP) where zircon growing in the presence of garnet have flat to slightly depleted REE patterns due to competition for M–HREE from the existing garnet (Fig. 4a) (Whitehouse and Platt, 2003; Hokada and Harley, 2004; Kelly and Harley, 2005; Harley and Kelly, 2007; Wu et al., 2008a; Wu et al., 2008b; Fornelli et al., 2014; Whitehouse et al., 2014). Partitioning coefficients (D_{REE}) for zircon over garnet (Zrc/Grt) may be graphically presented on a logarithmic plot with the growth of zircon in the presence of garnet seen as a curve with a M–HREE (Yb/Gd slope) slope of ~1 to a slightly curved profile (Fig. 3a; Taylor et al., 2015a). This logarithmic plot allows the comparison between REE partitioning patterns from empirical and experimental studies (Fig. 3a).

Experimental studies were conducted to quantify the partitioning of REE between zircon and garnet at set temperature conditions to link *T–t* constraints to empirical studies. The first experimental study was conducted by Rubatto and Hermann (2007) and looked at migmatitic granulites and eclogites. Experiments were conducted at ~20 kbar and granulite–UHT temperatures with Ca-rich garnet. The results of the experiments by Rubatto and Hermann (2007) showed a temperature-dependant control on the partitioning of M–HREE: a M–HREE slope of near 1 at ~1000°C but heavily favouring zircon at lower temperatures (Fig. 3a). The second experimental study was conducted by Taylor et al. (2015a) on pelitic migmatites with experiments conducted at 7 kbar and 900–1000°C. In contrast to the first experiments, the experimental results of Taylor et al. (2015a) showed no significant correlations between temperature and M–HREE

partitioning, with a M–HREE slope of near 1 for all temperatures. Whilst the two experiments alternate between two M–HREE partitioning patterns (more convex to a flatter pattern), this variation has also been noted in empirical studies (Fig. 3a). This variation in M–HREE partitioning patterns may reflect the pressure differences between the two studies or variations in garnet chemistry (Taylor et al. 2015a). The addition of more experiments testing the control of pressure and garnet chemistry may resolve this discrepancy and shed light on the factors controlling REE partitioning. These experiments still provide valuable information for empirical studies by relating partitioning patterns to ones generated through experiments at certain temperatures (using the experiment with appropriate bulk composition). If an empirical partitioning pattern matches one generated from an experiment this may be interpreted as the empirical partitioning relationship equilibrating at the temperature defined by the experimental pattern. A lack of partitioning relationships is also useful as shown by Harley and Nandakumar (2016) who interpreted garnet porphyroblast cores to predate zircon growth by a lack of partitioning between REE in zircon/garnet.

Zircon and garnet-bearing rocks, while abundant, are only some of the wide array of metamorphic parageneses. Partitioning relationships between zircon and melt (D_{REE}(Zrc/Melt)) are applicable to garnet-free rocks in supra-solidus conditions. D_{REE}(Zrc/Melt) have been experimentally quantified for pelitic (Taylor et al., 2015a), granulite and eclogite (Rubatto and Hermann, 2007) lithologies (Fig 3b). Many zircon-bearing rocks also contain monazite, but monazite can also be present in zircon-absent assemblages (Morrissey et al., 2016) and has been shown to be affected by bulk composition (Wing et al., 2003; Fitzsimons et al., 2005; Kelsey et al., 2008). Partitioning relationships have been experimentally quantified for monazite and melt (D_{REE}(Mnz/Melt))(Fig. 3c) within a peraluminous granitic composition (Stepanov et al., 2012) as well as within a number of empirical studies: Yurimoto et al. (1990) (pegmatitic granite), Ward et al. (1992) (granitic), Bea et al. (1994) (peraluminous migmatite). Andrehs and Heinrich (1998) experimentally quantified monazite and xenotime (D_{REE}(Mnz/Xen)) partitioning relationships for amphibolite to granulite temperatures using a bulk composition modelled from a metapelitic granulite (Fig. 3d), allowing additional *T–t* constraints from zircon-free rocks. Monazite and K-feldspar (D_{REE}(Mnz/Kfs)) has also been quantified but only empirically from granulites and felsic igneous rocks (Villaseca et al., 2003)(Fig. 3e).

All of the aforementioned partitioning relationships are typically applied by generating REE averages of certain textures or populations of each mineral and relating those in turn to experimental information if available. While this approach may be applicable for a simple interrogation of the dataset, the natural complexity and variability of the sample is lost. A new approach described by Taylor et al. (2017) uses data arrays with the capability of resolving large data. This array approach incorporates all zircon analyses from a sample to visualise partitioning relationships or trends within a logarithm plot of M–HREE slope ($\log(D_{Yb}/D_{Gd})$) versus HREE partitioning values ($\log(D_{Yb})$) (Fig. 3f). Natural samples may be compared to experimental data graphically, with each zircon analysis and their

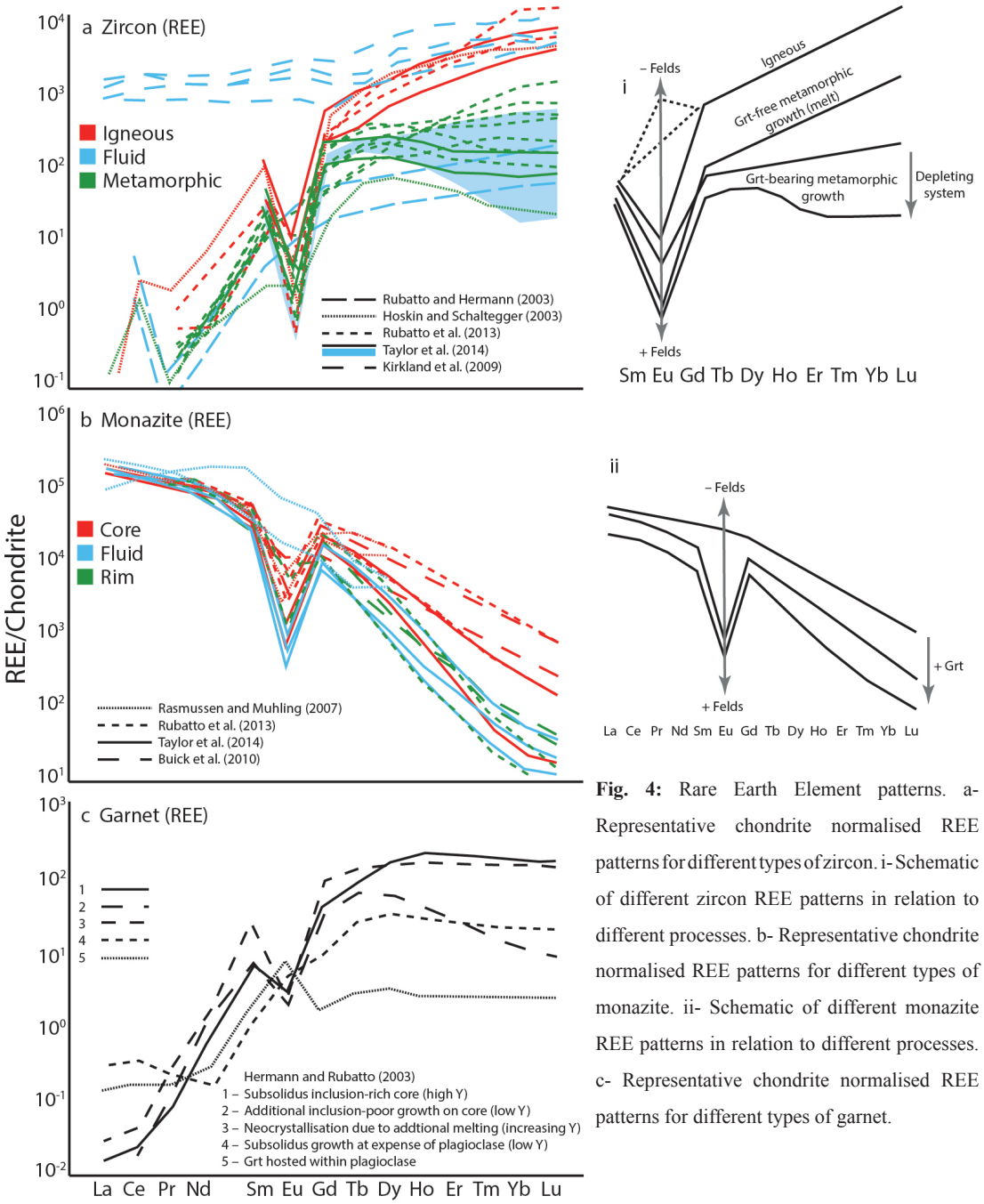

Fig. 4: Rare Earth Element patterns. a- Representative chondrite normalised REE patterns for different types of zircon. i- Schematic of different zircon REE patterns in relation to different processes. b- Representative chondrite normalised REE patterns for different types of monazite. ii- Schematic of different monazite REE patterns in relation to different processes. c- Representative chondrite normalised REE patterns for different types of garnet.

respective ages comparable to different garnet or orthopyroxene compositions within the sample (Taylor et al., 2017). Zircon analyses that partition with the selected garnet composition form linear arrays of data comparable to that defined by experimental data (Fig. 3f). By interrogating each individual analysis instead of averages this approach provides additional resolution to the timing of petrologic events (e.g. garnet resorption or orthopyroxene growth). Currently, partitioning relationships are only considered between two phases where in reality multiple phases may be interacting within an equilibration volume, potentially causing additional complications and unquantified relationships. Nonetheless, partitioning of REE between major and accessory

minerals is a key and important technique to petrochronological study.

3.4 The controls on the chemistry of high-grade accessory minerals

Rare Earth Element patterns can provide information on the formation geochemical environment at the time of mineral growth but are also controlled by growth and break down of other minerals, partial melts, fluids and diffusion. Zircon and monazite favour different REE, M–HREE and LREE respectively and can exert slight reductions in the concentration of their favoured elements in the opposing mineral during growth. However, many other minerals have stronger influences on the chemistry in zircon and monazite.

Garnet is a key REE-bearing mineral in metamorphic rocks and by having a huge capacity for REE (in particular M–HREE) has recognised influences on both zircon and monazite. Zircon grown in igneous lithologies (i.e. garnet-free) are characterised by steep M–HREE slopes e.g. (Schaltegger et al., 1999; Rubatto, 2002; Taylor et al., 2015b) (Fig 4a, i), reflecting incorporation of any available REE in the geochemical system if no other REE-bearing phases are present. In the presence of garnet, zircon shows flat M–HREE slopes representative of the competition for M–HREE regardless of the overall lithology (Fig. 4a, i): metapelites (Hermann and Rubatto, 2003; Taylor et al., 2015b), eclogites (Rubatto, 2002) and felsic gneisses (Taylor et al., 2015b). An important caveat to consider is flat M–HREE patterns in zircon can occur when zircon forms coevally with garnet as well as following garnet growth. This can result in chronology issues, with the only definitive interpretation based on REE data alone being the presence of garnet during zircon growth or modification. The textural location of the accessory mineral is also important as garnet can effectively shield even more reactive monazite from later modification as described by Montel et al. (2000), preserving earlier populations. Zhu and O'Nions (1999) showed monazite growing in the presence of or coeval with garnet can show depletion in M–HREE (Fig 4b, ii), a feature recognised in other studies (Foster et al., 2000; Foster et al., 2002; Kohn et al., 2005; McFarlane et al., 2005; Rubatto et al., 2006), and can be used as a complimentary or comparative indicator of garnet to zircon if both phases record similar ages. Other REE patterns in addition to flat M–HREE patterns occur in garnet and can provide information on processes predating zircon and monazite growth, such as the growth of garnet in zircon-absent, melt-present conditions which displays a convexity to the MREE (Fig. 4c) (Rubatto and Hermann, 2003). Increased concentrations of Y and HREE can occur in residual garnet resulting from resorption of available REE released during garnet breakdown (Baxter et al., 2017) resulting in enriched rims or 'annuli' structures in elemental maps (Pyle and Spear, 1999). The wide array of documented REE patterns of garnet permit detailed examinations of the geochemical evolution during metamorphism, including recognising multiple melting events during stages of growth (forming a 'bell curve' M–HREE pattern: Hermann and Rubatto, 2003).

One of the most common controls on REE is feldspar due to its wide *P–T* stability except for extreme *P* or *T*. The presence or absence of feldspar (plagioclase more so than K-feldspar

(Nagasawa, 1971)) can affect both zircon and monazite due to feldspar strongly partitioning Eu. When growing with plagioclase or in a rock with high amounts of plagioclase, zircon (Bea and Montero, 1999; Rubatto, 2002; Hermann and Rubatto, 2003; Möller et al., 2003) and monazite (Zhu and O'Nions, 1999; Hermann and Rubatto, 2003; Rubatto et al., 2006) are characterised by negative Eu anomalies (Fig. 4b, i–ii). Eu anomalies can be used to demonstrate increasing crystallisation of plagioclase in connection to partial melt crystallisation, as shown by Johnson et al. (2015) with a direct correlation between the negativity of the Eu anomaly in monazite with age. When growing in a feldspar-free rock, as long as the bulk composition is not already Eu depleted, crystallising zircon and monazite will have a positive Eu anomaly (Fig. 4 i).

Zircon readily grows within melt-bearing environments including metamorphic and igneous systems, however the two systems are readily told apart based on internal zircon textures and REE patterns. Zircon growing within partial melt formed during metamorphism in the absence of garnet will show steep M–HREE patterns with wholesale depletion in REE compared to igneous zircon (Schaltegger et al., 1999; Rubatto, 2002; Möller et al., 2003)(Fig. 4a, i). Whitehouse and Kamber (2003) showed there is a relationship between the REE composition of zircon growing in anatectic melts and the volume and composition of melt, resulting in the deviation from characteristically igneous REE patterns to steep REE patterns that are relatively depleted (Fig. 4 i).

Fluids have also shown to have variable influence on REE, with fluid altered zircon from Taylor et al. (2014) displaying increased scatter to the HREE but zircon related to a hydrothermal event from Kirkland et al. (2009) show uniformly enriched REE (Fig. 4a). As shown by Rubatto and Hermann (2003) zircon forming from a fluid under eclogite-facies can show wholesale depletion in nearly all trace elements and lacks a negative Eu anomaly (Fig. 4a). Despite the varied effects on REE composition, likely caused by variable fluid compositions, fluid related processes can be easily identified via internal textures (see earlier). The same fluids that modified zircon in Taylor et al. (2014) were also shown to affect HREE in monazite but to a lesser extent than in zircon due to the lower initial concentrations (Fig. 4b). This fluid event caused internal textural modification to both zircon and monazite that also correlated with age (Taylor et al., 2014).

All of the aforementioned REE patterns are dependant on the geochemical environment and diffusion. Recrystallisation (i.e. solid state) is a diffusion related process, with the effected mineral expelling elements that don't fit well within the atomic lattice or that are located within low energy sites in order for the mineral to reach equilibrium with the surrounding geochemical environment. Each element has its own unique diffusivity in a particular mineral which is a function of ionic radius and activation energy (which is inversely affected by temperature), causing complications to re-equilibrating systems as no two elements will re-equilibrate at the same rate. Due to very slow rates of diffusion in most geological settings REE are largely immobile within zircon, but diffusion is enhanced at elevated temperatures due to the positive exponential relationship between diffusivity and temperature as shown by Cherniak and Watson (2003). This

results in REE in recrystallised zircon largely representing the REE composition of the original zircon and not representing the surrounding evolving geochemical system. Recrystallised zircon may have steep REE patterns to relatively depleted REE patterns and may be associated with uniform low CL response textures, ghost zoning and discordant trends or spreads of ages (Fig. 2b) (Taylor et al., 2014). The REE patterns seen in recrystallised zircon are largely dependant on the starting composition of the zircon (measurable from relict regions or based on internal textures) as well as the conditions of metamorphism by being a diffusion related process. The bulk rock chemistry of the rock also exerts a first-order control over the available trace elements, so consideration of the rock bulk composition associated with the interpreted textural and geochemical context of accessory minerals is of key importance in order to avoid missleading interpretations when comparing different samples.

Higher temperatures, whilst increasing rates of diffusion, also affects equilibration volume and the associated effective bulk composition. Equilibration volume is an added level of complexity to a metamorphic system. Most interpretations are based purely on the overall mineral assemblage, i.e. garnet-bearing or garnet-absent, with the assumption that zircon growing in the rock was interacting with all the minerals within the whole rock. Conversely, it has been recognised that many metamorphic rocks can equilibrate on a smaller scale, forming subdomains within which minerals interact with an effective bulk composition that may differ on the small scale to a neighbouring domain (Palin et al., 2016; Lanari and Engi, 2017). This is important for accessory phases growing within such domains as mineral assemblages and recorded geochemical information may vary due to the absence or presence of phases rich in REE, resulting in range of potential REE patterns recorded in the same rock but from different bulk compositions or assemblages. The presence of different sized equilibrium domains is why establishing textural context of accessory minerals and their accompanying trace element geochemistry is essential in high-grade rocks.

4. LINKING PETROCHRONOLOGY TO METAMORPHIC FORWARD MODELS

The ultimate end point of petrochronology is forming the connection between various types of geochronological and geochemical data and *P–T* conditions built on phase equilibria and petrological interpretations. As discussed above, accessory minerals provide a wealth of information, in particular within high-grade rocks, surviving high temperatures whilst recording information on melt, fluids and remaining geochronologically and geochemically robust even after long timescales at high–*T*. Accessory mineral information (i.e. ages, chemistry) is commonly connected to metamorphic forward modelling (i.e. pseudosections) by using categorised relationships (through empirical and experimental studies) in regards to texture, chemistry and microstructures to form a connection between dated but not directly modelled minerals (e.g. monazite or zircon) and modelable minerals. Methods of linking accessory minerals to forward models will be illustrated using two synthetic models (Fig. 5) showing how this information can be coalesced into a qualitative *P–T–t* path, as well as evaluating

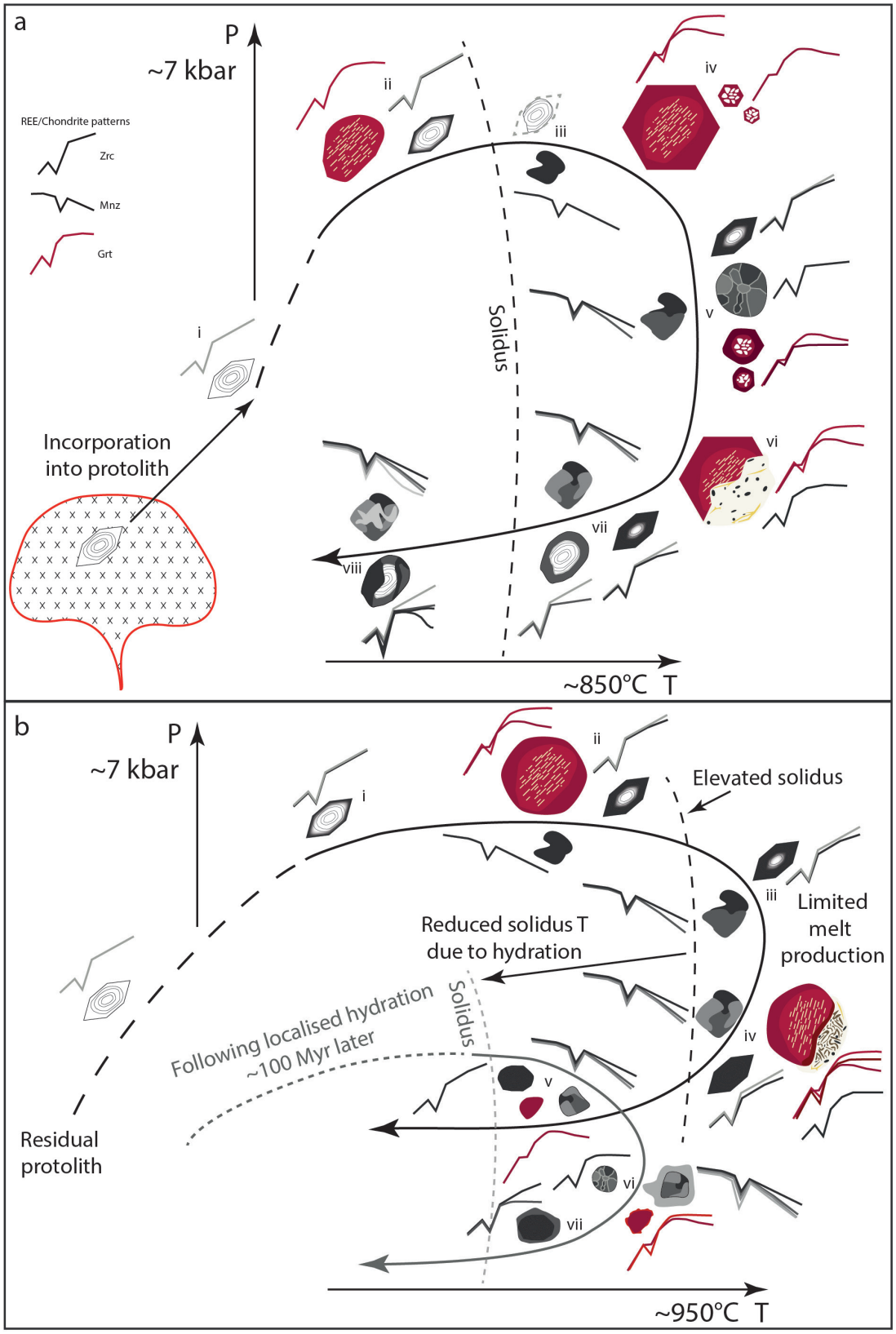
a
P
~7 kbar
REE/Chondrite patterns
Zrc
Mnz
Grt
i
ii
iii
iv
v
vi
vii
viii
Solidus
Incorporation
into protolith
~850°C T
b
P
~7 kbar
i
ii
iii
iv
v
vi
vii
Elevated solidus
Limited
melt
production
Reduced solidus T
due to hydration
Following localised hydration
~100 Myr later
Solidus
Residual
protolith
~950°C T

Fig. 5: Synthetic P–T evolutions with associated types of zircon and monazite, garnet growth/breakdown and potential REE systematics. a- Singular clockwise *P–T* evolution. (i) Incorporation of inherited zircon into metamorphic protolith. (ii) Primary garnet with sillimanite inclusions, recrystallisation of inherited zircon. (iii) Generation of relict zircon cores, initial monazite growth. (iv) Additional garnet growth and peritectic grains start to grow. (v) Neocrystallised 'soccer ball' zircon, continued monazite growth and recrystallisation of zircon. (vi) Garnet breakdown to cordierite forming micro-zircon within the breakdown texture. (vii) Melt crystallisation and majority of zircon growth (overgrowths) and final monazite growth, recrystallised zircon modification slows due to crystallisation of melt and cooling temperatures. (viii) A later fluid event causes modification to zircon and monazite forming lobate textures. b- A residual protolith along a clockwise polymetamorphic *P–T* path. (i) Inherited zircon starts to recrystallise. (ii) Subsolidus monazite growth along the prograde path in the presence of relict garnet, recrystallisation of zircon continues. (iii) Upon crossing an elevated solidus the generation of minor melt causes additional monazite growth and promotes recrystallisation of existing zircon but is insufficient to see new zircon growth. (iv) Garnet breakdown to plagioclase + orthopyroxene with neocrystallised micro-zircon, final monazite growth and complete 'ghost zoning' to recrystallised zircon. After a later localised hydration event, the hydrated areas followed the grey *P–T* path during a second metamorphic event. (v) Following localised hydration melt embays previously recrystallised zircon and previously grown monazite becoming relict cores stable with relict garnet grains. (vi) Neocrystallised zircon and monazite in equilibrium with minor garnet growth. (vii) Final melt crystallisation seen as zircon overgrowths.

and discussing limitations. These two *P–T* evolutions shown in the synthetic models could be produced from real samples. Such paths may be identified through forward modelling: generating a modelled *P–T* diagram from which associated mineral assemblages and microstructures within the sample may be linked to form a *P–T* path along which the sample evolved. Some of the assumptions and limitations of forward modelling will be discussed later.

The first *P–T* evolution (Fig. 5a) is representative of a standard granulite facies clockwise *P–T* evolution of a pelitic protolith containing inherited zircon (Fig. 5a i). Along the prograde path any inherited zircon may start to recrystallise as temperatures increase, coeval with primary garnet growth (Fig. 5a ii). Prograde information in high-grade rocks tends to be either difficult to constrain or completely absent from the preserved paragenesis and is one of the frequent gaps in the petrochronological record. Minerals growing during prograde metamorphism may have once dated prograde heating, but upon reaching peak conditions can be modified due to closure temperatures typically being exceeded (closure temperature below the metamorphic temperature = mineral is diffusively open) as well as due to high-grade processes (e.g. dissolution, fluid alteration) and perturbation will continue until cooling. No evidence of prograde metamorphism may be present at all due to no subsolidus geochronometer growth or complete overprinting by later metamorphism. Minor crystallisation of zircon during the prograde to peak metamorphic evolution has been shown to occur through the introduction of externally derived melts (Andersson et al., 2002; Flowerdew et al., 2006; Wu et al., 2007) as well as through local migration of melt (Harley and Nandakumar, 2014; Harley, 2016), but preservation of such phases is dependent on the evolution of the individual system and the location of the phase.

Upon crossing the solidus and with the generation of partial melts, inherited zircon may be

consumed/dissolved by the melt phase generating relict oscillatory zoned cores (Fig. 5a iii) or embayed grains (Keay et al., 2001; Rubatto et al., 2001; Andersson et al., 2002; Wu et al., 2007). First quantified by Watson and Harrison (1983) and more recently re-evaluated by Boehnke et al. (2013) and Gervasoni et al. (2016), inherited zircon may be completely dissolved if it is introduced to a melt phase rich in zirconium, resulting in a lack of inherited ages and promoting recrystallisation of pre-existing zircon over additional zircon growth. Monazite has been shown in natural samples to grow along both the prograde and retrograde path (Rubatto, 2002; Johnson et al., 2015) as well as during peak conditions (Kelsey et al., 2008; Rubatto et al., 2009) and just following peak conditions (Clark et al., 2014) (Fig. 5a iii, v, vii). However, this is contrary to predictive modelling by Kelsey et al. (2008) which show majority of monazite growth upon crossing the solidus and that prograde supersolidus monazite growth is unlikely and should be consumed instead (Kelsey et al., 2008; Yakymchuk, 2017). Modelling by Spear and Pyle (2010) showed monazite growing continuously throughout the high-*T* metamorphic evolution. Apatite breakdown to form monazite has been reported from experiments (Wolf and London, 1994) and has been proposed as a potential source of prograde monazite (Johnson et al., 2015), but recent forward modelling by Yakymchuk (2017) showed that only minor and small prograde monazite growth may occur at the interface between apatite and melt but would be unlikely to survive in the matrix of the rock unless shielded within peritectic minerals. A mechanism to grow and preserve large prograde monazite in the matrix following partial melting is still elusive.

Prograde garnet cores may see additional growth with the addition of partial melts as well as the formation of peritectic garnet (Fig. 5a iv), typically identifiable from large quartz inclusions or euhedral grain shapes, with both types of garnet showing similar REE patterns as a result of growing within the same geochemical system. The use of REE partitioning is one of the most common methods of linking zircon ages to an event such as peritectic garnet growth. In this example metamorphic ‘soccer ball’ zircon is growing during super/supra-solidus conditions (Schaltegger et al., 1999; Vavra and Schaltegger, 1999; Taylor et al., 2016) and shares similar REE as rims on peritectic garnet, which can be inferred to have grown and equilibrated at the same time as zircon (Fig. 5a v). Partitioning relationships are based on the assumption of equilibrium being achieved between minerals and the recorded information has not been perturbed since the end of metamorphism. As discussed above, the scale to which a metamorphic rock will achieve equilibrium is related to the equilibration volume which is typically at its largest during peak conditions due to the highest temperatures and highest rates of diffusion from the presence of fluids, melts as well as temperature. These factors lend themselves to the interpretation that in metamorphic rocks partitioning relationships are most likely achieved during peak conditions, but this is purely dependant on the occurrence of reactions causing new mineral growth, modification, or peak conditions being sufficient to re-equilibrate pre-existing minerals. Earlier relationships may be preserved but this must be investigated and evaluated on a case-by-case basis.

The stability of ferromagnesian minerals is an important control on the formation of zircon and monazite, as these contain elements necessary for crystallisation along the retrograde path (Brown and Korhonen, 2009). Following peak conditions during decompression Zr-bearing phases such as garnet may breakdown (e.g. to cordierite; Fig. 5a vi) and release Zr which has the potential to grow new micro-zircon (Fraser et al., 1997; Degeling et al., 2001; Tomkins et al., 2005; Wu et al., 2007) but only within the region directly adjacent to garnet as Zr is relatively insoluble and therefore difficult to transport (Whitehouse and Platt, 2003). This requirement of adjacency has also been illustrated by Bingen et al. (2001) with ilmenite breakdown forming new zircon in close proximity. However, the same relationships between garnet breakdown and zircon growth could not be replicated in predictive modelling by Kelsey and Powell (2011), with melt and rutile showing a greater control on zircon growth than garnet.

When approaching the solidus the majority of zircon growth occurs (Kelsey et al., 2008), nucleating on existing relict cores to form overgrowths such as low CL response rims reported by Taylor et al. (2014) and Johnson et al. (2015) (Fig. 5a vii) and potentially as entirely new grains at the initial stages of the cooling path (Roberts and Finger, 1997). A later subsolidus fluid event (e.g. fluids released from crystallisation of plutons) causes additional modification to zircon and monazite, forming lobate cross cutting textures (Fig. 5a viii), perturbing age and geochemical data (Kröner et al., 2014; Taylor et al., 2014). Fluids have been shown by Poitrasson et al. (2000) and Seydoux-Guillaume et al. (2012) to perturb monazite and zircon even at low–*T* (<400°C).

The second scenario is representative of metamorphism of a residual (already partially melted) pelitic protolith (Fig. 5b). Due to the residual nature of the protolith, the solidus temperature is more elevated than in the first scenario, with most of the prograde path staying at subsolidus conditions and the lack of melting along the prograde path promoting recrystallisation (Fig. 5b i, ii). White and Powell (2002) showed that melt loss will increase the preservation but limit the generation of new assemblages following initial high-grade metamorphism. Accessory minerals are also affected by melt loss as most trace elements from granitic melts are taken up by accessory minerals (Bea and Montero, 1999; White and Powell, 2002; Brown and Korhonen, 2009), limiting the growth of new accessory minerals but also increasing the potential of dissolution of existing phases to accommodate the growth of any new assemblages. The behaviour of monazite in high–*T* environments has been shown to contrast with zircon. For example, McFarlane et al. (2006) and Rubatto et al. (2013) both documented larger amounts of monazite growth with limited zircon growth during metamorphism. Monazite may grow despite the lack of zircon growth in a melt poor environment due to its higher reactivity (Morrissey et al., 2016)(Fig. 4b ii), resulting in monazite potentially recording information that might be missed by zircon. Högdahl et al. (2012) demonstrated that monazite was more capable than zircon at recording changing host rock conditions, permitting detailed time constraints from complex tectonic events. Monazite grew, dissolved and reprecipitated under both sub- and

supersolidus conditions with zircon restricted to melt-producing events, missing some of the age populations recorded by monazite (Högdahl et al., 2012).

Upon crossing the solidus, due to the residual bulk composition, melting is minimal, promoting additional recrystallisation (especially at elevated *T*) of zircon but no neocrystallisation (Fig. 5b iii). Morrissey et al. (2016) showed the importance of melt in residual compositions with new growth of zircon restricted to originally residual regions that experienced later retrogression, generating a more 'fertile' composition that produced more melt upon heating; the non-retrogressed remaining residual regions did not record the second event at all. The low abundance of neocrystallisation in residues compared to leucosomes has also been illustrated in predictive models by Yakymchuk and Brown (2014a). Similar to scenario one, relict garnet decompression breakdown to plagioclase + orthopyroxene permits micro-zircon growth dating decompression but due to the low volume of melt in scenario two no overgrowths representative of melt crystallisation occurs (Fig. 5b iv). The behaviour of zircon and monazite in melt bearing conditions are well categorised, being affected by factors such as the proportion (Rubatto et al., 2001) as well as chemistry (Watson and Harrison, 1983; Rapp et al., 1987) of melt and the rate of melt extraction (Watt et al., 1996). There is limited understanding as to what information geochronometers can record in prolonged, hot, residual systems with scare amounts of melt and fluids. Understanding the behaviour and responsiveness of geochronometers in anhydrous conditions is important for constraining the duration of geodynamic processes in the lower crust as well as generating quantitative *P–T–t* paths from residual lithologies, key to generating accurate geodynamic models of the crust.

Understanding the potential heterogeneity on a range of scales within a sample as well as the studied outcrop (e.g. microscopic, local, regional) is also important, as different ages may be preserved within different rocks from the same region due to melt loss and fluid incorporation (Morrissey et al., 2016). In scenario two, a later localised hydration event cause localised retrogression (e.g. introduction of externally derived fluid along fractures/shear zones), reducing the solidus temperature within the retrogressed areas (Fig. 5b). Retrogression permitted, during a second lower temperature event, additional melting only within these domains, similar to interpretations by Kelly et al. (2006) and Morrissey et al. (2016). This additional melting during the second event caused embayment of pre-existing grains (Fig. 5b v), followed by neocrystallisation of zircon (in equilibrium with relict garnet) and monazite only within the more 'fertile' compositions (Fig. 5b vi, vii), with the non-retrogressed samples showing no additional modification or younger ages.

High-grade terranes pose an additional problem, with geochronometers in most terranes recording a spread of ages rather than a singular statistical population, potentially related to prolonged thermal conditions or resetting from separate events (Taylor et al., 2016). Determining the process(es) responsible for the range of ages can be done petrochronologically, categorising the textures associated with the distribution of ages as well as any geochemical trends. As mentioned earlier if the spread of ages is associated

with recrystallisation or coupled dissolution-reprecipitation Pb loss has likely occurred. Pb loss through recrystallisation is one of the hardest processes to constrain as the amount of Pb loss can only be estimated through indirectly associated features (e.g. textures), with no quantitative method for estimating the volume of Pb lost as the whole system has likely been perturbed. The rate by which Pb is lost is dependent on diffusivity, which can vary in relation to temperature and grain size (Cherniak and Watson, 2003; Cherniak et al., 2004) but also features such as radiation damage (Mezger and Krogstad, 1997; Cherniak and Watson, 2001), fluids (Harlov et al., 2011; Williams et al., 2011) and deformation (Piazolo et al., 2016), implying that no two grains will evolve in the same way. Lead loss through diffusion may be further assisted through the presence of fractures as described by Ashwal et al. (1999). The simplest assumption is that the youngest recorded ages from modified grains are representative of complete Pb loss, and those with in-between ages are only partially modified. This kind of interpretation may be strengthened with relationships between Pb loss and internal texture or Pb loss and modifications of trace or major elements but there is still a degree of uncertainty to keep in mind.

Being able to accurately quantify the time-scales of events is key to accurately modelling geologic processes. However, there are two different interpretations in regard to the nature and time-scales of prolonged regional high-grade metamorphism recorded by geochronometers: (1) high-temperatures are regionally sustained throughout an entire event (>10 Myr) or (2) prolonged regional high–*T* events are made up of short temperature bursts. Korhonen et al. (2011) and Korhonen et al. (2013) used zircon and monazite to show that the Eastern Ghats Province potentially stayed continuously at UHT conditions for up to 200 Myr. Another example of prolonged high temperatures was documented by Walsh et al. (2015) and Smithies et al. (2011) who constrained the duration of high-grade metamorphism to ~100 Myr in the Musgrave Province with zircon and monazite. Diffusion experiments by Cherniak et al. (1997), Cherniak and Watson (2001) and Cherniak et al. (2004) quantified the resilience of zircon and monazite to perturbation via diffusion, requiring very-high and long-lived temperatures to cause modification and re-equilibration via diffusion. The implication of this for melt- and fluid-poor high–*T* terranes with limited new geochronometer growth but a wide spread of recorded ages is these regions must have sustained high–*T* in order to sufficiently modify geochronometers like zircon. Contrastingly, Viete and Lister (2017) propose that high-grade regional metamorphism represent transient thermal anomalies (1–10 Myr) related to localised heat production rather than prolonged ‘normal’ conditions within the associated tectonic setting. Walsh et al. (2015) suggested that a protracted spread of monazite ages could possibly represent crystallisation after multiple individual events occurring over short timescales that cannot be resolved with current analytical resolution, but could not rule out the possibility that the spread resulted from continuous elevated thermal conditions, similar to Korhonen et al. (2013). Clark et al. (2011) showed with numerical modelling that in order to achieve high-grade regional metamorphism the effected crust within a collisional orogen must be radiogenic element rich

and requires long time periods with low erosion rates, requiring extended periods at appropriate conditions for the achievement of wide-spread metamorphism without large scale magmatism or other heat sources that could potentially generate high temperatures over shorter time scales. Whilst short durations (<5–40 Myr: Kelsey and Hand, 2015; <10 Myr: Harley, 2016) of high-grade metamorphism are recognised (e.g. Kaapvaal Craton, 5–10 Myr: Schmitz and Bowring, 2003; Southern Madagascar, ~5 Myr: Jöns and Schenk, 2011), what types of internal textures have been dated in connection to the short metamorphic event is an important factor. Short durations of metamorphism would be best recorded by neocrystallisation but this requires the system to be primed to readily grow new accessory minerals. If the short range of ages were associated with recrystallisation either extreme temperatures would be required for equilibration of existing phases or potentially the data set has been over interpreted and the resolution of the techniques used (i.e. uncertainties on individual ages) should be questioned/considered (are the uncertainties small enough to separate two or multiple events?). These differing theories on the duration of high temperatures during metamorphism highlight the importance of resolution in terms of the duration of events and the limited nature of our current understanding of how responsive geochronometers are to an evolving high-T system. Does metamorphism occur over orogenic timescales (e.g. 10–100 Myr) or only as short thermal perturbations punctuating long-term subdued tectonism?

While very comprehensive, both of the posed synthetic scenarios are resolvable due to the application of petrochronological methodology, but are by no means absolute in their interpretation due to the high number of factors involved within even a simple metamorphic evolution. It is important keep in mind the number of factors affecting the information displayed here, in particular trace element geochemistry. REE signatures are dependant on a number of factors including bulk rock composition and the volume of REE minerals. A bulk composition enriched in HREE will allow zircon and garnet growing together within this bulk composition to have relatively high concentrations of these elements compared to a system within which these minerals would have to compete for limited volumes of these elements (Rubatto, 2017). Hermann et al. (2001) and Gauthiez-Putallaz et al. (2016) showed a similar bulk composition affect with zircon in a high pressure feldspar-free rocks where newly grown zircon still had an negative Eu anomaly despite the absence of feldspar due to the bulk composition being overall depleted in Eu. The volume of REE minerals (e.g. minor garnet) present within the sample can permit accessory minerals to have higher REE (i.e. HREE in terms of garnet) values than expected when growing in the presence of a REE bearing phase (Rubatto, 2017).

The petrochronological record is, put simply, a function of protolith, the presence of melt and *P–T–t* evolution. Different protoliths on the same *P–T–t* evolution will likely record different parts of and/or may not record parts of the *P–T–t* evolution if one protolith is more reactive than the other (more reactive = more likely to record more of the *P–T–t* evolution), as long as both have the ability to grow new geochronometers during

metamorphism. Conversely, similar protoliths on a singular vs. polymetamorphic evolution, if the rock remains sufficiently melt bearing during the whole evolution, may record one or multiple periods respectively of accessory mineral crystallisation during periods of cooling* (*– as long as cooling occurs between events in the polymetamorphic scenario). However, it is also possible that both a high-*T* protracted singular evolution and a polymetamorphic evolution with limited cooling could foreseeably produce similar geochronological data sets depending on a number of factors, but a petrochronological approach could be used to verify which kind of scenario likely occurred.

4.1 Limitations and complications with forward modelling

There is a large degree of complexity to consider when evaluating accessory minerals but there is also a degree of uncertainty involved in the generation of *P–T* models. Forward metamorphic models are inherently simplified in order to allow constraints to be quantified from complex natural processes. This simplification is applied through the use of a bulk composition that within *P–T* space does not vary (i.e. a closed system) and is modelled using a thermodynamic dataset of activity-composition models (*a–x)* that constrain mineral stability within a chosen chemical system of major elements. No natural chemical system is ever truly closed, but the degree to which they are open can vary and can only be estimated. Studies by Yakymchuk and Brown (2014b) have modelled conditionally open systems to replicate the extraction of partial melts which is a key process in the evolution of high-grade metamorphic rocks. Partial melting and melt loss however is a one-way process, resulting in evolved bulk compositions that experienced an unclear amount of melt loss. Forward modelling alone cannot quantify melt loss as the system models the rock 'forward' through time towards its current state. This is also why prograde conditions are typically not constrainable using metamorphic forward models as the modelled bulk composition represents an evolved composition, resulting in none to limited constraints on the prograde evolution. Attempts have been made to 'rewind' metamorphic processes such as Korhonen et al. (2010) and Yakymchuk and Brown (2014b), however this is still an evolving branch of research. The interrogation of a forward modelled *P–T* pseudosection by creating temperature- or pressure-composition (*T*– or *P–X*) diagrams allows the potential control of compositional factors on the modelled equilibrium assemblage to be assessed. As explained by Korhonen et al. (2012) *T–X* and *P–X* diagrams are commonly used to assess how the amount of H_2O or ferric iron changes the stability of the interpreted equilibrium assemblage, as well as correcting for later modification through retrogression or oxidation causing the modelled assemblage to contain rocks not observed within the natural sample.

Forward models currently have an over arching problem due to the lack of minor elements within thermodynamic *a–x* models that are built upon the behaviour of major element components within minerals. Minor elements such as Zn in spinel and F in biotite can expand the stability of these minerals in nature and experiments, but this currently cannot be replicated in forward models

(e.g. Vielzeuf, 1983; Harley, 1986; Chacko et al., 1987; Clarke et al., 1989; Motoyoshi et al., 1990; Nair and Chacko, 2002; White et al., 2002; Kelly and Harley, 2004; Tajčmanová et al., 2009; Diener and Powell, 2010). The continual updating of thermodynamic data sets allows for the increased accuracy of metamorphic forward models. White et al. (2014b) integrated manganese, permitting Mn substitution or Mn-bearing end members; however Mn has been shown to not have much impact at high temperature (Johnson et al., 2015) and may be excluded from studies with relevant conditions. Wheller and Powell (2014) created an updated sapphirine model incorporating ferric iron, which has been shown to effect and expand sapphirine stability to lower temperatures (Taylor-Jones and Powell, 2010; Wheller and Powell, 2014). Both of these updates are of particular importance to pelitic rocks, within which the stability of many minerals are affected by these elements. Pelitic to psammitic bulk compositions are modellable in the latest dataset 'ds6' since its public release in 2014 (White et al., 2014a; White et al., 2014b). The new activity models of Green et al. (2016) permit the modelling of melt bearing metabasic rocks, a key part of many metamorphic terranes. It is still the case that some minerals do not as of yet have updated *a–x* models for 'ds6' (e.g. osumilite) and must be modelled within the older dataset 'ds5'. The difference between these two models is discussed by Korhonen et al. (2014).

Another consideration is the rate at which the rock travelled through sections of the *P–T* evolution; similar rocks will not necessarily experience the same reactions if they move through *P–T* space at different rates due to reactions having variable activation energies and being subject to reaction kinetics. What is metamorphosed is also important, for example a sample experiencing no previous melt loss will be more sensitive to a rapid *P–T* excursions forming new microstructures and growing new minerals whereas a more residual composition may not have enough time to respond to a rapid *P–T* event, unless temperatures are sufficiently high. The formation of new microstructures during a metamorphic event (in particular during polymetamorphic scenarios) is incredibly important as microstructures and stable assemblages are what *P–T* paths are based on. Modelled assemblages are interpreted to be at equilibrium and were stable during a section of the *P–T* history, preserving the conditions the rock once experiences. However, it is entirely possible to model metastable conditions in forward modelling. The nature of equilibrium represented by an assemblage can be evaluated by comparing the stability of the modelled assemblage to the typical stability range of the individual minerals within the assemblage.

Petrochronology currently relies on *P–T* conditions constrained by major mineral assemblages that are indirectly correlated to accessory minerals. Accessory minerals are not readily considered during typical forward metamorphic modelling as they are a very small component of the rock (approximately ≤1%) and containing elements that are trace components within major minerals. Earlier attempts to integrate accessory minerals directly into phase equilibria such as Kelsey et al. (2008), combined data from dissolution experiments with phase equilibria as no mineral activity-composition models (*a–x*) existed at the time that enabled the incorporation

of Zr or LREE into minerals. An additional step towards integrating accessory minerals and phase equilibria came through the incorporation of Zr (Tomkins et al., 2007; Kelsey and Powell, 2011) and LREE (Spear and Pyle, 2010) into *a–x* models. However, these techniques are still evolving, but will be of great use to petrochronology following further development.

5. CONCLUSIONS

Quantitative constraints on the time-scales of high temperatures during metamorphism are essential for understanding lower crustal processes and the generation of accurate geodynamic models of the crust. Whilst the application of high-spatial resolution techniques are capable of analysing the internal complexities of accessory minerals, the variable behaviour of trace elements and the interaction of many geological processes during metamorphism generate complex heterogeneities in accessory minerals within high-grade metamorphic rocks. Whilst a lot of work has been done to categorise and constrain the processes associated with certain internal textures and geochemical signatures, there is limited understanding in regards to how accessory minerals behave when exposed to prolonged high temperatures. High temperatures can perturb recorded information as well as largely remove information connected to earlier events (e.g. prograde metamorphism), making it difficult to accurately constrain the duration of high-temperatures and resolve individual events from complex data sets. It is due to these complications that many high-grade terranes lack quantitative estimates of the duration of metamorphism. The increased study of accessory minerals within high-grade terranes will permit the assessment of the applicability of different geochronometers to constraining different geological processes at elevated temperatures and categorise what recorded information is representative of within a certain system. The petrochronological approach allows complex high-grade terranes to be evaluated to a high level of detail, enabling the discernment between melt, fluid and elevated temperature (diffusion) processes in addition to the quantification of accurate *P–T–t* constraints. The future development of new micro-analytical techniques and the continual updating of thermodynamic data sets will allow petrochronologic studies to achieve additional resolution in constraining rates, timescales and conditions of geological processes. The development and discovery of new geochronometers and their applicability to various geodynamic systems will also be beneficial to petrochronological studies.

6. RELEVANCE FOR THIS THESIS

This overview highlights key information that is applied in the following chapters and also provides a foundation of the current state of research and the current limitations of various petrochronological techniques and applications. The following chapters further develop this young field of research, highlighting the importance of a petrochronological approach by providing new insight into two debated high-*T* terranes and providing new insight into the behaviours of common geochronometers at high-*T,* of high importance for constraining quantitative *P–T–t* evolutions. As it is only a side project of this thesis (see Thesis structure) a summary of $^{40}Ar/^{39}Ar$

geochronology is not discussed here, see the following reviews for more information:

–Jourdan, F., Mark, D. F., and Verati, C., 2014, Advances in 40Ar/39Ar dating: from archaeology to planetary sciences – introduction: Geological Society, London, Special Publications, v. 378, no. 1, p. 1–8.

– Kelley, S., 2002, K-Ar and Ar-Ar Dating: Reviews in Mineralogy and Geochemistry, v. 47, no. 1, p. 785.

–McDougall, I., and Harrison, T. M., 1999, Geochronology and Thermochronology by the 40Ar/39Ar Method, Oxford University Press on Demand.

REFERENCES

Ahrens, L. H., 1965, Some observations on the uranium and thorium distributions in accessory zircon from granitic rocks: Geochimica et Cosmochimica Acta, v. 29, no. 6, p. 711-716.

Andersson, J., Möller, C., and Johansson, L., 2002, Zircon geochronology of migmatite gneisses along the Mylonite Zone (S Sweden): a major Sveconorwegian terrane boundary in the Baltic Shield: Precambrian Research, v. 114, no. 1–2, p. 121-147.

Andrehs, G., and Heinrich, W., 1998, Experimental determination of REE distributions between monazite and xenotime: potential for temperature-calibrated geochronology: Chemical Geology, v. 149, no. 1–2, p. 83-96.

Ashwal, L. D., Tucker, R. D., and Zinner, E. K., 1999, Slow cooling of deep crustal granulites and Pb-loss in zircon: Geochimica et Cosmochimica Acta, v. 63, no. 18, p. 2839-2851.

Ayers, J. C., Miller, C., Gorisch, B., and Milleman, J., 1999, Textural development of monazite during high-grade metamorphism: Hydrothermal growth kinetics, with implications for U,Th-Pb geochronology, American Mineralogist, Volume 84, p. 1766.

Baldwin, J. A., and Brown, M., 2008, Age and duration of ultrahigh-temperature metamorphism in the Anápolis-Itauçu Complex, Southern Brasília Belt, central Brazil - constraints from U-Pb geochronology, mineral rare earth element chemistry and trace-element thermometry: Journal of Metamorphic Geology, v. 26, p. 213-233.

Baxter, E. F., Caddick, M. J., and Dragovic, B., 2017, Garnet: A Rock-Forming Mineral Petrochronometer: Reviews in Mineralogy and Geochemistry, v. 83, no. 1, p. 469.

Bea, F., and Montero, P., 1999, Behavior of accessory phases and redistribution of Zr, REE, Y, Th, and U during metamorphism and partial melting of metapelites in the lower crust: an example from the Kinzigite Formation of Ivrea-Verbano, NW Italy: Geochimica et Cosmochimica Acta, v. 63, no. 7–8, p. 1133-1153.

Bea, F., Pereira, M. D., and Stroh, A., 1994, Mineral/leucosome trace-element partitioning in a peraluminous migmatite (a laser ablation-ICP-MS study): Chemical Geology, v. 117, no. 1, p. 291-312.

Bingen, B., Birkeland, A., Nordgulen, Ø., and Sigmond, E. M. O., 2001, Correlation of supracrustal sequences and origin of terranes in the Sveconorwegian orogen of SW Scandinavia: SIMS data on zircon in clastic metasediments: Precambrian Research, v. 108, p. 293-318.

Boehnke, P., Watson, E. B., Trail, D., Harrison, T. M., and Schmitt, A. K., 2013, Zircon saturation re-revisited: Chemical Geology, v. 351, p. 324-334.

Braun, I., Montel, J.-M., and Nicollet, C., 1998, Electron microprobe dating of monazites from high-grade gneisses and pegmatites of the Kerala Khondalite Belt, southern India: Chemical Geology including Isotope Geoscience, v. 146, p. 65-68.

Brown, M., and Korhonen, F. J., 2009, Some remarks on melting and exteme metamorphism of crustal rocks: Physic's and Chemistry of the Earth's Interior, p. 67-87.

Buick, I. S., Clark, C., Rubatto, D., Hermann, J., Pandit, M., and Hand, M., 2010, Constraints on the Proterozoic evolution of the Aravalli–Delhi Orogenic belt (NW India) from monazite geochronology and mineral trace element geochemistry: Lithos, v. 120, p. 511-528.

Buick, I. S., Hermann, J., Williams, I. S., Gibson, R. L., and Rubatto, D., 2006, A SHRIMP U–Pb and LA-ICP-MS trace element study of the petrogenesis of garnet–cordierite–orthoamphibole gneisses from the Central Zone of the Limpopo Belt, South Africa: Lithos, v. 88, no. 1–4, p. 150-172.

Chacko, T., Ravindra Kumar, G. R., and Newton, R. C., 1987, Metamorphic P–T conditions of the Kerala (South India) Khondalite Belt, a granulite facies supracrustal terrain: The Journal of Geology, v. 95, no. 3, p. 343-358.

Chen, R.-X., Zheng, Y.-F., and Xie, L., 2010, Metamorphic growth and recrystallization of zircon: Distinction by simultaneous in-situ analyses of trace elements, U–Th–Pb and Lu–Hf isotopes in zircons from eclogite-facies rocks in the Sulu orogen: Lithos, v. 114, no. 1–2, p. 132-154.

Cherniak, D. J., Hanchar, J. M., and Watson, E. B., 1997, Rare-earth diffusion in zircon: Chemical Geology, v. 134, no. 4, p. 289-301.

Cherniak, D. J., and Pyle, J. M., 2008, Th diffusion in monazite: Chemical Geology, v. 256, no. 1–2, p. 52-61.

Cherniak, D. J., and Watson, E. B., 2001, Pb diffusion in zircon: Chemical Geology, v. 172, no. 1–2, p. 5-24.

Cherniak, D. J., and Watson, E. B., 2003, Diffusion in zircon: Reviews in mineralogy and geochemistry, v. 53, no. 1, p. 113-143.

Cherniak, D. J., Watson, E. B., Grove, M., and Harrison, T. M., 2004, Pb diffusion in monazite: a combined RBS/SIMS study1: Geochimica et Cosmochimica Acta, v. 68, no. 4, p. 829-840.

Clark, C., Collins, A. S., Santosh, M., Taylor, R., and Wade, B. P., 2009, The P–T–t architecture of a Gondwanan suture: REE, U–Pb and Ti-in-zircon thermometric constraints from the Palghat Cauvery shear system, South India: Precambrian Research, v. 174, p. 129-144.

Clark, C., Fitzsimons, I. C. W., Healy, D., and Harley, S. L., 2011, How does the continental crust get really hot?: Elements, v. 7, p. 235-240.

Clark, C., Kirkland, C. L., Spaggiari, C. V., Oorschot, C., Wingate, M. T. D., and Taylor, R. J., 2014, Proterozoic granulite formation driven by mafic magmatism: An example from the Fraser Range Metamorphics, Western Australia: Precambrian Research, v. 240, p. 1-21.

Clarke, G. L., Powell, R., and Guiraud, M., 1989, Low-pressure granulite facies metapelitic assemblages and corona textures from MacRobertson Land, east Antarctica: the importance of Fe2O3 and TiO2 in accounting for spinel-bearing assemblages: Journal of Metamorphic Geology, v. 7, no. 3, p. 323-335.

Cocherie, A., and Albarede, F., 2001, An improved U-Th-Pb age calculation for electron microprobe dating of monazite: Geochimica et Cosmochimica Acta, v. 65, no. 24, p. 4509-4522.

Cocherie, A., Legendre, O., Peucat, J. J., and Kouamelan, A. N., 1998, Geochronology of polygenetic monazites constrained by in situ electron microprobe Th-U-total lead determination: implications for lead behaviour in monazite: Geochimica et Cosmochimica Acta, v. 62, no. 14, p. 2475-2497.

Compston, W., Williams, I. S., and Clement, S. W., U-Pb ages within single zircons using a sensitive high mass-resolution ion microprobe1982, p. 593-595.

Corfu, F., Hanchar, J. M., Hoskin, P. W. O., and Kinny, P., 2003, Atlas of zircon textures: Reviews in mineralogy and geochemistry, v. 53, no. 1, p. 469-500.

Cottle, J. M., Jessup, M. J., Newell, D. L., Horstwood, M. S. A., Noble, S. R., Parrish, R. R., Waters, D. J., and Searle, M. P., 2009a, Geochronology of granulitized eclogite from the Ama Drime Massif: Implications for the tectonic evolution of the South Tibetan Himalaya: Tectonics, v. 28, no. 1, p. 1-25.

Cottle, John M., Searle, Michael P., Horstwood, Matthew S. A., and Waters, David J., 2009b, Timing of Midcrustal Metamorphism, Melting, and Deformation in the Mount Everest Region of Southern Tibet Revealed by U(–Th)–Pb Geochronology: The Journal of Geology, v. 117, no. 6, p. 643-664.

Cutts, K. A., Kelsey, D. E., and Hand, M., 2013, Evidence for late Paleoproterozoic (ca 1690–1665 Ma) high- to ultrahigh-temperature metamorphism in southern Australia: Implications for Proterozoic supercontinent models: Gondwana Research, v. 23, no. 2, p. 617-640.

Dahl, P. S., Hamilton, M. A., Jercinovic, M. J., Terry, M. P., Williams, M. L., and Frei, R., 2005, Comparative isotopic and chemical geochronometry of monazite, with implications for U-Th-Pb dating by electron microprobe: An example from metamorphic rocks of the eastern Wyoming Craton (U.S.A.): American Mineralogist, v. 90, no. 4, p. 619.

Davis, D. W., Krogh, T. E., and Williams, I. S., 2003, Historical development of zircon geochronology: Reviews in mineralogy and geochemistry, v. 53, no. 1, p. 145-181.

Degeling, H., Eggins, S., and Ellis, D. J., 2001, Zr budgets for metamorphic reactions, and the formation of zircon from garnet breakdown: Mineralogical Magazine, v. 65, no. 6, p. 749-758.

Diener, J. F. A., and Powell, R., 2010, Influence of ferric iron on the stability of mineral assemblages: Journal of Metamorphic Geology, v. 28, p. 599-613.

Dumond, G., Goncalves, P., Williams, M. L., and Jercinovic, M. J., 2015, Monazite as a monitor of melting, garnet growth and feldspar recrystallization in continental lower crust: Journal of Metamorphic Geology, v. 33, no. 7, p. 735-762.

Engi, M., Lanari, P., and Kohn, M. J., 2017, Significant Ages—An Introduction to Petrochronology: Reviews in Mineralogy and Geochemistry, v. 83, no. 1, p. 1.

Erickson, T. M., Pearce, M. A., Taylor, R. J. M., Timms, N. E., Clark, C., Reddy, S. M., and Buick, I. S., 2015, Deformed monazite yields high-temperature tectonic ages: Geology, v. 43, no. 5, p. 383.

Feng, R., Machado, N., and Ludden, J., 1993, Lead geochronology of zircon by LaserProbe-inductively coupled plasma mass spectrometry (LP-ICPMS): Geochimica et Cosmochimica Acta, v. 57, no. 14, p. 3479-3486.

Fernández-Suárez, J., Gutiérrez-Alonso, G., Jenner, G. A., and Jackson, S. E., 1998, Geochronology and geochemistry of the Pola de Allande granitoids (northern Spain): their bearing on the Cadomian-Avalonian evolution of northwest Iberia: Canadian Journal of Earth Sciences, v. 35, no. 12, p. 1439-1453.

Ferry, J. M., and Watson, E. B., 2007, New thermodynamic models and revised calibrations for the Ti-in-zircon and Zr-in-rutile thermometers: Contributions to Mineralogy and Petrology, v. 154, no. 4, p. 429-437.

Fitzsimons, I. C. W., Kinny, P. D., Wetherley, S., and Hollingsworth, D. A., 2005, Bulk chemical control on metamorphic monazite growth in pelitic schists and implications for U–Pb age data: Journal of Metamorphic Geology, v. 23, no. 4, p. 261-277.

Flowerdew, M. J., Millar, I. L., Vaughan, A. P. M., Horstwood, M. S. A., and Fanning, C. M., 2006, The source of granitic gneisses and migmatites in the Antarctic Peninsula: a combined U–Pb SHRIMP and laser ablation Hf isotope study of complex zircons: Contributions to Mineralogy and Petrology, v. 151, no. 6, p. 751-768.

Fornelli, A., Langone, A., Micheletti, F., Pascazio, A., and Piccarreta, G., 2014, The role of trace element partitioning between garnet, zircon and orthopyroxene on the interpretation of zircon U–Pb ages: an example from high-grade basement in Calabria (Southern Italy): International Journal of Earth Sciences, v. 103, no. 2, p. 487-507.

Foster, G., Gibson, H. D., Parrish, R., Horstwood, M., Fraser, J., and Tindle, A., 2002, Textural, chemical and isotopic insights into the nature and behaviour of metamorphic monazite: Chemical Geology, v. 191, no. 1–3, p. 183-207.

Foster, G., Kinny, P., Vance, D., Prince, C., and Harris, N., 2000, The significance of monazite U–Th–Pb age data in metamorphic assemblages; a combined study of monazite and garnet chronometry: Earth and Planetary Science Letters, v. 181, no. 3, p. 327-340.

Foster, G., Parrish, R. R., Horstwood, M. S. A., Chenery, S., Pyle, J., and Gibson, H. D., 2004, The generation of prograde P–T–t points and paths; a textural, compositional, and chronological study of metamorphic monazite: Earth and Planetary Science Letters, v. 228, no. 1–2, p. 125-142.

Fraser, G., Ellis, D., and Eggins, S., 1997, Zirconium abundance in granulite-facies minerals, with implications for zircon geochronology in high-grade rocks: Geology, v. 25, no. 7, p. 607.

Friend, C. R. L., Strachan, R. A., Kinny, P. D., and Watt, G. R., 2003, Provenance of the Moine Supergroup of NW Scotland: evidence from geochronology of detrital and inherited zircons from (meta)sedimentary rocks, granites and migmatites: Journal of the Geological Society, v. 160, no. 2, p. 247.

Froude, D. O., Ireland, T. R., Kinny, P. D., Williams, I. S., Compston, W., Williams, I. R. t., and Myers, J. S., 1983, Ion microprobe identification of 4,100–4,200 Myr-old terrestrial zircons: Nature, v. 304, no. 5927, p. 616-618.

Fryer, B. J., Jackson, S. E., and Longerich, H. P., 1993, The application of laser ablation microprobe-inductively coupled plasma-mass spectrometry (LAM-ICP-MS) to in situ (U)–Pb geochronology: Chemical Geology, v. 109, no. 1, p. 1-8.

Gauthiez-Putallaz, L., Rubatto, D., and Hermann, J., 2016, Dating prograde fluid pulses during subduction by in situ U–Pb and oxygen isotope analysis: Contributions to Mineralogy and Petrology, v. 171, no. 2, p. 15.

Geisler, T., Schaltegger, U., and Tomaschek, F., 2007, Re-equilibration of Zircon in Aqueous Fluids and Melts: Elements, v. 3, no. 1, p. 43.

Gervasoni, F., Klemme, S., Rocha-Júnior, E. R. V., and Berndt, J., 2016, Zircon saturation in silicate melts: a new and improved model for aluminous and alkaline melts: Contributions to Mineralogy and Petrology, v. 171, no. 3, p. 21.

Gibson, H. D., Carr, S. D., Brown, R. L., and Hamilton, M. A., 2004, Correlations between chemical and age domains in monazite, and metamorphic reactions involving major pelitic phases: an integration of ID-TIMS and SHRIMP geochronology with Y–Th–U X-ray mapping: Chemical Geology, v. 211, no. 3–4, p. 237-260.

Gordon, S. M., Whitney, D. L., Teyssier, C., and Fossen, H., 2013, U–Pb dates and trace-element geochemistry of zircon from migmatite, Western Gneiss Region, Norway: Significance for history of partial melting in continental subduction: Lithos, v. 170–171, p. 35-53.

Gratz, R., and Heinrich, W., 1997, Monazite-xenotime thermobarometry: Experimental calibration of the miscibility gap in the binary system CePO4-YPO4: American Mineralogist, v. 82, no. 7-8, p. 772-780.

Green, E. C. R., White, R. W., Diener, J. F. A., Powell, R., Holland, T. J. B., and Palin, R. M., 2016, Activity–composition relations for the calculation of partial melting equilibria in metabasic rocks: Journal of Metamorphic Geology, v. 34, no. 9, p. 845-869.

Hanchar, J. M., and Miller, C. F., 1993, Zircon zonation patterns as revealed by cathodoluminescence and backscattered electron images: Implications for interpretation of complex crustal histories: Chemical Geology, v. 110, no. 1, p. 1-13.

Hanchar, J. M., and Rudnick, R. L., 1995, Revealing hidden structures: The application of cathodoluminescence and back-scattered electron imaging to dating zircons from lower crustal xenoliths: Lithos, v. 36, no. 3, p. 289-303.

Harley, S. L., 1986, A sapphirine-cordierite-garnet-sillimanite granulite from Enderby Land, Antarctica: implications for FMAS petrogenetic grids in the granulite facies: Contributions to Mineralogy and Petrology, v. 94, no. 4, p. 452-460.

Harley, S. L., 2016, A matter of time: The importance of the duration of UHT metamorphism: Journal of Mineralogical and Petrological Sciences, v. 111, p. 50–72.

Harley, S. L., and Kelly, N. M., 2007, The impact of zircon–garnet REE distribution data on the interpretation of zircon U–Pb ages in complex high-grade terrains: An example from the Rauer Islands, East Antarctica: Chemical Geology, v. 241, no. 1–2, p. 62-87.

Harley, S. L., Kelly, N. M., and Möller, A., 2007, Zircon behaviour and the thermal histories of mountain chains: Elements, v. 3, p. 25-30.

Harley, S. L., Kinny, P. D., Snape, I., and Black, L. P., Zircon chemistry and the definition of events in Archaean granulite terrains2001, Volume 37, p. 511-513.

Harley, S. L., and Nandakumar, V., 2014, Accessory mineral behaviour in granulite migmatites: a case study from the Kerala Khondalite Belt, India: Journal of Petrology, v. 55, no. 10, p. 1965-2002.

Harley, S. L., and Nandakumar, V., 2016, New evidence for Palaeoproterozoic high grade metamorphism in the Trivandrum Block, Southern India: Precambrian Research, v. 280, p. 120-138.

Harlov, D. E., 2011, Petrological and experimental application of REE- and actinide-bearing accessory mineral to the study of Precambrian high-grade gneiss terrains: Geological Society of America Memoirs, v. 207, p. 13-24.

Harlov, D. E., and Hetherington, C. J., 2010, Partial high-grade alteration of monazite using alkali-bearing fluids: Experiment and nature: American Mineralogist, v. 95, p. 1105-1108.

Harlov, D. E., Wirth, R., and Hetherington, C. J., 2011, Fluid-mediate partial alteration in monazite: the role of coupled dissolution-reprecipitation in element redistribution and mass transfer: Contributions to Mineralogy and Petrology, v. 162, p. 329-348.

Hermann, J., and Rubatto, D., 2003, Relating zircon and monazite domains to garnet growth zones: age and duration of granulite facies metamorphism in the Val Malenco lower crust: Journal of Metamorphic Geology, v. 21, p. 833-852.

Hermann, J., Rubatto, D., Korsakov, A., and Shatsky, V. S., 2001, Multiple zircon growth during fast exhumation of diamondiferous, deeply subducted continental crust (Kokchetav Massif, Kazakhstan): Contributions to Mineralogy and Petrology, v. 141, no. 1, p. 66-82.

Hirata, T., and Nesbitt, R. W., 1995, U-Pb isotope geochronology of zircon: evaluation of the laser probe-inductively coupled plasma mass spectrometry technique: Geochimica et Cosmochimica Acta, v. 59, no. 12, p. 2491-2500.

Högdahl, K., Majka, J., Sjöström, H., Nilsson, K. P., Claesson, S., and Konečný, P., 2012, Reactive monazite and robust zircon growth in diatexites and leucogranites from a hot, slowly cooled orogen: implications for the Palaeoproterozoic tectonic evolution of the central Fennoscandian Shield, Sweden: Contributions to Mineralogy and Petrology, v. 163, no. 1, p. 167-188.

Hokada, T., and Harley, S. L., 2004, Zircon growth in UHT leucosome: constraints from zircon-garnet rare earth elements (REE) relations in Napier Complex, East Antarctica: Journal of Mineralogical and Petrological Sciences, v. 99, no. 4, p. 180-190.

Holder, R. M., Hacker, B. R., Kylander-Clark, A. R. C., and Cottle, J. M., 2015, Monazite trace-element and isotopic signatures of (ultra)high-pressure metamorphism: Examples from the Western Gneiss Region, Norway: Chemical Geology, v. 409, p. 99-111.

Horn, I., Rudnick, R. L., and McDonough, W. F., 2000, Precise elemental and isotope ratio determination by simultaneous solution nebulization and laser ablation-ICP-MS: application to U–Pb geochronology: Chemical Geology, v. 164, no. 3–4, p. 281-301.

Hoskin, P. W. O., and Black, L. P., 2000, Metamorphic zircon formation by solid-state recrystallization of protolith igneous zircon: Journal of Metamorphic Geology, v. 18, p. 423-439.

Hoskin, P. W. O., and Ireland, T. R., 2000, Rare earth element chemistry of zircon and its use as a provenance indicator: Geology, v. 28, no. 7, p. 627-630.

Hoskin, P. W. O., and Schaltegger, U., 2003, The composition of zircon and igneous and metamorphic petrogenesis: Reviews in mineralogy and geochemistry, v. 53, no. 1, p. 27–62.

Ireland, T. R., Clement, S., Compston, W., Foster, J. J., Holden, P., Jenkins, B., Lanc, P., Schram, N., and Williams, I. S., 2008, Development of SHRIMP: Australian Journal of Earth Sciences, v. 55, no. 6-7, p. 937-954.

Ireland, T. R., and Williams, I. S., 2003, Considerations in zircon geochronology by SIMS: Reviews in Mineralogy and Geochemistry, v. 53, no. 1, p. 215-241.

Jackson, S. E., Pearson, N. J., Griffin, W. L., and Belousova, E. A., 2004, The application of laser ablation-inductively coupled plasma-mass spectrometry to in situ U–Pb zircon geochronology: Chemical Geology, v. 211, no. 1–2, p. 47-69.

Janots, E., Engi, M., Berger, A., Allaz, J., Schwarz, J. O., and Spandler, C., 2008, Prograde metamorphic sequence of REE minerals in pelitic rocks of the Central Alps: implications for allanite–monazite–xenotime phase relations from 250 to 610 °C: Journal of Metamorphic Geology, v. 26, no. 5, p. 509-526.

Janots, E., Engi, M., Rubatto, D., Berger, A., Gregory, C., and Rahn, M., 2009, Metamorphic rates in collisional orogeny from in situ allanite and monazite dating: Geology, v. 37, no. 1, p. 11.

Johnson, T., Clark, C., Taylor, R., Santosh, M., and Collins, A. S., 2015, Prograde and retrograde growth of monazite in migmatites: An example from the Nagercoil Block, southern India: Geoscience Frontiers, v. 6, no. 3, p. 373-387.

Jöns, N., and Schenk, V., 2011, The ultrahigh temperature granulites of southern Madagascar in a polymetamorphic context: implications for the amalgamation of the Gondwana supercontinent: European Journal of Mineralogy, v. 23, no. 2, p. 127.

Jourdan, F., Mark, D. F., and Verati, C., 2014, Advances in 40Ar/39Ar dating: from archaeology to planetary sciences – introduction: Geological Society, London, Special Publications, v. 378, no. 1, p. 1–8.

Keay, S., Lister, G., and Buick, I., 2001, The timing of partial melting, Barrovian metamorphism and granite intrusion in the Naxos metamorphic core complex, Cyclades, Aegean Sea, Greece: Tectonophysics, v. 342, no. 3–4, p. 275-312.

Kelley, S., 2002, K-Ar and Ar-Ar Dating: Reviews in Mineralogy and Geochemistry, v. 47, no. 1, p. 785.

Kelly, N. M., Clarke, G. L., and Harley, S. L., 2006, Monazite behaviour and age significance in polymetamorphic high-grade terrains: A case study from the western Musgrave Block, central Australia1: Lithos, v. 88, no. 1–4, p. 100-134.

Kelly, N. M., and Harley, S. L., 2004, Orthopyroxene–Corundum in Mg–Al-rich Granulites from the Oygarden Islands, East Antarctica: Journal of Petrology, v. 45, no. 7, p. 1481-1512.

Kelly, N. M., and Harley, S. L., 2005, An integrated microtextural and chemical approach to zircon geochronology: refining the Archaean history of the Napier Complex, east Antartica: Contributions to Mineralogy and Petrology, v. 149, p. 57-84.

Kelly, N. M., Harley, S. L., and Möller, A., 2012, Complexity in the behavior and recrystallization of monazite during high-T metamorphism and fluid infiltration: Chemical Geology, v. 322-323, p. 192-208.

Kelsey, D. E., Clark, C., and Hand, M., 2008, Thermobarometric modelling of zircon and monazite growth in melt-bearing systems: examples using model metapelitic and metapsammitic granulites: Journal of Metamorphic Geology, v. 26, p. 199-212.

Kelsey, D. E., and Hand, M., 2015, On ultrahigh temperature crustal metamorphism: Phase equilibria, trace element thermometry, bulk composition, heat sources, timescales and tectonic settings: Geoscience Frontiers, v. 6, p. 311-356.

Kelsey, D. E., and Powell, R., 2011, Progress in linking accessory mineral growth and breakdown to major mineral evolution in metamorphic rocks: a thermodynamic approach in the Na_2O-CaO-K_2O-FeO-MgO-Al_2O_3-SiO_2-H_2O-TiO_2-ZrO_2 system: Journal of Metamorphic Geology, v. 29, no. 1, p. 151-166.

Ketchum, J. W. F., Jackson, S. E., Culshaw, N. G., and Barr, S. M., 2001, Depositional and tectonic setting of the Paleoproterozoic Lower Aillik Group, Makkovik Province, Canada: evolution of a passive margin-foredeep sequence based on petrochemistry and U–Pb (TIMS and LAM-ICP-MS) geochronology: Precambrian Research, v. 105, no. 2–4, p. 331-356.

Kirkland, C. L., Erickson, T. M., Johnson, T. E., Danišík, M., Evans, N. J., Bourdet, J., and McDonald, B. J., 2016, Discriminating prolonged, episodic or disturbed monazite age spectra: An example from the Kalak Nappe Complex, Arctic Norway: Chemical Geology, v. 424, p. 96-110.

Kirkland, C. L., Whitehouse, M. J., and Slagstad, T., 2009, Fluid-assisted zircon and monazite growth within a shear zone: a case study from Finnmark, Arctic Norway: Contributions to Mineralogy and Petrology, v. 158, no. 5, p. 637-657.

Kohn, M. J., and Kelly, N., 2017, Petrology and Geochronology of Metamorphic Zircon: Microstructural Geochronology: Planetary Records Down to Atom Scale, v. 232, p. 35.

Kohn, M. J., and Malloy, M. A., 2004, Formation of monazite via prograde metamorphic reactions among common silicates: implications for age determinations: Geochimica et Cosmochimica Acta, v. 68, no. 1, p. 101-113.

Kohn, M. J., and Penniston-Dorland, S. C., 2017, Diffusion: Obstacles and Opportunities in Petrochronology: Reviews in Mineralogy and Geochemistry, v. 83, no. 1, p. 103.

Kohn, M. J., Wieland, M. S., Parkinson, C. D., and Upreti, B. N., 2005, Five generations of monazite in Langtang gneisses: implications for chronology of the Himalayan metamorphic core: Journal of Metamorphic Geology, v. 23, no. 5, p. 399-406.

Korhonen, F. J., Clark, C., Brown, M., Bhattacharya, S., and Taylor, R., 2013, How long-lived is ultrahigh temperature (UHT) metamorphism? Constraints from zircon and monazite geochronology in the Eastern Ghats orogenic belt, India: Precambrian Research, v. 234, p. 322-350.

Korhonen, F. J., Clark, C., Brown, M., and Taylor, R. J. M., 2014, Taking the temperature of Earth's hottest crust: Earth and Planetary Science Letters, v. 408, p. 341-354.

Korhonen, F. J., Powell, R., and Stout, J. H., 2012, Stability of sapphirine + quartz in the oxidised rocks of the Wilson Lake terrane, Labrador: calculated equilibria in NCKFMASHTO: Journal of Metamorphic Geology, v. 30, p. 21-36.

Korhonen, F. J., Saito, S., Brown, M., and Siddoway, C. S., 2010, Modeling multiple melt loss events in the evolution of an active continental margin: Lithos, v. 116, p. 230-248.

Korhonen, F. J., Saw, A. K., Clark, C., Brown, M., and Bhattacharya, S., 2011, New constraints on UHT metamorphism in the Eastern Ghats Province through the application of phase equilibria modelling and in situ geochronology: Gondwana Research, v. 20, p. 764-781.

Košler, J., Fonneland, H., Sylvester, P., Tubrett, M., and Pedersen, R.-B., 2002, U–Pb dating of detrital zircons for sediment provenance studies—a comparison of laser ablation ICPMS and SIMS techniques: Chemical Geology, v. 182, no. 2–4, p. 605-618.

Kröner, A., Wan, Y., Liu, X., and Liu, D., 2014, Dating of zircon from high-grade rocks: Which is the most reliable method?: Geoscience Frontiers, v. 5, no. 4, p. 515-523.

Kylander-Clark, A. R. C., Hacker, B. R., and Cottle, J. M., 2013, Laser-ablation split-stream ICP petrochronology: Chemical Geology, v. 345, p. 99-112.

Lanari, P., and Engi, M., 2017, Local Bulk Composition Effects on Metamorphic Mineral Assemblages: Reviews in Mineralogy and Geochemistry, v. 83, no. 1, p. 55.

Li, X.-h., Liang, X.-r., Sun, M., Guan, H., and Malpas, J. G., 2001, Precise 206Pb/238U age determination on zircons by laser ablation microprobe-inductively coupled plasma-mass spectrometry using continuous linear ablation: Chemical Geology, v. 175, no. 3–4, p. 209-219.

Mahan, K. H., Goncalves, P., Williams, M. L., and Jercinovic, M. J., 2006, Dating metamorphic reactions and fluid flow: application to exhumation of high-P granulites in a crustal-scale shear zone, western Canadian Shield: Journal of Metamorphic Geology, v. 24, no. 3, p. 193-217.

Martin, A. J., Gehrels, G. E., and DeCelles, P. G., 2007, The tectonic significance of (U,Th)/Pb ages of monazite inclusions in garnet from the Himalaya of central Nepal: Chemical Geology, v. 244, no. 1–2, p. 1-24.

McDougall, I., and Harrison, T. M., 1999, Geochronology and Thermochronology by the 40Ar/39Ar Method, Oxford University Press on Demand.

McFarlane, C. R. M., Connelly, J. N., and Carlson, W. D., 2005, Monazite and xenotime petrogenesis in the contact aureole of the Makhavinekh Lake Pluton, northern Labrador: Contributions to Mineralogy and Petrology, v. 148, no. 5, p. 524-541.

McFarlane, C. R. M., Connelly, J. N., and Carlson, W. D., 2006, Contrasting response of monazite and zircon to a high-T thermal overprint: Lithos, v. 88, no. 1–4, p. 135-149.

Mezger, K., and Krogstad, E. J., 1997, Interpretation of discordant U-Pb zircon ages: An evaluation: Journal of Metamorphic Geology, v. 15, no. 1, p. 127-140

.

Möller, A., O'Brien, P. J., Kennedy, A., and Kröner, A., 2002, Polyphase zircon in ultrahigh-temperature granulites (Rogaland, SW Norway): constraints for Pb diffusion in zircon: Journal of Metamorphic Geology, v. 20, p. 727-740.

Möller, A., O'Brien, P. J., Kennedy, A., and Kröner, A., 2003, Linking growth episodes of zircon and metamorphic textures to zircon chemistry: an example from the ultrahigh-temperature granulites of Rogaland (SW Norway): Geological Society, London, Special Publications, v. 220, no. From: Vance, D., Müller, W., & Villa, I. M. (eds) 2003. Geochronology: Linking the Isotopic Record with Petrology and Textures., p. 65-81.

Montel, Kornprobst, and Vielzeuf, 2000, Preservation of old U–Th–Pb ages in shielded monazite: example from the Beni Bousera Hercynian kinzigites (Morocco): Journal of Metamorphic Geology, v. 18, no. 3, p. 335-342.

Morrissey, L. J., Hand, M., Kelsey, D. E., and Wade, B. P., 2016, Cambrian High-temperature Reworking of the Rayner–Eastern Ghats Terrane: Constraints from the Northern Prince Charles Mountains Region, East Antarctica: Journal of Petrology, v. 57, no. 1, p. 53-92.

Motoyoshi, Y., Hensen, B. J., and Matsueda, H., 1990, Metastable growth of corundum adjacent to quartz in a spinel-bearing quartzite from the Archaean Napier Complex, Antarctica: Journal of Metamorphic Geology, v. 8, no. 1, p. 125-130.

Nagasawa, H., 1971, Partitioning of Eu and Sr between coexisting plagioclase and K-feldspar: Earth and Planetary Science Letters, v. 13, no. 1, p. 139-144.

Nair, R., and Chacko, T., 2002, Fluid-absent melting of high-grade semi-pelites: P-T constraints on orthopyroxene formation and implications for granulite genesis: Journal of Petrology, v. 43, no. 11, p. 2121-2142.

Nemchin, A. A., Horstwood, M. S. A., and Whitehouse, M. J., 2013, High-spatial-resolution geochronology: Elements, v. 9, no. 1, p. 31-37.

Nutman, A. P., McGregor, V. R., Shiraishi, K., Friend, C. R. L., Bennett, V. C., and Kinny, P. D., 2002, ≥3850 Ma BIF and mafic inclusions in the early Archaean Itsaq Gneiss Complex around Akilia, southern West Greenland? The difficulties of precise dating of zircon-free protoliths in migmatites: Precambrian Research, v. 117, no. 3, p. 185-224.

Palin, R. M., Weller, O. M., Waters, D. J., and Dyck, B., 2016, Quantifying geological uncertainty in metamorphic phase equilibria modelling; a Monte Carlo assessment and implications for tectonic interpretations: Geoscience Frontiers, v. 7, no. 4, p. 591-607.

Pidgeon, R. T., 1992, Recrystallisation of oscillatory zoned zircon: some geochronological and petrological implications: Contributions to Mineralogy and Petrology, v. 110, no. 4, p. 463-472.

Poitrasson, F., Chenery, S., and Bland, D. J., 1996, Contrasted monazite hydrothermal alteration mechanisms and their geochemical implications: Earth and Planetary Science Letters, v. 145, no. 1, p. 79-96.

Poitrasson, F., Chenery, S., and Shepherd, T. J., 2000, Electron microprobe and LA-ICP-MS study of monazite hydrothermal alteration:: Implications for U-Th-Pb geochronology and nuclear ceramics: Geochimica et Cosmochimica Acta, v. 64, no. 19, p. 3283-3297.

Pyle, J. M., and Spear, F. S., 1999, Yttrium zoning in garnet: coupling of major and accessory phases during metamorphic reactions: Geological Materials Research, v. 1, no. 6, p. 1-49.

Pyle, J. M., and Spear, F. S., 2000, An empirical garnet (YAG) – xenotime thermometer: Contributions to Mineralogy and Petrology, v. 138, no. 1, p. 51-58.

Pyle, J. M., and Spear, F. S., 2003, Four generations of accessory-phase growth in low-pressure migmatites from SW New Hampshire, American Mineralogist, Volume 88, p. 338.

Pyle, J. M., Spear, F. S., Rudnick, R. L., and McDonough, W. F., 2001, Monazite–Xenotime–Garnet Equilibrium in Metapelites and a New Monazite–Garnet Thermometer: Journal of Petrology, v. 42, no. 11, p. 2083-2107.

Rapp, R. P., Ryerson, F. J., and Miller, C. F., 1987, Experimental evidence bearing on the stability of monazite during crustal anaatexis: Geophysical Research Letters, v. 14, no. 3, p. 307-310.

Rasmussen, B., and Muhling, J. R., 2007, Monazite begets monazite: evidence for dissolution of detrital monazite and reprecipitation of syntectonic monazite during low-grade regional metamorphism: Contributions to Mineralogy and Petrology, v. 154, no. 6, p. 675-689.

Roberts, M. P., and Finger, F., 1997, Do U–Pb zircon ages from granulites reflect peak metamorphic conditions?: Geology, v. 25, p. 319-322.

Rubatto, D., 2002, Zircon trace element geochemistry: partitioning with garnet and the link between U–Pb ages and metamorphism: Chemical Geology, v. 184, p. 123-138.

Rubatto, D., 2017, Zircon: The Metamorphic Mineral: Reviews in Mineralogy and Geochemistry, v. 83, no. 1, p. 261.

Rubatto, D., Chakraborty, S., and Dasgupta, S., 2013, Timescales of crustal melting in the Higher Himalayan Crystallines (Sikkim, Eastern Himalaya) inferred from trace element-constrained monazite and zircon chronology: Contributions to Mineralogy and Petrology, v. 165, no. 2, p. 349-372.

Rubatto, D., and Hermann, J., 2003, Zircon formation during fluid circulation in eclogites (Monviso, Western Alps): implications for Zr and Hf budget in subduction zones: Geochimica et Cosmochimica Acta, v. 67, no. 12, p. 2173-2187.

Rubatto, D., and Hermann, J., 2007, Experimental zircon/melt and zircon/garnet trace element partitioning and implications for the geochronology of crustal rocks: Chemical Geology, v. 241, p. 38-61.

Rubatto, D., Hermann, J., Berger, A., and Engi, M., 2009, Protracted fluid-induced melting during Barrovian metamorphism in the Central Alps: Contributions to Mineralogy and Petrology, v. 158, p. 703-722.

Rubatto, D., Hermann, J., and Buick, I. S., 2006, Temperature and bulk composition control on the growth of monazite and zircon during low-pressure anatexis (Mount Stafford, Central Australia): Journal of Petrology, v. 47, no. 10, p. 1973-1996.

Rubatto, D., Williams, I. S., and Buick, I. S., 2001, Zircon and monazite response to prograde metamorphism in the Reynolds Range, central Australia: Contributions to Mineralogy and Petrology, v. 140, no. 4, p. 458-468.

Sanislav, I. V., 2011, A long-lived metamorphic history in the contact aureole of the Mooselookmeguntic pluton revealed by in situ dating of monazite grains preserved as inclusions in staurolite porphyroblasts: Journal of Metamorphic Geology, v. 29, no. 2, p. 251-273.

Santosh, M., Yokoyama, K., Biju-Sekhar, S., and Rogers, J. J. W., 2003, Multiple tectonothermal events in the granulite blocks of southern India revealed from EPMA dating: implications on the history of supercontinents: Gondwana Research, v. 6, no. 1, p. 29-63.

Schaltegger, U., Fanning, C. M., Gűnther, D., Maurin, J. C., Schulmann, K., and Gebauer, D., 1999, Growth, annealing and recrystallization of zircon and preservation of monazite in high-grade metamorphism: conventional and in-situ U-Pb isotope, cathodoluminesecence and microchemical evidence: Contributions to Mineralogy and Petrology, v. 134, p. 186-201.

Schärer, U., 1984, The effect of initial230Th disequilibrium on young UPb ages: the Makalu case, Himalaya: Earth and Planetary Science Letters, v. 67, no. 2, p. 191-204.

Schmitt, A. K., and Vazquez, J. A., 2017, Secondary Ionization Mass Spectrometry Analysis in Petrochronology: Reviews in Mineralogy and Geochemistry, v. 83, no. 1, p. 199.

Schmitz, M. D., and Bowring, S. A., 2003, Ultrahigh-temperature metamorphism in the lower crust during Neoarchean Ventersdorp rifting and magmatism, Kaapvaal Craton, southern Africa: Geological Society of America Bulletin, v. 115, no. 5, p. 533.

Seydoux-Guillaume, A.-M., Montel, J.-M., Bingen, B., Bosse, V., de Parseval, P., Paquette, J.-L., Janots, E., and Wirth, R., 2012, Low-temperature alteration of monazite: Fluid mediated coupled dissolution–precipitation, irradiation damage, and disturbance of the U–Pb and Th–Pb chronometers: Chemical Geology, v. 330–331, p. 140-158.

Shazia, J. R., Harlov, D. E., Suzuki, K., Kim, S. W., Girish-Kumar, M., Hayasaka, Y., Ishwar-Kumar, C., Windley, B. F., and Sajeev, K., 2015, Linking monazite geochronology with fluid infiltration and metamorphic histories: Nature and experiement: Lithos, v. 236-237, p. 1–15.

Smithies, R. H., Howard, H. M., Evins, P. M., Kirkland, C. L., Kelsey, D. E., Hand, M., Wingate, M. T. D., Collins, A. S., and Belousova, E., 2011, High-Temperature Granite Magmatism, Crust–Mantle Interaction and the Mesoproterozoic Intracontinental Evolution of the Musgrave Province, Central Australia: Journal of Petrology, v. 52, no. 5, p. 931-958.

Spear, F. S., and Pyle, J. M., 2010, Theoretical modeling of monazite growth in a low-Ca metapelite: Chemical Geology, v. 273, no. 1–2, p. 111-119.

Stepanov, A. S., Hermann, J., Rubatto, D., and Rapp, R. P., 2012, Experimental study of monazite/melt partitioning with implications for the REE, Th and U geochemistry of crustal rocks: Chemical Geology, v. 300–301, p. 200-220.

Štípská, P., Hacker, B. R., Racek, M., Holder, R., Kylander-Clark, A. R. C., Schulmann, K., and Hasalova, P., 2015, Monazite dating of prograde and retrograde P–T–d paths in the Barrovian terrane of the Thaya window, Bohemian Massif: Journal of Petrology, v. 56, no. 5, p. 1007-1035.

Suzuki, K., and Adachi, M., 1991, Precambrian provenance and Silurian metamorphism of the Tsubonosawa paragneiss in the South Kitakami terrane, Northeast Japan, revealed by the chemical Th-U-total Pb isochron ages of monazite, zircon and xenotime: GEOCHEMICAL JOURNAL, v. 25, no. 5, p. 357-376.

Suzuki, K., and Adachi, M., 1994, Middle Precambrian detrital monazite and zircon from the hida gneiss on Oki-Dogo Island, Japan: their origin and implications for the correlation of basement gneiss of Southwest Japan and Korea: Tectonophysics, v. 235, no. 3, p. 277-292.

Tajčmanová, L., Konopásek, J., and Košler, J., 2009, Distribution of zinc and its role in the stability of spinel in high-grade felsic rocks of the Moldanubian domain (Bohemian Massif): European Journal of Mineralogy, v. 21, p. 407-418.

Taylor, R., Clark, C., Fitzsimons, I. C. W., Santosh, M., Hand, M., Evans, N., and McDonald, B., 2014, Post-peak, fluid-mediated modification of granulite facies zircon and monazite in the Trivandrum Block, southern India: Contrib Mineral Petrol, v. 168, no. 2, p. 1-17.

Taylor, R., Harley, S. L., Hinton, R. W., Elphick, S., Clark, C., and Kelly, N. M., 2015a, Experimental determination of REE partition coefficients between zircon, garnet and melt: a key to understanding high-T crustal processes: Journal of Metamorphic Geology, v. 33, p. 231–248.

Taylor, R. J. M., Clark, C., Harley, S. L., Kylander-Clark, A. R. C., Hacker, B. R., and Kinny, P. D., 2017, Interpreting granulite facies events through rare earth element partitioning arrays: Journal of Metamorphic Geology, p. 1-17.

Taylor, R. J. M., Clark, C., Johnson, T. E., Santosh, M., and Collins, A. S., 2015b, Unravelling the complexities in high-grade rocks using multiple techniques: the Achankovil Zone of southern India: Contributions to Mineralogy and Petrology, v. 169, no. 5, p. 51.

Taylor, R. J. M., Kirkland, C. L., and Clark, C., 2016, Accessories after the facts: Constraining the timing, duration and conditions of high-temperature metamorphic processes: Lithos, v. 264, p. 239-257.

Taylor-Jones, K., and Powell, R., 2010, The stability of sapphirine + quartz: calculated phase equilibria in FeO–MgO–Al_2O_3–SiO_2–TiO_2–O: Journal of Metamorphic Geology, v. 28, no. 6, p. 615-633.

Tiepolo, M., 2003, In situ Pb geochronology of zircon with laser ablation–inductively coupled plasma–sector field mass spectrometry: Chemical Geology, v. 199, no. 1–2, p. 159-177.

Tomkins, H. S., and Pattison, D. R. M., 2007, Accessory phase petrogenesis in relation to major phase assemblages in pelites from the Nelson contact aureole, southern British Columbia: Journal of Metamorphic Geology, v. 25, no. 4, p. 401-421.

Tomkins, H. S., Powell, R., and Ellis, D. J., 2007, The pressure dependence of the zirconium-in-rutile thermometer: Journal of Metamorphic Geology, v. 25, no. 6, p. 703-713.

Tomkins, H. S., Williams, I. S., and Ellis, D. J., 2005, In situ U–Pb dating of zircon formed from retrograde garnet breakdown during decompression in Rogaland, SW Norway: Journal of Metamorphic Geology, v. 23, p. 201-215.

Tucker, N. M., Hand, M., Kelsey, D. E., and Dutch, R. A., 2015, A duality of timescales: Short-lived ultrahigh temperature metamorphism preserving a long-lived monazite growth history in the Grenvillian Musgrave–Albany–Fraser Orogen: Precambrian Research, v. 264, p. 204-234.

Vavra, G., 1990, On the kinematics of zircon growth and its petrogenetic significance: a cathodoluminescence study: Contributions to Mineralogy and Petrology, v. 106, no. 1, p. 90-99.

Vavra, G., Gebauer, D., Schmid, R., and Compston, W., 1996, Multiple zircon growth and recrystallization during polyphase Late Carboniferous to Triassic metamorphism in granulites of the Ivrea Zone (Southern Alps): an ion microprobe (SHRIMP) study: Contributions to Mineralogy and Petrology, v. 122, p. 337-358.

Vavra, G., and Schaltegger, U., 1999, Post-granulite facies monazite growth and rejuvenation during Permian to Lower Jurassic thermal and fluid events in the Ivrea Zone (Southern Alps): Contributions to Mineralogy and Petrology, v. 134, no. 4, p. 405-414.

Vielzeuf, D., 1983, The spinel and quartz associations in high grade xenoliths from Tallante (S.E. Spain) and their potential use in geothermometry and barometry: Contributions to Mineralogy and Petrology, v. 82, no. 4, p. 301-311.

Viete, D. R., and Lister, G. S., 2017, On the significance of short-duration regional metamorphism: Journal of the Geological Society, v. 174, no. 3, p. 377.

Villaseca, C., Martín Romera, C., De la Rosa, J., and Barbero, L., 2003, Residence and redistribution of REE, Y, Zr, Th and U during granulite-facies metamorphism: behaviour of accessory and major phases in peraluminous granulites of central Spain: Chemical Geology, v. 200, no. 3–4, p. 293-323.

Walsh, A. K., Kelsey, D. E., Kirkland, C. L., Hand, M., Smithies, R. H., Clark, C., and Howard, H. M., 2015, P–T–t evolution of a large, long-lived, ultrahigh-temperature Grenvillian belt in central Australia: Gondwana Research, v. 28, no. 2, p. 531–564.

Ward, C. D., McArthur, J. M., and Walsh, J. N., 1992, Rare Earth Element Behaviour During Evolution and Alteration of the Dartmoor Granite, SW England: Journal of Petrology, v. 33, no. 4, p. 785-815.

Watson, E. B., and Harrison, T. M., 1983, Zircon saturation revisited: temperature and composition effects in a variety of crustal magma types: Earth and Planetary Science Letters, v. 64, no. 2, p. 295-304.

Watson, E. B., and Harrison, T. M., 2005, Zircon Thermometer Reveals Minimum Melting Conditions on Earliest Earth: Science, v. 308, no. 5723, p. 841.

Watson, E. B., Wark, D. A., and Thomas, J. B., 2006, Crystallization thermometers for zircon and rutile: Contributions to Mineralogy and Petrology, v. 151, no. 4, p. 413.

Watt, G. R., Burns, I. M., and Graham, G. A., 1996, Chemical characteristics of migmatites: accessory phase distribution and evidence for fast melt segregation rates: Contributions to Mineralogy and Petrology, v. 125, no. 1, p. 100-111.

Wheller, C. J., and Powell, R., 2014, A new thermodynamic model for sapphirine: calculated phase equilibria in K_2O-FeO-MgO-Al_2O_3-SiO_2-H_2O-TiO_2-Fe_2O_3: Journal of Metamorphic Geology, v. 32, p. 287-299.

White, R. W., and Powell, R., 2002, Melt loss and the preservation of granulite facies mineral assemblages: Journal of Metamorphic Geology, v. 20, p. 621-632.

White, R. W., Powell, R., and Clarke, G. L., 2002, The interpretation of reaction textures in Fe-rich metapelitic granulites of the Musgrave Block, central Australia: constraints from mineral equilibria calculations in the system K_2O-FeO-MgO-Al_2O_3-SiO_2-H_2O-TiO_2-Fe_2O_3: Journal of Metamorphic Geology, v. 20, p. 41-55.

White, R. W., Powell, R., Holland, T. J. B., Johnson, T., and Green, E. C. R., 2014a, New mineral activity-composition relations for thermodynamic calculations in metapelitic systems: Journal of Metamorphic Geology, v. 32, p. 261-286.

White, R. W., Powell, R., and Johnson, T., 2014b, The effect of Mn on mineral stability in metapelites revisited: new a–x relations for manganese-bearing minerals: Journal of Metamorphic Geology, v. 32, p. 809-828.

Whitehouse, M. J., and Kamber, B. S., 2003, A rare earth element study of complex zircons from early Archaean Amîtsoq gneisses, Godthåbsfjord, south-west Greenland: Precambrian Research, v. 126, no. 3–4, p. 363-377.

Whitehouse, M. J., and Platt, J. P., 2003, Dating high-grade metamorphism- constraints from rare-earth elements in zircon and garnet: Contributions to Mineralogy and Petrology, v. 145, p. 61-74.

Whitehouse, M. J., Ravindra Kumar, G. R., and Rimša, A., 2014, Behaviour of radiogenic Pb in zircon during ultrahigh-temperature metamorphism: an ion imaging and ion tomography case study from the Kerala Khondalite Belt, southern India: Contributions to Mineralogy and Petrology, v. 168, no. 2, p. 1042.

Williams, I. S., Buick, I. S., and Cartwright, I., 1996, An extended episode of early Mesoproterozoic metamorphic fluid flow in the Reynolds Range, central Australia*: Journal of Metamorphic Geology, v. 14, no. 1, p. 29-47.

Williams, I. S., Compston, W., Collerson, K. D., Arriens, P. A., and Lovering, J. F., 1983, A reassessment of the age of the Windmill metamorphics, Casey area: Antarctic Earth Science. Austral Acad Sci, Canberra, p. 73-76.

Williams, M. L., and Jercinovic, M. J., 2002, Microprobe monazite geochronology: putting absolute time into microstructural analysis: Journal of Structural Geology, v. 24, no. 6–7, p. 1013-1028.

Williams, M. L., and Jercinovic, M. J., 2012, Tectonic interpretation of metamorphic tectonites: integrating compositional mapping, microstructural analysis and in situ monazite dating: Journal of Metamorphic Geology, v. 30, no. 7, p. 739-752.

Williams, M. L., Jercinovic, M. J., Goncalves, P., and Mahan, K., 2006, Format and philosophy for collecting, compiling, and reporting microprobe monazite ages: Chemical Geology, v. 225, no. 1–2, p. 1-15.

Williams, M. L., Jercinovic, M. J., Harlov, D. E., Budzyń, B., and Hetherington, C. J., 2011, Resetting monazite ages during fluid-related alteration: Chemical Geology, v. 283, p. 218-225.

Williams, M. L., Jercinovic, M. J., Mahan, K. H., and Dumond, G., 2017, Electron Microprobe Petrochronology: Reviews in Mineralogy and Geochemistry, v. 83, no. 1, p. 153.

Williams, M. L., Jercinovic, M. J., and Terry, M. P., 1999, Age mapping and dating of monazite on the electron microprobe: Deconvoluting multistage tectonic histories: Geology, v. 27, no. 11, p. 1023.

Wing, B. A., Ferry, J. M., and Harrison, T. M., 2003, Prograde destruction and formation of monazite and allanite during contact and regional metamorphism of pelites: petrology and geochronology: Contributions to Mineralogy and Petrology, v. 145, no. 2, p. 228-250.

Wolf, M. B., and London, D., 1994, Apatite dissolution into peraluminous haplogranitic melts: An experimental study of solubilities and mechanisms: Geochimica et Cosmochimica Acta, v. 58, no. 19, p. 4127-4145.

Wu, Y.-B., Gao, S., Zhang, H.-F., Yang, S.-H., Jiao, W.-F., Liu, Y.-S., and Yuan, H.-L., 2008a, Timing of UHP metamorphism in the Hong'an area, western Dabie Mountains, China: evidence from zircon U–Pb age, trace element and Hf isotope composition: Contributions to Mineralogy and Petrology, v. 155, no. 1, p. 123-133.

Wu, Y.-B., Zheng, Y.-F., Gao, S., Jiao, W.-F., and Liu, Y.-S., 2008b, Zircon U–Pb age and trace element evidence for Paleoproterozoic granulite-facies metamorphism and Archean crustal rocks in the Dabie Orogen: Lithos, v. 101, no. 3–4, p. 308-322.

Wu, Y. B., Zheng, Y. F., Zhang, S. B., Zhao, Z. F., Wu, F. Y., and Liu, X. M., 2007, Zircon U–Pb ages and Hf isotope compositions of migmatite from the North Dabie terrane in China: constraints on partial melting: Journal of Metamorphic Geology, v. 25, no. 9, p. 991-1009.

Xie, L., Zhang, Y., Zhang, H., Sun, J., and Wu, F., 2008, In situ simultaneous determination of trace elements, U-Pb and Lu-Hf isotopes in zircon and baddeleyite: Chinese Science Bulletin, v. 53, no. 10, p. 1565-1573.

Yakymchuk, C., 2017, Behaviour of apatite during partial melting of metapelites and consequences for prograde suprasolidus monazite growth: Lithos, v. 274–275, p. 412-426.

Yakymchuk, C., and Brown, M., 2014a, Behaviour of zircon and monazite during crustal melting: Journal of the Geological Society, v. 171, no. 4, p. 465.

Yakymchuk, C., and Brown, M., 2014b, Consequences of open-system melting in tectonics: Journal of the Geological Society, v. 171, no. 1, p. 21.

Yakymchuk, C., Clark, C., and White, R. W., 2017, Phase Relations, Reaction Sequences and Petrochronology: Reviews in Mineralogy and Geochemistry, v. 83, no. 1, p. 13.

Yuan, H.-L., Gao, S., Dai, M.-N., Zong, C.-L., Günther, D., Fontaine, G. H., Liu, X.-M., and Diwu, C., 2008, Simultaneous determinations of U–Pb age, Hf isotopes and trace element compositions of zircon by excimer laser-ablation quadrupole and multiple-collector ICP-MS: Chemical Geology, v. 247, no. 1–2, p. 100-118.

Yurimoto, H., Duke, E. F., Papike, J. J., and Shearer, C. K., 1990, Are discontinuous chondrite-normalized REE patterns in pegmatitic granite systems the results of monazite fractionation?: Geochimica et Cosmochimica Acta, v. 54, no. 7, p. 2141-2145.

Zack, T., Moraes, R., and Kronz, A., 2004, Temperature dependence of Zr in rutile: empirical calibration of a rutile thermometer: Contributions to Mineralogy and Petrology, v. 148, no. 4, p. 471-488.

Zhao, L., Zhou, X., Zhai, M., Santosh, M., and Geng, Y., 2015, Zircon U–Th–Pb–Hf isotopes of the basement rocks in northeastern Cathaysia block, South China: Implications for Phanerozoic multiple metamorphic reworking of a Paleoproterozoic terrane: Gondwana Research, v. 28, no. 1, p. 246-261.

Zhou, X., Zhao, G., Wei, C., Geng, Y., and Sun, M., 2008, EPMA U-Th-Pb monazite and SHRIMP U-Pb zircon geochronology of high-pressure pelitic granulites in the Jiaobei massif of the North China Craton: American Journal of Science, v. 308, no. 3, p. 328-350.

Zhu, X. K., and O'Nions, R. K., 1999, Zonation of monazite in metamorphic rocks and its implications for high temperature thermochronology: a case study from the Lewisian terrain: Earth and Planetary Science Letters, v. 171, no. 2, p. 209-220.

Zhu, X. K., O'Nions, R. K., Belshaw, N. S., and Gibb, A. J., 1997, Significance of in situ SIMS chronometry of zoned monazite from the Lewisian granulites, northwest Scotland: Chemical Geology, v. 135, no. 1, p. 35-53.

Chapter 2

Constraints on the timing and conditions of high-grade metamorphism, charnockite formation, and fluid-rock interaction in the Trivandrum Block, southern India

Eleanore Blereau[1*], Chris Clark[1], Richard J. M. Taylor[1], Tim E. Johnson[1], Ian C. W. Fitzsimons[1], M. Santosh[2,3]

[1]Department of Applied Geology, The Institute of Geoscience Research (TIGeR), Curtin University, GPO Box U1987, Perth WA 6845, Australia.

[2]School of the Earth Sciences and Resources, China University of Geosciences (Beijing), 29 Xueyuan Road, Beijing 100083, China.

[3]Centre for Tectonics, Resources and Exploration (TRaX), School of Earth and Environmental Sciences, University of Adelaide, SA 5005, Australia

This article is published in the Journal of Metamorphic Geology, vol. 34, pp. 527–549. doi:10.1111/jmg.12192 and reprinted with permission in Appendix A.

ABSTRACT

Incipient charnockites have been widely used as evidence for the infiltration of CO_2-rich fluids driving dehydration of the lower crust. Rocks exposed at Kakkod quarry in the Trivandrum Block of southern India allow for a thorough investigation of the metamorphic evolution by preserving not only orthopyroxene-bearing charnockite patches in a host garnet-biotite felsic gneiss but also layers of garnet-sillimanite metapelite gneiss. Thermodynamic phase equilibria modelling of all three bulk compositions indicates consistent peak metamorphic conditions of 830–925°C and 6–9 kbar with retrograde evolution involving suprasolidus decompression at high-temperature. These models suggest that orthopyroxene was most likely stabilised close to the metamorphic peak as a result of small compositional heterogeneities in the host garnet-biotite gneiss. There is insufficient evidence to determine whether the heterogeneities were inherited from the protolith or introduced during syn-metamorphic fluid flow. U–Pb geochronology of monazite and zircon from all three rock types constrains the peak of metamorphism and orthopyroxene growth to have occurred between the onset of high-grade metamorphism at c. 590 Ma and the onset of melt crystallisation at c. 540 Ma. The majority of metamorphic zircon growth occurred during protracted melt crystallisation between c. 540–510 Ma. Melt crystallisation was followed by the influx of aqueous, alkali-rich fluids likely derived from melts crystallizing at depth. This late fluid flow led to retrogression of orthopyroxene, the observed outcrop pattern and to the textural and isotopic modification of monazite grains at c. 525–490 Ma.

1. INTRODUCTION

The occurrence of orthopyroxene-bearing patches within otherwise orthopyroxene-free biotite- or hornblende-bearing host rocks, referred to as incipient or arrested charnockite, has been used as a key piece of evidence to support the notion that the infiltration of a low-H_2O activity, CO_2-rich fluid drives dehydration of the lower crust and the transition from amphibolite to granulite facies rocks (Newton, 1992; Santosh & Omori, 2008; Touret & Huizenga, 2012; Newton & Tsunogae, 2014). Whether dehydration of the lower crust to form granulite facies rocks was driven dominantly by interaction with CO_2-rich fluids (Newton et al., 1980; Newton, 1989) or by the removal of hydrous partial melt (Fyfe, 1973; White & Powell, 2002) is still the subject of debate.

Incipient charnockites have been described at many localities within the Trivandrum Block of southern India (Hansen et al., 1987; Stähle et al., 1987; Raith & Srikantappa, 1993; Perchuk et al., 2000; Ravindra Kumar, 2004; Rajesh & Santosh, 2012; Endo et al., 2013; Taylor et al., 2014). Exposures are generally confined to quarries, most of which contain either garnet–biotite gneiss (referred to locally as leptynite) and associated charnockite or more aluminous metapelitic gneiss (khondalite). However, a previously unstudied quarry at Kakkod (Fig. 1) preserves all three main rock types (incipient charnockite, host garnet–biotite gneiss and metapelitic gneiss), potentially enabling a study of charnockite formation within the context of the broader metamorphic history of the Trivandrum Block. We combine petrography, phase equilibria modelling, U–Pb geochronology and REE analyses of key minerals from the three

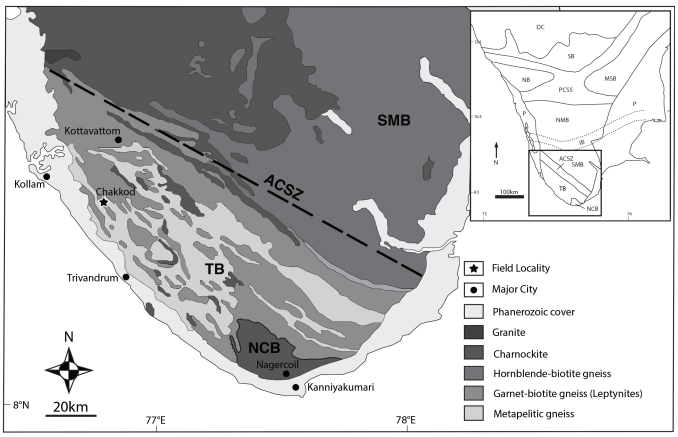

Fig. 1: Geological map of the Southern Granulite Terrane of southern India adapted from Taylor et al. (2014) with major rock types and field locations marked. Kakkod quarry is located at N 08° 48' 37.6" E 76° 48' 37.9", with the direction of view to the north. The Achankovil Shear Zone (ACSZ) separates the Trivandrum Block from the South Madurai Block. ACSZ, Achankovil Shear Zone; DC, Dharwar craton; SB, Salem Block; PCSS, Palghat-Cauvery Shear System; NB, Nilgiri Block; MSB, Madras Block; NMB, North Madurai Block; SMB, South Madurai Block; IB, Isotopic boundary; P, Phanerozoic cover; NCB, Nagercoil Block; TB, Trivandrum Block.

main lithotypes to better understand the conditions and timing of their formation. In addition, we use textural information from monazite and zircon to infer an episode of fluid flux in these rocks, and, coupled with U–Pb age data and the rare earth element compositions of garnet, zircon and monazite, investigate the relationship between the timing of peak metamorphism, charnockite formation and fluid influx.

2. GEOLOGICAL SETTING

The Southern Granulite terrane (SGT) of southern India, located to the south of the Dharwar Craton, has been subdivided into a series of crustal tectonic domains (Figure 1). These are the Coorg (Santosh et al., 2015; Santosh et al., 2016), Salem (Clark et al., 2009b), Nilgiri (Raith et al., 1990; Harris et al., 1994) and Madras Blocks (Harris et al., 1994; Santosh et al., 2003b) in the north, which are separated from more southerly domains by the Palghat-Cauvery shear zone system (Collins et al., 2007a; Clark et al., 2009a). To the south of the Palghat-Cauvery shear zone system are the northern and southern Madurai Blocks that are distinguished on the basis of different protolith ages (Plavsa et al., 2012; Plavsa et al., 2014; Clark et al., 2015). The Trivandrum Block is located to the south of the southern Madurai Block, from which it is separated by the Achankovil Zone (Drury et al., 1984; Sacks et al., 1997; Cenki et al., 2004; Chetty et al., 2006; Taylor et al., 2014). The southernmost domain, the Nagercoil Block, lies at the southern tip of peninsular India (Johnson et al., 2015; Kröner et al., 2015) (Fig. 1).

Cambrian deformation and granulite facies metamorphism in the Trivandrum Block has generally been attributed to the Malagasy Orogeny (550–510 Ma) and linked to the assembly of Gondwana (Collins & Pisarevsky, 2005; Santosh et al., 2009; Collins et al., 2014). The rocks in the Trivandrum Block are dominated by garnet- and biotite-bearing felsic gneiss (leptynite) and garnet–sillimanite–biotite or garnet–biotite–sillimanite–cordierite gneiss (khondalite), with minor calc–silicate, quartzite and mafic granulite (Ravindra Kumar et al., 1985; Chacko et al., 1987; Yoshida et al., 1991; Chacko et al., 1992; Jackson & Santosh, 1992; Raith & Srikantappa, 1993; Harley & Santosh, 1995; Braun et al., 1998; Fonarev et al., 2000; Nandakumar & Harley, 2000; Nair & Chacko, 2002; Morimoto et al., 2004; Shabeer et al., 2005; Braun, 2006; Tadokoro et

al., 2008; Endo et al., 2013; Collins et al., 2014; Harley & Nandakumar, 2014). The Trivandrum Block also contains particularly good examples of orthopyroxene-bearing felsic granulites (hereafter termed charnockites) that are commonly developed within garnet–biotite gneiss (Ravindra Kumar et al., 1985; Hansen et al., 1987; Raith & Srikantappa, 1993; Endo et al., 2013; Taylor et al., 2014). Charnockites within the Trivandrum Block have two main modes of occurrence: (1) decimetre-scale incipient charnockites with diffuse contacts that generally occur within the garnet–biotite gneisses and are interpreted to have a metamorphic origin; and (2) massive charnockite that forms discrete outcrops that have no reported contact relationships with garnet–biotite or metapelitic gneisses, and which are often ascribed an igneous origin or interpreted as an end-product of the incipient charnockitisation process (Ravindra Kumar et al., 1985; Srikantappa et al., 1985; Harley & Santosh, 1995; Rajesh & Santosh, 2004; Rajesh & Santosh, 2012; Touret & Huizenga, 2012). This study focuses on incipient charnockites.

The pressure–temperature–time (*P–T–t)* evolution recorded by rocks of the Trivandrum Block is the subject of on-going debate. Some authors have suggested peak temperatures in excess of 950°C and pressures up to ~12 kbar (Morimoto et al., 2004; Tadokoro et al., 2008). By contrast, other studies have documented lower pressures and a decrease in metamorphic grade towards the southwest from 900–1050 °C at ~8.5–9.5 kbar at the southern margin of the Achankovil Zone to 800–900 °C and 4.5–6.0 kbar further south (Chacko et al., 1996; Nandakumar & Harley, 2000; Pattison et al., 2003; Shabeer et al., 2005; Collins et al., 2014). However, there is general consensus that the rocks followed a clockwise *P–T* evolution (Cenki et al., 2004; Shabeer et al., 2005; Tadokoro et al., 2008; Collins et al., 2014).

A large proportion of U–Pb zircon data from rocks across the Trivandrum Block suggest zircon grew at ~515 Ma (Collins et al., 2007b), which was originally interpreted to constrain the age of peak metamorphism and later interpreted as the age of melt crystallization (Taylor et al., 2014). Taylor et al. (2014) constrained the age of peak metamorphism in the Trivandrum Block to c. 580–560 Ma based on U–Pb dating of monazite. Harley and Nandakumar (2014) suggested high temperature conditions prevailed until 545–535 Ma. Following peak metamorphism, Taylor et al. (2014) suggested that an episode of alkali-bearing fluid ingress occurred at ~500 Ma resulting in the modification of the accessory phases and the development of the distinctive patchiness observed in the outcrop.

3. FIELD RELATIONSHIPS AT KAKKOD QUARRY

The dominant rock type within the quarry at Kakkod is a pale-grey garnet–biotite gneiss (Fig. 2a). The gneiss has a centimetre-scale gneissic foliation defined by biotite with numerous pink garnet porphyroblasts. Garnet occurs mainly within 5–10 millimetre wide leucosome veins (Fig. 2b) that are parallel to the regional foliation, as well as within larger leucogranite sheets that vary from 5 centimetres to 3 metres in thickness. The leucogranite is coarser grained than the garnet–biotite gneiss and lacks biotite. The garnet in the leucogranite sheets typically occurs as grain aggregates 1–2 centimetres across and,

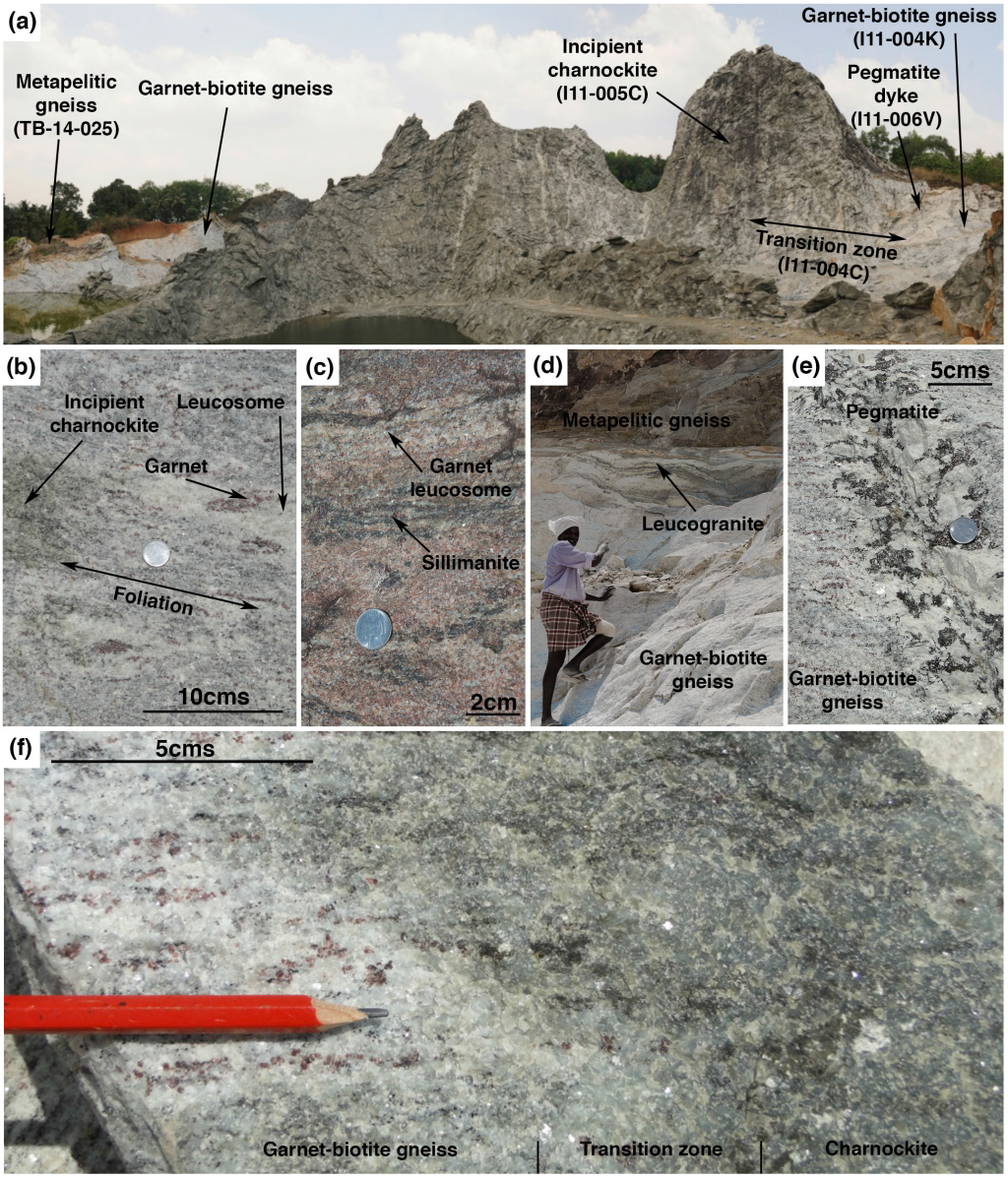

Fig. 2: Field photographs of Kakkod quarry. (a) Kakkod quarry showing three main rock types; garnet–sillimanite–cordierite gneiss (metapelitic gneiss) to the west with dark incipient charnockite patches within the grey garnet–biotite gneiss to the east. (b) Garnet–biotite gneiss with white leucosome patches. (c) Metapelitic gneiss. (d) Metapelitic gneiss (dark coloured) outcropping on top of the garnet–biotite gneiss with white leucogranite sheet. (e) Pegmatite dyke cross-cutting the garnet–biotite gneiss with yellow-brown monazite aggregates visible (f) Close-up of garnet–biotite gneiss and charnockite with a transition zone in-between.

less commonly, as large euhedral to subhedral grains 1.0–1.5 centimetres across. At the western end of the quarry (Fig. 2a) a layer of migmatitic garnet–sillimanite–cordierite gneiss (hereafter metapelitic gneiss) is exposed (Fig. 2c, d). No direct contact between the garnet–biotite gneiss and the metapelitic gneiss is exposed. The two rock types are always separated by a thin (5–10 cm) garnet-bearing leucogranite sheet that is similar in mineralogy to the leucogranite described above (Fig. 2d). A number of small dykes (~10–12 cm wide) of undeformed coarse-grained monazite-

and biotite-bearing but garnet-absent pegmatite cross cut the foliation within the garnet–biotite gneiss (Fig. 2e).

Incipient charnockites at Kakkod are characterized by the occurrence of diffuse, irregular dark patches that occur exclusively within the garnet–biotite gneiss (Fig. 2a, f). These patches comprise orthopyroxene-bearing quartzofeldspathic granofels ranging from 50 centimetres to 2 metres across and have no clear preferred orientation. A 2–5 centimetre transition zone between the garnet–biotite gneiss and the charnockite is characterised by a decrease in the abundance of biotite and a gradual change in colour into the darker green charnockite (Fig. 2f). Incipient charnockites rarely cross cut the leucogranite, although charnockite patches occur commonly at the margins of some of the larger leucogranite bodies. In this paper we present and discuss data collected from five samples that are representative of these various rock types.

4. PETROGRAPHY

4.1 Garnet-biotite gneiss

The garnet–biotite gneiss (I11-004K) is migmatitic and dominated by quartz (30–35%) and feldspar (35–40%). Garnet (10–14%) occurs as two distinct populations. Type-1 garnets are isolated rounded porphyroblasts (~3–6 mm) containing inclusions of biotite (Fig. 3a) and are located within the melanosome. Type-2 garnets occur as subhedral to anhedral clusters of grains 2 mm or less in size containing inclusions of both quartz and biotite and are located within the leucosome (Fig. 3b). Biotite (around 10%, 1–2 mm) is interpreted to record two generations of growth. The first, which occurs as inclusions within garnet (Fig. 3a, b – Bt 1) and as laths defining the gneissic foliation, is interpreted to have been stable during the prograde evolution and at the metamorphic peak. The second generation, which occurs as randomly orientated grains and replacing garnet at its margins (Fig. 3a, b – Bt 2), is interpreted as retrograde. The sample also contains minor ilmenite (~1%, ~1 mm). Most of the (partially sericitized) feldspar is perthite (30–35%, 2–4 mm) with minor plagioclase (2–5%, 1–2 mm); myrmekite is also present. The peak assemblage of the garnet–biotite gneiss sample I11-004K is interpreted as garnet, K-feldspar, quartz, biotite, ilmenite, plagioclase and melt. Along with some biotite, minor chlorite is interpreted to be retrograde.

Large grains of monazite (~240 μm) occur within K-feldspar and quartz, with some grains occurring near or directly adjacent to biotite. Back-scattered electron imaging (BSE) of monazite reveals low BSE response cores with complex irregular recrystallised zones displaying a high BSE response (Fig. 4a). Zircon (~100 μm) displays oscillatory-zoned cores under cathodoluminescence (CL) imaging with uniform CL response rims that sometimes truncate the zoning within the cores (Fig. 4b).

4.2 Transitional zone between garnet–biotite gneiss and charnockite

Sample I11-004C was collected from a gradational transition zone between garnet–biotite gneiss and charnockite (i.e. similar to Fig. 2f). Biotite (5–10%, 0.5–1.0 mm) and garnet (5–10%, 1–1.5 mm) are present but less abundant than in the garnet–biotite gneiss. The remainder of the sample is

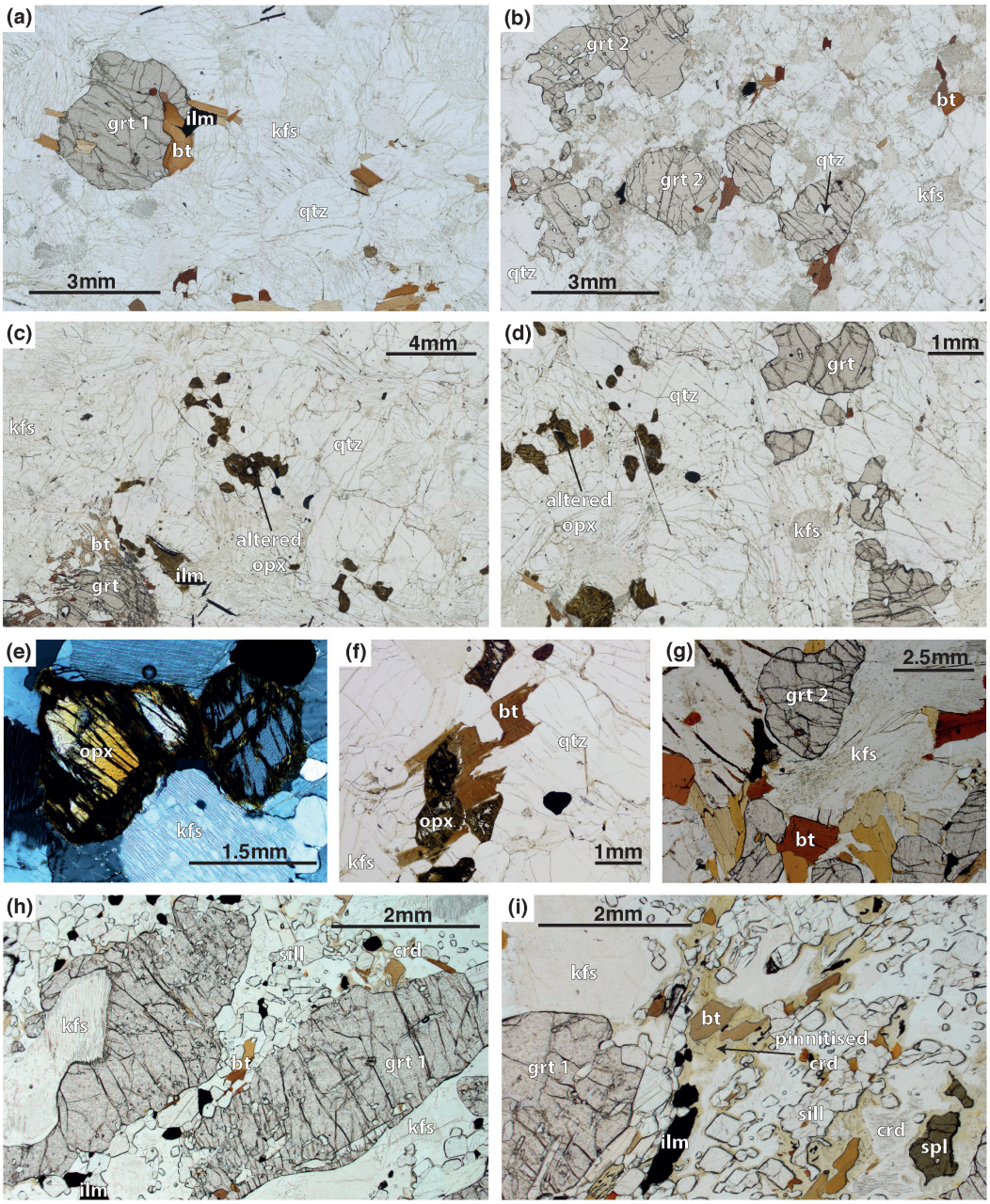

Fig. 3: Thin section photomicrographs. (a) Garnet–biotite gneiss with type-1 garnet porphyroblast. (b) Garnet–biotite gneiss with type-2 garnet porphyroblasts. (c) Transition zone showing garnet that has reacted with H_2O/melt to form retrograde biotite. (d) Partially retrogressed subhedral orthopyroxene within the charnockite with straight grain boundaries preserved. Biotite is seen replacing the orthopyroxene grain to the right on the image. (e) Orthopyroxene within the charnockite partially replaced by chlorite and other hydrosilicates. (f) Fully retrogressed orthopyroxene and anhedral garnets within the charnockite (g) Inclusion poor anhedral garnets (type-2) from the metapelitic gneiss. (h) Metapelitic gneiss with elongate garnet porphyroblasts (type-1) containing inclusions of sillimanite. (i) Metapelitic gneiss with sillimanite, green spinel and garnet porphyroblasts surrounded by variably pinitised cordierite.

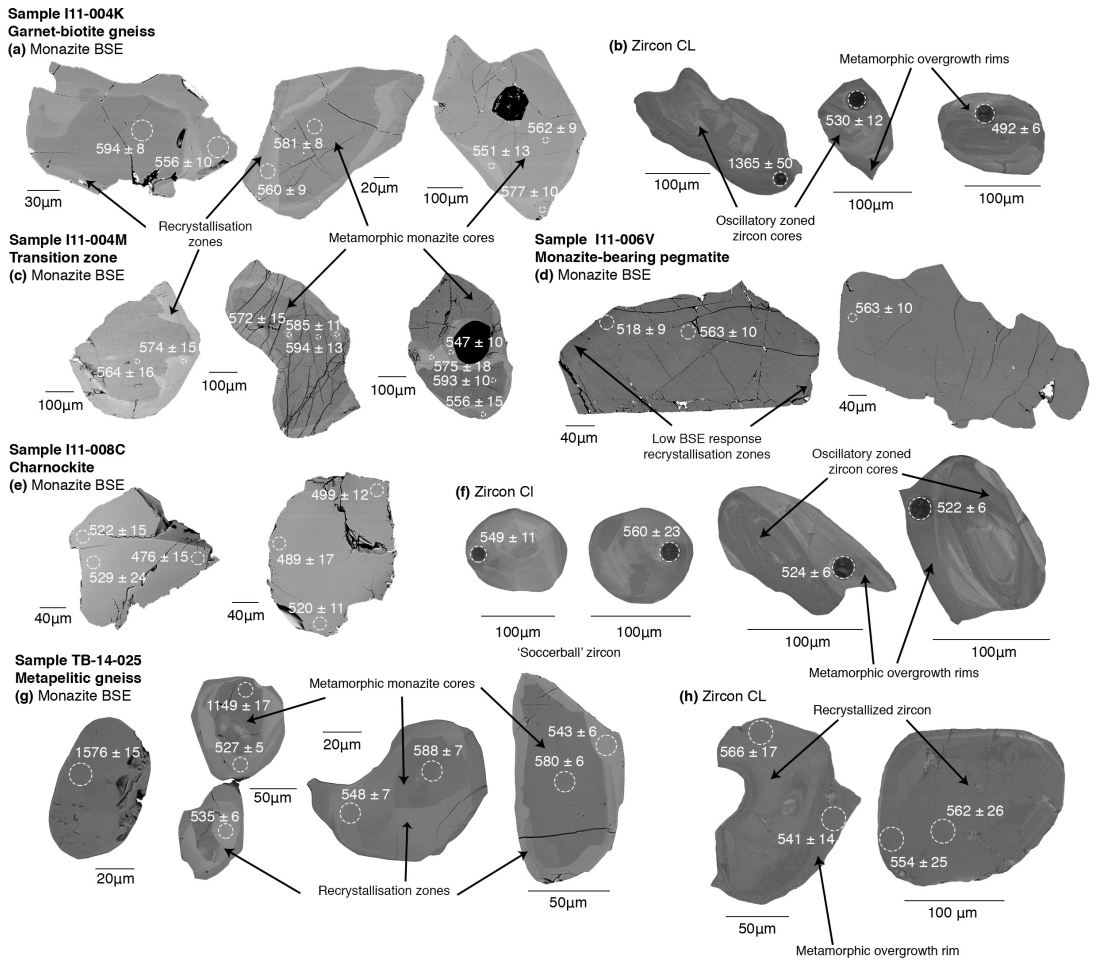

Fig. 4: BSE and CL images for monazite and zircon from all samples. Marked ages are $^{206}Pb/^{238}U$ SHRIMP ages for zircon and $^{207}Pb/^{235}U$ SHRIMP ages for monazite, both with 1σ errors. Circles represent LA-ICP-MS analytical spots that were placed over SHRIMP spots. (a) Monazite BSE images from the garnet–biotite gneiss (I11-004K). Monazite shows low BSE response cores with recrystallised zones of high BSE response. (b) Zircon CL images from the garnet–biotite gneiss with inherited oscillatory-zoned zircon cores and uniform to sector-zoned rims. (c) BSE images of monazite from the transition zone (I11-004C) showing low BSE response cores and recrystallised zones with high BSE response. (d) Monazite BSE images from the pegmatite (I11-006V) showing variable BSE response and limited zoning. A few grains have low BSE response recrystallised zones. (e) BSE images of monazite from the charnockite (I11-008C) with uniform BSE response and no internal structures. (f) Zircon CL images from the charnockite with a population of equant sector-zoned soccer ball zircon and a population of inherited oscillatory-zoned cores with uniform to sector-zoned rims. (g) Monazite BSE images from the metapelitic gneiss (TB-14-025) with most monazite showing low BSE response cores and high BSE response recrystallised zones, and a few grains with quite uniform BSE response. (h) Zircon CL images from the metapelitic gneiss with recrystallised zircon showing remnants of inherited cores and uniform CL response, and one grain with a uniform CL response rim.

dominated by quartz (35–40%, 1–4 mm), perthite (35–40%, 1–3 mm) and plagioclase (5–10%, 1–3 mm). Garnet has irregular grain boundaries with quartz and biotite inclusions, similar to type-2 garnet from the garnet–biotite gneiss. Garnet is commonly surrounded by an intergrowth of biotite and quartz, consistent with a reaction with melt (Fig. 3c). Some myrmekite is present.

Orthopyroxene (0.5–2.0 mm) is completely retrogressed to chlorite and other fine-grained hydrous phases (Fig. 3c). Monazite is similar to that within the garnet–biotite gneiss, with low BSE response cores and high BSE response recrystallised zones (Fig. 4e). Likewise, the zircon grains have a similar appearance to those in the garnet–biotite gneiss, with oscillatory-zoned cores and homogeneous rims.

4.3 Garnet-bearing charnockite

Sample I11-008C, a charnockite patch from within the garnet–biotite gneiss, is coarse grained and darker in colour than the host gneiss. The sample is dominated by irregular grains of feldspar (40–45% perthite 1–3 mm; 5–10% plagioclase, 1–3 mm) and quartz (35–40%, 1–4 mm) with some myrmekite. Orthopyroxene (2–3%, 0.5–2 mm) occurs as discrete subhedral grains in contact with quartzofeldspathic minerals (Fig. 3d, e, f) and does not appear to replace any ferromagnesian minerals, suggesting that it grew in equilibrium with other matrix minerals in the charnockite. All orthopyroxene grains are retrogressed at their margins and along cleavage plains (Fig. 3d, e) to a fine-grained aggregate of hydrous minerals including chlorite, with many grains completely pseudomorphed (Fig. 3f). Minor biotite (2–5%, 1–2 mm) generally occurs adjacent to or replacing orthopyroxene (Fig. 3d, f). Garnet (2–5%) forms irregular porphyroblasts 1–4 mm in diameter containing quartz inclusions, similar to the type-2 garnets of the garnet–biotite gneiss (Fig. 3f). Ilmenite (~1%, ~1 mm) and chlorite occur as minor phases. The main equilibrium assemblage of this sample is interpreted to be orthopyroxene, garnet, K-feldspar, quartz, plagioclase, ilmenite and melt. Given suggestions that incipient charnockite forms by fluid-driven recrystallisation, we acknowledge that this might not be the peak assemblage (an issue we address below using phase equilibria modelling). Biotite and chlorite are considered to be retrograde.

Monazite (~240 μm) shows uniform BSE response with no obvious zoning (Fig 4e). On the basis of CL imaging, zircon within the charnockite occurs in two forms: (i) grains with oscillatory-zoned cores with either uniform or sector-zoned rims (~160 μm) and, (ii) equant 'soccer-ball' grains (~130 μm) (Vavra et al., 1996; Schaltegger et al., 1999; Kelly & Harley, 2005) (Fig. 4f).

4. 4 Metapelitic gneiss

The metapelitic gneiss (TB-14-025) is meso- to melanocratic and migmatitic, comprising layers of melanosome and leucosome. Garnet (20–22%, 0.5–4.5 mm) is present in both melanosome and leucosome as two different types. Type-1 garnets, which are more abundant in melanosome, are anhedral, inclusion-rich (including sillimanite, plagioclase and biotite), elongate, and aligned parallel to the foliation (Fig. 3h). Type-2 garnets are inclusion-poor, anhedral (Fig. 3g) and occur within the leucosome. Sillimanite (20–25%) is abundant within the melanosome and defines the foliation, occurring as euhedral grains ranging from 0.5 to 2.0 mm in length (Fig. 3c). Sillimanite also occurs as inclusions in type-1 garnet that define a foliation subparallel to the matrix foliation. Perthite (15–18%, 0.5–4.0 mm) is present both in the melanosome and leucosome, whereas quartz (8–10%, 1–2 mm) is present only

in the leucosome. Spinel (2–3%, 0.2–1.0 mm) occurs as anhedral grains in the matrix of the quartz-free melanosome. The rock also contains minor plagioclase (2%, 0.1–0.5 mm), ilmenite (1%, 0.1–1.0 mm) and pyrite (<1%, 0.1–1.0 mm). Twinned and variably pinitised cordierite (~20%, 1–4 mm) surrounds garnet, sillimanite, ilmenite, spinel and biotite. Matrix biotite (7–10%, 0.1–2.0 mm) occurs as two generations. The first is present as inclusions within garnet and anhedral grains enclosed by cordierite (Fig. 3i – Bt 1). The second generation occurs as randomly orientated grains within the matrix and replacing garnet in both the melanosome and leucosome (Fig. 3g – Bt 2). The peak assemblage of this sample is interpreted to be garnet, ilmenite, plagioclase, K-feldspar, biotite and melt with sillimanite and spinel only present in the melanosome and quartz only present in the leucosome. Cordierite and some of the biotite is interpreted to be retrograde.

Zircon (~200 μm) occurs within quartz, feldspar and near ilmenite, biotite and sillimanite. Monazite (~60–100 μm) is present as inclusions within garnet, cordierite, K-feldspar, quartz and adjacent to sillimanite, ilmenite and spinel. Monazite generally shows low BSE response cores with lobate high BSE response recrystallised zones (Fig. 4g) although some grains are uniform (Fig. 4g). Zircon is recrystallised with most primary oscillatory-zoned cores replaced by uniform low-CL response domains (Fig. 4h). Some grains also have rims with uniform CL response (Fig. 4h).

4.5 Pegmatite

Sample I11-006V is dominated by quartz (20–25%), feldspar (~60%) and biotite (15–20%), all of which are 2 to 4mm across. The majority of feldspar is perthite comprising an approximate 1:1 ratio of sodic to potassic feldspar lamellae, along with minor plagioclase (~10%). Yellow monazite (~1 mm) is found both as clusters and isolated grains. It occurs as inclusions within biotite, within and in close association with ilmenite (~1%, 1–2 mm), and rarely within feldspar (both perthite and minor plagioclase). BSE imaging of monazite reveals little or no zoning in the majority of grains. Unzoned monazite shows high to low BSE response with a few grain showing low BSE response recrystallised zones (Fig. 4d).

5. ANALYTICAL METHODS

5.1 Phase equilibria modelling

Metamorphic *P–T* conditions were constrained using isochemical *P–T* pseudosections in the model pelite system Na_2O–CaO–K_2O–$FeO-MgO-Al_2O_3-SiO_2-H_2O-TiO_2-O$ (NCKFMASHTO). Pseudosections were calculated using THERMOCALC 3.40i and the internally consistent thermodynamic dataset of Holland and Powell (2011)(specifically the tc-ds62 dataset generated on 6 February 2014). The phases considered were: garnet (Grt), silicate melt (Liq), ternary feldspar (Kfs, Pl), muscovite (Ms), biotite (Bt), orthopyroxene (Opx), cordierite (Crd), ilmenite (Ilm) and magnetite–spinel (Mt, Spl). Activity–composition models are from White et al. (2014a). Mineral abbreviations follow Kretz (1983) and Whitney and Evans (2010).

Bulk rock compositions for I11-004K, I11-008C and TB-14-025 (garnet–biotite gneiss, charnockite and metapelitic gneiss) were determined by X-ray fluorescence analysis using

	Measured compositions from XRF (mol %)										
Sample	SiO_2	TiO_2	Al_2O_3	O	FeO	MgO	CaO	Na_2O	K_2O	LOI	Total
I11-004K Garnet-biotite gneiss	76.32	0.19	9.39	0.39	2.56	1.07	2.56	4.61	1.23	1.69	100.01
I11-005C Charnockite	74.72	0.16	9.23	0.35	2.27	1.04	2.6	4.59	1.36	3.67	99.99
TB-14-025 Metapelitic gneiss	64.83	0.59	11.93	1.34	6.62	3.66	1.30	3.49	3.36	2.87	99.99
	Modelled Bulk compositions (mol%)										
Sample	SiO_2	TiO_2	Al_2O_3	O	FeO	MgO	CaO	Na_2O	K_2O	LOI	Total
I11-004K Garnet-biotite gneiss	76.53	0.19	9.42	0.11	2.57	1.07	2.57	4.63	1.23	1.69	100.01
I11-005C Charnockite	77.00	0.16	9.52	0.11	2.34	1.08	2.68	4.73	1.40	1.00	100.02
TB-14-025 Metapelitic gneiss	65.45	0.60	12.04	0.40	6.68	3.69	1.32	3.53	3.39	2.9	100.00

Table 1: Bulk rock compositions as measured by XRF and modelled composition with modified ferric values. All values are in mol.%. Fe2O3 concentrations are recast into equivalent concentrations of FeO (added to the ferrous FeO concentration) and O (Diener & Powell, 2010).

a Panalytical 2404 instrument at Franklin and Marshall College, Pennsylvania; ferric and ferrous iron contents were determined by titration at the same institution. The bulk compositions (as mol.%) used in pseudosections are provided in Table 1. Although Mn-bearing solution models have recently been calibrated (White et al., 2014b), Mn has a negligible effect on phase stability at high–*T* and was excluded from the model system (Johnson et al., 2015). Modelled H_2O contents are taken from the total loss-on-ignition amounts in XRF data, except for the charnockitic composition in which a lower value of 1 mol.% was used to account for the significant hydrous retrogression of orthopyroxene in this sample.

Based on petrographic observations, none of the samples contained magnetite as a peak phase, an interpretation supported by energy dispersive spectral analysis using the TM3030 Tabletop Microscope (using Swift ED3000 at 15kv), in which all analysed opaque phases were ilmenite. Preliminary phase equilibria calculations using the measured amount of ferric iron oxide (Fe_2O_3, modelled in THERMOCALC as O in the bulk composition, Diener and Powell (2010); Table 1) contained no fields in which the interpreted peak assemblage did not coexist with magnetite, implying some oxidation of the rock after the metamorphic peak (either during exhumation and/or weathering of the rock or during sample preparation). To better constrain Fe_2O_3 contents at the metamorphic peak, $T/P–M_{Fe2O3}$ pseudosections were calculated for all modelled rocks, where M_{Fe2O3} is a binary compositional range expressing variable ferric iron contents (molecular proportion of Fe_2O_3 in the rock) from the titrated values (at $X=0$) to a minimal Fe_2O_3 content in the rock of 0.01 mol.% (at $X=1$; see supplementary data Fig. S1–3). These diagrams show that magnetite is removed from the interpreted peak assemblage at appropriate *P–T* conditions (> 5 kbar, c. 900 °C, see below) if *X* is increased to a value of ~0.7, equivalent to decreasing the molecular proportion of Fe_2O_3 in the rock to 30% of the measured value. Thus, for the charnockite and garnet–biotite gneiss, which have very similar measured Fe_2O_3 concentrations of 0.39 and 0.36 mol.% respectively, we have used a single Fe_2O_3 concentration of 0.11 mol.% for pseudosection modelling, while a corresponding value of 0.40 mol.% was used for the metapelitic gneiss (also equal to ~30% of the measured value).

5.2 SHRIMP U-Pb geochronology

Grains of monazite from all samples (and zircon from metapelitic gneiss) were extracted from polished thin sections (in situ) along with immediately adjacent minerals as 2-mm diameter pucks using a coring piece on a Dremel drill. Nineteen pucks were mounted and cast in a 25-mm diameter epoxy disk. Samples were cleaned and coated with a 30 µm gold coat to ensure conductivity during SIMS analysis. In addition to thin section mounts, grain separates of monazite and zircon were prepared via traditional methods of disaggregation, magnetic and heavy liquid separation. These grains were mounted in 25-mm diameter epoxy discs, polished then cleaned before applying a 30 µm gold coat. Mounts were characterised using BSE imaging for monazite with a Zeiss EVO 40XVP SEM and Tescan Mira3 FESEM, and CL imaging for zircon with a Philips XL 30 and a Tescan Mira3 FESEM (both at the John de Laeter Centre of Mass Spectrometry housed at Curtin University).

U–Pb isotopic data of zircon and monazite were collected using the Sensitive High Resolution Ion Microprobe (SHRIMP II) based in the John de Laeter Centre, Curtin University. The mass filtered O_2- primary beam strength was 0.3 nA with a 10 µm spot size for monazite, and 1.9 nA with a 20 µm spot size for zircon. A 6-scan duty cycle and a mass resolution of ≈5000 were used during analysis (Kennedy & de Laeter, 1994; de Laeter & Kennedy, 1998). Data was processed using SQUID II and Isoplot 3.75 (Ludwig, 2003; Ludwig, 2009) with the correction of measured isotopic ratios for common Pb based on Stacey and Kramers (1975). Standards were located in a separate mount for the analysis of monazite and zircon in thin section and this mount was Au-coated at the same time as their respective samples. For monazite, INDIA (Curtin internal laboratory standard, 509 Ma) was used as a primary standard (Korhonen et al., 2011) and GM-3 as a secondary standard (Curtin internal laboratory standard, 488 Ma). The same standards were used in the monazite grain mount. NBS glass (610, 612) was used for all zircon and monazite analyses to calibrate the position of the ^{204}Pb peak. For zircon analyses, BR266 (Stern & Amelin, 2003) was used as a primary standard and Temora 2 (Black et al., 2003) as a secondary standard in both grain and in situ mounts. Secondary standards (Temora 2 (417 Ma) and GM-3 (488 Ma)) for all sessions were within error (Temora 2: 414 ± 4 Ma, 413 ± 5 Ma; GM-3: 488 ± 5 Ma, 488 ± 3 Ma) of reported ages. ^{207}Pb/^{235}U monazite ages were used for reported ages and ranges over ^{206}Pb/^{238}U ages because of reduced effects of fractionation via incorporation of intermediate daughter products from ^{230}Th decay (Kirkland et al., 2009). Based on our data ^{207}Pb/^{235}U and ^{206}Pb/^{238}U monazite ages are within ~ 5% discordance and are near equivalent to each other, allowing for use of Terra-Wasserburg concordia plots. A high degree of discordance and smearing along concordia is typical of U–Pb zircon and monazite data from southern India. Recrystallised, inherited zircon show a large variation in discordance (up to 48%) due to partial U–Pb resetting. In comparison the majority of metamorphic zircon are less than 10% discordant. For the purpose of calculating metamorphic ages concordance is defined by the 2σ error ellipse overlapping with concordia (Spencer et al., 2015). Metamorphic zircon age ranges are defined using ^{206}Pb/^{238}U as these grains

are younger than ~1500 Ma (Spencer et al., 2015). Pooled age data from multiple grains is reported either as a weighted mean age (if MSWD <2.5) or a range of ages (if MSWD > 2.5). Error ellipses on concordia diagrams are at the 2σ level. Weighted means were calculated at 95% confidence. Errors cited for individual spot analysis in the text and data tables include errors from counting statistics, errors from the common Pb correction and U–Pb calibration errors based on reproducibility of U–Pb measurements of the standard, and are at the 1σ level. A minimum error of 1% was assigned to the external spot-to-spot error to reflect the long-term performance of the SHRIMP. Zircon was not analysed from the transition zone due to its similar morphology to that within the garnet–biotite gneiss. Complete data tables for all monazite and zircon geochronology can be found in supplementary data Tables S1 and S2.

5.3 LA-ICP-MS REE analysis of monazite, zircon and garnet

Rare earth element (REE) data were collected using Laser Ablation Inductively Coupled Plasma Mass Spectrometry (LA-ICP-MS) on an ASI Resolution M-50 with a 193-nm wavelength Ar–F excimer laser with an Agilent 7700 mass spectrometer at the GeoHistory Facility, John de Laeter Centre, Curtin University. Analyses were made directly on top of all SHRIMP spots in monazite and zircon in both in situ and grain mounts. Garnet (core and rims) within the garnet–biotite gneiss (I11-004K), charnockite (I11-008C) and metapelitic gneiss (TB-14-025) were also analysed in thin sections. Garnet was analysed using a 50-µm spot size, zircon with a 23-µm spot size and monazite with a 33-µm spot size. NIST glasses were used as reference material, specifically the 610 and 612 glasses with 610 used as the primary standard. Stoichiometric major elements were used for calibration of trace elements in each phase. Stoichiometric Si was used as the internal standardisation element for both zircon (14.76 wt%) and garnet (18 wt%). Ce (230526 ppm) was used as the internal standardisation element for monazite (Buick et al., 2010). All REE ppm values were normalized to CI chondrite values from Anders and Grevesse (1989), given as X_N values (X = relevant element). Europium anomalies were evaluated using Eu/Eu* values ($Eu/Eu^* = Eu_N/0.5*(Sm_N + Gd_N)$). Time-resolved data for all data points were reviewed following each session using the Iolite software package (Paton et al., 2010; Paton et al., 2011) and any monazite analyses that sampled inclusions (e.g. thorite) were removed. LREE data from zircon and garnet are not reported because relatively high values indicate that the LA–ICP–MS technique has sampled LREE-rich inclusions as well as the host mineral (e.g. LREE in zircon and garnet indicate monazite inclusions). Complete REE data tables can be found in supplementary data Tables S3, S4 and S5.

6. RESULTS

6.1 Phase equilibria modelling

In the *P–T* pseudosection for sample I11-004K (garnet–biotite gneiss; Fig. 5a) the calculated solidus is located at ~ 700–725 °C. The stability field for the inferred peak assemblage of garnet, ilmenite, K-feldspar, plagioclase, quartz, and melt both with and without biotite is highlighted, as natural biotite contains fluorine that will expand

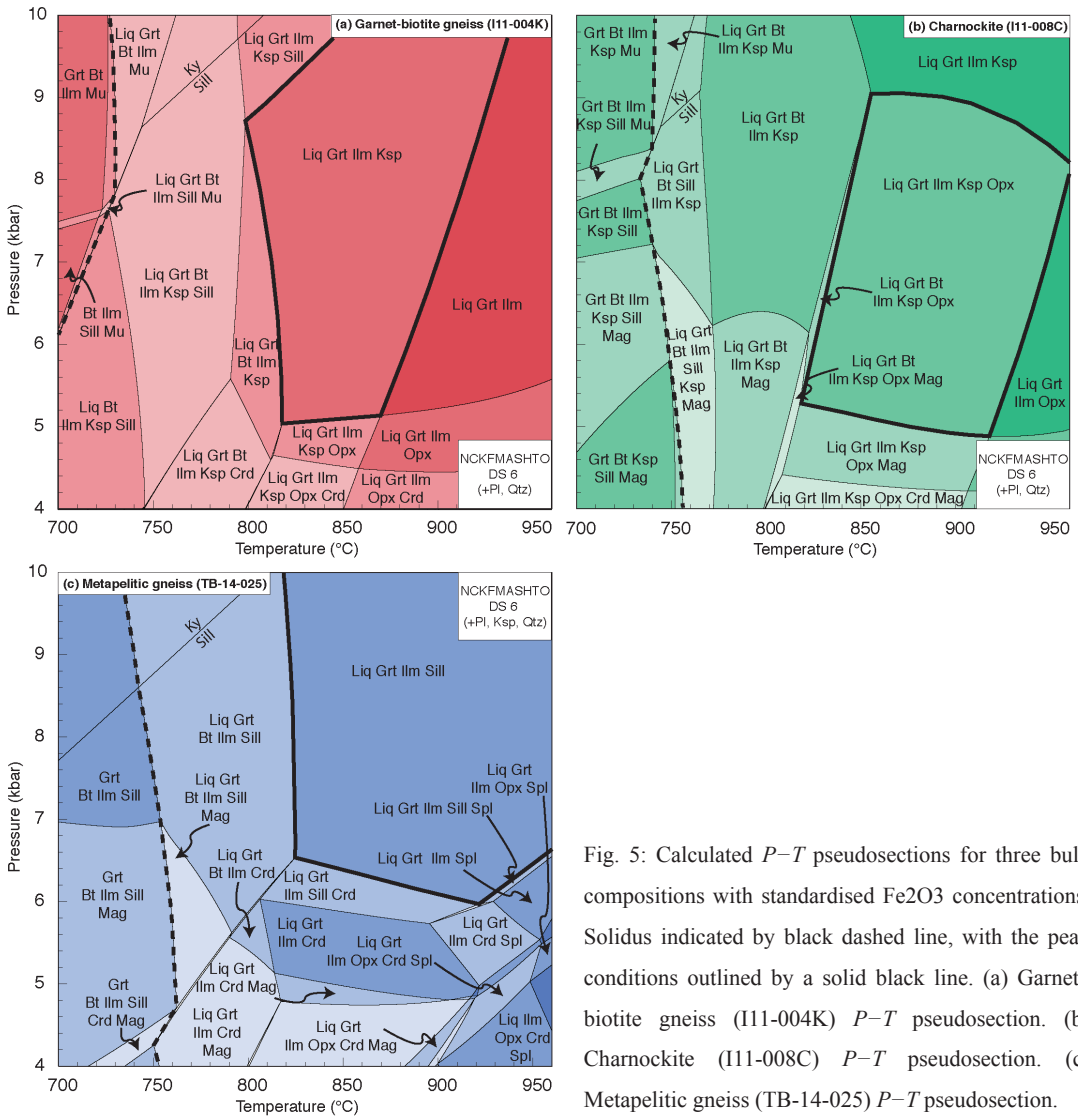

Fig. 5: Calculated *P*–*T* pseudosections for three bulk compositions with standardised Fe2O3 concentrations. Solidus indicated by black dashed line, with the peak conditions outlined by a solid black line. (a) Garnet–biotite gneiss (I11-004K) *P*–*T* pseudosection. (b) Charnockite (I11-008C) *P*–*T* pseudosection. (c) Metapelitic gneiss (TB-14-025) *P*–*T* pseudosection.

its stability to temperatures higher than predicted in the model system. These fields encompass a *P*–*T* range of 4.6 to >10 kbar and 790–940 °C. At lower pressures orthopyroxene and/or cordierite are predicted to be stable, neither of which occur in this sample.

In the *P*–*T* pseudosection for sample I11-008C (charnockite; Fig. 5b) the calculated solidus is located at ~ 735–750 °C. The stability field for the interpreted peak assemblage of garnet, orthopyroxene, ilmenite, plagioclase, K-feldspar, quartz and melt occurs at 820–950 °C at 4.9–9.0 kbar. At lower temperatures biotite is predicted. Magnetite is predicted to be stable at pressures of less than 7 kbar at 700 °C and less than 5 kbar at 950 °C, and therefore defines the lower pressure limit of the peak field. However, given that we adjusted the bulk Fe_2O_3 content specifically to move the magnetite stability field to lower pressure the *P*–*T* position of this field does not provide independent constraints on the metamorphic conditions in our samples. Instead, we take the lack of cordierite, which is predicted to be stable at P < 4.5 kbar, to provide a more robust lower pressure limit to peak conditions in this sample.

In the *P*–*T* pseudosection for sample TB-

14-025 (metapelitic gneiss; Fig. 5c) the calculated solidus is located at ~ 730–760 °C. Magnetite is predicted only at low pressures (below 7 kbar at 700 °C and below 4 kbar at 920 °C) for the chosen Fe_2O_3 content. The bulk composition of this sample contains both melanosome and leucosome and the pseudosection generated for this composition has quartz stable across the entire *P–T* range. Due to spinel only being stable in the quartz-free melanosome we have chosen to ignore it from the peak assemblage for this whole rock pseudosection. The stability field of the interpreted peak assemblage of garnet, ilmenite, sillimanite, plagioclase, K-feldspar, quartz and melt (both with and without biotite to account for likely differences between the natural and modelled stabilities of biotite) occurs at conditions of 740–960 °C and > 5.6 kbar. Cordierite, which is stable at P < 6–6.5 kbar, provides the lower pressure limit to the peak assemblage.

6.2 Monazite SHRIMP U–Pb dating

Monazite was analysed in thin section from a variety of textural settings such as inclusions in K-feldspar, quartz, garnet, cordierite and adjacent to ilmenite, biotite, sillimanite and spinel. No relationship was found between the textural location of accessory phases and their respective ages. Complete data tables for monazite U–Pb analyses can be found in supplementary data Table S1.

6.2.1 Garnet-biotite gneiss

Fifteen analyses were performed on monazite grains from sample I11-004K. Core and recrystallised zone textures were targeted that had previously been identified through BSE imaging. Low BSE response monazite cores from the garnet–biotite gneiss yielded a range of $^{207}Pb/^{235}U$ spot ages from 594 ± 8 to 529 ± 10 Ma (n=6) and Th/U ratios of 16.6–26.6. The recrystallised zones yield a range of $^{207}Pb/^{235}U$ spot ages from 587 ± 10 to 507 ± 17 Ma (n=9) and Th/U ratios of 30.6–87.1 (Fig. 6a).

6.2.2 Transition zone

Twenty-nine spots from ten grains were analysed from sample I11-004C. Ten analyses of low BSE response monazite cores yielded a weighted mean $^{207}Pb/^{235}U$ age of 584 ± 8 Ma (MSWD=0.7, n=10) and Th/U ratios of 17.1–23.5 with the high BSE response recrystallised zones giving a range of $^{207}Pb/^{235}U$ spot ages from 593 ± 13 to 517 ± 13 Ma and Th/U ratios of 20.0–98.4 (Fig. 6b).

6.2.3 Charnockite

Only two monazite grains were found in sample I11-008C. Both appear uniform, with no zoning or high BSE response recrystallised zones, and yielded a weighted mean $^{207}Pb/^{235}U$ age of 505 ± 12 Ma (MSWD=1.8, n=6) and Th/U ratios of 6.9–83.9 (Fig. 6c).

6.2.4 Metapelitic gneiss

Seventeen monazite grains were analysed from sample TB-14-025. The concordant monazite cores gave a range of $^{207}Pb/^{235}U$ ages from 586 ± 5 to 512 ± 6 Ma (n=12) and Th/U ratios of 4.0–45.9. A few discordant cores define a discordia with an upper intercept of 1946 ± 24 Ma (MSWD=0.66, n=5) (Fig. 6d). The lower intercept of this discordant array is based on the onset of high-temperature conditions using the oldest metamorphic monazite spots and

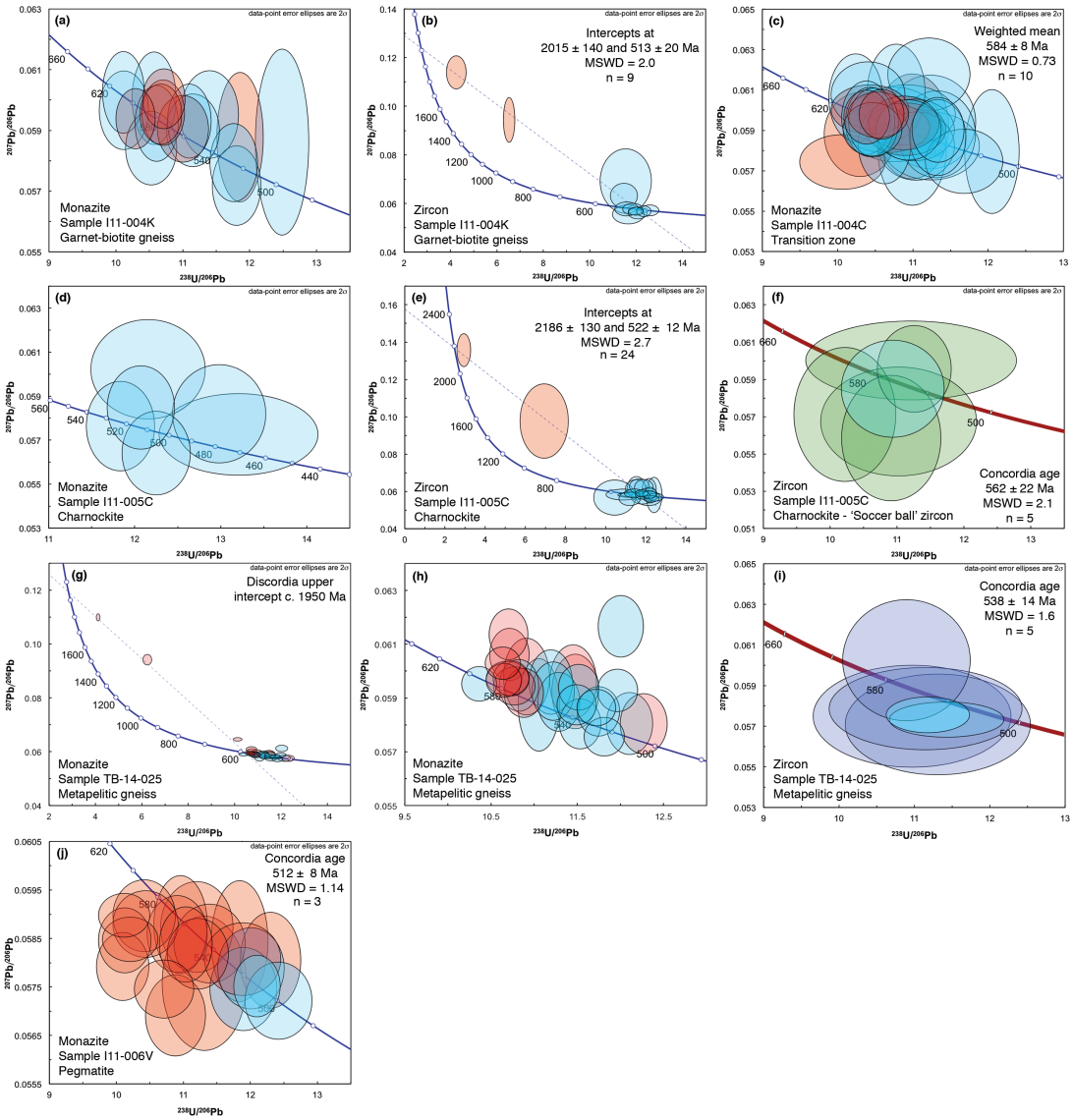

Fig. 6: U–Pb monazite and zircon data for the samples in this study. Colours indicate textural location the analysis (see online version): red- grain core; light blue- rim (zircon) or recrystallised zones (monazite); green- 'soccerball' zircon; dark blue- recrystallised zircon. (a) All monazite analyses for the garnet–biotite gneiss. (b) All monazite analyses for the transition zone with the weighted mean age of monazite cores. (c) All monazite analyses for the charnockite. (d) All monazite analyses for the metapelitic gneiss with a few inherited monazite defining a discordia. The lower intercept of this discordant array is based on the onset of high-temperature conditions using the oldest metamorphic monazite spots and should not be interpreted as a true metamorphic age. (e) Younger population of monazite analyses from the metapelitic gneiss. (f) All monazite analyses for the pegmatite with the weighted mean age of the recrystallised zones. (g) All zircon analyses for the garnet–biotite gneiss with a few inherited zircon defining a discordia. The lower intercept of this discordant array is a mean age of the complete range of rim ages. (h) All zircon core and rim analyses for the charnockite with discordia through discordant inherited zircon. Lower intercept of this discordant array is based on the onset of high-temperature conditions using the oldest rims and should not be interpreted as a true metamorphic age. (i) All analyses of the 'soccerball' zircon from the charnockite with weighted mean age of all analyses. (j) All zircon analyses for the metapelitic gneiss with weighted mean age of all analyses.

should not be interpreted as a true metamorphic age. The majority of ages are younger than c. 590 Ma and plot close to the concordia line (Fig. 6d, e). The recrystallised zones yielded a range of $^{207}Pb/^{235}U$ ages from 595 ± 6 to 513 ± 7 Ma (n=15) and Th/U ratios of 6.2–47.8.

6.2.5 Pegmatite

A total of seventeen analyses were conducted on monazite from sample I11-006V. The cores of nine grains gave a range of $^{207}Pb/^{235}U$ spot ages from 586 ± 12 to 510 ± 9 Ma (n=14) and Th/U ratios of 11.0–30.3. The low BSE response outer recrystallised zones yielded a younger concordant population with a weighted mean $^{207}Pb/^{235}U$ age of 512 ± 10 Ma (MSWD=1.5, n=3) and Th/U ratios of 5.5–17.1 (Fig. 6f).

6.3 Zircon SHRIMP U–Pb dating

Zircon was analysed within grain mounts except for the metapelitic gneiss sample, which was analysed in thin section. Complete data tables for zircon U–Pb analyses can be found in supplementary data Table S2.

6.3.1 Garnet-biotite gneiss

A total of eleven zircon U–Pb analyses were performed on the garnet–biotite gneiss (I11-004K). Two oscillatory cores were analysed with ages falling along a discordia trend (MSWD=2.0, n=11) that has a poorly constrained upper intercept at 2015 ± 140 Ma and a lower intercept of 513 ± 20 Ma, a mean age of the range of rim analyses (Fig. 6g). The rims yielded a range of $^{206}Pb/^{238}U$ spot ages from 538 ± 11 to 492 ± 6 Ma (n=9).

6.3.2 Charnockite

Twenty-nine U–Pb analyses were performed on zircon from the charnockite (I11-008C). The oscillatory zoned cores fall along a discordia with a poorly defined upper intercept of 2238 ± 110 Ma and a lower intercept 572 ± 23 Ma (MSWD=0.43, n=5; the lower intercept is based on the onset of high-temperature conditions using the oldest rims and should not be interpreted as a true metamorphic age) (Fig. 6h). The rims yielded a range of $^{206}Pb/^{238}U$ spot ages from 589 ± 23 Ma to 496 ± 6 (n=22). Zircon from this sample with a 'soccer-ball' morphology yielded a concordant population with a weighted mean $^{206}Pb/^{238}U$ age of 563 ± 14 Ma (MSWD=1.7, n=5) (Fig. 6i).

6.3.3 Metapelitic gneiss

Five U–Pb analyses were performed in thin section on zircon from the metapelitic gneiss (TB-14-025). This number was limited by the very low abundance of zircon and by cracks that left only a small portion of each grain available for analysis. Zircon grains were contained in quartz and K-feldspar and adjacent to ilmenite, biotite and sillimanite. No relationship was found between the textural location of accessory phases and their respective ages. The rim and recrystallised areas yielded a single concordant age population with a weighted mean $^{206}Pb/^{238}U$ age of 552 ± 17 Ma (MSWD=0.38, n=5) (Fig. 6j).

6.4 Rare Earth Element mineral chemistry

Key REE concentrations and ratios for monazite, zircon and garnet have been summarised in Table 2. A complete table of analysed trace elements for these phases can be found in supplementary data Tables S3, S4 and S5 respectively.

6.4.1 Monazite

Garnet–biotite gneiss (I11-004K). The cores and recrystallised zones have similar negative M–HREE slopes (Yb_N/Gd_N of 0.001–0.008 and 0.001–0.004 respectively) but with a relative HREE enrichment of almost one order of magnitude more in the most of the cores (Lu_N = 75–146 ppm/chondrite, n=8) compared to the recrystallised zones (Lu_N = 13–59 ppm/chondrite, n=13) (Fig. 7a). A few cores have HREE concentrations similar to the recrystallised zones (Lu_N = 16–30 ppm/chondrite, n=4). Some of the cores have less pronounced Eu anomalies than the recrystallised zones with Eu/Eu* values of 0.002–0.006 and 0.002–0.004, respectively.

Transition zone (I11-004C). Monazite from the transition zone sample shows similar M–HREE negative slopes for cores and recrystallised zones with Yb_N/Gd_N values of 0.001–0.002 and 0.0004–0.002 respectively. The recrystallised zones are relatively more depleted in the M–HREE (Lu_N = 8–57 ppm/chondrite, n=21) compared to the cores (Lu_N = 62–82 ppm/chondrite, n=9). One core had similar HREE concentration to recrystallised zones (21 ppm/chondrite). The Eu anomaly is the same from core to recrystallised zones with Eu/Eu* values of 0.001–0.004 (Fig. 7b).

Charnockite (I11-008C). Monazite from the charnockite shows no internal variation and has a M–HREE negative slope with Yb_N/Gd_N of 0.001 and Eu/Eu* of 0.002 (Fig. 7c).

Metapelitic gneiss (TB-14-025). Monazite cores from the metapelitic gneiss have a negative M–HREE slope (Yb_N/Gd_N = 0.0003–0.026). Those cores that preserved old discordant U–Pb ages have relatively high HREE concentrations (Lu_N= 778–942 ppm/chondrite, n=2) that are higher than those of recrystallised zones, while other cores have lower concentrations (Lu_N = 5–425 ppm/chondrite, n=10) comparable to those in the recrystallised zones (Lu_N = 3–253 ppm/chondrite, n=9) (Fig. 7d). The recrystallised zones also have a negative M–HREE slope (Yb_N/Gd_N = 0.0002–0.007) and a large spread of HREE concentrations, although the majority are lower than those of core analyses (Lu_N = 3–7 ppm/chondrite, n=6). Some of the cores preserve less pronounced negative Eu anomalies than the recrystallised zones with Eu/Eu* values of 0.002–0.075 and 0.002–0.034 respectively.

Pegmatite (I11-006V). The cores and recrystallised zones both show a negative M–HREE slope with Yb_N/Gd_N = 0.004–0.006 and 0.004–0.005 respectively (Fig. 7e). The cores are slightly more enriched in HREE than the recrystallised zones. The Eu anomaly is the same for the cores and recrystallised zones with Eu/Eu* values of 0.003–0.005 and 0.004–0.005 respectively.

6.4.2 Zircon

Garnet–biotite gneiss (I11-004K). Two distinct HREE patterns are present. Oscillatory-zoned cores show a steep positive M–HREE slope with Yb_N/Gd_N = 8–16 (Fig. 7f). These cores have a less pronounced negative Eu anomaly (Eu/Eu*= 0.70–0.97). Zircon rims show a flat HREE pattern (Yb_N/Gd_N = 0.7–1.3) on a chondrite-normalised plot. The rims exhibit a more pronounced negative Eu anomaly (Eu/Eu*= 0.03–0.38).

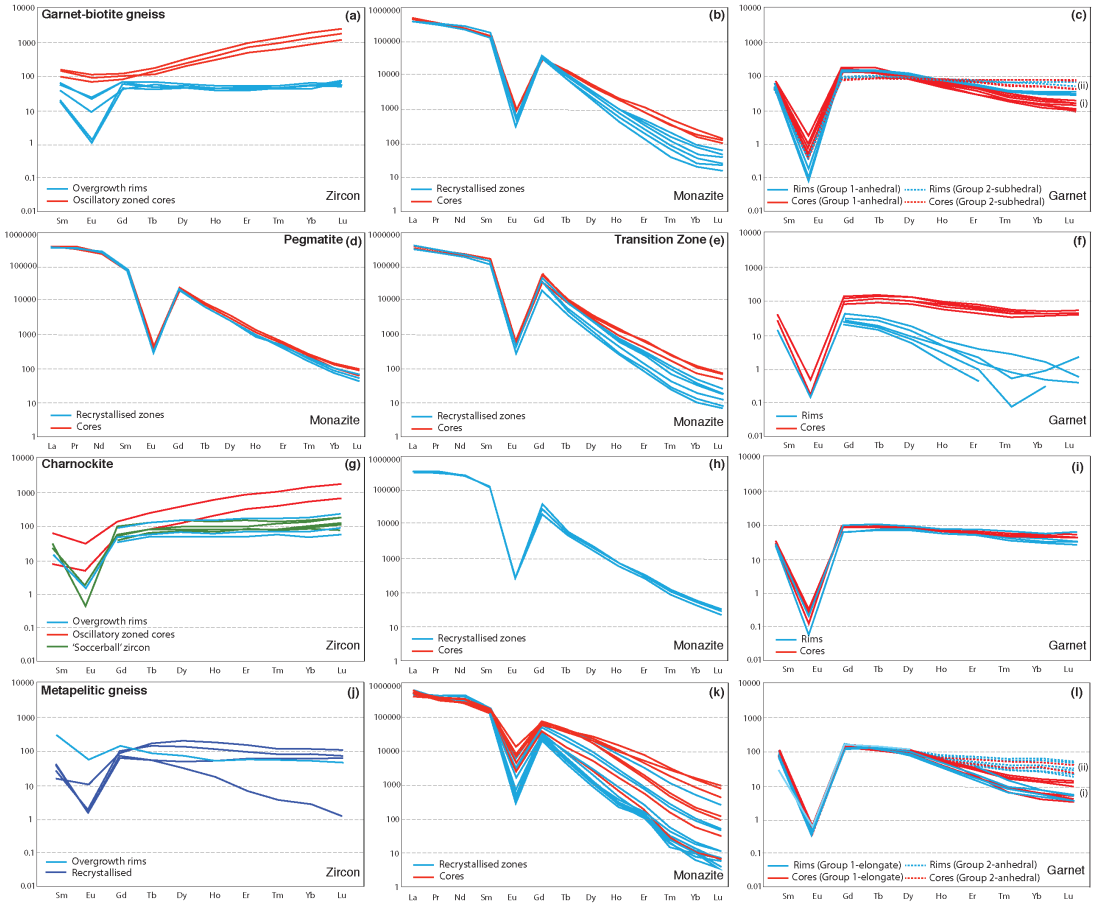

Fig. 7: Representative zircon, monazite and garnet REE analyses for samples in this study. Colours indicate textural location the analysis (see online version): red- core; light blue- rim (zircon) or recrystallised zones (monazite); green- Soccer ball zircon; dark blue- recrystallised zircon. (a) Garnet–biotite gneiss, monazite cores show little variation except for a few with low HREE compared to the recrystallised zones with lower HREE concentrations and almost an order of magnitude of variation. (b) Transition zone, monazite shows similar separation of cores and recrystallised zones to the garnet-biotite gneiss. (c) Charnockite, monazite recrystallised zones showing no variation in HREE. (d) Metapelitic gneiss, the monazite recrystallised zones mainly cluster at low HREE concentrations with a few grains with higher concentrations of HREE. The monazite cores show a high degree of scatter to the HREE and a range of Eu anomalies. (e) Pegmatite, monazite shows little differentiation between cores and recrystallised zones. (f) Garnet–biotite gneiss, zircon cores show a positive M–HREE slope with a flat M–HREE slope to the rims. (g) Charnockite, positive M–HREE slope to the cores with a less positive M–HREE slope to the rims and the soccer ball zircon. (h) Metapelitic gneiss, recrystallised zircon shows near flat M–HREE slope with some scatter, except one grain with a negative HREE slope. The zircon rim shows a near flat M–HREE slope. (i) Garnet–biotite gneiss, type-1 garnet (solid lines) show a slightly negative M–HREE slope for both cores and rims with slightly enriched rims. Type-2 garnet (dashed lines) show flat M–HREE slopes for both cores and rims. (j) Transition zone, garnet shows scatter and reduced concentration of HREE to the rims with an almost flat M–HREE slopes and little variation to the HREE concentration of the cores. (k) Charnockite, garnet from the charnockite shows a near flat M–HREE slope for the cores and rims with no separation. (l) Metapelitic gneiss, type-1 garnet (solid lines) show a negative M–HREE slope with slightly enriched cores and minor scatter to the rims. Type-2 garnet (dashed lines) show almost flat M–HREE slope with some limited scatter to cores and rims.

Monazite

Sample	Textural position	Y (ppm)	Ca (ppm)	Si (ppm)	Th (ppm)	U (ppm)	Yb/Gd	Eu/Eu*
Garnet–biotite gneiss	Core	548–4140	6630–10890	BDL–6710	91100–159800	9270–15870	0.001–0.008	0.002–0.006
I11-004K	Recrystallised zone	473–1370	10180–12240	4200–17100	146300–226400	5730–14900	0.001–0.004	0.002–0.004
Transition zone	Core	2222–3643	6690–9100	210–1710	91400–133800	8310–11340	0.001–0.002	0.001–0.004
I11-004C	Recrystallised zone	337–2695	6320–10410	1200–5020	115000–252700	3990–8510	0.0004–0.002	0.001–0.004
Charnockite	Recrystallised zone	1101–1640	1880–13390	98–2880	23200–279600	4390–4890	0.001	0.002
I11-008C								
Metapelitic gneiss	Core	346–19900	2860–11200	BDL–16500	32410–120100	2890–10480	0.0003–0.026	0.002–0.075
TB-14-025	Recrystallised zone	287–11260	6010–9970	2100–24300	64500–201900	1682–8560	0.0002–0.007	0.002–0.034
Pegmatite	Core	1214–1890	7170–14400	BDL–17100	97700–183900	10970–40400	0.004–0.006	0.003–0.005
I11-006V	Recrystallised zone	1250–1363	4520–9600	BDL–8300	46900–151200	11810–17500	0.004–0.005	0.004–0.005

Zircon

Sample	Textural position	Y (ppm)	Th/U	Yb/Gd	Eu/Eu*
Garnet–biotite gneiss	Core	816–1450	0.03–0.075	8.21–16.41	0.97–0.70
I11-004K	Rim	98–130	0.04–0.13	0.74–1.28	0.03–0.38
Charnockite	Core	115–980	0.11–0.31	11.70–14.26	0.13–0.28
I11-008C	Rim	414–1309	0.07–0.23	1.40–9.69	0.004–0.06
	'Soccerball' zircon	124–178	0.07–0.09	2.09–2.63	All Eu values BDL
Metapelitic gneiss	Rim	138	0.125	0.39	0.29
TB-14-025	Recrystallised	37–326	0.012–0.24	0.06–1.28	0.04–0.25

Garnet

Sample	Textural position	Y (ppm)	Yb/Gd	Eu/Eu*
Garnet–biotite gneiss	Type 1 - Core	121–141	0.53–0.91	0.001–0.002
I11-004K	Type 1 - Rim	117–141	0.58–0.84	0.005
	Type 2 - Core	79–117	0.06–0.12	0.001–0.010
	Type 2 - Rim	103–126	0.17–0.23	0.001–0.004
Transition zone	Core	94–150	0.31–0.44	0.002–0.005
I11-004C	Rim	4–13	0.012–0.038	0.005
Charnockite	Core	106–123	0.43–1.19	0.002–0.006
I11-008C	Rim	94–122	0.44–1.35	0.001–0.005
Metapelitic gneiss	Type 1 - Core	53–84	0.042–0.13	0.005–0.008
TB-14-025	Type 1 - Rim	56–75	0.043–0.091	0.005–0.011
	Type 2 - Core	72–100	0.175–0.363	0.005–0.007
	Type 2 - Rim	78–121	0.173–0.457	0.004–0.006

BDL- Below detection limit

Table 2: Summary table of compositional ranges of LA–ICP–MS REE and other elements from monazite, zircon and garnet. Values are in ppm for singular elements or ppm/chondrite for REE. BDL, below detection limit.

Charnockite (I11-008C). Zircon in the charnockite displays two distinct HREE patterns. Oscillatory-zoned cores have a positive M–HREE slope (Yb_N/Gd_N = 11.7–14.26), and a small Eu anomaly (Eu/Eu*= 0.13–0.28) (Fig. 7g). Zircon rims show a less positive M–HREE slope (Yb_N/Gd_N = 1.4–9.69) and have similar to more pronounced Eu anomalies than the cores (Eu/Eu*= 0.004–0.060). Soccer ball zircon displays a similar M–HREE slope (Yb_N/Gd_N = 2.09–2.63) and concentrations to the zircon rims (Fig. 7g) with all Eu values below detection limits.

Metapelitic gneiss (TB-14-025). Recrystallised zircons in the metapelite show a near flat M–HREE slope, except for one analysis (PA1-1.1) having a negative M–HREE slope (Yb_N/Gd_N = 0.06–1.28). This analysis also has lower Y concentration (37.5 ppm) compared to the other zircon in this sample. These zircons all have negative Eu anomalies (Eu/Eu* = 0.04–0.25) (Fig. 7h). The one rim analysed has a similar M–HREE slope to the recrystallised zircon (Yb_N/Gd_N = 0.39) and a similar Eu anomaly compared to the recrystallised zircon (Eu/Eu* =

0.29).

6.4.3 Garnet

Garnet–biotite gneiss (I11-004K). Type-1 garnet cores show a negative M–HREE slope (Yb_N/Gd_N = 0.53–0.91) on a chondrite-normalised plot with Eu anomalies yielding Eu/Eu* values = (0.001–0.002) (Fig. 7i). The rims show a similar M–HREE slope on a chondrite-normalised plot (Yb_N/Gd_N = 0.58–0.84), with a less pronounced Eu anomaly (Eu/Eu* = 0.005) and relative enrichment in M–HREE compared to the cores (Fig 7i).

Type-2 garnet shows limited core to rim variation and has a near flat M–HREE slope on a chondrite-normalised plot with Yb_N/Gd_N values of 0.06–0.12 for cores and slightly steeper slopes of 0.17–0.23 for the rims. The Eu anomaly is in the cores covers a range of values that includes the rims with Eu/Eu* values of 0.0005–0.010 in the cores and 0.001–0.004 in the rims (Fig 7i).

Transition zone (I11-004C). Garnet cores display a flat M–HREE slope on a chondrite-normalised plot (Yb_N/Gd_N = 0.31–0.44) with the rims showing a negative M–HREE slope (Yb_N/Gd_N = 0.012–0.038) (Fig. 7j). There is more variation in Eu anomaly in the cores compared to the rims with Eu/Eu* values of 0.002–0.005 and 0.005 respectively.

Charnockite (I11-008C). The cores and rims of the garnets from the charnockite show slightly negative to flat M–HREE slopes on a chondrite-normalised plot (Yb_N/Gd_N = 0.43–1.19 and 0.44–1.35 respectively) and Eu/Eu* of 0.002–0.006 for cores and 0.001–0.005 for rims (Fig. 7k).

Metapelitic gneiss (TB-14-025). Type-1 garnet cores and rims show a negative M–HREE slope (Yb_N/Gd_N = 0.042–0.13 and 0.043–0.091 respectively) with the majority of core analyses at higher HREE concentrations (Fig. 7l). The cores show a higher degree of scatter in the HREE than the rims. There is little variation in Eu anomaly between cores and rims in these garnets (Eu/Eu* values of 0.005–0.008 and 0.005–0.011 respectively).

Type-2 garnet core and rims show similar near flat to slightly negative M–HREE slopes with Yb_N/Gd_N values of 0.175–0.363 and 0.173–0.457 respectively (Fig. 7l). Both cores and rims show a spread in HREE concentrations but the rims show more scatter. There is little variation in Eu anomaly between the cores and rims in these garnets (Eu/Eu* = 0.005–0.007 and 0.004–0.006 respectively).

7. DISCUSSION

7.1 Pressure-temperature evolution

As all of the studied samples were collected from the same locality and no major structural discontinuities were observed that could have led to the juxtaposition of units with different tectonic histories, we assume all rocks share a common *P*–*T*–*t* history. We have modelled this history using pseudosections calculated in the NCKFMASHTO system, which can successfully account for all observed peak minerals with the exception of biotite and spinel. Small quantities of biotite are interpreted as part of the peak assemblage in both the metapelitic gneiss and the garnet–biotite gneiss (Fig. 3a, i), but biotite is likely to be stable at temperatures higher than those predicted in the NCKFMASHTO system due to additional components, in particular fluorine, which has been

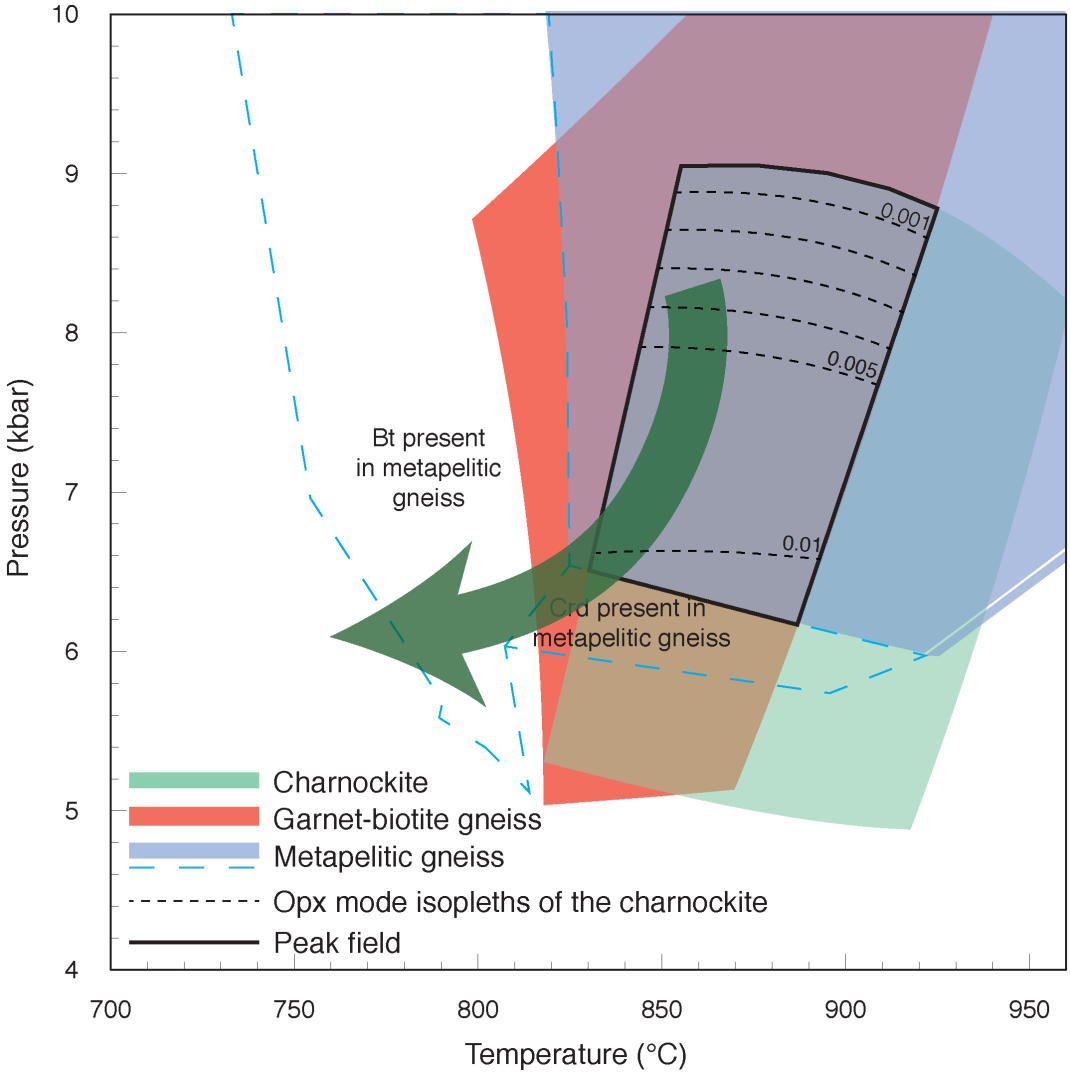

Fig. 8: Summary diagram of *P–T* estimates. Peak fields for each modelled *P–T* pseudosection are overlain to show a common field of peak conditions outlined in black. Mineral isopleths show predicted modal proportions of orthopyroxene in the charnockite composition. Dashed blue lines indicate the possible conditions through which the post peak evolution might have passed based on the growth of retrograde cordierite within the metapelitic gneiss. No prograde evolution is proposed because partial melting and melt segregation mean that the present-day bulk rock compositions are not representative of prograde conditions.

reported in incipient charnockites and associated rock types from southern India (Chacko et al., 1987; Stähle et al., 1987; Nair & Chacko, 2002; Santosh et al., 2003a; Ravindra Kumar, 2004). For this reason, both biotite-bearing and biotite-absent fields have been included in the inferred peak *P–T* conditions for the garnet–biotite and metapelitic gneisses. Spinel within the metapelitic gneiss is only stable within only the quartz-free melanosome and has been excluded from the inferred peak assemblage in the modelled pseudosection as this was calculated for a bulk composition that contains both melanosome and leucosome causing quartz to be predicted across the whole modelled interval.

This pseudosection modelling predicts that peak assemblages in the three main rock types at Kakkod have *P–T* stability fields of 4.6 to >10 kbar and 790–940 °C (garnet–biotite gneiss, Fig.

5a), 4.9–9.0 kbar and 820–960 °C (garnet-bearing charnockite, Fig. 5b) and 5.6 to >10 kbar, 740 °C to > 960 °C (metapelitic gneiss Fig. 5c). While these fields are different, there is a region of overlap (highlighted in Fig. 8) suggesting peak conditions of 6–9 kbar 830–925 °C. Such conditions are consistent with many peak *P–T* estimates from elsewhere in the Trivandrum block (Chacko et al., 1987; Santosh, 1987; Nandakumar & Harley, 2000; Pattison et al., 2003; Collins et al., 2014). On this basis we infer that mineral assemblages in the garnet–biotite gneiss, charnockite and metapelitic gneiss were stabilised at similar *P–T* conditions.

The metapelitic gneiss is best suited to constrain the *P−T* path at Kakkod as it contains a relatively low-variance mineral assemblage compared to the other samples and is a fairly typical (albeit residual) aluminous metapelite. However, due to the effects of melt loss, the calculated pseudosections based on residual compositions are not suitable for accurately constraining the prograde path (White & Powell, 2002; Diener et al., 2013) and therefore we focus here on the retrograde evolution. The growth of cordierite and biotite in the metapelite is interpreted to record high-temperature retrograde decompression to around 6.5–5.5 kbar followed by cooling (Fig. 8). The lack of orthopyroxene in this sample suggests that pressures did not drop below ~ 5 kbar (Fig. 5c), and this is also consistent with the lack of orthopyroxene in the garnet–biotite gneiss (Fig.5a). This evolution is likely to be part of a clockwise *P–T* path and is similar to many paths reported from other areas in southern India (Nandakumar & Harley, 2000; Shabeer et al., 2002; Cenki et al., 2004; Collins et al., 2014; Clark et al., 2015; Johnson et al., 2015). It is important to note that all three samples can be modelled with a single *P−T* path, although the *P–T* path suggested in Figure 8, which shows decompression from ~ 8 to ~ 6 kbar, is not a unique solution (for example a path with a smaller pressure decrease from ~ 7 to 6 kbar could also explain the observed assemblages).

Our findings that mineral assemblages in all three main rock types at Kakkod are stable at similar *P–T* conditions conflict with the conclusions of Endo et al. (2013), who argued that the metapelitic gneiss preserves evidence for higher-grade conditions than the garnet–biotite gneiss and charnockite. However, while Endo et al. (2013) used *P–T* pseudosections to derive estimates for peak metamorphic conditions in garnet–biotite gneiss and charnockite, they were unable to use this approach for the metapelite because this rock type was not exposed in the quarry that they studied. Instead they relied on the earlier study of Tadokoro et al. (2008) who used Zn-in-spinel barometry and feldspar-solvus thermometry to propose peak *P–T* conditions of 10–12 kbar and 900–1000°C for the Trivandrum Block metapelite. Tadokoro et al. (2008) provided only very brief descriptions of mineral-chemical relationships in their samples, and little information on how they selected mineral compositions for conventional thermobarometry, which makes it difficult to evaluate their *P–T* estimates. However, our results allow for a simpler and more consistent interpretation of metamorphic *P–T* conditions in the Trivandrum Block, and we therefore prefer a model in which all rocks underwent peak metamorphism and a high-*T* decompression within a pressure interval of 9–6 kbar.

7.2 A case for peak-metamorphic charnockite formation

As highlighted above, the matrix peak charnockite assemblage containing liquid, garnet, orthopyroxene, ilmenite, K-feldspar, plagioclase and quartz is predicted to be stable at conditions of 820–960 °C and ~ 4.9–9.0 kbar, and this field overlaps with those inferred for peak metamorphic assemblages in other rock compositions (Fig. 8). Thus it is permissible that the orthopyroxene-bearing charnockite assemblage formed at the same time as peak assemblages in the host garnet–biotite gneiss. A similar conclusion was reached by Endo et al. (2013) even though they assumed different peak conditions for the metapelite (as discussed above). Although charnockite stabilisation at the metamorphic peak is our preferred interpretation, the microstructural relationships are ambiguous and orthopyroxene may also have grown during high-temperature retrograde decompression. Mineral isopleths of orthopyroxene (Fig. 8) permit either of these scenarios, and the very low abundance of orthopyroxene in these felsic bulk compositions leads to large uncertainties in both observed and predicted mineral modes.

The modelled stability of orthopyroxene differs significantly between the charnockite and garnet–biotite gneiss (maximum pressure limits of 9 and 5 kbar, respectively) and this must reflect a difference in bulk composition between these two rock types. However, these two compositions are very similar (Table 1), making it difficult to precisely determine the components that are controlling orthopyroxene stability at Kakkod. Previous comparisons of incipient charnockite and host garnet–biotite gneiss in the Trivandrum Block have identified small differences in the concentrations of components such as SiO_2, K_2O, Na_2O, MgO and FeO/Fe_2O_3, but there seems little consistency in the magnitude of these variations or even in which rock has the higher and which the lower concentration (e.g. Hansen et al., 1987; Raith & Srikantappa, 1993; Endo et al., 2013). A recent study by Endo et al. (2012) of similar rocks further north in the Madurai Block used pseudosection modelling to argue that orthopyroxene in charnockite patches was stabilised by less-oxidised conditions; our study also indicates that ferric iron exhibits a strong control on orthopyroxene stability. In particular, a $P–M_{Fe2O3}$ pseudosection calculated for the Kakkod charnockite sample indicates that orthopyroxene is stabilised to higher pressures with a small reduction in the ferric/ferrous ratio (Fig. S2). However, our final *P–T* pseudosections (Fig. 5) were calculated for identical Fe_2O_3 concentrations in the charnockite and garnet–biotite gneiss, and marginally higher $Fe_2O_3/(Fe_2O_3+FeO)$ values in the charnockite, indicating that ferric iron is not responsible for the differences in orthopyroxene stability in our models.

The exact compositional variables that control the stability of orthopyroxene between the two rock compositions at Kakkod is not yet known, although we emphasize that the very low abundance of mafic minerals in these highly felsic bulk rock compositions means that their stability will be sensitive to small variations in bulk chemistry. Similarly, it is unclear what might have caused these local compositional variations, with insufficient information available to determine whether they were inherited from the protolith or a result of syn-metamorphic fluid flow.

7.3 Timing of peak metamorphism at Kakkod quarry

Zircons from the garnet–biotite gneiss and charnockite show oscillatory-zoned cores (Fig. 4b, f) and are interpreted to be inherited from the protolith to the garnet–biotite gneiss. The ages of these inherited cores fall within known ages of inherited Palaeoproterozoic igneous zircons for the Trivandrum Block (Fig. 6b, e) (Collins et al., 2007b; Collins et al., 2014) and show steep M–HREE slopes indicative of growth without garnet (Fig. 7f, g) (Hoskin & Schaltegger, 2003). A number of monazites from the metapelitic gneiss (Fig. 6g) also show older discordant ages (> c. 650 Ma) and again fall along a discordia with a Palaeoproterozoic upper intercept. These are likewise interpreted to be inherited grains that have undergone Pb-loss during the Late Neoproterozoic - Cambrian metamorphic event, and they have the most enriched HREE of any of monazite analyses.

The onset of high-grade metamorphism at Kakkod is interpreted to have occurred at c. 590 Ma based on the oldest metamorphic monazite ages (Fig. 9), an age that is consistent with other studies from the Trivandrum and Nagercoil Blocks (Taylor et al., 2014, Johnson et al., 2015). Monazite cores in the garnet–biotite gneiss, transition zone and metapelitic gneiss are all enriched in HREE suggesting they grew before or during the appearance of a HREE- enriched phase (i.e. c. 590 Ma) (Fig. 7a, b, c, d) (Hermann & Rubatto, 2003; Rubatto et al., 2006). This HREE-enriched phase is assumed to be garnet, which is present in all samples except the pegmatite. The monazite from the metapelitic gneiss has M–HREE concentrations an order of magnitude larger than the other samples (due to influence of HREE-enriched inherited monazite) and also has a greater spread of HREE contents (Fig. 7d). This scatter in HREE for the non-inherited monazite in the metapelitic gneiss and the few low HREE cores in the garnet–biotite gneiss and the transition zone is interpreted to represent the increasing influence of a HREE phase (i.e. garnet growth) during monazite crystallisation.

The type-1 garnets in both garnet–biotite gneiss and metapelitic gneiss are interpreted to be prograde with slightly negative M–HREE slopes (Hermann & Rubatto, 2003). The type-2 garnets from the garnet–biotite and metapelitic gneiss as well as the transition zone and charnockite are interpreted to be peritectic and grew in the presence of zircon based on their near flat M–HREE slope (Hokada & Harley, 2004). In both the garnet–biotite gneiss and the metapelitic gneiss the rims of type-1 garnet were likely modified by the influx of REE-enriched partial melt, resulting in rim compositions closer to type-2. The population of equant 'soccer ball' metamorphic zircon in the charnockite is interpreted to have precipitated as high–*T* subsolidus growth (Schaltegger et al., 1999; Harley et al., 2007) at 562 ± 22 Ma (Fig. 6f), rather than during post-peak melt crystallisation due to their age and sector zoned 'soccer ball' texture (Vavra et al., 1996; Schaltegger et al., 1999; Kelly & Harley, 2005). The 'soccer ball' zircon is inferred to have equilibrated with the flat-REE type-2 garnets is inferred to have equilibrated with flat-REE garnet in the charnockite, which is equivalent to type-2 garnet in other rock types. This is corroborated by the near 1:1 D_{REE} (zircon/garnet) ratio between garnet and the 'soccer ball'

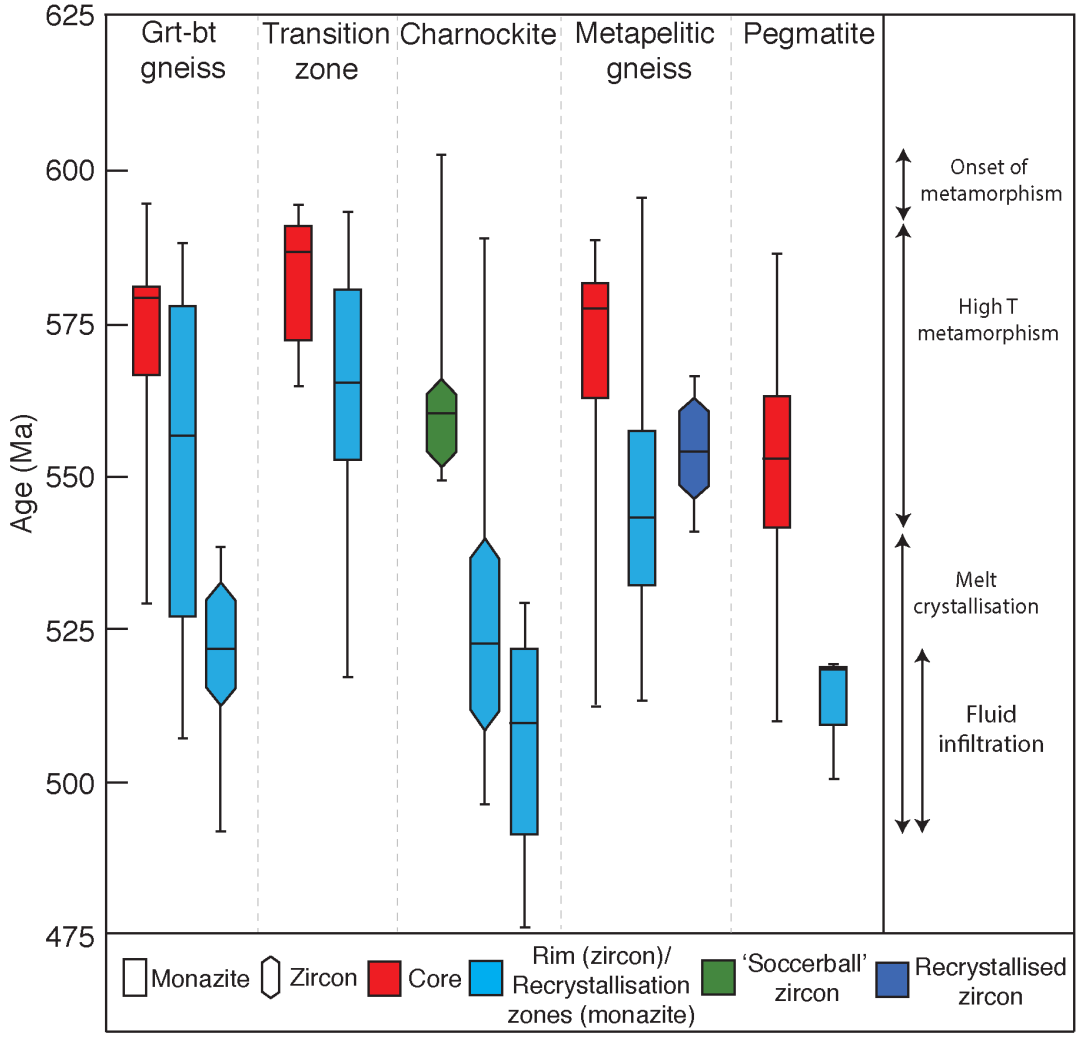

Fig. 9: Summary diagram of all monazite and zircon U–Pb geochronological data for Kakkod (excluding analyses of older inherited grains). Data are shown as box and whisker plots to illustrate the age spread of each analysis type. Box shape indicates the mineral (monazite versus zircon), while colours indicate the textural location of the analyses (see online version): red- core; light blue- rim (zircon) or recrystallised zones(monazite); green- Soccer ball zircon; dark blue- recrystallised zircon. Monazite is given as $^{207}Pb/^{235}U$ ages. Zircon is given as $^{206}Pb/^{238}U$ ages. The box represents the interquartile range (the middle 50% (median- horizontal bar) of the data from the 25th to 75th percentile), the whiskers represent the minimum and maximum ages within 1.5*interquartile range with outliers marked with an 'X'. Some of overlap between the age ranges is likely a representation of the analytical uncertainty of the data. Major events interpreted from geochronology are outlined by arrowed intervals based on quartile ranges and ignoring outliers.

zircon (Taylor et al., 2015). The garnet rims from the transition zone show HREE concentrations nearly an order of magnitude lower than any of the other samples. These low HREE concentrations are interpreted to reflect the retrograde reaction observed at garnet margins to an intergrowth of biotite and quartz, which is not seen in the other samples. The trend of increasing negative Eu anomaly from core to rim in zircon (garnet–biotite gneiss and charnockite), monazite (garnet–biotite gneiss, metapelitic gneiss) and garnet (garnet–biotite gneiss) could indicate the increasing crystallisation of plagioclase likely from partial melt whilst zircon, monazite and garnet was

recrystallising/growing or the presence of plagioclase before recrystallisation, sequestering much of the Eu (Johnson et al., 2015). Some samples show little to no differentiation in Eu anomalies between cores and rims.

Rims on inherited zircon from the charnockite contain a number of different ages that potentially relate to (1) partial to full recrystallisation during prograde metamorphism and (2) neocrystallisation during subsequent melt crystallisation (Vavra et al., 1996; Schaltegger et al., 1999; Kelly & Harley, 2005). The onset of melt crystallisation is interpreted to have occurred at c. 540 Ma based on the upper quartile distribution of zircon rim ages from the charnockite (Fig. 9). The majority of zircon crystallised between ~ 540–510 Ma matching that found in other studies of the Trivandrum Block and adjacent areas (Harley & Nandakumar, 2014; Taylor et al., 2014; Johnson et al., 2015). The ages calculated for the monazite cores and metamorphic zircon rims define a window of prograde to peak metamorphism of ~ 50 Myr from the onset at 590 Ma to 540 Ma, followed by a further 30 Myr during which melt crystallised (Fig. 9).

The zircon from the metapelitic gneiss shows remnants of oscillatory zoning that has become diffuse through recrystallisation (Hoskin & Black, 2000; Wang et al., 2014). Unlike similar zircon from the garnet–biotite gneiss and charnockite with partly reset pre-metamorphic ages and steep positive M–HREE slopes, this zircon from the metapelitic gneiss gives a concordant c. 550 Ma metamorphic age and mostly has flat HREE patterns interpreted as a result of recrystallisation and growth in the presence of garnet (Fig. 7h). The one analysis of recrystallised zircon with low HREE also has the youngest spot age and is interpreted to represent increasing recrystallisation with age. Metamorphic zircon rims in all samples are likely a result of post-peak melt crystallization (Roberts & Finger, 1997; Kelsey et al., 2008). Monazite cores from the pegmatite are interpreted to be inherited from the garnet–biotite gneiss with ages ranging from c. 580–512 Ma (Fig. 9). REE in the pegmatite monazite cores show similar HREE concentrations and M–HREE slope to monazites in the garnet–biotite gneiss (Fig. 7e). The ages from the recrystallised areas (weighted mean $^{207}Pb/^{235}U$ age 512 ± 10 Ma) are interpreted to represent the emplacement of the pegmatite (Fig. 9).

7.4 Age of post-peak fluid event

Lobate high-Th recrystallised zones in monazite grains (Fig. 4; Table 2) are interpreted to be the result of coupled dissolution-reprecipitation. These textures are similar to those observed in previous experimental and empirical studies (Harlov & Hetherington, 2010; Harlov et al., 2011; Williams et al., 2011; Kelly et al., 2012), and based on comparisons with the experiments Taylor et al. (2014) interpreted the same features in incipient charnockites at the nearby locality of Kottavattom to have formed during post-peak influx of hydrous alkali-rich fluid.

Monazite ages from the Kakkod samples show variable amounts of resetting (Pb-loss) with some grains showing distinct sections (lobate dissolution-reprecipitation structures) that are variably reset, and others with no internal structures at all that are fully reset, recording the

youngest ages of any of the samples. The effects of incomplete Pb-loss manifests itself as the presence of discordant monazite ages within the metapelitic gneiss (Fig. 6g) and the large spread of ages along concordia to a younger age. Similar manifestations of Pb-loss can occur in zircon from prolonged high–T localities like the Rayner Complex in Antarctica (Halpin et al., 2012). This spread is particularly well developed in the monazite analyses from the garnet–biotite gneiss and metapelitic gneiss (Fig. 6a, d, e). This spread along concordia records a range of ages from c. 590 Ma down to around c. 490 Ma. Samples that record the large spread in ages all contain fluid-related coupled dissolution-reprecipitation textures in the monazite (Fig. 4a, d, e). From our data the transition zone monazite appears to have seen the least overprint with limited smearing along concordia, and also shows coupled dissolution-reprecipitation textures. Monazite from the charnockite has no internal structures and recorded the youngest ages of any of the samples. We suggest that this represents complete resetting of the monazite in the charnockite, with partially reset monazite from the other samples smearing down concordia towards this same age. The significance of this apparently greater degree of fluid-driven monazite resetting in the charnockite is unclear, not least because only two monazite grains were found in the single sample of charnockite analysed in this study, and more analyses of more samples would be needed to establish if the charnockite monazite truly saw more resetting than monazite in other rock types.

The monazite recrystallised zones in the garnet–biotite gneiss, metapelitic gneiss and transition zone show large variations in HREE, with consistently lower concentrations compared to their respective cores (Fig. 7a, b, d). This is interpreted to represent the modification of monazite in the presence of garnet, after this latter phase had sequestered HREE.

Ages of c. 525–490 Ma for the monazite population in the charnockite and the youngest monazite recrystallised zones from the transition zone, garnet–biotite gneiss, and metapelitic gneiss are interpreted as the time of fluid infiltration and coupled dissolution-reprecipitation of monazite (Fig. 9). Based on the overlap between the inferred ages of melt crystallisation (~ 540–510 Ma) and hydrous fluid influx (~ 525–490 Ma), and the presence of the pegmatite dyke that cuts across the garnet–biotite gneiss, we suggest that the fluids were sourced from a local melt system, perhaps at deeper crustal levels, that crystallised slightly later than melt in the Kakkod samples. This is similar to the source of fluids proposed by Taylor et al. (2014). The presence of the coupled dissolution-reprecipitation textures within monazite from the garnet–biotite gneiss, transition zone, metapelitic gneiss as well as the homogenous charnockite monazite indicate that fluid influx was pervasive throughout the whole outcrop which reinforces the study by Taylor et al. (2014).

8. CONCLUSIONS

- Phase relationships in all three rock types at Kakkod (garnet–biotite gneiss, charnockite, and metapelitic gneiss) are consistent with peak metamorphic conditions of c. 830–925°C and 6–9 kbar.
- Peak metamorphism was followed by high-temperature decompression best recorded by

retrograde growth of cordierite and/or biotite in the metapelitic gneiss.

- The onset of high-grade metamorphism is dated at c. 590 Ma with melt crystallisation starting at c. 540 Ma. The majority of zircon grew at 540–510 Ma, which is taken as when most of the melt at Kakkod crystallised.
- Orthopyroxene-bearing charnockite assemblages replaced local patches of the garnet–biotite gneiss at or soon after peak metamorphism. They must reflect local compositional heterogeneities in the garnet–biotite gneiss, although we cannot determine if these heterogeneities were inherited from the protolith or introduced by high-temperature fluid influx.
- *T–P–X* sections highlight the sensitivity of orthopyroxene stability in metafelsic rocks to the local oxidation state, but this does not seem to have been the controlling factor in charnockite formation at Kakkod.
- Later lower-temperature fluid influx at c. 525–490 Ma led to coupled dissolution-reprecipitation of monazite and variable resetting of its U−Pb isotope system. Based on comparisons with monazite textures in experiments, we follow Taylor et al. (2014) in suggesting that these fluids were aqueous and perhaps rich in alkalis.
- The presence of coupled dissolution-reprecipitation textures in monazite from all samples at Kakkod indicates that late fluid flux was pervasive throughout the outcrop. It is likely to have driven hydrous retrogression of the charnockite, but played no role in its stabilization.
- The timing of monazite modification at Kakkod is very close to final melt crystallisation ages from this and other localities. This suggests that fluid influx was linked to cooling and solidification of local (and possibly deeper) melt systems, and could be related to the pegmatite dyke at Kakkod with a crystallisation age of ~ 512 Ma.

ACKNOWELDGEMENTS

Zircon and monazite U–Pb analyses were carried out using the SHRIMP II Ion Microprobe at the John de Laeter Centre for Isotope Research, Perth, managed by Allen Kennedy. LA-ICP-MS REE analyses were carried out at the GeoHistory Facility, John de Laeter Centre, Curtin University. Financial support for this project was provided by an ARC DECRA fellowship to CC and ARC Discovery Project Grant DP150102773 to ICWF and CC. We thank J. Halpin, S. Harley and N. Daczko for their thorough reviews and G. Clarke for his editorial handling.

REFERENCES

Anders, E. & Grevesse, N., 1989. Abundances of the elements: meteoric and solar. Geochimica et Cosmochimica Acta, 53, 197–214.

Black, L.P., Kamo, S.L., Allen, C.M. et al., 2003. TEMORA 1: a new zircon standard for Phanerozoic U-Pb geochronology. Chemical Geology, 200, 155–170.

Braun, I., 2006. Pan-African granitic magmatism in the Kerala Khondalite Belt, southern India. Journal of Asian Earth Sciences, 28, 38–45.

Braun, I., Montel, J.-M. & Nicollet, C., 1998. Electron microprobe dating of monazites from high-grade gneisses and pegmatites of the Kerala Khondalite Belt, southern India. Chemical Geology including Isotope Geoscience, 146, 65–68.

Buick, I.S., Clark, C., Rubatto, D., Hermann, J., Pandit, M. & Hand, M., 2010. Constraints on the Proterozoic evolution of the Aravalli-Delhi Orogenic belt (NW India) from monazite geochronology and mineral trace element geochemistry. Lithos, 120, 511–528.

Cenki, B., Braun, I. & Bro€cker, M., 2004. Evolution of the continental crust in the Kerala Khondalite Belt, southern-most India: evidence from Nd isotope mapping, U-Pb and Rb-Sr geochronology. Precambrian Research, 134, 275–292.

Chacko, T., Ravindra Kumar, G.R. & Newton, R.C., 1987. Metamorphic P-T conditions of the Kerala (South India) Khondalite Belt, a granulite facies supracrustal terrain. The Journal of Geology, 95, 343–358.

Chacko, T., Ravindra Kumar, G.R., Meen, J.K. & Rodgers, J.W., 1992. Geochemistry of high-grade supracrustal rocks from the Kerala Khondalite Belt and adjacent massif charnockites, South India. Precambrian Research, 55, 469– 489.

Chacko, T., Lamb, M. & Farquhar, J., 1996. Ultra-high tem- perature metamorphism in the Kerala Khondalite Belt. Gondwana Research Group Memoir, 3, 157–165.

Chetty, T.R.K., Fitzsimons, I.C.W., Brown, L., Dimri, V.P. & Santosh, M., 2006. Crustal structure and tectonic evolution of the Southern Granulite Terrane, India: introduction. Gondwana Research, 10, 3–5.

Clark, C., Collins, A.S., Santosh, M., Taylor, R. & Wade, B.P., 2009a. The P-T–t architecture of a Gondwanan suture: REE, U–Pb and Ti-in-zircon thermometric constraints fromthe Palghat Cauvery shear system, South India. PrecambrianResearch, 174, 129–144.

Clark, C., Collins, A.S., Timms, N.E., Kinny, P., Chetty, T.R.K. & Santosh, M., 2009b. SHRIMP U-Pb age constraints on magmatism and high-grade metamorphism in the Salem Block, southern India. Gondwana Research, 16, 27–36.

Clark, C., Healy, D., Johnson, T. et al., 2015. Hot orogens and supercontinent amalgamation: a Gondwanan example from southern India. Gondwana Research, 28(4), 1310–1328.

Collins, A.S. & Pisarevsky, S.A., 2005. Amalgamating eastern Gondwana: the evolution of the Circum-Indian Orogens. Earth-Science Reviews, 71, 229–270.

Collins, A.S., Clark, C., Sajeev, K., Santosh, M., Kelsey, D.E. & Hand, M., 2007a.Passage through India: the Mozambique Ocean suture, high-pressure granulites and the Palghat-Cauvery shear zone system. Terra Nova, 19, 141– 147.

Collins, A.S., Santosh, M., Braun, I. & Clark, C., 2007b. Age and sedimentary provenance of the Southern Granulites, South India: U-Th-Pb SHRIMP secondary ion mass spectrometry. Precambrian Research, 155, 125–138.

Collins, A.S., Clark, C. & Plavsa, D., 2014. Peninsula India in Gondwana: the tectonothermal evolution of the Southern Granulite Terrain and its Gondwanan counterparts. Gondwana Research, 25(1), 190–203.

Diener, J.F.A. & Powell, R., 2010. Influence of ferric iron on the stability of mineral assemblages. Journal of Metamorphic Geology, 28, 599–613.

Diener, J.F.A., White, R.W., Link, K., Dreyer, T.S. & Mood- ley, A., 2013. Clockwise, low-P metamorphism of the Aus granulite terrain, southern Namibia, during the Mesoproterozoic Namaqua Orogeny. Precambrian Research, 224, 629–652.

Drury, S.A., Harris, N.B.W., Holt, R.W., Reeves-Smith, G.J. & Wightman, R.T., 1984. Precambrian tectonics and crustal evolution in South India. The Journal of Geology, 92, 3–20.

Endo, T., Toshiaki, T., Santosh, M. & Shaji, E., 2012. Phase equilibrium modeling of incipient charnockite formation in NCKFMASHTO and MnNCKFMASHTO systems: a case study from Rajapalaiyam, Madurai Block, southern India. Geoscience Frontiers, 3, 801–812.

Endo, T., Toshiaki, T., Santosh, M., Shimizu, H. & Shaji, E., 2013. Granulite formation in a Gondwana fragment: petrology and mineral equilibrium modeling of incipient charnockite from Mavadi, southern India. Mineralogy and Petrology, 107, 727–738.

Fonarev, V.I., Konilov, A.N. & Santosh, M., 2000. Multistage metamorphic evolution of the Trivandrum Granulite Block, Southern India. Gondwana Research, 3, 293–314.

Fyfe, W.S., 1973. The granulite facies, partial melting and the Archaean crust. Philosophical Transactions of the Royal Society of London. Series A, Mathematical and Physical Sciences, 273, 457–461.

Halpin, J.A., Daczko, N.R., Milan, L.A. & Clarke, G.L., 2012. Decoding near-concordant U-Pb zircon ages spanning several hundred million years: recrystallisation, metamictisation or diffusion? Contributions to Mineralogy and Petrology, 163, 67–85.

Hansen, E.C., Janardhan, A.S., Newton, R.C., Prame, W.K.B.N. & Kumar, G.R.R., 1987. Arrested charnockite formation in southern India and Sri Lanka. Contributions to Mineralogy and Petrology, 96, 225–244.

Harley, S.L. & Nandakumar, V., 2014. Accessory mineral behaviour in granulite migmatites: a case study from the Kerala Khondalite Belt, India. Journal of Petrology, 55, 1965–2002.

Harley, S.L. & Santosh, M., 1995. Wollastonite at Nuliyam, Kerala, souterhn India: a reassessment of CO2-infiltration and charnockite formation at a classic locality Contributions to Mineralogy and Petrology, 120, 83–94.

Harley, S.L., Kelly, N.M. & Mo€ller, A., 2007. Zircon beha- viour and the thermal histories of mountain chains. Elements, 3, 25–30.

Harlov, D.E. & Hetherington, C.J., 2010. Partial high-grade alteration of monazite using alkali-bearing fluids: experiment and nature. American Mineralogist, 95, 1105–1108.

Harlov, D.E., Wirth, R. & Hetherington, C.J., 2011. Fluid-mediate partial alteration in monazite: the role of coupled dissolution-reprecipitation in element redistribution and mass transfer. Contributions to Mineralogy and Petrology, 162, 329–348.

Harris, N.B.W., Santosh, M. & Taylor, P.N., 1994. Crustal evolution in South India: constraints from Nd isotopes. The Journal of Geology, 102, 139–150.

Hermann, J. & Rubatto, D., 2003. Relating zircon and mon- azite domains to garnet growth zones: age and duration of granulite facies metamorphism in the Val Malenco lower crust. Journal of Metamorphic Geology, 21, 833–852.

Hokada, T. & Harley, S.L., 2004. Zircon growth in UHT leu- cosome: constraints from zircon-garnet rare earth elements (REE) relations in Napier Complex, East Antarctica. Journal of Mineralogical and Petrological Sciences, 99, 180–190.

Holland, T.J.B. & Powell, R., 2011. An improved and extended internally consistent thermodynamic dataset for phases of petrological interest, involving a new equation of state for solids. Journal of Metamorphic Geology, 29, 333– 383.

Hoskin, P.W.O. & Black, L.P., 2000. Metamorphic zircon for- mation by solid-state recrystallization of protolith igneous zircon. Journal of Metamorphic Geology, 18, 423–439.

Hoskin, P.W.O. & Schaltegger, U., 2003. The composition of zircon and igneous and metamorphic petrogenesis. Reviews in Mineralogy and Geochemistry, 53, 27–62.

Jackson, D.H. & Santosh, M., 1992. Dehydration reaction and isotope front transport induced by CO2 infiltration at Nuliyam, South India. Journal of Metamorphic Geology, 10, 365–382.

Johnson, T., Clark, C., Taylor, R., Santosh, M. & Collins, A.S., 2015. Prograde and retrograde growth of monazite in migmatites: an example from the Nagercoil Block, southern India. Geoscience Frontiers, 6, 373–387.

Kelly, N.M. & Harley, S.L., 2005. An integrated microtextu- ral and chemical approach to zircon geochronology: refin- ing the Archaean history of the Napier Complex, east Antartica. Contributions to Mineralogy and Petrology, 149, 57–84.

Kelly, N.M., Harley, S.L. & Möller, A., 2012. Complexity in the behavior and recrystallization of monazite during high-T metamorphism and fluid infiltration. Chemical Geology, 322– 323, 192–208.

Kelsey, D.E., Clark, C. & Hand, M., 2008. Thermobarometric modelling of zircon and monazite growth in melt-bearing systems: examples using model metapelitic and metapsam- mitic granulites. Journal of Metamorphic Geology, 26, 199–212.

Kennedy, A.K. & de Laeter, J.R., 1994. The performance characteristics of the WA SHRIMP II ion microprobe. US Geological Survey Circular, 1107, 166.

Kirkland, C.L., Whitehouse, M.J. & Slagstad, T., 2009. Fluid-assisted zircon and monazite growth within a shear zone: a case study from Finnmark, Arctic Norway. Contributions to Mineralogy and Petrology, 158, 637–657.

Korhonen, F.J., Saw, A.K., Clark, C., Brown, M. & Bhat- tacharya, S., 2011. New constraints on UHT metamorphism in the Eastern Ghats Province through the application of phase equilibria modelling and in situ geochronology. Gond- wana Research, 20, 764–781.

Kretz, R., 1983. Symbols for rock-forming minerals. American Mineralogist, 68, 277–279.

Kröner, A., Santosh, M., Hegner, E. et al., 2015. Palaeopro- terozoic ancestry of Pan-African high-grade granitoids in southernmost India: implications for Gondwana reconstructions. Gondwana Research, 27, 1–37.

de Laeter, J.R. & Kennedy, A.K., 1998. A double focussing mass spectrometer for geochronology. International Journal of Mass Spectrometry, 178, 43–50.

Ludwig, K.R., 2003. Isoplot 3.0. A Geochronological Toolkit for Microsoft Excel. Berkeley Geochronological Center Spe- cial Publication, 2, 70.

Ludwig, K.R., 2009. SQUID II. A user's manual. Berkeley Geochronological Center Special Publication, 2, 100.

Morimoto, T., Santosh, M., Tsunogae, T. & Yoshimura, Y., 2004. Spinel+Quartz association from the Kerala Khon- dalites, southern India: evidence for ultra-high temperature metamorphism. Journal of Mineralogical and Petrological Sciences, 99, 257–278.

Nair, R. & Chacko, T., 2002. Fluid-absent melting of high- grade semi-pelites: P-T constraints on orthopyroxene forma- tion and implications for granulite genesis. Journal of Petrology, 43, 2121–2142.

Nandakumar, V. & Harley, S.L., 2000. A reappraisal of the pressure-temperature path of granulites from the Kerala Khondalite Belt, southern India. The Journal of Geology, 108, 687–703.

Newton, R.C., 1989. Metamorphic fluids in the deep crust. Annual Review of Earth and Planetary Sciences, 17, 385–412.

Newton, R.C., 1992. Charnockitic alteration: evidence for CO2 infiltration in granulite facies metamorphism. Journal of Metamorphic Geology, 10, 383–400.

Newton, R.C. & Tsunogae, T., 2014. Incipient charnockite: characterization at the type localities. Precambrian Research, 253, 38–49.

Newton, R.C., Smith, J.V. & Windley, B.F., 1980. Carbonic metamorphism, granulites and crustal growth. Nature, 288, 45–50.

Paton, C., Woodhead, J., Hellstrom, J., Hergt, J., Greig, A. & Maas, R., 2010. Improved laser ablation U–Pb zircon and geochronology through robust downhole fractionation correction. Geochemistry, Geophysics, Geosystems, 11, 1–36.

Paton, C., Hellstrom, J., Paul, B., Woodhead, J. & Hergt, J., 2011. Iolite: freeware for the visualisation and processing of mass spectrometric data. Journal of Analytical Atomic Spectrometry, 26, 2508–2518.

Pattison, D.R.M., Chacko, T., Farquhar, J. & McFarlane, R.M., 2003. Temperature of granulite-facies metamorphism: constraints from experimental phase equilibria and thermo- barometry corrected for retrograde exchange. Journal of Petrology, 44, 867–900.

Perchuk, L.L., Safonov, O.G., Gerya, T.V., Fu, B. & Harlov, D.E., 2000. Mobility of components in metasomatic trans- formation and partial melting of gneisses: an example from Sri Lanka. Contributions to Mineralogy and Petrology, 140, 212–232.

Plavsa, D., Collins, A.S., Foden, J.F. et al., 2012. Delineating crustal domains in Peninsular India: age and chemistry of orthopyroxene-bearing felsic gneisses in the Madurai Block. Precambrian Research, 198–199, 77–93.

Plavsa, D., Collins, A.S., Payne, J.L., Foden, J.D., Clark, C. & Santosh, M., 2014. Detrital zircons in basement metasedimentary protoliths unveil the origins of southern India. Bulletin of the Geological Society of America, 126, 791–812.

Raith, M. & Srikantappa, C., 1993. Arrested charnockite formation at Kottavattam, southern India. Journal of Metamor- phic Geology, 11, 815–832.

Raith, M., Srikantappa, C., Ashamanjari, K.G. & Spiering, B., 1990. The granulite terrane of the Nilgiri Hills (Southern India): characterization of high-grade metamorphism. Gran- ulites and Crustal Evolution (eds. Vielzeuf, D. & Vidal, Ph), pp. 339–365. Springer, The Netherlands.

Rajesh, H.M. & Santosh, M., 2004. Charnockite magmatism in southern India. Proceedings of the Indian Academy of Sciences. A Earth and Planetary Sciences, 113, 565–585.

Rajesh, H.M. & Santosh, M., 2012. Charnockites and charnockites. Geoscience Frontiers, 3, 1–8.

Ravindra Kumar, G.R., 2004. Mechanism of arrested charnockite formation at Nemmara, Palghat region, south- ern India. Lithos, 75, 331–358.

Ravindra Kumar, G.R., Srikantappa, C. & Hansen, E.C., 1985. Charnockite formation at Ponmudi in southern India. Nature, 313, 207–209.

Roberts, M.P. & Finger, F., 1997. Do U-Pb zircon ages from granulites reflect peak metamorphic conditions? Geology, 25, 319–322.

Rubatto, D., Hermann, J. & Buick, I.S., 2006. Temperature and bulk composition contrl on the growth of monazite and zircon during low-pressure anatexis (Mount Stafford, Central Australia). Journal of Petrology, 47, 1973–1996.

Sacks, P.E., Nambiar, C.G. & Walters, L.J., 1997. Dextral Pan-African shear along the Southwestern edge of the Achankovil Shear Belt, South India: constraints on Gond- wana reconstructions. The Journal of Geology, 105, 275–284.

Santosh, M., 1987. Cordierite gneisses of southern Kerala, India: petrology, fluid inclusions and implications for crustal uplift history. Contributions to Mineralogy and Petrology, 96, 343–356.

Santosh, M. & Omori, S., 2008. CO_2 flushing: a plate tectonic perspective. Gondwana Research, 13, 86–102.

Santosh, M., Tagawa, M., Taguchi, S. & Yoshikura, S., 2003a. The Nagercoil Granulite Block, southern India: petrology, fluid inclusions and exhumation history. Journal of Asian Earth Sciences, 22, 131–155.

Santosh, M., Yokoyama, K., Biju-Sekhar, S. & Rogers, J.J.W., 2003b. Multiple tectonothermal events in the granulite blocks of southern India revealed from EPMA dating: impli- cations on the history of supercontinents. Gondwana Research, 6, 29–63.

Santosh, M., Maruyama, S. & Sato, K., 2009. Anatomy of a Cambrian suture in Gondwana: pacific-type orogeny in southern India. Gondwana Research, 16, 321–341.

Santosh, M., Yang, Q.Y., Shaji, E., Tsunogae, T., Mohan, M.R. & Satyanarayanan, M., 2015. An exotic Mesoarchean microcontinent: the Coorg Block, southern India. Gondwana Research, 27, 165–195.

Santosh, M., Yang, Q.Y., Shaji, E., Mohan, M.R., Tsunogae, T. & Satyanarayanan, M., 2016. Oldest rocks from Peninsular India: evidence for Hadean to Neoarchean crustal evolution. Gondwana Research, 29, 105–135.

Schaltegger, U., Fanning, C.M., Gũnther, D., Maurin, J.C., Schulmann, K. & Gebauer, D., 1999. Growth, annealing and recrystallization of zircon and preservation of monazite in high-grade metamorphism: conventional and in-situ U-Pb isotope, cathodoluminesecence and microchemical evidence. Contributions to Mineralogy and Petrology, 134, 186–201.

Shabeer, K.P., Sajeev, K., Okudaira, T. & Santosh, M., 2002. Two-stage spinel growth in the high-grade metapelites of the central Kerala Khondalite Belt: implications for prograde P-T path. Journal of Geosciences, Osaka City University, 45, 29–43.

Shabeer, K.P., Santish-Kumar, M., Armstrong, R. & Buick, I.S., 2005. Constraints on the timing of Pan-African gran- ulite-facies metamorphism in the Kerala Khondalite Belt of southern India: SHRIMP mineral ages and Nd isotopic sys- tematics. The Journal of Geology, 113, 95–106.

Spencer, C.J., Kirkland, C.L. & Taylor, R.J.M., 2015. Strategies toward statistically robust interpretations of in situ U– Pb zircon geochronology. Geoscience Frontiers, doi:10.1016/ j.gsf.2015.11.006.

Srikantappa, C., Raith, M. & Spiering, B., 1985. Progressive charnockitization of a leptynite-khondalite suite in southern Kerala, India-evidence for formation of charnockites through decrease in fluid pressure? Journal of the Geological Society of India, 26, 849–892.

Stacey, J.S. & Kramers, J.D., 1975. Approximation of terrestrial lead isotope evolution by a two-stage model. Earth and Planetary Science Letters, 26, 207–221.

Stähle, H.J., Raith, M., Hoernes, S. & Delfs, A., 1987. Element mobility during incipient granulite formation at Kabbaldurga, Southern India. Journal of Petrology, 28, 803–834.

Stern, R.S. & Amelin, Y., 2003. Assessment of errors in SIMS zircon U-Pb geochronology using a natural zircon standard and NIST SRM 610 glass. Chemical Geology, 197, 111–142.

Tadokoro, H., Tsunogae, T. & Santosh, M., 2008. Metamor- phic P-T path of eastern Trivandrum Granulite Block, southern India: implications for regional correlation of lower crustal fragments. Journal of Mineralogical and Petrological Sciences, 103, 279–284.

Taylor, R., Clark, C., Fitzsimons, I.C.W. et al., 2014. Post- peak, fluid-mediated modification of granulite facies zircon and monazite in the Trivandrum Block, southern India. Con- tributions to Mineralogy and Petrology, 168, 1–17.

Taylor, R., Harley, S.L., Hinton, R.W., Elphick, S., Clark, C. & Kelly, N.M., 2015. Experimental determination of REE partition coefficients between zircon, garnet and melt: a key to understanding high-T crustal processes. Journal of Metamorphic Geology, 33, 231–248.

Touret, J.L.R. & Huizenga, J.M., 2012. Charnockite microstructures: from magmatic to metamorphic. Geoscience Frontiers, 3, 1–9.

Vavra, G., Gebauer, D., Schmid, R. & Compston, W., 1996. Multiple zircon growth and recrystallization during polyphase Late Carboniferous to Triassic metamorphism in granulites of the Ivrea Zone (Southern Alps): an ion microprobe (SHRIMP) study. Contributions to Mineralogy and Petrology, 122, 337–358.

Wang, W., Dunkley, E., Clarke, G.L. & Daczko, N.R., 2014. The evolution of zircon during low-P partial melting of metapelitic rocks: theoretical predictions and a case study from Mt Stafford, central Australia. Journal of Metamorphic Geology, 32, 791–808.

White, R.W. & Powell, R., 2002. Melt loss and the preservation of granulite facies mineral assemblages. Journal of Metamorphic Geology, 20, 621–632.

White, R.W., Powell, R., Holland, T.J.B., Johnson, T. & Green, E.C.R., 2014a. New mineral activity-composition relations for thermodynamic calculations in metapelitic systems. Journal of Metamorphic Geology, 32, 261–286.

White, R.W., Powell, R. & Johnson, T., 2014b. The effect of Mn on mineral stability in metapelites revisited: new a–x relations for manganese-bearing minerals. Journal of Meta- morphic Geology, 32, 809–828.

Whitney, D.L. & Evans, B.W., 2010. Abbreviations for names of rock-forming minerals. American Mineralogist, 95, 185– 187.

Williams, M.L., Jercinovic, M.J., Harlov, D.E., Budzyn', B. & Hetherington, C.J., 2011. Resetting monazite ages during fluid-related alteration. Chemical Geology, 283, 218–225.

Yoshida, M., Santosh, M. & Shirahata, H., 1991. Geochemistry of gneiss-granulite transformation in the "incipient charnockite" zones of southern India. Mineralogy and Petrology, 45, 69–83.

Supplementary material: See Appendix B

Chapter 3

Reappraising the *P–T* evolution of the Rogaland–Vest Agder Sector, southwestern Norway

Eleanore Blereau[1*], Tim E. Johnson[1], Chris Clark[1], Richard J. M. Taylor[1], Peter D. Kinny[1], Martin Hand[2]

[1]Department of Applied Geology, The Institute of Geoscience Research (TIGeR), Curtin University, GPO Box U1987, Perth WA 6845, Australia.

[2]Centre for Tectonics, Resources and Exploration (TRaX), School of Earth and Environmental Sciences, University of Adelaide, Adelaide 5005, South Australia

This article is published in Geoscience Frontiers, vol 8, pp. 1–14.
http://dx.doi.org/10.1016/j.gsf.2016.07.003 and reprinted with permission in Appendix A.

ABSTRACT

The Rogaland–Vest Agder Sector of southwestern Norway comprises high-grade metamorphic rocks intruded by voluminous plutonic bodies that include the ~1000 km^2 Rogaland Igneous Complex (RIC). New petrographic observations and thermodynamic phase equilibria modelling of three metapelitic samples collected at various distances (30 km, 10 km and ~10 m) from one of the main bodies of RIC anorthosite were undertaken to assess two alternative *P–T–t* models for the metamorphic evolution of the area. The results are consistent with a revised two-phase evolution. Regional metamorphism followed a clockwise *P–T* path reaching peak conditions of ~850–950 °C and ~7–8 kbar at ~1035 Ma followed by high-temperature decompression to ~5 kbar at ~950 Ma, and resulted in extensive anatexis and melt loss to produce highly residual rocks. Subsequent emplacement of the RIC at ~930 Ma caused regional-scale contact metamorphism that affected country rocks 10 km or more from their contact with the anorthosite. This thermal overprint is expressed in the sample proximal to the anorthosite by replacement of sillimanite by coarse intergrowths of cordierite plus spinel and growth of a second generation of garnet, and in the intermediate (10 km) sample by replacement of sapphirine by coarse intergrowths of cordierite, spinel and biotite. The formation of late biotite in the intermediate sample may suggest the rocks retained small quantities of melt produced by regional metamorphism and remained at temperatures above the solidus for up to 100 Ma. Our results are more consistent with an accretionary rather than a collisional model for the Sveconorwegian Orogen.

1. INTRODUCTION

The Rogaland–Vest Agder Sector of SW Norway is a metamorphic province dominated by high-grade gneisses and intrusive igneous rocks (Maijer et al., 1981; Tobi et al., 1985; Jansen and Tobi, 1987; Maijer et al., 1987). Together these rocks represent the core of the ca 1200–900 Ma Sveconorwegian Orogen (Falkum and Petersen, 1980; Falkum, 1985). The intrusive rocks include the Rogaland Igneous Complex (RIC) that is exposed over ~1000 km^2 and comprised largely of three massif-type anorthosite plutons emplaced around 930 Ma (Schärer et al., 1996). Two contrasting tectonic models have been proposed to explain the evolution of the Sveconorwegian Orogen, one involving continent–continent collision (Bingen et al., 2008) and the other involving protracted subduction–accretion (Slagstad et al., 2013; Coint et al., 2015; Roberts and Slagstad, 2015). Collisional models generally require long timescales for the rocks to reach high-grade metamorphism (Clark et al., 2011; Slagstad et al., 2013), whereas in accretionary orogens such conditions may be attained much faster (Slagstad et al., 2013; Coint et al., 2015). However, clockwise *P–T* paths are not diagnostic of either tectonic setting (Brown, 2007).

The role of the RIC in the metamorphic history of the gneisses of the Rogaland–Vest Agder Sector is controversial, and two different *P–T–t* models have been advanced (Fig. 3). Möller et al. (2003) and Tomkins et al. (2005) proposed a two-stage metamorphic evolution, in which an upper amphibolite facies regional event characterized

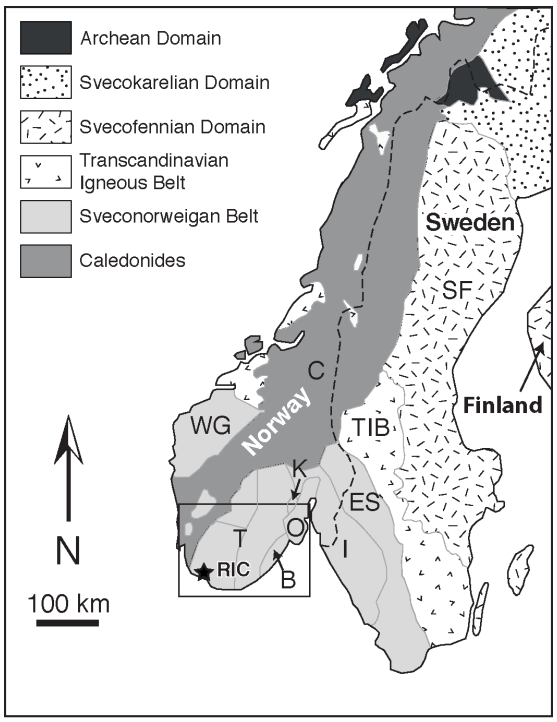

Fig. 1: Map showing the main geological subdivisions of Scandinavia (after Bergh et al., 2012). Abbreviations: T- Telemarkia Terrane; B- Bamble Sector; O- Oslo Graben; K- Kongsberg Sector; I- Idefjorden Terrane; ES- Eastern Segment; C- Caledonides; TIB- Transcandinavian Igneous Belt; SF- Svecofennian Domain; WG- Western Gneiss Region.

by a clockwise *P–T* evolution was followed by ultra-high temperature (UHT) metamorphism at lower pressure related to intrusion of the RIC. By contrast, Drüppel et al. (2013) proposed a single-stage, protracted clockwise regional metamorphic evolution that reached a UHT metamorphic peak some 70 Ma prior to emplacement of the RIC; in this model, high-grade metamorphism and intrusion are considered to have been unrelated.

In this study, we combine new petrographic observations with phase equilibria modelling of three metapelitic samples collected at different distances from the RIC (30 km, 10 km and <50 m) to re-evaluate their metamorphic evolution. We discuss the implications of the results for the tectonic evolution of the Sveconorwegian Belt.

2. REGIONAL GEOLOGY

The rocks of southern Scandinavia experienced three Proterozoic orogenic events: in Sweden and Finland the ca 1900–1750 Ma Svecofennian orogeny, in SE Norway and Sweden the ca 1750–1550 Ma Gothian orogeny, and in southern Norway and SW Sweden the ca 1200–900 Ma Sveconorwegian orogeny (Andersen et al., 2002). The Sveconorwegian Belt lies to the west of the Svecofennian Domain and the ca 1850–1650 Ma Transcandinavian Igneous Belt and is bounded obliquely to the northwest by the Caledonides (Fig. 1). It comprises a number of lithotectonic domains, including the Eastern Segment, Idefjorden Terrane, Bamble, Kongsberg and Telemarkia Terranes, all of which are bounded by major shear zones (Fig. 1). The Telemarkia Terrane is interpreted to have formed in a short magmatic event between 1520–1480 Ma (Bingen et al., 2005; Bingen et al., 2006; Bogdanova et al., 2008; Roberts and Slagstad, 2015) and is further divided into the Telemark, Hardangervidda, Sudal and Rogaland–Vest Agder Sectors (Fig. 2).

The focus of this study, the Rogaland–Vest Agder (RVA) Sector, is a high-grade gneiss complex intruded by voluminous synorogenic plutons that represents the core of the Sveconorwegian Orogen (Falkum and Petersen, 1980; Falkum, 1985). The complex consists of felsic orthogneiss, much of which contains orthopyroxene, and subordinate garnet-bearing paragneiss (Hermans et al., 1975; Falkum, 1982, 1985; Tobi et al., 1985; Bingen et al., 2005; Tomkins et al., 2005; Coint et al., 2015), with minor

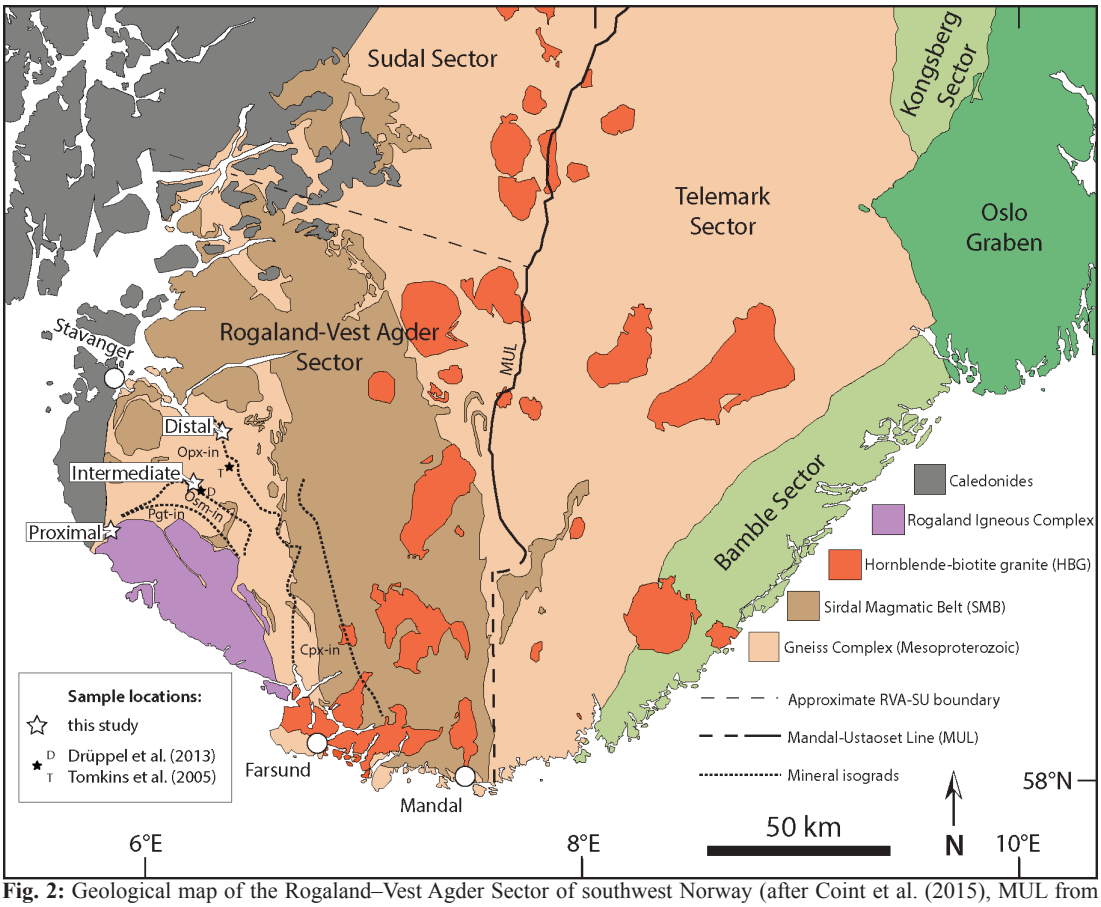

Fig. 2: Geological map of the Rogaland–Vest Agder Sector of southwest Norway (after Coint et al. (2015), MUL from Vander Auwera et al. (2011) and mineral isograds from Bolle et al. (2010)). Samples from this study are marked as large white stars with locations from previous studies as smaller black stars.

amphibolite, quartzite, calc-silicate and marble (Huijsmans et al., 1981; Falkum, 1982, 1985; Tobi et al., 1985; Jansen and Tobi, 1987; Bingen et al., 2005; Harlov, 2011). The orthopyroxene-bearing orthogneiss is variably migmatitic, in which migmatised varieties have protolith ages of ca 1450 Ma whereas non-migmatised varieties have younger protolith ages of ca 1230–1210 Ma (Coint et al., 2015). Migmatitic garnet-bearing paragneiss contains abundant garnet as well as sillimanite and/or cordierite-bearing layers indicating pelitic to semi-pelitic protoliths (Hermans et al., 1975; Coint et al., 2015). Detrital zircon U–Pb ages between ca 3000–1200 Ma have been reported from one of these migmatitic metapelites (Tomkins et al., 2005).

The RVA Sector contains three suites of intrusive rocks: (i) the Sirdal Magmatic Belt (SMB); (ii) the hornblende-biotite granites (HBG) and (iii) the Rogaland Igneous Complex (RIC). The 1060–1020 Ma SMB, which covers an aerial extent of ~10,000 km^2, is a weakly deformed calc-alkaline granitic batholith that preserves igneous textures (Slagstad et al., 2013; Coint et al., 2015). The main constituent is porphyritic biotite granite with lesser amounts of leucogranite, garnet granite and zones rich in xenoliths including migmatitic gneiss (Coint et al., 2015). The arc-like compositions of the SMB (Slagstad et al., 2013) may reflect characteristics inherited from the source rocks, which were probably ca 1500 Ma calc-alkaline metavolcanics and granitoid

rocks such as are common in southern Norway, in particular in the Telemark and Hardangervidda Sector (Coint et al., 2015).

The 990–932 Ma HBG suite occurs as discrete 'A-type' plutons that crop out across the Telemarkia Terrane (Bogaerts et al., 2003; Vander Auwera et al., 2011). The range in composition in the HBG Suite from gabbronorite to granite (50–77 wt% SiO_2) is interpreted to reflect extreme fractional crystallization of several batches of basaltic magma (Bogaerts et al., 2003). The HBG suite was likely derived from an undepleted to slightly depleted hydrous mafic source that was underplated during a previous orogenic event (Bogaerts et al., 2003; Vander Auwera et al., 2011; Vander Auwera et al., 2014).

The ~1000 km^2 RIC, also referred to as the Rogaland Anorthosite Complex (Pasteels et al., 1979; Schärer et al., 1996; Bogaerts et al., 2003; Westphal et al., 2003) and Rogaland Anorthosite Province (Sauer et al., 2013; Coint et al., 2015), is composed of three massif-type anorthosites (Egersund-Ogna, Håland-Heleren and Åna-Sira) as well as a large layered polyphase intrusion (Bjerkreim-Sokundal lopolith), two smaller leuconorite bodies (Hidra and Garsaknatt) and a small number of mafic dykes (high-Al gabbros to orthopyroxene monzonorite) (Pasteels et al., 1979; Wilmart et al., 1991; Vander Auwera and Longhi, 1994; Nijland et al., 1996; Schärer et al., 1996; Duchesne and Wilmart, 1997; Bolle et al., 2002; Marker et al., 2003; Möller et al., 2003; Bolle et al., 2010). The three anorthosite massifs contain subophitic aggregates of megacrystic plagioclase and aluminous orthopyroxene within fine-grained leuconorite (Schärer et al., 1996; Bybee et al., 2014). U–Pb ages of zircon and baddeleyite inclusions within orthopyroxene megacrysts in the Egersund-Ogna, Håland-Heleren and Åna-Sira anorthosites are identical within uncertainty at ca 930 Ma (Schärer et al., 1996). Based on the complex spread of zircon U–Pb ages reported by Möller et al. (2003) the RIC is suggested by Coint et al. (2015) to have had a protracted, episodic emplacement history. The margin of the Egersund-Ogna massif has a magmatic foliation parallel to both its boundary and to the foliation of the adjacent host gneisses (Schärer et al., 1996; Bolle et al., 2002) that has been used as evidence for diapiric emplacement of a ~1150 °C crystal mush (Duchesne and Michot, 1987; Longhi et al., 1993; Schärer et al., 1996; Bolle et al., 2002). The anorthosites were emplaced at mid crustal depths (minimum of 5.0–7.7 kbar, ~20–30 km) based on conventional thermobarometry and numerical modelling (Wilmart and Duchesne, 1987; Barnichon et al., 1999).

Within the RIC, the Bjerkreim-Sokundal lopolith is a layered intrusion with four main phases; a basal phase of anorthosite–leuconorite and norite with rhythmic layering is overlain by monzonorite that is in turn overlain by monzonite and, lastly, by quartz monzonite (Versteeve, 1975; Wilmart et al., 1991; Duchesne and Wilmart, 1997; Bolle et al., 2002). The lopolith, which is separated from the anorthosite intrusions by a thin septum of gneissic country rocks, was emplaced at approximately the same time (Wilmart et al., 1991; Vander Auwera and Longhi, 1994; Schärer et al., 1996; Duchesne and Wilmart, 1997). Geochemical and isotopic data indicate that the RIC had a relatively anhydrous, lower crustal source (Bogaerts et al., 2003) with more recent studies suggesting that the parent magmas originated

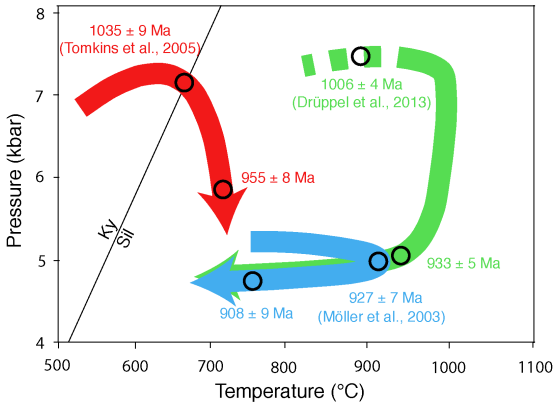

Fig. 3: Two alternative *P–T* models proposed for the Rogaland–Vest Agder sector (modified after Drüppel et al. (2013)); two-stage metamorphic evolution (Möller et al., 2003; Tomkins et al., 2005) versus protracted, single-stage metamorphic evolution (Drüppel et al., 2013).

at the Moho with anorthosite formation tied to protracted magmatism in a convergent arc (Bybee et al., 2014). Previous studies suggest multiple parental melt compositions for the RIC suite, with source rocks possibly ranging from high Al-basalt to primitive orthopyroxene monzonorite (Vander Auwera et al., 2011, and references within).

The high-grade gneisses of the RVA Sector are considered by some authors to have experienced a polymetamorphic evolution, and to preserve textural evidence for a regional metamorphic event followed by a high temperature contact metamorphic overprint (Verschure et al., 1980; Maijer et al., 1981; Wielens et al., 1981; Demaiffe and Michot, 1985; Jansen et al., 1985; Tobi et al., 1985; Maijer, 1987; Bingen and van Breemen, 1998; Möller et al., 2003; Tomkins et al., 2005; Coint et al., 2015). Evidence for an amphibolite facies regional metamorphic event (commonly termed M1) at ca 1035 Ma (Tomkins et al., 2005) is based on isotopic data from a garnet–biotite–sillimanite metapelite, ~25–30 km from the contact with the RIC (Möller et al., 2003). Coint et al. (2015) also suggests a similar age of regional metamorphism of ca 1030 Ma. The subsequent growth in this rock of cordierite containing zircon dated at ca 955 Ma indicates that peak metamorphic conditions were followed by decompression (shown in red, Fig. 3) (Möller et al., 2003; Tomkins et al., 2005). These events predate the emplacement of the RIC at ca 930 Ma (Schärer et al., 1996), which caused large-scale contact metamorphism (M2) at UHT conditions (shown in blue, Fig. 3)(Scharer et al., 1996; Möller et al., 2003; Westphal et al., 2003). Pressure–temperature estimates of ~750 °C at 5–7 kbar for the regional event and 700–1050 °C at ~4 kbar for the contact metamorphism were derived using conventional thermobarometry (Jansen et al., 1985). A later retrograde overprint (so-called M3) to upper amphibolite to granulite facies at 908 Ma (550–700 °C and 3–5 kbar) is interpreted to be related to the isobaric cooling of intrusive bodies with the partial replacement of high grade minerals such as osumilite (Kars et al., 1980; Maijer et al., 1981; Wielens et al., 1981; Jansen et al., 1985; Bol et al., 1989; Nijland et al., 1996; Möller et al., 2003; Tomkins et al., 2005; Bolle et al., 2010).

In contrast to the previous interpretations, Drüppel et al. (2013) reinterpreted the gneisses as having experienced a single, long-lived regional metamorphic event that peaked at UHT conditions some 70 Ma prior to intrusion of the RIC (shown in green, Fig. 3). This interpretation, based on phase equilibria modelling in the Na_2O–CaO–K_2O–FeO–MgO–Al_2O_3–SiO_2–H_2O–TiO_2 (NCKFMASHT) model system of samples ~10 km from the RIC contact, indicated peak conditions of ~1000 °C at ~7.5 kbar were followed by near isothermal decompression to <5.5 kbar at 900–1000 °C

(M2) before near isobaric cooling (Drüppel et al., 2013). These authors concluded that no second thermal pulse is recorded by the silicate mineral assemblage in the RVA Sector. Zircon U–Pb ages are consistent with a metamorphic age at ca 1000 Ma; epitaxial xenotime yields U–Pb ages within error of the emplacement of the RIC at ca 930 Ma (Drüppel et al., 2013).

A series of high-*T* mineral-in isograds, including inverted pigeonite in felsic orthogneiss, osumilite in paragneiss, orthopyroxene in felsic orthogneiss and clinopyroxene in granodioritic gneiss, are broadly parallel to the margin of the RIC (Fig. 2) (Hermans et al., 1975; Pasteels et al., 1979; Sauter, 1981; Jansen et al., 1985; Tobi et al., 1985; Maijer, 1987; Bol et al., 1989). These isograds represent a temperature range from ~700 °C at the orthopyroxene-in isograd to over 900 °C (UHT) at the pigeonite-in isograd (Jansen et al., 1985; Tobi et al., 1985; Bol et al., 1989; Möller et al., 2003; Tomkins et al., 2005). Whereas most studies have interpreted the osumilite and pigeonite-in isograds as the products of contact metamorphism at ca 930 Ma superimposed upon granulite to amphibolite-facies regional metamorphic assemblages, others regard the orthopyroxene isograd to pre-date the contact event (Bingen and van Breemen, 1998), More recently, Coint et al. (2015) have proposed that the orthopyroxene-in isograd separates granulite-facies rocks to the west from non-metamorphosed granites to the east and should not be regarded as an isograd at all.

3. SAMPLE DESCRIPTIONS AND PETROLOGY

Three samples collected from different distances from the RIC–country rock contact were investigated in order to evaluate their metamorphic histories. Hereafter, these samples are referred to as distal (collected ~30 km from the RIC), intermediate (~10 km) and proximal (~10 m), as shown in Fig. 2. Mineral abbreviations follow Kretz (1983) and Whitney and Evans (2010).

3.1. Distal sample (N 58°49’49.4”, E 6°16’49.2”)

The distal sample (ROG13/11) is a garnet–sillimanite–cordierite metapelite collected a short distance up-grade of the orthopyroxene-in isograd. The sample site, ~400m NW of Giljastølsvatnet, is ~5 km north of the sample locality of Degeling et al. (2001) and Tomkins et al. (2005) (Fig. 2). The sample is a migmatite comprising melanosome rich in garnet, sillimanite and cordierite and garnet-bearing leucosomes that are continuous at an outcrop scale and oriented sub-parallel to the regional foliation (Fig. 4a).

In thin section, the melanosome contains anhedral garnet porphyroblasts (2–8 mm) within which abundant inclusions of sillimanite define a folded foliation that curves into parallelism with the matrix foliation (Fig. 4b, c) that is also defined by sillimanite (0.2–1 mm). Variably pinitised cordierite (2–6 mm, 10–15%) surrounds garnet, sillimanite, ilmenite and quartz (Fig. 4b, c). Minor feldspar is also present within the matrix. Minor singular grains of ilmenite (0.5–1 mm) is partially to completely replaced by intergrowths of differently orientated rutile and chlorite. The leucosome is composed of sub-equal proportions of quartz (2–6 mm), plagioclase (1–4 mm) and K-feldspar (2–4 mm), along with anhedral to rounded garnet (1–3 mm) that contains abundant inclusions of quartz but no sillimanite (Fig. 4d).

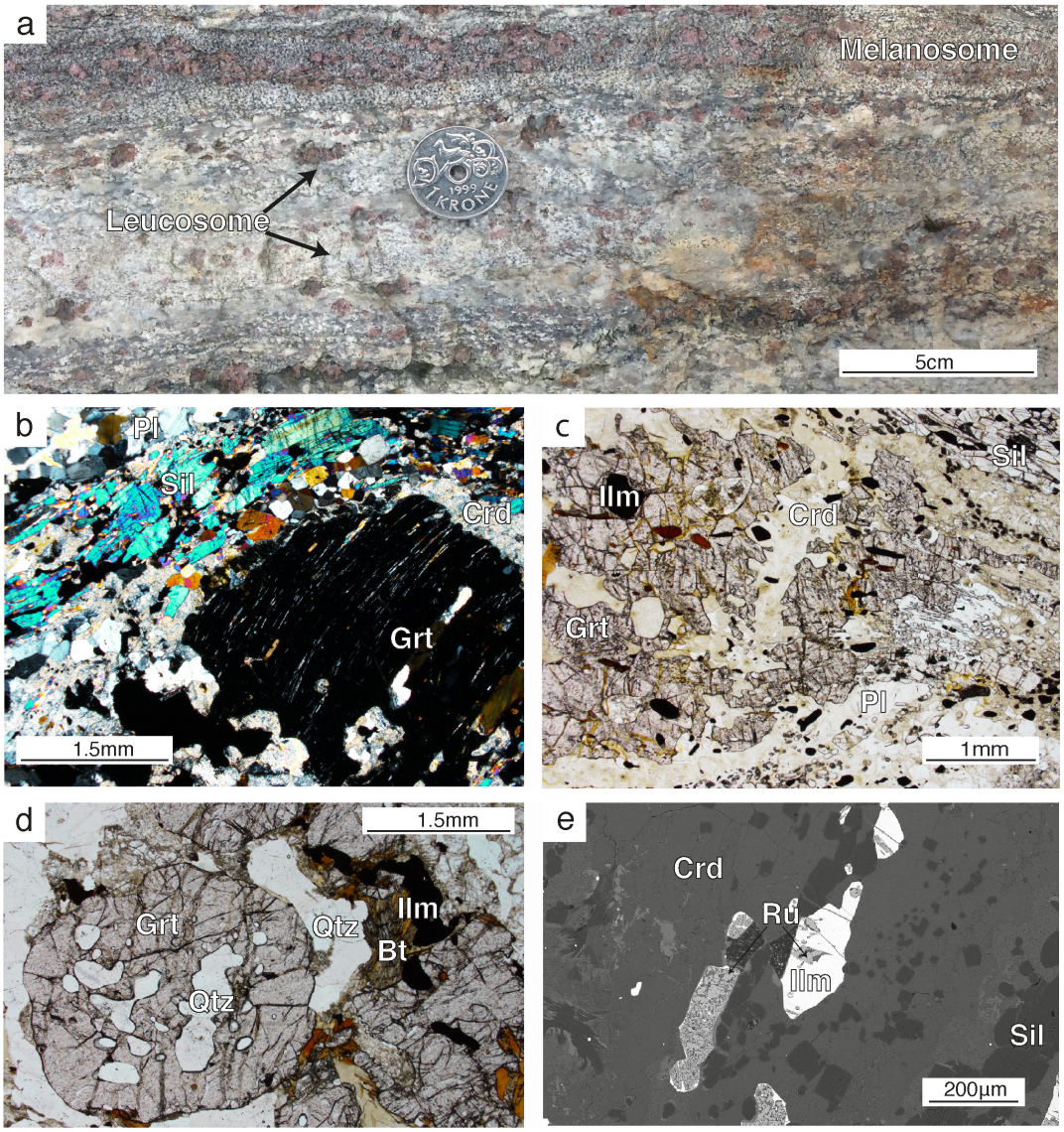

Fig. 4: Field photograph and photomicrographs from the 'Distal' locality. a- Garnet–cordierite–sillimanite melanosome with garnet-bearing leucosome at outcrop scale. b- Garnet porphyroblast within melanosome (xpl) containing ilmenite, sillimanite and minor biotite inclusions, surrounded by pinitised cordierite and sillimanite. c- Garnet porphyroblast within melanosome with sillimanite inclusions defining a relict foliation. Coarse sillimanite in the matrix defines a new foliation. d- Peritectic garnet with quartz inclusions within leucosome, with late biotite. e- Back scattered electron (BSE) image showing ilmenite being replaced by an intergrowth of rutile and chlorite within the melanosome.

Minor biotite is present (0.5–1 mm) along with small amounts of muscovite.

The interpreted peak assemblage in sample ROG13/11 is garnet, sillimanite, plagioclase, K-feldspar, quartz, ilmenite and melt. Matrix garnet containing sillimanite inclusions is interpreted to mainly represent subsolidus growth, whereas leucosome garnet that lacks sillimanite inclusions is regarded as a peritectic product of melting reactions consuming biotite. Cordierite and biotite are considered to be retrograde minerals.

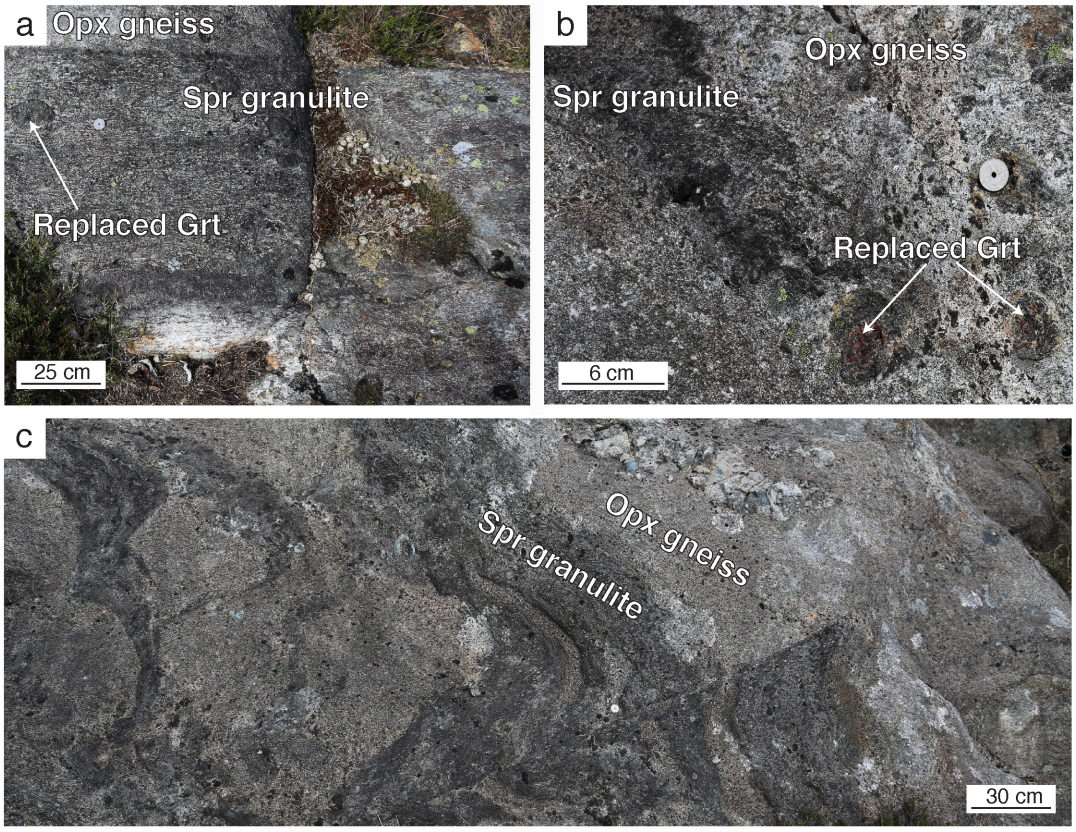

Fig. 5: Field photographs from the 'Intermediate' locality. a- Dark sapphirine granulite layer with completely replaced garnet. b- Sapphirine granulite and orthopyroxene gneiss containing partially replaced garnets with orthopyroxene coronas. c- Irregular dark layers of sapphirine granulite interleaved with orthopyroxene gneiss, cut by minor faults.

3.2. Intermediate sample (N 58°42'9.7", E 6°10'1.4")

The intermediate sample (ROG13/10) is a residual sapphirine-bearing metapelite from a locality near Ivesdal, ~10 km NE of the RIC contact (Fig. 2), which has been described previously by Hermans et al. (1976) and Drüppel et al. (2013). The exposure consists of irregular, dark sapphirine-bearing layers within a host orthopyroxene-bearing gneiss (Figs 5). Minor and sporadically dispersed large garnets (~3–8 cm) within the sapphirine-bearing granulite and, less commonly, within the orthopyroxene gneiss have coronae of orthopyroxene with or without plagioclase, and in some cases have been replaced completely (Fig. 5a, b). Garnet-bearing leucosome occurs as rare patches within orthopyroxene gneiss. Sparse quartz veins occur within, and cross-cut both lithologies. Irregular orthopyroxene-rich selvedges and schlieren occur within the orthopyroxene gneiss and occasionally along contacts between orthopyroxene gneiss and sapphirine-bearing metapelite.

In thin section, subhedral to euhedral sapphirine porphyroblasts (1–8 mm, 10–15%) are partially to completely replaced by coarse intergrowths of spinel and cordierite, along with variable amounts of biotite that appears to be replacing cordierite (Fig. 6a, b, d). The matrix consists of cordierite (0.5–3 mm), orthopyroxene (0.5–3 mm), plagioclase (0.5–2 mm), K-feldspar (0.5–1 mm) and biotite (up to 2 mm) (Fig.

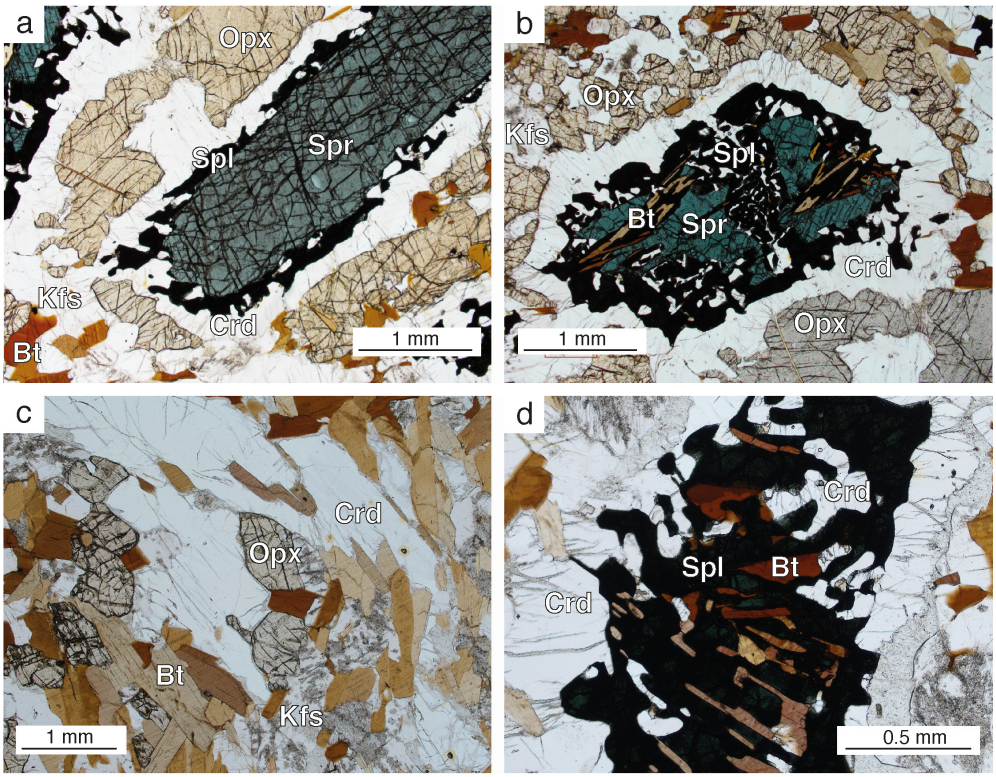

Fig. 6: Photomicrographs from the 'Intermediate' locality. a- Sapphirine porphyroblast rimmed by spinel plus cordierite and a cordierite rim separating the symplectite from orthopyroxene. b- Sapphirine partially replaced by a spinel–cordierite symplectite, with later biotite replacing cordierite within the symplectite. An outer rim of cordierite is present between the symplectite and orthopyroxene. c- Irregular grains of orthopyroxene and cordierite within the matrix with some grains almost completely surrounded by late biotite. d- Spinel plus cordierite symplectite with biotite partially replacing cordierite.

6c). Orthopyroxene grains are separated from sapphirine porphyroblasts by layers of cordierite and spinel plus cordierite (Fig. 6a, b). Feldspar grains are variably sericitised. Spinel contains ilmenite and minor exsolved magnetite. Quartz is absent.

We interpret sample ROG13/10 to have contained an earlier assemblage of sapphirine, orthopyroxene, plagioclase, K-feldspar, cordierite, ilmenite and melt that later underwent replacement of sapphirine and orthopyroxene by coarse intergrowths of spinel and cordierite. Subsequent growth of biotite may reflect retrograde reaction in the presence of melt.

3.3. Proximal sample (N 58°35'46.5", E 5°46'59.0")

The proximal sample ROG14/5 is from country rocks ~10 m from the northwest margin of the RIC (Fig. 2). The sample is a migmatitic garnet–sillimanite–spinel–cordierite metapelitic gneiss (Fig. 7a) that is intruded by several small sheets of garnet-bearing anorthosite (Fig. 7b). The metapelite consists of melanosome rich in garnet and cordierite, within which occurs narrow, foliation-parallel leucosome layers (<1 cm in width). Larger (~0.5–1 m) irregular bodies of garnet-bearing and garnet-free leucosome cross-cut the foliation and contain schollen of

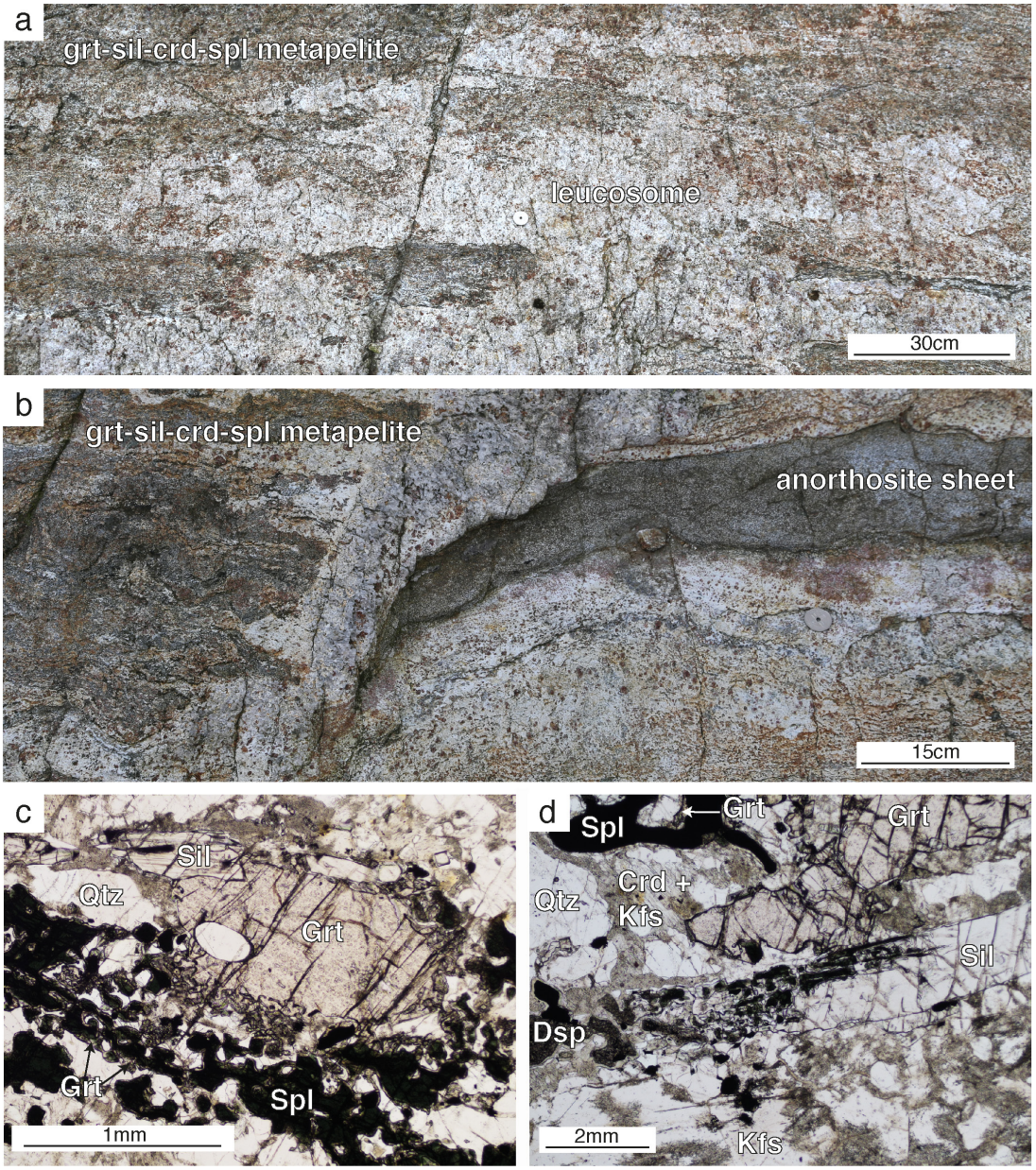

Fig. 7: Field photographs and photomicrographs from the 'Proximal' locality. a- Garnet–sillimanite–cordierite–spinel migmatite overprinted by a large irregular garnet-bearing leucosome containing shollen of the metapelite. b- Metapelite with intruded anorthosite sheet. c- Garnet porphyroblast with secondary garnet overgrowing spinel. d- Sillimanite partly replaced by spinel plus cordierite, with some of the spinel replaced by diaspore.

melanosome (Fig. 7a). Minor quartz veins are also present. The anorthosite sheets are discontinuous, up to 15 cm wide and 4 m in length and oriented parallel to the foliation (Fig. 7b).

In thin section, sample ROG14/5 is dominated by melanosome containing equant to elongate anhedral garnet porphyroblasts (0.5–4 mm) containing sillimanite inclusions (Fig. 7c, d). A second generation of garnet forms narrow (~100 µm) rims around pre-existing garnet porphyroblasts and adjacent to spinel (Fig. 7c, d). Coarse matrix sillimanite (0.5–4 mm) defines a foliation that wraps around garnet, and is partially replaced by intergrowths of spinel plus cordierite (Fig. 7d).

Sample	SiO_2	TiO_2	Al_2O_3	O	FeO	MgO	CaO	Na_2O	K_2O	LOI	Total
ROG13/11 (Distal)	68.95	0.78	12.95	0.67	6.86	3.68	1.39	1.82	2.80	0.10	100
ROG13/10 (Intermediate)	51.45	0.64	14.98	1.13	6.73	17.99	1.33	1.78	2.94	1.03	100
ROG14/5 (Proximal)	63.19	0.83	16.71	0.57	9.29	4.85	1.28	1.11	2.06	0.11	100

Table 1: Bulk compositions as molar oxide (mol.%) used in phase equilibria modelling.

Spinel occurs both within the symplectite and as aggregates of grains surrounded by a thin rind of cordierite or garnet (Fig. 7d). The leucosome contains large (2–8 mm) slightly elongate grains along with smaller (0.5–2 mm) grains of quartz, plagioclase (1–2 mm) and K-feldspar (1–2 mm). Cordierite surrounds garnet, sillimanite and, less commonly, quartz and spinel (1–2 mm) and is sometimes intergrown with K–feldspar (Fig. 7d). Minor ilmenite is partially to completely replaced by late intergrowths of rutile and chlorite.

This sample is interpreted to contain an earlier assemblage of garnet, sillimanite, plagioclase, K-feldspar, quartz, spinel, ilmenite and melt. Replacement of sillimanite by cordierite plus spinel, and growth of a second generation of garnet occurred subsequently.

4. PHASE EQUILIBRIA MODELLING

Metamorphic *P–T* conditions were constrained using *P–T*, *P–X* and *T–X* pseudosections modelled in the $Na_2O-CaO-K_2O-FeO-MgO-Al_2O_3-SiO_2-H_2O-TiO_2-O$ system using THERMOCALC 3.40i and the internally consistent thermodynamic dataset of Holland and Powell (2011) (specifically the tc-ds62 dataset generated on 06/02/2014). Activity–composition models are from White et al. (2014a). Although Mn-bearing solution models have been calibrated (White et al., 2014b), Mn has a negligible effect at high temperatures and was not considered (Johnson et al., 2015). Calculations consider the phases garnet, silicate melt, plagioclase, K-feldspar, sillimanite, sapphirine, quartz, muscovite, biotite, orthopyroxene, cordierite, ilmenite, rutile and magnetite-spinel. Osumilite was not included as there is no solution model calibrated against the ds6 dataset.

Bulk rock compositions were determined by X-ray fluorescence analysis using a Panalytical 2404 XRF unit at Franklin and Marshall College, Pennsylvania, for which ferric and ferrous iron contents were determined by titration. The bulk compositions (expressed as mol.% oxides) used in the pseudosections are given in Table 1. Modelled H_2O contents were constrained using *T–X* or *P–X* pseudosections ranging from a quantity assuming all analysed loss on ignition (LOI) as H_2O to lower values (0.1 mol.%). The H_2O content chosen for *P–T* modelling was such that the solidus intersected, or was as close as possible to the field containing the interpreted peak assemblage (see Supplementary data Fig. S1–3). Calculations using the composition of the distal sample (ROG13/11), the most altered of the studied rocks, measured ferric iron concentrations were too high with all calculated fields containing magnetite, which is not observed in the rock. Thus, to account for post-peak oxidation, appropriate ferric iron contents were constrained using a *P–X* pseudosection ranging from the titrated value (1.31 mol.% Fe_2O_3) to a minimal content (0.01 mol.%; see Supplementary data Fig. S4). A value of $X = 0.5$ (Fe_2O_3 = O = 0.67 mol.%) was chosen, as it is the minimum required to eliminate magnetite from the interpreted peak assemblage. Note that the stability field of spinel in nature is likely to be larger than the calculated

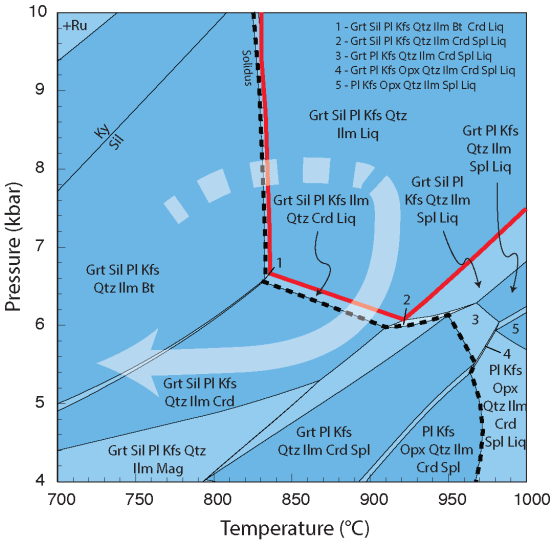

Fig. 8: Modelled *P–T* pseudosection of the distal sample (ROG13/11) with peak field outlined in red and solidus marked by a black dashed line. The interpreted, clockwise *P–T* path traces the post-peak growth of cordierite and biotite. Positioning of the *P–T* path is based on modal isopleths generated using TCInvestigator (Pearce et al., 2015).

stability due to the presence of minor components (e.g. Zn, V, Cr) that cannot currently be modelled (Tajčmanová et al., 2009). Drüppel et al. (2013) report average concentrations of Cr_2O_3 and ZnO in spinel in the sapphirine-bearing sample as 0.07 and 0.15 wt. %, respectively (Drüppel et al., 2013). For reference, *P–T* pseudosections contoured for the abundance of particular phases calculated using TCInvestigator (Pearce et al., 2015) are given in the Supplementary data (Fig. S5).

4.1. Distal sample

In the *P–T* pseudosection for sample ROG13/11 (Fig. 8), the solidus for the chosen H_2O content is located at ~830 °C at pressures above 7 kbar. Between 6–7 kbar the solidus inflects to higher temperatures (~970 °C) due to the presence of cordierite that partitions some of the H_2O that at higher pressures is contained within melt. For the chosen ferric iron content and *P–T* range, ilmenite is stable throughout and magnetite is predicted only at low temperatures and pressures. The interpreted peak assemblage of garnet, sillimanite, plagioclase, K-feldspar, quartz, ilmenite and melt occupies a large stability field at >850 °C and >6 kbar (outlined in red, Fig. 8). At lower temperatures biotite is stable, and at lower pressures cordierite, which occurs replacing garnet at its margins, is predicted. The calculated stability fields of spinel and orthopyroxene occur at higher temperatures and lower pressures than the inferred peak, respectively.

4.2. Intermediate sample

In the *P–T* pseudosection for sample ROG13/10 (Fig. 9) the solidus for the chosen H_2O content is located at ~900–950 °C. The stability field for the interpreted earlier assemblage of sapphirine, orthopyroxene, plagioclase, K-feldspar, cordierite, ilmenite and melt is relatively narrow (in *T*) between 910–980 °C and between 4 and 8 kbar (outlined in red, Fig. 9). Cordierite is consumed at higher *T* and biotite is predicted at lower *T*, and garnet is stable at higher *P* and spinel at lower *P*. Compositional isopleths of Al–in–orthopyroxene are shown on Fig. 9. Maximum measured values of X(Al) (Al cations in the formula unit based on six oxygens) from samples from this locality are 0.18 according to Drüppel et al. (2013), and this isopleth, along with the one sigma uncertainty on its position, is shown as the shaded field. The measured Al content in orthopyroxene is consistent with the higher pressure part of the preferred peak field, implying peak conditions of around 7–8 kbar

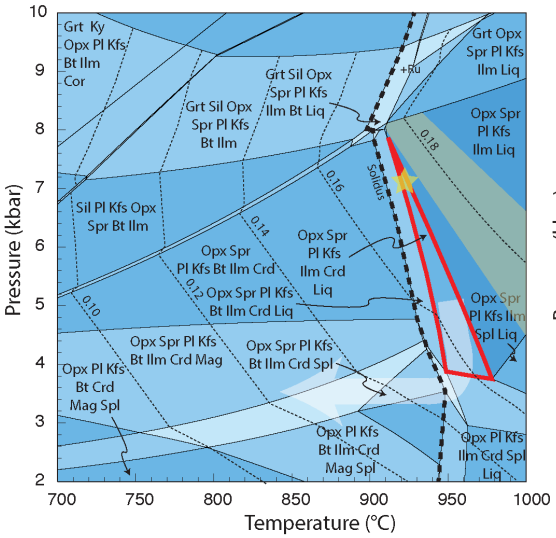

Fig. 9: Modelled *P–T* pseudosection of the intermediate sample (ROG13/10) with peak field outlined in red, solidus marked by a black dashed line and y(opx) isopleths marked by fine dashed lines labelled with their respective values. Grey shaded area indicates uncertainty on the y(opx)=0.18 isopleth. The presence of garnet defines the upper pressure limit of the peak assemblage, while cordierite defines the lower temperature limit. The star indicates the interpreted peak conditions reached during regional metamorphism. The illustrated portion of the *P–T* path traces the growth of spinel and cordierite and later biotite. Positioning of the *P–T* path is based on modal isopleths generated using TCInvestigator (Pearce et al., 2015).

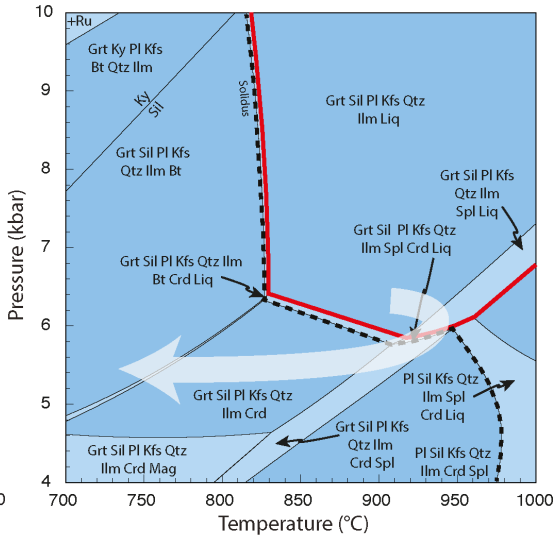

Fig. 10: Modelled *P–T* pseudosection of the proximal sample (ROG14/5) with peak field outline in red and solidus marked by a black dashed line. The interpreted *P–T* path traces the growth of spinel, cordierite and secondary garnet.

and 900–950 °C (Fig. 9). The subsequent evolution of the rock, expressed by the growth of cordierite, spinel and biotite at the expense of sapphirine, requires significantly lower pressures but similar temperatures that was followed by cooling into fields containing biotite.

4.3. Proximal sample

In the *P–T* pseudosection for proximal sample ROG14/5 (Fig. 10), the solidus for the chosen H_2O content is located at ~815 °C above 6.3 kbar but inflects to higher temperatures (~950–975 °C) below 6 kbar due to the presence of cordierite which partitions some of the H_2O that, at higher pressures, is contained within melt. The interpreted earlier assemblage of garnet, sillimanite, plagioclase, K-feldspar, quartz, ilmenite and melt but without spinel, defines a large stability field at 820 to >1000 °C and ~6 to >10 kbar (outlined in red, Fig. 10); spinel is predicted to become stable at higher temperatures. As spinel may be stabilised by non-system components, our preferred interpretation is that the earlier assemblage is consistent with the high *T* end of the modelled spinel-absent field or with the field containing spinel (i.e. >900 °C and >6 kbar). The subsequent evolution of this sample, indicated by the replacement of sillimanite by cordierite and spinel and the growth of a second generation of garnet and cordierite (shown by the arrow on Fig. 10), require lower pressures (~5–6 kbar) but similar temperatures.

5. DISCUSSION

5.1 *P–T* conditions of regional metamorphism

At a distance of ~30 km from the contact, the distal sample is considered to be beyond the effects of contact metamorphism associated with the emplacement of the RIC and to preserve the regional metamorphic history. This is supported by a pronounced regional foliation and the lack of symplectitic replacement of porphyroblast phases that characterises the other samples. Petrographic observations coupled with phase equilibria modelling suggest that this sample experienced a clockwise regional *P–T* path, reaching peak conditions of >850 °C at >6 kbar. Partial replacement of garnet by cordierite implies high-temperature decompression to conditions of ~850 °C at 5 kbar, while the growth of biotite implies crystallisation of the last vestiges of melt upon cooling. A *P–T* path consistent with these observations is shown on Fig. 8. Peak conditions are poorly constrained due to the size and the calculated compositional and modal homogeneity of the phases within the inferred peak field. The high temperature subsolidus prograde path is constrained to the sillimanite field, with no evidence for the former presence of kyanite.

The inferred early assemblages developed within the intermediate sample (sapphirine, orthopyroxene, plagioclase, K-feldspar, cordierite, ilmenite and melt) and the proximal sample (garnet, sillimanite plagioclase, K-feldspar, quartz, ilmenite, spinel and melt), are similarly consistent with growth during regional metamorphism. Modelling of these compositions gives *P–T* conditions that are similar to those derived for the distal sample, namely 900–950 °C and ~7–8 kbar for the intermediate sample (Fig. 9) and >900 °C and >6 kbar for the proximal sample (Fig. 10). Clearly, all three samples cannot have followed an identical regional *P–T* path. However, we propose that a generalised, clockwise regional metamorphic evolution was experienced by all samples, which attained peak conditions of around 850–950 °C at 7–8 kbar, and was followed by high-temperature decompression to ~5 kbar, followed by near isobaric cooling (Fig. 8). Under such conditions, pelitic and greywacke protoliths will produce significant quantities of melt (Johnson et al., 2008; White et al., 2014a), most of which will have been lost to higher crustal levels to leave low a (H_2O) granulite facies residua, consistent with observation.

Clockwise regional *P–T* paths were proposed by both Tomkins et al. (2005) and Drüppel et al. (2013). However, our inferred regional peak conditions are at least ~200 °C higher than those reported by Tomkins et al., (2005) based on conventional thermobarometry, and ~50 °C lower than the UHT regional conditions proposed by Drüppel et al. (2013), based on phase equilibria modelling (Fig. 11). Possible reasons for these differences are detailed below.

5.2. *P–T* conditions of contact metamorphism

Petrographic observations of the intermediate and proximal samples in conjunction with phase equilibria modelling suggest a two-stage evolution which we equate to: (i) high- to ultra-high *T* regional metamorphism with associated partial melting and melt loss (detailed above); and (ii) subsequent high- to ultra-high *T* contact metamorphism of the residual rocks caused by emplacement of the RIC.

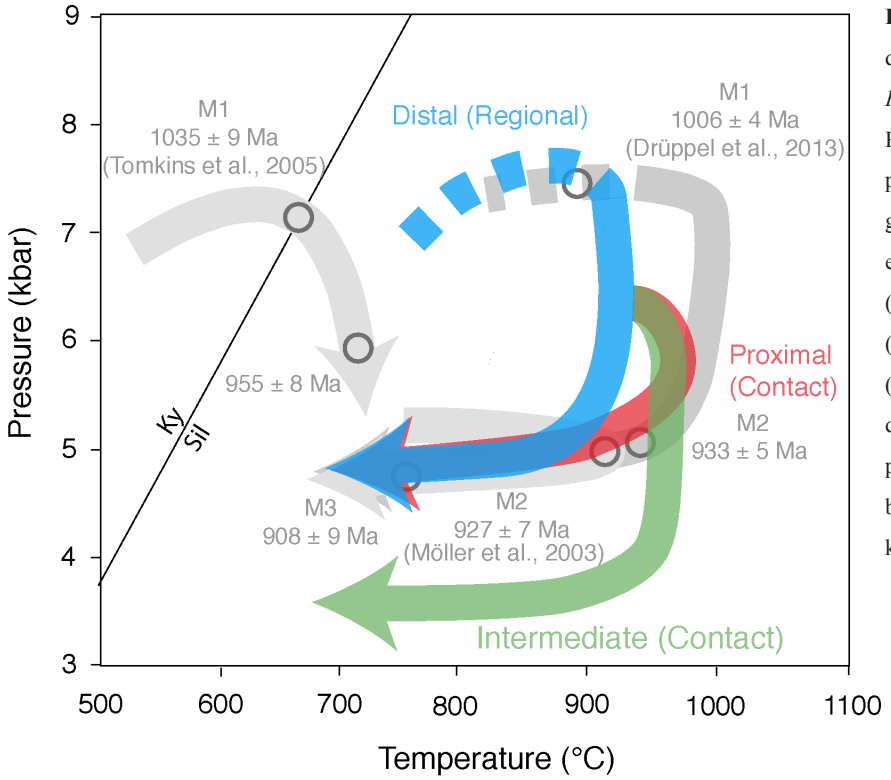

Fig. 11: Summary diagram of the revised *P–T* evolution of the RVA Sector, with previous models in grey. Interpreted *P–T* evolution for the distal (blue), intermediate (green) and proximal (red) samples. The dashed approximate prograde evolution is based on the lack of kyanite in all samples.

Importantly, the distal and proximal samples have strikingly similar bulk compositions, confirmed by the similarity in the *P–T* pseudosections for each (see Figs 8 & 10). However, the petrographic features of the rocks are very different. Both are inferred to have had a regional peak assemblage containing garnet, sillimanite, plagioclase, K-feldspar, quartz, ilmenite, and melt, with the proximal sample inferred to have additionally contained a small quantity of spinel. However, the proximal sample contains a second generation of garnet (and spinel) that is lacking from the distal sample. In addition, sillimanite in the proximal sample is extensively replaced by a coarse intergrowth of cordierite plus spinel, whereas sillimanite in the distal sample is pristine. We interpret the coarse intergrowths of cordierite and spinel after sapphirine in the intermediate sample and after sillimanite in the proximal sample as prograde reaction products that formed as a result of heating associated with emplacement of the RIC. Similar prograde reaction textures have been described elsewhere (Pitra and Waal, 2001; White et al., 2002; Johnson et al., 2004).

In the proximal sample, the reaction textures are consistent with contact metamorphic conditions of ~950 °C at ~5 kbar (Fig. 10, 11). In the intermediate sample, the reaction textures are consistent with temperatures of ~950 °C and lower pressures of ~3–4 kbar (Fig. 9, 11). The lower pressures inferred for the intermediate sample suggests it was at higher levels in the crust when the RIC was emplaced and implies tilting of the section and/or differential uplift and erosion post intrusion of the RIC. Overall, the pressures inferred for the contact metamorphism (3–6 kbar, Fig. 11) are similar to those reported by other authors (Möller et al., 2003; Tomkins et al., 2005). The high temperatures inferred for

the contact metamorphism in the intermediate sample may suggest the anorthosite sits at shallow levels beneath these rocks. However, with no borehole data, the similarity in density between the anorthosite and host gneisses makes this difficult to test using geophysical means.

Within the intermediate sample, the growth of biotite replacing cordierite in the spinel-cordierite symplectites, which are themselves replacing sapphirine, suggests that the rocks may have retained small quantities of melt and that, on cooling and exhumation from the regional peak, the intermediate sample did not cross the solidus before the onset of contact metamorphism. This could indicate that the rocks stayed at high temperature for 100 Ma or more.

Our interpretation that the intermediate and proximal samples followed a two-stage *P–T* evolution (Fig. 11), with contact metamorphism superimposed upon the regional metamorphic evolution path, differs from the work of Drüppel et al. (2013). These authors suggest the rocks followed a clockwise, single-stage regional metamorphic evolution peaking at UHT conditions based on their interpretation that the age of UHT metamorphism pre-dates the intrusion of the RIC. We suggest that the 1021 ± 23 to 999 ± 17 Ma metamorphic ages of Drüppel et al. (2013) may represent growth of zircon from crystallising melt following peak metamorphism at ca 1035 Ma (Tomkins et al., 2005).

5.3. *P–T* evolution of the RVA Sector

We present a revised *P–T* evolution for gneisses of the RVA Sector during the Sveconorwegian orogeny: For rocks outside the influence of the RIC (our distal sample), regional metamorphism followed a clockwise *P–T* path with peak conditions of ~850–950 °C at ~7–8 kbar followed by high-temperature, retrograde decompression to conditions of ~900 °C at 5 kbar and, subsequently, isobaric cooling to below 700 °C (Fig. 11). Whereas the distal sample preserves no compelling evidence for having experienced contact metamorphism, rocks closer to the RIC (our intermediate and proximal samples) contain evidence for a static thermal overprint (contact metamorphism) that records pressures of 3–6 kbar and reached a maximum temperature in the sample immediately adjacent to the RIC contact of over 950 °C.

The proposed *P–T* evolution outlined in this study reconciles the previous interpretations made by Degeling et al. (2001) and Drüppel et al. (2013). Degeling et al. (2001) underestimated the temperature of peak regional metamorphism by ~200 °C, due to their reliance on petrogenetic grids in the KFMASH model system, which is an oversimplification of natural rocks (White et al., 2007; White et al., 2014a), and by their use of conventional thermobarometric techniques which, due to post-peak diffusion, commonly lead to underestimates of peak temperatures (Fitzsimons and Harley, 1994; Pattison et al., 2003). Assuming our results are reliable, Drüppel et al. (2013) overestimated the temperature experienced by the rocks at Ivesdal, our intermediate locality, by ~50 °C. This is most likely due to their omission of ferric iron (modelled as O) from their model system, that affects the bulk $X_{(Mg)}$ of the modelled composition. In particular, these authors used an older solution model for sapphirine that does not include ferric iron, which can significantly reduce

the temperature at which sapphirine is stable (Kelsey et al., 2005; Wheller and Powell, 2014). Furthermore, Drüppel et al. (2013) rely in part on spinel to constrain their *P–T* trajectories. However, the presence of elements such as Cr and Zn that are not currently incorporated into thermodynamic models, will stabilise spinel to lower temperatures than predicted by the pseudosection modelling (Tajčmanová et al., 2009).

5.4. Implications for the tectonic setting of the Sveconorwegian orogeny

The revised metamorphic evolution proposed here has implications for tectonic models for the development of the RVA Sector during the Sveconorwegian orogeny. There are at present two different tectonic models for the Sveconorwegian orogeny, a continent-continent collisional model proposed by Bingen et al. (2008) and an accretionary model of Slagstad et al. (2013a), which has been further refined by Coint et al. (2015). The collisional model postulates that at ~1140 Ma Fennoscandia collided with an as yet unidentified continent (possibly Amazonia), resulting in widespread Barrovian-type regional metamorphism. At ~930 Ma a phase of orogenic collapse was initiated that resulted in the emplacement of the RIC and formation of a regional-scale UHT contact aureole (Bingen et al., 2008). The long timescales of high-temperature conditions interpreted in this study are sufficient for the generation of high-grade metamorphic conditions within a collisional system (Clark et al., 2011). However, the lack of any obvious colliding continental block and the evidence for a series of magmatic events with arc-like chemistry that post-date the proposed collision led Slagstad et al. (2013a) to develop an alternative Andean-style accretionary model to explain the geological evolution of SW Norway. According to Slagstad et al. (2013a), the long-lived accretionary margin underwent periodic extension and compression (as a result of steep and flat slab subduction) and to alternate between periods of metamorphism (1020–990 Ma) and magmatism (1050–1020 and 990–920 Ma) to generate the SMB, HBG and RIC suites.

In contrast to the *P–T–t* proposed by Drüppel et al. (2013), which consists of a single clockwise *P–T* loop with UHT metamorphism occurring 10–15 Myr after the cessation of SMB magmatism, Slagstad and co-workers argued that the metamorphic history of rocks in SW Norway could not have been produced by a collisional orogeny (Slagstad et al., 2013b). They suggest that to generate temperatures of ~1000 °C at mid to lower crustal depths in a collisional system requires on the order of ca 100 Ma (e.g. Clark et al., 2011; Clark et al., 2015).

All of the available evidence from this and previous studies indicates that a period of crustal thickening must have occurred prior to the attainment of peak regional metamorphic conditions (Bingen et al., 2008; Drüppel et al., 2013; Slagstad et al., 2013a). Possible mechanisms for crustal thickening include collision, flat-slab subduction and accretion. Whilst continental collision is a key part of the four-phase model of Bingen et al. (2008), with subduction interpreted to have ceased at 1140 Ma, this is inconsistent with the presence of the 1060–1020 Ma calc-alkaline SMB as well as the presence of contemporaneous and later arc-related features across the terranes

of the Sveconorwegian Belt. These include the widespread arc geochemical signatures (Brewer et al., 2002; Andersen et al., 2007; Corfu and Laajoki, 2008; Petersson et al., 2015), multiple periods of back-arc basin formation (Brewer et al., 2002; Söderlund and Ask, 2006; Söderlund et al., 2006; Andersen et al., 2007; Spencer et al., 2014; Petersson et al., 2015) and related bimodal magmatism (Söderlund and Ask, 2006; Bingen et al., 2008; Corfu and Laajoki, 2008; Spencer et al., 2014) as well as the overall younging to the west caused by westerly arc retreat with subduction beneath Fennoscandia (Slagstad et al., 2013a; Spencer et al., 2014 and references within; Coint et al., 2015; Petersson et al., 2015; Roberts and Slagstad, 2015).

Flat-slab subduction has been previously proposed by Slagstad et al. (2013a) to have driven crustal thickening and develop medium–*P*, high–*T* regional metamorphism within the geographically restricted area of the RVA Sector. This interpretation is consistent with magmatism starting 15 Myr prior to the onset of regional metamorphism, in which the magmas could not have been produced from partial melting related to crustal thickening (Slagstad et al., 2013a, b). Therefore, we therefore favour the Slagstad et al. (2013a) accretionary model for the RVA Sector. Similar styles of accretionary tectonics have been invoked to form regional-scale granulite facies terranes in a number of other Mesoproterozoic Orogens (Karlstrom et al., 2001; Clark et al., 2014; Korhonen et al., 2014) and have been singled out as sites of crustal growth and granulite generation throughout Earth history (Collins, 2002; Cawood and Buchan, 2007), at least since the Archaean.

More problematic is exactly how the RIC formed. Most geochronology of the RIC indicates that it was emplaced in a restricted time span at ~930 Ma. However, Coint et al. (2015) hypothesise that it may have had a protracted, episodic emplacement history based on the complex spread of zircon U–Pb ages that may record multiple intrusive events and resulted in the formation of complex growth and dissolution of zircon and monazite over an extended time interval (<1000 Ma to 920 Ma) (Möller et al., 2003 and references within). In the absence of unequivocal geochronological evidence that suggests emplacement over a prolonged period, we favour a short-lived intrusive event at ~930 Ma, with magmas emplaced into rocks that still retained small amounts of melt. Small volumes of melt in the rocks could have resulted in the reported zircon textures (Möller et al., 2003) and a single thermal pulse is consistent with the relatively simple petrographic textures documented in this study and the pluton sub-parallel isograds observed at the map scale. There is no clear evidence for slab breakoff as the causal mechanism for generation of the RIC. Recent work by Bybee et al. (2013) suggests that the RIC formed as part of a long-lived magmatic system, consistent with an accretionary setting. It is difficult to determine what caused the end of the Sveconorwegian orogeny as this margin was significantly modified during the Caledonian orogeny, leaving no obvious geological record of what previously lay to the west.

6. CONCLUSIONS

- Regional metamorphism in the RVA Sector during the Sveconorwegian orogeny followed a clockwise *P–T* path attaining peak conditions of ~850–950 °C and ~7–8 kbar at ca

1035 Ma. Partial melting and melt loss led to the production of highly residual rock compositions.

- Rocks located up to at least 10km from the RIC experienced an additional static, low-pressure, high-temperature event ~100 Myr after the peak of regional metamorphism that reached a maximum *T* of ~950 °C at 3–6 kbar. The source of this additional heat was the RIC itself, which was emplaced into slightly cooler but residual crust and resulted in the series of high-*T* isograds concentric with its margin.
- The collisional model of Bingen et al. (2008) cannot satisfactorily explain the metamorphic and magmatic evolution of the Sveconorwegian orogeny in the RVA Sector as it lacks a plausible heat source to drive UHT metamorphism. A model that has the Sveconorwegian Orogen as an east facing accretionary margin that experienced long-lived subduction associated with periods of flat slab subduction, rollback and arc accretion, akin to that proposed by Slagstad et al. (2013) better explains the metamorphic and magmatic evolution of the RVA Sector.

ACKNOWELDGEMENTS

We thank two anonymous reviewers for their detailed comments and Prof. M. Santosh for his editorial handling. Financial support for this project was provided by an ARC DECRA fellowship (DE120103067) to CC.

REFERENCES

Andersen, T., Griffin, W. L., and Pearson, N. J., 2002. Crustal evolution in the SW part of the Baltic Shield: the Hf isotope evidence. Journal of Petrology 43(9), 1725-1747.

Andersen, T., Griffin, W. L., and Sylvester, A. G., 2007. Sveconorwegian crustal underplating in southwestern Fennoscandia: LAM-ICPMS U-Pb and Lu-Hf isotope evidence from granites and gneisses in Telemark, southern Norway. Lithos 93, 273-287.

Barnichon, J. D., Havenith, H., Hoffer, B., Charlier, R., Jongmans, D., and Duchesne, J. C., 1999. The deformation of the Egersund-Ogna anorthosite massif, south Norway: finite-element modelling of diapirism. Tectonophysics 303, 109-130.

Bergh, S. G., Chattopadhya, A., Ravna, E. K., Corfu, F., Kullerud, K., Swaan, K. B., Armitage, P. E. B., Myhre, P. I., and Holdsworth, R. E., 2012. Was the Precambrian basement of Western Troms and Lofoten-Vesterålen in northern Norway linked to the Lewisian of Scotland? A comparison of crustal components, tectonic evolution and amalgamation history, In: Sharkov, E. (Ed) Tectonics – Recent Advances. In Tech Open Access Publisher, 283-330.

Bingen, B., Nordgulen, Ø., and Viola, G., 2008. A four-phase model for the Sveconorwegian orogeny, SW Scandinavia. Norwegian Journal of Geology 88, 43-72.

Bingen, B., Skår, Ø., Marker, M., Sigmond, E. M. O., Nordgulen, Ø., Ragnhildstveit, J., Mansfeld, J., Tucker, R. D., and Liégeois, J-P., 2005. Timing of continental building in the Sveconorwegian orogen, SW Scandinavia. Norwegian Journal of Geology 85, 87-116.

Bingen, B., Stein, H. J., Bogaerts, M., Bolle, O., and Mansfeld, J., 2006. Molybdenite Re–Os dating constrains gravitational collapse of the Sveconorwegian orogen, SW Scandinavia. Lithos 87, 328-346.

Bingen, B., and van Breemen, O., 1998. U–Pb monazite ages in amphibolite- to granulite-facies orthogneiss reflect hydrous mineral breakdown reactions: Sveconorwegian Province of SW Norway. Contributions to Mineralogy and Petrology 132, 336-353.

Bogaerts, M., Scaillet, B., Liégeois, J.-P., and Vander Auwera, J., 2003. Petrology and geochemistry of the Lyngdal granodiorite (Southern Norway) and the role of fractional crystallization in the genesis of Proterozoic ferro-potassic A-type granites. Precambrian Research 124, 149-184.

Bogdanova, S. V., Bingen, B., Gorbatschev, R., Kheraskova, T. N., Kozlov, V. I., Puchkov, V. N., and Volozh, Y. A., 2008. The East European craton (Baltica) before and during the assembly of Rodinia. Precambrian Research, 160, 23-45.

Bol, L. C. G. M., Maijer, C., and Jansen, B. H., 1989. Premetamorphic lateritisation in Proterozoic metabasites of Rogaland, SW Norway. Contributions to Mineralogy and Petrology 103, 306-316.

Bolle, O., Diot, H., Liégeois, J.-P., and Auwera, J. V., 2010. The Farsund intrusion (SW Norway): a marker of late-Sveconorwegian (Grenvillian) tectonism emplaced along a newly defined major shear zone. Journal of Structural Geology 32, 1500-1518.

Bolle, O., Trindade, R. I. F., Bouches, J. L., and Duchesne, J.-C., 2002. Imaging downward granitic transport in the Rogaland Igneous Complex, SW Norway. Terra Nova 14, 87-92.

Brewer, T. S., Åhäll, K. I., Darbyshire, D. P. F., and Menuge, J. F., 2002. Geochemistry of late Mesoproterozoic volcanism in southwestern Scandinavia: implications for Sveconorwegian/ Grenvillian plate tectonic models. Journal of the Geological Society, London 159, 129-144.

Brown, M., 2007. Metamorphic conditions in orogenic belts: a record of secular change. International Geology Review 49, 193-234.

Bybee, G. M., Ashwal, L. D., Shirey, S. B., Horan, M., Mock, T., and Andersen, T. B., 2014. Pyroxene megacrysts in Proterozoic anorthosites: Implications for tectonic setting, magma source and magmatic processes at the Moho. Earth and Planetary Science Letters 389, 74–85.

Cawood, P. A., and Buchan, C., 2007. Linking accretionary orogenesis with supercontinent assembly. Earth-Science Reviews 82, 217-256.

Clark, C., Fitzsimons, I. C. W., Healy, D., and Harley, S. L., 2011. How does the continental crust get really hot?. Elements 7, 235-240.

Clark, C., Healy, D., Johnson, T., Collins, A. S., Taylor, R., Santosh, M., and Timms, N. E., 2015. Hot orogens and supercontinent amalgamation: A Gondwanan example from southern India. Gondwana Research 28(4), 1310-1328.

Clark, C., Kirkland, C. L., Spaggiari, C. V., Oorschot, C., Wingate, M. T. D., and Taylor, R. J., 2014. Proterozoic granulite formation driven by mafic magmatism: An example from the Fraser Range Metamorphics, Western Australia. Precambrian Research 240, 1-21.

Coint, N., Slagstad, T., Roberts, N. M. W., Marker, M., Røhr, T. S., and Sørensen, B. E., 2015. The Late Mesoproterozoic Sirdal Magmatic Belt, SW Norway: Relationships between magmatism and metamorphism and implications for Sveconorwegian orogenesis. Precambrian Research 265, 57-77.

Collins, W. J., 2002. Hot orogens, tectonic switching, and creation of continental crust. Geology 30(6), 535-538.

Corfu, F., and Laajoki, K., 2008. An uncommon episode of mafic magmatism at 1347 Ma in the Mesoproterozoic Telemark supracrustals, Sveconorwegian orogen–Implications for stratigraphy and tectonic evolution. Precambrian Research 160, 299-307.

Degeling, H., Eggins, S., and Ellis, D. J., 2001. Zr budgets for metamorphic reactions, and the formation of zircon from garnet breakdown. Mineralogical Magazine 65(6), 749-758.

Demaiffe, D., and Michot, J., 1985. Isotope geochronology of the Proterozoic crustal segment of Southern Norway: a review. In: Tobi, A. C. & Touret, J. L. R. (Eds) The Deep Proterozoic Crust in the North Atlantic Provinces, D. Reidel Publishing Co, 411-435.

Drüppel, K., Elsäßer, L., Brandt, S., and Gerdes, A., 2013. Sveconorwegian Mid-crustal Ultrahigh-temperature Metamorphism in Rogaland, Norway: U-Pb LA-ICP-MS Geochronology and Pseudosections of Sapphrine Granulites and Associated Paragneisses. Journal of Petrology 54(2), 305-350.

Duchesne, J.-C., and Wilmart, E., 1997. Igneous charnockites and related rocks from the Bjerkreim-Sokndal Layered Intrusion (Southwest Norway): a jotunite (hypersthene monzodiorite)-derived A-type granitoid suite. Journal of Petrology 38(3), 337-369.

Duchesne, J. C., and Michot, J., 1987. The Rogaland intrusive masses: Introduction. In: Maijer, C. & Padget, P. (Eds) The geology of Southernmost Norway. Norges Geologisk Undersøkelse Special Publication 1, 48-59.

Falkum, T., 1982. Geologisk kart over Norge, berggrunnskart MANDAL, 1:250,000. Norges Geologisk Undersøkelse.

Falkum, T., 1985. Geotectonic evolution of southern Scandinavia in light of a late-Proterozoic plate-collision. In: Tobi, A. C. & Touret, J. L. R. (Eds) The Deep Proterozoic Crust in the North Atlantic Provinces, D. Reidel Publishing Co, 309-322.

Falkum, T., and Petersen, J. S., 1980. The Sveconorwegian orogenic belt, a case of late-Proterozoi plate-collision: Geologische Rundschau 69(3), 622-647.

Fitzsimons, I. C. W., and Harley, S. L., 1994. The influence of retrograde cation exchange on granulite P–T estimates and a convergence technique for the recovery of peak metamorphic conditions. Journal of Petrology 35(2), 543-576.

Harlov, D. E., 2011. Petrological and experimental application of REE- and actinide-bearing accessory mineral to the study of Precambrian high-grade gneiss terrains. Geological Society of America Memoirs 207, 13-24.

Hermans, G. A. E. M., Hakstege, A. L., Jansen, J. B. H., and Poorter, R. P. E., 1976. Sapphrine occurrence near Vikeså in Rogaland, Southwestern Norway. Norsk Geologisk Tidsskrift 56, 397-412.

Hermans, G. A. E. M., Tobi, A. C., Poorter, R. P. E., and Maijer, C., 1975. The high-grade metamorphic Precambrian of the Sirdal-Ørsdal area, Rogaland/Vest-Agder, South-west Norway. Norges Geologisk Undersøkelse 318, 51-74.

Holland, T. J. B., and Powell, R., 2011. An improved and extended internally consistent thermodynamic dataset for phases of petrological interest, involving a new equation of state for solids. Journal of Metamorphic Geology 29, 333-383.

Huijsmans, J. P. P., Kabel, A. B. E. T., and Steenstra, S. E., 1981. On the structure of high-grade metamorphic Precambrian terrain in Rogaland, south Norway. Norsk Geologisk Tidsskrift 61, 183-192.

Jansen, B. H., Blok, R. J. P., Bos, M., and Scheelings, M., 1985. Geothermometry and geobarometry in Rogaland and preliminary results from the Bamble area, S Norway. In: Tobi, A. C. & Touret, J. L. R. (Eds) The Deep Proterozoic Crust in the North Atlantic Provinces, D. Reidel Publishing Co, 499-516.

Jansen, B. H., and Tobi, A. C., 1987. Introduction to the Faurefjell metasediments: In: Maijer, C. & Padget, P. (Eds) The geology of Southernmost Norway. Norges Geologisk Undersøkelse Special Publication 1, 88-89.

Johnson, T., Brown, M., Gibson, R. & Wing, B., 2004. Spinel-cordierite symplectites replacing andalusite: evidence for melt-assisted diapirism in the Bushveld Complex, South Africa. Journal of Metamorphic Geology 22, 529–545.

Johnson, T., Clark, C., Taylor, R., Santosh, M., and Collins, A. S., 2015. Prograde and retrograde growth of monazite in migmatites: An example from the Nagercoil Block, southern India. Geoscience Frontiers 6(3), 373-387.

Johnson, T. E., White, R. W. & Powell, R., 2008. Partial melting of metagreywacke – a calculated mineral equilibria study. Journal of Metamorphic Geology, 26, 837–853.

Karlstrom, K. E., Åhäll, K. I., Harlan, S. S., Williams, M. L., McLelland, J., and Geissman, J. W., 2001. Long-lived (1.8-1.0 Ga) convergent orogen in southern Laurentia, its extensions to Australia and Baltica, and implications for refining Rodinia. Precambrian Research 111, 5–30.

Kars, H., Jansen, B. H., Tobi, A. C., and Poorter, R. P. E., 1980. The metapelitic rocks of the polymetamorphic Precambrian of Rogaland, SW Norway: Part II- Mineral relations between cordierite, hercynite and magnetite within the osumilite-in isograd. Contributions to Mineralogy and Petrology 74, 235-244.

Kelsey, D. E., White, R. W., and Powell, R., 2005. Calculated phase equilibria in K_2O–FeO–MgO–Al_2O_3–SiO_2–H_2O for silica-undersaturated sapphrine-bearing mineral assemblages. Journal of Metamorphic Geology 23, 217-239.

Korhonen, F. J., Clark, C., Brown, M., and Taylor, R. J. M., 2014. Taking the temperature of Earth's hottest crust. Earth and Planetary Science Letters 408, 341-354.

Kretz, R., 1983. Symbols for rock-forming minerals. American Mineralogist 68, 277-279.

Longhi, J., Fram, M. S., Auwera, J. V., and Montieth, J. N., 1993. Pressure effects, kinetics, and rheology of anorthositic and related magmas. American Mineralogist 78, 1016-1030.

Maijer, C., 1987. The metamorphic envelope of the Rogaland intrusive complex. Norges Geologisk Undersøkelse- Special Publication 1, 68-73.

Maijer, C., Andriessen, P. A. M., Hebeda, E. H., Jansen, B. H., and Verschure, R. H., 1981. Osumilite, an approximately 970 Ma old high-temperature index mineral of the granulite-facies metamorphism in Rogaland, SW Norway. Geologie en Mijnbouw 60, 267-272.

Marker, M., Schiellerup, H., Meyer, G., Robins, B., and Bolle, O., 2003. Introduction to the geological map of the Rogaland Anorthosite Province 1:75000. Norges Geologisk Undersøkelse- Special Publication 9, 109-116.

Möller, A., O'Brien, P. J., Kennedy, A., and Kröner, A., 2002. Polyphase zircon in ultrahigh-temperature granulites (Rogaland, SW Norway): constraints for Pb diffusion in zircon. Journal of Metamorphic Geology 20, 727-740.

Möller, A., O'Brien, P. J., Kennedy, A., and Kröner, A., 2003. Linking growth episodes of zircon and metamorphic textures to zircon chemistry: an example from the ultrahigh-temperature granulites of Rogaland (SW Norway). In: Vance, D. Müller, W. & Villa, I. M. (Eds) Geochronology: Linking the Isotopic Record with Petrology and Textures. The Geological Society, London, Special Publications 220, 65-81

Nijland, T. G., Maijer, C., and de Haas, G.-J. L. M., 1996. The Stokkafjell Troctolite, SW Norway: its bearing on the early P-T evolution of the Rogaland terrane. Neues Jahrbuch fur Mineralogie Abhandlungen 171, 91-117.

Pasteels, P., Demaiffe, D., and Michot, J., 1979. U–Pb and Rb–Sr geochronology of the eastern part of the south Rogaland igneous complex, southern Norway. Lithos 12, 199-208.

Pattison, D. R. M., Chacko, T., Farquhar, J., and McFarlane, R. M., 2003. Temperature of granulite-facies metamorphism: constraints from experimental phase equilibria and thermobarometry corrected for retrograde exchange. Journal of Petrology 44(5), 867-900.

Pearce, M. A., White, A. J. R., and Gazley, M. F., 2015. TCInvestigator: automated calculation of mineral mode and composition contour for THERMOCALC pseudosections. Journal of Metamorphic Geology 33, 413-425.

Petersson, A., Scherstén, A., Bingen, B., Gerdes, A., and Whitehouse, M. J., 2015. Mesoproterozoic continental growth: U–Pb–Hf–O zircon record in the Idefjorden Terrane, Sveconorwegian Orogen. Precambrian Research 261, 75-95.

Pitra, P., and Waal, S. A. D., 2001. High-temperature, low-pressure metamorphism and development of prograde symplectites, Marble Hall Fragment, Bushveld Complex (South Africa). Journal of Metamorphic Geology 19(3), 311-325.

Rivers, T., 1997. Lithotectonic elements of the Grenville Province: review and tectonic implications. Precambrian Research 86,117–154.

Roberts, N. M. W. and Slagstad, T., 2015. Continental growth and reworking on the edge of the Columbia and Rodinia supercontinents; 1.86-0.9 Ga accretionary orogeny in southwest Fennoscandia. International Geology Review 57, 1582-1606.

Sauer, S., Slagstad, T., Andersen, T., and Kirkland, C. L., 2013. Zircon Lu-Hf isotopes in high-alumina orthopyroxene megacrysts from the Neoproterozoic Rogaland Anorthosite Province, SW Norway: A window into the Sveconorwegian lower crust. EGU General Assembly Conference Abstracts 15, 13958.

Sauter, P. C. C., 1981. Mineral relations in siliceous dolomites and related rocks in the high-grade metamorphic Precambrian of Rogaland, SW Norway. Norsk Geologisk Tidsskrift 61, 35-45.

Schärer, U., Wilmart, E., and Duchesne, J-C., 1996. The short duration and anorogenic character of anorthosite magmatism: U–Pb dating of the Rogaland complex, Norway. Earth and Planetary Science Letters 139, 335-350.

Slagstad, T., Roberts, N. M. W., Marker, M., Røhr, T. S., and Schiellerup, H., 2013a. A non-collisional, accretionary Sveconorwegian orogen. Terra Nova 25, 30-37.

Slagstad, T., Roberts, N. M. W., Marker, M., Røhr, T. S., and Schiellerup, H., 2013b. A non-collisional, accretionary Sveconorwegian orogen – Reply. Terra Nova 25(2), 169-171.

Söderlund, U., and Ask, R., 2006. Mesoproterozoic bimodal magmatism along the Protogine Zone, S Sweden: three magmatic pulses at 1.56, 1.22 and 1.205 Ga, and regional implications. GFF 128, 303-310.

Söderlund, U., Elming, S.-Å., Ernst, R. E., and Schissel, D., 2006. The Central Scandinavian Dolerite Group–Protracted hotspot activity or back-arc magmatism? Constraints from U–Pb baddeleyite geochronology and Hf isotopic data. Precambrian Research 150, 136-152.

Spencer, C. J., Roberts, N. M. W., Cawood, P. A., Hawkesworth, C. J., Prave, A. R., Antonini, A. S. M., Horstwood, M. S. A., and EIMF, 2014. Intermontane basins and bimodal volcanism at the onset of the Sveconorwegian Orogeny, southern Norway. Precambrian Research 252, 107-118.

Tajčmanová, L., Konopásek, J., and Košler, J., 2009. Distribution of zinc and its role in the stability of spinel in high-grade felsic rocks of the Moldanubian domain (Bohemian Massif). European Journal of Mineralogy 21, 407-418.

Tobi, A. C., Hermans, G. A. E. M., Maijer, C., and Jansen, B. H., 1985. Metamorphic zoning in the high-grade Proterozoic of Rogaland-Vest Agder, SW Norway. In: Tobi, A. C. & Touret, J. L.R. (Eds) The Deep Proterozoic Crust in the North Atlantic Provinces, D. Reidel Publishing Co., 477-497

Tomkins, H. S., Williams, I. S., and Ellis, D. J., 2005. In situ U–Pb dating of zircon formed from retrograde garnet breakdown during decompression in Rogaland, SW Norway. Journal of Metamorphic Geology 23, 201-215.

Vander Auwera, J., Bolle, O., Bingen, B., Liégeois, J.-P., Bogaerts, M., Duchesne, J.-C., Waele, B. D., and Longhi, J., 2011. Sveconorwegian massif-type anorthosites and related granitoids result from post-collisional melting of a continental arc root. Earth-Science Reviews 107, 375-397.

Vander Auwera, J., Bolle, O., Dupont, A., Pin, C., Paquette, J.-L., Charlier, B., Duchesne, J.-C., Mattielli, N., and Bogaerts, M., 2014. Source-derived heterogeneities in the composite (charnockite-granite) ferroan Farsund intrusion (SW Norway). Precambrian Research 251, 141-163.

Vander Auwera, J., and Longhi, J., 1994. Experimental study of a joutunite (hypersthene monzodiorite): constraints on the parent magma composition and crystallization conditions (P, T, fO_2) of the Bjerkreim-Sokndal layered intrusion (Norway). Contributions to Mineralogy and Petrology 118, 60-78.

Verschure, R. H., Andriessen, P. A. M., Boelrijk, N. A. I. M., Hebeda, E. H., Maier, W. D., Priem, H. N. A., and Verdurmen, E. A. T., 1980. On the thermal stability of Rb–Sr and K–Ar biotite systems: evidence from coexisting Sveconorwegian (ca 870 Ma) and Caledonian (ca 400 Ma) biotites in SW Norway. Contributions to Mineralogy and Petrology 74, 245-252.

Versteeve, A. J., 1975. Isotope geochronology in the high-grade metamorphic Precambrian of Southwestern Norway. Norges Geologisk Undersøkelse 318, 1-50.

Westphal, M., Schumacher, J. C., and Boschert, S., 2003. High-Temperature Metamorphism and the Role of Magmatic Heat Sources at the Rogaland Anorthosite Complex in Southwestern Norway. Journal of Petrology 44(6), 1145-1162.

Wheller, C. J., and Powell, R., 2014. A new thermodynamic model for sapphirine: calculated phase equilibria in K_2O-FeO-MgO-Al_2O_3-SiO_2-H_2O-TiO_2-Fe_2O_3. Journal of Metamorphic Geology 32, 287-299.

White, R. W., Powell, R., and Clarke, G. L., 2002. The interpretation of reaction textures in Fe-rich metapelitic granulites of the Musgrave Block, central Australia: constraints from mineral equilibria calculations in the system K_2O-FeO-MgO-Al_2O_3-SiO_2-H_2O-TiO_2-Fe_2O_3. Journal of Metamorphic Geology 20, 41-55.

White, R. W., Powell, R., and Holland, T. J. B., 2007. Progress relating to calculation of partial melting equilibria for metapelites. Journal of Metamorphic Geology 25, 511-527.

White, R. W., Powell, R., Holland, T. J. B., Johnson, T., and Green, E. C. R., 2014a. New mineral activity-composition relations for thermodynamic calculations in metapelitic systems. Journal of Metamorphic Geology 32, 261-286.

White, R. W., Powell, R., and Johnson, T., 2014b. The effect of Mn on mineral stability in metapelites revisited: new a–x relations for manganese-bearing minerals. Journal of Metamorphic Geology 32, 809-828.

Whitney, D. L., and Evans, B. W., 2010. Abbreviations for names of rock-forming minerals. American Mineralogist 95, 185-187.

Wielens, J. B. W., Andriessen, P. A. M., Boelrijk, N. A. I. M., Hebeda, E. H., Priem, H. N. A., Verdurmen, E. A. T., and Verschure, R. H., 1981. Isotope geochronology in the High-grade metamorphic Precambrian of Southwestern Norway: new data and reinterpretations. Norges Geologisk Undersøkelse 359, 1-30.

Wilmart, E., Clocchiatti, R., Duchesne, J.-C., and Touret, J. L. R., 1991. Fluid inclusions in charnockites from the Bjerkreim-Sokndal massif (Rogaland, southwestern Norway): fluid origin and in situ evolution. Contributions to Mineralogy and Petrology 108, 453-462.

Wilmart, E., and Duchesne, J.-C., 1987. Geothermobarometry of igneous and metamorphic rocks around the Åna-sira anorthosite massif: Implications for the depth of emplacement of the South Norwegian anorthosites. Norsk Geologisk Tidsskrift 67, 185-196.

Supplementary material: See Appendix C

Chapter 4

Constraining the timing of prograde metamorphism in long-lived hot orogens

Eleanore Blereau[1*], Chris Clark[1], Fred Jourdan[1,2], Tim E. Johnson[1], Richard J. M. Taylor[1], Peter D. Kinny[1], Martin Hand[3] and Ela Eroglu[2,4]

[1]Department of Applied Geology, The Institute of Geoscience Research (TIGeR), Curtin University, GPO Box U1987, Perth WA 6845, Australia.

[2]Western Australian Argon Isotope Facility, John de Laeter Centre, Curtin University, GPO Box U1987, Perth WA 6845, Australia.

[3]Centre for Tectonics, Resources and Exploration (TRaX), School of Earth and Environmental Sciences, University of Adelaide, Adelaide 5005, South Australia

[4]Department of Chemical Engineering, Curtin University, GPO Box U1987, Perth WA 6845, Australia.

This article is under review in *GEOLOGY* (since June 7 2017)

ABSTRACT

We present results of the first $^{40}Ar/^{39}Ar$ dating of osumilite, a high-temperature mineral that occurs in volcanic and high-grade metamorphic rocks. The metamorphic osumilite studied here is from the Rogaland–Vest Agder Sector, Norway, an area that experienced high temperatures (>850°C) for ~100 Myr. The results of diffusion experiments indicate that, for a cooling rate of 10°C/Ma and a crystal radius of 175 µm, the closure temperature for argon in osumilite is high (~770°C). The large grain size of osumilite in the Rogaland rocks (~1 cm) allows for the preservation of two apparent age populations. The first dates growth of osumilite during prograde granulite facies regional metamorphism at ca 1070–1050 Ma; the second population records growth and equilibration during contact metamorphism at ca 920–880 Ma following emplacement of the Rogaland Igneous Complex. The ability to date osumilite provides a valuable new thermochronometer that can be used to constrain the timing and duration of high-temperature magmatic and metamorphic events and potentially archaeological events.

1. INTRODUCTION

Establishing robust temporal constraints on long-lived orogenic events and associated pressure–temperature–time (*P–T–t*) paths is key to developing an in-depth, quantitative understanding of the processes of mountain building and collapse. There is increasing evidence to suggest that the deep crust of some large orogenic belts may have remained at high temperatures (>800 °C) in which melt is likely to have been present for long durations (>>10 Myrs; e.g. Clark et al., 2015; Kelsey and Hand, 2015; Harley, 2016). The presence of melt exerts a fundamental control on the strength of the lower crust and its ability to flow and redistribute mass. As such, accurate *P–T–t* information is critical to the construction of robust and realistic thermo-rheological models of the crust (Jamieson and Beaumont, 2013; Gerya, 2014; Sizova et al., 2014).

A well-recognised complication when attempting to establish the duration of orogenic events where temperatures are elevated for >>10 Myrs is that the geochronometers most commonly applied to constrain the timing of part of the *P–T* evolution, such as zircon or monazite, are subject to modification by diffusion thereby limiting their ability to constrain the timing of prograde to peak events (Kelsey and Hand, 2015; Harley, 2016). By contrast, major rock forming minerals commonly have much larger grain sizes (100s to 1000s of µm versus 10s to 100s of µm for zircon and monazite) resulting in far greater diffusional length scales that greatly increase the potential of preserving age information from the prograde and peak portions of the *P–T* evolution. In addition, the growth and breakdown of major rock forming minerals can be forward modelled using thermodynamic datasets and software (e.g. THERMOCALC) enabling direct constraints to be placed on the timing of mineral growth along a *P–T* path. However, at temperatures >500 °C and/or where cooling rates are slow (<20°C Myr^{-1}), these isotopic systems are also open to diffusion (Baxter and Scherer, 2013; Smit et al., 2013). Therefore, it is crucial to seek out minerals that are resistant to elemental

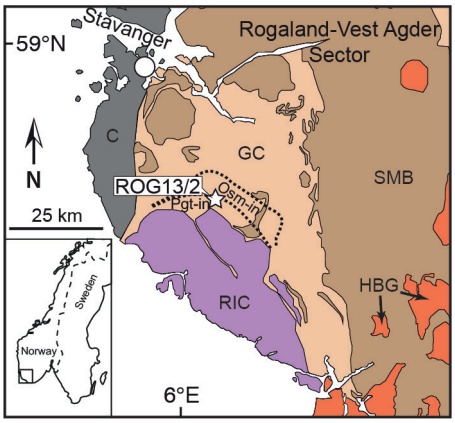

Fig. 1: Simplified geological map of the Rogaland Vest–Agder Sector with sample location (N 58°38'37.12", E 6°6'48.90"; WGS 84), modified after Coint et al. (2015). GC-Gneiss complex; SMB-Sirdal Magmatic Belt; HBG-Hornblende-biotite granites; RIC-Rogaland Igneous Complex; C-Caledonides; Osm–in- osumilite isograd; Pgt–in- pigeonite isograd.

diffusion at high temperatures and that have a grain size sufficiently large to preserve the age information near the peak of metamorphism.

Here we present the first $^{40}Ar/^{39}Ar$ analyses of osumilite, a K-bearing silicate mineral that is found in both volcanic and high-temperature metamorphic rocks. Using an example from Rogaland, SW Norway, we use diffusion experiments to demonstrate a high closure temperature of the Ar system in osumilite, and thermodynamic modelling to constrain the metamorphic conditions under which it grew. The utility of osumilite as a high temperature chronometer opens up a number of applications, such as dating volcanism (Miyashiro, 1956; Balassone et al., 2008), high and ultrahigh temperature regional metamorphism (Ellis et al., 1980; Adjerid et al., 2013) and potentially archaeological events through analysing the by-products of ceramic making processes (Artioli et al., 2013).

2. GEOLOGICAL SETTING AND SAMPLE DESCRIPTION

The Rogaland–Vest Agder Sector (RVA) of southwestern Norway experienced a long-lived (~100 Myr) high–*T* metamorphic evolution during the Sveconorwegian orogeny. Regional metamorphism reached peak conditions of ~850–950°C and 7–8 kbar at ca 1035 Ma (Degeling et al., 2001; Möller et al., 2003; Drüppel et al., 2013; Laurent et al., 2016; Blereau et al., 2017). On emplacement of the Rogaland Igneous Complex (RIC) at ca 930 Ma (Schärer et al., 1996), rocks up to 10 km from the margin of the RIC experienced contact metamorphism, with conditions of ~950°C and 3–6 kbar at the RIC–country rock contact (Tomkins et al., 2005).

The studied osumilite occurs in a migmatite (ROG13/2) ~2 km from the RIC contact (Fig. 1). Osumilite, which comprises ~20% of the rock, occurs in the melanosome where it coexists with orthopyroxene, quartz, spinel/magnetite, ilmenite and rare garnet. The leucosome mainly comprises plagioclase, K-feldspar, orthopyroxene and quartz (Fig. 2a). Based on petrographic observations, minor biotite is interpreted to be retrograde. Osumilite occurs in two different textural associations: (i) as large grains (~10 mm), the outer parts of which are intergrown with quartz (Fig. 2a) and, (ii) as rims (~0.3–0.5 mm wide) at the margins of rare garnet (Fig. S1). The large grains of osumilite (type i) are interpreted to have grown during the prograde to peak regional evolution, whereas the osumilite overgrowths replacing garnet (type ii) are interpreted to have grown during the subsequent contact metamorphism. In some places both variants of osumilite are replaced

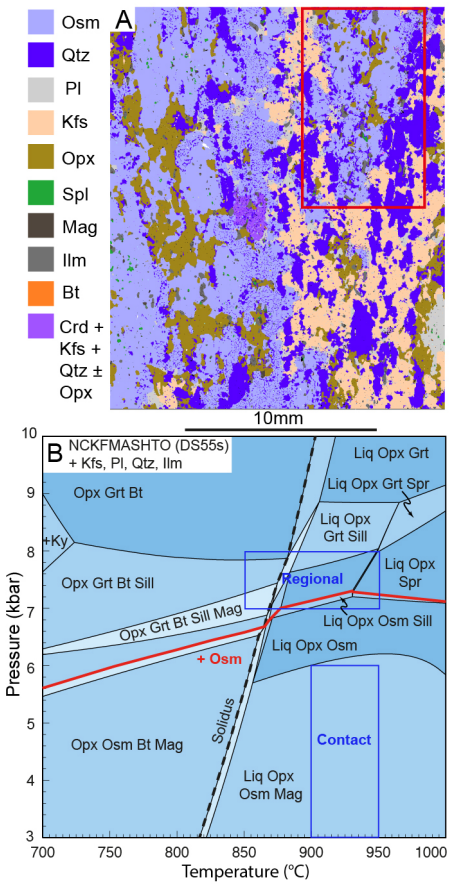

Fig. 2: A- TIMA mineral map of the osumilite migmatite (ROG13/2) with colour mineral legend, abbreviations after Kretz (1983). Single large grain of osumilite (red box). B- Modelled pseudosection of ROG13/2 with osumilite stability at low-*P* (outlined in red) compared to the *P–T* conditions determined by Blereau et al., (2017) (blue boxes).

by a symplectitic intergrowth of cordierite–K-feldspar–quartz ± orthopyroxene (Fig. 2a).

3. METHODS AND RESULTS

Detailed methods are given in Appendix 1. A pseudosection in the Na_2O–CaO–K_2O–FeO–MgO–Al_2O_3–SiO_2–H_2O–TiO_2–O model system for sample ROG13/2 indicates that osumilite was stable with melt at >815°C and <7.2 kbar (Fig. 2b), broadly consistent with existing *P–T* constraints for both regional and contact metamorphism (Blereau et al., 2017).

For $^{40}Ar/^{39}Ar$ dating, fifty-five inclusion- and alteration-free fragments of osumilite were hand picked from the 355–450 µm size fraction following SELFRAG electrical pulse disaggregation of samples. Fragments were loaded into a 1.9 x 0.3 cm Cd-shielded aluminium disc then irradiated for 40 hours in the Oregon State University TRIGA reactor (Oregon, USA). $^{40}Ar/^{39}Ar$ analyses (Appendix 2) were performed on eight single-grain aliquots using a laser and furnace on a MAP 215–50 mass spectrometer at the Western Australian Argon Isotope Facility, part of the John de Laeter Centre at Curtin University. There were no obvious optical differences between the analysed fragments.

Of the eight analyses, six produced $^{40}Ar/^{39}Ar$ plateau ages associated with probability of fit values (P, which are considered to be statistically valid if >0.05) between 0.16 and 0.59, and each was calculated from combined steps representing >73% of the total ^{39}Ar released (Fig. 3). The results fall into two age clusters, with two fragments yielding plateau ages of 1070.0 ± 2.1 [±3.3*] (*=internal error plus decay constant error, 2σ) and 1055.7 ± 3.2 [±4.0] Ma and another four yielding younger plateau ages ranging from 920.6 ± 2.1 [±2.9] to 880.3 ± 2.4 [±3.1] Ma (Fig. 3). The remaining two fragments did not yield a statistically acceptable plateau (Appendix 1, Fig. S2). Although the apparent ages of the remaining two fragments converge on the two age clusters defined by the other analyses, they are not discussed further.

Diffusion parameters in osumilite were measured on three aliquots of five fragments, heated in stages using a Pond Engineering furnace. ^{39}Ar was chosen as the diffusant with each

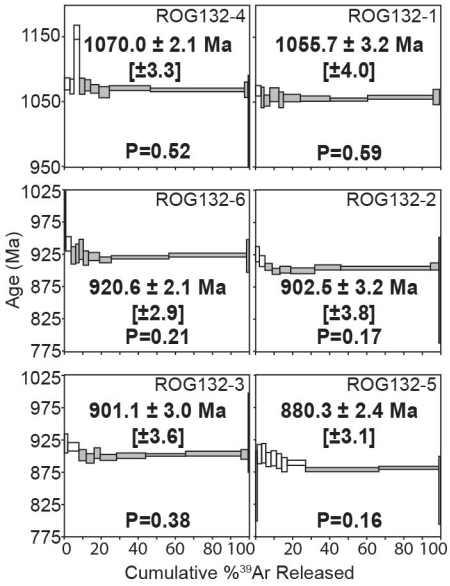

Fig. 3: $^{40}Ar/^{39}Ar$ age spectra and respective plateau ages. Steps included in the plateaux are shaded grey; errors on the plateau ages are 2σ. The errors in square brackets are the internal error plus the decay constant error (2σ).

extraction step lasting 10 minutes (2 minutes with increasing temperature, then 8 minutes at a fixed temperature). The fraction of ^{39}Ar released and the duration of each step were used to calculate the *D* values (Dodson, 1973), which are shown on Arrhenius plots (Fig. S4). Activation energy (E_a) and pre-exponential frequency factor (D_0) were calculated from the arrays defined on the Arrhenius plots. Calculations used a crystal radius of 175 µm (the smallest grain size analysed) and a spherical geometry. The three experimental runs yielded a range of E_a and related D_0 values (Table 1). The corresponding closure temperatures (T_c) and their uncertainties (2σ) were calculated using a Monte Carlo simulation (Scibiorski et al., 2015) incorporating the uncertainties of E_a, D_0 and crystal radius.

For a cooling rate of 10 °C/Ma (e.g. Cassata et al., 2009; Cassata et al., 2011) and a crystal radius of 175 µm, the E_a and D_0 values correspond to a range of T_c values (Table 1). The E_a and D_0 values, and consequently the lower calculated T_c, of the third run, are considerably lower than the first two runs. This might be the result of grain fracturing (osumilite has no discernable cleavage), facilitating escape of argon. The Ar closure temperature of osumilite has a lower limit of ~600 °C but the similarity between the results of experiment 1 and 2 and the relatively small 2σ error on experiment 1 implies a T_c closer to 770°C for a crystal radius of 175 µm. A T_c of 770°C makes osumilite is one of the most retentive crystals to argon diffusion, comparable with clinopyroxene (~750°C) (Cassata et al., 2011).

4. DISCUSSION

The six osumilite fragments that produced $^{40}Ar/^{39}Ar$ plateau ages yielded two distinct age clusters that correspond with known high-*T* metamorphic events in the RVA Sector. The TIMA mineral map in Figure 2a shows a grain of osumilite with approximate dimensions of >10,000 by 5000 µm. In such large grains, isotopic equilibration of Ar by diffusion is unlikely, preserving a gradient in $^{40}Ar/^{39}Ar$ with older apparent ages toward the core (Harrison, 1983). Using the diffusion parameters of experiment 1 (Table 1), the core of a grain with a radius of 5000 µm would have an approximate closure temperature of ~910°C for a cooling rate of 10°C/Ma.

The distribution of ages is further illustrated by diffusion models generated using the ArArDiff algorithm (Jourdan and Eroglu, 2017) that show the theoretical shape of $^{40}Ar/^{39}Ar$ age spectra obtained for an osumilite grain of a given radius and time-temperature history. Due

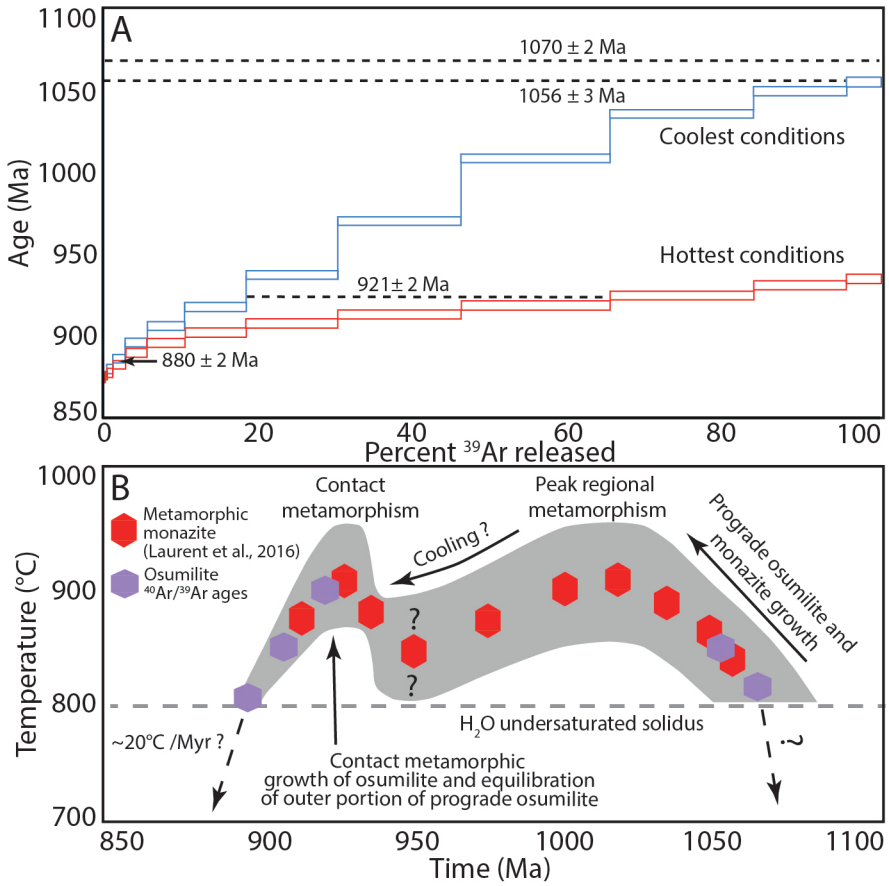

Fig. 4: A- Modelled age spectra for a 5000 µm radius grain of osumilite (Parameters summarised in Appendix 1, Table S1). B- Temperature-time path (shaded) defined by phase equilibria (Blereau et al., 2017), U–Pb monazite and ^{40}Ar/^{39}Ar osumilite geochronology.

to the range of possible temperatures for regional and contact metamorphism (Blereau et al., 2017), two alternative diffusion models were calculated based on the coldest (~800–900°C) and hottest (~900–950°C) temperatures proposed for the two events (Table S1, Fig. 4). In the lower temperature scenario, the modelled 5000 µm radius osumilite grain developed a strong internal age profile (Fig. 4a) with apparent ages ranging from ca 1055 Ma in the core to ca 870 Ma at the edge of the grain. For such a profile, ~35% of the gas release steps would yield apparent ages of 1030 Ma or older (Fig. 4a). These results demonstrate how various fragments of a single large crystal that experienced the Rogaland metamorphic history would yield a series of plateau ages spanning 180 million years. Furthermore, since a 175 µm-radius grain fragment represents only 3.5% of the radius of a 5000-µm radius crystal, the step-age gradient measured for the 175 µm grain would be small enough (3.5% of ^{39}Ar released on Fig. 4a) to yield the observed plateau age.

In the higher temperature scenario it was not possible to generate step ages older than the age of the contact metamorphism (> 930 Ma) (Fig. 4a.), suggesting that the lower temperature scenario is more realistic. However, even with the lower temperature model, the 1070 Ma age obtained for the oldest grain (Fig. 3) could not be achieved using the model parameters listed

in Table S1. One possible reason for this is that the numerical models do not account for pressure effects. A lithostatic pressure of 5 kbar could cause approximately 10–15°C difference in closure temperature (Lister and Baldwin, 1996), resulting in an age shift of 6 Ma towards older ages, still not within error of 1070 Ma. Alternatively, unaccounted factors might influence the retention of Ar in osumilite or that factors such as the initial age of crystallization (here considered to be 1070 Ma) might be inaccurate.

Finally, the results of the lower temperature model suggest that, in order to retain a ca 1050 Ma age signature, the temperature conditions during the metamorphic evolution must not have exceeded ~900°C within rocks ~2km from the RIC, broadly comparable to the lower-*T* estimates of Blereau et al., (2017).

Existing geochronology on monazite constrained peak regional metamorphism in Rogaland to ca 1035 Ma, with a few older monazite ages at ca 1060–1050 Ma (Laurent et al., 2016). However, as a result of growing during the prograde evolution, osumilite provides age constraints along the prograde path. The older osumilite $^{40}Ar/^{39}Ar$ age of 1070 ± 2.1 Ma provides a refined estimate for prograde heating through approximately 815°C (based on phase equilibria modelling). Contact metamorphism resulted in both additional osumilite growth around the margins of garnet (type ii), and equilibration of the outer regions of larger osumilite grains (type i) at 920–900 Ma. The youngest age, ca 880 Ma, is interpreted to represent cooling after which no further growth or modification of osumilite occured. The combination of high closure temperature, large grain size of osumilite and the similarity between the U–Pb and $^{40}Ar/^{39}Ar$ ages all provide evidence for the $^{40}Ar/^{39}Ar$ ages reported here to not be the product of excess argon.

Osumilite has previously been interpreted by some as a mineral that grew only as the result of contact metamorphism in the RVA Sector (e.g. Tobi et al., 1985). However, some osumilite grain fragments preserve ages that predate the contact metamorphism by more than 100 Myr, demonstrating that the mapped osumilite isograd in the RVA sector is not a true contact metamorphic isograd, but formed in appropriate bulk compositions during regional metamorphism associated with the Sveconorwegian Orogeny, as has previously been suggested by Drüppel et al. (2013).

The $^{40}Ar/^{39}Ar$ closure temperature of osumilite (up to 771 ± 11°C for a 175 µm-radius grain and a cooling rate of 10°C/Ma) is higher than the $^{40}Ar/^{39}Ar$ closure temperatures of equivalent sized pyroxene (~750°C; Cassata et al., 2011) and hornblende (~550°C; Harrison, 1981). Osumilite also has the advantage of potentially growing to very large grain sizes increasing its retentiveness to Ar (Fig. 4a), making it very suitable for providing insight into extreme crustal conditions and prolonged orogenic processes. A knowledge of the $^{40}Ar/^{39}Ar$ diffusional properties as determined in this study allows the *T–t* history to be deduced. This information is not typically obtainable from other high-temperature geochronometers, such as zircon and monazite, due to their small grain size and limitations on the analytical spot sizes.

5. CONCLUSIONS

Osumilite provides a novel means of retrieving *T–t* points along a high-*T* prograde metamorphic

path, allowing for better constraints on the duration of orogenesis. Grain size permitting, osumilite may retain multiple age populations in high-grade terrains as it is very resilient to Ar diffusion. $^{40}Ar/^{39}Ar$ dating of osumilite provides geochronological data that can be directly connected to thermodynamic modelling, a feature not as readily applicable to accessory minerals such as monazite and zircon. Using the diffusion systematics of osumilite and the presence of certain age populations, additional constraints on the maximum temperatures experienced can be interpreted. Osumilite is also present within igneous rocks and in by-products of the ceramic making process and therefore this technique can be applied to a wider set of geological and archaeological problems than those discussed here.

ACKNOWLEDGEMENTS

$^{40}Ar/^{39}Ar$ analyses and diffusion experiments were carried out at the West Australian Argon Isotope Facility (WAAIF) of the John de Laeter Centre, Curtin University. The Tescan Integrated Mineral Analysis (TIMA) instrument at the John de Laeter Centre, was funded by a grant from the Australian Research Council (LE140100150) and is operated with the support of the Geological Survey of Western Australia, University of Western Australia and Murdoch University. Financial support for this project was provided by an ARC DECRA fellowship (DE120103067) to CC. Many thanks to Fawna Korhonen for supplying the updated *a-X* models.

REFERENCES

Adjerid, Z., Godard, G., Ouzegane, K. H., and Kienast, J.-R., 2013, Multistage progressive evolution of rare osumilite-bearing assemblages preserved in ultrahigh-temperature granulites from In Ouzzal (Hoggar, Algeria): Journal of Metamorphic Geology, v. 31, p. 505–524.

Artioli, G., Angelini, I., and Nestola, F., 2013, New milarite/osumilite-type phase formed during ancient glazing of an Egyptian scarab: Applied Physics A, v. 110, no. 2, p. 371-377.

Balassone, G., Mormone, A., Rossi, M., Bernardi, A., Fisch, M., Armbruster, T., Malsy, K., and Berger, A., 2008, Crystal chemical and structural characterisation of an Mg-rich Osumilite from Vesuvius volcano (Italy): European Journal of Mineralogy, v. 20, p. 713-720.

Baxter, E. F., and Scherer, E. E., 2013, Garnet Geochronology: Timekeeper of Tectonometamorphic Processes: Elements, v. 9, no. 6, p. 433.

Blereau, E., Johnson, T. E., Clark, C., Taylor, R. J. M., Kinny, P. D., and Hand, M., 2017, Reappraising the P–T evolution of the Rogaland–Vest Agder Sector, southwestern Norway: Geoscience Frontiers, v. 8, no. 1, p. 1–14.

Cassata, W. S., Renne, P. R., and Shuster, D. L., 2009, Argon diffusion in plagioclase and implications for thermochronometry: A case study from the Bushveld Complex, South Africa: Geochimica et Cosmochimica Acta, v. 73, no. 21, p. 6600-6612.

Cassata, W. S., Renne, P. R., and Shuster, D. L., 2011, Argon diffusion in pyroxenes: Implications for thermochronometry and mantle degassing: Earth and Planetary Science Letters, v. 304, no. 3–4, p. 407–416.

Clark, C., Healy, D., Johnson, T., Collins, A. S., Taylor, R., Santosh, M., and Timms, N. E., 2015, Hot orogens and supercontinent amalgamation: A Gondwanan example from southern India: Gondwana Research, v. 28, no. 4, p. 1310-1328.

Coint, N., Slagstad, T., Roberts, N. M. W., Marker, M., Røhr, T. S., and Sørensen, B. E., 2015, The Late Mesoproterozoic Sirdal Magmatic Belt, SW Norway: Relationships between magmatism and metamorphism and implications for Sveconorwegian orogenesis: Precambrian Research, v. 265, p. 57-77.

Degeling, H., Eggins, S., and Ellis, D. J., 2001, Zr budgets for metamorphic reactions, and the formation of zircon from garnet breakdown: Mineralogical Magazine, v. 65, no. 6, p. 749-758.

Dodson, M. H., 1973, Closure temperature in cooling geochronological and petrological systems: Contributions to Mineralogy and Petrology, v. 40, no. 3, p. 259-274.

Drüppel, K., Elsäßer, L., Brandt, S., and Gerdes, A., 2013, Sveconorwegian Mid-crustal Ultrahigh-temperature Metamorphism in Rogaland, Norway: U-Pb LA-ICP-MS Geochronology and Pseudosections of Sapphrine Granulites and Associated Paragneisses: Journal of Petrology, v. 54, no. 2, p. 305-350.

Ellis, D. J., Sheraton, J. W., England, R. N., and Dallwitz, W. B., 1980, Osumilite-sapphirine-quartz granulites from Enderby Land Antarctica - mineral assemblages and reactions: Contributions to Mineralogy and Petrology, v. 72, p. 123-143.

Gerya, T., 2014, Precambrian geodynamics: Concepts and models: Gondwana Research, v. 25, no. 2, p. 442-463.

Harley, S. L., 2016, A matter of time: The importance of the duration of UHT metamorphism: Journal of Mineralogical and Petrological Sciences, v. 111, p. 50–72.

Harrison, T. M., 1981, Diffusion of 40Ar in Hornblende: Contributions to Mineralogy and Petrology, v. 78, p. 324-331.

Harrison, T. M., 1983, Some observations on the interpretation of 40Ar/39Ar age spectra: Chemical Geology, v. 41, p. 319-338.

Jamieson, R. A., and Beaumont, C., 2013, On the origin of orogens: Geological Society of America Bulletin, v. 125, no. 11-12, p. 1671.

Jourdan, F., and Eroglu, E., 2017, 40Ar/39Ar and (U-Th)/He model age signatures of elusive mercurian and venusian meteorites: Meteoritics & Planetary Science, v. In press.

Kelsey, D. E., and Hand, M., 2015, On ultrahigh temperature crustal metamorphism: Phase equilibria, trace element thermometry, bulk composition, heat sources, timescales and tectonic settings: Geoscience Frontiers, v. 6, p. 311-356.

Kretz, R., 1983, Symbols for rock-forming minerals: American Mineralogist, v. 68, p. 277-279.

Laurent, A. T., Seydoux-Guillaume, A.-M., Duchene, S., Bingen, B., Bosse, V., and Datas, L., 2016, Sulphate incorporation in monazite lattice and dating the cycle of sulphur in metamorphic belts: Contributions to Mineralogy and Petrology, v. 171, no. 11, p. 94.

Lister, G. S., and Baldwin, S. L., 1996, Modelling the effect of arbitrary P-T-t histories on argon diffusion in minerals using the MacArgon program for the Apple Macintosh: Tectonophysics, v. 253, no. 1, p. 83-109.

Miyashiro, A., 1956, Osumilite, a new silicate mineral, and its crystal structure: American Mineralogist, v. 41, p. 104-116.

Möller, A., O'Brien, P. J., Kennedy, A., and Kröner, A., 2003, Linking growth episodes of zircon and metamorphic textures to zircon chemistry: an example from the ultrahigh-temperature granulites of Rogaland (SW Norway): Geological Society, London, Special Publications, v. 220, no. From: Vance, D., Müller, W., & Villa, I. M. (eds) 2003. Geochronology: Linking the Isotopic Record with Petrology and Textures., p. 65-81.

Schärer, U., Wilmart, E., and Duchesne, J-C., 1996, The short duration and anorogenic character of anorthosite magmatism: U–Pb dating of the Rogaland complex, Norway: Earth and Planetary Science Letters, v. 139, p. 335-350.

Scibiorski, E., Tohver, E., and Jourdan, F., 2015, Rapid cooling and exhumation in the western part of the Mesoproterozoic Albany-Fraser Orogen, Western Australia: Precambrian Research, v. 265, p. 232-248.

Sizova, E., Gerya, T., and Brown, M., 2014, Contrasting styles of Phanerozoic and Precambrian continental collision: Gondwana Research, v. 25, no. 2, p. 522-545.

Smit, M. A., Scherer, E. E., and Mezger, K., 2013, Lu–Hf and Sm–Nd garnet geochronology: Chronometric closure and implications for dating petrological processes: Earth and Planetary Science Letters, v. 381, p. 222-233.

Tobi, A. C., Hermans, G. A. E. M., Maijer, C., and Jansen, B. H., 1985, Metamorphic zoning in the high-grade Proterozoic of Rogaland-Vest Agder, SW Norway: The Deep Proterozoic Crust in the North Atlantic Provinces, p. 477-497.

Tomkins, H. S., Williams, I. S., and Ellis, D. J., 2005, In situ U–Pb dating of zircon formed from retrograde garnet breakdown during decompression in Rogaland, SW Norway: Journal of Metamorphic Geology, v. 23, p. 201-215.

Supplementary material: See Appendix D

Chapter 5

Using accessory minerals to unravel thermal histories in polymetamorphic terranes: an example from Rogaland, SW Norway

Eleanore Blereau[1*], Chris Clark[1], Richard J. M. Taylor[1, 2], Peter D. Kinny[1], Tim E. Johnson[1], Eleanor Sansom[1], Martin Hand[3]

[1]Department of Applied Geology, The Institute of Geoscience Research (TIGeR), Curtin University, GPO Box U1987, Perth WA 6845, Australia.

[2]Department of Earth Sciences, University of Cambridge, Cambridge CB2 3EQ, United Kingdom

[3] Centre for Tectonics, Resources and Exploration (TRaX), School of Earth and Environmental Sciences, University of Adelaide, Adelaide 5005, South Australia

This article is under review in the *Journal of Metamorphic Geology* (since June 23 2017)

ABSTRACT

The age spectra from accessory minerals from the Rogaland–Vest Agder Sector (RVA) in southwestern Norway are complex and difficult to interpret due to polymetamorphism and prolonged residence at high temperatures. A suite of samples collected various distances from the Rogaland Igneous Complex (RIC) (30 km, 10 km, 2 km and at the contact) were used to study the effects of anorthosite emplacement on the country rocks of the RVA as well as to investigate the effects of high to ultra-high temperature (UHT) metamorphism on the rare earth element (REE) systematics of zircon. Prograde (regional) heating sufficient to recrystallise zircon occurred at 1059 ± 12 Ma, culminating in peak metamorphism at c. 1035–995 Ma and final melt crystallisation outside the aureole at 951 ± 14 Ma. Samples within the aureole of the RIC show a continuum of ages rather than two discrete age peaks, with no clear melt crystallisation event until c. 900 Ma, some 30 Myr after the emplacement of the RIC. This is explained by prolonged residence at high-temperature and a slow cooling rate following regional metamorphism. Diffusion modelling shows that the REE in recrystallised zircon may be modified sufficiently to reflect the surrounding geochemical environment rather than the growth conditions of the original zircon and so can provide additional constraints on the metamorphic *T*–*t* path. The observed variations in zircon REE across the sample suite suggest that the RIC was emplaced rapidly, as a series of pulses between 1 and 5 Myr in overall duration.

1. INTRODUCTION

The U–Pb decay schemes are the most commonly used radiogenic isotope systems for constraining timescales of metamorphism within high-grade metamorphic terranes. However, the perturbation of U–Pb and trace elements within accessory minerals such as zircon at high temperatures is a problem, especially in situations where high–*T* conditions were prolonged (Clark et al., 2015; Halpin, Daczko, Milan, & Clarke, 2012; Harley, Kelly, & Möller, 2007; Kelly & Harley, 2005). The partitioning of REE between zircon and garnet is now widely used for linking accessory minerals to a metamorphic evolution (Rubatto, 2002; Rubatto & Hermann, 2007; Taylor et al., 2015; Taylor, Kirkland, & Clark, 2016). This approach is readily applicable to newly grown zircon, or grains undergoing coupled dissolution-reprecipitation, but these processes require fluids or melt which may be scarce within residual high–*T* granulites, leaving recrystallisation as the dominant mechanism by which zircon may be modified. Recrystallised zircon may not record REE information representative of later events due to the slow pace of solid-state diffusion (Cherniak & Watson, 2003). However, diffusion is strongly temperature and time dependent, increasing the cumulative effects of diffusion during prolonged high–*T* metamorphism.

The Sveconorwegian Belt of SW Norway and Sweden has experienced a complex orogenic history including emplacement of anorthosite massifs. Much of SW Norway also shows little or no evidence for later overprinting from Caledonian tectonothermal events (Verschure et

al., 1980). This allows for an investigation into the thermal effects of anorthosite emplacement on the surrounding country rocks as well as providing a natural laboratory to investigate the geochemical effects of prolonged high–*T* on geochronometers. The geological history of the Rogaland–Vest Agder Sector (RVA) is well constrained and has been the focus of many investigations (Bingen, Nordgulen, & Viola, 2008 and references within; Blereau et al., 2017; Drüppel, Elsäßer, Brandt, & Gerdes, 2013; Laurent et al., 2016; Möller, O'Brien, Kennedy, & Kröner, 2003; Tomkins, Williams, & Ellis, 2005) making this region an ideal case study. Blereau et al. (2017) re-evaluated the *P–T* evolution of the RVA sector, concluding that the RVA sector experienced a two-stage rather than single-stage evolution, in which a high-grade regional event was followed by a later contact metamorphic event coeval with the emplacement of the voluminous anorthosite bodies (cf. Drüppel et al., 2013; Möller et al., 2003; Tomkins et al., 2005). Blereau et al. (2017) also provided evidence that high-temperature conditions were maintained in the interval between peak regional and later contact metamorphism.

In this study, we integrate SHRIMP U–Pb data and LA–ICP–MS REE compositions of zircon, monazite and garnet to constrain the timing of metamorphism and to investigate the variability in response of geochronometers to distance from the RIC. We also use diffusion modelling to provide additional constraints to the *T–t* history, based on the modification of REE in recrystallised zircon, providing insight into the assembly of the RIC.

2. REGIONAL GEOLOGY

The regional geology of the RVA has been described most recently by Blereau et al. (2017). Here we summarise previous geochronological studies and the timing of geological events of the Sveconorwegian Belt. Three Proterozoic orogenic events are recorded in southern Scandinavia: the 1.9–1.75 Ga Svecofennian Orogeny, the 1.75–1.55 Ga Gothian Orogeny and the 1.2–0.9 Ga Sveconorwegian Orogeny (Andersen, Griffin, & Pearson, 2002) during which the Rogaland Igneous Complex (RIC) was emplaced. The Sveconorwegian Belt connects with the Fennoscandia Foreland and is comprised of a number of lithotectonic domains: the Eastern Segment, Idefjorden Terrane, Bamble-Kongsberg Terranes and Telemarkia Terrane, all of which are separated by major shear zones (Figure 1a). The Sveconorwegian Belt has previously been interpreted to have developed in a continent–continent collision setting (Bingen et al., 2008). However, in more recent studies the tectonic setting has been proposed to record protracted subduction–accretion (Blereau et al., 2017; Coint et al., 2015; Roberts & Slagstad, 2015; Slagstad, Roberts, & Kulakov, 2017; Slagstad, Roberts, Marker, Røhr, & Schiellerup, 2013; Spencer et al., 2014). The Sveconorwegian Belt has experienced periods of pre- to syn-Sveconorwegian magmatism including 1920–1640 Ma (Fennoscandian Foreland, TIB, Eastern Segment), 1659–1455 Ma (Eastern Segment, Idefjorden, Bamble, Kongsberg, Telemarkia), 1399–1204 Ma (Eastern Segment, Idfjorden, Telemarkia), 1198–1130 Ma (Bamble, Telemarkia) (Bingen & Solli, 2009 and references within) and 1060–914 Ma (Idefjorden, Bamble, Telemarkia) (Bingen & Solli, 2009 and

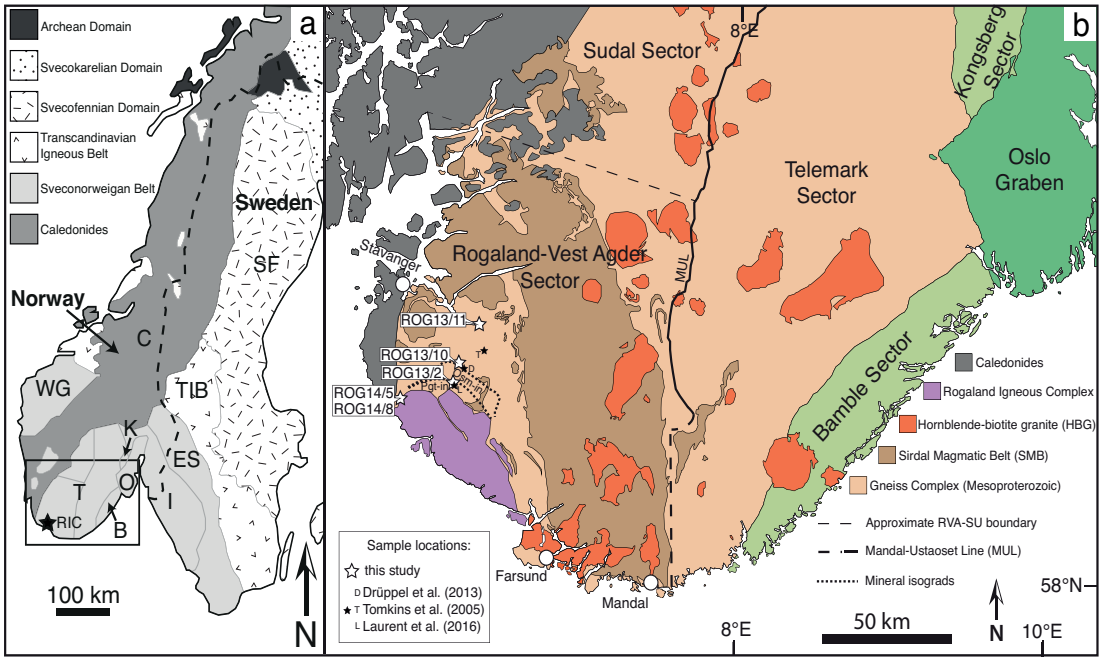

Fig. 1: a- Map showing the main geological domains of Scandinavia (after Bergh et al., 2012). Abbreviations: T- Telemarkia Terrane; B- Bamble Sector; O- Oslo Graben; K- Kongsberg Sector; I- Idefjorden Terrane; ES- Eastern Segment; C- Caledonides; TIB- Transcandinavian Igneous Belt; SF- Svecofennian Foreland (Domain); WG- Western Gneiss Region. b- Geological map of the Rogaland-Vest Agder Sector (mineral isograds from Bolle, Diot, Liégeois, & Auwera, 2010; after Coint et al., 2015; and MUL from Vander Auwera et al., 2011). Samples from this study are marked as white stars with locations from previous studies marked as smaller black stars.

references within; Coint et al., 2015; Slagstad et al., 2013).

The Telemarkia Terrane was formed during a magmatic event at 1555–1459 Ma with no older magmatic rocks currently known (Bingen et al., 2008; Bingen & Solli, 2009). The Telemarkia Terrane is subdivided into the Telemark, Hardangervidda, Sudal and Rogaland–Vest Agder Sectors (Figure 1b), the latter of which is the focus of this study. The RVA is a high-grade gneiss complex composed mainly of orthopyroxene-bearing felsic orthogneisses and subordinate garnet-bearing paragneisses. Migmatised orthogneisses have recorded protolith ages of c. 1450 Ma, while non-migmatised orthogneisses have recorded protolith ages of 1210–1230 Ma (Coint et al., 2015). A migmatitic paragneiss has recorded inherited, detrital zircon ages between 3.0–1.2 Ga (Tomkins et al., 2005). Sapphirine granulites (paragneisses) have recorded detrital zircon 207Pb/206Pb ages ranging from 1841 ± 26 to 1220 ± 40 Ma and 1501 ± 21 to 1265 ± 54 Ma (Drüppel et al., 2013).

The RVA has been intruded by three syn-orogenic magmatic suites: the 1060–1020 Ma Sirdal Magmatic Belt (Coint et al., 2015; Slagstad et al., 2013); the 970–932 Ma hornblende-biotite granites (Bogaerts, Scaillet, Liégeois, & Vander Auwera, 2003; Vander Auwera et al., 2011); and the 930–920 Ma RIC (Bogaerts et al., 2003; Pasteels, Demaiffe, & Michot, 1979; Schärer, Wilmart, & Duchesne, 1996; Westphal, Schumacher, & Boschert, 2003). The emplacement of the RIC is interpreted to form a contact aureole represented by a series of approximately concentric isograds mapped in the surrounding gneiss complex,

including pigeonite and osumilite (-in) (Figure 1). SHRIMP U–Pb dating of zircons by Möller et al. (2003) from a combination of ortho- and paragneisses within the aureole yielded five $^{206}Pb/^{238}U$ age populations: c. 1050 Ma (magmatic cores), c. 1035 Ma (magmatic cores), c. 1000 Ma (metamorphic zircon), 927 ± 7 Ma (metamorphic rims, n=11) and 908 ± 9 Ma (metamorphic rims, lower Th/U, n=6). LA–ICP–MS dating of monazite from an osumilite-bearing paragneiss within the aureole by Laurent et al. (2016) yielded similar age populations to Möller et al. (2003), with three age population interpreted: 1034 ± 6 Ma (sulphate rich core), 1005 ± 7 Ma (secondary sulphate-bearing domains) and 935 ± 7 Ma (S-free Y-rich domains). SHRIMP U–Pb dating of zircons by Tomkins et al. (2005) from a metapelitic gneiss outside the aureole yielded a range of $^{206}Pb/^{238}U$ age populations also: c. 3.05–1.34 Ga (detrital zircon), c. 1.04–0.97 Ga (recrystallised zircon), 1035 ± 9 Ma (metamorphic zircon, n=10) and 955 ± 8 Ma (metamorphic zircon in cordierite, n=14). Tomkins et al. (2005) also defined an upper age limit of 1068 ± 14 Ma for regional metamorphism. LA–ICP–MS U–Pb dating of zircons from a sapphirine granulite (paragneiss) within the aureole by Drüppel et al. (2013) yielded $^{207}Pb/^{206}Pb$ ages ranging from 1064 ± 38 to 989 ± 49 Ma (metamorphic rims), 1029 ± 32 to 993 ± 23 Ma (metamorphic zircon) with a Concordia age of 1006 ± 4 Ma calculated from one sample (14 zircon rims, 4 xenotime analyses). Single grains of xenotime yielded $^{207}Pb/^{206}Pb$ ages ranging from c. 1001 to 979 Ma with epitaxial xenotime yielding younger Concordia ages of 933 ± 5 Ma (n=8), and 928 ± 10 Ma (n=3) (Drüppel et al., 2013). Based on differing interpretations of the geochronological data, two different ages for peak regional metamorphism have been proposed: c. 1035 Ma (Laurent et al., 2016; Tomkins et al., 2005) and c. 1006 Ma (Drüppel et al., 2013). While there is general agreement that the RIC was emplaced at c. 930 Ma (Bingen et al., 2008; Roberts & Slagstad, 2015; Schärer et al., 1996; Vander Auwera et al., 2011).

3. SAMPLE DESCRIPTIONS

Geochronology and REE geochemistry were conducted on five samples from the RVA in order to determine the duration of the contact metamorphism subsequent to the regional metamorphic event, as well as the effects of high-grade metamorphism on U–Pb and REE systematics in zircon and monazite. Three samples were collected in the regionally metamorphosed country rocks, at various distances from the RIC contact - ROG13/11 – 30 km, ROG13/10 – 10 km, and ROG13/2 – 2 km. Two further samples - metapelite ROG14/5 and anorthosite ROG14/8 were collected adjacent to the contact. Three of these samples (ROG13/11, ROG13/10 and ROG14/5) were described in detail by Blereau et al. (2017) and are summarised below with additional zircon and monazite morphological information. The petrographic and accessory mineral descriptions for the two remaining samples (ROG13/2 and ROG14/8) are presented below.

3.1 Garnet–sillimanite–cordierite migmatite (ROG13/11, 30 km)

This sample is of a migmatitic metapelite 30 km from the RIC (Figure 1b). The rock comprises

foliated melanosome rich in garnet, sillimanite and cordierite together with felsic stromatic leucosome containing peritectic garnet (Blereau et al., 2017).

Zircon occurs within the leucosome and melanosome as equant to slightly elongate grains 25–200 μm long. Some of the grains contain oscillatory-zoned cores with bright cathodoluminescence (CL) response, that are surrounded and sometimes truncated by uniform rims of dark CL response (Figure 2a i, iv). Other grains show internal features commonly associated with recrystallisation such as diffuse, remnant oscillatory zoning with dark CL response (Figure 2a ii, iii), resembling the 'ghost textures' of Hoskin and Black (2000).

Monazite (40–100 μm) occurs throughout the sample in association with garnet, cordierite, sillimanite, ilmenite and K-feldspar. The studied grains appeared internally uniform in backscattered electron (BSE) images (Figure 2f).

3.2 Sapphirine–orthopyroxene–cordierite–spinel granulite (ROG13/10, 10 km)

This sample is from a residual, silica undersaturated, sapphirine-bearing granulite (paragneiss) situated approximately 10 km from the RIC (Blereau et al., 2017) (Figure 1b).

Zircon (20–100 μm) occurs throughout the sample in association with cordierite, biotite, orthopyroxene and spinel. Grain shapes vary from equant to elongate along the c-axis. The zircon grains contain bright CL response oscillatory-zoned cores (Figure 2b i, ii) as well as more diffuse 'ghost zoning' (Hoskin & Black, 2000) indicative of recrystallization (Figure 2b iii, iv). Some grains have uniform, presumed recrystallised areas with dark CL response that appear to truncate the zoning of the bright CL cores (Figure 2b i, ii). No monazite was found in this sample.

3.3 Osumilite–orthopyroxene–spinel migmatite (ROG13/2, 2 km)

This sample is from a migmatite situated approximately 2 km from the RIC (Figure 1b). The rock consists of melanosome containing osumilite, orthopyroxene, spinel, garnet, quartz and feldspar, and leucosome containing quartz, K-feldspar (perthite) and plagioclase. Osumilite occurs as large, irregular shaped, pale purple grains (>5 mm) that are colourless to pale pink in thin section, some containing inclusions of spinel/magnetite and garnet (Figure 3a, b). Osumilite also occurs in fine-grained symplectites with quartz and cordierite. (Figure 3d, e). Orthopyroxene occurs in trails of (0.5–4 mm) grains aligned with the fabric and contains inclusions of quartz, spinel/magnetite, ilmenite and biotite. Garnet (~0.2 mm) is present as relict inclusions within osumilite. Quartz occurs as large elongate grains (~4–6 mm) in the leucosome as well as smaller grains (~1 mm) in the melanosome. Cordierite occurs intergrown with K-feldspar, quartz and sometimes orthopyroxene, together with inclusions of opaques/spinel and phlogopite (Figure 3b, d). The symplectite of cordierite–K-feldspar–quartz (± orthopyroxene) appears to be retrograde after osumilite (Figure 3 b, d) (Bhattacharya & Kar, 2002; Ellis, Sheraton, England, & Dallwitz, 1980; Kelsey, 2008; Korhonen, Brown, Clark, & Bhattacharya, 2013). Small sheets (~0.1 mm) of late phlogopite occur in K-feldspar and next to

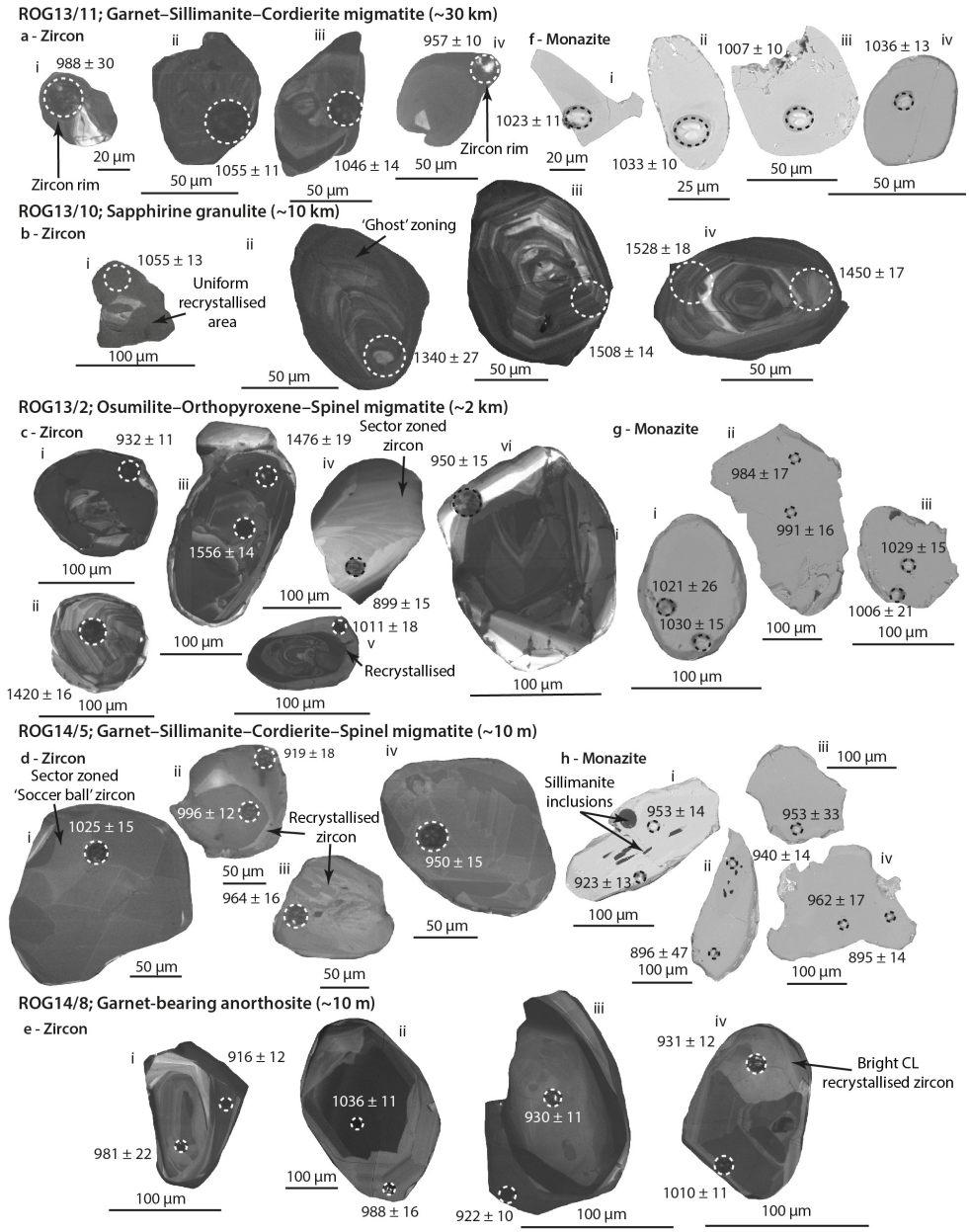

Fig 2: Representative zircon and monazite grains imaged using CL (zircon) and BSE imaging (monazite). Marked spots are LA–ICP–MS spots placed over SHRIMP spots, except for ROG13/10 (SHRIMP spots only). a- Zircons from ROG13/11, i, iv- Grains with bright CL response cores and dark uniform overgrowths. ii, iii- Recrystallised zircons with diffuse zoning. b- Zircons from ROG13/10, i- Bright CL response core with dark uniform recrystallised zircon. ii-iv- Recrystallised zircon with diffuse oscillatory zoning. c- Zircon from ROG13/2, i- Recrystallised oscillatory zoned core with dark overgrowth. ii, iii- oscillatory zoned inherited cores with dark recrystallised area. iv- Bright CL response sector zoned grain. v- Recrystallised grain with bright CL response overgrowth. d- Zircon from ROG14/5, i, iv- Sector zoned zircon. ii, iii- Recrystallised zircon with convoluted zoning. e- Zircon from ROG14/8, i, iii- Recrystallised zircon with dark overgrowths. ii, iv- recrystallised zircon with bright CL response regions. f- Monazite from ROG13/11, i-iv- uniform BSE response monazite. g- Monazite from ROG13/2, i-iii- uniform BSE response monazite. h- Monazite from ROG14/5, i, ii- Monazite with dark BSE response core with sillimanite inclusions and bright BSE response outer region. iii, iv- Inclusion free monazite with limited variation in BSE response.

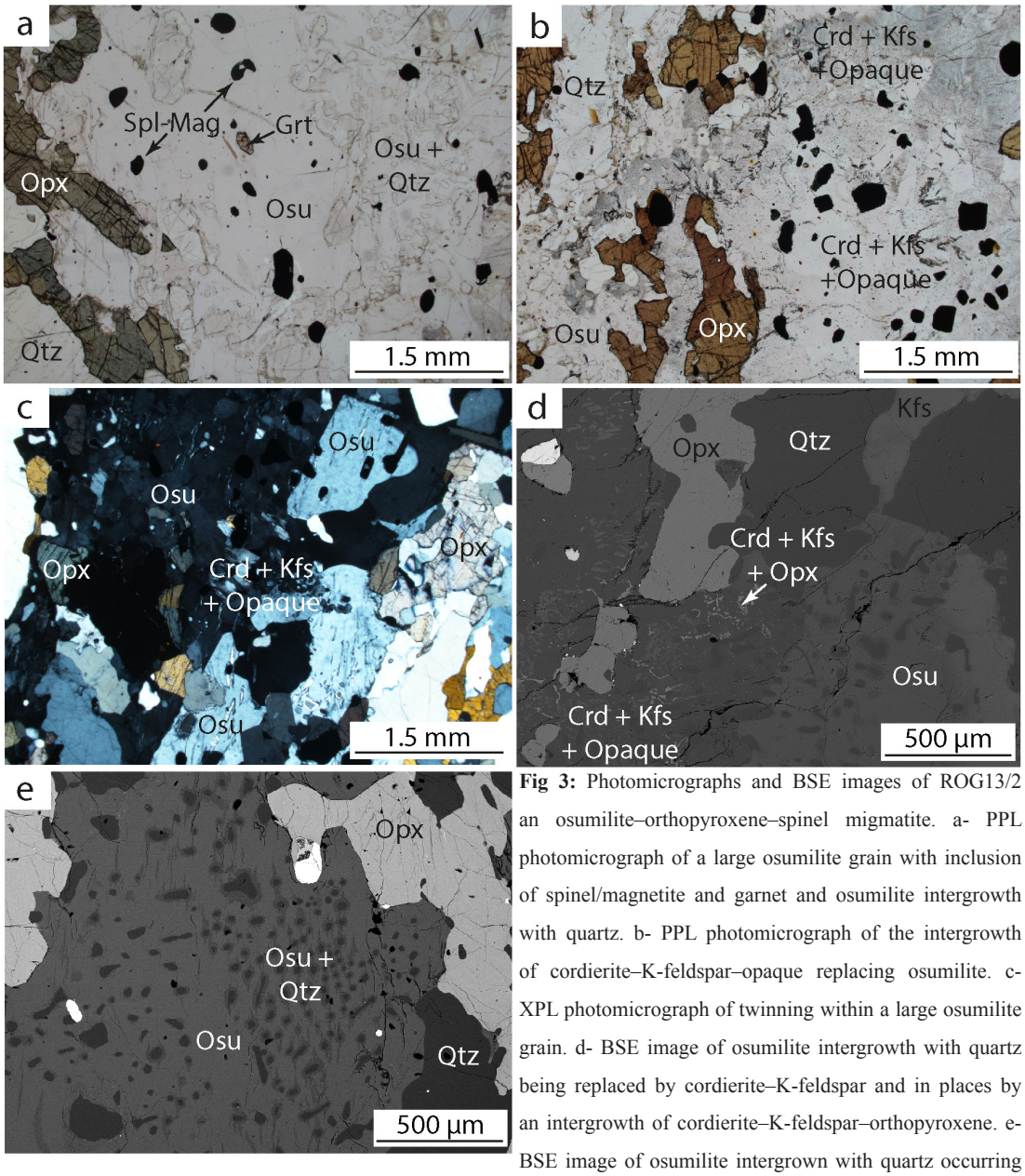

Fig 3: Photomicrographs and BSE images of ROG13/2 an osumilite–orthopyroxene–spinel migmatite. a- PPL photomicrograph of a large osumilite grain with inclusion of spinel/magnetite and garnet and osumilite intergrowth with quartz. b- PPL photomicrograph of the intergrowth of cordierite–K-feldspar–opaque replacing osumilite. c- XPL photomicrograph of twinning within a large osumilite grain. d- BSE image of osumilite intergrowth with quartz being replaced by cordierite–K-feldspar and in places by an intergrowth of cordierite–K-feldspar–orthopyroxene. e- BSE image of osumilite intergrown with quartz occurring next to orthopyroxene and quartz.

some of the opaque grains in cordierite.

Zircon grains in this sample are variable in size (50–200 µm) and shape and show complex internal structures in CL. Grains either contain oscillatory-zoned cores with moderate CL response (Figure 2c ii) or recrystallised cores with diffuse oscillatory-zoning (Fig 2c iii, v) that are truncated and surrounded by uniform overgrowths. One sector-zoned grain was also analysed (Figure 2c iv). Overgrowths show variable CL response from dark (Figure 2c, i) to bright (Figure 2c iii, v). A few grains of monazite (100–400 µm) were extracted from the sample for analysis also. These show no internal variation in BSE images (Figure 2g).

3.4 Garnet–sillimanite–cordierite–spinel migmatite (ROG14/5, at contact)

This sample is of a migmatitic garnet–sillimanite–cordierite–spinel metapelitic gneiss located at the contact of the RIC (Figure 1b). The sample consists of melanosome rich in garnet and cordierite together with small mm-scale leucosome (Blereau et al., 2017).

Zircon grains (60–200 μm) from this sample have multifaceted 'soccer ball' morphologies indicating metamorphic recrystallization (Vavra et al., 1996). Internally, they are either sector zoned (Figure 2d i, iv) or weakly zoned to uniform in their CL response (Figure 2d ii, iii). Monazite grains in this sample are similar in size (100–200 μm) to the zircon grains; many host sillimanite inclusions (Figure 2h i). A number of monazite grains show minor brightness variation in BSE images (Figure 2h i), others display no variation in BSE response (Figure 2h iii).

3.5 Garnet-bearing anorthosite (ROG14/8, at contact)

This sample was obtained from adjacent to ROG14/5 (Figure 1b) and is one of a series of garnet-bearing anorthosite sheets (~30 cm to ~2 m long, ~5–10 cm wide) that intrude into the country rock (garnet–sillimanite–spinel–cordierite metapelitic gneiss) adjacent to the main RIC contact (Figure 4a). The anorthosite sheets are parallel to the foliation of the surrounding migmatite. The sample is dominated by equant, 1–2 mm subhedral plagioclase that shows minor sericitization (Figure 4b, c). Orthopyroxene occurs in millimetre scale layers as subhedral to anhedral grains of varying size (1–8 mm) (Figure 4b, c). Garnet forms clusters of small, subhedral, inclusion-free grains (<1 mm) and larger euhedral grains (~1.5 mm) (Figure 4b). Minor phases are ilmenite (~0.5 mm), biotite (~1 mm) and quartz (1–2 mm).

Only zircon was analysed from this sample as there were no monazite grains large enough for analysis. The zircon grains (50–300 μm) have oscillatory cores (Figure 2e i, ii, iv) with some cores showing more diffuse zoning with low CL response (Figure 2e iii), surrounded, and sometimes crosscut by sector-zoned to uniform regions with high CL response (Figure 2e iv). A few grains have overgrowths with low CL response (Figure 2e i, iii).

4. ANALYTICAL METHODS

All sample preparation and analytical work was conducted using the facilities of the John de Laeter Centre, Curtin University, including the SelFRAG Electric Pulse Disaggregation (EPD) unit, Tescan Mira3 FESEM, SHRIMP II ion microprobe and GeoHistory Facility LA-ICP-MS.

4.1 SHRIMP U–Pb geochronology

Monazite and zircon from sample ROG13/11 and zircon from sample ROG13/10 were extracted from polished thin sections for in situ analysis as 2 mm diameter pucks, using a coring piece on a Dremel drill. The pucks were cast in 25 mm diameter epoxy discs that were cleaned and gold-coated prior to SIMS analysis. In addition, monazite and zircon grain separates were obtained from all samples. Samples were disaggregated

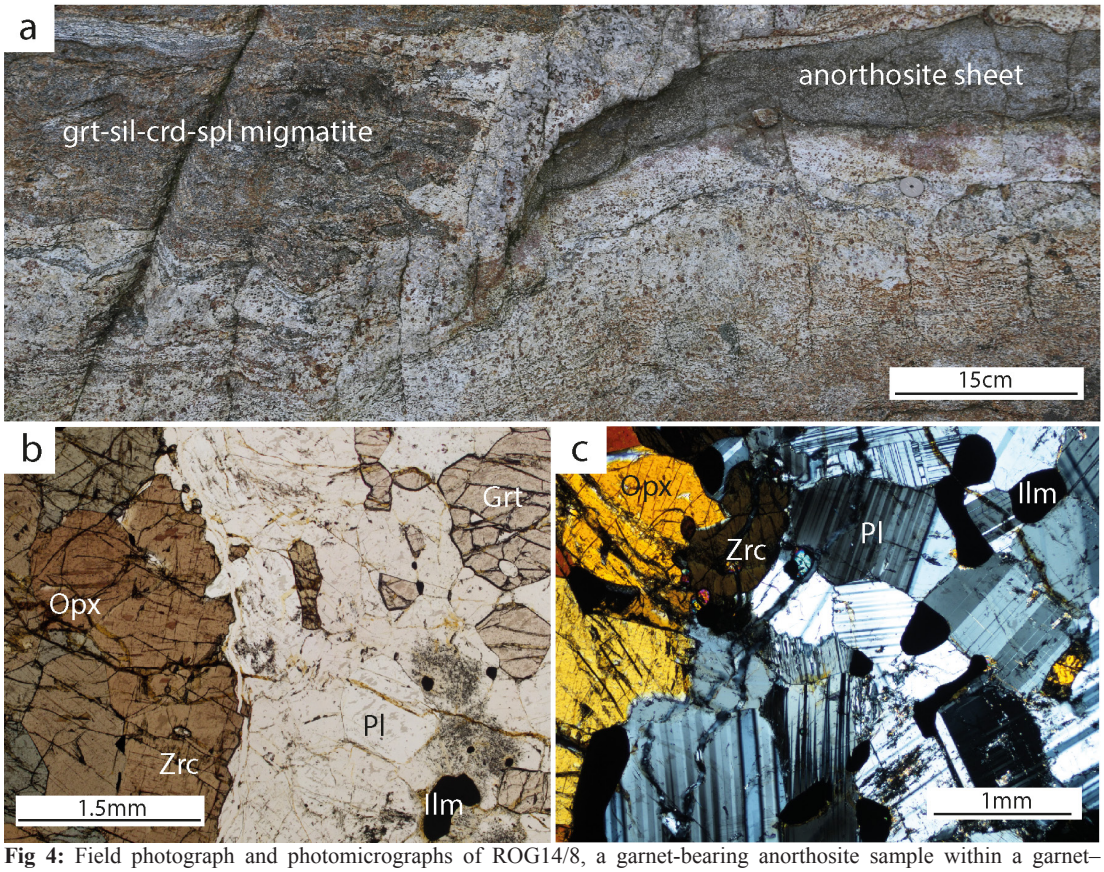

Fig 4: Field photograph and photomicrographs of ROG14/8, a garnet-bearing anorthosite sample within a garnet–cordierite–sillimanite–spinel migmatite. a- Field photograph of the garnet-bearing anorthosite sheet aligned with the foliation of the surrounding garnet–sillimanite–spinel migmatite, (after Blereau et al., 2017). b- PPL photomicrograph of coarse aggregates of orthopyroxene and garnet grains. c- XPL photomicrograph showing the plagioclase rich matrix.

using a SelFRAG EPD unit, except for ROG14/5 from which grains were released using traditional crushing methods. All separates were prepared via magnetic and heavy liquid separation. Selected grains were mounted in 25 mm diameter epoxy discs that were polished, cleaned and Au-coated prior to SIMS analysis. Grains were imaged using BSE imaging for monazite and CL imaging for zircon, with a Tescan Mira3 FESEM.

U–Pb isotopic data for zircon and monazite were collected using a SHRIMP II high mass-resolution SIMS ion microprobe. The mass-filtered O_2- primary beam settings were: for monazite 0.3 nA, 10 µm spot size, and for zircon 1.8 nA, 20 µm spot size. A 6-scan duty cycle was used, with mass resolution set at >5000 (de Laeter & Kennedy, 1998; Kennedy & de Laeter, 1994). NBS glass was used to calibrate the position of the ^{204}Pb peak.

Age data were processed using SQUID II (v2.5) and Isoplot (v3.75) (Ludwig, 2003, 2009). Corrections of measured isotopic ratios for common Pb were based on Stacey and Kramers (1975) model parameters. For the analysis of thin section mounts, standards were located in a separate mount that was gold coated at the same time. For zircon analyses, BR266 (Stern & Amelin, 2003) was used as the primary standard and Temora 2 (Black et al., 2003) or Plešovice (Sláma et al., 2008) as a secondary standard. Both secondary standards were within error of their reported ages for each analytical session

(Temora 2: 413 ± 4, 415 ± 4; Plešovice: 341 ± 5). For monazite analyses, Curtin internal laboratory standard INDIA (509 Ma) was used as the primary standard (Korhonen, Saw, Clark, Brown, & Bhattacharya, 2011) and Curtin internal laboratory standard GM-3 (488 Ma) was used as a secondary standard (Secondary standard ages from each session: GM-3: 485 ± 6, 482 ± 6, 485 ± 6). $^{206}Pb/^{238}U$ ages were used for monazite pooled ages. Corrections for excessive counts on ^{206}Pb and matrix effects related to Th content were conducted on monazite sessions (based on Fletcher, McNaughton, Davis, & Rasmussen, 2010), some spots were still discordant after correction and were excluded from the calculation of any pooled ages.

Uncertainties cited in the text and data tables for individual spot analyses include errors from counting statistics, errors from the common Pb correction and U–Pb calibration errors based on the reproducibility of U–Pb measurements of the primary standards and are cited at the 1σ level. A minimum error of 1% was assigned to the external spot-to-spot error in Pb/U for the standard, reflecting the long-term performance of the SHRIMP. Error ellipses on Concordia diagrams are presented at the 2σ level. Uncertainties of weighted mean ages are quoted at 95% confidence unless indicated.

4.2 REE analysis by LA–ICP–MS

Rare earth element (REE) and other trace element compositions of zircon, monazite and garnet were measured using Laser Ablation Inductively Coupled Plasma Mass Spectrometry (LA–ICP–MS) on an ASI Resolution M-50 193-nm wavelength Ar-F excimer laser with an Agilent 7700 mass spectrometer. Analyses of monazite and zircon were made directly over selected SHRIMP spots. Garnets were analysed in thin section, and in one case from a grain mount (ROG13/2). A 33 µm spot size was used for garnet, a 23 µm spot size for zircon and a 15 µm spot size for monazite. For garnet and zircon analysis, ablation length was 30 seconds with a repetition rate of 7 Hz. For monazite analysis, ablation length was with 20 seconds with a repetition rate of 4 Hz. NIST glasses (610, 612) (Pearce et al., 1997) were used as calibration reference materials. NIST 610 was used as the primary standard for garnet, while GJ1 (Liu et al., 2010) was used for zircon calibration and 44069 (Aleinikoff et al., 2006) was used for monazite calibration. Stoichiometric major element compositions were used for calibration of trace elements in zircon (Zr = 43.14 wt%) and garnet (Si = 18 wt%). For monazite analyses, Ce (230526 ppm) was used as an internal normalisation element (Buick et al., 2010; Taylor et al., 2014). Time-resolved data were reviewed following each session using the Iolite software package (Paton, Hellstrom, Paul, Woodhead, & Hergt, 2011; Paton et al., 2010), in order to detect and eliminate data affected by inclusions. All REE plots use the chondrite normalisation values of Anders and Grevesse (1989).

5. RESULTS

5.1 Zircon U–Pb Geochronology

Data tables for zircon U–Pb analyses can be found in supplementary data Table S1. Concordia plots summarising the results are presented in Figure 5. Typical discordance is less than 10% for zircon,

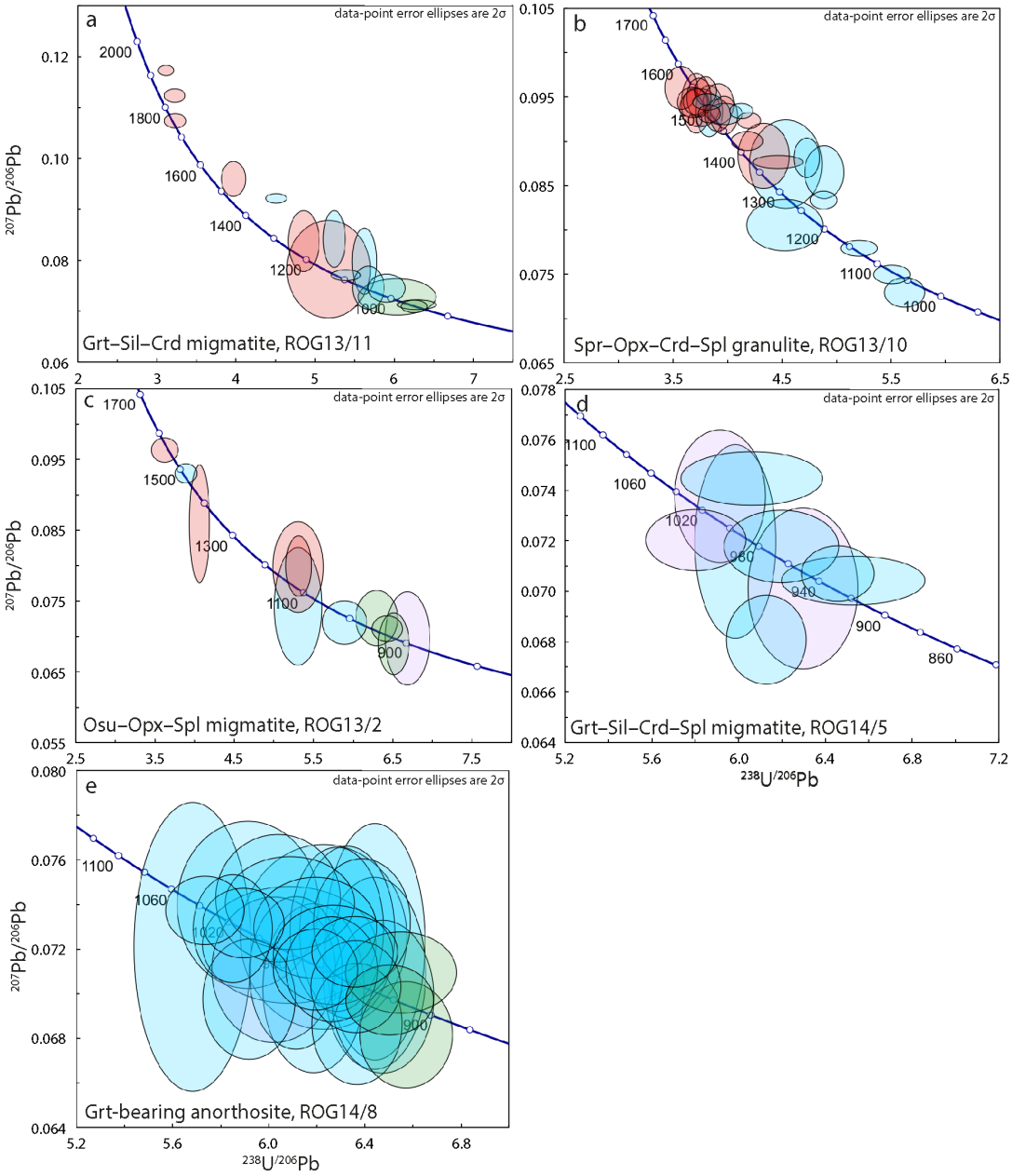

Fig 5: Zircon U–Pb Concordia diagrams. Analyses are shaded for the textural location of the analysis: red – oscillatory zoned core, blue – recrystallised zircon, green – zircon rim, purple – sector zoned zircon. See online version for colour.

however in some cases ancient Pb-loss has resulted in some analyses falling along a discordia trend.

5.1.1 Garnet–sillimanite–cordierite migmatite (ROG13/11 – 30 km)

Fifteen U–Pb analyses were performed on zircon grains from ROG13/11 (Figure 5a). Six oscillatory-zoned cores yielded concordant to slightly discordant ages ranging from 1917 ± 6 ($^{207}Pb/^{206}Pb$) to 1140 ± 43 Ma ($^{206}Pb/^{238}U$), with Th/U ratios of 0.77–0.23. Analyses of parts of grains showing diffuse, recrystallised oscillatory zoning yielded discordant $^{206}Pb/^{238}U$ ages ranging from 1292 ± 14 to 1126 ± 11 Ma and younger concordant $^{206}Pb/^{238}U$ ages ranging from 1098 ±

14 to 1009 ± 15 Ma (Th/U= 0.18–0.03). Three analyses of zircon rims form a concordant group with a weighted mean $^{206}Pb/^{238}U$ age of 957 ± 15 Ma (MSWD= 0.62, prob= 0.54, n=3; Th/U=0.11–0.03).

5.1.2 Sapphirine–orthopyroxene–cordierite–Spinel granulite (ROG13/10 – 10 km)

Twenty-seven U–Pb analyses were performed on zircon grains from ROG13/10 (Figure 5b). A group of seven concordant analyses of oscillatory-zoned cores yielded a weighted mean $^{206}Pb/^{238}Pb$ age of 1535 ± 14 (MSWD=1.7, prob=0.12, n=7; Th/U= 0.33–0.25). Zircon showing textures in CL indicative of recrystallization yielded a mixture of discordant and concordant data with $^{206}Pb/^{238}U$ ages ranging from 1502 ± 19 to 1133 ± 14 Ma with the largest range of Th/U ratios (Th/U=0.32–0.10). A number of additional oscillatory zoned zircon cores younger than the oldest recrystallised core yielded a mixture of discordant and concordant data with $^{206}Pb/^{238}U$ ages ranging from 1496 ± 15 to 1304 ± 25 Ma with Th/U ratios of 0.40–0.21. Two uniform recrystallised domains yielded the youngest $^{206}Pb/^{238}U$ ages of 1076 ± 12 and 1055 ± 13 Ma, and also have the lowest Th/U ratios (Th/U= 0.18–0.09).

5.1.3 Osumilite–orthopyroxene–spinel migmatite (ROG13/2 – 2 km)

Eleven U–Pb analyses were performed on zircon grains from ROG13/2 (Figure 5c). Four oscillatory-zoned cores yielded $^{206}Pb/^{238}Pb$ ages ranging from 1574 ± 27 to 1113 ± 13 Ma (Th/U=0.43–0.12). Analyses from more recrystallised parts of grains yielded an overlapping range of $^{206}Pb/^{238}Pb$ ages from 1476 ± 19 to 1011 ± 18 Ma (Th/U=1.02–0.18). Three analyses of overgrowths (both bright and dark in CL) yielded a weighted mean $^{206}Pb/^{238}U$ age of 920 ± 13 Ma (MSWD=1.7, prob=0.18, n=3; Th/U= 1.08–0.54). The youngest $^{206}Pb/^{238}U$ age, 899 ± 15 Ma with a Th/U ratio of 2.79, was obtained from the only sector-zoned grain analysed.

5.1.4 Garnet–sillimanite–cordierite–spinel migmatite (ROG14/5 – at contact)

Nine U–Pb analyses were performed on zircon grains from ROG14/5 (Figure 5d). Three sector zoned zircons yielded $^{206}Pb/^{238}U$ ages ranging from 1025 ± 15 to 950 ± 14 Ma with Th/U ratios of 0.09–0.03. Analyses of recrystallised zircon yielded concordant to slightly discordant $^{206}Pb/^{238}U$ ages ranging from 996 ± 12 to 919 ± 18 Ma with a broader range of Th/U ratios of 0.14–0.02.

5.1.5 Garnet-bearing anorthosite (ROG14/8 – at contact)

Twenty-nine U–Pb analyses were performed on zircons from sample ROG14/8 (Figure 5e). The oldest $^{206}Pb/^{238}U$ ages of 1045 ± 17 and 1036 ± 11 were obtained from two unzoned zircon cores with poor CL response (Th/U= 0.50–0.25). Recrystallised zircon with diffuse oscillatory zoning yielded a range of younger $^{206}Pb/^{238}U$ ages from 1017 ± 11 to 926 ± 12 Ma with Th/U ratios of 0.51–0.09. Three overgrowths with poor CL response yielded the youngest $^{206}Pb/^{238}U$ ages with a weighted mean of 917 ± 12 Ma (MSWD=0.21, prob=0.81, n=3) and the highest Th/U ratios (Th/

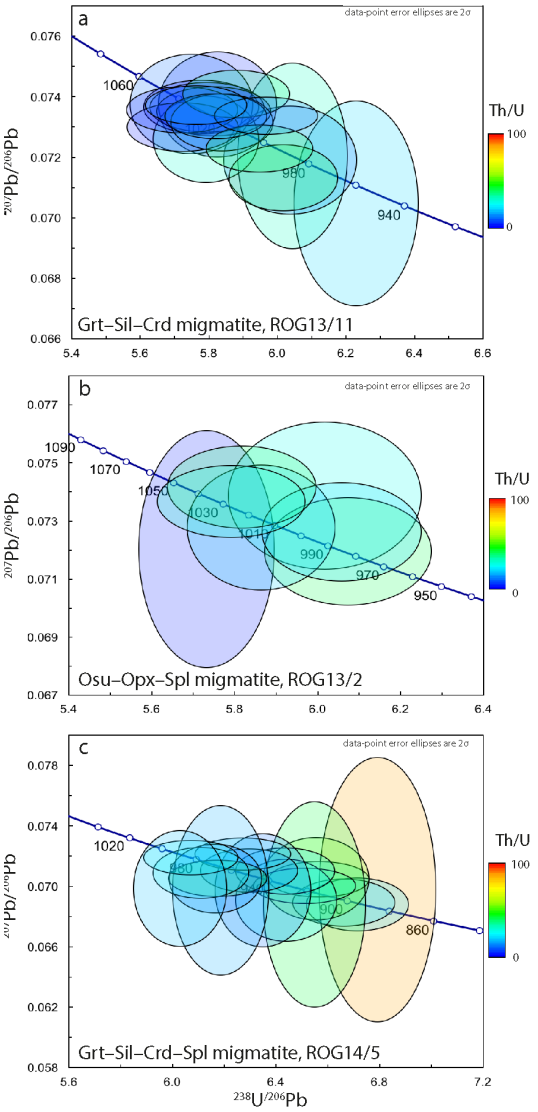

Fig 6: Monazite U–Pb Concordia diagrams. Analyses are shaded for Th/U content. See online version for colour.

U= 0.72–0.59).

5.2 Monazite U–Pb Geochronology

Data tables for monazite U–Pb analyses can be found in supplementary data Table S2. Concordia plots summarising the results are presented in Figure 6. Typical discordance is less than 10% for monazite.

5.2.1 Garnet–sillimanite–cordierite migmatite (ROG13/11 – 30 km)

Eighteen U–Pb analyses were performed on monazite grains from this sample. The analyses overlap Concordia (Figure 6a) and show a range of $^{206}Pb/^{238}U$ ages from 1038 ± 11 to 960 ± 11 Ma (Th/U = 40–1.6) with the twelve oldest analyses forming a cluster on Concordia (the remaining analyses spread along Concordia and have lower Th/U ratios) with a weighted mean $^{206}Pb/^{238}U$ age of 1028 ± 7 Ma (MSWD=0.37, prob=0.96, n=12).

5.2.2 Osumilite–orthopyroxene–spinel migmatite (ROG13/2 – 2 km)

Seven U–Pb analyses were performed on monazite grains from this sample. The analyses overlap Concordia (Figure 6b) and have $^{206}Pb/^{238}U$ ages ranging from 1037 ± 11 to 983 ± 12 Ma (Th/U = 40–2.2).

5.2.3 Garnet–sillimanite–cordierite–spinel migmatite (ROG14/5 – at contact)

Eighteen U–Pb analyses were performed on monazite grains from this sample, each concordant to within error. $^{206}Pb/^{238}U$ ages range from 990 ± 11 to 886 ± 11 Ma (Th/U = 88–10) (Figure 6c). Sillimanite inclusion-bearing cores (983 ± 11 to 931 ± 11) and inclusion-free monazite cores (990 ± 11 to 915 ± 11) show similar ranges of ages. Brighter BSE response recrystallised areas on inclusion-bearing (954 ± 11 to 886 ± 11) and absent (968 ± 11 to 895 ± 10) cores also show similar ranges of ages.

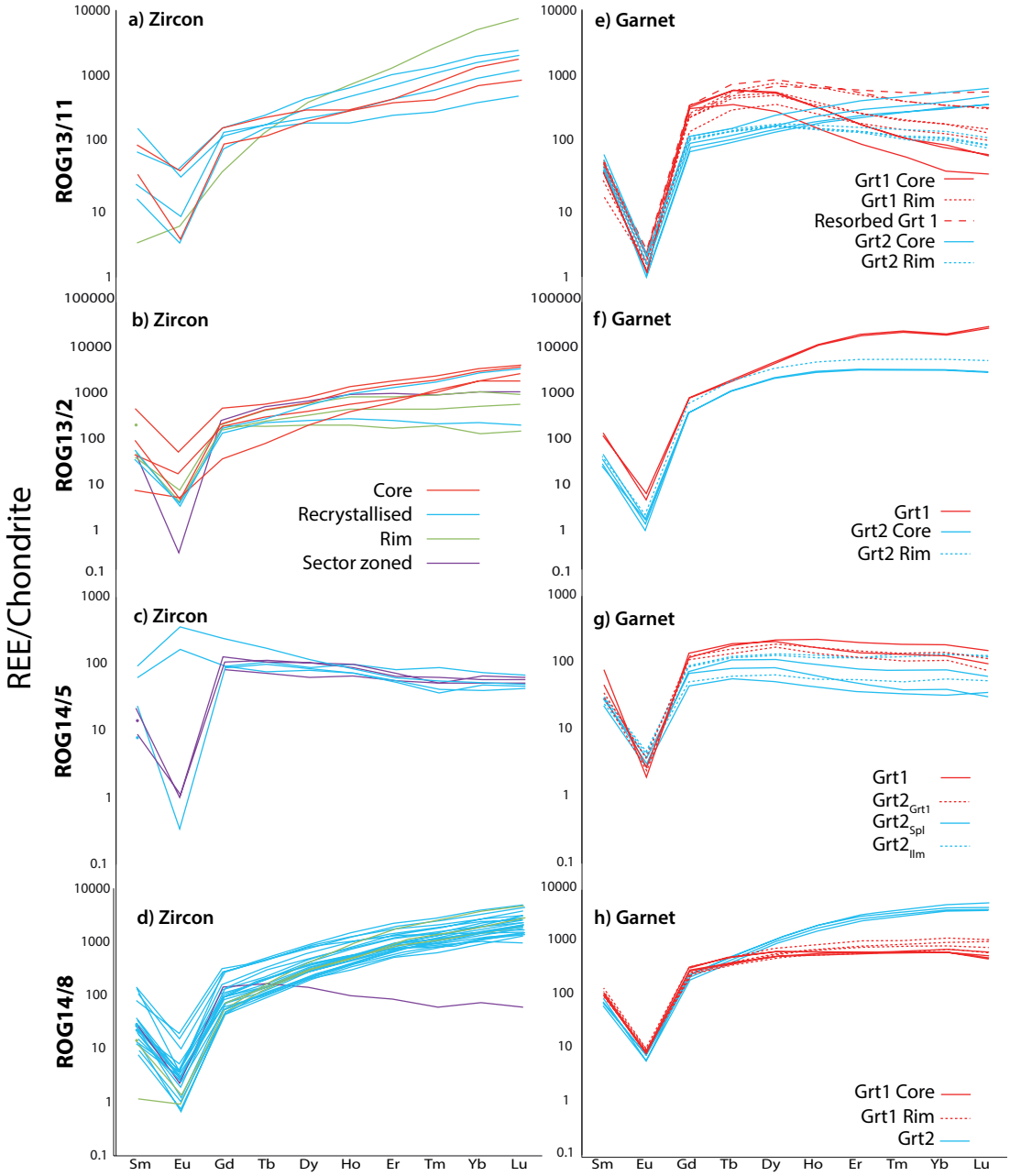

Fig 7: REE/Chondrite normalised plots for zircon and garnet. Zircon REE analyses are shaded for age, garnet analyses are shaded for analysed texture. See online version for colour. Zircon REE analyses –a-d. Garnet analyses from ROG13/11 -e: grt1 contains a sillimanite rich core, inclusion poor rims. Resorbed garnet is located next to cordierite, related to garnet break down and is the most enriched. Grt2 is located within the leucosome and is interpreted as peritectic with inclusion rich cores and inclusion poor rims. Garnet from ROG13/2 -f: grt1 was picked from a mineral separate. Grt2 is small garnet grain within osumilite. Garnet from ROG14/5 -g: grt1 are inclusion free porphyroblasts, grt2grt1 secondary garnet nucleating on primary garnet, grt2spl secondary garnet nucleating on spinel, grt2ilm secondary garnet nucleating on ilmenite. Garnet from ROG14/8 -h: grt1 is a large garnet porphyroblast. grt2 are small garnet grains.

5.3 Rare Earth Elements

REE and other trace elements were analysed from selected concordant zircon and monazite grains in all garnet-bearing samples. Texturally distinct generations of garnet (e.g. inclusion free rims, inclusion bearing cores) in thin section was also analysed for trace elements. Results can be found in supplementary data Tables S3–S6 respectively, and summarised on chondrite-normalised plots in Figures 7 and 8.

5.3.1 Zircon

Garnet–sillimanite–cordierite migmatite (ROG13/11 – 30 km). Analyses of oscillatory zoned zircon cores show moderately positive middle-to-heavy REE (M–HREE) slopes with normalised ($_N$) Yb/Gd (Yb_N/Gd_N) = 7.2–8.4 and an order of magnitude of range in the normalised HREE abundances (Lu_N = 840–1708 (n=2) (Figure 7a). Analyses of recrystallised zircon display steep positive M–HREE slope also with greater variation than the cores with Yb_N/Gd_N = 5.1–12.4 and Lu_N = 486–2354 (n=4). Both the cores and recrystallised zircon have a similar range of negative Eu anomalies with Eu/Eu* (Eu/Eu*=Eu_N/0.5*(Sm_N + Gd_N)) values of 0.06–0.3 and 0.07–0.3 respectively. A dark BSE response rim was analysed, and has a steep M–HREE slope (Yb_N/Gd_N = 122) as a result of having lower MREE concentrations (Gd_N = 38.1) than the other analyses (Gd_N = >76.8).

Osumilite–orthopyroxene–spinel migmatite (ROG13/2 – 2 km). Oscillatory zoned zircon cores display positive M–HREE slope with Yb_N/Gd_N = 6.9–16.4, with some scatter to the M–HREE (Gd_N = 33–417; Lu_N = 1630–3589 (n=4)) and a range of negative Eu anomalies (Eu/Eu* = 0.03–0.2) (Figure 7b). Recrystallised zircon shows some variation, with one flat M–HREE slope (Yb_N/Gd_N = 1.6; Lu_N = 166), and one steep slope (Yb_N/Gd_N = 16.8; Lu_N = 2856) but both analyses have similar negative Eu anomalies (Eu/Eu* = 0.03–0.05). Two dark CL response rims (R13-2-4 and R13-2-10) were analysed with flat to shallow M–HREE slope (Yb_N/Gd_N = 0.7–3.4) and are depleted in HREE relative to the cores (Lu_N = 522–128). Dark CL rims show a negative Eu anomaly with some values below detection (Eu/Eu* = 0.04). One bright CL response rim (R13-2-7) yielded a moderate M–HREE slope (Yb_N/Gd_N = 5.5), more enriched in HREE (Lu_N = 868) than the dark rims with a negative Eu anomaly (Eu/Eu* = 0.06). One bright CL response sector zoned grain (R13-2-8) was analysed yielding a moderate M–HREE slope with Yb_N/Gd_N = 4.2 with similar HREE concentrations as the bright rim (Lu_N = 938) and has the most prominent negative Eu anomaly of any of the analyses (Eu/Eu* = 0.002).

Garnet–sillimanite–cordierite–spinel migmatite (ROG14/5 – at contact). Sector zoned zircon yielded slightly negatively sloped to flat M–HREE (Yb_N/Gd_N = 0.4–0.8) (Figure 7c) with similar HREE concentrations (Lu_N = 41.6–63.0, n=4) and yielded a negative Eu anomaly (Eu/Eu* = 0.02) to Eu below detection limit. Recrystallised zircon analysis yielded similar M–HREE slopes (Yb_N/Gd_N = 0.22–0.82) similar HREE concentrations (Lu_N = 45.3–61.3, n=3) with two of the analyses (R114-5-1 and R114-5-2) showing positive Eu anomalies (Eu/Eu* = 2.15–2.16) with

the remaining analysis displaying a negative Eu anomaly (R114-5-9; Eu/Eu* = 0.01).

Garnet-bearing anorthosite (ROG14/8 – at contact). Two uniform dark CL response recrystallised cores yielded consistent steep M–HREE slope (Yb_N/Gd_N = 14.8–15.6) limited scatter in the HREE (Lu_N = 1296–2634, n=2) and similar negative Eu anomalies (Eu/Eu* = 0.04–0.08) (Figure 7d). Recrystallised zircon with diffuse oscillatory zoning displayed moderate to steep M–HREE slope (Yb_N/Gd_N = 5.6–52.4) with almost half an order of magnitude of scatter to the HREE (Lu_N = 971–4967, n=16) with a range of negative Eu anomalies (Eu/Eu* = 0.02–0.1). One sector zoned core yielded the only flat M–HREE slope (Yb_N/Gd_N = 0.5) with lower HREE concentrations (Lu_N = 60.1) but a similar negative Eu anomaly (Eu/Eu* = 0.03). Bright CL response, recrystallised zircon also yielded steep M–HREE slope with little variation (Yb_N/Gd_N = 21.3–29.3) with less variation to HREE (Lu_N = 1498–2761, n=4) compared to the dark CL recrystallised zircon and prominent negative Eu anomalies (Eu/Eu* = 0.03–0.09) to Eu below detection limit. Dark uniform CL response overgrowths show steep M–HREE slope (Yb_N/Gd_N = 17.2–76.4) with some scatter to the HREE (Lu_N = 1984–5066, n=3) with negative Eu anomalies (Eu/Eu* = 0.03–0.04) to Eu below detection limit.

5.3.2 Garnet

Garnet–sillimanite–cordierite migmatite (ROG13/11 – 30 km). Nine analyses were conducted on a garnet porphyroblast (grt1) from within the melanosome, with sillimanite inclusion rich cores and inclusion free rims. All grt1 analyses show a 'convex' pattern with a pronounced decrease in the HREE in the core (Yb_N/Gd_N = 0.12–2.1; Dy_N = 306–911, n=3; Lu_N = 36–591, n=3) and a range of Y values (450–1000 ppm) (Figure 7e). The inclusion free rims show similar MREE values but have elevated HREE relative to cores (Yb_N/Gd_N = 0.70–1.33; Dy_N = 391–816; Lu_N = 114–334 (n=4)) as well as a smaller range of Y values (250–539 ppm). Both the core and rim have negative Eu anomalies with the rim being slightly less pronounced with Eu/Eu* values of 0.005–0.02 and 0.009–0.02 respectively. Resorption texture associated with the formation of cordierite show increased HREE values (Lu_N = 348–591, n=2), with flat to near flat M–HREE slope (Yb_N/Gd_N = 0.99–2.1) and negative Eu anomalies (Eu/Eu* = 0.006–0.02) and the highest Y concentrations (958–1037 ppm).

Garnet within the leucosome (grt2) shows quartz inclusions in the core and an inclusion-free rim. The inclusion-rich core shows moderate M–HREE slopes (Yb_N/Gd_N = 3.9–4.6) with a small amount of spread to the M–HREE (Dy_N = 153–267; Lu_N = 377–679 (n=4)) and lower Y values (290–452 ppm) compared to the melanosome core. The inclusion-free rim shows a flat M–HREE slope (Yb_N/Gd_N = 0.9–1.2) with less spread to the HREE compared to the inclusion rich core (Lu_N = 86.4–123, n=4). Both the core and rim have negative Eu anomalies (Eu/Eu* values of 0.02 and 0.02–0.03 respectively) with the cores having higher Y values than the rims (Y = 290–452 ppm and 267–310 ppm respectively).

Osumilite–orthopyroxene–spinel migmatite (ROG13/2 – 2 km). The only garnet present in thin

section occurred within osumilite (grt1). Three analyses on grt1 yielded a steep M–HREE slope (Yb_N/Gd_N = 23.1–23.7) with a slight enrichment from Ho to Tm with a slight depletion in Yb but overall enrichment in HREE (Lu_N = 26296–28231, n=3) (Figure 7f). All analyses yielded high Y values (Y = 11640–12100 ppm).

Four analyses (3 core, 1 rim) were conducted on a whole garnet grain (grt2) as a mineral separate mounted in epoxy. REE values from this grain showed moderate M–HREE slope (Yb_N/Gd_N = 8.4–9.1) with flat HREE approximately an order of magnitude lower than the garnet included in osumilite. The rim of grt2 is more enriched in HREE and Y than the core (Lu_N = 2914–3033 (n=3) and 5136 (n=1) respectively; Y = 7100 ppm and 4210–4380 ppm respectively). Both have negative Eu anomalies but the grt2 is more pronounced with Eu/Eu* values of 0.005–0.009 compared to 0.01–0.02 in grt1.

Garnet–sillimanite–cordierite–spinel migmatite (ROG14/5 – at contact). Four analyses were conducted on inclusion free primary garnet (grt1) with near flat H–MREE slopes (Yb_N/Gd_N = 0.9–1.9) with almost half an order of magnitude of spread to the HREE (Lu_N = 96.3–445, n=2) and a pronounced Eu anomaly (Eu/Eu*= 0.01–0.04) with limited spread in Y (Y = 301–391 ppm) (Figure 7g). Secondary garnet (grt2) was also analysed on primary garnet ($grt2_{grt1}$), around ilmenite ($grt2_{ilm}$) and around spinel ($grt2_{sp}$) (three analyses each). $Grt2_{grt1}$ showed similar M–HREE slope (Yb_N/Gd_N = 0.98–2.7) to grt1 but with a slight depletion in M–HREE (Lu_N = 77.0–296, n=2) and Y (Y = 207–275 ppm), and shows a negative Eu anomaly (Eu/Eu* = 0.04–0.05). Both $grt2_{ilm}$ and $grt2_{sp}$ shows similar near flat M–HREE slopes (Yb_N/Gd_N =1.1–1.5 and 0.6–1.1 respectively) with garnet around spinel being the most depleted in M–HREE and Y (Lu_N = 32.5–64.2, n=3; Y = 95–205 ppm) followed by garnet around ilmenite (Lu_N = 54.7–125.1, n=3; Y = 76–161 ppm). Both $grt2_{ilm}$ and $grt2_{sp}$ are depleted in M–HREE relative to $grt2_{grt1}$.

Garnet-bearing anorthosite (ROG14/8 – at contact). Sample contains large subhedral (grt1), and small subhedral garnet (grt2). Eight analyses were conducted on grt1 that is surrounded by plagioclase. Grt1 cores show near flat M–HREE slope (Yb_N/Gd_N =1.8–2.5) with limited scatter to the HREE (Lu_N = 410–540, n=4) and Y (Y = 791–899 ppm) (Figure 7h). Grt1 rims show similar near flat M–HREE slope (Yb_N/Gd_N =2.9–3.6) but with more scatter to the HREE (Lu_N = 532–905, n=4) and higher Y than the cores (Y = 769–1134 ppm). Four analyses were conducted on grt2. Grt2 show steep M–HREE slopes (Yb_N/Gd_N =16.5–18.5) compared to grt1 with similar HREE concentrations and limited scatter (Lu_N = 3214–4148, n=4) but relative enrichment of Y concentrations (Y = 1940–2400 ppm).

5.3.3 Monazite

Garnet–sillimanite–cordierite migmatite (ROG13/11 – 30 km). Monazite grains from this sample show negative M–HREE slopes (Yb_N/Gd_N = 0.001–0.02) with an order of magnitude of scatter to the HREE (Lu_N = 36–580, n=16) (Figure 8a). All analyses show negative Eu anomalies with Eu/Eu* values of 0.002–0.005 and Y values ranging from 833–22210 ppm.

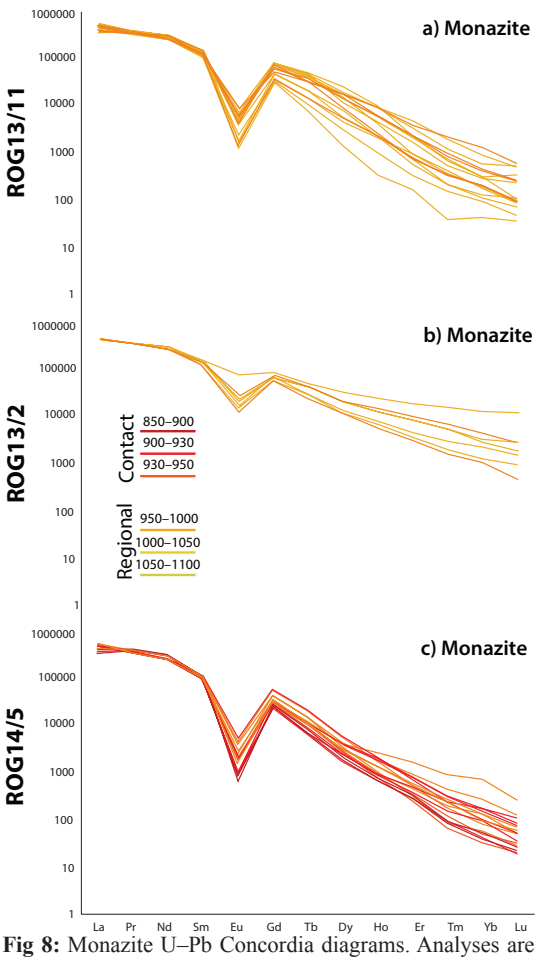

Fig 8: Monazite U–Pb Concordia diagrams. Analyses are shaded for Th/U content. See online version for colour.

Osumilite–orthopyroxene–spinel migmatite (ROG13/2 – 2 km). Monazite from this sample shows no internal textural variation. Negative M–HREE slopes are variable with no consistent group (Yb_N/Gd_N = 0.02–0.16), and more than an order of magnitude of scatter to the HREE (Lu_N = 453–123505, n=7) (Figure 8b). All analyses show negative Eu anomalies with one analysis with a less prominent negative anomaly (Eu/Eu* =0.002–0.006) with Y values ranging from 48400–12280 ppm.

Garnet–sillimanite–cordierite–spinel migmatite (ROG14/5 – at contact). Sillimanite inclusion-bearing and inclusion-free, darker BSE response cores both show negative M–HREE slopes (Yb_N/Gd_N = 0.001–0.004 and 0.001–0.02 respectively) with an order of magnitude of scatter to the HREE (Lu_N = 20–53 (n=3) and 18–253 (n=6) respectively) and negative Eu anomalies (Eu/Eu* = 0.001–0.002 and 0.001–0.004 respectively) (Figure 8c). The inclusion-free cores have a slightly larger range of Y values than the inclusion bearing cores with values of 1709–5610 ppm and 1850–2428 ppm respectively. Brighter BSE response recrystallised areas on inclusion bearing and inclusion free cores both show negative M–HREE slopes (Yb_N/Gd_N =0.001–0.008 and 0.002–0.006 respectively) with an order of magnitude of scatter to the HREE (Lu_N = 23–84 (n=3) and 26–103 (n=5) respectively) and negative Eu anomalies (Eu/Eu* = 0.004 and 0.001–0.004 respectively). Similar to the cores the recrystallised areas associated with inclusion-free cores (Y=1629–4780 ppm) show a larger range of Y values than the recrystallised areas of inclusion-bearing monazite (Y=1404–3011 ppm). Analysis of sillimanite inclusion-bearing and inclusion-free monazite are similar in their M–HREE patterns, however the rims of both show slightly elevated HREE values.

6. DISCUSSION

6.1 Metamorphic events in SW Norway

Having two temporally close metamorphic events, regional and contact, in the same geographical area provides some challenges for the determination of distinct time frames for each. Indeed they may be so intrinsically linked as to make some aspects indistinguishable. However, the sampling strategy employed in this study, with samples from varying distances from the RIC, enables some distinction to be made between samples far enough removed

from the intrusion that they have been modified only by regional metamorphism (ROG13/11, 13/10), from those dominated by the extreme conditions close to the anorthosite intrusion (ROG14/5).

The interval of regional metamorphism recorded by ROG13/11 falls between a cluster of zircon ages at ~1052 Ma, and a later cluster at ~955 Ma (Figure 9). The ~1052 Ma cluster comprises analyses of inherited zircon grains that have been recrystallised and fully isotopically reset at high–*T* (falling at the end of a discordant array), whilst the later cluster is defined by zircon rims resulting from the crystallisation of partial melt (based on rim textures combined with youngest ages) (Taylor et al., 2016). The zircon analyses falling within the 1052 Ma age peak show characteristically low Th/U ratios expected of grains formed or recrystallised during metamorphism (Harley et al., 2007; Hoskin & Black, 2000; Hoskin & Schaltegger, 2003; Schaltegger et al., 1999) related to the expulsion of Pb and Th during recrystallisation (Harley et al., 2007; Hoskin & Black, 2000). All of the analyses of metamorphic monazite in this sample fall within this time window also, with a major peak at ~1025 Ma. REE abundances in zircon from ROG13/11 show an order of magnitude more scatter of the M–HREE in recrystallised zircon when compared to oscillatory zoned cores. Garnet from ROG13/11 exhibits the most geochemical and textural variation of all the samples (Figure 7e); preserving M–HREE patterns indicative of growth during fluid absent partial melting (Grt1 core; Hermann & Rubatto, 2003), growth with higher concentrations of partial melt (Grt1 rim; Hermann & Rubatto, 2003), peritectic growth (Grt2; Rubatto, 2002) and later resorption (Resorbed Grt1).

Few zircon analyses from ROG13/10 yielded metamorphic ages (as defined by ROG13/11), likely due to the anhydrous (residual), unreactive nature of the bulk composition, hindering additional zircon growth (e.g. Vavra, Gebauer, Schmid, & Compston, 1996). However, two uniform recrystallised areas yielded the youngest ages of 1076 ± 12 and 1055 ± 13 Ma. These fall at the end of a discordant array, within error of the oldest regional metamorphic ages recorded in ROG13/11. A pooled weighted mean age of the ~1050 Ma recrystallised zircon from ROG13/11 and the two recrystallised areas from ROG13/10 yielded a weighted mean $^{206}Pb/^{238}U$ age of 1059 ± 12 Ma (MSWD=0.98, prob=0.40, n=4, 2σ), interpreted to date the recrystallisation of zircon during prograde heating (~>700°C). This age is within error of $^{40}Ar/^{39}Ar$ osumilite ages interpreted to represent prograde regional growth (Blereau et al., In review). Prograde recrystallisation of zircon is further corroborated by the oldest monazite analyses from ROG13/11, with two grains yielding the same age of 1038 ± 11 Ma, within error of the pooled age. Our 1059 ± 12 Ma interpreted age of prograde heating predates previous onset estimates (~1035 Ma: Bingen et al., 2008) and previous estimates of peak regional metamorphism by ~25–55 Ma (c. 1006 Ma: Drüppel et al., 2013; c. 1034 Ma: Laurent et al., 2016; c. 1035 Ma: Möller et al., 2003). The interval for peak regional metamorphism indicated in this study, 1035–995 Ma, is based on the majority of monazite ages (1028 ± 7 Ma) and on the youngest recrystallised zircon (1009 ± 15 Ma) from ROG13/11. This interval lies within the range

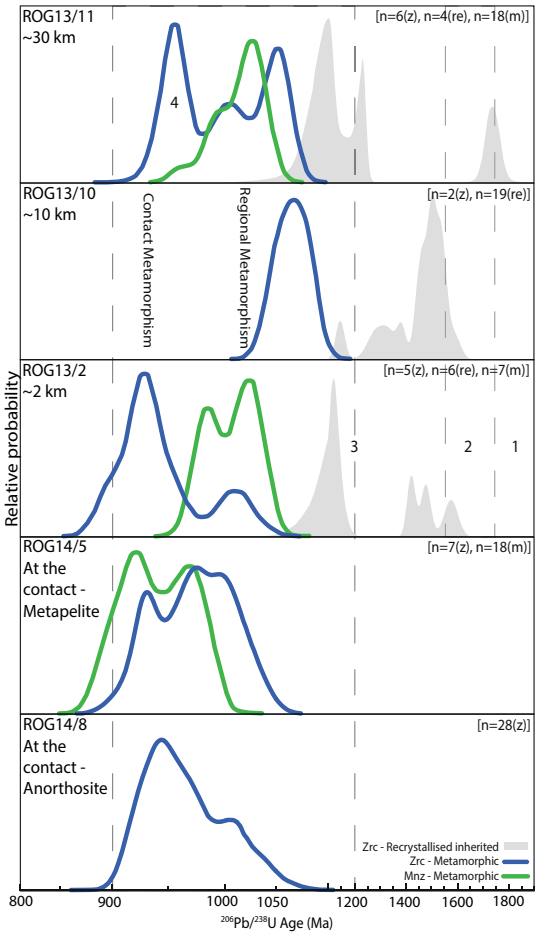

Fig 9: Relative probability plots of all concordant U–Pb zircon and monazite SHRIMP analyses. Samples are arranged according to their relative distance from the pluton. Zircon and monazite data is given as 206Pb/238U ages. All inherited and recrystallised zircon that may be partially reset are shown as filled grey plots; distinguished from zircon (of a range of textures) recording ages related to the onset of regional metamorphism and younger. 1 – Svecofennian Orogeny, 2 – Gothian Orogeny, 3 – Sveconorwegian Orogeny, 4 – Regional melt crystallisation.

of previous estimates for peak metamorphism (Drüppel et al., 2013; Laurent et al., 2016; Möller et al., 2003). The bulk of monazite growth is generally interpreted to occur immediately after the metamorphic peak during melt crystallisation (Clark et al., 2014; Kelsey, Clark, & Hand, 2008) but can also occur during prograde metamorphism (Johnson, Clark, Taylor, Santosh, & Collins, 2015; Taylor et al., 2016).

Zircon rims interpreted to be the result of final regional melt crystallisation are dated at 951 ± 14 Ma based on the youngest analysis, after which no further zircon or monazite growth occurred in the samples that experienced regional metamorphism only. This age is within error of the c. 955 Ma age previously reported for zircon growth related to garnet breakdown during decompression (Tomkins et al., 2005).

Following regional metamorphism, high–*T* conditions were prolonged and accentuated by the intrusion of the RIC (Blereau et al., 2017). This is reflected in the monazite and zircon ages in samples ROG13/2, 14/5 and 14/8, that extend beyond the period of regional metamorphism defined above (~1050–950 Ma) to ages relating to the RIC (~932 Ma: Schärer et al., 1996) and younger.

Zircon and monazite data for ROG13/2 (2 km from the RIC) include analyses recording regional metamorphic ages between ~1030 and 970 Ma. However, in addition, three analyses of zircon rims record a weighted mean age of 920 ± 13 Ma, within error of the emplacement of the RIC. The youngest zircon age from ROG13/2 is from a sector-zoned grain interpreted to have crystallised from melt, with an age of 899 ± 15 Ma, within error of the previously mentioned population of rims.

The samples on the RIC contact lack any ages older than the time of onset of regional metamorphism (c. 1050 Ma). Zircon overgrowths from ROG14/8 yielded a weighted mean age of 917 ± 15 Ma, within error of ages of 928 ± 9 and 919 ± 8 Ma obtained from recrystallised zircon in ROG14/5. Monazite from ROG14/5 yielded

the youngest ages of any sample, ranging from 990 ± 11 to 886 ± 11 Ma, as well as the most depleted HREE concentrations, with consistently flat M–HREE. With reduced distance from the RIC, M–HREE in zircon show reduced scatter (homogenisation) while M–HREE in garnet show simpler textural and geochemical relationships (e.g. core and rims only), compared to the distal samples that experienced only regional metamorphism. A single zircon analysis (a sector zoned core) from ROG14/8 shows the same, negative sloping M–HREE pattern (Figure 7d) as analyses from the metapelite sample ROG14/5 (Figure 7c). Flat M–HREE slopes were also recorded from the core and rim of a large garnet (grt1) within ROG14/8, with smaller garnet grains showing steep M–HREE slopes (grt2; Figure 7h). It is likely that both the zircon and grt1 (Figure 7h) in the anorthosite sheet have been entrained from the metapelite given the similarities in REE patterns and ages of both samples, with grt1 being interpreted as xenocrystic.

Based on the continuum of zircon and monazite ages in all samples from within the aureole (ROG13/2, 14/5 and 14/8) and the lack of evidence for new zircon growth at c. 955 Ma (only recrystallised zircon is present), the samples within the aureole show little evidence for significant cooling following regional metamorphism prior to the emplacement of the RIC (Blereau et al., 2017; Blereau et al., in review), and are thus interpreted to have experienced very slow cooling following regional metamorphism. This interpretation is preferred over a more cyclic evolution, which would require multiple reheating and re-melting events in already residual lithologies as a result of significant cooling in-between events in order to allow for the growth of the observed melt-bearing mineral reaction microstructures in the aureole samples during contact metamorphism as well as the growth of new zircon. Whilst a more cyclic scenario cannot be entirely ruled out, it is far simpler for the region to have stayed above the solidus than cooling and re-melting residual lithologies repeatedly.

Based on the results presented here and by Blereau et al. (2017) and Blereau et al. (In review), high temperature conditions in the RVA Sector were prolonged; prograde regional conditions sufficient to modify zircon were reached at 1059 ± 12 Ma with peak metamorphism (temperatures of ~850–950°C) reached at c. 1035–995 Ma. Final melt crystallisation within the most distal sample occurred at 951 ± 14 Ma. Samples closer to the RIC show no clear melt crystallisation event at 951 ± 14 Ma due to limited cooling until after the c. 930 Ma contact metamorphic event (~950°C at the RIC contact) (Figure 9). Final melt crystallisation in samples from within the aureole was delayed by c. 50 Myr (to c. 900 Ma based on youngest zircon and monazite ages, compared to 951 ± 14 Ma) due to the contact event. Therefore, we conclude that high temperature conditions were sustained in the RVA Sector for ~100–160 Myr, (cf. Drüppel et al., 2013).

6.2 Modification of REE during high–*T* conditions

Rare Earth Element abundances in zircon and monazite can be used to interpret growth conditions as well as potential modification by processes such as fluid-induced coupled dissolution-reprecipitation or recrystallisation (Taylor et al., 2016). In this study, monazite

textures were relatively simple, with no textural evidence for modification by fluids or partial melts. Rare Earth Elements also showed limited variations in concentration, defining no distinct geochemical trends associated with increasing temperatures from the RIC. Variations in REE between samples do not correlate with bulk compositional differences (13/11 and 14/5 metapelitic, 13/2 high-Mg metapelite). This combination of features is interpreted to suggest monazite was growing throughout the high-temperature metamorphic evolution, potentially along both the prograde and retrograde path (cf. Johnson et al., 2015), providing information on the duration of high-*T* conditions. In this context the mechanism of monazite growth (dominantly neocrystallisation) is not able to record systematic changes in the REE related to the thermal history of the RVA. By contrast, there is little evidence for new growth of zircon in samples inferred to have been melt-bearing until crystallisation of the last vestiges of melt and none at all in highly residual samples. The chemistry and recorded metamorphic ages in zircon are therefore interpreted to be related to recrystallisation and diffusion over neocrystallisation. Recrystallised zircon, unlike monazite, shows a systematic variation in REE with increasing temperature in association with decreasing distance from the RIC.

Zircon and garnet both favour HREE and can influence each other during growth and during elevated temperatures when the geochemical system is open to diffusive processes. The partitioning relationships of REE between garnet and zircon have been quantified experimentally (Johnson et al., 2015; Rubatto & Hermann, 2007) and are readily applicable to neocrystallised zircon and to zircon undergoing coupled dissolution-reprecipitation, making it possible to interpret whether such zircon grew in a garnet-bearing or garnet-absent system. However, the same partitioning relationships may not be present in recrystallised zircon, even when garnet has been present during the entire metamorphic evolution, due to the sluggish nature of volume diffusion during recrystallisation that is also affected by grain size, temperature and duration at high temperature. The modification of REE is further complicated by different elements having different diffusivities (e.g. Dy < Pb < Yb) (Cherniak, Hanchar, & Watson, 1997; Cherniak & Watson, 2001; Johnson et al., 2015; Rubatto & Hermann, 2007), potentially causing mixed analyses due to incomplete modification of all REE within an analytical volume (Taylor et al., 2016). Whether the REE in recrystallised zircon will equilibrate fully to record abundance patterns similar to those of contemporary neocrystallised zircon depends on the conditions and timescale of metamorphism.

We have calculated theoretical diffusion profiles to model the changes in REE composition that would be expected during recrystallisation of an originally igneous zircon (with steep

$$C = Co \times \frac{1}{2}\left\{erf\left[\frac{a+r}{2\sqrt{(Dt)}}\right] + erf\left[\frac{a-r}{2\sqrt{(Dt)}}\right]\right\} - \left\{\left(\frac{1}{r}\right)\sqrt{\left(\frac{Dt}{\pi}\right)} \times \left(exp\left[\frac{-(a-r)^2}{4Dt}\right] - exp\left[\frac{-(a+r)^2}{4Dt}\right]\right)\right\} \quad (1)$$

Element	IR (Å)	E_a	D_0
La	1.16	1298 ±172	9.76E+17
Pr	1.126	1100 ±112	1.96E+13
Nd	1.109	1017 ±88	2.10E+11
Sm	1.079	897 ±57	2.88E+08
Eu	1.066	856 ±47	2.91E+07
Gd	1.053	820 ±41	4.12E+06
Tb	1.04	791 ±36	8.19E+05
Dy	1.027	768 ±35	2.29E+05
Ho	1.015	753 ±35	9.52E+04
Er	1.004	743 ±38	5.50E+04
Tm	0.994	739 ±42	4.13E+04
Yb	0.985	737 ±47	3.78E+04
Lu	0.977	739 ±52	4.01E+04

Table 1: Parameters used for the calculation of diffusion coefficients and diffusion coefficients used in diffusion modelling. IR- ionic radius, E_a- activation energy, D_0- pre-exponential factor. IR from Shannon (1976) for coordination number: 8, valence: 3+.

	Diffusion coefficients (m^2s^{-1})					
T (°C)	850	900	950	1000	1050	1100
Gd	2.1226E-30	7.4758E-29	1.9678E-27	4.0061E-26	6.4945E-25	8.5952E-24
Tb	6.0721E-30	1.9089E-28	4.5266E-27	8.3707E-26	1.2416E-24	1.5132E-23
Dy	1.6654E-29	4.7510E-28	1.0305E-26	1.7552E-25	2.4130E-24	2.7408E-23
Ho	3.8870E-29	1.0301E-27	2.0880E-26	3.3415E-25	4.3363E-24	4.6691E-23
Er	8.2141E-29	2.0596E-27	3.9684E-26	6.0604E-25	7.5320E-24	7.7913E-23
Tm	1.5637E-28	3.7681E-27	7.0002E-26	1.0337E-24	1.2454E-23	1.2517E-22
Yb	2.7518E-28	6.4509E-27	1.1684E-25	1.6856E-24	1.9875E-23	1.9579E-22
Lu	4.3139E-28	9.9435E-27	1.7733E-25	2.5220E-24	2.9346E-23	2.8559E-22

M–HREE; C_O) to a modified composition in equilibrium with garnet (flat M–HREE; C_{Eq}), for different temperature conditions and timescales. A composition in equilibrium with garnet was used for the modified composition C_{Eq}, as all of the samples analysed for REE in this study have garnet present. ROG13/11 shows textural evidence for having contained garnet throughout the metamorphic evolution. Due to increased textural complexity the presence of garnet in ROG14/5 for the duration of the metamorphic evolution is less clear but cannot be ruled out, hence for the purposes of the modelling, all samples are assumed to have had garnet present during the entire metamorphic evolution. The light REE (La–Eu) were not considered due to large possible variations in their concentration and given that the process being modelled involves a M–HREE rich phase (i.e. garnet). The modelling algorithm required simplification of the typically prismatic zircon grain shape to a spherical volume and the assumption that only volume diffusion was acting, with no additional influences on diffusion rates (e.g. radiation damage, fluids). A radius '*r*' of 50 µm (representing a zircon grain 100 µm in the shortest dimension) was used for the spherical volume, within which, multiple ~20 µm SHRIMP spots could theoretically be placed. In the model, the diffusant element is initially distributed uniformly (with concentration C_O) within the 50 µm radius sphere and diffuses into an infinite volume, with concentration (C) calculated at time periods of interest (t = Myr, between 0.5–200 Myr) at the radius of interest (a, where $a \leq r$). When C_{Eq} for a diffusing element is reached, the concentration of that element is buffered for

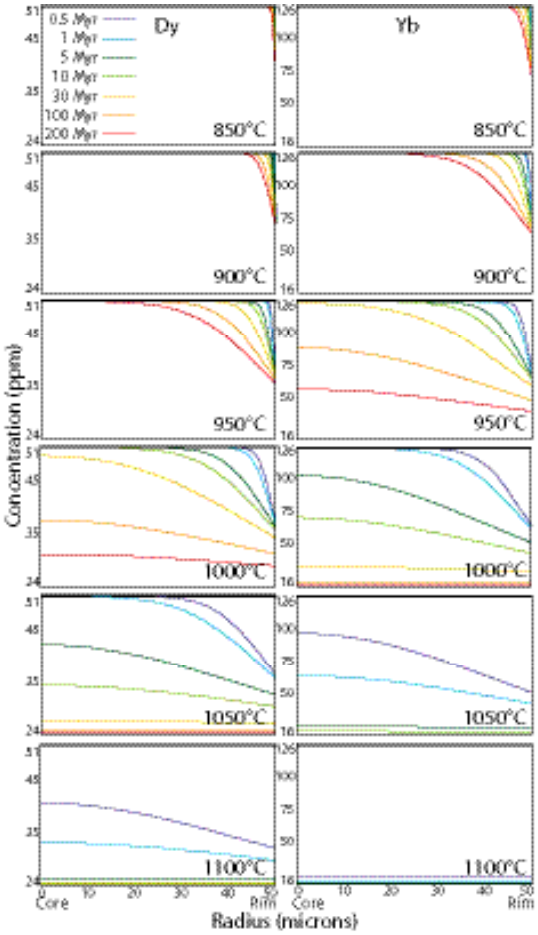

Fig 10: Modelled diffusion profiles of Dy and Yb in a theoretical zircon for different *T–t* scenarios. See online version for colour.

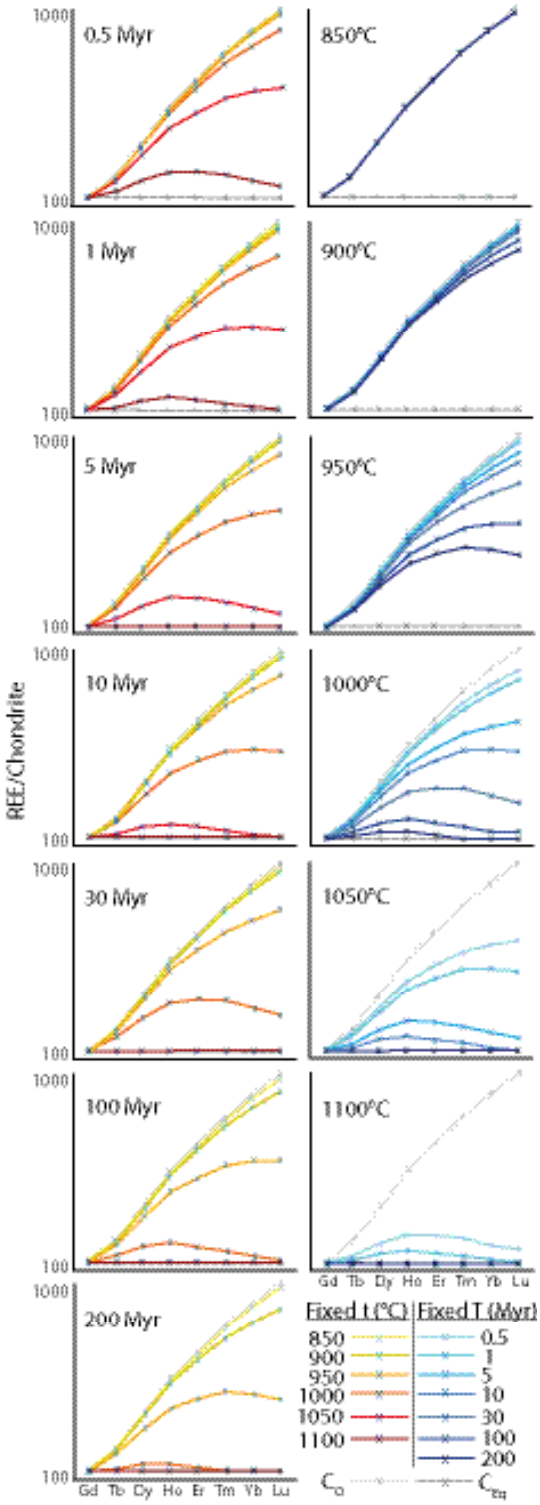

Fig 11: Diffusion-modified M–HREE compositions expected for a 20 µm SHRIMP spot analysis on the edge of the modelled theoretical zircon. Compositions are given for set temperature or time periods. See online version for colour.

the remainder of the run. For these calculations, a corrected version of equation 3.8 of Crank (1975) was used (Equation 1): see below.

The formula was corrected from that published in Crank (1975) where both error functions (*erf*) had the same sign (+) within the numerator, resulting in unusual curve profiles.

Diffusion coefficients (D in m^2s^{-1}) for Dy and Yb for a range of temperatures (850–1100°C) were calculated using the Arrhenius functions of Cherniak et al. (1997). Using the polynomial relationships between ionic radius (IR), activation energy (E_a) and pre-exponential factor (D_0) from Cherniak et al. (1997), E_a and

D_0 values for the remaining M–HREE were extrapolated to calculate D values for all pertinent elements (Table 1). The uncertainty on E_a from the Arrhenius functions (Cherniak et al., 1997) generates a wide range of possible diffusion coefficients; for the purpose of this model we used the average diffusion coefficient of each element. Diffusion profiles were calculated in MATLAB using Equation 1 and are shown in Figure 10 for Dy and Yb. Diffusion profiles in Figure 10 show the strong control of temperature on diffusional modification, with increased propagation of the modification front from rim to core with increasing temperature. Time is also an important factor, with longer time periods at lower temperatures also causing perturbation to the trace elements at the edge of the grain. The differing amounts of modification between Dy and Yb highlight the increased diffusivity of HREE over MREE due to their smaller ionic radii.

The same suite of temperature conditions and time periods used to generate the diffusion profiles of Dy and Yb were used to calculate profiles for the remaining M–HREE (Gd–Lu). To simulate a 20 μm diameter SHRIMP spot placed on the edge of the theoretical zircon, an average REE composition was extracted from each set of profiles (Table S7). The calculated compositions were averaged from 1 μm segments along the diffusion profile that were then assigned to a section of the 20 μm circular spot area and normalised with respect to chondritic REE abundances using the values of Anders and Grevesse (1989). The results show that for temperatures of 850–900°C, even after extended time periods, little to no modification to the M–HREE occurs (Figure 11). This implies that REE within recrystallised zircon from rocks experiencing such conditions will be largely representative of the original zircon composition as long as volume diffusion is the only process acting. Prolonged periods at 950°C have the potential to cause significant modification to the REE, but will not cause complete equilibration within the analytical volume. However, at much more extreme temperatures for relatively short periods of time it is possible to fully equilibrate zircon, with near flat to slightly curved patterns being produced. 1000°C, an important temperature in UHT metamorphism, appears to be a key threshold at which large amounts of modification becomes possible, albeit still requiring very long time periods at this temperature for near complete modification of all REE. By varying the placement of the analytical spot along the modelled profiles, the resultant theoretical spread of REE compositions generated by incomplete modification is shown (Figure 12a–d) (Table S7).

6.3 Implications for the assembly of the RIC

The diffusion modelling presented above can help explain the systematic variations of the zircon REE profiles observed among the Rogaland samples. REE abundance patterns in recrystallised zircon are scattered with no evidence for equilibration with garnet REE across most of the studied region except in close proximity with the RIC, where all recrystallised zircon appears to be in equilibrium with garnet. Based on the thermodynamic and diffusion modelling of Blereau et al. (2017) and Blereau et al. (In review), sample ROG13/11, the most distant from the RIC, only experienced regional metamorphism at ~850–900°C for at least 100 Myr. The prediction of the REE diffusion

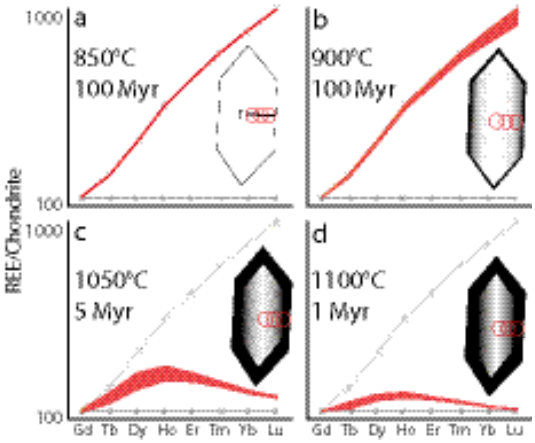

Fig 12: Theoretical REE datasets from multiple spot analyses on the modelled zircon: a- 100 Myr at 850°C; b- 100 Myr at 900°C; c- 5 Myr at 1050°C; d- 1 Myr at 1100°C. Red circles represent 20 µm SHRIMP spots. The grey lines represent C_O (steep) and C_{Eq} (flat) compositions, *r*- modelled radius (50 µm). See online version for colour.

model for such conditions matches the observed limited modification and a degree of scatter in the M–HREE arising from variations in the original REE concentrations of the grains (Figure 12a–b, 7a). In contrast, ROG14/5 on the RIC contact potentially reached more extreme temperatures, given that the anorthosite intrusion temperature is estimated at ~1200°C (Westphal et al., 2003). In order to achieve the flat REE patterns in apparent equilibrium with garnet observed in ROG14/5 (Figure 7c), for average rates of diffusion, the sample would need to have reached either ~1100°C for 1 to 5 Myr or ~1050°C for >10 Myr (Figure 12c–d). The period of emplacement of the RIC has been previously constrained by geochronology to <10 Myr (Schärer et al., 1996), therefore the 1100°C scenario is more likely. Emplacement of the RIC in a single magmatic pulse would see most heat lost to the surrounding country rock without generating a significant temperature change at the contact, and certainly would not sustain elevated temperatures for >1 Myr (Cao, Kaus, & Paterson, 2016). The simplest geodynamic scenario that would generate significant heating at the contact for up to 5 Myr but also limited heating at greater distances is a rapid multiple-pulse intrusion (Cao et al., 2016) of the RIC.

Previous 2–D thermal modelling by Westphal et al. (2003) undertaken to explain the distribution of high-*T* mineral isograds adjacent to the intrusion, suggested a two-pulse scenario; an initial pulse to raise the country rock temperatures followed by emplacement (3 Myr later) of a smaller hotter intrusion over 2 Myr. However, their modelling used a starting country rock temperature of 600°C; ~200°C colder than the minimum temperatures preceding contact metamorphism interpreted by recent studies (Blereau et al., In review; Blereau et al., 2017). An initial country rock temperature of ≥ 800°C would reduce the rate of heat loss, enabling the retention of extreme temperatures at the RIC contact, and reducing the required assembly time of the RIC to less than 5 Myr. However, the higher initial country rock temperature combined with Westphal's model would also increase the temperature effects in the surrounding country rocks to a degree that is not seen within the recrystallised zircon. Westphal's model required a large thermal aureole in order to generate the metamorphic isograds. Recent studies have shown that the osumilite (Blereau et al., In review) and orthopyroxene (Coint et al., 2015) isograds are not true contact isograds, but the location of appropriate bulk composition effected by regional metamorphism or the mix between several granulite facies events respectively. The intrusion of many small pulses over 1–5 Myr would generate a smaller but higher temperature aureole

whilst also prolonging high-temperatures in the surrounding rocks with minimal modification.

7. CONCLUSIONS

Prograde heating to temperatures sufficient to recrystallise zircon was reached at 1059 ± 12 Ma with peak metamorphism occurring at c. 1035–995 Ma and final melt crystallisation outside the aureole by 951 ± 14 Ma.

Samples within the RIC aureole show a continuum of ages rather than two discrete age events, with no clear melt crystallisation event until after the emplacement of the RIC (c. 900 Ma). This is explained by prolonged residence at high-temperature conditions associated with a slow cooling rate following regional metamorphism.

Whilst largely considered as immobile, under appropriate high-grade conditions REE abundances in recrystallised zircon may be modified and possibly equilibrated to reflect the contemporary geochemical environment of the host rock rather than that of the growth conditions of the original zircon.

REE in recrystallised zircon can provide additional constraints on the *T–t* path experienced during metamorphism as long as volume diffusion is the main process acting.

Based on REE-in-zircon diffusion modelling, the emplacement of the RIC occurred rapidly as multiple magmatic pulses over 1 to 5 Myr, resulting in significantly elevated temperatures at the contact but minimal modification of rocks at a greater distance; retaining high temperatures for longer than the rocks far removed from the aureole.

ACKNOWLEDGEMENTS

Financial support for this project was provided by an ARC DECRA fellowship (DE120103067) to CC.

REFERENCES

Aleinikoff, J. N., Schenck, W. S., Plank, M. O., Srogi, L., Fanning, C. M., Kamo, S. L., & Bosbyshell, H. (2006). Deciphering igneous and metamorphic events in high-grade rocks of the Wilmington Complex, Delaware: Morphology, cathodoluminescence and backscattered electron zoning, and SHRIMP U-Pb geochronology of zircon and monazite. Geological Society of America Bulletin, 118(1-2), 39.

Anders, E., & Grevesse, N. (1989). Abundances of the elements: Meteoric and solar. Geochimica et Cosmochimica Acta, 53, 197-214.

Andersen, T., Griffin, W. L., & Pearson, N. J. (2002). Crustal evolution in the SW part of the Baltic Shield: the Hf isotope evidence. Journal of Petrology, 43(9), 1725-1747.

Bergh, S. G., Chattopadhya, A., Ravna, E. K., Corfu, F., Kullerud, K., Swaan, K. B., . . . Holdsworth, R. E. (2012). Was the Precambrian basement of Western Troms and Lofoten-Vesterålen in northern Norway linked to the Lewisian of Scotland? A comparison of crustal components, tectonic evolution and amalgamation history: INTECH Open Access Publisher.

Bhattacharya, S., & Kar, R. (2002). High-temperature dehydration melting and decompressive P–T path in a granulite complex from the Eastern Ghats, India. Contributions to Mineralogy and Petrology, 143(2), 175-191.

Bingen, B., Nordgulen, Ø., & Viola, G. (2008). A four-phase model for the Sveconorwegian orogeny, SW Scandinavia. Norwegian Journal of Geology, 88, 43-72.

Bingen, B., & Solli, A. (2009). Geochronology of magmatism in the Caledonian and Sveconorwegian belts of Baltic: synopsis for detrital zircon provenance studies. Norwegian Journal of Geology, 89, 267-290.

Black, L. P., Kamo, S. L., Allen, C. M., Aleinikoff, J. N., Davis, D. W., Korscha, R. J., & Foudoulis, C. (2003). TEMORA 1: a new zircon standard for Phanerozoic U-Pb geochronology. Chemical Geology, 200, 155-170.

Blereau, E., Clark, C., Jourdan, F., Johnson, T. E., Taylor, R. J. M., Kinny, P. D., . . . Eroglu, E. (In review). Constraining the timing of prograde metamorphism in long-lived hot orogens.

Blereau, E., Johnson, T. E., Clark, C., Taylor, R. J. M., Kinny, P. D., & Hand, M. (2017). Reappraising the P–T evolution of the Rogaland–Vest Agder Sector, southwestern Norway. Geoscience Frontiers, 8(1), 1–14.

Bogaerts, M., Scaillet, B., Liégeois, J.-P., & Vander Auwera, J. (2003). Petrology and geochemistry of the Lyngdal granodiorite (Southern Norway) and the role of fractional crystallization in the genesis of Proterozoic ferro-potassic A-type granites. Precambrian Research, 124, 149-184.

Bolle, O., Diot, H., Liégeois, J.-P., & Auwera, J. V. (2010). The Farsund intrusion (SW Norway): a marker of late-Sveconorwegian (Grenvillian) tectonism emplaced along a newly defined major shear zone. Journal of Structural Geology, 32, 1500-1518.

Buick, I. S., Clark, C., Rubatto, D., Hermann, J., Pandit, M., & Hand, M. (2010). Constraints on the Proterozoic evolution of the Aravalli–Delhi Orogenic belt (NW India) from monazite geochronology and mineral trace element geochemistry. Lithos, 120, 511-528.

Cao, W., Kaus, B. J. P., & Paterson, S. (2016). Intrusion of granitic magma into the continental crust facilitated by magma pulsing and dike-diapir interactions: Numerical simulations. Tectonics, 35(6), 1575-1594.

Cherniak, D. J., Hanchar, J. M., & Watson, E. B. (1997). Rare-earth diffusion in zircon. Chemical Geology, 134(4), 289-301.

Cherniak, D. J., & Watson, E. B. (2001). Pb diffusion in zircon. Chemical Geology, 172(1–2), 5-24.

Cherniak, D. J., & Watson, E. B. (2003). Diffusion in zircon. Reviews in mineralogy and geochemistry, 53(1), 113-143.

Clark, C., Healy, D., Johnson, T., Collins, A. S., Taylor, R., Santosh, M., & Timms, N. E. (2015). Hot orogens and supercontinent amalgamation: A Gondwanan example from southern India. Gondwana Research, 28(4), 1310-1328.

Clark, C., Kirkland, C. L., Spaggiari, C. V., Oorschot, C., Wingate, M. T. D., & Taylor, R. J. (2014). Proterozoic granulite formation driven by mafic magmatism: An example from the Fraser Range Metamorphics, Western Australia. Precambrian Research, 240, 1-21.

Coint, N., Slagstad, T., Roberts, N. M. W., Marker, M., Røhr, T. S., & Sørensen, B. E. (2015). The Late Mesoproterozoic Sirdal Magmatic Belt, SW Norway: Relationships between magmatism and metamorphism and implications for Sveconorwegian orogenesis. Precambrian Research, 265, 57-77.

Crank, J. (1975). The Mathematics of Diffusion: 2d Ed.: Oxford University Press.

de Laeter, J. R., & Kennedy, A. K. (1998). A double focussing mass spectrometer for geochronology. International Journal of Mass Spectrometry, 178, 43-50.

Drüppel, K., Elsäßer, L., Brandt, S., & Gerdes, A. (2013). Sveconorwegian Mid-crustal Ultrahigh-temperature Metamorphism in Rogaland, Norway: U-Pb LA-ICP-MS Geochronology and Pseudosections of Sapphrine Granulites and Associated Paragneisses. Journal of Petrology, 54(2), 305-350.

Ellis, D. J., Sheraton, J. W., England, R. N., & Dallwitz, W. B. (1980). Osumilite-sapphirine-quartz granulites from Enderby Land Antarctica - mineral assemblages and reactions. Contributions to Mineralogy and Petrology, 72, 123-143.

Fletcher, I. R., McNaughton, N. J., Davis, W. J., & Rasmussen, B. (2010). Matrix effects and calibration limitations in ion probe U–Pb and Th–Pb dating of monazite. Chemical Geology, 270, 31-44.

Halpin, J. A., Daczko, N. R., Milan, L. A., & Clarke, G. L. (2012). Decoding near-concordant U–Pb zircon ages spanning several hundred million years: recrystallisation, metamictisation or diffusion? Contrib Mineral Petrol, 163(1), 67-85.

Harley, S. L., Kelly, N. M., & Möller, A. (2007). Zircon behaviour and the thermal histories of mountain chains. Elements, 3, 25-30.

Hermann, J., & Rubatto, D. (2003). Relating zircon and monazite domains to garnet growth zones: age and duration of granulite facies metamorphism in the Val Malenco lower crust. Journal of Metamorphic Geology, 21, 833-852.

Hoskin, P. W. O., & Black, L. P. (2000). Metamorphic zircon formation by solid-state recrystallization of protolith igneous zircon. Journal of Metamorphic Geology, 18, 423-439.

Hoskin, P. W. O., & Schaltegger, U. (2003). The composition of zircon and igneous and metamorphic petrogenesis. Reviews in mineralogy and geochemistry, 53(1), 27–62.

Johnson, T., Clark, C., Taylor, R., Santosh, M., & Collins, A. S. (2015). Prograde and retrograde growth of monazite in migmatites: An example from the Nagercoil Block, southern India. Geoscience Frontiers, 6(3), 373-387.

Kelly, N. M., & Harley, S. L. (2005). An integrated microtextural and chemical approach to zircon geochronology: refining the Archaean history of the Napier Complex, east Antartica. Contributions to Mineralogy and Petrology, 149, 57-84.

Kelsey, D. E. (2008). On ultrahigh-temperature crustal metamorphism. Gondwana Research, 13, 1-29.

Kelsey, D. E., Clark, C., & Hand, M. (2008). Thermobarometric modelling of zircon and monazite growth in melt-bearing systems: examples using model metapelitic and metapsammitic granulites. Journal of Metamorphic Geology, 26, 199-212.

Kennedy, A. K., & de Laeter, J. R. (1994). The performance characteristics of the WA SHRIMP II ion microprobe. US Geological survey circular, 1107, 166.

Korhonen, F. J., Brown, M., Clark, C., & Bhattacharya, S. (2013). Osumilite-melt interactions in the ultrahigh temperatures granulites: phase equilibria modelling and implications for the P-T-t evolution of the Eastern Ghats Provincee, India. Journal of Metamorphic Geology, 31, 881-907.

Korhonen, F. J., Saw, A. K., Clark, C., Brown, M., & Bhattacharya, S. (2011). New constraints on UHT metamorphism in the Eastern Ghats Province through the application of phase equilibria modelling and in situ geochronology. Gondwana Research, 20, 764-781.

Laurent, A. T., Seydoux-Guillaume, A.-M., Duchene, S., Bingen, B., Bosse, V., & Datas, L. (2016). Sulphate incorporation in monazite lattice and dating the cycle of sulphur in metamorphic belts. Contributions to Mineralogy and Petrology, 171(11), 94.

Liu, Y., Hu, Z., Zong, K., Gao, C., Gao, S., Xu, J., & Chen, H. (2010). Reappraisement and refinement of zircon U-Pb isotope and trace element analyses by LA-ICP-MS. Chinese Science Bulletin, 55(15), 1535-1546.

Ludwig, K. R. (2003). Isoplot 3.0. A Geochronological Toolkit for Microsoft Excel. Berkeley Geochronological Center Special Publication, 4, 70.

Ludwig, K. R. (2009). SQUID II: A user's manual. Berkeley Geochronological Center Special Publication, 5, 110.

Möller, A., O'Brien, P. J., Kennedy, A., & Kröner, A. (2003). Linking growth episodes of zircon and metamorphic textures to zircon chemistry: an example from the ultrahigh-temperature granulites of Rogaland (SW Norway). Geological Society, London, Special Publications, 220(From: Vance, D., Müller, W., & Villa, I. M. (eds) 2003. Geochronology: Linking the Isotopic Record with Petrology and Textures.), 65-81.

Pasteels, P., Demaiffe, D., & Michot, J. (1979). U–Pb and Rb–Sr geochronology of the eastern part of the south Rogaland igneous complex, southern Norway. Lithos, 12, 199-208.

Paton, C., Hellstrom, J., Paul, B., Woodhead, J., & Hergt, J. (2011). Iolite: freeware for the visualisation and processing of mass spectrometric data. Journal of Analytical Atomic Spectrometry, 26, 2508-2518.

Paton, C., Woodhead, J., Hellstrom, J., Hergt, J., Greig, A., & Maas, R. (2010). Improved laser ablation U–Pb zircon and geochronology through robust downhole fractionation correction. Geochemistry, Geophysics, Geosystems, 11, 1-36.

Pearce, N. J. G., Perkins, W. T., Westgate, J. A., Gorton, M. P., Jackson, S. E., Neal, C. R., & Chenery, S. P. (1997). A compilation of new and published major and trace element data for NIST SRM 610 and NIST SRM 612 glass reference materials. Geostandards Newsletter, 21, 115-144.

Roberts, N. M. W., & Slagstad, T. (2015). Continental growth and reworking on the edge of the Columbia and Rodinia supercontinents; 1.86–0.9 Ga accretionary orogeny in southwest Fennoscandia. International Geology Review, 57(11-12), 1582-1606.

Rubatto, D. (2002). Zircon trace element geochemistry: partitioning with garnet and the link between U–Pb ages and metamorphism. Chemical Geology, 184, 123-138.

Rubatto, D., & Hermann, J. (2007). Experimental zircon/melt and zircon/garnet trace element partitioning and implications for the geochronology of crustal rocks. Chemical Geology, 241, 38-61.

Schaltegger, U., Fanning, C. M., Gűnther, D., Maurin, J. C., Schulmann, K., & Gebauer, D. (1999). Growth, annealing and recrystallization of zircon and preservation of monazite in high-grade metamorphism: conventional and in-situ U-Pb isotope, cathodoluminesecence and microchemical evidence. Contributions to Mineralogy and Petrology, 134, 186-201.

Schärer, U., Wilmart, E., & Duchesne, J-C. (1996). The short duration and anorogenic character of anorthosite magmatism: U–Pb dating of the Rogaland complex, Norway. Earth and Planetary Science Letters, 139, 335-350.

Shannon, R. (1976). Revised effective ionic radii and systematic studies of interatomic distances in halides and chalcogenides. Acta Crystallographica Section A, 32(5), 751-767.

Slagstad, T., Roberts, N. M. W., & Kulakov, E. (2017). Linking orogenesis across a supercontinent; the Grenvillian and Sveconorwegian margins on Rodinia. Gondwana Research, 44, 109-115.

Slagstad, T., Roberts, N. M. W., Marker, M., Røhr, T. S., & Schiellerup, H. (2013). A non-collisional, accretionary Sveconorwegian orogen. Terra Nova, 25, 30-37.

Sláma, J., Košler, J., Condon, D. J., Crowley, J. L., Gerdes, A., Hanchar, J. M., . . . Whitehouse, M. J. (2008). Plešovice zircon – A new natural reference material for U–Pb and Hf isotopic microanalysis`. Chemical Geology, 249, 1–35.

Spencer, C. J., Roberts, N. M. W., Cawood, P. A., Hawkesworth, C. J., Prave, A. R., Antonini, A. S. M., . . . EIMF. (2014). Intermontane basins and bimodal volcanism at the onset of the Sveconorwegian Orogeny, southern Norway. Precambrian Research, 252, 107-118.

Stacey, J. S., & Kramers, J. D. (1975). Approximation of terrestrial lead isotope evolution by a two-stage model. Earth and Planetary Science Letters, 26, 207-221.

Stern, R. S., & Amelin, Y. (2003). Assessment of errors in SIMS zircon U–Pb geochronology using a natural zircon standard and NIST SRM 610 glass. Chemical Geology, 197, 111-142.

Taylor, R., Clark, C., Fitzsimons, I. C. W., Santosh, M., Hand, M., Evans, N., & McDonald, B. (2014). Post-peak, fluid-mediated modification of granulite facies zircon and monazite in the Trivandrum Block, southern India. Contrib Mineral Petrol, 168(2), 1-17.

Taylor, R., Harley, S. L., Hinton, R. W., Elphick, S., Clark, C., & Kelly, N. M. (2015). Experimental determination of REE partition coefficients between zircon, garnet and melt: a key to understanding high-T crustal processes. Journal of Metamorphic Geology, 33, 231–248.

Taylor, R. J. M., Kirkland, C. L., & Clark, C. (2016). Accessories after the facts: Constraining the timing, duration and conditions of high-temperature metamorphic processes. Lithos, 264, 239-257.

Tomkins, H. S., Williams, I. S., & Ellis, D. J. (2005). In situ U–Pb dating of zircon formed from retrograde garnet breakdown during decompression in Rogaland, SW Norway. Journal of Metamorphic Geology, 23, 201-215.

Vander Auwera, J., Bolle, O., Bingen, B., Liégeois, J.-P., Bogaerts, M., Duchesne, J.-C., . . . Longhi, J. (2011). Sveconorwegian massif-type anorthosites and related granitoids result from post-collisional melting of a continental arc root. Earth-Science Reviews, 107, 375-397.

Vavra, G., Gebauer, D., Schmid, R., & Compston, W. (1996). Multiple zircon growth and recrystallization during polyphase Late Carboniferous to Triassic metamorphism in granulites of the Ivrea Zone (Southern Alps): an ion microprobe (SHRIMP) study. Contributions to Mineralogy and Petrology, 122, 337-358.

Verschure, R. H., Andriessen, P. A. M., Boelrijk, N. A. I. M., Hebeda, E. H., Maier, W. D., Priem, H. N. A., & Verdurmen, E. A. T. (1980). On the thermal stability of Rb–Sr and K–Ar biotite systems: evidence from coexisting Sveconorwegian (ca 870 Ma) and Caledonian (ca 400 Ma) biotites in SW Norway. Contributions to Mineralogy and Petrology, 74, 245-252.

Westphal, M., Schumacher, J. C., & Boschert, S. (2003). High-Temperature Metamorphism and the Role of Magmatic Heat Sources at the Rogaland Anorthosite Complex in Southwestern Norway. Journal of Petrology, 44(6), 1145-1162.

Supplementary material: See Appendix E

Chapter 6

CONCLUSIONS AND FUTURE RESEARCH DIRECTIONS

This thesis endeavoured to investigate and constrain the effects of metamorphic, melt and fluid processes in the lower crust through the application of a range of analytical techniques in a petrochronological approach. The chapters in this thesis investigated two high-grade terranes as case studies, with the aim of providing new and additional constraints on the duration and conditions of metamorphism, evaluate previous interpretations, whilst studying the effects of prolonged high temperatures and lower crustal processes on common geochronometer minerals zircon and monazite. The following discussion summarises the state of knowledge in regard to the key outcomes of this study in terms of the aims defined in the introduction. This chapter also discusses potential areas for future research.

1. TIMING, CONDITIONS AND CONTROLLING FACTORS ON HIGH-T METAMORPHIC PROCESSES IN SOUTHERN INDIA AND SOUTHWESTERN NORWAY

1.1 S India (**Chapter 2**)

Kakkod was a previously unstudied incipient charnockite locality that provided an opportunity in this thesis to investigate the charnockite formation process and assess the scale over which this process acted (localised or regional), whilst also providing new geochronological and *P–T* constraints. The *P–T* conditions of the Trivandrum Block (TB) as well as the mechanism through which incipient charnockites form (a purely fluid related process or a metamorphic process) have both been highly debated for many years. SHRIMP U–Pb dating of zircon and monazite constrained the onset of high-*T* conditions to *ca* 590 Ma with the onset of melt crystallisation following peak metamorphism at *ca* 540 Ma, with high temperatures sustained for ~50 Myrs. The majority of zircon growth was associated with melt crystallisation, forming zircon rims between *ca* 540–510 Ma. Zircon rims older than 540 Ma (up to *ca* 590 Ma) were also analysed but were less prevalent. These ages are consistent with previous ages of metamorphism within the TB. A later fluid event was dated using monazite between *ca* 525–490 Ma, causing perturbation of existing monazite through Pb loss within the regions undergoing coupled dissolution-reprecipitation. From the presence of fluid related monazite textures in each rock type the fluid event was interpreted to be pervasive through the whole outcrop, similar to the nearby charnockite locality Kottavattom (Taylor et al., 2014). The closeness in age between melt crystallisation and the fluid event is interpreted to suggest that the fluid influx was linked to cooling of the local melt system. Kakkod also provided a unique opportunity to constrain the *P–T* conditions of charnockite formation as well as providing additional constraints on metamorphic conditions of the TB due to the fact that all three main rock types found in the TB (garnet-biotite gneiss, incipient charnockite and metapelite) were present. Using the latest thermodynamic dataset ('ds62' released early 2014), metamorphic forward modelling of the three rock types yielded consistent peak metamorphic conditions of 830–925°C and 6–9 kbar. Modelling and dating of these rocks showed that incipient charnockite formation (i.e. the patchy appearance of orthopyroxene within an originally

orthopyroxene-free gneiss) could occur as part of the metamorphic evolution rather than being an exclusively fluid related process. Based on mineral textures and phase equilibria, orthopyroxene could have grown during peak metamorphism and was retrogressed by the later fluid event recorded by monazite. However, our study could not completely rule out previous interpretations at this point (i.e. orthopyroxene grew from the later fluid), with further investigations required into the control of local variations of bulk composition on the growth of orthopyroxene. If the growth of orthopyroxene is indeed a peak metamorphic process, based on the fluid source and the absence of fluid modification to zircon that was recorded at Kottavattom (Taylor et al., 2014), the formation of the characteristic patchy appearance of incipient charnockites likely occurred on a localised scale rather than as a widespread fluid event as previously postulated.

1.2 SW Norway (**Chapter 3–5**)

The Rogaland–Vest Agder Sector (RVA) in SW Norway had two contrasting *P–T* evolution from previous studies: (1) a polymetamorphic evolution (Möller et al., 2003; Tomkins et al., 2005) and (2) a singular *P–T* evolution (Drüppel et al., 2013), with the emplacement of the Rogaland Igneous Complex (RIC) having a relationship to the generation of high temperatures in the former evolution but not the latter. This thesis aimed to re-evaluate the timing and conditions of metamorphism in Rogaland to discern which *P–T* evolution is most appropriate and to determine if the emplacement of the RIC was a controlling factor or a product of metamorphism. Both of these aims were assessed by using a transect of samples at different distances from the RIC. The most removed sample (~30 km from the RIC) experienced regional metamorphism along singular clockwise *P–T* path, peaking at 850–950°C and 7–8 kbar, followed by decompression and slow cooling (**Chapter 3**). Rocks less than and up to 10 km from the RIC experienced similar regional peak conditions but also experienced a secondary event up to ~950°C and 3–6 kbar. No significant cooling was interpreted in between the two events, with cooling occuring after the second event based on the presence of secondary melt related microstructures within residual samples (**Chapter 3**). The second event is interpreted to be a contact metamorphic event tied to the emplacement of the RIC based on the spatial distribution of the second event, confirming a polymetamorphic evolution for the RIC.

Osumilite provided a potential opportunity to directly link age data to phase equilibria by being potentially datable using $^{40}Ar/^{39}Ar$ (containing ~4wt% potassium) and by having quantified thermodynamic models for its stability in *P–T* space. This kind of direct connection cannot be made with zircon and monazite. Osumilite also had the added appeal as a mineral stable in high temperature terranes to potentially retain age information in relation to high temperatures, something that is very difficult to do with most thermochronometers. With the exception of pyroxene (T_c of >700°C), most argon analyses relate to cooling through temperatures below granulite facies due to low closure temperatures. Phase equilibria modelling was conducted on the osumilite samples and yielded comparable conditions to previous modelling,

but the modelling of the osumilite sample is only broadly consistent with modelling in **Chapter 3** as osumilite cannot be modelled in the current thermodynamic data set ('ds62', only available in 'ds55' which was used in **Chapter 4**). The *P–T* conditions of both metamorphic events were further refined in **Chapter 4** through diffusion modelling using the $^{40}Ar/^{39}Ar$ systematics of osumilite (T_c ~770°C for 175 µm grain radius and a cooling rate of 10°C/Myr). In order to preserve the recorded age populations, metamorphic temperatures must not have exceeded ~900°C within rocks ~2 km from the RIC (for both regional and contact metamorphism), indicating conditions reached the lower-*T* end of the earlier mentioned phase equilibria estimates (**Chapter 4**).

Diffusion modelling of zircon in **Chapter 5** showed that rocks at the contact of the RIC experienced 1100°C for between 1–5 Myr in order to sufficiently modify REE in zircon to achieve equilibrium. In order to achieve and maintain such conditions, this *T–t* scenario requires a rapid multiple pulse emplacement model for the RIC (**Chapter 5**), differing from previous two pulse emplacement models (Westphal et al., 2003). The discontinuity in temperature between phase equilibria and diffusion modelling (~950°C compared to 1100°C from diffusion modelling) is potentially a product of the inability to model osumilite in 'ds6' (ROG14/5 contains intergrowths of cordierite + K-feldspar that could be formed after replacing osumilite), the lack of minor elements in mineral models (in particular Zn in spinel, which is highly abundant in ROG13/10 and to a lesser extent in the other contact metamorphosed samples) and the simple nature of the diffusion model.

A range of different ages for peak metamorphism have been reported from previous studies (~1035 Ma: Möller et al., 2003; Tomkins et al., 2005; Laurent et al., 2016; or ~1000 Ma: (Drüppel et al., 2013) with limited constraints on prograde heating. Only the emplacement age of the RIC at *ca* 930 Ma is widely accepted. In **Chapter 4**, using the $^{40}Ar/^{39}Ar$ method, osumilite was successfully dated using single grain aliquots from a mineral separate. Picking grain fragments from a mineral separate is typical for $^{40}Ar/^{39}Ar$ analysis, however, this was conducted before the true grain size of osumilite was realised: due to its colourless nature the grain size of osumilite was not apparent until TIMA maps were conducted, resulting in the identification of very large grains (at least a 1 cm in diameter). The very large grain size allowed for the preservation of older ages (*ca* 1070–1050 Ma) within the core and the youngest ages at the edge of the grain as well as in later osumilite growth around garnet (*ca* 920–880 Ma). By using a mineral separate, none of the analysed grain fragments had any context, so future osumilite studies should, where able, use micro-drilling approaches to generate textural context. The oldest $^{40}Ar/^{39}Ar$ ages are interpreted to relate to prograde heating with the growth of large osumilite grains at *ca* 1070–1050 Ma (**Chapter 4**), ages that are also seen in zircon marking the end of a discordant resetting trend associated with recrystallisation within distal regionally metamorphosed samples (**Chapter 5**). Peak regional metamorphism is interpreted based on monazite and zircon to fall between *ca* 1035–995 Ma, between previous estimates, with final regional melt crystallisation at 951 ± 14 Ma (**Chapter 5**). Samples closer to the RIC did not experience this melt crystallisation

event, containing zircon and monazite recording ages younger than *ca* 950 Ma, with no melt crystallisation (i.e. neocrystallisation) till 30 Myr after the emplacement of the RIC at *ca* 900 Ma. The youngest osumilite ages are interpreted to relate to the edge of the large grains as well later osumilite growth around garnet during contact metamorphism (*ca* 920–880 Ma). This new geochronology extended previous estimates of the time-scale of high-*T* metamorphism in SW Norway to at least 100 Myr to ~150 Myr.

2. TECTONIC IMPLICATIONS FOR SW NORWAY

Two tectonic models have been previously proposed for SW Norway and more broadly the Sveconorwegian Belt as a whole. In **Chapter 3**, based on an assessment of current literature, the earlier continent-continent collisional model proposed by Bingen et al. (2008) could not satisfactorily explain the metamorphic and magmatic evolution of the Sveconorwegian Belt, based on features such as the presence subduction related magmatic suites postdating proposed subduction cessation, as well as contemporaneous and later arc-related features. The accretionary model suggested by Slagstad et al. (2013) and developed further by Coint et al. (2015) and Roberts and Slagstad (2015), permits crustal thickening sufficient to generate the recorded metamorphic conditions (3–8 kbar) whilst explaining the distribution of magmatic suites and metamorphic events as well as the progressive younging of terranes from east to west. This model is more consistent with the *P–T* results of **Chapter 3** as well as the geochronological and geodynamic results of **Chapters 4** and **5**. Whilst diffusion modelling in **Chapter 5** showed that the RIC was assembled rapidly as a series of multiple pulses, the exact mechanism to generate the anorthosite magmas remains unclear. Increased understanding on the generation of anorthositic melts and the required tectonic settings may provide additional insight into the tectonic setting of the Sveconorwegian Belt.

3. BEHAVIOUR OF TRADITIONAL GEOCHRONOMETERS DURING HIGH-T CONDITIONS

3.1 S India (**Chapter 2**)

Zircon from Kakkod showed protracted growth during high-*T* conditions, recorded as zircon overgrowths with a range of ages, but showed no textural features related to fluid influx, unlike the nearby charnockite locality Kottavattom (Taylor et al., 2014). Zircon at Kakkod was controlled by the presence of melt, permitting neocrystallisation over recrystallisation, which dominates in melt absent conditions. Due to their formational relationship, zircon showed no effects of bulk compositional variation between the garnet-biotite gneiss and the incipient charnockite, with both lithologies showing zircon overgrowths by retaining melt, seen in outcrop as numerous large-scale leucogranites and small-scale leucosomes. Zircon growth in the metapelite was limited and all grains showed recrystallisation as a result of a more residual composition, with the metapelite displaying a smaller amount of melt in outcrop compared to the other lithologies. Monazite at Kakkod, like Kottavattom, best records the fluid event, containing coupled dissolution-reprecipitation textures in connection with the

youngest monazite ages in all lithologies. As mentioned above the fluid source is interpreted to be locally sourced from the crystallisation of the local melt system, supported by the lack of fluid modification of zircon at Kakkod, indicating a different fluid composition to that experienced by Kottavattom (Taylor et al., 2014). The proportion or activity of fluid may also be deduced from monazite. Monazite from within the charnockite show increased amounts of modification as well as the youngest ages; potentially indicating a larger volume of fluid or the fluid was more active in the rock evolution, either interpretation is plausible as the charnockite shows the most alteration.

3.2 SW Norway (**Chapter 5**)

The conditions experienced by zircon and monazite within the Rogaland samples are more highly varied as a number of different bulk compositions were used, with different levels of partial melting/melt extraction, variable temperature for the contact metamorphosed samples, as well as all samples being very anhydrous. Zircon was present within all samples and was mainly modified through recrystallisation due to the extreme temperatures and anhydrous nature of the samples. All samples bar one saw new zircon growth in relation to crystallisation of melt, with the most residual sample (ROG13/10) showing only recrystallisation of zircon. The effect of variable temperature during contact metamorphism on the recorded age range is highlighted by ROG13/10 and ROG14/8, both of which contained only zircon but are located at different distances from the RIC (10 km and at the contact respectively). As a consequence of experiencing more extreme temperatures during contact metamorphism, a larger range of zircon ages was recorded in ROG14/8 as a result of increased diffusional modification during recrystallisation. Similar distributions of zircon ages were also recorded in the monazite-bearing contact sample ROG14/5. Neocrystallisation as zircon overgrowths only occurred during the samples respective melt crystallisation event (i.e. distal samples after regional, samples closer to the RIC after contact metamorphism), with the exception of ROG13/10 due to complete melt extraction. Monazite showed little to no internal textures within all samples, with monazite growth interpreted to be controlled by precipitation within appropriate composition and conditions. No fluid related textures were present, consistent with the anhydrous nature of the samples. REE in zircon showed a systematic variation with distance from the RIC, with increasing modification of REE towards equilibrium with garnet with decreasing distance from the RIC. Whilst thought to be typically immobile during most geological conditions, through diffusion modelling, REE in zircon were shown to be modifiable during geologically short-lived extreme temperature conditions as well as during prolonged UHT conditions. This allows diffusion of REE-in-zircon to be used to provide constraints on the duration and temperature of metamorphism. Diffusion modelling determined that the rocks at the contact of the RIC experienced temperatures of ~1100°C in order for the system to achieve geochemical equilibrium. The attainment of such temperatures for a given time period in order to achieve zircon re-equilibration also provided constraints on the method of emplacement of the RIC (as mentioned

above).

4. THE IMPORTANCE OF A PETROCHRONOLOGICAL APPROACH IN ASSESSING HIGH-GRADE TERRANES

Due to the large array of processes acting during lower crustal metamorphism it can be difficult to unravel what processes were acting when as well as the true duration of events, as no single rock may record the entire metamorphic evolution. The application of petrochronological techniques in **Chapters 2–5** allowed the quantification of the time-scales of metamorphism (S India: ~50 Myr; SW Norway: ~100–150 Myr), refining previous estimates in Rogaland in particular. Despite the prolonged nature of high-*T* conditions, by using a range of samples and techniques, quantitative *P–T–t* paths were derived for both case studies. Both regions experienced regional style metamorphism, with SW Norway being characterised by a secondary more localised contact metamorphic event and S India experiencing a later fluid event. These events were recorded in both case studies as a combination of different internal textures within geochronometers, variations in geochemistry and microstructures connected to geochronological populations and phase equilibria.

This thesis shows that zircon and monazite, if present, are adept at recording and preserving a wide array of geochronological and geochemical data even when exposed to prolonged high temperatures. Whilst not entirely impervious to modification due to the increased action of many processes at elevated temperatures, this modification may be used to provide additional information on the durations and conditions of metamorphism and is not a hindrance to petrochronological studies if all potential affects and limitations are properly considered. Nonetheless, the availability of zircon and monazite and the information recorded is strongly affected by key lower crustal processes, such as the availability of melt and the presence of fluids. The unique combination and interaction of particular processes along a metamorphic evolution will result in a unique data set and mineral paragenesis. Whilst both case studies produced geochronological data sets that from the outset appear similar (older inherited ages, discordant trends to younger populations, spreads of younger data along concordia), the processes controlling and causing this age distribution are dissimilar. At Kakkod the distribution of zircon ages was controlled by neocrystallisation resulting in protracted zircon growth; compared to Rogaland where recrystallisation was the dominant process affecting zircon, smearing ages along concordia due to Pb loss. Monazite in Rogaland provided information on the duration of metamorphism, where as at Kakkod monazite best recorded fluid infiltration, with the duration of metamorphism best defined by zircon. This contrasting behaviour between regions and individual geochronometers makes a petrochronological approach even more critical, as the combination of geochronological information with textural, petrological and geochemical information was key in identifying the involvement or action of a combination of different processes as well as differentiating between the factors controlling the distribution of ages. The application of multiple geochronometers where available is also highly beneficial due to their variable response to evolving geodynamic and geochemical systems. Monazite can provide

complimentary information to zircon by growing throughout supra-solidus conditions (and sometimes during sub-solidus conditions) where zircon may not grow or react depending on the geochemical system. Both the consideration of the effects of sample characteristics on recorded age and geochemical information as well as the careful categorisation of internal geochronometer textures within a wider petrological context are of equal importance to unravelling complex metamorphic terranes and quantitative petrochronological studies and should be the focus of detailed analysis within every study.

5. FUTURE RESEARCH DIRECTIONS

–Further investigation is required into the effects of subtle compositional variations on the stability of orthopyroxene in charnockites. In particular, identifying which compositional variables are responsible. The variable amount of fluid flux recorded across the outcrop could also be further investigated.

–Future studies could conduct texturally constrained sampling of osumilite grains as well as a trace element/structural investigation into the distribution of cores and rims in osumilite to better quantify the range of ages recorded. Further study into the complex diffusion behaviour of osumilite could also be conducted (i.e. cycled step heating).

–Detailed geodynamic modelling could be conducted, applying this new data, to better understand the emplacement/formation of the RIC and the tectonic setting of the RVA Sector.

REFERENCES

Bingen, B., Nordgulen, Ø., and Viola, G., 2008, A four-phase model for the Sveconorwegian orogeny, SW Scandinavia: Norwegian Journal of Geology, v. 88, p. 43-72.

Coint, N., Slagstad, T., Roberts, N. M. W., Marker, M., Røhr, T. S., and Sørensen, B. E., 2015, The Late Mesoproterozoic Sirdal Magmatic Belt, SW Norway: Relationships between magmatism and metamorphism and implications for Sveconorwegian orogenesis: Precambrian Research, v. 265, p. 57-77.

Drüppel, K., Elsäßer, L., Brandt, S., and Gerdes, A., 2013, Sveconorwegian Mid-crustal Ultrahigh-temperature Metamorphism in Rogaland, Norway: U-Pb LA-ICP-MS Geochronology and Pseudosections of Sapphrine Granulites and Associated Paragneisses: Journal of Petrology, v. 54, no. 2, p. 305-350.

Laurent, A. T., Seydoux-Guillaume, A.-M., Duchene, S., Bingen, B., Bosse, V., and Datas, L., 2016, Sulphate incorporation in monazite lattice and dating the cycle of sulphur in metamorphic belts: Contributions to Mineralogy and Petrology, v. 171, no. 11, p. 94.

Möller, A., O'Brien, P. J., Kennedy, A., and Kröner, A., 2003, Linking growth episodes of zircon and metamorphic textures to zircon chemistry: an example from the ultrahigh-temperature granulites of Rogaland (SW Norway): Geological Society, London, Special Publications, v. 220, no. From: Vance, D., Müller, W., & Villa, I. M. (eds) 2003. Geochronology: Linking the Isotopic Record with Petrology and Textures., p. 65-81.

Roberts, N. M. W., and Slagstad, T., 2015, Continental growth and reworking on the edge of the Columbia and Rodinia supercontinents; 1.86–0.9 Ga accretionary orogeny in southwest Fennoscandia: International Geology Review, v. 57, no. 11-12, p. 1582-1606.

Slagstad, T., Roberts, N. M. W., Marker, M., Røhr, T. S., and Schiellerup, H., 2013, A non-collisional, accretionary Sveconorwegian orogen: Terra Nova, v. 25, p. 30-37.

Taylor, R., Clark, C., Fitzsimons, I. C. W., Santosh, M., Hand, M., Evans, N., and McDonald, B., 2014, Post-peak, fluid-mediated modification of granulite facies zircon and monazite in the Trivandrum Block, southern India: Contrib Mineral Petrol, v. 168, no. 2, p. 1-17.

Tomkins, H. S., Williams, I. S., and Ellis, D. J., 2005, In situ U–Pb dating of zircon formed from retrograde garnet breakdown during decompression in Rogaland, SW Norway: Journal of Metamorphic Geology, v. 23, p. 201-215.

Westphal, M., Schumacher, J. C., and Boschert, S., 2003, High-Temperature Metamorphism and the Role of Magmatic Heat Sources at the Rogaland Anorthosite Complex in Southwestern Norway: Journal of Petrology, v. 44, no. 6, p. 1145-1162.

Chapter 7

BIBLIOGRAPHY

Adjerid, Z., Godard, G., Ouzegane, K. H., and Kienast, J.-R., 2013, Multistage progressive evolution of rare osumilite-bearing assemblages preserved in ultrahigh-temperature granulites from In Ouzzal (Hoggar, Algeria): Journal of Metamorphic Geology, v. 31, p. 505–524.

Ahrens, L. H., 1965, Some observations on the uranium and thorium distributions in accessory zircon from granitic rocks: Geochimica et Cosmochimica Acta, v. 29, no. 6, p. 711-716.

Aleinikoff, J. N., Schenck, W. S., Plank, M. O., Srogi, L., Fanning, C. M., Kamo, S. L., and Bosbyshell, H., 2006, Deciphering igneous and metamorphic events in high-grade rocks of the Wilmington Complex, Delaware: Morphology, cathodoluminescence and backscattered electron zoning, and SHRIMP U-Pb geochronology of zircon and monazite: Geological Society of America Bulletin, v. 118, no. 1-2, p. 39.

Anders, E., and Grevesse, N., 1989, Abundances of the elements: Meteoric and solar: Geochimica et Cosmochimica Acta, v. 53, p. 197-214.

Andersen, T., Griffin, W. L., and Pearson, N. J., 2002, Crustal evolution in the SW part of the Baltic Shield: the Hf isotope evidence: Journal of Petrology, v. 43, no. 9, p. 1725-1747.

Andersen, T., Griffin, W. L., and Sylvester, A. G., 2007, Sveconorwegian crustal underplating in southwestern Fennoscandia: LAM-ICPMS U-Pb and Lu-Hf isotope evidence from granites and gneisses in Telemark, southern Norway: Lithos, v. 93, p. 273-287.

Andersson, J., Möller, C., and Johansson, L., 2002, Zircon geochronology of migmatite gneisses along the Mylonite Zone (S Sweden): a major Sveconorwegian terrane boundary in the Baltic Shield: Precambrian Research, v. 114, no. 1–2, p. 121-147.

Andrehs, G., and Heinrich, W., 1998, Experimental determination of REE distributions between monazite and xenotime: potential for temperature-calibrated geochronology: Chemical Geology, v. 149, no. 1–2, p. 83-96.

Artioli, G., Angelini, I., and Nestola, F., 2013, New milarite/osumilite-type phase formed during ancient glazing of an Egyptian scarab: Applied Physics A, v. 110, no. 2, p. 371-377.

Ashwal, L. D., Tucker, R. D., and Zinner, E. K., 1999, Slow cooling of deep crustal granulites and Pb-loss in zircon: Geochimica et Cosmochimica Acta, v. 63, no. 18, p. 2839-2851.

Ayers, J. C., Miller, C., Gorisch, B., and Milleman, J., 1999, Textural development of monazite during high-grade metamorphism: Hydrothermal growth kinetics, with implications for U,Th-Pb geochronology, American Mineralogist, Volume 84, p. 1766.

Balassone, G., Mormone, A., Rossi, M., Bernardi, A., Fisch, M., Armbruster, T., Malsy, K., and Berger, A., 2008, Crystal chemical and structural characterisation of an Mg-rich Osumilite from Vesuvius volcano (Italy): European Journal of Mineralogy, v. 20, p. 713-720.

Baldwin, J. A., and Brown, M., 2008, Age and duration of ultrahigh-temperature metamorphism in the Anápolis-Itauçu Complex, Southern Brasília Belt, central Brazil - constraints from U-Pb geochronology, mineral rare earth element chemistry and trace-element thermometry: Journal of Metamorphic Geology, v. 26, p. 213-233.

Barnichon, J. D., Havenith, H., Hoffer, B., Charlier, R., Jongmans, D., and Duchesne, J. C., 1999, The deformation of the Egersund-Ogna anorthosite massif, south Norway: finite-element modelling of diapirism: Tectonophysics, v. 303, p. 109-130.

Baxter, E. F., Caddick, M. J., and Dragovic, B., 2017, Garnet: A Rock-Forming Mineral Petrochronometer: Reviews in Mineralogy and Geochemistry, v. 83, no. 1, p. 469.

Baxter, E. F., and Scherer, E. E., 2013, Garnet Geochronology: Timekeeper of Tectonometamorphic Processes: Elements, v. 9, no. 6, p. 433.

Bea, F., and Montero, P., 1999, Behavior of accessory phases and redistribution of Zr, REE, Y, Th, and U during metamorphism and partial melting of metapelites in the lower crust: an example from the Kinzigite Formation of Ivrea-Verbano, NW Italy: Geochimica et Cosmochimica Acta, v. 63, no. 7–8, p. 1133-1153.

Bea, F., Pereira, M. D., and Stroh, A., 1994, Mineral/leucosome trace-element partitioning in a peraluminous migmatite (a laser ablation-ICP-MS study): Chemical Geology, v. 117, no. 1, p. 291-312.

Bergh, S. G., Chattopadhya, A., Ravna, E. K., Corfu, F., Kullerud, K., Swaan, K. B., Armitage, P. E. B., Myhre, P. I., and Holdsworth, R. E., 2012, Was the Precambrian basement of Western Troms and Lofoten-Vesterålen in northern Norway linked to the Lewisian of Scotland? A comparison of crustal components, tectonic evolution and amalgamation history, INTECH Open Access Publisher, Tectonics- Recent Advances, 283-330 p.

Bhattacharya, S., and Kar, R., 2002, High-temperature dehydration melting and decompressive P–T path in a granulite complex from the Eastern Ghats, India: Contributions to Mineralogy and Petrology, v. 143, no. 2, p. 175-191.

Bingen, B., Birkeland, A., Nordgulen, Ø., and Sigmond, E. M. O., 2001, Correlation of supracrustal sequences and origin of terranes in the Sveconorwegian orogen of SW Scandinavia: SIMS data on zircon in clastic metasediments: Precambrian Research, v. 108, p. 293-318.

Bingen, B., Nordgulen, Ø., and Viola, G., 2008, A four-phase model for the Sveconorwegian orogeny, SW Scandinavia: Norwegian Journal of Geology, v. 88, p. 43-72.

Bingen, B., Skår, Ø., Marker, M., Sigmond, E. M. O., Nordgulen, Ø., Ragnhildstveit, J., Mansfeld, J., Tucker, R. D., and Liégeois, J-P., 2005, Timing of continental building in the Sveconorwegian orogen, SW Scandinavia: Norwegian Journal of Geology, v. 85, p. 87-116.

Bingen, B., and Solli, A., 2009, Geochronology of magmatism in the Caledonian and Sveconorwegian belts of Baltic: synopsis for detrital zircon provenance studies: Norwegian Journal of Geology, v. 89, p. 267-290.

Bingen, B., Stein, H. J., Bogaerts, M., Bolle, O., and Mansfeld, J., 2006, Molybdenite Re–Os dating constrains gravitational collapse of the Sveconorwegian orogen, SW Scandinavia: Lithos, v. 87, p. 328-346.

Bingen, B., and van Breemen, O., 1998, U–Pb monazite ages in amphibolite- to granulite-facies orthogneiss reflect hydrous mineral breakdown reactions: Sveconorwegian Province of SW Norway: Contributions to Mineralogy and Petrology, v. 132, p. 336-353.

Black, L. P., Kamo, S. L., Allen, C. M., Aleinikoff, J. N., Davis, D. W., Korscha, R. J., and Foudoulis, C., 2003, TEMORA 1: a new zircon standard for Phanerozoic U-Pb geochronology: Chemical Geology, v. 200, p. 155-170.

Blereau, E., Clark, C., Jourdan, F., Johnson, T. E., Taylor, R. J. M., Kinny, P. D., Hand, M., and Eroglu, E., In review, Constraining the timing of prograde metamorphism in long-lived hot orogens: Geology.

Blereau, E., Johnson, T. E., Clark, C., Taylor, R. J. M., Kinny, P. D., and Hand, M., 2017, Reappraising the P–T evolution of the Rogaland–Vest Agder Sector, southwestern Norway: Geoscience Frontiers, v. 8, no. 1, p. 1–14.

Boehnke, P., Watson, E. B., Trail, D., Harrison, T. M., and Schmitt, A. K., 2013, Zircon saturation re-revisited: Chemical Geology, v. 351, p. 324-334.

Bogaerts, M., Scaillet, B., Liégeois, J.-P., and Vander Auwera, J., 2003, Petrology and geochemistry of the Lyngdal granodiorite (Southern Norway) and the role of fractional crystallization in the genesis of Proterozoic ferro-potassic A-type granites: Precambrian Research, v. 124, p. 149-184.

Bogdanova, S. V., Bingen, B., Gorbatschev, R., Kheraskova, T. N., Kozlov, V. I., Puchkov, V. N., and Volozh, Y. A., 2008, The East European craton (Baltica) before and during the assembly of Rodinia: Precambrian Research, v. 160, p. 23-45.

Bol, L. C. G. M., Maijer, C., and Jansen, B. H., 1989, Premetamorphic lateritisation in Proterozoic metabasites of Rogaland, SW Norway: Contributions to Mineralogy and Petrology, v. 103, p. 306-316.

Bolle, O., Diot, H., Liégeois, J.-P., and Auwera, J. V., 2010, The Farsund intrusion (SW Norway): a marker of late-Sveconorwegian (Grenvillian) tectonism emplaced along a newly defined major shear zone: Journal of Structural Geology, v. 32, p. 1500-1518.

Bolle, O., Trindade, R. I. F., Bouches, J. L., and Duchesne, J.-C., 2002, Imaging downward granitic transport in the Rogaland Igneous Complex, SW Norway: Terra Nova, v. 14, p. 87-92.

Braun, I., 2006, Pan-African granitic magmatism in the Kerala Khondalite Belt, southern India: Journal of Asian Earth Sciences, v. 28, p. 38-45.

Braun, I., Montel, J.-M., and Nicollet, C., 1998, Electron microprobe dating of monazites from high-grade gneisses and pegmatites of the Kerala Khondalite Belt, southern India: Chemical Geology including Isotope Geoscience, v. 146, p. 65-68.

Brewer, T. S., Åhäll, K. I., Darbyshire, D. P. F., and Menuge, J. F., 2002, Geochemistry of late Mesoproterozoic volcanism in southwestern Scandinavia: implications for Sveconorwegian/Grenvillian plate tectonic models: Journal of the Geological Society, London, v. 159, p. 129-144.

Brown, M., 2007, Metamorphic condtitions in orogenic belts: a record of secular change: International Geology Review, v. 49, no. 3, p. 193-234.

Brown, M., and Korhonen, F. J., 2009, Some remarks on melting and exteme metamorphism of crustal rocks: Physic's and Chemistry of the Earth's Interior, p. 67-87.

Buick, I. S., Clark, C., Rubatto, D., Hermann, J., Pandit, M., and Hand, M., 2010, Constraints on the Proterozoic evolution of the Aravalli–Delhi Orogenic belt (NW India) from monazite geochronology and mineral trace element geochemistry: Lithos, v. 120, p. 511-528.

Buick, I. S., Hermann, J., Williams, I. S., Gibson, R. L., and Rubatto, D., 2006, A SHRIMP U–Pb and LA-ICP-MS trace element study of the petrogenesis of garnet–cordierite–orthoamphibole gneisses from the Central Zone of the Limpopo Belt, South Africa: Lithos, v. 88, no. 1–4, p. 150-172.

Bybee, G. M., Ashwal, L. D., Shirey, S. B., Horan, M., Mock, T., and Andersen, T. B., 2014, Pyroxene megacrysts in Proterozoic anorthosites: Implications for tectonic setting, magmaa source and magmatic processes at the Moho: Earth and Planetary Science Letters, v. 389, p. 74-85.

Cao, W., Kaus, B. J. P., and Paterson, S., 2016, Intrusion of granitic magma into the continental crust facilitated by magma pulsing and dike-diapir interactions: Numerical simulations: Tectonics, v. 35, no. 6, p. 1575-1594.

Cassata, W. S., Renne, P. R., and Shuster, D. L., 2009, Argon diffusion in plagioclase and implications for thermochronometry: A case study from the Bushveld Complex, South Africa: Geochimica et Cosmochimica Acta, v. 73, no. 21, p. 6600-6612.

Cassata, W. S., Renne, P. R., and Shuster, D. L., 2011, Argon diffusion in pyroxenes: Implications for thermochronometry and mantle degassing: Earth and Planetary Science Letters, v. 304, no. 3–4, p. 407–416.

Cawood, P. A., and Buchan, C., 2007, Linking accretionary orogenesis with supercontinent assembly: Earth-Science Reviews, v. 82, p. 217-256.

Cenki, B., Braun, I., and Bröcker, M., 2004, Evolution of the continental crust in the Kerala Khondalite Belt, southernmost India: evidence from Nd isotope mapping, U-Pb and Rb-Sr geochronology: Precambrian Research, v. 134, p. 275-292.

Chacko, T., Lamb, M., and Farquhar, J., 1996, Ultra-high temperature metamorphism in the Kerala Khondalite Belt: Gondwana Research Group Memoir, v. 3, p. 157-165.

Chacko, T., Ravindra Kumar, G. R., Meen, J. K., and J. W. Rodgers, J, 1992, Geochemistry of high-grade supracrustal rocks from the Kerala Khondalite Belt and adjacent massif charnockites, South India: Precambrian Research, v. 55, p. 469-489.

Chacko, T., Ravindra Kumar, G. R., and Newton, R. C., 1987, Metamorphic P–T conditions of the Kerala (South India) Khondalite Belt, a granulite facies supracrustal terrain: The Journal of Geology, v. 95, no. 3, p. 343-358.

Chen, R.-X., Zheng, Y.-F., and Xie, L., 2010, Metamorphic growth and recrystallization of zircon: Distinction by simultaneous in-situ analyses of trace elements, U–Th–Pb and Lu–Hf isotopes in zircons from eclogite-facies rocks in the Sulu orogen: Lithos, v. 114, no. 1–2, p. 132-154.

Cherniak, D. J., Hanchar, J. M., and Watson, E. B., 1997, Rare-earth diffusion in zircon: Chemical Geology, v. 134, no. 4, p. 289-301.

Cherniak, D. J., and Pyle, J. M., 2008, Th diffusion in monazite: Chemical Geology, v. 256, no. 1–2, p. 52-61.

Cherniak, D. J., and Watson, E. B., 2001, Pb diffusion in zircon: Chemical Geology, v. 172, no. 1–2, p. 5-24.

Cherniak, D. J., and Watson, E. B., 2003, Diffusion in zircon: Reviews in mineralogy and geochemistry, v. 53, no. 1, p. 113-143.

Cherniak, D. J., Watson, E. B., Grove, M., and Harrison, T. M., 2004, Pb diffusion in monazite: a combined RBS/SIMS study1: Geochimica et Cosmochimica Acta, v. 68, no. 4, p. 829-840.

Chetty, T. R. K., Fitzsimons, I. C. W., Brown, L., Dimri, V. P., and Santosh, M., 2006, Crustal structure and tectonic evolution of the Southern Granulite Terrane, India: introduction: Gondwana Research, v. 10, no. 1-2, p. 3-5.

Clark, C., Collins, A. S., Santosh, M., Taylor, R., and Wade, B. P., 2009a, The P–T–t architecture of a Gondwanan suture: REE, U–Pb and Ti-in-zircon thermometric constraints from the Palghat Cauvery shear system, South India: Precambrian Research, v. 174, p. 129-144.

Clark, C., Collins, A. S., Timms, N. E., Kinny, P., Chetty, T. R. K., and Santosh, M., 2009b, SHRIMP U–Pb age constraints on magmatism and high-grade metamorphism in the Salem Block, southern India: Gondwana Research, v. 16, p. 27-36.

Clark, C., Fitzsimons, I. C. W., Healy, D., and Harley, S. L., 2011, How does the continental crust get really hot?: Elements, v. 7, p. 235-240.

Clark, C., Healy, D., Johnson, T., Collins, A. S., Taylor, R., Santosh, M., and Timms, N. E., 2015, Hot orogens and supercontinent amalgamation: A Gondwanan example from southern India: Gondwana Research, v. 28, no. 4, p. 1310-1328.

Clark, C., Kirkland, C. L., Spaggiari, C. V., Oorschot, C., Wingate, M. T. D., and Taylor, R. J., 2014, Proterozoic granulite formation driven by mafic magmatism: An example from the Fraser Range Metamorphics, Western Australia: Precambrian Research, v. 240, p. 1-21.

Clarke, G. L., Powell, R., and Guiraud, M., 1989, Low-pressure granulite facies metapelitic assemblages and corona textures from MacRobertson Land, east Antarctica: the importance of Fe2O3 and TiO2 in accounting for spinel-bearing assemblages: Journal of Metamorphic Geology, v. 7, no. 3, p. 323-335.

Cocherie, A., and Albarede, F., 2001, An improved U-Th-Pb age calculation for electron microprobe dating of monazite: Geochimica et Cosmochimica Acta, v. 65, no. 24, p. 4509-4522.

Cocherie, A., Legendre, O., Peucat, J. J., and Kouamelan, A. N., 1998, Geochronology of polygenetic monazites constrained by in situ electron microprobe Th-U-total lead determination: implications for lead behaviour in monazite: Geochimica et Cosmochimica Acta, v. 62, no. 14, p. 2475-2497.

Coint, N., Slagstad, T., Roberts, N. M. W., Marker, M., Røhr, T. S., and Sørensen, B. E., 2015, The Late Mesoproterozoic Sirdal Magmatic Belt, SW Norway: Relationships between magmatism and metamorphism and implications for Sveconorwegian orogenesis: Precambrian Research, v. 265, p. 57-77.

Collins, A. S., Clark, C., and Plavsa, D., 2014, Peninsula India in Gondwana: the tectonothermal evolution of the Southern Granulite Terraine and its Gondwanan counterparts: Gondwana Research, v. 25, no. 1, p. 190-203.

Collins, A. S., Clark, C., Sajeev, K., Santosh, M., Kelsey, D. E., and Hand, M., 2007a, Passage through India: the Mozambique Ocean suture, high-pressure granulites and the Palghat-Cauvery shear zone system: Terra Nova, v. 19, p. 141-147.

Collins, A. S., and Pisarevsky, S. A., 2005, Amalgamating eastern Gondwana: the evolution of the Circum-Indian Orogens: Earth-Science Reviews, v. 71, p. 229-270.

Collins, A. S., Santosh, M., Braun, I., and Clark, C., 2007b, Age and sedimentary provenance of the Southern Granulites, South India: U-Th-Pb SHRIMP secondary ion mass spectrometry: Precambrian Research, v. 155, p. 125-138.

Collins, W. J., 2002, Hot orogens, tectonic switching, and creation of continental crust: Geology, v. 30, no. 6, p. 535-538.

Compston, W., Williams, I. S., and Clement, S. W., U-Pb ages within single zircons using a sensitive high mass-resolution ion microprobe1982, p. 593-595.

Corfu, F., Hanchar, J. M., Hoskin, P. W. O., and Kinny, P., 2003, Atlas of zircon textures: Reviews in mineralogy and geochemistry, v. 53, no. 1, p. 469-500.

Corfu, F., and Laajoki, K., 2008, An uncommon episode of mafic magmatism at 1347 Ma in the Mesoproterozoic Telemark supracrustals, Sveconorwegian orogen–Implications for stratigraphy and tectonic evolution: Precambrian Research, v. 160, p. 299-307.

Cottle, J. M., Jessup, M. J., Newell, D. L., Horstwood, M. S. A., Noble, S. R., Parrish, R. R., Waters, D. J., and Searle, M. P., 2009a, Geochronology of granulitized eclogite from the Ama Drime Massif: Implications for the tectonic evolution of the South Tibetan Himalaya: Tectonics, v. 28, no. 1, p. 1–25.

Cottle, John M., Searle, Michael P., Horstwood, Matthew S. A., and Waters, David J., 2009b, Timing of Midcrustal Metamorphism, Melting, and Deformation in the Mount Everest Region of Southern Tibet Revealed by U(–Th)–Pb Geochronology: The Journal of Geology, v. 117, no. 6, p. 643-664.

Crank, J., 1975, The Mathematics of Diffusion: 2d Ed., Oxford University Press.

Cutts, K. A., Kelsey, D. E., and Hand, M., 2013, Evidence for late Paleoproterozoic (ca 1690–1665 Ma) high- to ultrahigh-temperature metamorphism in southern Australia: Implications for Proterozoic supercontinent models: Gondwana Research, v. 23, no. 2, p. 617-640.

Dahl, P. S., Hamilton, M. A., Jercinovic, M. J., Terry, M. P., Williams, M. L., and Frei, R., 2005, Comparative isotopic and chemical geochronometry of monazite, with implications for U-Th-Pb dating by electron microprobe: An example from metamorphic rocks of the eastern Wyoming Craton (U.S.A.): American Mineralogist, v. 90, no. 4, p. 619.

Davis, D. W., Krogh, T. E., and Williams, I. S., 2003, Historical development of zircon geochronology: Reviews in mineralogy and geochemistry, v. 53, no. 1, p. 145-181.

de Laeter, J. R., and Kennedy, A. K., 1998, A double focussing mass spectrometer for geochronology: International Journal of Mass Spectrometry, v. 178, p. 43-50.

Degeling, H., Eggins, S., and Ellis, D. J., 2001, Zr budgets for metamorphic reactions, and the formation of zircon from garnet breakdown: Mineralogical Magazine, v. 65, no. 6, p. 749-758.

Demaiffe, D., and Michot, J., 1985, Isotope geochronology of the Proterozoic crustal segment of Southern Norway: a review: The Deep Proterozoic Crust in the North Atlantic Provinces, p. 499-516.

Diener, J. F. A., and Powell, R., 2010, Influence of ferric iron on the stability of mineral assemblages: Journal of Metamorphic Geology, v. 28, p. 599-613.

Diener, J. F. A., White, R. W., Link, K., Dreyer, T. S., and Moodley, A., 2013, Clockwise, low-P metamorphism of the Aus granulite terrain, southern Namibia, during the Mesoproterozoic Namaqua Orogeny: Precambrian Research, v. 224, p. 629-652.

Dodson, M. H., 1973, Closure temperature in cooling geochronological and petrological systems: Contributions to Mineralogy and Petrology, v. 40, no. 3, p. 259-274.

Drüppel, K., Elsäßer, L., Brandt, S., and Gerdes, A., 2013, Sveconorwegian Mid-crustal Ultrahigh-temperature Metamorphism in Rogaland, Norway: U-Pb LA-ICP-MS Geochronology and Pseudosections of Sapphrine Granulites and Associated Paragneisses: Journal of Petrology, v. 54, no. 2, p. 305-350.

Drury, S. A., Harris, N. B. W., Holt, R. W., Reeves-Smith, G. J., and Wightman, R. T., 1984, Precambrian Tectonics and Crustal Evolution in South India: The Journal of Geology, v. 92, no. 1, p. 3-20.

Duchesne, J.-C., and Wilmart, E., 1997, Igneous charnockites and related rocks from the Bjerkreim-Sokndal Layered Intrusion (Southwest Norway): a jotunite (hypersthene monzodiorite)-derived A-type granitoid suite: Journal of Petrology, v. 38, no. 3, p. 337-369.

Duchesne, J. C., and Michot, J., 1987, The Rogaland intrusive massives: introduction: Norges Geologisk Undersøkelse- Special Publication, v. 1, p. 48-59.

Dumond, G., Goncalves, P., Williams, M. L., and Jercinovic, M. J., 2015, Monazite as a monitor of melting, garnet growth and feldspar recrystallization in continental lower crust: Journal of Metamorphic Geology, v. 33, no. 7, p. 735-762.

Ellis, D. J., Sheraton, J. W., England, R. N., and Dallwitz, W. B., 1980, Osumilite-sapphirine-quartz granulites from Enderby Land Antarctica - mineral assemblages and reactions: Contributions to Mineralogy and Petrology, v. 72, p. 123-143.

Endo, T., Toshiaki, T., Santosh, M., and Shaji, E., 2012, Phase equilibrium modeling of incipient charnockite formation in NCKFMASHTO and MnNCKFMASHTO systems: A case study from Rajapalaiyam, Madurai Block, southern India: Geoscience Frontiers, v. 3, no. 6, p. 801-812.

Endo, T., Toshiaki, T., Santosh, M., Shimizu, Hisako, and Shaji, E., 2013, Granulite formation in a Gondwana fragment: petrology and mineral equilibrium modeling of incipient charnockite from Mavadi, southern India: Mineralogy and Petrology, v. 107, no. 5, p. 727–738.

Engi, M., Lanari, P., and Kohn, M. J., 2017, Significant Ages—An Introduction to Petrochronology: Reviews in Mineralogy and Geochemistry, v. 83, no. 1, p. 1.

Erickson, T. M., Pearce, M. A., Taylor, R. J. M., Timms, N. E., Clark, C., Reddy, S. M., and Buick, I. S., 2015, Deformed monazite yields high-temperature tectonic ages: Geology, v. 43, no. 5, p. 383.

Falkum, T., 1982, Geologisk kart over Norge, berggrunnskart MANDAL, 1:250,000: Norges Geol. Unders.

Falkum, T., 1985, Geotectonic evolution of southern Scandinavia in light of a late-Proterozoic plate-collision: The Deep Proterozoic Crust in the North Atlantic Provinces, p. 309-322.

Falkum, T., and Petersen, J. S., 1980, The Sveconorwegian orogenic belt, a case of late-Proterozoi plate-collision: Geologische Rundschau, v. 69, no. 3, p. 622-647.

Feng, R., Machado, N., and Ludden, J., 1993, Lead geochronology of zircon by LaserProbe-inductively coupled plasma mass spectrometry (LP-ICPMS): Geochimica et Cosmochimica Acta, v. 57, no. 14, p. 3479-3486.

Fernández-Suárez, J., Gutiérrez-Alonso, G., Jenner, G. A., and Jackson, S. E., 1998, Geochronology and geochemistry of the Pola de Allande granitoids (northern Spain): their bearing on the Cadomian-Avalonian evolution of northwest Iberia: Canadian Journal of Earth Sciences, v. 35, no. 12, p. 1439-1453.

Ferry, J. M., and Watson, E. B., 2007, New thermodynamic models and revised calibrations for the Ti-in-zircon and Zr-in-rutile thermometers: Contributions to Mineralogy and Petrology, v. 154, no. 4, p. 429-437.

Fitzsimons, I. C. W., and Harley, S. L., 1994, The influence of retrograde cation exchange on granulite P–T estimates and a convergence technique for the recovery of peak metamorphic conditions: Journal of Petrology, v. 35, no. 2, p. 543-576.

Fitzsimons, I. C. W., Kinny, P. D., Wetherley, S., and Hollingsworth, D. A., 2005, Bulk chemical control on metamorphic monazite growth in pelitic schists and implications for U–Pb age data: Journal of Metamorphic Geology, v. 23, no. 4, p. 261-277.

Fletcher, I. R., McNaughton, N. J., Davis, W. J., and Rasmussen, B., 2010, Matrix effects and calibration limitations in ion probe U–Pb and Th–Pb dating of monazite: Chemical Geology, v. 270, p. 31-44.

Flowerdew, M. J., Millar, I. L., Vaughan, A. P. M., Horstwood, M. S. A., and Fanning, C. M., 2006, The source of granitic gneisses and migmatites in the Antarctic Peninsula: a combined U–Pb SHRIMP and laser ablation Hf isotope study of complex zircons: Contributions to Mineralogy and Petrology, v. 151, no. 6, p. 751-768.

Fonarev, V. I., Konilov, A. N., and Santosh, M., 2000, Multistage metamorphic evolution of the Trivandrum Granulite Block, Southern India: Gondwana Research, v. 3, no. 3, p. 293-314.

Fornelli, A., Langone, A., Micheletti, F., Pascazio, A., and Piccarreta, G., 2014, The role of trace element partitioning between garnet, zircon and orthopyroxene on the interpretation of zircon U–Pb ages: an example from high-grade basement in Calabria (Southern Italy): International Journal of Earth Sciences, v. 103, no. 2, p. 487-507.

Foster, G., Gibson, H. D., Parrish, R., Horstwood, M., Fraser, J., and Tindle, A., 2002, Textural, chemical and isotopic insights into the nature and behaviour of metamorphic monazite: Chemical Geology, v. 191, no. 1–3, p. 183-207.

Foster, G., Kinny, P., Vance, D., Prince, C., and Harris, N., 2000, The significance of monazite U–Th–Pb age data in metamorphic assemblages; a combined study of monazite and garnet chronometry: Earth and Planetary Science Letters, v. 181, no. 3, p. 327-340.

Foster, G., Parrish, R. R., Horstwood, M. S. A., Chenery, S., Pyle, J., and Gibson, H. D., 2004, The generation of prograde P–T–t points and paths; a textural, compositional, and chronological study of metamorphic monazite: Earth and Planetary Science Letters, v. 228, no. 1–2, p. 125-142.

Fraser, G., Ellis, D., and Eggins, S., 1997, Zirconium abundance in granulite-facies minerals, with implications for zircon geochronology in high-grade rocks: Geology, v. 25, no. 7, p. 607.

Friend, C. R. L., Strachan, R. A., Kinny, P. D., and Watt, G. R., 2003, Provenance of the Moine Supergroup of NW Scotland: evidence from geochronology of detrital and inherited zircons from (meta)sedimentary rocks, granites and migmatites: Journal of the Geological Society, v. 160, no. 2, p. 247.

Froude, D. O., Ireland, T. R., Kinny, P. D., Williams, I. S., Compston, W., Williams, I. R. t., and Myers, J. S., 1983, Ion microprobe identification of 4,100–4,200 Myr-old terrestrial zircons: Nature, v. 304, no. 5927, p. 616-618.

Fryer, B. J., Jackson, S. E., and Longerich, H. P., 1993, The application of laser ablation microprobe-inductively coupled plasma-mass spectrometry (LAM-ICP-MS) to in situ (U)–Pb geochronology: Chemical Geology, v. 109, no. 1, p. 1-8.

Fyfe, W. S., 1973, The granulite facies, partial melting and the Archaean crust: Phiosophical Transactions of the Royal Society of London. Series A, Mathematical and Physical Sciences, v. 273, no. 1235, p. 457-461.

Gauthiez-Putallaz, L., Rubatto, D., and Hermann, J., 2016, Dating prograde fluid pulses during subduction by in situ U–Pb and oxygen isotope analysis: Contributions to Mineralogy and Petrology, v. 171, no. 2, p. 15.

Geisler, T., Schaltegger, U., and Tomaschek, F., 2007, Re-equilibration of Zircon in Aqueous Fluids and Melts: Elements, v. 3, no. 1, p. 43.

Gervasoni, F., Klemme, S., Rocha-Júnior, E. R. V., and Berndt, J., 2016, Zircon saturation in silicate melts: a new and improved model for aluminous and alkaline melts: Contributions to Mineralogy and Petrology, v. 171, no. 3, p. 21.

Gerya, T., 2014, Precambrian geodynamics: Concepts and models: Gondwana Research, v. 25, no. 2, p. 442-463.

Gibson, H. D., Carr, S. D., Brown, R. L., and Hamilton, M. A., 2004, Correlations between chemical and age domains in monazite, and metamorphic reactions involving major pelitic phases: an integration of ID-TIMS and SHRIMP geochronology with Y–Th–U X-ray mapping: Chemical Geology, v. 211, no. 3–4, p. 237-260.

Gordon, S. M., Whitney, D. L., Teyssier, C., and Fossen, H., 2013, U–Pb dates and trace-element geochemistry of zircon from migmatite, Western Gneiss Region, Norway: Significance for history of partial melting in continental subduction: Lithos, v. 170–171, p. 35-53.

Gratz, R., and Heinrich, W., 1997, Monazite-xenotime thermobarometry: Experimental calibration of the miscibility gap in the binary system CePO4-YPO4: American Mineralogist, v. 82, no. 7-8, p. 772-780.

Green, E. C. R., White, R. W., Diener, J. F. A., Powell, R., Holland, T. J. B., and Palin, R. M., 2016, Activity–composition relations for the calculation of partial melting equilibria in metabasic rocks: Journal of Metamorphic Geology, v. 34, no. 9, p. 845-869.

Halpin, J. A., Daczko, N. R., Milan, L. A., and Clarke, G. L., 2012, Decoding near-concordant U–Pb zircon ages spanning several hundred million years: recrystallisation, metamictisation or diffusion?: Contrib Mineral Petrol, v. 163, no. 1, p. 67-85.

Hanchar, J. M., and Miller, C. F., 1993, Zircon zonation patterns as revealed by cathodoluminescence and backscattered electron images: Implications for interpretation of complex crustal histories: Chemical Geology, v. 110, no. 1, p. 1-13.

Hanchar, J. M., and Rudnick, R. L., 1995, Revealing hidden structures: The application of cathodoluminescence and back-scattered electron imaging to dating zircons from lower crustal xenoliths: Lithos, v. 36, no. 3, p. 289-303.

Hansen, E. C., Janardhan, A. S., Newton, R. C., Prame, W. K. B. N., and Kumar, G. R. R., 1987, Arrested charnockite formation in southern India and Sri Lanka: Contributions to Mineralogy and Petrology, v. 96, p. 225-244.

Harley, S. L., 1986, A sapphirine-cordierite-garnet-sillimanite granulite from Enderby Land, Antarctica: implications for FMAS petrogenetic grids in the granulite facies: Contributions to Mineralogy and Petrology, v. 94, no. 4, p. 452-460.

Harley, S. L., 2016, A matter of time: The importance of the duration of UHT metamorphism: Journal of Mineralogical and Petrological Sciences, v. 111, p. 50–72.

Harley, S. L., and Kelly, N. M., 2007, The impact of zircon–garnet REE distribution data on the interpretation of zircon U–Pb ages in complex high-grade terrains: An example from the Rauer Islands, East Antarctica: Chemical Geology, v. 241, no. 1–2, p. 62-87.

Harley, S. L., Kelly, N. M., and Möller, A., 2007, Zircon behaviour and the thermal histories of mountain chains: Elements, v. 3, p. 25-30.

Harley, S. L., Kinny, P. D., Snape, I., and Black, L. P., Zircon chemistry and the definition of events in Archaean granulite terrains2001, Volume 37, p. 511-513.

Harley, S. L., and Nandakumar, V., 2014, Accessory mineral behaviour in granulite migmatites: a case study from the Kerala Khondalite Belt, India: Journal of Petrology, v. 55, no. 10, p. 1965-2002.

Harley, S. L., and Nandakumar, V., 2016, New evidence for Palaeoproterozoic high grade metamorphism in the Trivandrum Block, Southern India: Precambrian Research, v. 280, p. 120-138.

Harley, S. L., and Santosh, M., 1995, Wollastonite at Nuliyam, Kerala, souterhn India: a reassessment of CO2-infiltration and charnockite formation at a classic locality: Contrib Mineral Petrol, v. 120, p. 83-94.

Harlov, D. E., 2011, Petrological and experimental application of REE- and actinide-bearing accessory mineral to the study of Precambrian high-grade gneiss terrains: Geological Society of America Memoirs, v. 207, p. 13-24.

Harlov, D. E., and Hetherington, C. J., 2010, Partial high-grade alteration of monazite using alkali-bearing fluids: Experiment and nature: American Mineralogist, v. 95, p. 1105-1108.

Harlov, D. E., Wirth, R., and Hetherington, C. J., 2011, Fluid-mediate partial alteration in monazite: the role of coupled dissolution-reprecipitation in element redistribution and mass transfer: Contributions to Mineralogy and Petrology, v. 162, p. 329-348.

Harris, N. B. W., Santosh, M., and Taylor, P. N., 1994, Crustal evolution in South India: constraints from Nd isotopes: The Journal of Geology, v. 102, no. 2, p. 139-150.

Harrison, T. M., 1981, Diffusion of 40Ar in Hornblende: Contributions to Mineralogy and Petrology, v. 78, p. 324-331.

Harrison, T. M., 1983, Some observations on the interpretation of 40Ar/39Ar age spectra: Chemical Geology, v. 41, p. 319-338.

Hermann, J., and Rubatto, D., 2003, Relating zircon and monazite domains to garnet growth zones: age and duration of granulite facies metamorphism in the Val Malenco lower crust: Journal of Metamorphic Geology, v. 21, p. 833-852.

Hermann, J., Rubatto, D., Korsakov, A., and Shatsky, V. S., 2001, Multiple zircon growth during fast exhumation of diamondiferous, deeply subducted continental crust (Kokchetav Massif, Kazakhstan): Contributions to Mineralogy and Petrology, v. 141, no. 1, p. 66-82.

Hermans, G. A. E. M., Hakstege, A. L., Jansen, J. B. H., and Poorter, R. P. E., 1976, Sapphrine occurrence near Vikeså in Rogaland, Southwestern Norway: Norsk Geologisk Tidsskrift, v. 56, p. 397-412.

Hermans, G. A. E. M., Tobi, A. C., Poorter, R. P. E., and Maijer, C., 1975, The high-grade metamorphic Precambrian of the Sirdal-Ørsdal area, Rogaland/Vest-Agder, South-west Norway: Norges Geol. Unders., v. 318, p. 51-74.

Hirata, T., and Nesbitt, R. W., 1995, U-Pb isotope geochronology of zircon: evaluation of the laser probe-inductively coupled plasma mass spectrometry technique: Geochimica et Cosmochimica Acta, v. 59, no. 12, p. 2491-2500.

Högdahl, K., Majka, J., Sjöström, H., Nilsson, K. P., Claesson, S., and Konečný, P., 2012, Reactive monazite and robust zircon growth in diatexites and leucogranites from a hot, slowly cooled orogen: implications for the Palaeoproterozoic tectonic evolution of the central Fennoscandian Shield, Sweden: Contributions to Mineralogy and Petrology, v. 163, no. 1, p. 167-188.

Hokada, T., and Harley, S. L., 2004a, Zircon growth in UHT leucosome: constraints from zircon-garnet rare earth elements (REE) relations in Napier Complex, East Antarctica: Journal of Mineralogical and Petrological Sciences, v. 99, p. 180-190.

Hokada, T., and Harley, S. L., 2004b, Zircon growth in UHT leucosome: constraints from zircon-garnet rare earth elements (REE) relations in Napier Complex, East Antarctica: Journal of Mineralogical and Petrological Sciences, v. 99, no. 4, p. 180-190.

Holder, R. M., Hacker, B. R., Kylander-Clark, A. R. C., and Cottle, J. M., 2015, Monazite trace-element and isotopic signatures of (ultra)high-pressure metamorphism: Examples from the Western Gneiss Region, Norway: Chemical Geology, v. 409, p. 99-111.

Holland, T. J. B., and Powell, R., 2011, An improved and extended internally consistent thermodynamic dataset for phases of petrological interest, involving a new equation of state for solids: Journal of Metamorphic Geology, v. 29, p. 333-383.

Horn, I., Rudnick, R. L., and McDonough, W. F., 2000, Precise elemental and isotope ratio determination by simultaneous solution nebulization and laser ablation-ICP-MS: application to U–Pb geochronology: Chemical Geology, v. 164, no. 3–4, p. 281-301.

Hoskin, P. W. O., and Black, L. P., 2000, Metamorphic zircon formation by solid-state recrystallization of protolith igneous zircon: Journal of Metamorphic Geology, v. 18, p. 423-439.

Hoskin, P. W. O., and Ireland, T. R., 2000, Rare earth element chemistry of zircon and its use as a provenance indicator: Geology, v. 28, no. 7, p. 627-630.

Hoskin, P. W. O., and Schaltegger, U., 2003, The composition of zircon and igneous and metamorphic petrogenesis: Reviews in mineralogy and geochemistry, v. 53, no. 1, p. 27–62.

Huijsmans, J. P. P., Kabel, A. B. E. T., and Steenstra, S. E., 1981, On the structure of high-grade metamorphic Precambrian terrain in Rogaland, south Norway: Norsk Geologisk Tidsskrift, v. 61, p. 183-192.

Ireland, T. R., Clement, S., Compston, W., Foster, J. J., Holden, P., Jenkins, B., Lanc, P., Schram, N., and Williams, I. S., 2008, Development of SHRIMP: Australian Journal of Earth Sciences, v. 55, no. 6-7, p. 937-954.

Ireland, T. R., and Williams, I. S., 2003, Considerations in zircon geochronology by SIMS: Reviews in Mineralogy and Geochemistry, v. 53, no. 1, p. 215-241.

Jackson, D. H., and Santosh, M., 1992, Dehydration reaction and isotope front transport induced by CO2 infiltration at Nuliyam, South India: Journal of Metamorphic Geology, v. 10, p. 365-382.

Jackson, S. E., Pearson, N. J., Griffin, W. L., and Belousova, E. A., 2004, The application of laser ablation-inductively coupled plasma-mass spectrometry to in situ U–Pb zircon geochronology: Chemical Geology, v. 211, no. 1–2, p. 47-69.

Jamieson, R. A., and Beaumont, C., 2013, On the origin of orogens: Geological Society of America Bulletin, v. 125, no. 11-12, p. 1671.

Janots, E., Engi, M., Berger, A., Allaz, J., Schwarz, J. O., and Spandler, C., 2008, Prograde metamorphic sequence of REE minerals in pelitic rocks of the Central Alps: implications for allanite–monazite–xenotime phase relations from 250 to 610 °C: Journal of Metamorphic Geology, v. 26, no. 5, p. 509-526.

Janots, E., Engi, M., Rubatto, D., Berger, A., Gregory, C., and Rahn, M., 2009, Metamorphic rates in collisional orogeny from in situ allanite and monazite dating: Geology, v. 37, no. 1, p. 11.

Jansen, B. H., Blok, R. J. P., Bos, M., and Scheelings, M., 1985, Geothermometry and geobarometry in Rogaland and preliminary results from the Bamble area, S Norway: The Deep Proterozoic Crust in the North Atlantic Provinces, p. 499-516.

Jansen, B. H., and Tobi, A. C., 1987, Introduction to the Faurefjell metasediments: Norges Geologisk Undersøkelse- Special Publication, v. 1, p. 88-89.

Johnson, T., Brown, M., Gibson, R., and Wing, B., 2004, Spinel–cordierite symplectites replacing andalusite: evidence for melt-assisted diapirism in the Bushveld Complex, South Africa: Journal of Metamorphic Geology, v. 22, no. 6, p. 529-545.

Johnson, T., Clark, C., Taylor, R., Santosh, M., and Collins, A. S., 2015, Prograde and retrograde growth of monazite in migmatites: An example from the Nagercoil Block, southern India: Geoscience Frontiers, v. 6, no. 3, p. 373-387.

Johnson, T. E., White, R. W., and Powell, R., 2008, Partial melting of metagreywacke: a calculated mineral equilibria study: Journal of Metamorphic Geology, v. 26, no. 8, p. 837-853.

Jöns, N., and Schenk, V., 2011, The ultrahigh temperature granulites of southern Madagascar in a polymetamorphic context: implications for the amalgamation of the Gondwana supercontinent: European Journal of Mineralogy, v. 23, no. 2, p. 127.

Jourdan, F., and Eroglu, E., 2017, 40Ar/39Ar and (U-Th)/He model age signatures of elusive Mercurian and Venusian meteorites: Meteoritics & Planetary Science, p. 884-905.

Jourdan, F., Mark, D. F., and Verati, C., 2014, Advances in 40Ar/39Ar dating: from archaeology to planetary sciences – introduction: Geological Society, London, Special Publications, v. 378, no. 1, p. 1–8.

Karlstrom, K. E., Åhäll, K. I., Harlan, S. S., Williams, M. L., McLelland, J., and Geissman, J. W., 2001, Long-lived (1.8-1.0 Ga) convergent orogen in southern Laurentia, its extensions to Australia and Baltica, and implications for refining Rodinia: Precambrian Research, v. 111, p. 5–30.

Kars, H., Jansen, B. H., Tobi, A. C., and Poorter, R. P. E., 1980, The metapelitic rocks of the polymetamorphic Precambrian of Rogaland, SW Norway: Part II- Mineral relations between cordierite, hercynite and magnetite within the osumilite-in isograd: Contributions to Mineralogy and Petrology, v. 74, p. 235-244.

Keay, S., Lister, G., and Buick, I., 2001, The timing of partial melting, Barrovian metamorphism and granite intrusion in the Naxos metamorphic core complex, Cyclades, Aegean Sea, Greece: Tectonophysics, v. 342, no. 3–4, p. 275-312.

Kelley, S., 2002, K-Ar and Ar-Ar Dating: Reviews in Mineralogy and Geochemistry, v. 47, no. 1, p. 785.

Kelly, N. M., Clarke, G. L., and Harley, S. L., 2006, Monazite behaviour and age significance in poly-metamorphic high-grade terrains: A case study from the western Musgrave Block, central Australia1: Lithos, v. 88, no. 1–4, p. 100-134.

Kelly, N. M., and Harley, S. L., 2004, Orthopyroxene–Corundum in Mg–Al-rich Granulites from the Oygarden Islands, East Antarctica: Journal of Petrology, v. 45, no. 7, p. 1481-1512.

Kelly, N. M., and Harley, S. L., 2005, An integrated microtextural and chemical approach to zircon geochronology: refining the Archaean history of the Napier Complex, east Antartica: Contributions to Mineralogy and Petrology, v. 149, p. 57-84.

Kelly, N. M., Harley, S. L., and Möller, A., 2012, Complexity in the behavior and recrystallization of monazite during high-T metamorphism and fluid infiltration: Chemical Geology, v. 322-323, p. 192-208.

Kelsey, D. E., 2008, On ultrahigh-temperature crustal metamorphism: Gondwana Research, v. 13, p. 1-29.

Kelsey, D. E., Clark, C., and Hand, M., 2008, Thermobarometric modelling of zircon and monazite growth in melt-bearing systems: examples using model metapelitic and metapsammitic granulites: Journal of Metamorphic Geology, v. 26, p. 199-212.

Kelsey, D. E., and Hand, M., 2015, On ultrahigh temperature crustal metamorphism: Phase equilibria, trace element thermometry, bulk composition, heat sources, timescales and tectonic settings: Geoscience Frontiers, v. 6, p. 311-356.

Kelsey, D. E., and Powell, R., 2011, Progress in linking accessory mineral growth and breakdown to major mineral evolution in metamorphic rocks: a thermodynamic approach in the Na_2O-CaO-K_2O-FeO-MgO-Al_2O_3-SiO_2-H_2O-TiO_2-ZrO_2 system: Journal of Metamorphic Geology, v. 29, no. 1, p. 151-166.

Kelsey, D. E., White, R. W., and Powell, R., 2005, Calculated phase equilibria in K_2O–FeO–MgO–Al_2O_3–Si_2O–H_2O for silica-undersaturated sapphrine-bearing mineral assemblages: Journal of Metamorphic Geology, v. 23, p. 217-239.

Kennedy, A. K., and de Laeter, J. R., 1994, The performance characteristics of the WA SHRIMP II ion microprobe: US Geological survey circular, v. 1107, p. 166.

Ketchum, J. W. F., Jackson, S. E., Culshaw, N. G., and Barr, S. M., 2001, Depositional and tectonic setting of the Paleoproterozoic Lower Aillik Group, Makkovik Province, Canada: evolution of a passive margin-foredeep sequence based on petrochemistry and U–Pb (TIMS and LAM-ICP-MS) geochronology: Precambrian Research, v. 105, no. 2–4, p. 331-356.

Kirkland, C. L., Erickson, T. M., Johnson, T. E., Danišík, M., Evans, N. J., Bourdet, J., and McDonald, B. J., 2016, Discriminating prolonged, episodic or disturbed monazite age spectra: An example from the Kalak Nappe Complex, Arctic Norway: Chemical Geology, v. 424, p. 96-110.

Kirkland, C. L., Whitehouse, M. J., and Slagstad, T., 2009a, Fluid-assisted zircon and monazite growth within a shear zone: a case study from Finnmark, Arctic Norway: Contrib Mineral Petrol, v. 158, p. 637-657.

Kirkland, C. L., Whitehouse, M. J., and Slagstad, T., 2009b, Fluid-assisted zircon and monazite growth within a shear zone: a case study from Finnmark, Arctic Norway: Contributions to Mineralogy and Petrology, v. 158, no. 5, p. 637-657.

Kohn, M. J., and Kelly, N., 2017, Petrology and Geochronology of Metamorphic Zircon: Microstructural Geochronology: Planetary Records Down to Atom Scale, v. 232, p. 35.

Kohn, M. J., and Malloy, M. A., 2004, Formation of monazite via prograde metamorphic reactions among common silicates: implications for age determinations: Geochimica et Cosmochimica Acta, v. 68, no. 1, p. 101-113.

Kohn, M. J., and Penniston-Dorland, S. C., 2017, Diffusion: Obstacles and Opportunities in Petrochronology: Reviews in Mineralogy and Geochemistry, v. 83, no. 1, p. 103.

Kohn, M. J., Wieland, M. S., Parkinson, C. D., and Upreti, B. N., 2005, Five generations of monazite in Langtang gneisses: implications for chronology of the Himalayan metamorphic core: Journal of Metamorphic Geology, v. 23, no. 5, p. 399-406.

Korhonen, F. J., Brown, M., Clark, C., and Bhattacharya, S., 2013a, Osumilite-melt interactions in the ultrahigh temperatures granulites: phase equilibria modelling and implications for the P-T-t evolution of the Eastern Ghats Provincee, India: Journal of Metamorphic Geology, v. 31, p. 881-907.

Korhonen, F. J., Clark, C., Brown, M., Bhattacharya, S., and Taylor, R., 2013b, How long-lived is ultrahigh temperature (UHT) metamorphism? Constraints from zircon and monazite geochronology in the Eastern Ghats orogenic belt, India: Precambrian Research, v. 234, p. 322-350.

Korhonen, F. J., Clark, C., Brown, M., and Taylor, R. J. M., 2014, Taking the temperature of Earth's hottest crust: Earth and Planetary Science Letters, v. 408, p. 341-354.

Korhonen, F. J., Powell, R., and Stout, J. H., 2012, Stability of sapphirine + quartz in the oxidised rocks of the Wilson Lake terrane, Labrador: calculated equilibria in NCKFMASHTO: Journal of Metamorphic Geology, v. 30, p. 21-36.

Korhonen, F. J., Saito, S., Brown, M., and Siddoway, C. S., 2010, Modeling multiple melt loss events in the evolution of an active continental margin: Lithos, v. 116, p. 230-248.

Korhonen, F. J., Saw, A. K., Clark, C., Brown, M., and Bhattacharya, S., 2011, New constraints on UHT metamorphism in the Eastern Ghats Province through the application of phase equilibria modelling and in situ geochronology: Gondwana Research, v. 20, p. 764-781.

Košler, J., Fonneland, H., Sylvester, P., Tubrett, M., and Pedersen, R.-B., 2002, U–Pb dating of detrital zircons for sediment provenance studies—a comparison of laser ablation ICPMS and SIMS techniques: Chemical Geology, v. 182, no. 2–4, p. 605-618.

Kretz, R., 1983, Symbols for rock-forming minerals: American Mineralogist, v. 68, p. 277-279.

Kröner, A., Santosh, M., Hegner, E., Shaji, E., Geng, H., Wong, J., Xie, H., Wan, Y., Shang, C. K., Liu, D., Sun, M., and Nanda-Kumar, V., 2015, Palaeoproterozoic ancestry of Pan-African high-grade granitoids in southernmost India: Implications for Gondwana reconstructions: Gondwana Research, v. 27, p. 1-37.

Kröner, A., Wan, Y., Liu, X., and Liu, D., 2014, Dating of zircon from high-grade rocks: Which is the most reliable method?: Geoscience Frontiers, v. 5, no. 4, p. 515-523.

Kylander-Clark, A. R. C., Hacker, B. R., and Cottle, J. M., 2013, Laser-ablation split-stream ICP petrochronology: Chemical Geology, v. 345, p. 99-112.

Lanari, P., and Engi, M., 2017, Local Bulk Composition Effects on Metamorphic Mineral Assemblages: Reviews in Mineralogy and Geochemistry, v. 83, no. 1, p. 55.

Laurent, A. T., Seydoux-Guillaume, A.-M., Duchene, S., Bingen, B., Bosse, V., and Datas, L., 2016, Sulphate incorporation in monazite lattice and dating the cycle of sulphur in metamorphic belts: Contributions to Mineralogy and Petrology, v. 171, no. 11, p. 94.

Li, X.-h., Liang, X.-r., Sun, M., Guan, H., and Malpas, J. G., 2001, Precise 206Pb/238U age determination on zircons by laser ablation microprobe-inductively coupled plasma-mass spectrometry using continuous linear ablation: Chemical Geology, v. 175, no. 3–4, p. 209-219.

Lister, G. S., and Baldwin, S. L., 1996, Modelling the effect of arbitrary P-T-t histories on argon diffusion in minerals using the MacArgon program for the Apple Macintosh: Tectonophysics, v. 253, no. 1, p. 83-109.

Liu, Y., Hu, Z., Zong, K., Gao, C., Gao, S., Xu, J., and Chen, H., 2010, Reappraisement and refinement of zircon U-Pb isotope and trace element analyses by LA-ICP-MS: Chinese Science Bulletin, v. 55, no. 15, p. 1535-1546.

Longhi, J., Fram, M. S., Auwera, J. V., and Montieth, J. N., 1993, Pressure effects, kinetics, and rheology of anorthositic and related magmas: American Mineralogist, v. 78, p. 1016-1030.

Ludwig, K. R., 2003, Isoplot 3.0. A Geochronological Toolkit for Microsoft Excel: Berkeley Geochronological Center Special Publication, v. 4, p. 70.

Ludwig, K. R., 2009, SQUID II: A user's manual: Berkeley Geochronological Center Special Publication, v. 5, p. 110.

Mahan, K. H., Goncalves, P., Williams, M. L., and Jercinovic, M. J., 2006, Dating metamorphic reactions and fluid flow: application to exhumation of high-P granulites in a crustal-scale shear zone, western Canadian Shield: Journal of Metamorphic Geology, v. 24, no. 3, p. 193-217.

Maijer, C., 1987, The metamorphic envelope of the Rogaland intrusive complex: Norges Geologisk Undersøkelse- Special Publication, v. 1, p. 68-73.

Maijer, C., Andriessen, P. A. M., Hebeda, E. H., Jansen, B. H., and Verschure, R. H., 1981, Osumilite, an approximately 970 Ma old high-temperature index mineral of the granulite-facies metamorphism in Rogaland, SW Norway: Geol. Mijnbouw, v. 60, p. 267-272.

Marker, M., Schiellerup, H., Meyer, G., Robins, B., and Bolle, O., 2003, Introduction to the geological map of the Rogaland Anorthosite Province 1:75000: Norges Geologisk Undersøkelse- Special Publication, v. 9, p. 109-116.

Martin, A. J., Gehrels, G. E., and DeCelles, P. G., 2007, The tectonic significance of (U,Th)/Pb ages of monazite inclusions in garnet from the Himalaya of central Nepal: Chemical Geology, v. 244, no. 1–2, p. 1-24.

McFarlane, C. R. M., Connelly, J. N., and Carlson, W. D., 2005, Monazite and xenotime petrogenesis in the contact aureole of the Makhavinekh Lake Pluton, northern Labrador: Contributions to Mineralogy and Petrology, v. 148, no. 5, p. 524-541.

McFarlane, C. R. M., Connelly, J. N., and Carlson, W. D., 2006, Contrasting response of monazite and zircon to a high-T thermal overprint: Lithos, v. 88, no. 1–4, p. 135-149.

Mezger, K., and Krogstad, E. J., 1997, Interpretation of discordant U-Pb zircon ages: An evaluation: Journal of Metamorphic Geology, v. 15, no. 1, p. 127-140.

Miyashiro, A., 1956, Osumilite, a new silicate mineral, and its crystal structure: American Mineralogist, v. 41, p. 104-116.

Möller, A., O'Brien, P. J., Kennedy, A., and Kröner, A., 2002, Polyphase zircon in ultrahigh-temperature granulites (Rogaland, SW Norway): constraints for Pb diffusion in zircon: Journal of Metamorphic Geology, v. 20, p. 727-740.

Möller, A., O'Brien, P. J., Kennedy, A., and Kröner, A., 2003, Linking growth episodes of zircon and metamorphic textures to zircon chemistry: an example from the ultrahigh-temperature granulites of Rogaland (SW Norway): Geological Society, London, Special Publications, v. 220, no. From: Vance, D., Müller, W., & Villa, I. M. (eds) 2003. Geochronology: Linking the Isotopic Record with Petrology and Textures., p. 65-81.

Montel, Kornprobst, and Vielzeuf, 2000, Preservation of old U–Th–Pb ages in shielded monazite: example from the Beni Bousera Hercynian kinzigites (Morocco): Journal of Metamorphic Geology, v. 18, no. 3, p. 335-342.

Morimoto, T., Santosh, M., Tsunogae, T., and Yoshimura, Y., 2004, Spinel+Quartz association from the Kerala Khondalites, southern India: evidence for ultra-high temperature metamorphism: Journal of Mineralogical and Petrological Sciences, v. 99, p. 257-278.

Morrissey, L. J., Hand, M., Kelsey, D. E., and Wade, B. P., 2016, Cambrian High-temperature Reworking of the Rayner–Eastern Ghats Terrane: Constraints from the Northern Prince Charles Mountains Region, East Antarctica: Journal of Petrology, v. 57, no. 1, p. 53-92.

Motoyoshi, Y., Hensen, B. J., and Matsueda, H., 1990, Metastable growth of corundum adjacent to quartz in a spinel-bearing quartzite from the Archaean Napier Complex, Antarctica: Journal of Metamorphic Geology, v. 8, no. 1, p. 125-130.

Nagasawa, H., 1971, Partitioning of Eu and Sr between coexisting plagioclase and K-feldspar: Earth and Planetary Science Letters, v. 13, no. 1, p. 139-144.

Nair, R., and Chacko, T., 2002, Fluid-absent melting of high-grade semi-pelites: P-T constraints on orthopyroxene formation and implications for granulite genesis: Journal of Petrology, v. 43, no. 11, p. 2121-2142.

Nandakumar, V., and Harley, S. L., 2000, A reappraisal of the pressure-temperature path of granulites from the Kerala Khondalite Belt, southern India: The Journal of Geology, v. 108, no. 6, p. 687-703.

Nemchin, A. A., Horstwood, M. S. A., and Whitehouse, M. J., 2013, High-spatial-resolution geochronology: Elements, v. 9, no. 1, p. 31-37.

Newton, R. C., 1989, Metamorphic fluids in the deep crust: Annual Review of Earth and Planetary Sciences, v. 17, p. 385-412.

Newton, R. C., 1992, Charnockitic alteration: evidence for CO2 infiltration in granulite facies metamorphism: Journal of Metamorphic Geology, v. 10, p. 383-400.

Newton, R. C., Smith, J. V., and Windley, B. F., 1980, Carbonic metamorphism, granulites and crustal growth: Nature, v. 288, p. 45-50.

Newton, R. C., and Tsunogae, T., 2014, Incipient charnockite: characterization at the type localities: Precambrian Research, v. 253, p. 38-49.

Nijland, T. G., Maijer, C., and de Haas, G.-J. L. M., 1996, The Stokkafjell Troctolite, SW Norway: its bearing on the early P-T evolution of the Rogaland terrane: Neues Jahrbuch fur Mineralogie Abhandlungen, v. 171, p. 91-117.

Nutman, A. P., McGregor, V. R., Shiraishi, K., Friend, C. R. L., Bennett, V. C., and Kinny, P. D., 2002, ≥3850 Ma BIF and mafic inclusions in the early Archaean Itsaq Gneiss Complex around Akilia, southern West Greenland? The difficulties of precise dating of zircon-free protoliths in migmatites: Precambrian Research, v. 117, no. 3, p. 185-224.

Palin, R. M., Weller, O. M., Waters, D. J., and Dyck, B., 2016, Quantifying geological uncertainty in metamorphic phase equilibria modelling; a Monte Carlo assessment and implications for tectonic interpretations: Geoscience Frontiers, v. 7, no. 4, p. 591-607.

Pasteels, P., Demaiffe, D., and Michot, J., 1979, U–Pb and Rb–Sr geochronology of the eastern part of the south Rogaland igneous complex, southern Norway: Lithos, v. 12, p. 199-208.

Paton, C., Hellstrom, J., Paul, B., Woodhead, J., and Hergt, J., 2011, Iolite: freeware for the visualisation and processing of mass spectrometric data: Journal of Analytical Atomic Spectrometry, v. 26, p. 2508-2518.

Paton, C., Woodhead, J., Hellstrom, J., Hergt, J., Greig, A., and Maas, R., 2010, Improved laser ablation U–Pb zircon and geochronology through robust downhole fractionation correction: Geochemistry, Geophysics, Geosystems, v. 11, p. 1-36.

Pattison, D. R. M., Chacko, T., Farquhar, J., and McFarlane, R. M., 2003, Temperature of granulite-facies metamorphism: constraints from experimental phase equilibria and thermobarometry corrected for retrograde exchange: Journal of Petrology, v. 44, no. 5, p. 867-900.

Pearce, M. A., White, A. J. R., and Gazley, M. F., 2015, TCInvestigator: automated calculation of mineral mode and composition contour for THERMOCALC pseudosections: Journal of Metamorphic Geology, v. 33, p. 413-425.

Pearce, N. J. G., Perkins, W. T., Westgate, J. A., Gorton, M. P., Jackson, S. E., Neal, C. R., and Chenery, S. P., 1997, A compilation of new and published major and trace element data for NIST SRM 610 and NIST SRM 612 glass reference materials: Geostandards Newsletter, v. 21, p. 115-144.

Perchuk, L. L., Safonov, O. G., Gerya, T. V., Fu, B., and Harlov, D. E., 2000, Mobility of components in metasomatic transformation and partial melting of gneisses: an example from Sri Lanka: Contrib Mineral Petrol, v. 140, no. 2, p. 212-232.

Petersson, A., Scherstén, A., Bingen, B., Gerdes, A., and Whitehouse, M. J., 2015, Mesoproterozoic continental growth: U–Pb–Hf–O zircon record in the Idefjorden Terrane, Sveconorwegian Orogen: Precambrian Research, v. 261, p. 75-95.

Piazolo, S., Fontaine, A. L., Trimby, P., Harley, S., Yang, L., Armstrong, R., and Cairney, J. M., 2016, Deformation-induced trace element redistribution in zircon revealed using atom probe tomography: Nature Communications, v. 7, p. 10490.

Pidgeon, R. T., 1992, Recrystallisation of oscillatory zoned zircon: some geochronological and petrological implications: Contributions to Mineralogy and Petrology, v. 110, no. 4, p. 463-472.

Pitra, P., and Waal, S. A. D., 2001, High-temperature, low-pressure metamorphism and development of prograde symplectites, Marble Hall Fragment, Bushveld Complex (South Africa): Journal of Metamorphic Geology, v. 19, no. 3, p. 311-325.

Plavsa, D., Collins, A. S., Foden, J. F., Kropinski, L., Santosh, M., Chetty, T. R. K., and Clark, C., 2012, Delineating crustal domains in Peninsular India: Age and chemistry of orthopyroxene-bearing felsic gneisses in the Madurai Block: Precambrian Research, v. 198-199, p. 77-93.

Plavsa, D., Collins, A. S., Payne, J. L., Foden, J. D., Clark, C., and Santosh, M., 2014, Detrital zircons in basement metasedimentary protoliths unveil the origins of southern India: Bulletin of the Geological Society of America, v. 126, p. 791-812.

Poitrasson, F., Chenery, S., and Bland, D. J., 1996, Contrasted monazite hydrothermal alteration mechanisms and their geochemical implications: Earth and Planetary Science Letters, v. 145, no. 1, p. 79-96.

Poitrasson, F., Chenery, S., and Shepherd, T. J., 2000, Electron microprobe and LA-ICP-MS study of monazite hydrothermal alteration:: Implications for U-Th-Pb geochronology and nuclear ceramics: Geochimica et Cosmochimica Acta, v. 64, no. 19, p. 3283-3297.

Pyle, J. M., and Spear, F. S., 1999, Yttrium zoning in garnet: coupling of major and accessory phases during metamorphic reactions: Geological Materials Research, v. 1, no. 6, p. 1-49.

Pyle, J. M., and Spear, F. S., 2000, An empirical garnet (YAG) – xenotime thermometer: Contributions to Mineralogy and Petrology, v. 138, no. 1, p. 51-58.

Pyle, J. M., and Spear, F. S., 2003, Four generations of accessory-phase growth in low-pressure migmatites from SW New Hampshire, American Mineralogist, Volume 88, p. 338.

Pyle, J. M., Spear, F. S., Rudnick, R. L., and McDonough, W. F., 2001, Monazite–Xenotime–Garnet Equilibrium in Metapelites and a New Monazite–Garnet Thermometer: Journal of Petrology, v. 42, no. 11, p. 2083-2107.

Raith, M., and Srikantappa, C., 1993, Arrested charnockite formation at Kottavattam, southern India: Journal of Metamorphic Geology, v. 11, p. 815-832.

Raith, M., Srikantappa, C., Ashamanjari, K. G., and Spiering, B., 1990, The granulite terrane of the Nilgiri Hills (Southern India): characterization of high-grade metamorphism, in Vielzeuf, D., and Vidal, P., eds., Granulites and Crustal Evolution, Springer Netherlands, p. 339-365.

Rajesh, H. M., and Santosh, M., 2004, Charnockite magmatism in southern India: Proceedings of the Indian Academy of Sciences. A Earth and Planetary Sciences, v. 113, p. 565-585.

Rajesh, H. M., and Santosh, M., 2012, Charnockites and charnockites: Geoscience Frontiers, v. 3, no. 6, p. 1-8.

Rapp, R. P., Ryerson, F. J., and Miller, C. F., 1987, Experimental evidence bearing on the stability of monazite during crustal anaatexis: Geophysical Research Letters, v. 14, no. 3, p. 307-310.

Rasmussen, B., and Muhling, J. R., 2007, Monazite begets monazite: evidence for dissolution of detrital monazite and reprecipitation of syntectonic monazite during low-grade regional metamorphism: Contributions to Mineralogy and Petrology, v. 154, no. 6, p. 675-689.

Ravindra Kumar, G. R., 2004, Mechanism of arrested charnockite formation at Nemmara, Palghat region, southern India: Lithos, v. 75, p. 331-358.

Ravindra Kumar, G. R., Srikantappa, C., and Hansen, E. C., 1985, Charnockite formation at Ponmudi in southern India: Nature, v. 313, no. 17, p. 207-209.

Rivers, T., 1997, Lithotectonic elements of the Grenville Province: review and tectonic implications: Precambrian Research, v. 86, p. 117–154.

Roberts, M. P., and Finger, F., 1997, Do U–Pb zircon ages from granulites reflect peak metamorphic conditions?: Geology, v. 25, p. 319-322.

Roberts, N. M. W., and Slagstad, T., 2015, Continental growth and reworking on the edge of the Columbia and Rodinia supercontinents; 1.86–0.9 Ga accretionary orogeny in southwest Fennoscandia: International Geology Review, v. 57, no. 11-12, p. 1582-1606.

Rubatto, D., 2002, Zircon trace element geochemistry: partitioning with garnet and the link between U–Pb ages and metamorphism: Chemical Geology, v. 184, p. 123-138.

Rubatto, D., 2017, Zircon: The Metamorphic Mineral: Reviews in Mineralogy and Geochemistry, v. 83, no. 1, p. 261.

Rubatto, D., Chakraborty, S., and Dasgupta, S., 2013, Timescales of crustal melting in the Higher Himalayan Crystallines (Sikkim, Eastern Himalaya) inferred from trace element-constrained monazite and zircon chronology: Contributions to Mineralogy and Petrology, v. 165, no. 2, p. 349-372.

Rubatto, D., and Hermann, J., 2003, Zircon formation during fluid circulation in eclogites (Monviso, Western Alps): implications for Zr and Hf budget in subduction zones: Geochimica et Cosmochimica Acta, v. 67, no. 12, p. 2173-2187.

Rubatto, D., and Hermann, J., 2007, Experimental zircon/melt and zircon/garnet trace element partitioning and implications for the geochronology of crustal rocks: Chemical Geology, v. 241, p. 38-61.

Rubatto, D., Hermann, J., Berger, A., and Engi, M., 2009, Protracted fluid-induced melting during Barrovian metamorphism in the Central Alps: Contributions to Mineralogy and Petrology, v. 158, p. 703-722.

Rubatto, D., Hermann, J., and Buick, I. S., 2006, Temperature and bulk composition control on the growth of monazite and zircon during low-pressure anatexis (Mount Stafford, Central Australia): Journal of Petrology, v. 47, no. 10, p. 1973-1996.

Rubatto, D., Williams, I. S., and Buick, I. S., 2001, Zircon and monazite response to prograde metamorphism in the Reynolds Range, central Australia: Contributions to Mineralogy and Petrology, v. 140, no. 4, p. 458-468.

Sacks, P. E., Nambiar, C. G., and Walters, L. J., 1997, Dextral Pan–African Shear along the Southwestern Edge of the Achankovil Shear Belt, South India: Constraints on Gondwana Reconstructions: The Journal of Geology, v. 105, no. 2, p. 275-284.

Sanislav, I. V., 2011, A long-lived metamorphic history in the contact aureole of the Mooselookmeguntic pluton revealed by in situ dating of monazite grains preserved as inclusions in staurolite porphyroblasts: Journal of Metamorphic Geology, v. 29, no. 2, p. 251-273.

Santosh, M., 1987, Cordierite gneisses of southern Kerala, India: petrology, fluid inclusions and implications for crustal uplift history: Contributions to Mineralogy and Petrology, v. 96, p. 343-356.

Santosh, M., Maruyama, S., and Sato, K., 2009, Anatomy of a Cambrian suture in Gondwana: Pacific-type orogeny in southern India: Gondwana Research, v. 16, p. 321-341.

Santosh, M., and Omori, S., 2008, CO2 flushing: A plate tectonic perspective: Gondwana Research, v. 13, p. 86-102.

Santosh, M., Tagawa, M., Taguchi, S., and Yoshikura, S., 2003a, The Nagercoil Granulite Block, southern India: petrology, fluid inclusions and exhumation history: Journal of Asian Earth Sciences, v. 22, p. 131-155.

Santosh, M., Yang, Q. Y., Shaji, E., Mohan, M. R., Tsunogae, T., and Satyanarayanan, M., 2016, Oldest rocks from Peninsular India: evidence for Hadean to Neoarchean crustal evolution: Gondwana Research, v. 29, no. 1, p. 105-135.

Santosh, M., Yang, Q. Y., Shaji, E., Tsunogae, T., Mohan, M. R., and Satyanarayanan, M., 2015, An exotic Mesoarchean microcontinent: the Coorg Block, southern India: Gondwana Research, v. 27, no. 1, p. 165–195.

Santosh, M., Yokoyama, K., Biju-Sekhar, S., and Rogers, J. J. W., 2003b, Multiple tectonothermal events in the granulite blocks of southern India revealed from EPMA dating: implications on the history of supercontinents: Gondwana Research, v. 6, no. 1, p. 29-63.

Sauer, S., Slagstad, T., Andersen, T., and Kirkland, C. L., 2013, Zircon Lu-Hf isotopes in high-alumina orthopyroxene megacrysts from the Neoproterozoic Rogaland Anorthosite Province, SW Norway: A window into the Sveconorwegian lower crust: EGU General Assembly Conference Abstracts, v. 15, p. 13958.

Sauter, P. C. C., 1981, Mineral relations in siliceous dolomites and related rocks in the high-grade metamorphic Precambrian of Rogaland, SW Norway: Norsk Geologisk Tidsskrift, v. 61, p. 35-45.

Schaltegger, U., Fanning, C. M., Gűnther, D., Maurin, J. C., Schulmann, K., and Gebauer, D., 1999, Growth, annealing and recrystallization of zircon and preservation of monazite in high-grade metamorphism: conventional and in-situ U-Pb isotope, cathodoluminesecence and microchemical evidence: Contributions to Mineralogy and Petrology, v. 134, p. 186-201.

Schärer, U., 1984, The effect of initial230Th disequilibrium on young UPb ages: the Makalu case, Himalaya: Earth and Planetary Science Letters, v. 67, no. 2, p. 191-204.

Schärer, U., Wilmart, E., and Duchesne, J-C., 1996, The short duration and anorogenic character of anorthosite magmatism: U–Pb dating of the Rogaland complex, Norway: Earth and Planetary Science Letters, v. 139, p. 335-350.

Schmitt, A. K., and Vazquez, J. A., 2017, Secondary Ionization Mass Spectrometry Analysis in Petrochronology: Reviews in Mineralogy and Geochemistry, v. 83, no. 1, p. 199.

Schmitz, M. D., and Bowring, S. A., 2003, Ultrahigh-temperature metamorphism in the lower crust during Neoarchean Ventersdorp rifting and magmatism, Kaapvaal Craton, southern Africa: Geological Society of America Bulletin, v. 115, no. 5, p. 533.

Scibiorski, E., Tohver, E., and Jourdan, F., 2015, Rapid cooling and exhumation in the western part of the Mesoproterozoic Albany-Fraser Orogen, Western Australia: Precambrian Research, v. 265, p. 232-248.

Seydoux-Guillaume, A.-M., Montel, J.-M., Bingen, B., Bosse, V., de Parseval, P., Paquette, J.-L., Janots, E., and Wirth, R., 2012, Low-temperature alteration of monazite: Fluid mediated coupled dissolution–precipitation, irradiation damage, and disturbance of the U–Pb and Th–Pb chronometers: Chemical Geology, v. 330–331, p. 140-158.

Shabeer, K. P., Sajeev, K., Okudaira, T., and Santosh, M., 2002, Two-stage spinel growth in the high-grade metapelites of the central Kerala Khondalite Belt: implications for prograde P–T path: Journal of Geosciences, Osaka City University, v. 45, no. 3, p. 29-43.

Shabeer, K. P., Santish-Kumar, M., Armstrong, R., and Buick, I. S., 2005, Constraints on the timing of Pan-African granulite-facies metamorphism in the Kerala Khondalite Belt of southern India: SHRIMP mineral ages and Nd isotopic systematics: The Journal of Geology, v. 113, no. 1, p. 95-106.

Shannon, R., 1976, Revised effective ionic radii and systematic studies of interatomic distances in halides and chalcogenides: Acta Crystallographica Section A, v. 32, no. 5, p. 751-767.

Shazia, J. R., Harlov, D. E., Suzuki, K., Kim, S. W., Girish-Kumar, M., Hayasaka, Y., Ishwar-Kumar, C., Windley, B. F., and Sajeev, K., 2015, Linking monazite geochronology with fluid infiltration and metamorphic histories: Nature and experiement: Lithos, v. 236-237, p. 1–15.

Sizova, E., Gerya, T., and Brown, M., 2014, Contrasting styles of Phanerozoic and Precambrian continental collision: Gondwana Research, v. 25, no. 2, p. 522-545.

Slagstad, T., Roberts, N. M. W., and Kulakov, E., 2017, Linking orogenesis across a supercontinent; the Grenvillian and Sveconorwegian margins on Rodinia: Gondwana Research, v. 44, p. 109-115.

Slagstad, T., Roberts, N. M. W., Marker, M., Røhr, T. S., and Schiellerup, H., 2013a, A non-collisional, accretionary Sveconorwegian orogen: Terra Nova, v. 25, p. 30-37.

Slagstad, T., Roberts, N. M. W., Marker, M., Røhr, T. S., and Schiellerup, H., 2013b, A non-collisional, accretionary Sveconorwegian orogen - Reply: Terra Nova, v. 25, no. 2, p. 169-171.

Sláma, J., Košler, J., Condon, D. J., Crowley, J. L., Gerdes, A., Hanchar, J. M., Horstwood, M. S. A., Morris, G. A., Nasdala, L., Norberg, N., Schaltegger, U., Schoene, B., Tubrett, M. N., and Whitehouse, M. J., 2008, Plešovice zircon – A new natural reference material for U–Pb and Hf isotopic microanalysis`: Chemical Geology, v. 249, p. 1–35.

Smit, M. A., Scherer, E. E., and Mezger, K., 2013, Lu–Hf and Sm–Nd garnet geochronology: Chronometric closure and implications for dating petrological processes: Earth and Planetary Science Letters, v. 381, p. 222-233.

Smithies, R. H., Howard, H. M., Evins, P. M., Kirkland, C. L., Kelsey, D. E., Hand, M., Wingate, M. T. D., Collins, A. S., and Belousova, E., 2011, High-Temperature Granite Magmatism, Crust–Mantle Interaction and the Mesoproterozoic Intracontinental Evolution of the Musgrave Province, Central Australia: Journal of Petrology, v. 52, no. 5, p. 931-958.

Söderlund, U., and Ask, R., 2006, Mesoproterozoic bimodal magmatism along the Protogine Zone, S Sweden: three magmatic pulses at 1.56, 1.22 and 1.205 Ga, and regional implications: GFF, v. 128, p. 303-310.

Söderlund, U., Elming, S.-Å., Ernst, R. E., and Schissel, D., 2006, The Central Scandinavian Dolerite Group–Protracted hotspot activity or back-arc magmatism? Constraints from U–Pb baddeleyite geochronology and Hf isotopic data: Precambrian Research, v. 150, p. 136-152.

Spear, F. S., and Pyle, J. M., 2010, Theoretical modeling of monazite growth in a low-Ca metapelite: Chemical Geology, v. 273, no. 1–2, p. 111-119.

Spencer, C. J., Kirkland, C. L., and Taylor, R. J. M., 2015, Strategies toward statistically robust interpretations of in situ U–Pb zircon geochronology: Geoscience Frontiers, v. 7, no. 4, p.581-589.

Spencer, C. J., Roberts, N. M. W., Cawood, P. A., Hawkesworth, C. J., Prave, A. R., Antonini, A. S. M., Horstwood, M. S. A., and EIMF, 2014, Intermontane basins and bimodal volcanism at the onset of the Sveconorwegian Orogeny, southern Norway: Precambrian Research, v. 252, p. 107-118.

Srikantappa, C., Raith, M., and Spiering, B., 1985, Progressive charnockitization of a leptynite-khondalite suite in southern Kerala, India-evidence for formation of charnockites through decrease in fluid pressure?: Journal of the Geological Society of India, v. 26, no. 12, p. 849-892.

Stacey, J. S., and Kramers, J. D., 1975, Approximation of terrestrial lead isotope evolution by a two-stage model: Earth and Planetary Science Letters, v. 26, p. 207-221.

Stähle, H. J., Raith, M., Hoernes, S., and Delfs, A., 1987, Element mobility during incipient granulite formation at Kabbaldurga, Southern India: Journal of Petrology, v. 28, no. 5, p. 803-834.

Stepanov, A. S., Hermann, J., Rubatto, D., and Rapp, R. P., 2012, Experimental study of monazite/melt partitioning with implications for the REE, Th and U geochemistry of crustal rocks: Chemical Geology, v. 300–301, p. 200-220.

Stern, R. S., and Amelin, Y., 2003, Assessment of errors in SIMS zircon U–Pb geochronology using a natural zircon standard and NIST SRM 610 glass: Chemical Geology, v. 197, p. 111-142.

Štípská, P., Hacker, B. R., Racek, M., Holder, R., Kylander-Clark, A. R. C., Schulmann, K., and Hasalova, P., 2015, Monazite dating of prograde and retrograde P–T–d paths in the Barrovian terrane of the Thaya window, Bohemian Massif: Journal of Petrology, v. 56, no. 5, p. 1007-1035.

Suzuki, K., and Adachi, M., 1991, Precambrian provenance and Silurian metamorphism of the Tsubonosawa paragneiss in the South Kitakami terrane, Northeast Japan, revealed by the chemical Th-U-total Pb isochron ages of monazite, zircon and xenotime: GEOCHEMICAL JOURNAL, v. 25, no. 5, p. 357-376.

Suzuki, K., and Adachi, M., 1994, Middle Precambrian detrital monazite and zircon from the hida gneiss on Oki-Dogo Island, Japan: their origin and implications for the correlation of basement gneiss of Southwest Japan and Korea: Tectonophysics, v. 235, no. 3, p. 277-292.

Tadokoro, H., Tsunogae, T., and Santosh, M., 2008, Metamorphic P-T path of eastern Trivandrum Granulite Block, southern India: implications for regional correlation of lower crustal fragments: Journal of Mineralogical and Petrological Sciences, v. 103, p. 279-284.

Tajčmanová, L., Konopásek, J., and Košler, J., 2009, Distribution of zinc and its role in the stability of spinel in high-grade felsic rocks of the Moldanubian domain (Bohemian Massif): European Journal of Mineralogy, v. 21, p. 407-418.

Taylor, R., Clark, C., Fitzsimons, I. C. W., Santosh, M., Hand, M., Evans, N., and McDonald, B., 2014, Post-peak, fluid-mediated modification of granulite facies zircon and monazite in the Trivandrum Block, southern India: Contrib Mineral Petrol, v. 168, no. 2, p. 1-17.

Taylor, R., Harley, S. L., Hinton, R. W., Elphick, S., Clark, C., and Kelly, N. M., 2015a, Experimental determination of REE partition coefficients between zircon, garnet and melt: a key to understanding high-T crustal processes: Journal of Metamorphic Geology, v. 33, p. 231–248.

Taylor, R. J. M., Clark, C., Harley, S. L., Kylander-Clark, A. R. C., Hacker, B. R., and Kinny, P. D., 2017, Interpreting granulite facies events through rare earth element partitioning arrays: Journal of Metamorphic Geology, p. 1-17.

Taylor, R. J. M., Clark, C., Johnson, T. E., Santosh, M., and Collins, A. S., 2015b, Unravelling the complexities in high-grade rocks using multiple techniques: the Achankovil Zone of southern India: Contributions to Mineralogy and Petrology, v. 169, no. 5, p. 51.

Taylor, R. J. M., Kirkland, C. L., and Clark, C., 2016, Accessories after the facts: Constraining the timing, duration and conditions of high-temperature metamorphic processes: Lithos, v. 264, p. 239-257.

Taylor-Jones, K., and Powell, R., 2010, The stability of sapphirine + quartz: calculated phase equilibria in FeO–MgO–Al_2O_3–SiO_2–TiO_2–O: Journal of Metamorphic Geology, v. 28, no. 6, p. 615-633.

Tiepolo, M., 2003, In situ Pb geochronology of zircon with laser ablation–inductively coupled plasma–sector field mass spectrometry: Chemical Geology, v. 199, no. 1–2, p. 159-177.

Tobi, A. C., Hermans, G. A. E. M., Maijer, C., and Jansen, B. H., 1985, Metamorphic zoning in the high-grade Proterozoic of Rogaland-Vest Agder, SW Norway: The Deep Proterozoic Crust in the North Atlantic Provinces, p. 477-497.

Tomkins, H. S., and Pattison, D. R. M., 2007, Accessory phase petrogenesis in relation to major phase assemblages in pelites from the Nelson contact aureole, southern British Columbia: Journal of Metamorphic Geology, v. 25, no. 4, p. 401-421.

Tomkins, H. S., Powell, R., and Ellis, D. J., 2007, The pressure dependence of the zirconium-in-rutile thermometer: Journal of Metamorphic Geology, v. 25, no. 6, p. 703-713.

Tomkins, H. S., Williams, I. S., and Ellis, D. J., 2005, In situ U–Pb dating of zircon formed from retrograde garnet breakdown during decompression in Rogaland, SW Norway: Journal of Metamorphic Geology, v. 23, p. 201-215.

Touret, J. L. R., and Huizenga, Jan Marten, 2012, Charnockite microstructures: From magmatic to metamorphic: Geoscience Frontiers, v. 3, no. 6, p. 1-9.

Tucker, N. M., Hand, M., Kelsey, D. E., and Dutch, R. A., 2015, A duality of timescales: Short-lived ultrahigh temperature metamorphism preserving a long-lived monazite growth history in the Grenvillian Musgrave–Albany–Fraser Orogen: Precambrian Research, v. 264, p. 204-234.

Vander Auwera, J., 1993, Diffusion controlled growth of pyroxene-bearing margins on amphibolite bands in the granulite facies of Rogaland (Southwestern Norway): implications for granulite formation: Contributions to Mineralogy and Petrology, v. 114, p. 203-220.

Vander Auwera, J., Bolle, O., Bingen, B., Liégeois, J.-P., Bogaerts, M., Duchesne, J.-C., Waele, B. D., and Longhi, J., 2011, Sveconorwegian massif-type anorthosites and related granitoids result from post-collisional melting of a continental arc root: Earth-Science Reviews, v. 107, p. 375-397.

Vander Auwera, J., Bolle, O., Dupont, A., Pin, C., Paquette, J.-L., Charlier, B., Duchesne, J.-C., Mattielli, N., and Bogaerts, M., 2014, Source-derived heterogeneities in the composite (charnockite-granite) ferroan Farsund intrusion (SW Norway): Precambrian Research, v. 251, p. 141-163.

Vander Auwera, J., and Longhi, J., 1994, Experimental study of a joutunite (hypersthene monzodiorite): constraints on the parent magma composition and crystallization conditions (P, T, fO2) of the Bjerkreim-Sokndal layered intrusion (Norway): Contributions to Mineralogy and Petrology, v. 118, p. 60-78.

Vavra, G., 1990, On the kinematics of zircon growth and its petrogenetic significance: a cathodoluminescence study: Contributions to Mineralogy and Petrology, v. 106, no. 1, p. 90-99.

Vavra, G., Gebauer, D., Schmid, R., and Compston, W., 1996, Multiple zircon growth and recrystallization during polyphase Late Carboniferous to Triassic metamorphism in granulites of the Ivrea Zone (Southern Alps): an ion microprobe (SHRIMP) study: Contributions to Mineralogy and Petrology, v. 122, p. 337-358.

Vavra, G., and Schaltegger, U., 1999, Post-granulite facies monazite growth and rejuvenation during Permian to Lower Jurassic thermal and fluid events in the Ivrea Zone (Southern Alps): Contributions to Mineralogy and Petrology, v. 134, no. 4, p. 405-414.

Verschure, R. H., Andriessen, P. A. M., Boelrijk, N. A. I. M., Hebeda, E. H., Maier, W. D., Priem, H. N. A., and Verdurmen, E. A. T., 1980, On the thermal stability of Rb–Sr and K–Ar biotite systems: evidence from coexisting Sveconorwegian (ca 870 Ma) and Caledonian (ca 400 Ma) biotites in SW Norway: Contributions to Mineralogy and Petrology, v. 74, p. 245-252.

Versteeve, A. J., 1975, Isotope geochronology in the high-grade metamorphic Precambrian of Southwestern Norway: Norges Geol. Unders., v. 318, p. 1-50.

Vielzeuf, D., 1983, The spinel and quartz associations in high grade xenoliths from Tallante (S.E. Spain) and their potential use in geothermometry and barometry: Contributions to Mineralogy and Petrology, v. 82, no. 4, p. 301-311.

Viete, D. R., and Lister, G. S., 2017, On the significance of short-duration regional metamorphism: Journal of the Geological Society, v. 174, no. 3, p. 377.

Villaseca, C., Martín Romera, C., De la Rosa, J., and Barbero, L., 2003, Residence and redistribution of REE, Y, Zr, Th and U during granulite-facies metamorphism: behaviour of accessory and major phases in peraluminous granulites of central Spain: Chemical Geology, v. 200, no. 3–4, p. 293-323.

Walsh, A. K., Kelsey, D. E., Kirkland, C. L., Hand, M., Smithies, R. H., Clark, C., and Howard, H. M., 2015, P–T–t evolution of a large, long-lived, ultrahigh-temperature Grenvillian belt in central Australia: Gondwana Research, v. 28, no. 2, p. 531–564.

Wang, W., Dunkley, E., Clarke, G. L., and Daczko, N. R., 2014, The evolution of zircon during low-P partial melting of metapelitic rocks: theoretical predictions and a case study from Mt Stafford, central Australia: Journal of Metamorphic Geology, v. 32, p. 791-808.

Ward, C. D., McArthur, J. M., and Walsh, J. N., 1992, Rare Earth Element Behaviour During Evolution and Alteration of the Dartmoor Granite, SW England: Journal of Petrology, v. 33, no. 4, p. 785-815.

Watson, E. B., and Harrison, T. M., 1983, Zircon saturation revisited: temperature and composition effects in a variety of crustal magma types: Earth and Planetary Science Letters, v. 64, no. 2, p. 295-304.

Watson, E. B., and Harrison, T. M., 2005, Zircon Thermometer Reveals Minimum Melting Conditions on Earliest Earth: Science, v. 308, no. 5723, p. 841.

Watson, E. B., Wark, D. A., and Thomas, J. B., 2006, Crystallization thermometers for zircon and rutile: Contributions to Mineralogy and Petrology, v. 151, no. 4, p. 413.

Watt, G. R., Burns, I. M., and Graham, G. A., 1996, Chemical characteristics of migmatites: accessory phase distribution and evidence for fast melt segregation rates: Contributions to Mineralogy and Petrology, v. 125, no. 1, p. 100-111.

Westphal, M., Schumacher, J. C., and Boschert, S., 2003, High-Temperature Metamorphism and the Role of Magmatic Heat Sources at the Rogaland Anorthosite Complex in Southwestern Norway: Journal of Petrology, v. 44, no. 6, p. 1145-1162.

Wheller, C. J., and Powell, R., 2014, A new thermodynamic model for sapphirine: calculated phase equilibria in K_2O-FeO-MgO-Al_2O_3-SiO_2-H_2O-TiO_2-Fe_2O_3: Journal of Metamorphic Geology, v. 32, p. 287-299.

White, R. W., and Powell, R., 2002, Melt loss and the preservation of granulite facies mineral assemblages: Journal of Metamorphic Geology, v. 20, p. 621-632.

White, R. W., Powell, R., and Clarke, G. L., 2002, The interpretation of reaction textures in Fe-rich metapelitic granulites of the Musgrave Block, central Australia: constraints from mineral equilibria calculations in the system K_2O-FeO-MgO-Al_2O_3-SiO_2-H_2O-TiO_2-Fe_2O_3: Journal of Metamorphic Geology, v. 20, p. 41-55.

White, R. W., Powell, R., and Holland, T. J. B., 2007, Progress relating to calculation of partial melting equilibria for metapelites: Journal of Metamorphic Geology, v. 25, p. 511-527.

White, R. W., Powell, R., Holland, T. J. B., Johnson, T., and Green, E. C. R., 2014a, New mineral activity-composition relations for thermodynamic calculations in metapelitic systems: Journal of Metamorphic Geology, v. 32, p. 261-286.

White, R. W., Powell, R., and Johnson, T., 2014b, The effect of Mn on mineral stability in metapelites revisited: new a–x relations for manganese-bearing minerals: Journal of Metamorphic Geology, v. 32, p. 809-828.

Whitehouse, M. J., and Kamber, B. S., 2003, A rare earth element study of complex zircons from early Archaean Amîtsoq gneisses, Godthåbsfjord, south-west Greenland: Precambrian Research, v. 126, no. 3–4, p. 363-377.

Whitehouse, M. J., and Platt, J. P., 2003, Dating high-grade metamorphism- constraints from rare-earth elements in zircon and garnet: Contributions to Mineralogy and Petrology, v. 145, p. 61-74.

Whitehouse, M. J., Ravindra Kumar, G. R., and Rimša, A., 2014, Behaviour of radiogenic Pb in zircon during ultrahigh-temperature metamorphism: an ion imaging and ion tomography case study from the Kerala Khondalite Belt, southern India: Contributions to Mineralogy and Petrology, v. 168, no. 2, p. 1042.

Whitney, D. L., and Evans, B. W., 2010, Abbreviations for names of rock-forming minerals: American Mineralogist, v. 95, p. 185-187.

Wielens, J. B. W., Andriessen, P. A. M., Boelrijk, N. A. I. M., Hebeda, E. H., Priem, H. N. A., Verdurmen, E. A. T., and Verschure, R. H., 1981, Isotope geochronology in the High-grade metamorphic Precambrian of Southwestern Norway: new data and reinterpretations: Norges Geol. Unders., v. 359, p. 1-30.

Williams, I. S., Buick, I. S., and Cartwright, I., 1996, An extended episode of early Mesoproterozoic metamorphic fluid flow in the Reynolds Range, central Australia*: Journal of Metamorphic Geology, v. 14, no. 1, p. 29-47.

Williams, I. S., Compston, W., Collerson, K. D., Arriens, P. A., and Lovering, J. F., 1983, A reassessment of the age of the Windmill metamorphics, Casey area: Antarctic Earth Science. Austral Acad Sci, Canberra, p. 73-76.

Williams, M. L., and Jercinovic, M. J., 2002, Microprobe monazite geochronology: putting absolute time into microstructural analysis: Journal of Structural Geology, v. 24, no. 6–7, p. 1013-1028.

Williams, M. L., and Jercinovic, M. J., 2012, Tectonic interpretation of metamorphic tectonites: integrating compositional mapping, microstructural analysis and in situ monazite dating: Journal of Metamorphic Geology, v. 30, no. 7, p. 739-752.

Williams, M. L., Jercinovic, M. J., Goncalves, P., and Mahan, K., 2006, Format and philosophy for collecting, compiling, and reporting microprobe monazite ages: Chemical Geology, v. 225, no. 1–2, p. 1-15.

Williams, M. L., Jercinovic, M. J., Harlov, D. E., Budzyń, B., and Hetherington, C. J., 2011, Resetting monazite ages during fluid-related alteration: Chemical Geology, v. 283, p. 218-225.

Williams, M. L., Jercinovic, M. J., Mahan, K. H., and Dumond, G., 2017, Electron Microprobe Petrochronology: Reviews in Mineralogy and Geochemistry, v. 83, no. 1, p. 153.

Williams, M. L., Jercinovic, M. J., and Terry, M. P., 1999, Age mapping and dating of monazite on the electron microprobe: Deconvoluting multistage tectonic histories: Geology, v. 27, no. 11, p. 1023.

Wilmart, E., Clocchiatti, R., Duchesne, J.-C., and Touret, J. L. R., 1991, Fluid inclusions in charnockites from the Bjerkreim-Sokndal massif (Rogaland, southwestern Norway): fluid origin and in situ evolution: Contributions to Mineralogy and Petrology, v. 108, p. 453-462.

Wilmart, E., and Duchesne, J.-C., 1987, Geothermobarometry of igneous and metamorphic rocks around the Åna-sira anorthosite massif: Implications for the depth of emplacement of the South Norwegian anorthosites: Norsk Geologisk Tidsskrift, v. 67, p. 185-196.

Wing, B. A., Ferry, J. M., and Harrison, T. M., 2003, Prograde destruction and formation of monazite and allanite during contact and regional metamorphism of pelites: petrology and geochronology: Contributions to Mineralogy and Petrology, v. 145, no. 2, p. 228-250.

Wolf, M. B., and London, D., 1994, Apatite dissolution into peraluminous haplogranitic melts: An experimental study of solubilities and mechanisms: Geochimica et Cosmochimica Acta, v. 58, no. 19, p. 4127-4145.

Wu, Y.-B., Gao, S., Zhang, H.-F., Yang, S.-H., Jiao, W.-F., Liu, Y.-S., and Yuan, H.-L., 2008a, Timing of UHP metamorphism in the Hong'an area, western Dabie Mountains, China: evidence from zircon U–Pb age, trace element and Hf isotope composition: Contributions to Mineralogy and Petrology, v. 155, no. 1, p. 123-133.

Wu, Y.-B., Zheng, Y.-F., Gao, S., Jiao, W.-F., and Liu, Y.-S., 2008b, Zircon U–Pb age and trace element evidence for Paleoproterozoic granulite-facies metamorphism and Archean crustal rocks in the Dabie Orogen: Lithos, v. 101, no. 3–4, p. 308-322.

Wu, Y. B., Zheng, Y. F., Zhang, S. B., Zhao, Z. F., Wu, F. Y., and Liu, X. M., 2007, Zircon U–Pb ages and Hf isotope compositions of migmatite from the North Dabie terrane in China: constraints on partial melting: Journal of Metamorphic Geology, v. 25, no. 9, p. 991-1009.

Xie, L., Zhang, Y., Zhang, H., Sun, J., and Wu, F., 2008, In situ simultaneous determination of trace elements, U-Pb and Lu-Hf isotopes in zircon and baddeleyite: Chinese Science Bulletin, v. 53, no. 10, p. 1565-1573.

Yakymchuk, C., 2017, Behaviour of apatite during partial melting of metapelites and consequences for prograde suprasolidus monazite growth: Lithos, v. 274–275, p. 412-426.

Yakymchuk, C., and Brown, M., 2014a, Behaviour of zircon and monazite during crustal melting: Journal of the Geological Society, v. 171, no. 4, p. 465.

Yakymchuk, C., and Brown, M., 2014b, Consequences of open-system melting in tectonics: Journal of the Geological Society, v. 171, no. 1, p. 21.

Yakymchuk, C., Clark, C., and White, R. W., 2017, Phase Relations, Reaction Sequences and Petrochronology: Reviews in Mineralogy and Geochemistry, v. 83, no. 1, p. 13.

Yoshida, M., Santosh, M., and Shirahata, H., 1991, Geochemistry of gneiss-granulite transformation in the “incipient charnockite” zones of southern India: Mineralogy and Petrology, v. 45, p. 69-83.

Yuan, H.-L., Gao, S., Dai, M.-N., Zong, C.-L., Günther, D., Fontaine, G. H., Liu, X.-M., and Diwu, C., 2008, Simultaneous determinations of U–Pb age, Hf isotopes and trace element compositions of zircon by excimer laser-ablation quadrupole and multiple-collector ICP-MS: Chemical Geology, v. 247, no. 1–2, p. 100-118.

Yurimoto, H., Duke, E. F., Papike, J. J., and Shearer, C. K., 1990, Are discontinuous chondrite-normalized REE patterns in pegmatitic granite systems the results of monazite fractionation?: Geochimica et Cosmochimica Acta, v. 54, no. 7, p. 2141-2145.

Zack, T., Moraes, R., and Kronz, A., 2004, Temperature dependence of Zr in rutile: empirical calibration of a rutile thermometer: Contributions to Mineralogy and Petrology, v. 148, no. 4, p. 471-488.

Zhao, L., Zhou, X., Zhai, M., Santosh, M., and Geng, Y., 2015, Zircon U–Th–Pb–Hf isotopes of the basement rocks in northeastern Cathaysia block, South China: Implications for Phanerozoic multiple metamorphic reworking of a Paleoproterozoic terrane: Gondwana Research, v. 28, no. 1, p. 246-261.

Zhou, X., Zhao, G., Wei, C., Geng, Y., and Sun, M., 2008, EPMA U-Th-Pb monazite and SHRIMP U-Pb zircon geochronology of high-pressure pelitic granulites in the Jiaobei massif of the North China Craton: American Journal of Science, v. 308, no. 3, p. 328-350.

Zhu, X. K., and O'Nions, R. K., 1999, Zonation of monazite in metamorphic rocks and its implications for high temperature thermochronology: a case study from the Lewisian terrain: Earth and Planetary Science Letters, v. 171, no. 2, p. 209-220.

Zhu, X. K., O'Nions, R. K., Belshaw, N. S., and Gibb, A. J., 1997, Significance of in situ SIMS chronometry of zoned monazite from the Lewisian granulites, northwest Scotland: Chemical Geology, v. 135, no. 1, p. 35-53.

Appendix A

This appendix contains formatted copies of all published papers contained within this thesis, author contributions and copyright information where required.

Contents:

Statement of Authorship

Title of Paper: Constraints on the timing and conditions of high-grade metamorphism, charnockite formation and fluid–rock interaction in the Trivandrum Block, southern India

Publication Status: ■ Published ☐ Accepted for Publication ☐ Submitted for Publication ☐ Publication Style

Publication Details:
Blereau, E., Clark, C., Taylor, R. J. M., Johnson, T. E., Fitzsimons, I. C. W., and Santosh M., 2016. Constraints on the timing and conditions of high-grade metamorphism, charnockite formation and fluid-rock interaction in the Trivandrum Block, southern India. Journal of Metamorphic Geology, 34, 527–549. doi:10.1111/jmg.12192.

Author Contributions

By signing the Statement of Authorship, each author certifies that their stated contribution to the publication is accurate and that permission is granted for the publication to be included in the candidate's thesis.

Name of Principal Author (Candidate): Eleanore R. Blereau
Contributions to the Paper: Conducted sample preparation, geochronological and geochemical data collection, processing and interpretation, petrography, phase equilibria modelling and drafting the manuscript
Overall percentage: 75%

Signature Date: 7 / 7 /2017

Name of Co-Author: Chris Clark
Contributions to the Paper: Assisted with data interpretation, petrography and editing of the manuscript, field work
Overall percentage: 7%

Signature Digitally signed by Chris Clark Date: 2017.07.07 09:53:25 +08'00' Date: 7 / 7 /2017

Name of Co-Author: Richard J. M. Taylor
Contributions to the Paper: Assisted with geochronological and geochemical data collection, processing and interpretation and editing of the manuscript, field work
Overall percentage: 7%

Signature Date: 7 / 4 /2017

Name of Co-Author: Tim E. Johnson
Contributions to the Paper: Assisted with data interpretation, phase equilibria modelling, petrography and editing of the manuscript
Overall percentage: 7%

Signature Date: 7 / 7 /2017

Name of Co-Author: Ian C. W. Fitzsimons
Contributions to the Paper: Assisted with editing of the manuscript
Overall percentage: 2%

Signature Date: 11 / 4 /2017

Name of Co-Author: M. Santosh
Contributions to the Paper: Assisted with editing of the manuscript and field logistics
Overall percentage: 1%

Signature Date: 28 / 3 /2017

Copyright: Please see below for copyright license for typeset Chapter 2.

JOHN WILEY AND SONS LICENSE
TERMS AND CONDITIONS

Jul 01, 2017

This Agreement between Eleanore R Blereau ("You") and John Wiley and Sons ("John Wiley and Sons") consists of your license details and the terms and conditions provided by John Wiley and Sons and Copyright Clearance Center.

License Number	4140040837595
License date	Jul 01, 2017
Licensed Content Publisher	John Wiley and Sons
Licensed Content Publication	Journal of Metamorphic Geology
Licensed Content Title	Constraints on the timing and conditions of high-grade metamorphism, charnockite formation and fluid–rock interaction in the Trivandrum Block, southern India
Licensed Content Author	E. Blereau,C. Clark,R. J. M. Taylor,T. E. Johnson,I. C. W. Fitzsimons,M. Santosh
Licensed Content Date	May 19, 2016
Licensed Content Pages	23
Type of use	Dissertation/Thesis
Requestor type	Author of this Wiley article
Format	Print and electronic
Portion	Full article
Will you be translating?	No
Title of your thesis / dissertation	A Petrochronological Investigation of Metamorphic, Melt and Fluid Related Processes in Lower Crustal Rocks from Southwestern Norway and Southern India
Expected completion date	Jul 2017
Expected size (number of pages)	300
Requestor Location	Eleanore R Blereau 14 Onslow St Chidlow Perth, Western Australia 6556 Australia Attn: Eleanore R Blereau
Publisher Tax ID	EU826007151
Billing Type	Invoice
Billing Address	Eleanore R Blereau 14 Onslow St Chidlow Perth, Australia 6556 Attn: Eleanore R Blereau
Total	0.00 AUD
Terms and Conditions	

TERMS AND CONDITIONS

This copyrighted material is owned by or exclusively licensed to John Wiley & Sons, Inc. or one of its group companies (each a"Wiley Company") or handled on behalf of a society with which a Wiley Company has exclusive publishing rights in relation to a particular work

(collectively "WILEY"). By clicking "accept" in connection with completing this licensing transaction, you agree that the following terms and conditions apply to this transaction (along with the billing and payment terms and conditions established by the Copyright Clearance Center Inc., ("CCC's Billing and Payment terms and conditions"), at the time that you opened your RightsLink account (these are available at any time at http://myaccount.copyright.com).

Terms and Conditions

- The materials you have requested permission to reproduce or reuse (the "Wiley Materials") are protected by copyright.

- You are hereby granted a personal, non-exclusive, non-sub licensable (on a stand-alone basis), non-transferable, worldwide, limited license to reproduce the Wiley Materials for the purpose specified in the licensing process. This license, **and any CONTENT (PDF or image file) purchased as part of your order,** is for a one-time use only and limited to any maximum distribution number specified in the license. The first instance of republication or reuse granted by this license must be completed within two years of the date of the grant of this license (although copies prepared before the end date may be distributed thereafter). The Wiley Materials shall not be used in any other manner or for any other purpose, beyond what is granted in the license. Permission is granted subject to an appropriate acknowledgement given to the author, title of the material/book/journal and the publisher. You shall also duplicate the copyright notice that appears in the Wiley publication in your use of the Wiley Material. Permission is also granted on the understanding that nowhere in the text is a previously published source acknowledged for all or part of this Wiley Material. Any third party content is expressly excluded from this permission.

- With respect to the Wiley Materials, all rights are reserved. Except as expressly granted by the terms of the license, no part of the Wiley Materials may be copied, modified, adapted (except for minor reformatting required by the new Publication), translated, reproduced, transferred or distributed, in any form or by any means, and no derivative works may be made based on the Wiley Materials without the prior permission of the respective copyright owner.**For STM Signatory Publishers clearing permission under the terms of the STM Permissions Guidelines only, the terms of the license are extended to include subsequent editions and for editions in other languages, provided such editions are for the work as a whole in situ and does not involve the separate exploitation of the permitted figures or extracts,** You may not alter, remove or suppress in any manner any copyright, trademark or other notices displayed by the Wiley Materials. You may not license, rent, sell, loan, lease, pledge, offer as security, transfer or assign the Wiley Materials on a stand-alone basis, or any of the rights granted to you hereunder to any other person.

- The Wiley Materials and all of the intellectual property rights therein shall at all times remain the exclusive property of John Wiley & Sons Inc, the Wiley Companies, or their respective licensors, and your interest therein is only that of having possession of and the right to reproduce the Wiley Materials pursuant to Section 2 herein during the continuance of this Agreement. You agree that you own no right, title or interest in or to the Wiley Materials or any of the intellectual property rights therein. You shall have no rights hereunder other than the license as provided for above in Section 2. No right, license or interest to any trademark, trade name, service mark or other branding ("Marks") of WILEY or its licensors is granted hereunder, and you agree that you shall not assert any such right, license or interest with respect thereto

- NEITHER WILEY NOR ITS LICENSORS MAKES ANY WARRANTY OR REPRESENTATION OF ANY KIND TO YOU OR ANY THIRD PARTY, EXPRESS, IMPLIED OR STATUTORY, WITH RESPECT TO THE MATERIALS OR THE ACCURACY OF ANY INFORMATION CONTAINED IN THE

MATERIALS, INCLUDING, WITHOUT LIMITATION, ANY IMPLIED WARRANTY OF MERCHANTABILITY, ACCURACY, SATISFACTORY QUALITY, FITNESS FOR A PARTICULAR PURPOSE, USABILITY, INTEGRATION OR NON-INFRINGEMENT AND ALL SUCH WARRANTIES ARE HEREBY EXCLUDED BY WILEY AND ITS LICENSORS AND WAIVED BY YOU.

- WILEY shall have the right to terminate this Agreement immediately upon breach of this Agreement by you.
- You shall indemnify, defend and hold harmless WILEY, its Licensors and their respective directors, officers, agents and employees, from and against any actual or threatened claims, demands, causes of action or proceedings arising from any breach of this Agreement by you.
- IN NO EVENT SHALL WILEY OR ITS LICENSORS BE LIABLE TO YOU OR ANY OTHER PARTY OR ANY OTHER PERSON OR ENTITY FOR ANY SPECIAL, CONSEQUENTIAL, INCIDENTAL, INDIRECT, EXEMPLARY OR PUNITIVE DAMAGES, HOWEVER CAUSED, ARISING OUT OF OR IN CONNECTION WITH THE DOWNLOADING, PROVISIONING, VIEWING OR USE OF THE MATERIALS REGARDLESS OF THE FORM OF ACTION, WHETHER FOR BREACH OF CONTRACT, BREACH OF WARRANTY, TORT, NEGLIGENCE, INFRINGEMENT OR OTHERWISE (INCLUDING, WITHOUT LIMITATION, DAMAGES BASED ON LOSS OF PROFITS, DATA, FILES, USE, BUSINESS OPPORTUNITY OR CLAIMS OF THIRD PARTIES), AND WHETHER OR NOT THE PARTY HAS BEEN ADVISED OF THE POSSIBILITY OF SUCH DAMAGES. THIS LIMITATION SHALL APPLY NOTWITHSTANDING ANY FAILURE OF ESSENTIAL PURPOSE OF ANY LIMITED REMEDY PROVIDED HEREIN.
- Should any provision of this Agreement be held by a court of competent jurisdiction to be illegal, invalid, or unenforceable, that provision shall be deemed amended to achieve as nearly as possible the same economic effect as the original provision, and the legality, validity and enforceability of the remaining provisions of this Agreement shall not be affected or impaired thereby.
- The failure of either party to enforce any term or condition of this Agreement shall not constitute a waiver of either party's right to enforce each and every term and condition of this Agreement. No breach under this agreement shall be deemed waived or excused by either party unless such waiver or consent is in writing signed by the party granting such waiver or consent. The waiver by or consent of a party to a breach of any provision of this Agreement shall not operate or be construed as a waiver of or consent to any other or subsequent breach by such other party.
- This Agreement may not be assigned (including by operation of law or otherwise) by you without WILEY's prior written consent.
- Any fee required for this permission shall be non-refundable after thirty (30) days from receipt by the CCC.
- These terms and conditions together with CCC's Billing and Payment terms and conditions (which are incorporated herein) form the entire agreement between you and WILEY concerning this licensing transaction and (in the absence of fraud) supersedes all prior agreements and representations of the parties, oral or written. This Agreement may not be amended except in writing signed by both parties. This Agreement shall be binding upon and inure to the benefit of the parties' successors, legal representatives, and authorized assigns.

- In the event of any conflict between your obligations established by these terms and conditions and those established by CCC's Billing and Payment terms and conditions, these terms and conditions shall prevail.

- WILEY expressly reserves all rights not specifically granted in the combination of (i) the license details provided by you and accepted in the course of this licensing transaction, (ii) these terms and conditions and (iii) CCC's Billing and Payment terms and conditions.

- This Agreement will be void if the Type of Use, Format, Circulation, or Requestor Type was misrepresented during the licensing process.

- This Agreement shall be governed by and construed in accordance with the laws of the State of New York, USA, without regards to such state's conflict of law rules. Any legal action, suit or proceeding arising out of or relating to these Terms and Conditions or the breach thereof shall be instituted in a court of competent jurisdiction in New York County in the State of New York in the United States of America and each party hereby consents and submits to the personal jurisdiction of such court, waives any objection to venue in such court and consents to service of process by registered or certified mail, return receipt requested, at the last known address of such party.

WILEY OPEN ACCESS TERMS AND CONDITIONS
Wiley Publishes Open Access Articles in fully Open Access Journals and in Subscription journals offering Online Open. Although most of the fully Open Access journals publish open access articles under the terms of the Creative Commons Attribution (CC BY) License only, the subscription journals and a few of the Open Access Journals offer a choice of Creative Commons Licenses. The license type is clearly identified on the article.
The Creative Commons Attribution License
The Creative Commons Attribution License (CC-BY) allows users to copy, distribute and transmit an article, adapt the article and make commercial use of the article. The CC-BY license permits commercial and non-
Creative Commons Attribution Non-Commercial License
The Creative Commons Attribution Non-Commercial (CC-BY-NC)License permits use, distribution and reproduction in any medium, provided the original work is properly cited and is not used for commercial purposes.(see below)

Creative Commons Attribution-Non-Commercial-NoDerivs License
The Creative Commons Attribution Non-Commercial-NoDerivs License (CC-BY-NC-ND) permits use, distribution and reproduction in any medium, provided the original work is properly cited, is not used for commercial purposes and no modifications or adaptations are made. (see below)
Use by commercial "for-profit" organizations
Use of Wiley Open Access articles for commercial, promotional, or marketing purposes requires further explicit permission from Wiley and will be subject to a fee.
Further details can be found on Wiley Online Library
http://olabout.wiley.com/WileyCDA/Section/id-410895.html

Other Terms and Conditions:

v1.10 Last updated September 2015

Questions? customercare@copyright.com or +1-855-239-3415 (toll free in the US) or +1-978-646-2777.

The accepted and formatted version of the paper 'Constraints on the timing and conditions of high-grade metamorphism, charnockite formation and fluid–rock interaction in the Trivandrum Block, southern India' is unable to be reproduced here due to copyright restrictions. The paper 'Constraints on the timing and conditions of high-grade metamorphism, charnockite formation and fluid–rock interaction in the Trivandrum Block, southern India' can instead be accessed via DOI: 10.1111/jmg.12192.

Statement of Authorship

Title of Paper: Reappraising the P–T evolution of the Rogaland–Vest Agder Sector, southerwestern Norway

Publication Status: ■ Published ☐ Accepted for Publication ☐ Submitted for Publication ☐ Publication Style

Publication Details:
Blereau, E., Johnson, T. E., Clark, C., Taylor, R. J. M., Kinny, P. D., and Hand, M., 2017. Reappraising the P–T evolution of the Rogaland–Vest Agder Sector, southwestern Norway. Geoscience Frontiers, 8, 1–14. doi: http://dx.doi.org/10.1016/j.gsf.2016.07.003

Author Contributions

By signing the Statement of Authorship, each author certifies that their stated contribution to the publication is accurate and that permission is granted for the publication to be included in the candidate's thesis.

Name of Principal Author (Candidate): Eleanore R. Blereau
Contributions to the Paper: Conducted sample preparation, field work, phase equilibria modelling, petrography, sample interpretation and drafting of the manuscript
Overall percentage: 74%

Signature Date: 7 / 7 /2017

Name of Co-Author: Tim E. Johnson
Contributions to the Paper: Assisted with phase equilibria modelling, petrography, sample interpretation and editing of the manuscript
Overall percentage: 6%

Signature Date: 7 / 7 /2017

Name of Co-Author: Chris Clark
Contributions to the Paper: Assisted with field work, sample interpretation and editing of the manuscript
Overall percentage: 6%

Digitally signed by Chris Clark
Date: 2017.07.07 09:54:30 +08'00'

Signature Date: 7 / 7 /2017

Name of Co-Author: Richard J. M. Taylor
Contributions to the Paper: Assisted with field work, sample interpretation and editing of the manuscript
Overall percentage: 6%

Signature Date: 7 / 4 /2017

Name of Co-Author: Peter D. Kinny
Contributions to the Paper: Assisted with field work, sample interpretation and editing of the manuscript
Overall percentage: 6%

Signature Date: 7 / 7 /2017

Name of Co-Author: Martin Hand
Contributions to the Paper: Assisted with field work and editing of the manuscript
Overall percentage: 2%

Signature Date: 10 / 4 /2017

Geoscience Frontiers 8 (2017) 1–14

HOSTED BY ELSEVIER

Contents lists available at ScienceDirect

China University of Geosciences (Beijing)

Geoscience Frontiers

journal homepage: www.elsevier.com/locate/gsf

Research paper

Reappraising the *P–T* evolution of the Rogaland–Vest Agder Sector, southwestern Norway

Eleanore Blereau [a,*], Tim E. Johnson [a], Chris Clark [a], Richard J.M. Taylor [a], Peter D. Kinny [a], Martin Hand [b]

[a] Department of Applied Geology, The Institute for Geoscience Research (TIGeR), Curtin University, Perth 6845, Western Australia, Australia
[b] Centre for Tectonics, Resources and Exploration (TRaX), School of Earth and Environmental Sciences, University of Adelaide, Adelaide 5005, South Australia, Australia

ARTICLE INFO

Article history:
Received 14 April 2016
Received in revised form
12 July 2016
Accepted 16 July 2016
Available online 10 August 2016

Keywords:
UHT
Phase equilibria modelling
Rogaland Igneous Complex
THERMOCALC
Sveconorwegian Orogen

ABSTRACT

The Rogaland–Vest Agder Sector of southwestern Norway comprises high-grade metamorphic rocks intruded by voluminous plutonic bodies that include the ~1000 km^2 Rogaland Igneous Complex (RIC). New petrographic observations and thermodynamic phase equilibria modelling of three metapelitic samples collected at various distances (30 km, 10 km and ~10 m) from one of the main bodies of RIC anorthosite were undertaken to assess two alternative *P–T–t* models for the metamorphic evolution of the area. The results are consistent with a revised two-phase evolution. Regional metamorphism followed a clockwise *P–T* path reaching peak conditions of ~850–950 °C and ~7–8 kbar at ~1035 Ma followed by high-temperature decompression to ~5 kbar at ~950 Ma, and resulted in extensive anatexis and melt loss to produce highly residual rocks. Subsequent emplacement of the RIC at ~930 Ma caused regional-scale contact metamorphism that affected country rocks 10 km or more from their contact with the anorthosite. This thermal overprint is expressed in the sample proximal to the anorthosite by replacement of sillimanite by coarse intergrowths of cordierite plus spinel and growth of a second generation of garnet, and in the intermediate (10 km) sample by replacement of sapphirine by coarse intergrowths of cordierite, spinel and biotite. The formation of late biotite in the intermediate sample may suggest the rocks retained small quantities of melt produced by regional metamorphism and remained at temperatures above the solidus for up to 100 Ma. Our results are more consistent with an accretionary rather than a collisional model for the Sveconorwegian Orogen.

1. Introduction

The Rogaland–Vest Agder Sector of SW Norway is a metamorphic province dominated by high-grade gneisses and intrusive igneous rocks (Maijer et al., 1981; Tobi et al., 1985; Jansen and Tobi, 1987; Maijer, 1987). Together these rocks represent the core of the *ca.* 1200–900 Ma Sveconorwegian Orogen (Falkum and Petersen, 1980; Falkum, 1985). The intrusive rocks include the Rogaland Igneous Complex (RIC) that is exposed over ~1000 km^2 and comprised largely of three massif-type anorthosite plutons emplaced around 930 Ma (Schärer et al., 1996). Two contrasting tectonic models have been proposed to explain the evolution of the Sveconorwegian Orogen, one involving continent-continent collision (Bingen et al., 2008) and the other involving protracted subduction-accretion (Slagstad et al., 2013a,b; Coint et al., 2015; Roberts and Slagstad, 2015). Collisional models generally require long timescales for the rocks to reach high-grade metamorphism (Clark et al., 2011; Slagstad et al., 2013a,b), whereas in accretionary orogens such conditions may be attained much faster (Slagstad et al., 2013a,b; Coint et al., 2015). However, clockwise *P–T* paths are not diagnostic of either tectonic setting (Brown, 2007).

The role of the RIC in the metamorphic history of the gneisses of the Rogaland–Vest Agder Sector is controversial, and two different *P–T–t* models have been advanced (Fig. 3). Möller et al. (2003) and Tomkins et al. (2005) proposed a two-stage metamorphic evolution, in which an upper amphibolite facies regional event characterized by a clockwise *P–T* evolution was followed by ultra-high

* Corresponding author.
E-mail address: eleanore.blereau@postgrad.curtin.edu.au (E. Blereau).
Peer-review under responsibility of China University of Geosciences (Beijing).

http://dx.doi.org/10.1016/j.gsf.2016.07.003

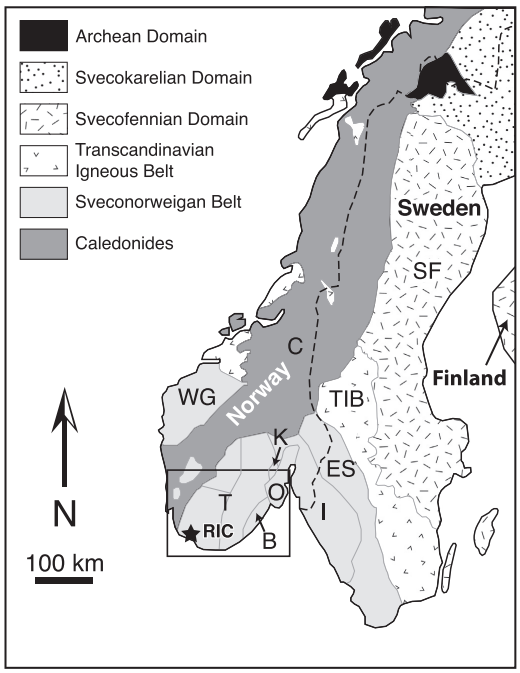

Figure 1. Map showing the main geological subdivisions of Scandinavia (after Bergh et al., 2012). Abbreviations: T – Telemarkia Terrane; B – Bamble Sector; O – Oslo Graben; K – Kongsberg Sector; I – Idefjorden Terrane; ES – Eastern Segment; C – Caledonides; TIB – Transcandinavian Igneous Belt; SF – Svecofennian Domain; WG – Western Gneiss Region.

temperature (UHT) metamorphism at lower pressure related to intrusion of the RIC. By contrast, Drüppel et al. (2013) proposed a single-stage, protracted clockwise regional metamorphic evolution that reached a UHT metamorphic peak some 70 Ma prior to emplacement of the RIC; in this model, high-grade metamorphism and intrusion are considered to have been unrelated.

In this study, we combine new petrographic observations with phase equilibria modelling of three metapelitic samples collected at different distances from the RIC (30 km, 10 km and <50 m) to re-evaluate their metamorphic evolution. We discuss the implications of the results for the tectonic evolution of the Sveconorwegian Belt.

2. Regional geology

The rocks of southern Scandinavia experienced three Proterozoic orogenic events: in Sweden and Finland the *ca.* 1900–1750 Ma Svecofennian orogeny, in SE Norway and Sweden the *ca.* 1750–1550 Ma Gothian orogeny, and in southern Norway and SW Sweden the *ca.* 1200–900 Ma Sveconorwegian orogeny (Andersen et al., 2002). The Sveconorwegian Belt lies to the west of the Svecofennian Domain and the *ca.* 1850–1650 Ma Transcandinavian Igneous Belt and is bounded obliquely to the northwest by the Caledonides (Fig. 1). It comprises a number of lithotectonic domains, including the Eastern Segment, Idefjorden Terrane, Bamble, Kongsberg and Telemarkia Terranes, all of which are bounded by major shear zones (Fig. 1). The Telemarkia Terrane is interpreted to have formed in a short magmatic event between 1520–1480 Ma (Bingen et al., 2005, 2006; Bogdanova et al., 2008; Roberts and Slagstad, 2015) and is further divided into the Telemark, Hardangervidda, Sudal and Rogaland–Vest Agder Sectors (Fig. 2).

The focus of this study, the Rogaland–Vest Agder (RVA) Sector, is a high-grade gneiss complex intruded by voluminous synorogenic plutons that represents the core of the Sveconorwegian Orogen (Falkum and Petersen, 1980; Falkum, 1985). The complex consists of felsic orthogneiss, much of which contains orthopyroxene, and subordinate garnet-bearing paragneiss (Hermans et al., 1975; Falkum, 1982, 1985; Tobi et al., 1985; Bingen et al., 2005; Tomkins et al., 2005; Coint et al., 2015), with minor amphibolite, quartzite, calc-silicate and marble (Huijsmans et al., 1981; Falkum, 1982, 1985; Tobi et al., 1985; Jansen and Tobi, 1987; Bingen et al., 2005; Harlov, 2011). The orthopyroxene-bearing orthogneiss is variably migmatitic, in which migmatised varieties have protolith ages of *ca.* 1450 Ma whereas non-migmatised varieties have younger protolith ages of *ca.* 1230–1210 Ma (Coint et al., 2015). Migmatitic garnet-bearing paragneiss contains abundant garnet as well as sillimanite and/or cordierite-bearing layers indicating pelitic to semi-pelitic protoliths (Hermans et al., 1975; Coint et al., 2015). Detrital zircon U–Pb ages between *ca.* 3000–1200 Ma have been reported from one of these migmatitic metapelites (Tomkins et al., 2005).

The RVA Sector contains three suites of intrusive rocks: (1) the Sirdal Magmatic Belt (SMB); (2) the hornblende-biotite granites (HBG) and (3) the Rogaland Igneous Complex (RIC). The 1060–1020 Ma SMB, which covers an aerial extent of ~10,000 km^2, is a weakly deformed calc-alkaline granitic batholith that preserves igneous textures (Slagstad et al., 2013a,b; Coint et al., 2015). The main constituent is porphyritic biotite granite with lesser amounts of leucogranite, garnet granite and zones rich in xenoliths including migmatitic gneiss (Coint et al., 2015). The arc-like compositions of the SMB (Slagstad et al., 2013a,b) may reflect characteristics inherited from the source rocks, which were probably *ca.* 1500 Ma calc-alkaline metavolcanics and granitoid rocks such as are common in southern Norway, in particular in the Telemark and Hardangervidda Sector (Coint et al., 2015).

The 990–932 Ma HBG suite occurs as discrete 'A-type' plutons that crop out across the Telemarkia Terrane (Bogaerts et al., 2003; Vander Auwera et al., 2011). The range in composition in the HBG Suite from gabbronorite to granite (50–77 wt.% SiO_2) is interpreted to reflect extreme fractional crystallization of several batches of basaltic magma (Bogaerts et al., 2003). The HBG suite was likely derived from an undepleted to slightly depleted hydrous mafic source that was underplated during a previous orogenic event (Bogaerts et al., 2003; Vander Auwera et al., 2011, 2014).

The ~1000 km^2 RIC, also referred to as the Rogaland Anorthosite Complex (Pasteels et al., 1979; Schärer et al., 1996; Bogaerts et al., 2003; Westphal et al., 2003) and Rogaland Anorthosite Province (Sauer et al., 2013; Coint et al., 2015), is composed of three massif-type anorthosites (Egersund-Ogna, Håland-Heleren and Åna-Sira) as well as a large layered polyphase intrusion (Bjerkreim-Sokndal lopolith), two smaller leuconorite bodies (Hidra and Garsaknatt) and a small number of mafic dykes (high-Al gabbros to orthopyroxene monzonorite) (Pasteels et al., 1979; Wilmart et al., 1991; Vander Auwera and Longhi, 1994; Nijland et al., 1996; Schärer et al., 1996; Duchesne and Wilmart, 1997; Bolle et al., 2002; Marker et al., 2003; Möller et al., 2003; Bolle et al., 2010). The three anorthosite massifs contain subophitic aggregates of megacrystic plagioclase and aluminous orthopyroxene within fine-grained leuconorite (Schärer et al., 1996; Bybee et al., 2014). U–Pb ages of zircon and baddeleyite inclusions within orthopyroxene megacrysts in the Egersund-Ogna, Håland-Heleren and Åna-Sira anorthosites are identical within uncertainty at *ca.* 930 Ma (Schärer

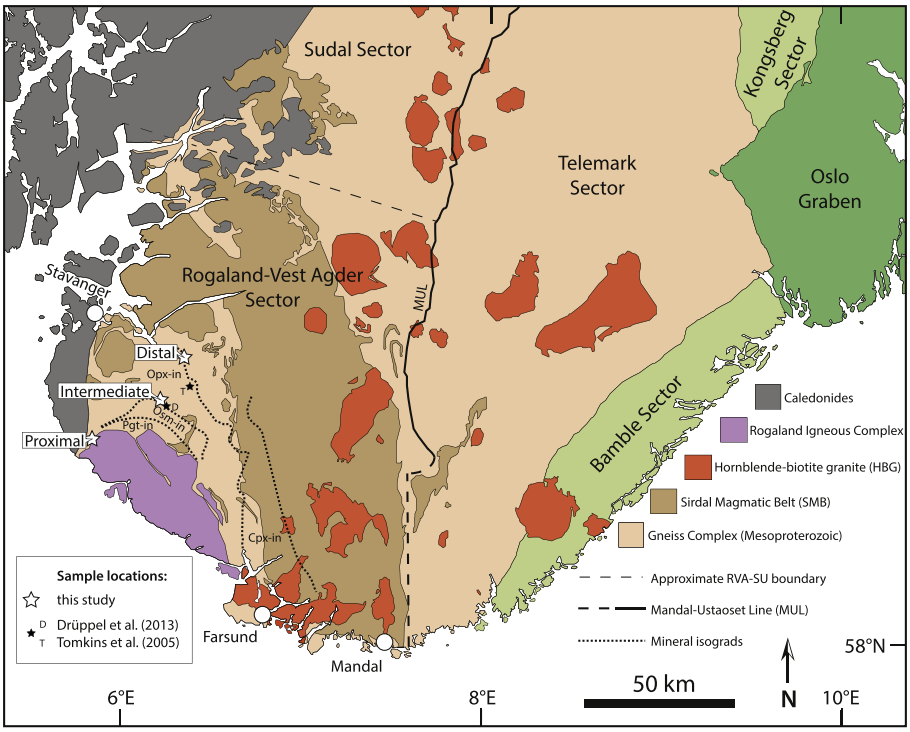

Figure 2. Geological map of the Rogaland–Vest Agder Sector of southwest Norway (after Coint et al. (2015), MUL from Vander Auwera et al. (2011) and mineral isograds from Bolle et al. (2010)). Samples from this study are marked as large white stars with locations from previous studies as smaller black stars.

et al., 1996). Based on the complex spread of zircon U–Pb ages reported by Möller et al. (2003), the RIC suggested by Coint et al. (2015) has a protracted, episodic emplacement history. The margin of the Egersund-Ogna massif has a magmatic foliation parallel to both its boundary and to the foliation of the adjacent host gneisses (Schärer et al., 1996; Bolle et al., 2002) that has been used as evidence for diapiric emplacement of a ~1150 °C crystal mush (Duchesne and Michot, 1987; Longhi et al., 1993; Schärer et al., 1996; Bolle et al., 2002). The anorthosites were emplaced at mid crustal depths (minimum of 5.0–7.7 kbar, ~20–30 km) based on conventional thermobarometry and numerical modelling (Wilmart and Duchesne, 1987; Barnichon et al., 1999).

Within the RIC, the Bjerkreim-Sokndal lopolith is a layered intrusion with four main phases; a basal phase of anorthosite–leuconorite and norite with rhythmic layering is overlain by monzonorite that is in turn overlain by monzonite and, lastly, by quartz monzonite (Versteeve, 1975; Wilmart et al., 1991; Duchesne and Wilmart, 1997; Bolle et al., 2002). The lopolith, which is separated from the anorthosite intrusions by a thin septum of gneissic country rocks, was emplaced at approximately the same time (Wilmart et al., 1991; Vander Auwera and Longhi, 1994; Schärer et al., 1996; Duchesne and Wilmart, 1997). Geochemical and isotopic data indicate that the RIC had a relatively anhydrous, lower crustal source (Bogaerts et al., 2003) with more recent studies suggesting that the parent magmas originated at the Moho with anorthosite formation tied to protracted magmatism in a convergent arc (Bybee et al., 2014). Previous studies suggested multiple parental melt compositions for the RIC suite, with source rocks possibly ranging from high Al-basalt to primitive orthopyroxene monzonorite (Vander Auwera et al., 2011, and references therein).

The high-grade gneisses of the RVA Sector are considered by some authors to have experienced a polymetamorphic evolution, and to preserve textural evidence for a regional metamorphic event followed by a high temperature contact metamorphic overprint (Verschure et al., 1980; Maijer et al., 1981; Wielens et al., 1981; Demaiffe and Michot, 1985; Jansen et al., 1985; Tobi et al., 1985; Maijer, 1987; Bingen and van Breemen, 1998; Möller et al., 2003; Tomkins et al., 2005; Coint et al., 2015). Evidence for an amphibolite facies regional metamorphic event (commonly termed M_1) at *ca.* 1035 Ma (Tomkins et al., 2005) is based on isotopic data from a garnet–biotite–sillimanite metapelite, ~25–30 km from the contact with the RIC (Möller et al., 2003). Coint et al. (2015) also suggested a similar age of regional metamorphism of *ca.* 1030 Ma. The subsequent growth in this rock of cordierite containing zircon dated at *ca.* 955 Ma indicates that peak metamorphic conditions were followed by decompression (shown in red, Fig. 3) (Möller et al., 2003; Tomkins et al., 2005). These events predate the emplacement of the RIC at *ca.* 930 Ma (Schärer et al., 1996), which caused large-scale contact metamorphism (M_2) at UHT conditions (shown in blue, Fig. 3) (Schärer et al., 1996; Möller et al., 2003; Westphal et al., 2003). Pressure–temperature estimates of ~750 °C at 5–7 kbar for the regional event and 700–1050 °C at ~4 kbar for the contact metamorphism were derived using

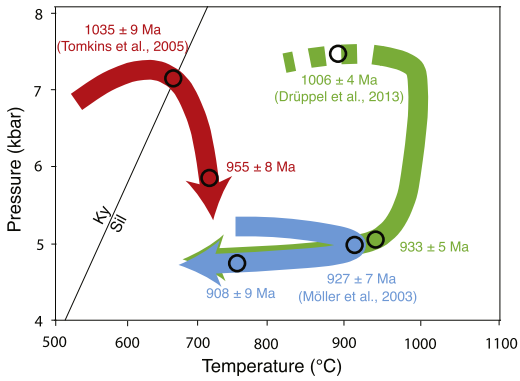

Figure 3. Two alternative *P–T* models proposed for the Rogaland–Vest Agder sector (modified after Drüppel et al., 2013); two-stage metamorphic evolution (Möller et al., 2003; Tomkins et al., 2005) versus protracted, single-stage metamorphic evolution (Drüppel et al., 2013).

conventional thermobarometry (Jansen et al., 1985). A later retrograde overprint (so-called M_3) to upper amphibolite to granulite facies at 908 Ma (550–700 °C and 3–5 kbar) is interpreted to be related to the isobaric cooling of intrusive bodies with the partial replacement of high grade minerals such as osumilite (Kars et al., 1980; Maijer et al., 1981; Wielens et al., 1981; Jansen et al., 1985; Bol et al., 1989; Nijland et al., 1996; Möller et al., 2003; Tomkins et al., 2005; Bolle et al., 2010).

In contrast to the previous interpretations, Drüppel et al. (2013) reinterpreted the gneisses as having experienced a single, long-lived regional metamorphic event that peaked at UHT conditions some 70 Ma prior to intrusion of the RIC (shown in green, Fig. 3). This interpretation, based on phase equilibria modelling in the $Na_2O–CaO–K_2O–FeO–MgO–Al_2O_3–SiO_2–H_2O–TiO_2$ (NCKFMASHT) model system of samples ~10 km from the RIC contact, indicated peak conditions of ~1000 °C at ~7.5 kbar were followed by near isothermal decompression to <5.5 kbar at 900–1000 °C (M_2) before near isobaric cooling (Drüppel et al., 2013). These authors concluded that no second thermal pulse is recorded by the silicate mineral assemblage in the RVA Sector. Zircon U–Pb ages are consistent with a metamorphic age at *ca.* 1000 Ma; epitaxial xenotime yields U–Pb ages within error of the emplacement of the RIC at *ca.* 930 Ma (Drüppel et al., 2013).

A series of high-*T* mineral-in isograds, including inverted pigeonite in felsic orthogneiss, osumilite in paragneiss, orthopyroxene in felsic orthogneiss and clinopyroxene in granodioritic gneiss, are broadly parallel to the margin of the RIC (Fig. 2) (Hermans et al., 1975; Pasteels et al., 1979; Sauter, 1981; Jansen et al., 1985; Tobi et al., 1985; Maijer, 1987; Bol et al., 1989). These isograds represent a temperature range from ~700 °C at the orthopyroxene-in isograd to over 900 °C (UHT) at the pigeonite-in isograd (Jansen et al., 1985; Tobi et al., 1985; Bol et al., 1989; Möller et al., 2002, 2003; Tomkins et al., 2005). Whereas most studies have interpreted the osumilite and pigeonite-in isograds as the products of contact metamorphism at *ca.* 930 Ma superimposed upon granulite to amphibolite-facies regional metamorphic assemblages, others regard the orthopyroxene isograd to pre-date the contact event (Bingen and van Breemen, 1998), More recently, Coint et al. (2015) have proposed that the orthopyroxene-in isograd separates granulite-facies rocks to the west from non-metamorphosed granites to the east and should not be regarded as an isograd at all.

3. Sample descriptions and petrology

Three samples collected from different distances from the RIC–country rock contact were investigated in order to evaluate their metamorphic histories. Hereafter, these samples are referred to as distal (collected ~30 km from the RIC), intermediate (~10 km) and proximal (~10 m), as shown in Fig. 2. Mineral abbreviations follow Kretz (1983) and Whitney and Evans (2010).

3.1. Distal sample (N58°49′49.4″, E6°16′49.2″)

The distal sample (ROG13/11) is a garnet–sillimanite–cordierite metapelite collected a short distance up-grade of the orthopyroxene-in isograd. The sample site, ~400 m NW of Giljastølsvatnet, is ~5 km north of the sample locality of Degeling et al. (2001) and Tomkins et al. (2005) (Fig. 2). The sample is a migmatite comprising melanosome rich in garnet, sillimanite and cordierite and garnet-bearing leucosomes that are continuous at an outcrop scale and oriented sub-parallel to the regional foliation (Fig. 4a).

In thin section, the melanosome contains anhedral garnet porphyroblasts (2–8 mm) within which abundant inclusions of sillimanite define a folded foliation that curves into parallelism with the matrix foliation (Fig. 4b, c) that is also defined by sillimanite (0.2–1 mm). Variably pinitised cordierite (2–6 mm, 10–15%) surrounds garnet, sillimanite, ilmenite and quartz (Fig. 4b, c). Minor feldspar is also present within the matrix. Minor singular grains of ilmenite (0.5–1 mm) are partially to completely replaced by intergrowths of differently orientated rutile and chlorite. The leucosome is composed of sub-equal proportions of quartz (2–6 mm), plagioclase (1–4 mm) and K-feldspar (2–4 mm), along with anhedral to rounded garnet (1–3 mm) that contains abundant inclusions of quartz but no sillimanite (Fig. 4d). Minor biotite is present (0.5–1 mm) along with small amounts of muscovite.

The interpreted peak assemblage in sample ROG13/11 is garnet, sillimanite, plagioclase, K-feldspar, quartz, ilmenite and melt. Matrix garnet containing sillimanite inclusions is interpreted to mainly represent subsolidus growth, whereas leucosome garnet that lacks sillimanite inclusions is regarded as a peritectic product of melting reactions consuming biotite. Cordierite and biotite are considered to be retrograde minerals.

3.2. Intermediate sample (N58°42′9.7″, E6°10′1.4″)

The intermediate sample (ROG13/10) is a residual sapphirine-bearing metapelite from a locality near Ivesdal, ~10 km NE of the RIC contact (Fig. 2), which has been described previously by Hermans et al. (1976) and Drüppel et al. (2013). The exposure consists of irregular, dark sapphirine-bearing layers within a host orthopyroxene-bearing gneiss (Fig. 5). Minor and sporadically dispersed large garnets (~3–8 cm) within the sapphirine-bearing granulite and, less commonly, within the orthopyroxene gneiss have coronae of orthopyroxene with or without plagioclase, and in some cases have been replaced completely (Fig. 5a, b). Garnet-bearing leucosome occurs as rare patches within orthopyroxene gneiss. Sparse quartz veins occur within, and cross-cut both lithologies. Irregular orthopyroxene-rich selvedges and schlieren occur within the orthopyroxene gneiss and occasionally along contacts between orthopyroxene gneiss and sapphirine-bearing metapelite.

In thin section, subhedral to euhedral sapphirine porphyroblasts (1–8 mm, 10–15%) are partially to completely replaced by coarse intergrowths of spinel and cordierite, along with variable amounts of biotite that appears to be replacing cordierite (Fig. 6a, b, d). The matrix consists of cordierite (0.5–3 mm), orthopyroxene

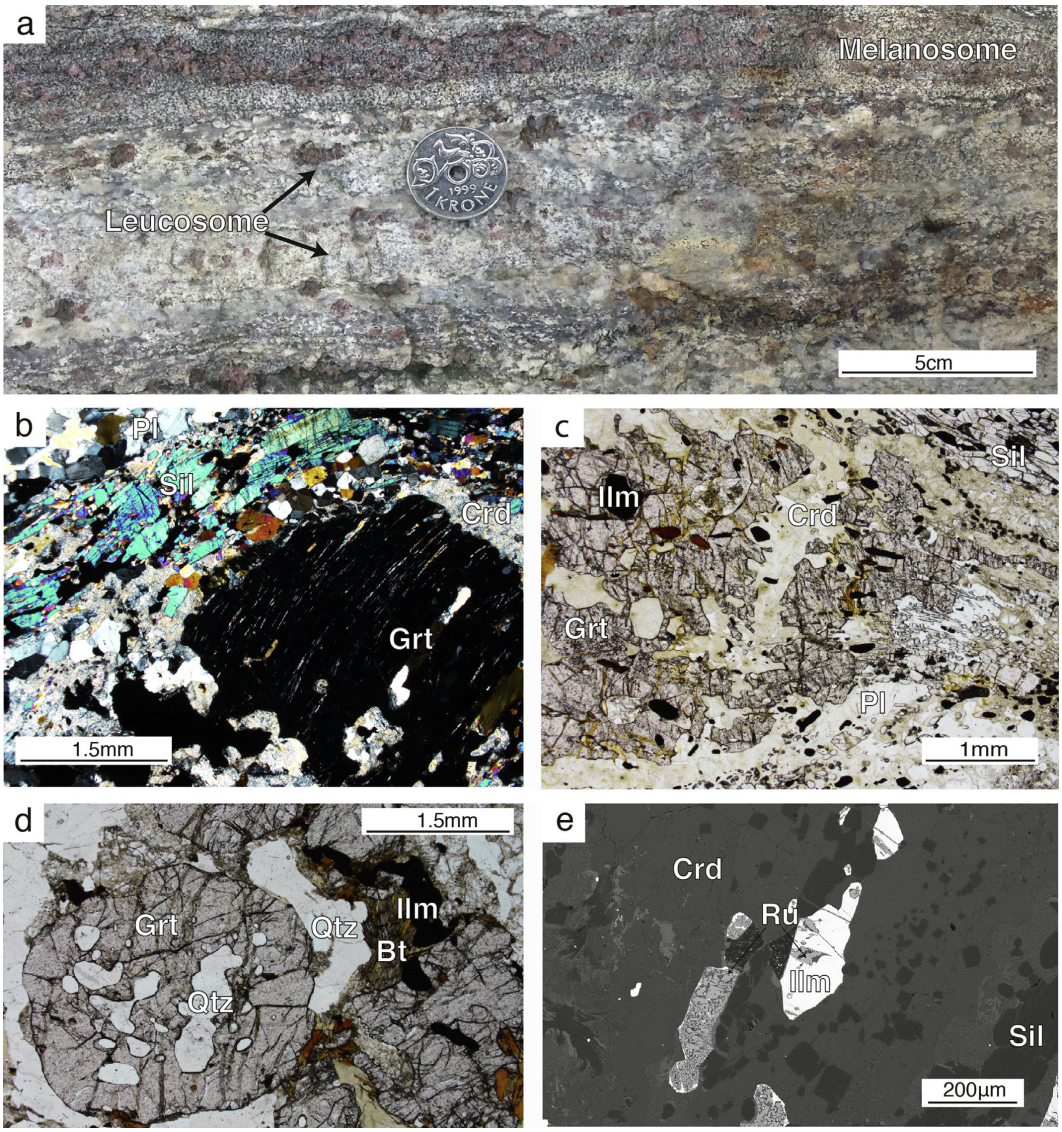

Figure 4. Field photograph and photomicrographs from the 'Distal' locality. (a) Garnet–cordierite–sillimanite melanosome with garnet-bearing leucosome at outcrop scale. (b) Garnet porphyroblast within melanosome (xpl) containing ilmenite, sillimanite and minor biotite inclusions, surrounded by pinitised cordierite and sillimanite. (c) Garnet porphyroblast within melanosome with sillimanite inclusions defining a relict foliation. Coarse sillimanite in the matrix defines a new foliation. (d) Peritectic garnet with quartz inclusions within leucosome, with late biotite. (e) Back scattered electron (BSE) image showing ilmenite being replaced by an intergrowth of rutile and chlorite within the melanosome.

(0.5–3 mm), plagioclase (0.5–2 mm), K-feldspar (0.5–1 mm) and biotite (up to 2 mm) (Fig. 6c). Orthopyroxene grains are separated from sapphirine porphyroblasts by layers of cordierite and spinel plus cordierite (Fig. 6a, b). Feldspar grains are variably sericitised. Spinel contains ilmenite and minor exsolved magnetite. Quartz is absent.

We interpret sample ROG13/10 to have contained an earlier assemblage of sapphirine, orthopyroxene, plagioclase, K-feldspar, cordierite, ilmenite and melt that later underwent replacement of sapphirine and orthopyroxene by coarse intergrowths of spinel and cordierite. Subsequent growth of biotite may reflect retrograde reaction in the presence of melt.

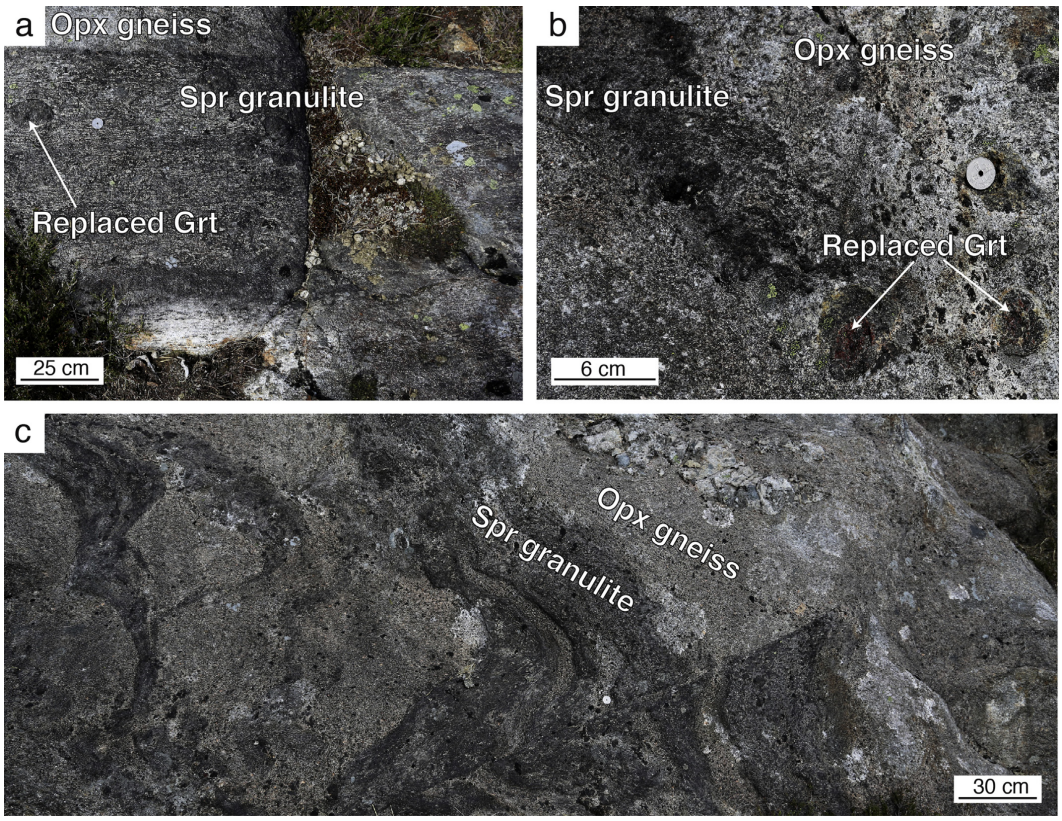

Figure 5. Field photographs from the 'Intermediate' locality. (a) Dark sapphirine granulite layer with completely replaced garnet. (b) Sapphirine granulite and orthopyroxene gneiss containing partially replaced garnets with orthopyroxene coronas. (c) Irregular dark layers of sapphirine granulite interleaved with orthopyroxene gneiss, cut by minor faults.

3.3. *Proximal sample (N58°35′46.5″, E5°46′59.0″)*

The proximal sample ROG14/5 is from country rocks ~10 m from the northwest margin of the RIC (Fig. 2). The sample is a migmatitic garnet–sillimanite–spinel–cordierite metapelitic gneiss (Fig. 7a) that is intruded by several small sheets of garnet-bearing anorthosite (Fig. 7b). The metapelite consists of melanosome rich in garnet and cordierite, within which occurs narrow, foliation-parallel leucosome layers (<1 cm in width). Larger (~0.5–1 m) irregular bodies of garnet-bearing and garnet-free leucosome cross-cut the foliation and contain schollen of melanosome (Fig. 7a). Minor quartz veins are also present. The anorthosite sheets are discontinuous, up to 15 cm wide and 4 m in length and oriented parallel to the foliation (Fig. 7b).

In thin section, sample ROG14/5 is dominated by melanosome containing equant to elongate anhedral garnet porphyroblasts (0.5–4 mm) containing sillimanite inclusions (Fig. 7c, d). A second generation of garnet forms narrow (~100 μm) rims around pre-existing garnet porphyroblasts and adjacent to spinel (Fig. 7c, d). Coarse matrix sillimanite (0.5–4 mm) defines a foliation that wraps around garnet, and is partially replaced by intergrowths of spinel plus cordierite (Fig. 7d). Spinel occurs both within the symplectite and as aggregates of grains surrounded by a thin rind of cordierite or garnet (Fig. 7d). The leucosome contains large (2–8 mm) slightly elongate grains along with smaller (0.5–2 mm) grains of quartz, plagioclase (1–2 mm) and K-feldspar (1–2 mm). Cordierite surrounds garnet, sillimanite and, less commonly, quartz and spinel (1–2 mm) and is sometimes intergrown with K–feldspar (Fig. 7d). Minor ilmenite is partially to completely replaced by late intergrowths of rutile and chlorite.

This sample is interpreted to contain an earlier assemblage of garnet, sillimanite, plagioclase, K-feldspar, quartz, spinel, ilmenite and melt. Replacement of sillimanite by cordierite plus spinel, and growth of a second generation of garnet occurred subsequently.

4. Phase equilibria modelling

Metamorphic *P–T* conditions were constrained using *P–T*, *P–X* and *T–X* pseudosections modelled in the Na_2O–CaO–K_2O–FeO–MgO–Al_2O_3–SiO_2–H_2O–TiO_2–O system using THERMOCALC 3.40i and the internally consistent thermodynamic dataset of Holland and Powell (2011) (specifically the tc-ds62 dataset generated on 06/02/2014). Activity–composition models are from White et al. (2014a). Although Mn-bearing solution models have been

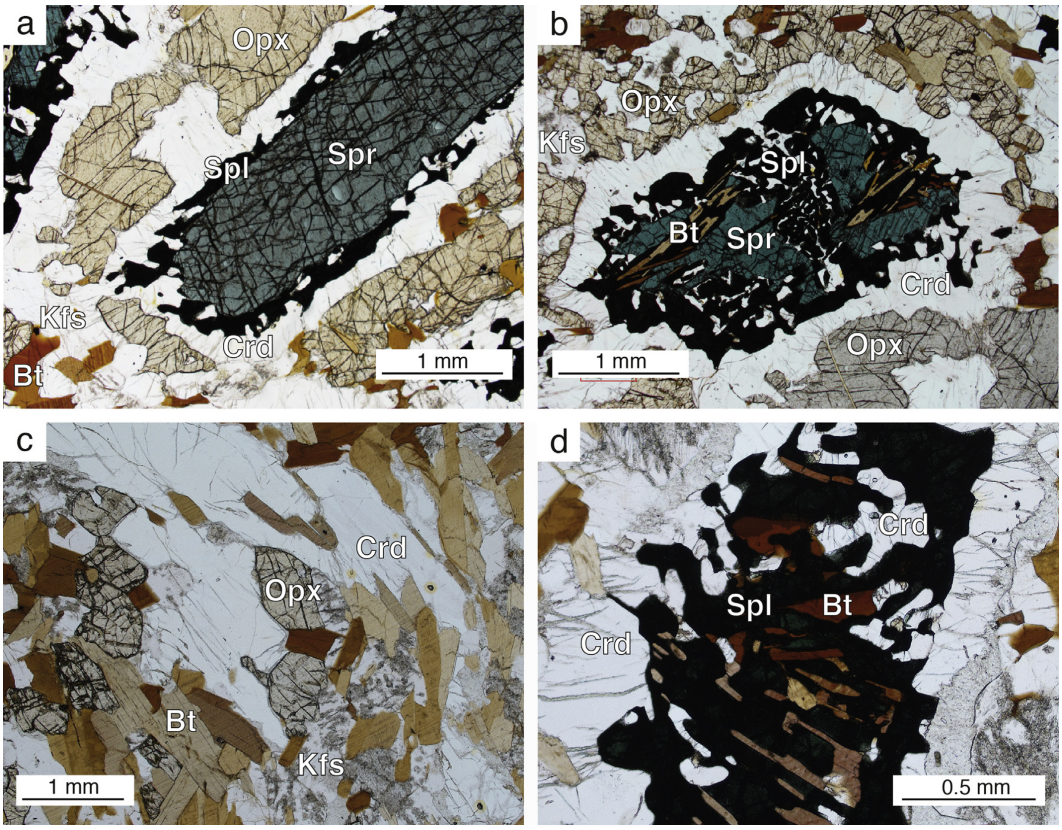

Figure 6. Photomicrographs from the 'Intermediate' locality. (a) Sapphirine porphyroblast rimmed by spinel plus cordierite and a cordierite rim separating the symplectite from orthopyroxene. (b) Sapphirine partially replaced by a spinel–cordierite symplectite, with later biotite replacing cordierite within the symplectite. An outer rim of cordierite is present between the symplectite and orthopyroxene. (c) Irregular grains of orthopyroxene and cordierite within the matrix with some grains almost completely surrounded by late biotite. (d) Spinel plus cordierite symplectite with biotite partially replacing cordierite.

calibrated (White et al., 2014b), Mn has a negligible effect at high temperatures and was not considered (Johnson et al., 2015). Calculations consider the phases garnet, silicate melt, plagioclase, K-feldspar, sillimanite, sapphirine, quartz, muscovite, biotite, orthopyroxene, cordierite, ilmenite, rutile and magnetite-spinel. Osumilite was not included as there is no solution model calibrated against the ds6 dataset.

Bulk rock compositions were determined by X-ray fluorescence analysis using a Panalytical 2404 XRF unit at Franklin and Marshall College, Pennsylvania, for which ferric and ferrous iron contents were determined by titration. The bulk compositions (expressed as mol.% oxides) used in the pseudosections are given in Table 1. Modelled H_2O contents were constrained using *T–X* or *P–X* pseudosections ranging from a quantity assuming all analysed loss on ignition (LOI) as H_2O to lower values (0.1 mol.%). The H_2O content chosen for *P–T* modelling was such that the solidus intersected, or was as close as possible to the field containing the interpreted peak assemblage (see Supplementary data Figs. S1–3). Calculations using the composition of the distal sample (ROG13/11), the most altered of the studied rocks, measured ferric iron concentrations were too high with all calculated fields containing magnetite, which is not observed in the rock. Thus, to account for post-peak oxidation, appropriate ferric iron contents were constrained using a *P–X* pseudosection ranging from the titrated value (1.31 mol.% Fe_2O_3) to a minimal content (0.01 mol.%; see Supplementary data Fig. S4). A value of X = 0.5 (Fe_2O_3 = O = 0.67 mol.%) was chosen, as it is the minimum required to eliminate magnetite from the interpreted peak assemblage. Note that the stability field of spinel in nature is likely to be larger than the calculated stability due to the presence of minor components (e.g. Zn, V, Cr) that cannot currently be modelled (Tajčmanová et al., 2009). Drüppel et al. (2013) reported average concentrations of Cr_2O_3 and ZnO in spinel in the sapphirine-bearing sample as 0.07 and 0.15 wt.%, respectively. For reference, *P–T* pseudosections contoured for the abundance of particular phases calculated using TCInvestigator (Pearce et al., 2015) are given in the Supplementary data (Fig. S5).

4.1. Distal sample

In the *P–T* pseudosection for sample ROG13/11 (Fig. 8), the solidus for the chosen H_2O content is located at ~830 °C at pressures above 7 kbar. Between 6–7 kbar the solidus inflects to higher

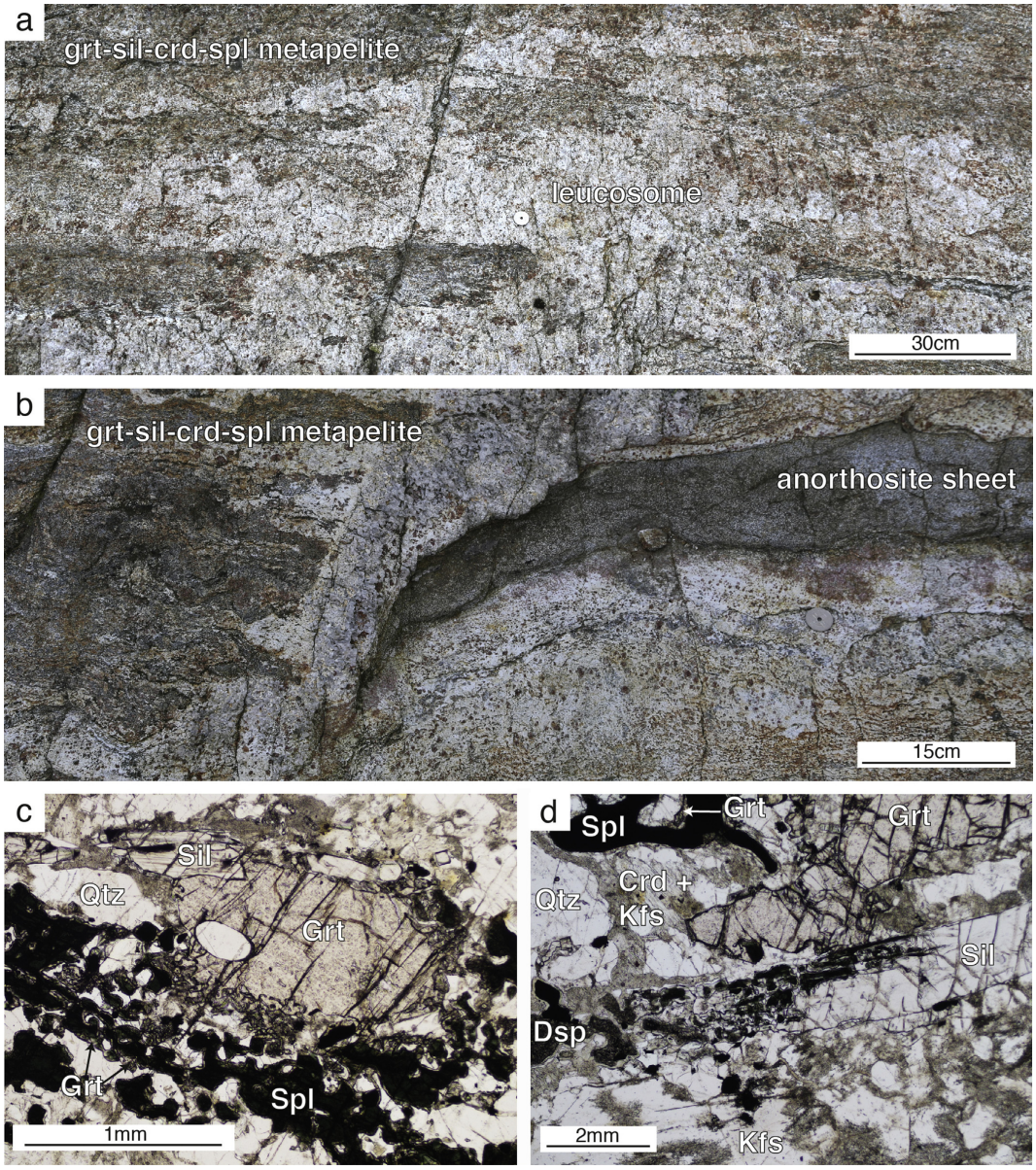

Figure 7. Field photographs and photomicrographs from the 'Proximal' locality. (a) Garnet–sillimanite–cordierite–spinel migmatite overprinted by a large irregular garnet-bearing leucosome containing schollen of the metapelite. (b) Metapelite with intruded anorthosite sheet. (c) Garnet porphyroblast with secondary garnet overgrowing spinel. (d) Sillimanite partly replaced by spinel plus cordierite, with some of the spinel replaced by diaspore.

temperatures (~970 °C) due to the presence of cordierite that partitions some of the H_2O that at higher pressures is contained within melt. For the chosen ferric iron content and *P*–*T* range, ilmenite is stable throughout and magnetite is predicted only at low temperatures and pressures. The interpreted peak assemblage of garnet, sillimanite, plagioclase, K-feldspar, quartz, ilmenite and melt occupies a large stability field at >850 °C and >6 kbar (outlined in red, Fig. 8). At lower temperatures biotite is stable, and at lower pressures cordierite, which occurs replacing garnet at its margins, is predicted. The calculated stability fields of spinel and

Table 1
Bulk compositions as molar oxide (mol.%) used in phase equilibria modelling.

Sample	SiO_2	TiO_2	Al_2O_3	O	FeO	MgO	CaO	Na_2O	K_2O	H_2O	Total
ROG13/11 (Distal)	68.95	0.78	12.95	0.67	6.86	3.68	1.39	1.82	2.80	0.10	100
ROG13/10 (Intermediate)	51.45	0.64	14.98	1.13	6.73	17.99	1.33	1.78	2.94	1.03	100
ROG14/5 (Proximal)	63.19	0.83	16.71	0.57	9.29	4.85	1.28	1.11	2.06	0.11	100

orthopyroxene occur at higher temperatures and lower pressures than the inferred peak, respectively.

4.2. Intermediate sample

In the *P–T* pseudosection for sample ROG13/10 (Fig. 9) the solidus for the chosen H_2O content is located at ~900–950 °C. The stability field for the interpreted earlier assemblage of sapphirine, orthopyroxene, plagioclase, K-feldspar, cordierite, ilmenite and melt is relatively narrow (in *T*) between 910–980 °C and between 4 and 8 kbar (outlined in red, Fig. 9). Cordierite is consumed at higher *T* and biotite is predicted at lower *T*, and garnet is stable at higher *P* and spinel at lower *P*. Compositional isopleths of Al–in–orthopyroxene are shown in Fig. 9. Maximum measured values of *X*(Al) (Al cations in the formula unit based on six oxygens) from samples from this locality are 0.18 according to Drüppel et al. (2013), and this isopleth, along with the one sigma uncertainty on its position, is shown as the shaded field. The measured Al content in orthopyroxene is consistent with the higher pressure part of the preferred peak field, implying peak conditions of around 7–8 kbar and 900–950 °C (Fig. 9). The subsequent evolution of the rock, expressed by the growth of cordierite, spinel and biotite at the expense of sapphirine, requires significantly lower pressures but similar temperatures that was followed by cooling into fields containing biotite.

4.3. Proximal sample

In the *P–T* pseudosection for proximal sample ROG14/5 (Fig. 10), the solidus for the chosen H_2O content is located at ~815 °C above 6.3 kbar but inflects to higher temperatures (~950–975 °C) below 6 kbar due to the presence of cordierite which partitions some of the H_2O that, at higher pressures, is contained within melt. The interpreted earlier assemblage of garnet, sillimanite, plagioclase, K-feldspar, quartz, ilmenite and melt but without spinel, defines a large stability field at 820 to >1000 °C and ~6 to >10 kbar (outlined in red, Fig. 10); spinel is predicted to become stable at higher temperatures. As spinel may be stabilised by non-system components, our preferred interpretation is that the earlier assemblage is consistent with the high *T* end of the modelled spinel-absent field or with the field containing spinel (i.e. >900 °C and >6 kbar). The subsequent evolution of this sample, indicated by the replacement of sillimanite by cordierite and spinel and the growth of a second generation of garnet and cordierite (shown by the arrow in Fig. 10), require lower pressures (~5–6 kbar) but similar temperatures.

5. Discussion

5.1. P–T conditions of regional metamorphism

At a distance of ~30 km from the contact, the distal sample is considered to be beyond the effects of contact metamorphism associated with the emplacement of the RIC and to preserve the regional metamorphic history. This is supported by a pronounced regional foliation and the lack of symplectitic replacement of porphyroblast phases that characterises the other samples. Petrographic observations coupled with phase equilibria modelling suggest that this sample experienced a clockwise regional *P–T* path, reaching peak conditions of >850 °C at >6 kbar. Partial replacement of garnet by cordierite implies high-temperature decompression to conditions of ~850 °C at 5 kbar, while the growth of biotite implies crystallisation of the last vestiges of melt upon cooling. A *P–T* path consistent with these observations is shown in Fig. 8. Peak conditions are poorly constrained due to the size and the calculated compositional and modal homogeneity of the phases within the inferred peak field. The high temperature subsolidus prograde path is constrained to the sillimanite field, with no evidence for the former presence of kyanite.

The inferred early assemblages developed within the intermediate sample (sapphirine, orthopyroxene, plagioclase, K-feldspar, cordierite, ilmenite and melt) and the proximal sample (garnet, sillimanite plagioclase, K-feldspar, quartz, ilmenite, spinel and melt), are similarly consistent with growth during regional metamorphism. Modelling of these compositions gives *P–T* conditions that are similar to those derived for the distal sample, namely 900–950 °C and ~7–8 kbar for the intermediate sample (Fig. 9) and >900 °C and >6 kbar for the proximal sample (Fig. 10). Clearly,

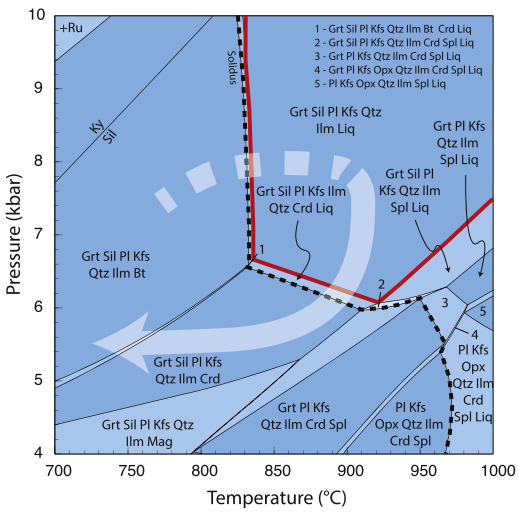

Figure 8. Modelled *P–T* pseudosection of the distal sample (ROG13/11) with peak field outlined in red and solidus marked by a black dashed line. The interpreted, clockwise *P–T* path traces the post-peak growth of cordierite and biotite. Positioning of the *P–T* path is based on modal isopleths generated using TCInvestigator (Pearce et al., 2015).

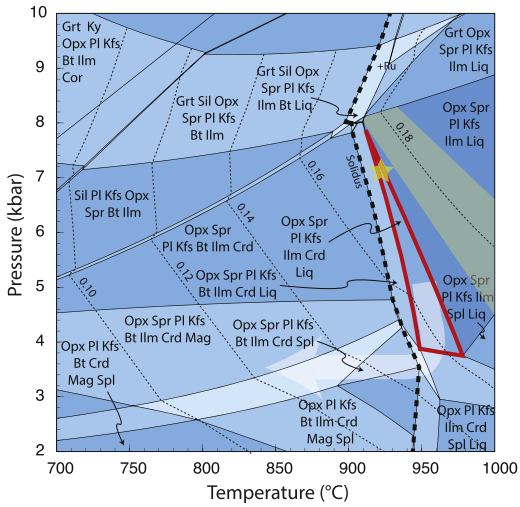

Figure 9. Modelled *P–T* pseudosection of the intermediate sample (ROG13/10) with peak field outlined in red, solidus marked by a black dashed line and y(opx) isopleths marked by fine dashed lines labelled with their respective values. Grey shaded area indicates uncertainty on the y(opx) = 0.18 isopleth. The presence of garnet defines the upper pressure limit of the peak assemblage, while cordierite defines the lower temperature limit. The star indicates the interpreted peak conditions reached during regional metamorphism. The illustrated portion of the *P–T* path traces the growth of spinel and cordierite and later biotite. Positioning of the *P–T* path is based on modal isopleths generated using TCInvestigator (Pearce et al., 2015).

all three samples cannot have followed an identical regional *P–T* path. However, we propose that a generalised, clockwise regional metamorphic evolution was experienced by all samples, which attained peak conditions of around 850–950 °C at 7–8 kbar, and

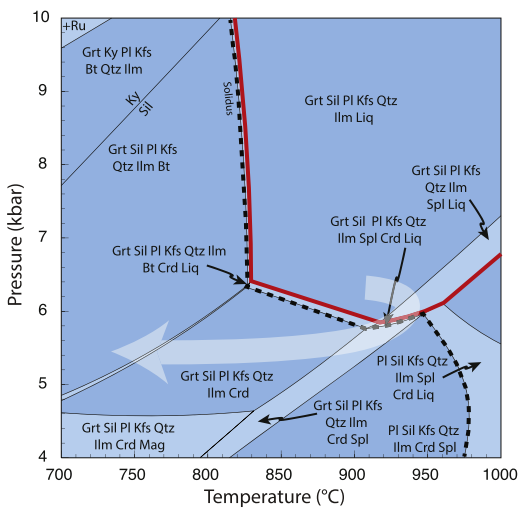

Figure 10. Modelled *P–T* pseudosection of the proximal sample (ROG14/5) with peak field outline in red and solidus marked by a black dashed line. The interpreted *P–T* path traces the growth of spinel, cordierite and secondary garnet.

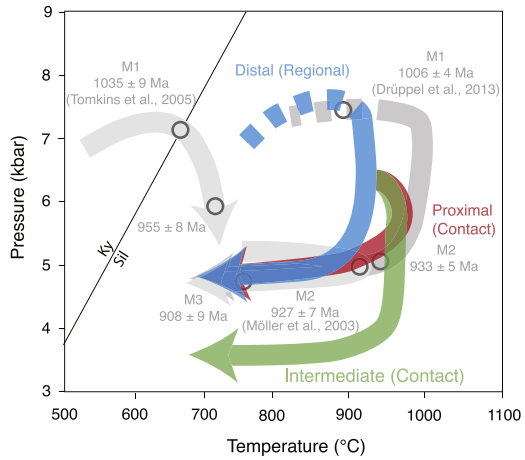

Figure 11. Summary diagram of the revised *P–T* evolution of the RVA Sector, with previous models in grey. Interpreted *P–T* evolution for the distal (blue), intermediate (green) and proximal (red) samples. The dashed approximate prograde evolution is based on the lack of kyanite in all samples.

was followed by high-temperature decompression to ~5 kbar, followed by near isobaric cooling (Fig. 8). Under such conditions, pelitic and greywacke protoliths will produce significant quantities of melt (Johnson et al., 2008; White et al., 2014a), most of which will have been lost to higher crustal levels to leave low $a(H_2O)$ granulite facies residua, consistent with observation.

Clockwise regional *P–T* paths were proposed by both Tomkins et al. (2005) and Drüppel et al. (2013). However, our inferred regional peak conditions are at least ~200 °C higher than those reported by Tomkins et al. (2005) based on conventional thermobarometry, and ~50 °C lower than the UHT regional conditions proposed by Drüppel et al. (2013), based on phase equilibria modelling (Fig. 11). Possible reasons for these differences are detailed below.

5.2. *P–T* conditions of contact metamorphism

Petrographic observations of the intermediate and proximal samples in conjunction with phase equilibria modelling suggest a two-stage evolution which we equate to: (1) high- to ultra-high *T* regional metamorphism with associated partial melting and melt loss (detailed above); and (2) subsequent high- to ultra-high *T* contact metamorphism of the residual rocks caused by emplacement of the RIC.

Importantly, the distal and proximal samples have strikingly similar bulk compositions, confirmed by the similarity in the *P–T* pseudosections for each (see Figs. 8 and 10). However, the petrographic features of the rocks are very different. Both are inferred to have had a regional peak assemblage containing garnet, sillimanite, plagioclase, K-feldspar, quartz, ilmenite, and melt, with the proximal sample inferred to have additionally contained a small quantity of spinel. However, the proximal sample contains a second generation of garnet (and spinel) that is lacking from the distal sample. In addition, sillimanite in the proximal sample is extensively replaced by a coarse intergrowth of cordierite plus spinel, whereas sillimanite in the distal sample is pristine. We interpret the coarse intergrowths of cordierite and spinel after sapphirine in the intermediate sample and after sillimanite in the proximal sample as

prograde reaction products that formed as a result of heating associated with emplacement of the RIC. Similar prograde reaction textures have been described elsewhere (Pitra and Waal, 2001; White et al., 2002; Johnson et al., 2004).

In the proximal sample, the reaction textures are consistent with contact metamorphic conditions of ~950 °C at ~5 kbar (Figs. 10 and 11). In the intermediate sample, the reaction textures are consistent with temperatures of ~950 °C and lower pressures of ~3–4 kbar (Figs. 9 and 11). The lower pressures inferred for the intermediate sample suggests it was at higher levels in the crust when the RIC was emplaced and implies tilting of the section and/or differential uplift and erosion post intrusion of the RIC. Overall, the pressures inferred for the contact metamorphism (3–6 kbar, Fig. 11) are similar to those reported by other authors (Möller et al., 2003; Tomkins et al., 2005). The high temperatures inferred for the contact metamorphism in the intermediate sample may suggest the anorthosite sits at shallow levels beneath these rocks. However, with no borehole data, the similarity in density between the anorthosite and host gneisses makes this difficult to test using geophysical means.

Within the intermediate sample, the growth of biotite replacing cordierite in the spinel-cordierite symplectites, which are themselves replacing sapphirine, suggests that the rocks may have retained small quantities of melt and that, on cooling and exhumation from the regional peak, the intermediate sample did not cross the solidus before the onset of contact metamorphism. This could indicate that the rocks stayed at high temperature for 100 Ma or more.

Our interpretation that the intermediate and proximal samples followed a two-stage *P–T* evolution (Fig. 11), with contact metamorphism superimposed upon the regional metamorphic evolution path, differs from the work of Drüppel et al. (2013). These authors suggest the rocks followed a clockwise, single-stage regional metamorphic evolution peaking at UHT conditions based on their interpretation that the age of UHT metamorphism predates the intrusion of the RIC. We suggest that the 1021 ± 23 to 999 ± 17 Ma metamorphic ages of Drüppel et al. (2013) may represent growth of zircon from crystallising melt following peak metamorphism at *ca.* 1035 Ma (Tomkins et al., 2005).

5.3. *P–T* evolution of the RVA sector

We present a revised *P–T* evolution for gneisses of the RVA Sector during the Sveconorwegian orogeny: For rocks outside the influence of the RIC (our distal sample), regional metamorphism followed a clockwise *P–T* path with peak conditions of ~850–950 °C at ~7–8 kbar followed by high-temperature, retrograde decompression to conditions of ~900 °C at 5 kbar and, subsequently, isobaric cooling to below 700 °C (Fig. 11). Whereas the distal sample preserves no compelling evidence for having experienced contact metamorphism, rocks closer to the RIC (our intermediate and proximal samples) contain evidence for a static thermal overprint (contact metamorphism) that records pressures of 3–6 kbar and reached a maximum temperature in the sample immediately adjacent to the RIC contact of over 950 °C.

The proposed *P–T* evolution outlined in this study reconciles the previous interpretations made by Degeling et al. (2001) and Drüppel et al. (2013). Degeling et al. (2001) underestimated the temperature of peak regional metamorphism by ~200 °C, due to their reliance on petrogenetic grids in the KFMASH model system, which is an oversimplification of natural rocks (White et al., 2007, 2014a), and by their use of conventional thermobarometric techniques which, due to post-peak diffusion, commonly lead to underestimates of peak temperatures (Fitzsimons and Harley, 1994; Pattison et al., 2003). Assuming our results are reliable, Drüppel et al. (2013) overestimated the temperature experienced by the rocks at Ivesdal, our intermediate locality, by ~50 °C. This is most likely due to their omission of ferric iron (modelled as O) from their model system, that affects the bulk X(Mg) of the modelled composition. In particular, these authors used an older solution model for sapphirine that does not include ferric iron, which can significantly reduce the temperature at which sapphirine is stable (Kelsey et al., 2005; Wheller and Powell, 2014). Furthermore, Drüppel et al. (2013) relied in part on spinel to constrain their *P–T* trajectories. However, the presence of elements such as Cr and Zn that are not currently incorporated into thermodynamic models, will stabilise spinel to lower temperatures than predicted by the pseudosection modelling (Tajčmanová et al., 2009).

5.4. Implications for the tectonic setting of the Sveconorwegian orogeny

The revised metamorphic evolution proposed here has implications for tectonic models for the development of the RVA Sector during the Sveconorwegian orogeny. There are at present two different tectonic models for the Sveconorwegian orogeny, a continent-continent collisional model proposed by Bingen et al. (2008) and an accretionary model of Slagstad et al. (2013a), which has been further refined by Coint et al. (2015). The collisional model postulates that at ~1140 Ma Fennoscandia collided with an as yet unidentified continent (possibly Amazonia), resulting in widespread Barrovian-type regional metamorphism. At ~930 Ma a phase of orogenic collapse was initiated that resulted in the emplacement of the RIC and formation of a regional-scale UHT contact aureole (Bingen et al., 2008). The long timescales of high-temperature conditions interpreted in this study are sufficient for the generation of high-grade metamorphic conditions within a collisional system (Clark et al., 2011). However, the lack of any obvious colliding continental block and the evidence for a series of magmatic events with arc-like chemistry that post-date the proposed collision led Slagstad et al. (2013a) to develop an alternative Andean-style accretionary model to explain the geological evolution of SW Norway. According to Slagstad et al. (2013a), the long-lived accretionary margin underwent periodic extension and compression (as a result of steep and flat slab subduction) and to alternate between periods of metamorphism (1020–990 Ma) and magmatism (1050–1020 and 990–920 Ma) to generate the SMB, HBG and RIC suites.

In contrast to the *P–T–t* proposed by Drüppel et al. (2013), which consists of a single clockwise *P–T* loop with UHT metamorphism occurring 10–15 Myr after the cessation of SMB magmatism, Slagstad and co-workers argued that the metamorphic history of rocks in SW Norway could not have been produced by a collisional orogeny (Slagstad et al., 2013b). They suggest that to generate temperatures of ~1000 °C at mid to lower crustal depths in a collisional system requires on the order of *ca.* 100 Ma (e.g. Clark et al., 2011; Clark et al., 2015).

All of the available evidence from this and previous studies indicates that a period of crustal thickening must have occurred prior to the attainment of peak regional metamorphic conditions (Bingen et al., 2008; Drüppel et al., 2013; Slagstad et al., 2013a). Possible mechanisms for crustal thickening include collision, flat-slab subduction and accretion. Whilst continental collision is a key part of the four-phase model of Bingen et al. (2008), with subduction interpreted to have ceased at 1140 Ma, this is inconsistent with the presence of the 1060–1020 Ma calc-alkaline SMB as well as the presence of contemporaneous and later arc-related features across the terranes of the Sveconorwegian Belt. These include the widespread arc geochemical signatures (Brewer et al., 2002; Andersen et al., 2007; Corfu and Laajoki, 2008; Petersson et al., 2015),

multiple periods of back-arc basin formation (Brewer et al., 2002; Söderlund and Ask, 2006; Söderlund et al., 2006; Andersen et al., 2007; Spencer et al., 2014; Petersson et al., 2015) and related bimodal magmatism (Söderlund and Ask, 2006; Bingen et al., 2008; Corfu and Laajoki, 2008; Spencer et al., 2014) as well as the overall younging to the west caused by westerly arc retreat with subduction beneath Fennoscandia (Slagstad et al., 2013a; Spencer et al., 2014 and references within; Coint et al., 2015; Petersson et al., 2015; Roberts and Slagstad, 2015).

Flat-slab subduction has been previously proposed by Slagstad et al. (2013a) to have driven crustal thickening and develop medium–*P*, high–*T* regional metamorphism within the geographically restricted area of the RVA Sector. This interpretation is consistent with magmatism starting 15 Myr prior to the onset of regional metamorphism, in which the magmas could not have been produced from partial melting related to crustal thickening (Slagstad et al., 2013a,b). Therefore, we therefore favour the Slagstad et al. (2013a) accretionary model for the RVA Sector. Similar styles of accretionary tectonics have been invoked to form regional-scale granulite facies terranes in a number of other Mesoproterozoic Orogens (Karlstrom et al., 2001; Clark et al., 2014; Korhonen et al., 2014) and have been singled out as sites of crustal growth and granulite generation throughout Earth history (Collins, 2002; Cawood and Buchan, 2007), at least since the Archaean.

More problematic is exactly how the RIC formed. Most geochronology of the RIC indicates that it was emplaced in a restricted time span at ~930 Ma. However, Coint et al. (2015) hypothesised that it may have had a protracted, episodic emplacement history based on the complex spread of zircon U–Pb ages that may record multiple intrusive events and resulted in the formation of complex growth and dissolution of zircon and monazite over an extended time interval (<1000 Ma to 920 Ma) (Möller et al., 2003 and references within). In the absence of unequivocal geochronological evidence that suggests emplacement over a prolonged period, we favour a short-lived intrusive event at ~930 Ma, with magmas emplaced into rocks that still retained small amounts of melt. Small volumes of melt in the rocks could have resulted in the reported zircon textures (Möller et al., 2003) and a single thermal pulse is consistent with the relatively simple petrographic textures documented in this study and the pluton sub-parallel isograds observed at the map scale. There is no clear evidence for slab breakoff as the causal mechanism for generation of the RIC. Recent work by Bybee et al. (2014) suggested that the RIC formed as part of a long-lived magmatic system, consistent with an accretionary setting. It is difficult to determine what caused the end of the Sveconorwegian orogeny as this margin was significantly modified during the Caledonian orogeny, leaving no obvious geological record of what previously lay to the west.

6. Conclusions

(1) Regional metamorphism in the RVA Sector during the Sveconorwegian orogeny followed a clockwise *P–T* path attaining peak conditions of ~850–950 °C and ~7–8 kbar at *ca.* 1035 Ma. Partial melting and melt loss led to the production of highly residual rock compositions.
(2) Rocks located up to at least 10 km from the RIC experienced an additional static, low-pressure, high-temperature event ~100 Myr after the peak of regional metamorphism that reached a maximum *T* of ~950 °C at 3–6 kbar. The source of this additional heat was the RIC itself, which was emplaced into slightly cooler but residual crust and resulted in the series of high-*T* isograds concentric with its margin.
(3) The collisional model of Bingen et al. (2008) cannot satisfactorily explain the metamorphic and magmatic evolution of the Sveconorwegian orogeny in the RVA Sector as it lacks a plausible heat source to drive UHT metamorphism. A model that has the Sveconorwegian Orogen as an east facing accretionary margin that experienced long-lived subduction associated with periods of flat slab subduction, rollback and arc accretion, akin to that proposed by Slagstad et al. (2013a,b) better explains the metamorphic and magmatic evolution of the RVA Sector.

Acknowledgements

We thank two anonymous reviewers for their detailed comments and Prof. M. Santosh for his editorial handling. Financial support for this project was provided by an ARC DECRA fellowship (DE120103067) to CC.

Appendix A. Supplementary data

Supplementary data related to this article can be found at http://dx.doi.org/10.1016/j.gsf.2016.07.003.

References

Andersen, T., Griffin, W.L., Pearson, N.J., 2002. Crustal evolution in the SW part of the Baltic Shield: the Hf isotope evidence. Journal of Petrology 43 (9), 1725–1747.
Andersen, T., Griffin, W.L., Sylvester, A.G., 2007. Sveconorwegian crustal underplating in southwestern Fennoscandia: LAM-ICPMS U-Pb and Lu-Hf isotope evidence from granites and gneisses in Telemark, southern Norway. Lithos 93, 273–287.
Barnichon, J.D., Havenith, H., Hoffer, B., Charlier, R., Jongmans, D., Duchesne, J.C., 1999. The deformation of the Egersund-Ogna anorthosite massif, south Norway: finite-element modelling of diapirism. Tectonophysics 303, 109–130.
Bergh, S.G., Chattopadhya, A., Ravna, E.K., Corfu, F., Kullerud, K., Swaan, K.B., Armitage, P.E.B., Myhre, P.I., Holdsworth, R.E., 2012. Was the Precambrian basement of Western Troms and Lofoten-Vesterålen in northern Norway linked to the Lewisian of Scotland? A comparison of crustal components, tectonic evolution and amalgamation history. In: Sharkov, E. (Ed.), Tectonics – Recent Advances. In Tech Open Access Publisher, pp. 283–330.
Bingen, B., Nordgulen, Ø., Viola, G., 2008. A four-phase model for the Sveconorwegian orogeny, SW Scandinavia. Norwegian Journal of Geology 88, 43–72.
Bingen, B., Skår, Ø., Marker, M., Sigmond, E.M.O., Nordgulen, Ø., Ragnhildstveit, J., Mansfeld, J., Tucker, R.D., Liégeois, J.-P., 2005. Timing of continental building in the Sveconorwegian orogen, SW Scandinavia. Norwegian Journal of Geology 85, 87–116.
Bingen, B., Stein, H.J., Bogaerts, M., Bolle, O., Mansfeld, J., 2006. Molybdenite Re–Os dating constrains gravitational collapse of the Sveconorwegian orogen, SW Scandinavia. Lithos 87, 328–346.
Bingen, B., van Breemen, O., 1998. U–Pb monazite ages in amphibolite- to granulite-facies orthogneiss reflect hydrous mineral breakdown reactions: Sveconorwegian Province of SW Norway. Contributions to Mineralogy and Petrology 132, 336–353.
Bogaerts, M., Scaillet, B., Liégeois, J.-P., Vander Auwera, J., 2003. Petrology and geochemistry of the Lyngdal granodiorite (Southern Norway) and the role of fractional crystallization in the genesis of proterozoic ferro-potassic A-type granites. Precambrian Research 124, 149–184.
Bogdanova, S.V., Bingen, B., Gorbatschev, R., Kheraskova, T.N., Kozlov, V.I., Puchkov, V.N., Volozh, Y.A., 2008. The East European craton (Baltica) before and during the assembly of Rodinia. Precambrian Research 160, 23–45.
Bol, L.C.G.M., Maijer, C., Jansen, B.H., 1989. Premetamorphic lateritisation in proterozoic metabasites of Rogaland, SW Norway. Contributions to Mineralogy and Petrology 103, 306–316.
Bolle, O., Diot, H., Liégeois, J.-P., Auwera, J.V., 2010. The Farsund intrusion (SW Norway): a marker of late-Sveconorwegian (Grenvillian) tectonism emplaced along a newly defined major shear zone. Journal of Structural Geology 32, 1500–1518.
Bolle, O., Trindade, R.I.F., Bouches, J.L., Duchesne, J.-C., 2002. Imaging downward granitic transport in the Rogaland Igneous Complex, SW Norway. Terra Nova 14, 87–92.
Brewer, T.S., Åhäll, K.I., Darbyshire, D.P.F., Menuge, J.F., 2002. Geochemistry of late mesoproterozoic volcanism in southwestern Scandinavia: implications for Sveconorwegian/Grenvillian plate tectonic models. Journal of the Geological Society, London 159, 129–144.
Brown, M., 2007. Metamorphic conditions in orogenic belts: a record of secular change. International Geology Review 49, 193–234.
Bybee, G.M., Ashwal, L.D., Shirey, S.B., Horan, M., Mock, T., Andersen, T.B., 2014. Pyroxene megacrysts in proterozoic anorthosites: implications for tectonic setting, magma source and magmatic processes at the Moho. Earth and Planetary Science Letters 389, 74–85.

Cawood, P.A., Buchan, C., 2007. Linking accretionary orogenesis with supercontinent assembly. Earth-Science Reviews 82, 217–256.

Clark, C., Fitzsimons, I.C.W., Healy, D., Harley, S.L., 2011. How does the continental crust get really hot? Elements 7, 235–240.

Clark, C., Healy, D., Johnson, T., Collins, A.S., Taylor, R., Santosh, M., Timms, N.E., 2015. Hot orogens and supercontinent amalgamation: a Gondwanan example from southern India. Gondwana Research 28 (4), 1310–1328.

Clark, C., Kirkland, C.L., Spaggiari, C.V., Oorschot, C., Wingate, M.T.D., Taylor, R.J., 2014. Proterozoic granulite formation driven by mafic magmatism: an example from the Fraser Range Metamorphics, Western Australia. Precambrian Research 240, 1–21.

Coint, N., Slagstad, T., Roberts, N.M.W., Marker, M., Røhr, T.S., Sørensen, B.E., 2015. The Late Mesoproterozoic Sirdal Magmatic Belt, SW Norway: relationships between magmatism and metamorphism and implications for Sveconorwegian orogenesis. Precambrian Research 265, 57–77.

Collins, W.J., 2002. Hot orogens, tectonic switching, and creation of continental crust. Geology 30 (6), 535–538.

Corfu, F., Laajoki, K., 2008. An uncommon episode of mafic magmatism at 1347 Ma in the mesoproterozoic Telemark supracrustals, Sveconorwegian orogen–implications for stratigraphy and tectonic evolution. Precambrian Research 160, 299–307.

Degeling, H., Eggins, S., Ellis, D.J., 2001. Zr budgets for metamorphic reactions, and the formation of zircon from garnet breakdown. Mineralogical Magazine 65 (6), 749–758.

Demaiffe, D., Michot, J., 1985. Isotope geochronology of the Proterozoic crustal segment of Southern Norway: a review. In: Tobi, A.C., Touret, J.L.R. (Eds.), The Deep Proterozoic Crust in the North Atlantic Provinces. D. Reidel Publishing Co, pp. 411–435.

Drüppel, K., Elsäßer, L., Brandt, S., Gerdes, A., 2013. Sveconorwegian mid-crustal ultrahigh-temperature metamorphism in Rogaland, Norway: U-Pb LA-ICP-MS geochronology and pseudosections of sapphrine granulites and associated paragneisses. Journal of Petrology 54 (2), 305–350.

Duchesne, J.-C., Wilmart, E., 1997. Igneous charnockites and related rocks from the Bjerkreim-Sokndal layered intrusion (Southwest Norway): a jotunite (hypersthene monzodiorite)-derived A-type granitoid suite. Journal of Petrology 38 (3), 337–369.

Duchesne, J.C., Michot, J., 1987. The Rogaland intrusive masses: introduction. In: Maijer, C., Padget, P. (Eds.), The Geology of Southernmost Norway, Norges Geologisk Undersøkelse Special Publication, vol. 1, pp. 48–59.

Falkum, T., 1982. Geologisk kart over Norge, berggrunnskart MANDAL, 1:250,000. Norges Geologisk Undersøkelse.

Falkum, T., 1985. Geotectonic evolution of southern Scandinavia in light of a late-proterozoic plate-collision. In: Tobi, A.C., Touret, J.L.R. (Eds.), The Deep Proterozoic Crust in the North Atlantic Provinces. D. Reidel Publishing Co, pp. 309–322.

Falkum, T., Petersen, J.S., 1980. The Sveconorwegian orogenic belt, a case of late-proterozoi plate-collision. Geologische Rundschau 69 (3), 622–647.

Fitzsimons, I.C.W., Harley, S.L., 1994. The influence of retrograde cation exchange on granulite P–T estimates and a convergence technique for the recovery of peak metamorphic conditions. Journal of Petrology 35 (2), 543–576.

Harlov, D.E., 2011. Petrological and experimental application of REE- and actinide-bearing accessory mineral to the study of Precambrian high-grade gneiss terrains. Geological Society of America Memoirs 207, 13–24.

Hermans, G.A.E.M., Hakstege, A.L., Jansen, J.B.H., Poorter, R.P.E., 1976. Sapphrine occurrence near Vikeså in Rogaland, Southwestern Norway. Norsk Geologisk Tidsskrift 56, 397–412.

Hermans, G.A.E.M., Tobi, A.C., Poorter, R.P.E., Maijer, C., 1975. The high-grade metamorphic Precambrian of the Sirdal-Ørsdal area, Rogaland/Vest-Agder, South-west Norway. Norges Geologisk Undersøkelse 318, 51–74.

Holland, T.J.B., Powell, R., 2011. An improved and extended internally consistent thermodynamic dataset for phases of petrological interest, involving a new equation of state for solids. Journal of Metamorphic Geology 29, 333–383.

Huijsmans, J.P.P., Kabel, A.B.E.T., Steenstra, S.E., 1981. On the structure of high-grade metamorphic Precambrian terrain in Rogaland, south Norway. Norsk Geologisk Tidsskrift 61, 183–192.

Jansen, B.H., Blok, R.J.P., Bos, M., Scheelings, M., 1985. Geothermometry and geobarometry in Rogaland and preliminary results from the Bamble area, S Norway. In: Tobi, A.C., Touret, J.L.R. (Eds.), The Deep Proterozoic Crust in the North Atlantic Provinces. D. Reidel Publishing Co, pp. 499–516.

Jansen, B.H., Tobi, A.C., 1987. Introduction to the Faurefjell metasediments. In: Maijer, C., Padget, P. (Eds.), The Geology of Southernmost Norway, Norges Geologisk Undersøkelse Special Publication, vol. 1, pp. 88–89.

Johnson, T., Brown, M., Gibson, R., Wing, B., 2004. Spinel-cordierite symplectites replacing andalusite: evidence for melt-assisted diapirism in the Bushveld Complex, South Africa. Journal of Metamorphic Geology 22, 529–545.

Johnson, T., Clark, C., Taylor, R., Santosh, M., Collins, A.S., 2015. Prograde and retrograde growth of monazite in migmatites: an example from the Nagercoil Block, southern India. Geoscience Frontiers 6 (3), 373–387.

Johnson, T.E., White, R.W., Powell, R., 2008. Partial melting of metagreywacke – a calculated mineral equilibria study. Journal of Metamorphic Geology 26, 837–853.

Karlstrom, K.E., Åhäll, K.I., Harlan, S.S., Williams, M.L., McLelland, J., Geissman, J.W., 2001. Long-lived (1.8-1.0 Ga) convergent orogen in southern Laurentia, its extensions to Australia and Baltica, and implications for refining Rodinia. Precambrian Research 111, 5–30.

Kars, H., Jansen, B.H., Tobi, A.C., Poorter, R.P.E., 1980. The metapelitic rocks of the polymetamorphic Precambrian of Rogaland, SW Norway: part II- mineral relations between cordierite, hercynite and magnetite within the osumilite-in isograd. Contributions to Mineralogy and Petrology 74, 235–244.

Kelsey, D.E., White, R.W., Powell, R., 2005. Calculated phase equilibria in K_2O–FeO–MgO–Al_2O_3–SiO_2–H_2O for silica-undersaturated sapphrine-bearing mineral assemblages. Journal of Metamorphic Geology 23, 217–239.

Korhonen, F.J., Clark, C., Brown, M., Taylor, R.J.M., 2014. Taking the temperature of Earth's hottest crust. Earth and Planetary Science Letters 408, 341–354.

Kretz, R., 1983. Symbols for rock-forming minerals. American Mineralogist 68, 277–279.

Longhi, J., Fram, M.S., Auwera, J.V., Montieth, J.N., 1993. Pressure effects, kinetics, and rheology of anorthositic and related magmas. American Mineralogist 78, 1016–1030.

Maijer, C., 1987. The metamorphic envelope of the Rogaland intrusive complex. Norges Geologisk Undersøkelse – Special Publication 1, 68–73.

Maijer, C., Andriessen, P.A.M., Hebeda, E.H., Jansen, B.H., Verschure, R.H., 1981. Osumilite, an approximately 970 Ma old high-temperature index mineral of the granulite-facies metamorphism in Rogaland, SW Norway. Geologie en Mijnbouw 60, 267–272.

Marker, M., Schiellerup, H., Meyer, G., Robins, B., Bolle, O., 2003. Introduction to the geological map of the Rogaland Anorthosite Province 1:75000. Norges Geologisk Undersøkelse – Special Publication 9, 109–116.

Möller, A., O'Brien, P.J., Kennedy, A., Kröner, A., 2002. Polyphase zircon in ultrahigh-temperature granulites (Rogaland, SW Norway): constraints for Pb diffusion in zircon. Journal of Metamorphic Geology 20, 727–740.

Möller, A., O'Brien, P.J., Kennedy, A., Kröner, A., 2003. Linking growth episodes of zircon and metamorphic textures to zircon chemistry: an example from the ultrahigh-temperature granulites of Rogaland (SW Norway). In: Vance, D., Müller, W., Villa, I.M. (Eds.), Geochronology: Linking the Isotopic Record with Petrology and Textures, The Geological Society, London, Special Publications, vol. 220, pp. 65–81.

Nijland, T.G., Maijer, C., de Haas, G.-J.L.M., 1996. The Stokkafjell Troctolite, SW Norway: its bearing on the early P-T evolution of the Rogaland terrane. Neues Jahrbuch fur Mineralogie Abhandlungen 171, 91–117.

Pasteels, P., Demaiffe, D., Michot, J., 1979. U–Pb and Rb–Sr geochronology of the eastern part of the south Rogaland igneous complex, southern Norway. Lithos 12, 199–208.

Pattison, D.R.M., Chacko, T., Farquhar, J., McFarlane, R.M., 2003. Temperature of granulite-facies metamorphism: constraints from experimental phase equilibria and thermobarometry corrected for retrograde exchange. Journal of Petrology 44 (5), 867–900.

Pearce, M.A., White, A.J.R., Gazley, M.F., 2015. TCInvestigator: automated calculation of mineral mode and composition contour for THERMOCALC pseudosections. Journal of Metamorphic Geology 33, 413–425.

Petersson, A., Scherstén, A., Bingen, B., Gerdes, A., Whitehouse, M.J., 2015. Mesoproterozoic continental growth: U–Pb–Hf–O zircon record in the Idefjorden Terrane, Sveconorwegian Orogen. Precambrian Research 261, 75–95.

Pitra, P., Waal, S.A.D., 2001. High-temperature, low-pressure metamorphism and development of prograde symplectites, marble hall fragment, Bushveld complex (South Africa). Journal of Metamorphic Geology 19 (3), 311–325.

Roberts, N.M.W., Slagstad, T., 2015. Continental growth and reworking on the edge of the Columbia and Rodinia supercontinents; 1.86-0.9 Ga accretionary orogeny in southwest Fennoscandia. International Geology Review 57, 1582–1606.

Sauer, S., Slagstad, T., Andersen, T., Kirkland, C.L., 2013. Zircon Lu-Hf Isotopes in High-alumina Orthopyroxene Megacrysts from the Neoproterozoic Rogaland Anorthosite Province, SW Norway: A Window into the Sveconorwegian Lower Crust. EGU General Assembly Conference Abstracts 15, p. 13958.

Sauter, P.C.C., 1981. Mineral relations in siliceous dolomites and related rocks in the high-grade metamorphic Precambrian of Rogaland, SW Norway. Norsk Geologisk Tidsskrift 61, 35–45.

Schärer, U., Wilmart, E., Duchesne, J.-C., 1996. The short duration and anorogenic character of anorthosite magmatism: U–Pb dating of the Rogaland complex, Norway. Earth and Planetary Science Letters 139, 335–350.

Slagstad, T., Roberts, N.M.W., Marker, M., Røhr, T.S., Schiellerup, H., 2013a. A non-collisional, accretionary Sveconorwegian orogen. Terra Nova 25, 30–37.

Slagstad, T., Roberts, N.M.W., Marker, M., Røhr, T.S., Schiellerup, H., 2013b. A non-collisional, accretionary Sveconorwegian orogen – reply. Terra Nova 25 (2), 169–171.

Söderlund, U., Ask, R., 2006. Mesoproterozoic bimodal magmatism along the Protogine Zone, S Sweden: three magmatic pulses at 1.56, 1.22 and 1.205 Ga, and regional implications. GFF 128, 303–310.

Söderlund, U., Elming, S.-Å., Ernst, R.E., Schissel, D., 2006. The Central Scandinavian Dolerite Group–protracted hotspot activity or back-arc magmatism? Constraints from U–Pb baddeleyite geochronology and Hf isotopic data. Precambrian Research 150, 136–152.

Spencer, C.J., Roberts, N.M.W., Cawood, P.A., Hawkesworth, C.J., Prave, A.R., Antonini, A.S.M., Horstwood, M.S.A., Elmf, 2014. Intermontane basins and bimodal volcanism at the onset of the Sveconorwegian Orogeny, southern Norway. Precambrian Research 252, 107–118.

Tajčmanová, L., Konopásek, J., Košler, J., 2009. Distribution of zinc and its role in the stability of spinel in high-grade felsic rocks of the Moldanubian domain (Bohemian Massif). European Journal of Mineralogy 21, 407–418.

Tobi, A.C., Hermans, G.A.E.M., Maijer, C., Jansen, B.H., 1985. Metamorphic zoning in the high-grade proterozoic of Rogaland-Vest Agder, SW Norway. In: Tobi, A.C., Touret, J.L.R. (Eds.), The Deep Proterozoic Crust in the North Atlantic Provinces. D. Reidel Publishing Co., pp. 477–497

Tomkins, H.S., Williams, I.S., Ellis, D.J., 2005. In situ U–Pb dating of zircon formed from retrograde garnet breakdown during decompression in Rogaland, SW Norway. Journal of Metamorphic Geology 23, 201–215.

Vander Auwera, J., Bolle, O., Bingen, B., Liégeois, J.-P., Bogaerts, M., Duchesne, J.-C., Waele, B.D., Longhi, J., 2011. Sveconorwegian massif-type anorthosites and related granitoids result from post-collisional melting of a continental arc root. Earth-Science Reviews 107, 375–397.

Vander Auwera, J., Bolle, O., Dupont, A., Pin, C., Paquette, J.-L., Charlier, B., Duchesne, J.-C., Mattielli, N., Bogaerts, M., 2014. Source-derived heterogeneities in the composite (charnockite-granite) ferroan Farsund intrusion (SW Norway). Precambrian Research 251, 141–163.

Vander Auwera, J., Longhi, J., 1994. Experimental study of a joutunite (hypersthene monzodiorite): constraints on the parent magma composition and crystallization conditions (P, T, f_{O2}) of the Bjerkreim-Sokndal layered intrusion (Norway). Contributions to Mineralogy and Petrology 118, 60–78.

Verschure, R.H., Andriessen, P.A.M., Boelrijk, N.A.I.M., Hebeda, E.H., Maier, W.D., Priem, H.N.A., Verdurmen, E.A.T., 1980. On the thermal stability of Rb–Sr and K–Ar biotite systems: evidence from coexisting Sveconorwegian (ca 870 Ma) and Caledonian (ca 400 Ma) biotites in SW Norway. Contributions to Mineralogy and Petrology 74, 245–252.

Versteeve, A.J., 1975. Isotope geochronology in the high-grade metamorphic Precambrian of Southwestern Norway. Norges Geologisk Undersøkelse 318, 1–50.

Westphal, M., Schumacher, J.C., Boschert, S., 2003. High-temperature metamorphism and the role of magmatic heat sources at the Rogaland anorthosite complex in Southwestern Norway. Journal of Petrology 44 (6), 1145–1162.

Wheller, C.J., Powell, R., 2014. A new thermodynamic model for sapphirine: calculated phase equilibria in K_2O-FeO-MgO-Al_2O_3-SiO_2-H_2O-TiO_2-Fe_2O_3. Journal of Metamorphic Geology 32, 287–299.

White, R.W., Powell, R., Clarke, G.L., 2002. The interpretation of reaction textures in Fe-rich metapelitic granulites of the Musgrave Block, central Australia: constraints from mineral equilibria calculations in the system K_2O-FeO-MgO-Al_2O_3-SiO_2-H_2O-TiO_2-Fe_2O_3. Journal of Metamorphic Geology 20, 41–55.

White, R.W., Powell, R., Holland, T.J.B., 2007. Progress relating to calculation of partial melting equilibria for metapelites. Journal of Metamorphic Geology 25, 511–527.

White, R.W., Powell, R., Holland, T.J.B., Johnson, T., Green, E.C.R., 2014a. New mineral activity-composition relations for thermodynamic calculations in metapelitic systems. Journal of Metamorphic Geology 32, 261–286.

White, R.W., Powell, R., Johnson, T., 2014b. The effect of Mn on mineral stability in metapelites revisited: new a–x relations for manganese-bearing minerals. Journal of Metamorphic Geology 32, 809–828.

Whitney, D.L., Evans, B.W., 2010. Abbreviations for names of rock-forming minerals. American Mineralogist 95, 185–187.

Wielens, J.B.W., Andriessen, P.A.M., Boelrijk, N.A.I.M., Hebeda, E.H., Priem, H.N.A., Verdurmen, E.A.T., Verschure, R.H., 1981. Isotope geochronology in the high-grade metamorphic Precambrian of Southwestern Norway: new data and reinterpretations. Norges Geologisk Undersøkelse 359, 1–30.

Wilmart, E., Clocchiatti, R., Duchesne, J.-C., Touret, J.L.R., 1991. Fluid inclusions in charnockites from the Bjerkreim-Sokndal massif (Rogaland, southwestern Norway): fluid origin and in situ evolution. Contributions to Mineralogy and Petrology 108, 453–462.

Wilmart, E., Duchesne, J.-C., 1987. Geothermobarometry of igneous and metamorphic rocks around the Åna-sira anorthosite massif: implications for the depth of emplacement of the South Norwegian Anorthosites. Norsk Geologisk Tidsskrift 67, 185–196.

Statement of Authorship

Title of Paper: Constraining the timing of prograde metamorphism in long-lived hot orogens

Publication Status: ☐ Published ☐ Accepted for Publication
☒ Submitted for Publication ☐ Publication Style

Publication Details:
Blereau, E., Clark, C., Jourdan, F., Johnson, T. E., Taylor, R. J. M., Kinny, P. D., Hand, M., and Eroglu, E., in review. Constraining the timing of prograde metamorphism in long-lived hot orogens, GEOLOGY (in review since 7/6/2017).

Author Contributions

By signing the Statement of Authorship, each author certifies that their stated contribution to the publication is accurate and that permission is granted for the publication to be included in the candidate's thesis.

Name of Principal Author (Candidate): Eleanore R. Blereau
Contributions to the Paper: Assisted with diffusion modelling and conducted feild work, sample preparation, petrography, phase equilibria modelling, $^{40}Ar/^{39}Ar$ data interpretation and drafting of the manuscript
Overall percentage: 70%

Signature Date: 7 / 7 /2017

Name of Co-Author: Chris Clark
Contributions to the Paper: Assisted with field work, $^{40}Ar/^{39}Ar$ data interpretation and editing of the manuscript
Overall percentage: 7%

Signature Digitally signed by Chris Clark Date: 2017.07.07 09:55:22 +08'00' Date: 7 / 7 /2017

Name of Co-Author: Fred Jourdan
Contributions to the Paper: Collected $^{40}Ar/^{39}Ar$ data, diffusion modelling and assisted with $^{40}Ar/^{39}Ar$ data interpretation and editing of the manuscript
Overall percentage: 10%

Signature Date: 4 / 4 /2017

Name of Co-Author: Tim E. Johnson
Contributions to the Paper: Assisted with phase equilibria modelling, interpreting $^{40}Ar/^{39}Ar$ data and editing of the manuscript
Overall percentage: 7%

Signature Date: 7 / 7 /2017

Name of Co-Author: Richard J. M. Taylor
Contributions to the Paper: Assisted with field work and editing of the manuscript
Overall percentage: 2%

Signature Date: 7 / 4 /2017

Name of Co-Author: Peter D. Kinny
Contributions to the Paper: Assisted with field work and editing of the manucript
Overall percentage: 2%

Signature Date: 7 / 7 /2017

Name of Co-Author: Martin Hand
Contributions to the Paper: Assisted with field work and editing of the manuscript
Overall percentage: 1%

Signature Date: 10 / 4 /2017

Name of Co-Author: Ela Eroglu
Contributions to the Paper: Diffusion modelling
Overall percentage: 1%

Signature Date: 4 / 4 /2017

Statement of Authorship

Title of Paper: Using accessory minerals to unravel thermal histories in polymetamorphic terranes: an example from Rogaland, SW Norway

Publication Status: ☐ Published ☐ Accepted for Publication
■ Submitted for Publication ☐ Publication Style

Publication Details:
Blereau, E., Clark, C., Taylor, R. J. M., Kinny, P. D., Johnson, T. E., Sansom, E., Hand, M., in review. Using accessory minerals to unravel thermal histories in polymetamorphic terranes: an example from Rogaland, SW Norway, Journal of Metamorphic Geology (in review since 23/6/2017).

Author Contributions

By signing the Statement of Authorship, each author certifies that their stated contribution to the publication is accurate and that permission is granted for the publication to be included in the candidate's thesis.

Name of Principal Author (Candidate): Eleanore R. Blereau
Contributions to the Paper: Conducted sample preparation, field work, geochronological and geochemical data collection, processing and interpretation, diffusion modelling and drafting the manuscript
Overall percentage: 75%

Signature Date: 7 / 7 /2017

Name of Co-Author: Chris Clark
Contributions to the Paper: Assisted with field work, data interpretation, editing of the manuscript
Overall percentage: 6%

Signature Digitally signed by Chris Clark Date: 2017.07.07 09:56:21 +08'00' Date: 7 / 7 /2017

Name of Co-Author: Richard J. M. Taylor
Contributions to the Paper: Assisted with field work, geochronological and geochemical data collection, processing and interpretation, diffusion modelling and editing of the manuscript
Overall percentage: 6%

Signature Date: 7 / 4 /2017

Name of Co-Author: Peter D. Kinny
Contributions to the Paper: Assisted with field work, data interpretation and editing of the manuscript
Overall percentage: 5%

Signature Date: 7 / 7 /2017

Name of Co-Author: Tim. E. Johnson
Contributions to the Paper: Assisted with data interpretation, editing of the manuscript
Overall percentage: 5%

Signature Date: 7 / 7 /2017

Name of Co-Author: Eleanor Sansom
Contributions to the Paper: Assisted with MATLAB coding for diffusion modelling
Overall percentage: 2%

Signature Date: 3 / 7 /2017

Name of Co-Author: Martin Hand
Contributions to the Paper: Assisted with field work and editing of the manuscript
Overall percentage: 1%

Signature Date: 10 / 4 /2017

Appendix B

This appendix contains the supplementary tables S1–5 and supplementary figures S1–S3 from the paper 'Constraints on the timing and conditions of high-grade metamorphism, charnockite formation and fluid–rock interaction in the Trivandrum Block, southern India'.

Contents:

Constraints on the timing and conditions of high-grade metamorphism, charnockite formation, and fluid-rock interaction in the Trivandrum Block, southern India

E. BLEREAU, C. CLARK, R. J. M. TAYLOR, T. E. JOHNSON, I. C. W. FITZSIMONS, M. SANTOSH

Table S1: All data for monazite SHRIMP U−Pb analyses

Table S1: SHRIMP analytical results for monazite from sample I11-004K: Garnet-biotite gneiss, Chakkod

Texture	Spot	238U	232Th	232Th	206Pb	206Pb/238U		207Pb*/206Pb*		207Pb*/235U		238U/206Pb*		207Pb*/206Pb*		207Pb*/235U		Disc.	Disc.
ID	no.	(ppm)	(ppm)	238U	(c/sec)	date (Ma) ± 1σ		date (Ma) ± 1σ		date (Ma) ± 1σ		± %		± %		± %		Pb-Pb %	U-Pb %
R	EB3-59.3L	2873	242128	87.08	778	496	±7	555	±64	507	±17	12.5	1.3	0.059	2.1	0.648	3.4	+11	+2
C	EB3-62.1D	6879	127887	19.21	1912	522	±6	560	±32	529	±10	11.9	1.2	0.059	1.5	0.683	1.9	+7	+1
R	EB3-62.2M	4264	157578	38.18	1355	524	±6	501	±22	520	±8	11.8	1.2	0.057	0.9	0.668	1.6	-5	-1
R	EB3-60.2M	3606	136320	39.06	1431	526	±6	529	±26	526	±9	11.8	1.2	0.058	0.9	0.679	1.7	+1	+0
R	EB3-61.3L	3193	175395	56.75	1164	542	±8	588	±36	551	±13	11.4	1.6	0.060	1.0	0.720	2.3	+8	+2
R	EB3-66.2M	4367	160414	37.96	1681	553	±8	568	±23	556	±10	11.2	1.4	0.059	0.8	0.729	1.8	+3	+1
R	EB3-64.2M	4026	124013	31.82	1608	556	±7	580	±21	560	±9	11.1	1.2	0.059	0.8	0.737	1.6	+4	+1
C	EB3-61.1D	6561	114009	17.95	2524	560	±8	571	±16	562	±9	11.0	1.4	0.059	0.7	0.740	1.6	+2	+0
C	EB3-64.1D	6119	100591	16.99	2559	574	±7	606	±15	581	±8	10.7	1.2	0.060	0.7	0.772	1.4	+5	+1
C	EB3-59.1D	4517	116476	26.64	2049	575	±7	590	±17	578	±8	10.7	1.2	0.060	0.7	0.767	1.4	+3	+1
C	EB3-60.1D	5865	105287	18.55	2415	577	±7	588	±16	579	±8	10.7	1.2	0.060	0.7	0.769	1.4	+2	+0
R	EB3-59.2M	3384	154796	47.26	1555	580	±7	577	±20	580	±9	10.6	1.2	0.059	0.8	0.770	1.5	-0	-0
R	EB3-62.3L	2607	180148	71.39	1044	582	±7	607	±26	587	±10	10.6	1.3	0.060	1.0	0.783	1.8	+4	+1
R	EB3-61.2M	3792	112247	30.59	1640	584	±8	548	±19	577	±10	10.5	1.5	0.058	0.8	0.765	1.7	-7	-1

Errors are 1-sigma (abs) or % where indicated. Pb* indicate radiogenic proportions. All ages are common Pb corrected using measured 204Pb. R-Recrystallised zone, C-Core

Table S1. continued: SHRIMP analytical results for monazites from sample I11-004C: Transition zone, Chakkod

Texture	Spot	238U	232Th	232Th	206Pb	206Pb/238U		207Pb*/206Pb*		207Pb*/235U		238U/206Pb*		207Pb*/206Pb*		207Pb*/235U		Disc.	Disc.
ID	no.	(ppm)	(ppm)	238U	(c/sec)	date (Ma) ± 1σ		date (Ma) ± 1σ		date (Ma) ± 1σ		± %		± %		± %		Pb-Pb %	U-Pb %

C	EB3-66.1D	6092	97703	16.57	2536	597	±7	583	±14	594	±8	10.3	1.2	0.059	0.7	0.795	1.4	-3	-1
R	004-8.1	896	3648	31.86	896	514	±6	528	±51	517	±13	12.0	1.2	0.058	2.2	0.664	2.6	+3	+0
R	004-6.5	889	3269	33.45	889	530	±9	510	±37	526	±13	11.7	1.8	0.057	1.1	0.679	2.5	-4	-1
R	004-7.2	655	2563	47.96	655	546	±7	555	±30	547	±10	11.3	1.3	0.059	1.3	0.714	1.9	+2	+0
R	004-1.2	506	2935	90.16	506	547	±10	561	±71	549	±21	11.3	1.8	0.059	1.5	0.718	3.9	+3	+1
R	004-5.4	819	3492	36.60	819	550	±12	539	±33	548	±15	11.2	2.3	0.058	1.2	0.715	2.8	-2	-0
R	004-2.2	443	2437	98.39	443	550	±12	583	±96	557	±28	11.2	2.2	0.059	1.6	0.730	5.2	+6	+1
R	004-3.2	776	4016	47.08	776	551	±11	667	±43	574	±15	11.2	2.0	0.062	1.2	0.761	2.9	+18	+4
R	004-9.2	817	2920	46.93	817	559	±10	539	±33	555	±13	11.0	1.9	0.058	1.2	0.728	2.4	-4	-1
R	004-10.2	1016	3668	35.14	1016	561	±11	569	±36	563	±14	11.0	2.0	0.059	1.1	0.741	2.6	+1	+0
C	004-3.1	1462	6920	19.20	1462	562	±10	575	±48	564	±16	11.0	1.8	0.059	1.8	0.744	2.9	+2	+0
R	004-7.4	812	3066	40.77	812	562	±9	529	±49	556	±15	11.0	1.7	0.058	1.9	0.728	2.8	-6	-1
R	004-5.1	1048	3605	22.90	1048	564	±9	568	±43	565	±14	10.9	1.6	0.059	1.0	0.745	2.6	+1	+0
R	004-4.2	1078	3919	31.79	1078	566	±13	596	±25	572	±15	10.9	2.4	0.060	1.0	0.756	2.7	+5	+1
C	004-1.1	1389	6309	20.29	1389	566	±11	570	±28	567	±13	10.9	2.0	0.059	0.9	0.748	2.4	+1	+0
C	004-2.1	1328	6498	20.01	1328	567	±10	581	±30	570	±13	10.9	1.8	0.059	0.9	0.753	2.3	+2	+0
R	004-6.4	450	1733	90.64	450	573	±8	637	±43	586	±14	10.8	1.5	0.061	1.6	0.781	2.5	+11	+2
R	004-7.1	697	2832	56.98	697	574	±13	578	±46	575	±18	10.7	2.4	0.059	1.3	0.761	3.2	+1	+0
C	004-9.1	1543	5343	17.68	1543	579	±12	573	±22	578	±14	10.6	2.2	0.059	0.9	0.767	2.4	-1	-0
R	004-9.3	601	2291	75.45	601	581	±8	542	±50	573	±15	10.6	1.3	0.058	1.4	0.758	2.7	-7	-1
C	004-8.2	1579	5262	17.32	1579	583	±6	597	±20	585	±8	10.6	1.2	0.060	0.8	0.780	1.5	+2	+0
C	004-5.2	1836	6055	10.94	1836	585	±9	596	±19	587	±10	10.5	1.6	0.060	0.8	0.783	1.8	+2	+0

Errors are 1-sigma (abs) or % where indicated. Pb* indicate radiogenic proportions. All ages are common Pb corrected using measured 204Pb. R-Recrystallised zone, C-Core

Table S1. continued: SHRIMP analytical results for monazites from sample I11-004C: Transition zone, Chakkod

R	004-10.3	811	2866	46.56	811	588	±7	582	±33	587	±12	10.5	1.3	0.059	1.2	0.782	2.0	-1	-0
R	004-4.3	1335	4999	19.97	1335	589	±9	570	±25	585	±11	10.5	1.5	0.059	0.9	0.779	1.9	-4	-1
R	004-6.3	807	3176	52.76	807	590	±7	583	±41	589	±13	10.4	1.3	0.059	1.2	0.786	2.3	-1	-0
C	004-4.1	1640	5049	17.05	1640	591	±11	606	±21	594	±13	10.4	2.0	0.060	0.8	0.795	2.2	+3	+1
R	004-8.3	719	2649	58.06	719	593	±7	591	±38	593	±13	10.4	1.3	0.060	1.3	0.793	2.2	-0	-0
C	004-7.3	1327	4187	18.23	1327	593	±7	592	±25	593	±10	10.4	1.2	0.060	0.9	0.793	1.7	-0	-0

C	004-6.2	1349	4472	18.95	1349	598	±11	560	±32	590	±14	10.3	1.9	0.059	1.4	0.789	2.4	-7	-1
C	004-10.1	1236	3875	23.54	1236	611	±13	509	±24	590	±15	10.1	2.3	0.057	1.0	0.788	2.5	-21	-4
SHRIMP analytical results for monazite from sample I11-008C: Charnockite, Chakkod																			
Texture	Spot	238U	232Th	232Th	206Pb	206Pb/238U		207Pb*/206Pb*		207Pb*/235U		238U/206Pb*		207Pb*/206Pb*		207Pb*/235U		Disc.	Disc.
ID	no.	(ppm)	(ppm)	238U	(c/sec)	date (Ma) ± 1σ		date (Ma) ± 1σ		date (Ma) ± 1σ		± %		± %		± %		Pb-Pb %	U-Pb %
R	008-2.3	2649	17551	6.85	663	471	±13	502	±31	476	±15	13.2	2.9	0.057	1.3	0.598	3.2	6	+1
R	008-1.1	3035	119409	40.66	471	478	±8	538	±70	489	±17	13.0	1.7	0.058	1.6	0.618	3.7	11	+2
Table S1. continued: SHRIMP analytical results for monazite from sample I11-008C: Charnockite, Chakkod																			
Texture	Spot	238U	232Th	232Th	206Pb	206Pb/238U		207Pb*/206Pb*		207Pb*/235U		238U/206Pb*		207Pb*/206Pb*		207Pb*/235U		Disc.	Disc.
ID	no.	(ppm)	(ppm)	238U	(c/sec)	date (Ma) ± 1σ		date (Ma) ± 1σ		date (Ma) ± 1σ		± %		± %		± %		Pb-Pb %	U-Pb %
R	008-1.3	2315	66941	29.88	629	506	±6	468	±42	499	±12	12.3	1.3	0.056	1.4	0.635	2.3	-8	-1
R	008-2.1	2814	228374	83.86	473	510	±11	612	±87	529	±24	12.1	2.3	0.060	1.5	0.684	4.8	17	+4
R	008-1.2	2498	86688	35.86	646	513	±7	549	±40	520	±11	12.1	1.3	0.059	1.3	0.668	2.3	7	+1
R	008-2.2	2399	179974	77.52	544	523	±7	516	±56	522	±15	11.8	1.4	0.058	1.4	0.672	2.9	-1	-0
Errors are 1-sigma (abs) or % where indicated. Pb* indicate radiogenic proportions. All ages are common Pb corrected using measured 204Pb. R-Recrystallised zone, C-Core																			
SHRIMP analytical results for monazite from sample TB-14-025: Metapelitic gneiss, Chakkod																			
Texture	Spot	238U	232Th	232Th	206Pb	206Pb/238U		207Pb*/206Pb*		207Pb*/235U		238U/206Pb*		207Pb*/206Pb*		207Pb*/235U		Disc.	Disc.
ID	no.	(ppm)	(ppm)	238U	(c/sec)	date (Ma) ± 1σ		date (Ma) ± 1σ		date (Ma) ± 1σ		± %		± %		± %		Pb-Pb %	U-Pb %
C	PB-2.1	256	1884	7.59	1841	505	±4	546	±19	512	±6	12.3	0.9	0.058	0.8	0.657	1.3	+8	+1
R	PA-5.2	215	4132	19.86	1760	512	±4	521	±20	513	±7	12.1	0.9	0.058	0.8	0.658	1.3	+2	+0

R	PA-1.1	275	7519	28.21	1902	515	±4	579	±27	526	±8	12.0	0.9	0.062	0.8	0.680	1.5	+12	+2
R	PB-6.3	591	18303	32.02	3852	518	±4	609	±15	535	±6	12.0	0.8	0.059	0.5	0.694	1.0	+16	+3
R	PB-6.2	559	10910	20.17	4433	525	±4	541	±13	527	±5	11.8	0.8	0.058	0.5	0.681	1.0	+3	+0
R	PA-3.1	395	10425	27.29	2777	527	±4	581	±17	537	±6	11.7	0.9	0.059	0.6	0.698	1.2	+10	+2
R	PB-4.1	729	13859	19.64	5082	529	±4	602	±14	543	±6	11.7	0.8	0.059	0.5	0.707	1.0	+13	+3
R	PA-16.1	338	6644	20.30	2656	536	±4	501	±19	529	±6	11.5	0.9	0.058	0.7	0.684	1.2	-7	-1
R	PA-2.2	457	9583	21.68	3276	537	±4	569	±14	543	±6	11.5	0.8	0.059	0.6	0.707	1.1	+6	+1
R	PA-13.1B	483	8582	18.35	4213	538	±4	554	±12	540	±5	11.5	0.8	0.059	0.5	0.704	1.0	+3	+0
C	PA-6.2	154	5259	35.23	1287	539	±5	553	±27	541	±9	11.4	1.0	0.060	0.9	0.705	1.6	+3	+0
C	PA-2.1	170	7564	45.85	1239	540	±5	646	±30	561	±10	11.5	1.0	0.059	1.0	0.737	1.7	+17	+4
R	PA-4.2	225	5153	23.72	1999	547	±5	548	±19	548	±7	11.3	0.9	0.059	0.8	0.715	1.2	+0	+0
R	PA-17.1	259	5154	20.58	2051	551	±5	611	±20	563	±7	11.2	0.9	0.059	0.7	0.741	1.3	+10	+2
R	PB-5.2	191	8834	47.75	1684	553	±5	646	±25	572	±8	11.2	0.9	0.060	0.8	0.756	1.5	+15	+3
R	PA-12.2	206	6555	32.84	1975	558	±5	523	±30	551	±9	11.0	0.9	0.059	1.2	0.721	1.6	-7	-1
C	PA-6.1	140	6085	44.89	1183	565	±5	555	±29	563	±9	10.9	1.0	0.060	1.0	0.741	1.7	-2	-0
C	PB-7.2	303	4914	16.75	2836	568	±5	608	±17	576	±7	10.9	0.9	0.059	0.6	0.764	1.2	+7	+1
R	PA-3.2	332	7910	24.63	2610	571	±5	617	±18	580	±7	10.8	0.9	0.059	0.7	0.771	1.2	+8	+2
Table S1 continued: SHRIMP analytical results for monazite from sample TB-14-025: Metapelitic gneiss, Chakkod																			
Texture	Spot	238U	232Th	232Th	206Pb	206Pb/238U		207Pb*/206Pb*		207Pb*/235U		238U/206Pb*		207Pb*/206Pb*		207Pb*/235U		Disc.	Disc.
ID	no.	(ppm)	(ppm)	238U	(c/sec)	date (Ma) ± 1σ		date (Ma) ± 1σ		date (Ma) ± 1σ		± %		± %		± %		Pb-Pb %	U-Pb %
C	PB-4.2	451	4948	11.33	4714	573	±5	606	±12	580	±6	10.8	0.9	0.059	0.5	0.771	1.1	+6	+1
Errors are 1-sigma (abs) or % where indicated. Pb* indicate radiogenic proportions. All ages are common Pb corrected using measured 204Pb. R-Recrystallised zone, C-Core																			
Table S1 continued: SHRIMP analytical results for monazite from sample TB-14-025: Metapelitic gneiss, Chakkod continued																			
Texture	Spot	238U	232Th	232Th	206Pb	206Pb/238U		207Pb*/206Pb*		207Pb*/235U		238U/206Pb*		207Pb*/206Pb*		207Pb*/235U		Disc.	Disc.
ID	no.	(ppm)	(ppm)	238U	(c/sec)	date (Ma) ± 1σ		date (Ma) ± 1σ		date (Ma) ± 1σ		± %		± %		± %		Pb-Pb %	U-Pb %
C	PA-13.2B	481	3048	6.55	5642	575	±4	592	±10	578	±5	10.7	0.8	0.060	0.4	0.768	0.9	+3	+1
C	PB-8.1	335	5910	18.21	2810	576	±5	623	±17	585	±7	10.7	0.9	0.061	0.6	0.780	1.2	+8	+2

C	PA-4.1	277	3415	12.76	2585	576	±5	636	±15	588	±7	10.7	0.9	0.061	0.7	0.785	1.1	+10	+2
C	PA-5.1	559	2594	4.79	5735	577	±5	592	±10	580	±6	10.7	1.0	0.060	0.4	0.771	1.1	+3	+0
C	PB-7.1	598	4076	7.05	6050	579	±4	567	±12	576	±6	10.6	0.8	0.060	0.4	0.764	1.0	-2	-0
C	PB-8.2	722	2816	4.03	6655	580	±4	609	±9	586	±5	10.6	0.8	0.060	0.4	0.780	0.9	+5	+1
R	PA-12.1	475	2856	6.21	5708	595	±5	597	±10	595	±6	10.3	0.8	0.060	0.4	0.797	0.9	+0	+0
C	PB-5.1	853	3097	3.75	9517	609	±4	764	±8	642	±6	10.1	0.8	0.065	0.4	0.883	0.9	+21	+5
C	PB-6.1	540	2829	5.42	9486	965	±11	1514	±16	1149	±17	6.2	1.3	0.094	0.8	2.101	1.5	+39	+16
C	PB-1.1	405	2952	7.53	9057	1415	±11	1799	±9	1576	±15	4.1	0.8	0.110	0.5	3.721	1.0	+24	+10
SHRIMP analytical results for monazite from sample I11-006V: Pegmatite, Chakkod																			
Texture	Spot	238U	232Th	232Th	206Pb	206Pb/238U		207Pb*/206Pb*		207Pb*/235U		238U/206Pb*		207Pb*/206Pb*		207Pb*/235U		Disc.	Disc.
ID	no.	(ppm)	(ppm)	238U	(c/sec)	date (Ma) ± 1σ		date (Ma) ± 1σ		date (Ma) ± 1σ		± %		± %		± %		Pb-Pb %	U-Pb %
R	006-24.4	6735	33560	5.50	3667	500	±8	500	±12	500	±8	12.39	1.6	0.057	0.6	0.636	1.7	-0	-0
C	006-5.2	5417	121002	24.67	2393	505	±7	531	±20	510	±9	12.28	1.5	0.058	0.7	0.652	1.8	+5	+1
R	006-27.1	5745	71774	13.80	3344	517	±8	525	±15	518	±9	11.99	1.7	0.058	0.6	0.666	1.8	+2	+0
R	006-4.2	6314	97874	17.12	3169	521	±9	509	±17	519	±10	11.88	1.7	0.057	0.6	0.667	1.9	-2	-0
C	006-12.1	10071	126549	13.88	4203	521	±10	532	±14	523	±10	11.87	1.9	0.058	0.5	0.674	2.0	+2	+0
C	006-4.1	8976	116564	14.34	3896	523	±7	546	±20	528	±9	11.82	1.5	0.058	0.9	0.681	1.7	+4	+1
C	006-6.2	6527	120368	20.37	3554	543	±10	544	±17	543	±11	11.38	1.9	0.058	0.6	0.707	2.1	+0	+0
C	006-24.3	6333	79929	13.94	3153	547	±12	514	±22	540	±13	11.30	2.3	0.058	1.0	0.703	2.5	-7	-1
C	006-4.3	9049	113016	13.79	4953	551	±9	536	±12	548	±9	11.20	1.7	0.058	0.5	0.716	1.8	-3	-1
C	006-7.2	5237	121020	25.52	2742	552	±10	557	±19	553	±11	11.18	1.9	0.059	0.6	0.724	2.1	+1	+0
Errors are 1-sigma (abs) or % where indicated. Pb* indicate radiogenic proportions. All ages are common Pb corrected using measured 204Pb. R-Recrystallised zone, C-Core																			
Table S1. continued: SHRIMP analytical results for monazite from sample I11-006V: Pegmatite, Chakkod																			
Texture	Spot	238U	232Th	232Th	206Pb	206Pb/238U		207Pb*/206Pb*		207Pb*/235U		238U/206Pb*		207Pb*/206Pb*		207Pb*/235U		Disc.	Disc.
ID	no.	(ppm)	(ppm)	238U	(c/sec)	date (Ma) ± 1σ		date (Ma) ± 1σ		date (Ma) ± 1σ		± %		± %		± %		Pb-Pb %	U-Pb %
C	006-11.1	7427	109865	16.34	3832	560	±8	543	±16	557	±9	11.02	1.5	0.058	0.5	0.730	1.6	-3	-1
C	006-22.2	4368	119695	30.27	2317	564	±8	558	±23	563	±10	10.94	1.5	0.059	0.7	0.740	1.8	-1	-0

C	006-6.1	6915	105552	16.86	3810	566	±9	552	±14	563	±10	10.90	1.7	0.059	0.5	0.741	1.8	-3	-1
C	006-12.2	5811	103615	19.69	3248	567	±9	488	±14	552	±10	10.87	1.7	0.057	0.6	0.722	1.8	-17	-3
C	006-27.2	9615	95745	11.00	6456	576	±9	509	±10	563	±10	10.70	1.7	0.057	0.4	0.740	1.7	-14	-2
C	006-24.1	8397	107720	14.17	4895	590	±11	559	±12	584	±12	10.43	1.9	0.059	0.5	0.777	2.0	-6	-1
C	006-5.1	8544	113088	14.62	4363	591	±10	565	±17	586	±12	10.41	1.8	0.059	0.5	0.781	2.0	-5	-1

Errors are 1-sigma (abs) or % where indicated. Pb* indicate radiogenic proportions. All ages are common Pb corrected using measured 204Pb. R-Recrystallised zone, C-Core

Table S2: SHRIMP analytical results for zircons from sample I11-004K: Garnet-biotite gneiss, Chakkod

Texture	Spot	238U	232Th	232Th	f204	206Pb/238U		207Pb*/206Pb*		207Pb*/235U		238U/206Pb*		207Pb*/206Pb*		207Pb*/235U		Disc.
ID	no.	(ppm)	(ppm)	238U	(%)	date (Ma) ± 1σ		date (Ma) ± 1σ		date (Ma) ± 1σ		± %		± %		± %		(%)
R	004G-2.1	398	131	0.34	0.28	492	±6	497	±36	493	±10	12.616	1.2	0.057	1.6	0.624	2.0	1
R	004G-9.1	448	146	0.34	0.32	502	±5	477	±36	498	±10	12.349	1.1	0.057	1.6	0.632	1.9	-5
R	004G-3.1	349	189	0.56	0.28	513	±7	451	±39	501	±11	12.082	1.3	0.056	1.8	0.639	2.2	-14
R	004G-6.1	490	130	0.27	0.11	516	±5	481	±26	510	±8	11.999	1.1	0.057	1.2	0.652	1.6	-8
R	004G-5.1	585	115	0.20	0.24	521	±7	519	±37	521	±12	11.870	1.5	0.058	1.7	0.671	2.3	-0
R	004G-10.1	296	218	0.76	0.28	530	±12	427	±64	511	±19	11.671	2.4	0.055	2.9	0.654	3.7	-25
R	004G-4.1	402	252	0.65	0.05	533	±9	516	±45	529	±14	11.612	1.8	0.058	2.1	0.684	2.7	-3
R	004G-8.1	475	165	0.36	0.19	534	±20	901	±162	610	±54	11.569	3.9	0.069	7.9	0.823	8.8	42
R	004G-7.1	501	136	0.28	1.74	538	±11	715	±70	573	±22	11.485	2.1	0.063	3.3	0.759	3.9	26
C	004G-11.1	665	120	0.19	3.62	919	±13	1514	±76	1112	±48	6.530	1.5	0.094	4.0	1.991	4.3	42
C	004G-1.1A	1664	77	0.05	0.09	1365	±50	1866	±44	1573	±74	4.239	4.1	0.114	2.4	3.711	4.7	30

SHRIMP analytical results for zircons from sample I11-008C: Garnet-bearing charnockite, Chakkod

Texture	Spot	238U	232Th	232Th	f204	206Pb/238U		207Pb*/206Pb*		207Pb*/235U		238U/206Pb*		207Pb*/206Pb*		207Pb*/235U		Disc.
ID	no.	(ppm)	(ppm)	238U	(%)	date (Ma) ± 1σ		date (Ma) ± 1σ		date (Ma) ± 1σ		± %		± %		± %		(%)
R	008C-5.1	277	109	0.41	0.08	496	±6	477	±34	493	±10	12.499	1.3	0.057	1.5	0.625	2.0	-4
R	008C-4.1	673	197	0.30	4.76	499	±6	521	±147	503	±34	12.417	1.3	0.058	6.7	0.641	6.8	4
R	008C-16.1	457	195	0.44	0.13	504	±6	442	±29	493	±9	12.285	1.3	0.056	1.3	0.626	1.8	-15
R	008C-24.1	321	170	0.55	0.22	507	±5	521	±66	509	±16	12.228	1.1	0.058	3.0	0.651	3.2	3
R	008C-23.1	251	101	0.41	--	508	±5	531	±32	512	±9	12.198	1.1	0.058	1.4	0.656	1.8	5
R	008C-9.2	850	181	0.22	0.01	508	±8	501	±37	507	±12	12.192	1.6	0.057	1.7	0.647	2.3	-1
R	008C-12.1	569	191	0.35	0.58	508	±6	639	±82	533	±21	12.184	1.2	0.061	3.8	0.690	4.0	21
R	008C-26.1	263	181	0.71	0.67	510	±10	458	±62	500	±18	12.156	2.1	0.056	2.8	0.637	3.5	-12
R	008C-7.1	631	180	0.30	0.13	511	±7	558	±40	520	±12	12.119	1.5	0.059	1.8	0.669	2.4	9
R	008C-14.1	517	461	0.92	--	519	±8	675	±62	549	±18	11.917	1.6	0.062	2.9	0.718	3.3	24

Errors are 1-sigma (abs) or % where indicated. Pb* indicate radiogenic proportions. All ages are common Pb corrected using measured 204Pb. f204 is % of common 206Pb. R-Rim, C-Core, RE-Recrystallised, SB-'Soccer ball'

Table S2. continued: SHRIMP analytical results for zircons from sample I11-008C: Garnet-bearing charnockite, Chakkod continued

Texture	Spot	238U	232Th	232Th	f204	206Pb/238U		207Pb*/206Pb*		207Pb*/235U		238U/206Pb*		207Pb*/206Pb*		207Pb*/235U		Disc.
ID	no.	(ppm)	(ppm)	238U	(%)	date (Ma) ± 1σ		date (Ma) ± 1σ		date (Ma) ± 1σ		± %		± %		± %		(%)
R	008C-3.1	607	180	0.31	0.44	522	±6	516	±33	521	±10	11.860	1.2	0.058	1.5	0.670	1.9	-1
R	008C-11.1	302	129	0.44	0.07	523	±10	483	±60	515	±17	11.837	1.9	0.057	2.7	0.661	3.3	-9
R	008C-13.1	319	208	0.67	--	524	±6	561	±28	530	±9	11.820	1.1	0.059	1.3	0.686	1.7	7
R	008C-9.1	282	191	0.70	0.28	529	±9	686	±57	559	±18	11.696	1.7	0.062	2.7	0.735	3.2	24
R	008C-19.1	270	101	0.39	--	535	±8	658	±88	559	±25	11.552	1.6	0.062	4.1	0.734	4.4	19
R	008C-18.1	243	164	0.70	1.01	536	±10	658	±67	560	±20	11.531	1.9	0.062	3.1	0.736	3.6	19
R	008C-29.1	768	183	0.25	--	541	±9	556	±35	543	±13	11.433	1.8	0.059	1.6	0.708	2.4	3
R	008C-8.1	607	155	0.26	--	542	±13	533	±20	540	±14	11.396	2.4	0.058	0.9	0.703	2.6	-2
R	008C-20.1	521	265	0.53	--	549	±12	522	±20	543	±14	11.259	2.4	0.058	0.9	0.708	2.5	-5
SB	008C-27.1	238	168	0.73	0.09	549	±11	588	±35	557	±14	11.250	2.0	0.060	1.6	0.730	2.6	7
R	008C-21.1	254	88	0.36	0.16	551	±10	455	±61	532	±18	11.213	2.0	0.056	2.7	0.689	3.4	-22
SB	008C-15.1	265	97	0.38	0.04	551	±30	604	±31	562	±33	11.201	5.7	0.060	1.4	0.739	5.9	9
SB	008C-17.1	263	113	0.45	--	560	±23	482	±47	545	±26	11.020	4.3	0.057	2.1	0.710	4.8	-17
SB	008C-6.1A	260	87	0.35	0.08	565	±15	447	±55	542	±20	10.909	2.8	0.056	2.5	0.706	3.7	-28
R	008C-2.1	257	94	0.38	--	567	±17	537	±43	561	±21	10.884	3.2	0.058	2.0	0.737	3.8	-6
R	008C-28.1	275	182	0.68	0.28	589	±23	471	±151	565	±45	10.454	4.0	0.056	6.8	0.745	7.9	-26
SB	008C-1.1	254	86	0.35	--	602	±18	496	±57	580	±23	10.214	3.1	0.057	2.6	0.771	4.0	-22
C	008C-22.1	394	167	0.44	1.21	867	±58	1580	±157	1095	±121	6.943	7.1	0.098	8.4	1.939	11.0	48
C	008C-25.1	372	94	0.26	0.49	1894	±79	2175	±46	2031	±111	2.928	4.8	0.136	2.7	6.396	5.5	15

Errors are 1-sigma (abs) or % where indicated. Pb* indicate radiogenic proportions. All ages are common Pb corrected using measured 204Pb. f204 is % of common 206Pb. R-Rim, C-Core, RE-Recrystallised, SB-'Soccer ball'

Table S2. continued: SHRIMP analytical results for zircons from sample TB-14-025: Metapelitic gneiss, Chakkod

Texture	Spot	238U	232Th	232Th	f204	206Pb/238U		207Pb*/206Pb*		207Pb*/235U		238U/206Pb*		207Pb*/206Pb*		207Pb*/235U		Disc.
ID	no.	(ppm)	(ppm)	238U	(%)	date (Ma) ± 1σ		date (Ma) ± 1σ		date (Ma) ± 1σ		± %		± %		± %		(%)
R	PB1-1.1	1806	162	0.09	0.08	541	±14	506	±14	534	±15	11.432	2.7	0.057	0.6	0.692	2.8	-7
RE	PA1-1.1	1855	141	0.08	0.13	546	±23	497	±39	536	±26	11.316	4.5	0.057	1.8	0.696	4.8	-10
RE	PB2-1.1	1323	22	0.02	0.16	554	±25	527	±31	548	±27	11.152	4.7	0.058	1.4	0.716	4.9	-5
RE	PB2-1.2	2273	20	0.01	0.05	562	±26	512	±39	552	±29	10.972	4.9	0.058	1.8	0.723	5.2	-10
RE	PB1-1.4	1265	180	0.15	0.16	566	±17	615	±44	575	±22	10.897	3.2	0.060	2.0	0.763	3.8	+8

Errors are 1-sigma (abs) or % where indicated. Pb* indicate radiogenic proportions. All ages are common Pb corrected using measured 204Pb. f204 is % of common 206Pb. R-Rim, C-Core, RE-Recrystallised, SB-'Soccer ball'

Table S3: LA-ICP-MS monazite REE and trace element analyses: Sample I11-004K Garnet-biotite gneiss

	EB3 MNZ 59.1	EB3 MNZ 59.2	EB3 MNZ 59.3	EB3 MNZ 60.1	EB3 MNZ 60.2	EB3 MNZ 60.3	EB3 MNZ 61.1	EB3 MNZ 61.2	EB3 MNZ 61.3	EB3 MNZ 62.1	EB3 MNZ 62.2	EB3 MNZ 62.3
Position	C	R	R	C	R	R	C	R	R	C	R	R
Y	548	680	688	2870	926	636	3660	944	1271	2840	827	1370
La	104000	95300	93700	102000	94100	95200	102000	93300	96100	102000	96200	101000
Ce	230526	230526	230526	230526	230526	230526	230526	230526	230526	230526	230526	230526
Pr	28080	29550	30060	28610	29830	29190	28650	30100	30470	29530	30260	29540
Nd	105000	119000	118000	111000	120000	116000	105000	118000	119000	108000	113000	110000
Sm	17900	20600	19200	24700	25300	17800	23600	26100	24800	22500	21300	20200
Eu	36.5	17	17.4	54	18.8	14.9	54.6	16.6	28	51.7	18.5	33.1
Gd	5860	6110	5980	7550	7210	5580	7110	7250	6910	7410	6290	6100
Tb	304	281	284	470	369	262.2	483	364	365	460	318	323
Dy	510	508	517	1164	661	452	1204	677	743	1120	588	699
Ho	24.8	32.1	32.3	103.8	40.8	28.3	103	41.9	55	99	36.5	57.2
Er	19.3	32	32.1	136	38.7	29.1	130.5	39	61.5	132.2	35.8	71.7
Tm	0.99	1.91	1.71	8.82	2.04	1.44	7.97	1.78	3.87	8.31	2.01	4.78
Yb	3.27	5.59	4.59	29.6	5.92	4.68	26.5	5.25	12.7	28	4.48	15.1
Lu	0.385	0.56	0.59	2.43	0.64	0.43	2.4	0.59	1.09	2.74	0.55	1.44
LaN	441841	406050	399233	433319	400937	405624	435876	397529	409459	433745	409885	428206
PrN	315152	331650	337374	321100	334792	327609	321549	337823	341975	331425	339618	331538
NdN	231211	263042	259726	245579	266136	255747	232095	260831	262157	238285	249116	242706
SmN	121686	140041	130523	167913	171992	121006	160435	177430	168593	152957	144799	137322
EuN	652	304	311	964	336	266	975	296	500	923	330	591
GdN	29807	31078	30417	38403	36673	28383	36165	36877	35148	37691	31994	31027
TbN	8375	7741	7824	12948	10165	7223	13306	10028	10055	12672	8760	8898
DyN	2101	2093	2130	4796	2724	1862	4961	2789	3061	4615	2423	2880
HoN	446	577	581	1867	734	509	1853	754	989	1781	656	1029
TmN	121	201	202	856	244	183	821	245	387	832	225	451
ErN	41	79	71	364	84	60	329	74	160	343	83	198
YbN	20	34	28	182	36	29	163	32	78	172	28	93
LuN	16	23	24	100	26	18	99	24	45	113	23	59
Th (ppm)	139900	222800	226400	121500	170000	223100	122000	146300	184800	129600	170400	196100
U (ppm)	9270	7730	7660	12200	6910	5730	13390	10030	10620	15870	9870	9450
Ca (ppm)	10180	11620	10900	8980	11400	11260	9950	10180	12240	10890	10410	11520
Si (ppm)	2400	8800	7000	2800	12400	12320	6710	10900	7400	6300	12300	7100
Yb/Gd	0.001	0.001	0.001	0.005	0.001	0.001	0.005	0.001	0.002	0.005	0.001	0.003
Eu/Eu*	0.005	0.002	0.002	0.005	0.002	0.002	0.005	0.002	0.003	0.005	0.002	0.004

Values of - indicate elements are below detection limit of the instrument. Monazite trace elements calibrated against stoichiometric Ce fixed at 230526 ppm (Ce*)(Buick et al., 2010). C-core, R-Recrystallised zone

Table S3 continued: LA-ICP-MS monazite REE and trace element analyses: Sample I11-004K Garnet-biotite gneiss continued (EB3)

	EB3 MNZ 64.1	EB3 MNZ 64.2	EB3 MNZ 64.3	EB3 MNZ 66.1	EB3 MNZ 66.2	EB3 MNZ 66.3	EB3 MNZ 68.1	EB3 MNZ 68.2	EB3 MNZ 68.3	EB3 MNZ 69.2	EB3 MNZ 71.1	EB3 MNZ 71.2
Position	C	R	R	C	R	R	C	C	R	C	C	C
Y	3120	1249	473	2320	937	1143	2700	2700	1088	4140	967	810
La	103600	93400	100400	101400	93700	98000	102100	103800	93100	110100	91700	94900
Ce	230526	230526	230526	230526	230526	230526	230526	230526	230526	230526	230526	230526
Pr	29250	30460	29590	28850	30980	29990	28140	28260	29940	27490	31240	30460
Nd	106800	117200	110400	108900	119100	113300	105000	105100	120800	102200	123100	118100
Sm	23780	24630	16900	22500	22300	20700	22610	23010	20800	20530	25700	26020
Eu	51.9	17.6	23	49.9	19.2	27.2	47.7	44.5	17.7	50.4	19.8	20.25
Gd	7550	7220	5330	7060	7130	6250	6770	6580	6980	6410	8850	7350
Tb	475	385	234.3	430	363	322	410	406	372	454	402	370.3
Dy	1202	787	387	1037	699	673	944	918	697	1207	740	669
Ho	101.5	52.9	20.94	84.2	41.1	47.3	81.9	80.5	48.2	115.9	43.2	38.9
Er	134	56.6	22.2	106.4	41.1	56.6	111.8	109.2	48.6	167.8	40.6	35.2
Tm	8	2.88	1.19	6.95	1.8	3.26	7	7.2	2.33	11.83	1.85	1.39
Yb	26.7	8.06	3.09	18.7	4.96	10.5	23	24.5	6.9	41.2	5.71	4.72
Lu	2.34	0.97	0.312	1.83	0.64	0.88	1.96	2.08	0.94	3.54	0.62	0.52
LaN	441415	397955	427780	432041	399233	417554	435023	442267	396677	469110	390712	404346
PrN	328283	341863	332099	323793	347699	336588	315825	317172	336027	308530	350617	341863
NdN	236074	259063	244032	240716	263263	250442	232095	232317	267020	225906	272104	261052
SmN	161659	167437	114888	152957	151598	140721	153705	156424	141400	139565	174711	176886
EuN	927	314	411	891	343	486	852	795	316	900	354	362
GdN	38403	36724	27111	35910	36267	31790	34435	33469	35504	32604	45015	37386
TbN	13085	10606	6455	11846	10000	8871	11295	11185	10248	12507	11074	10201
DyN	4953	3243	1595	4273	2880	2773	3890	3782	2872	4973	3049	2756
HoN	1826	951	377	1514	739	851	1473	1448	867	2085	777	700
TmN	843	356	140	670	259	356	704	687	306	1056	256	222
ErN	331	119	49	287	74	135	289	298	96	489	76	57
YbN	164	50	19	115	31	65	142	151	42	254	35	29
LuN	96	40	13	75	26	36	81	86	39	146	26	21
Th (ppm)	114100	173200	226400	123400	168000	186900	98400	96600	176000	111700	159800	150200
U (ppm)	12380	9420	7680	13030	9680	10830	11300	10860	8260	14990	12800	12200
Ca (ppm)	9300	10180	11540	9290	11430	11620	8220	9110	10580	8740	10720	9190
Si (ppm)	800	7600	6200	1000	17100	7500	2140	3000	4200	3180	-	-
Yb/Gd	0.004	0.004	0.001	0.001	0.003	0.001	0.004	0.005	0.001	0.008	0.001	0.001
Eu/Eu*	0.005	0.002	0.003	0.005	0.002	0.003	0.005	0.005	0.002	0.006	0.002	0.002

Values of - indicate elements are below detection limit of the instrument. Monazite trace elements calibrated against stoichiometric Ce fixed at 230526 ppm (Ce*)(Buick et al., 2010). C-core, R-Recrystallised zone

Table S3 continued: LA-ICP-MS monazite REE and trace element analyses: Sample I11-004K Garnet-biotite gneiss continued (EB3), Sample I11-004C Transition zone (004)

	EB3 MNZ 71.3	004 MNZ-1-1	004 MNZ-1-2	004 MNZ-2-1	004 MNZ-2-2	004 MNZ-3-1	004 MNZ-3-2	004 MNZ-4-1	004 MNZ-4-2	004 MNZ-4-3	004 MNZ-5-1	004 MNZ-5-2
Position	C	C	R	C	R	C	R	C	R	R	R	C
Y	999	2801	382	3570	398	3643	599.9	3448	2695	1610	1610	3264
La	92800	100500	98700	100600	94700	101800	95410	99510	97900	97320	98450	98320
Ce	230526	230526	230526	230526	230526	230526	230526	230526	230526	230526	230526	230526
Pr	30750	28560	28970	28650	29890	28580	29920	29080	29330	29790	28980	29060
Nd	118800	109700	113600	108800	119500	108200	117500	109200	109500	114600	111200	110100
Sm	27330	24660	19990	25410	22150	24600	23720	25280	24500	24430	24760	26070
Eu	22	38.8	15.82	43	12.25	45.9	14.6	43.2	36.5	25.1	18.61	48.8
Gd	8000	11690	4410	12950	7190	12860	10230	12480	11560	11370	11520	12500
Tb	406	325.5	156.4	410	177.5	409	231.3	369.3	327.3	300.7	309.5	366.7
Dy	748	797	280.8	999	303.1	1013	418.5	909	766	634	649	889
Ho	45.5	69	17.34	85.3	18.11	85.6	27.15	82.6	65.2	46.65	44.7	78
Er	42.9	89.2	17.96	107.2	18.58	107.4	25.74	112	82.5	53.4	46.1	102.9
Tm	1.77	5.47	0.78	6.51	0.809	6.42	1.18	6.95	4.92	2.97	2.25	6.33
Yb	5.41	17.76	2.69	21.2	2.36	20.5	3.55	22.8	15.69	9.05	5.99	20.73
Lu	0.74	1.56	0.223	1.8	0.262	1.732	0.347	1.95	1.39	0.748	0.522	1.75
LaN	395398	428206	420537	428632	403494	433745	406519	423988	417128	414657	419472	418918
PrN	345118	320539	325140	321549	335466	320763	335802	326375	329181	334343	325253	326150
NdN	262599	242485	251105	240495	264147	239169	259726	241379	242042	253316	245800	243369
SmN	185792	167641	135894	172740	150578	167233	161251	171856	166553	166077	168321	177226
EuN	393	693	283	768	219	820	261	771	652	448	332	871
GdN	40692	59461	22431	65870	36572	65412	52035	63479	58800	57833	58596	63581
TbN	11185	8967	4309	11295	4890	11267	6372	10174	9017	8284	8526	10102
DyN	3082	3284	1157	4116	1249	4174	1724	3745	3156	2612	2674	3663
HoN	818	1241	312	1534	326	1540	488	1486	1173	839	804	1403
TmN	270	561	113	675	117	676	162	705	519	336	290	648
ErN	73	226	32	269	33	265	49	287	203	123	93	262
YbN	33	109	17	130	15	126	22	140	97	56	37	128
LuN	30	64	9	74	11	71	14	80	57	31	21	72
Th (ppm)	91100	114900	252700	122500	237800	129900	201600	132400	115200	164600	115000	91400
U (ppm)	11770	9290	4250	10050	3990	11340	6340	10260	8510	7300	6800	9970
Ca (ppm)	6630	7190	8450	7690	9690	8410	8990	8180	7230	8980	6320	6880
Si (ppm)	6300	210	4480	840	3510	916	2940	570	1200	2020	1240	970
Yb/Gd	0.001	0.002	0.001	0.002	0.000	0.002	0.000	0.002	0.002	0.001	0.001	0.002
Eu/Eu*	0.002	0.004	0.002	0.004	0.001	0.004	0.001	0.004	0.003	0.002	0.004	0.002

Values of - indicate elements are below detection limit of the instrument. Monazite trace elements calibrated against stoichiometric Ce fixed at 230526 ppm (Ce*)(Buick et al., 2010). C-core, R-Recrystallised zone

Table S3 continued: LA-ICP-MS monazite REE and trace element analysesL Sample I11-004C Transition zone continued (004)

	004 MNZ-5-3	004 MNZ-5-4	004 MNZ-6-1	004 MNZ-6-2	004 MNZ-6-3	004 MNZ-6-4	004 MNZ-6-5	004 MNZ-7-1	004 MNZ-7-2	004 MNZ-7-3	004 MNZ-7-4	004 MNZ-8-1
Position	R	R	R	C	R	R	R	R	R	C	R	R
Y	838	678	1039	3196	455	499	720	337.2	698	2714	678	751
La	96340	95430	93340	100230	98400	94200	93900	96930	94860	98930	93480	95500
Ce	230526	230526	230526	230526	230526	230526	230526	230526	230526	230526	230526	230526
Pr	29270	29510	29710	28280	28800	30080	29730	29350	29970	28820	30130	29500
Nd	113500	115500	116900	107000	111200	117900	118200	113400	117600	107120	119000	115300
Sm	23690	24940	25490	24580	20700	22970	26160	20740	25340	24190	24710	24670
Eu	18.84	16.26	16.06	42.09	17.7	13.01	13.97	13.98	14.52	40.7	15.17	16.29
Gd	10410	11380	11500	11820	6350	9200	11910	6410	11150	11210	10680	11210
Tb	264.7	279	293.7	352	181.8	202.6	288.1	162.3	269.2	320.4	253.3	282.8
Dy	525	511.9	585	884	327	358	525	260.1	498.9	747.3	465.4	517
Ho	35.9	30.19	39.14	76.4	19	21.78	31.37	14.88	30.58	66.03	30.28	33.37
Er	38.7	27.46	40.5	101.4	19.7	22.25	28.05	15.42	28.56	86.5	30	31.8
Tm	1.77	1.054	1.85	6.32	0.87	0.946	1.26	0.589	1.19	5.52	1.33	1.39
Yb	5.7	3.4	5.09	21.2	2.72	3.39	3.51	2.14	4.16	18.77	4.01	4.1
Lu	0.459	0.323	0.451	1.76	0.207	0.291	0.341	0.188	0.372	1.51	0.359	0.353
LaN	410481	406604	397699	427056	419259	401363	400085	412995	404176	421517	398296	406902
PrN	328507	331201	333446	317396	323232	337598	333670	329405	336364	323457	338159	331089
NdN	250884	255305	258400	236516	245800	260610	261273	250663	259947	236782	263042	254863
SmN	161047	169545	173283	167097	140721	156152	177838	140993	172264	164446	167981	167709
EuN	336	290	287	752	316	232	249	250	259	727	271	291
GdN	52950	57884	58494	60122	32299	46796	60580	32604	56714	57019	54323	57019
TbN	7292	7686	8091	9697	5008	5581	7937	4471	7416	8826	6978	7791
DyN	2163	2109	2410	3642	1347	1475	2163	1072	2056	3079	1918	2130
HoN	646	543	704	1374	342	392	564	268	550	1188	545	600
TmN	244	173	255	638	124	140	177	97	180	544	189	200
ErN	73	44	76	261	36	39	52	24	49	228	55	57
YbN	35	21	31	130	17	21	22	13	26	116	25	25
LuN	19	13	19	72	9	12	14	8	15	62	15	15
Th (ppm)	174200	155800	167000	120800	238900	234900	172500	236800	172900	106000	198300	159800
U (ppm)	6730	6770	7290	9270	6600	5200	6380	5400	6570	8310	5870	6410
Ca (ppm)	9490	9050	8730	8530	9900	10380	9500	9670	9330	6690	9540	8010
Si (ppm)	1940	1700	2440	630	4210	3870	2000	4270	2790	1710	2400	5020
Yb/Gd	0.001	0.000	0.001	0.002	0.001	0.000	0.000	0.000	0.000	0.002	0.000	0.000
Eu/Eu*	0.002	0.004	0.001	0.001	0.002	0.004	0.002	0.001	0.001	0.004	0.002	0.001

Values of - indicate elements are below detection limit of the instrument. Monazite trace elements calibrated against stoichiometric Ce fixed at 230526 ppm (Ce*)(Buick et al., 2010). C-core, R-Recrystallised zone

Table S3 continued: LA-ICP-MS monazite REE and trace element analyses: Sample I11-004C Transition zone continued (004), Sample I11-008C Chamockite (008)

	004 MNZ-8-2	004 MNZ-8-3	004 MNZ-9-1	004 MNZ-9-2	004 MNZ-9-3	004 MNZ-10-1	004 MNZ-10-2	004 MNZ-10-3	008 MNZ-1-1	008 MNZ-1-2	008 MNZ-1-3	008 MNZ-2-1
Position	C	R	C	R	R	C	R	R	R	R	R	R
Y	3522	524	3491	803	892	2222	538	406.8	1570	1620	1640	1101
La	98000	94000	99700	97970	98980	105700	93770	96380	89290	89700	88440	90950
Ce	230526	230526	230526	230526	230526	230526	230526	230526	230526	230526	230526	230526
Pr	29080	29960	29320	29850	29460	28080	30020	29930	31090	31160	31230	31130
Nd	109700	118490	109100	115200	111500	104300	119500	117300	134400	134000	136000	131000
Sm	26100	23460	25180	22850	21860	21410	25010	23240	21530	21440	21730	19770
Eu	44.5	13.93	42.7	19.67	23.8	37.73	13.9	13.73	15.91	16.39	16.46	16.89
Gd	12780	9630	12400	9970	9330	10480	10810	8650	8230	7870	8360	4160
Tb	392	216.1	373.1	244.4	235	311.4	246.2	199.3	226.9	226.3	228.8	219.6
Dy	938	380.6	929	479.8	499	729	429.3	328.1	549	550	559	538
Ho	83	23.94	83.9	34.47	36.7	52.8	24.05	18.37	43.8	43.9	45.1	43.1
Er	114.4	23.58	111.3	39.1	44.3	54.7	21.4	16.94	55.8	54.1	56	56.4
Tm	7.07	1.09	6.8	2.05	2.67	2.68	0.766	0.667	3.06	2.97	3.24	3.31
Yb	22.93	3.5	23.7	6.28	7.74	7.11	2.55	2.01	9.3	9.55	9.96	9.17
Lu	1.93	0.275	1.99	0.553	0.69	0.511	0.237	0.207	0.862	0.739	0.851	0.729
LaN	417554	400511	424798	417427	421730	450362	399531	410652	380443	382190	376821	387516
PrN	326375	336251	329068	335017	330640	315152	336925	335915	348934	349719	350505	349383
NdN	242485	261914	241158	254642	246463	230548	264147	259284	297082	296198	300619	289567
SmN	177430	159483	171176	155337	148606	145547	170020	157988	146363	145751	147723	134398
EuN	795	249	763	351	425	674	248	245	284	293	294	302
GdN	65005	48983	63072	50712	47457	53306	54985	43998	41862	40031	42523	21160
TbN	10799	5953	10278	6733	6474	8579	6782	5490	6251	6234	6303	6050
DyN	3865	1568	3828	1977	2056	3004	1769	1352	2262	2266	2303	2217
HoN	1493	431	1509	620	660	950	433	330	788	790	811	775
TmN	720	148	700	246	279	344	135	107	351	340	352	355
ErN	292	45	281	85	110	111	32	28	126	123	134	137
YbN	141	22	146	39	48	44	16	12	57	59	61	56
LuN	79	11	82	23	28	21	10	9	35	30	35	30
Th (ppm)	126400	227600	133800	213200	217400	133100	200300	209900	111100	114300	95300	231800
U (ppm)	10400	5850	10220	6250	6220	9170	7040	5620	4470	4670	4390	4430
Ca (ppm)	9100	10410	8080	9220	9510	8610	8380	9100	6660	6160	5860	11990
Si (ppm)	1080	2900	990	3100	3660	1020	2930	3400	1040	910	500	1560
Yb/Gd	0.002	0.000	0.002	0.001	0.001	0.001	0.000	0.000	0.001	0.001	0.001	0.003
Eu/Eu*	0.001	0.002	0.001	0.004	0.001	0.001	0.004	0.001	0.002	0.002	0.002	0.002

Values of - indicate elements are below detection limit of the instrument. Monazite trace elements calibrated against stoichiometric Ce fixed at 230526 ppm (Ce*)(Buick et al., 2010). C-core, R-Recrystallised zone

Table S3 continued: LA-ICP-MS monazite REE and trace element analyses: Sample I11-008C Charnockite continued (008), Sample TB-14-025 Metapelitic gneiss (PA/PB)

	008 MNZ-2-2	008 MNZ-2-3	PA-1.1	PA-4.1	PA-4.2	PA-5.1	PA-5.2	PA-6.1	PA-12.1	PA-12.2	PA-13.1B	PB-1.1
Position	R	R	R	C	R	C	R	C	R	R	R	C
Y	1198	1114	329	3920	396	7960	288	346	319	338	11260	19900
La	90500	90300	97600	135300	119300	137600	105300	114700	115900	109900	140400	131600
Ce	230526	230526	230526	230526	230526	230526	230526	230526	230526	230526	230526	230526
Pr	31160	31160	32220	24980	27070	26970	32300	31240	30100	30960	27200	26680
Nd	132100	129500	152700	104700	124700	110300	151200	141700	135900	146900	112900	115700
Sm	20040	19270	21940	18900	18620	20030	20990	19320	19110	20840	21160	17380
Eu	17.6	17.56	20.9	146.5	26.7	353.5	21.82	28.1	27.5	23.6	342	394
Gd	4150	6580	5116	10810	5160	14660	5190	5700	4900	5450	14580	11140
Tb	224.9	193.2	191.7	775	222.7	1456	209.2	254	193.9	214.5	1489	1394
Dy	564	460	285.9	1998	361.1	4110	310	386	292	311.1	4730	6340
Ho	43.8	35.76	14.68	159.8	18.17	320	14.64	17.5	14.4	15.08	438	803
Er	58.3	45.2	16.62	149.8	18.12	298	14.38	16.4	16.6	16.69	509	1177
Tm	3.21	2.33	0.443	6.16	0.52	13.61	0.366	0.427	0.52	0.573	27.8	75.2
Yb	9.82	7.67	1.25	15	1.51	34.8	1.38	1.46	1.17	1.58	81.1	240
Lu	0.813	0.606	0.142	1.22	0.159	2.86	0.117	0.122	0.14	0.143	6.14	18.9
LaN	385599	384746	415850	576481	508308	586280	448658	488709	493822	468257	598210	560716
PrN	349719	349719	323232	361616	280359	302694	362514	350617	337823	347475	305275	299439
NdN	291998	286251	305040	337533	231432	243811	334218	313218	300398	324713	249558	255747
SmN	136234	130999	147111	149150	128484	136166	142692	131339	129912	141672	143848	118151
EuN	314	314	584	373	2616	6313	390	502	491	421	6107	7036
GdN	21109	33469	28230	26022	54985	74568	26399	28993	24924	27721	74161	56663
TbN	6196	5322	5620	5281	21350	40110	5763	6997	5342	5909	41019	38402
DyN	2324	1895	1199	1178	8232	16934	1277	1590	1203	1282	19489	26123
HoN	788	643	228	264	2874	5755	263	315	259	271	7878	14442
TmN	367	284	77	105	943	1875	90	103	104	105	3203	7407
ErN	133	96	10	18	255	562	15	18	21	24	1149	3107
YbN	60	47	12	8	92	214	8	9	7	10	499	1477
LuN	33	25	3	6	50	118	5	5	6	6	253	778
Th (ppm)	279600	23200	191000	57200	87800	56700	126200	120100	114800	134500	64500	74400
U (ppm)	4890	4770	4160	3684	3280	9940	2939	2890	2960	4970	8560	8290
Ca (ppm)	13390	1880	7680	6380	6010	8540	6500	8100	9970	7310	8420	11200
Si (ppm)	2880	98	15000	6500	10900	-	6300	1500	24300	5700	2100	-
Yb/Gd	0.003	0.001	0.000	0.000	0.002	0.003	0.000	0.000	0.000	0.000	0.007	0.026
Eu/Eu*	0.002	0.002	0.004	0.002	0.017	0.036	0.002	0.003	0.003	0.003	0.034	0.048

Values of - indicate elements are below detection limit of the instrument. Monazite trace elements calibrated against stoichiometric Ce fixed at 230526 ppm (Ce*)(Buick et al., 2010). C-core, R-Recrystallised zone

Table S3 continued: LA-ICP-MS monazite REE and trace element analyses: Sample TB-14-025 Metapelitic gneiss (PA/PB), Sample I11-006V Pegmatite (EB1)

	PB-2.1	PB-4.1	PB-4.2	PB-5.1	PB-5.2	PB-6.1	PB-6.2	PB-7.1	PB-7.2	PB-8.1	PB-8.2	EB1 MNZ 4.1
Position	C	R	C	C	R	C	R	C	C	C	C	C
Y	457.4	3120	3995	7850	286.5	13300	313.2	2310	1160	14980	11670	1700
La	96700	128600	140800	142600	110800	139300	96500	133300	126900	138100	141100	90600
Ce	230526	230526	230526	230526	230526	230526	230526	230526	230526	230526	230526	230526
Pr	31820	29650	28070	27670	32740	28610	35610	28230	29320	26780	26540	31080
Nd	149100	131200	118100	111800	147800	120400	180700	120700	129800	111200	110200	120000
Sm	22420	20380	19200	20500	17670	20290	24780	17490	18550	20000	20010	11740
Eu	15.95	136.2	175.1	443	24.38	250	18.84	136	91	721	563	20.1
Gd	4877	9600	11370	14520	3981	12380	5040	7100	6130	13610	14150	4520
Tb	179.5	679	867	1405	143.1	1250	179.4	447	325	1463	1512	281
Dy	304.4	1749	2217	4000	211.2	4650	262.3	1210	720	5650	5180	763
Ho	19.56	125.5	155.9	291	12.61	540	14.16	92	48.3	570	433	70.3
Er	25.9	117.8	137	257	17.87	820	18.2	86	40.8	690	373.8	99.9
Tm	1.05	5.21	6.46	11.31	0.624	66	0.654	3.8	1.34	44.3	14.81	6.27
Yb	2.89	14.36	16.63	29.3	1.86	251	1.67	9.2	3.4	136	35.2	21.7
Lu	0.273	1.15	1.25	2.24	0.168	22.9	0.152	0.76	0.271	10.32	2.56	2.09
LaN	412015	547934	599915	607584	472092	593524	411163	567959	540690	588411	601193	386025
PrN	357127	332772	315039	310550	367452	321100	399663	316835	329068	300561	297868	348822
NdN	329576	290009	261052	247126	326702	266136	399425	266799	286914	245800	243590	264589
SmN	152413	138545	130523	139361	120122	137933	168457	118899	126105	135962	136030	79810
EuN	285	2432	3127	7911	435	4464	336	2429	1625	12875	10054	359
GdN	24807	48830	57833	73856	20249	62970	25636	36114	31180	69227	71974	22991
TbN	4945	18705	23884	38705	3942	34435	4942	12314	8953	40303	41653	7741
DyN	1254	7206	9135	16481	870	19159	1081	4986	2967	23280	21343	3144
HoN	352	2257	2804	5234	227	9712	255	1655	869	10252	7788	1264
TmN	163	741	862	1617	112	5160	115	541	257	4342	2352	629
ErN	43	215	267	467	26	2727	27	157	55	1831	612	259
YbN	18	88	102	180	11	1545	10	57	21	837	217	134
LuN	11	47	51	92	7	942	6	31	11	425	105	86
Th (ppm)	32410	148000	92100	64710	134700	94000	201900	84300	109500	79100	60500	144200
U (ppm)	3120	7530	6540	10480	1682	7040	7420	3600	3320	7880	9190	23200
Ca (ppm)	2860	9370	10290	9630	8700	9180	8110	6890	6360	9820	9170	10930
Si (ppm)	1800	4900	3550	6200	13400	6100	15200	4000	4300	6000	16500	1800
Yb/Gd	0.001	0.002	0.002	0.002	0.001	0.025	0.000	0.002	0.001	0.012	0.003	0.006
Eu/Eu*	0.002	0.015	0.020	0.045	0.003	0.026	0.002	0.018	0.011	0.075	0.058	0.004

Values of - indicate elements are below detection limit of the instrument. Monazite trace elements calibrated against stoichiometric Ce fixed at 230526 ppm (Ce*)(Buick et al., 2010). C-core, R-Recrystallised zone

Table S3 continued: LA-ICP-MS monazite REE and trace element analyses, Sample I11-006V Pegmatite continued (EB1)

	EB1 MNZ 4.2	EB1 MNZ 4.3	EB1 MNZ 5.1	EB1 MNZ 5.2	EB1 MNZ 6.1	EB1 MNZ 6.2	EB1 MNZ 7.1	EB1 MNZ 7.2	EB1 MNZ 11.1	EB1 MNZ 12.1	EB1 MNZ 12.2	EB1 MNZ 22.1
Position	R	C	C	C	C	C	C	C	C	C	C	C
Y	1362	1235	1632	1322	1464	1415	1670	1710	1514	1890	1428	1678
La	92700	92000	89400	92300	91100	91800	92800	92700	90800	91500	92300	89500
Ce	230526	230526	230526	230526	230526	230526	230526	230526	230526	230526	230526	230526
Pr	29630	30610	31370	30330	31130	30220	31140	30490	31650	31450	30790	30950
Nd	116000	118000	119000	117000	123000	116000	124000	118000	120000	124000	120000	124000
Sm	12600	11010	11550	11010	13200	11700	13500	15400	11370	13300	12120	12040
Eu	21	20	20	20	19	21	23	20	19	22	19	22
Gd	4020	4010	4410	3930	4630	4010	4410	4390	4450	4680	4120	4840
Tb	241.2	238	281	239	284	256	274	269	274	297	260	299
Dy	627	590	748	608	692	648	738	711	714	803	656	764
Ho	53.4	51.9	67.8	53	61.7	55.4	69.7	65.4	64.6	71.1	57.4	70.7
Er	76.3	69.3	91.7	73.4	86.6	78.4	96.1	94.1	91.7	106.1	74	94.1
Tm	4.46	4.24	6.51	4.83	5.01	5.06	6.29	5.81	5.62	6.91	4.9	6.95
Yb	14	14.2	22.2	14.7	16	15.7	21.1	20.8	19	22.3	15.1	22
Lu	1.19	1.19	2.04	1.46	1.32	1.62	1.91	1.56	1.63	1.92	1.47	2.35
LaN	394972	391990	380912	393268	388155	391138	395398	394972	386877	389859	393268	381338
PrN	332548	343547	352076	340404	349383	339169	349495	342200	355219	352974	345567	347363
NdN	256189	260831	263926	259063	270778	256189	273431	261273	264589	273873	265694	274978
SmN	85656	74847	78518	74847	89735	79538	91774	104691	77294	90415	82393	81849
EuN	368	354	348	354	346	366	405	354	346	400	341	386
GdN	20448	20397	22431	19990	23550	20397	22431	22330	22635	23805	20956	24619
TbN	6645	6556	7741	6584	7824	7052	7548	7410	7548	8182	7163	8237
DyN	2583	2431	3082	2505	2851	2670	3041	2930	2942	3309	2703	3148
HoN	960	933	1219	953	1110	996	1254	1176	1162	1279	1032	1272
TmN	480	436	577	462	545	493	605	592	577	668	466	592
ErN	184	175	269	200	207	209	260	240	232	286	202	287
YbN	86	87	137	90	98	97	130	128	117	137	93	135
LuN	49	49	84	60	54	67	79	64	67	79	60	97
Th (ppm)	134200	152300	146300	155900	142500	148200	146900	143000	153700	147100	149700	143900
U (ppm)	15410	20000	20800	19000	23000	38800	30900	23300	17000	19100	15000	19400
Ca (ppm)	9440	10590	11330	11370	11500	11320	11380	13000	10600	12300	11400	11320
Si (ppm)	8300	5200	1660	10600	100	6600	-	10500	-	6000	5100	4280
Yb/Gd	0.004	0.004	0.006	0.005	0.004	0.005	0.006	0.006	0.005	0.006	0.004	0.005
Eu/Eu*	0.004	0.004	0.004	0.004	0.003	0.004	0.004	0.003	0.004	0.004	0.004	0.004

Values of - indicate elements are below detection limit of the instrument. Monazite trace elements calibrated against stoichiometric Ce fixed at 230526 ppm (Ce*)(Buick et al., 2010). C-core, R-Recrystallised zone

Table S3 continued: LA-ICP-MS monazite REE and trace element analyses, Sample I11-006V Pegmatite continued (EB1)

	EB1 MNZ 22.2	EB1 MNZ 24.1	EB1 MNZ 24.2	EB1 MNZ 24.3	EB1 MNZ 24.4	EB1 MNZ 25.1	EB1 MNZ 25.2	EB1 MNZ 26.1	EB1 MNZ 26.2	EB1 MNZ 27.1	EB1 MNZ 27.2	EB1 MNZ 27.3
Position	C	C	C	C	R	C	C	C	R	R	C	C
Y	1218	1763	1345	1214	1363	1690	1390	1430	1250	1314	1480	1540
La	90300	92800	90600	92000	87400	86700	95000	89800	91200	92300	90600	90200
Ce	230526	230526	230526	230526	230526	230526	230526	230526	230526	230526	230526	230526
Pr	30810	31170	30220	30580	32030	31000	30400	30070	30180	30060	30130	30800
Nd	120000	124000	114000	117000	127000	124000	116000	117000	119000	118000	116000	117000
Sm	10570	11610	9790	10050	11720	12000	17000	10300	11280	10580	13900	11700
Eu	19	21	20	18	26	23	21	19	18	19	21	21
Gd	4260	4923	4020	4050	4800	4690	4640	4130	4280	4240	4160	4300
Tb	250.9	297.9	253	235	280	310	236	257	253	249	259	275
Dy	627	807	646	600	690	719	617	643	626	644	667	714
Ho	51.8	74.3	55.4	51.1	58.2	66.3	53.3	57.3	54	54.4	57.3	60.8
Er	73.8	105	80.2	69.9	78.2	104	71	77.3	71.5	76.7	78.3	82.4
Tm	4.63	7.03	5.02	4.39	4.47	6.6	4.5	5.51	4.65	4.82	5.99	6.3
Yb	12.9	22.3	17.1	13.6	14.9	17.4	14.6	18.1	12.6	15.9	14.9	18.3
Lu	1.31	2.57	1.57	1.4	1.37	1.69	1.25	1.36	1.07	1.34	1.75	1.7
LaN	384746	395398	386025	391990	372390	369408	404772	382616	388581	393268	386025	384320
PrN	345791	349832	339169	343210	359484	347924	341190	337486	338721	337374	338159	345679
NdN	264368	274757	251768	258621	281388	274094	256410	258621	262157	260168	256631	258621
SmN	71856	78926	66553	68321	79674	81577	115568	70020	76683	71924	94494	79538
EuN	338	373	352	313	459	409	377	341	313	338	370	368
GdN	21668	25041	20448	20600	24415	23856	23601	21007	21770	21567	21160	21872
TbN	6912	8207	6970	6474	7713	8540	6501	7080	6970	6860	7135	7576
DyN	2583	3325	2662	2472	2843	2963	2542	2649	2579	2653	2748	2942
HoN	932	1336	996	919	1047	1192	959	1031	971	978	1031	1094
TmN	464	661	505	440	492	654	447	486	450	483	493	519
ErN	191	290	207	181	185	273	186	228	192	199	248	260
YbN	79	137	105	84	92	107	90	111	78	98	92	113
LuN	54	106	65	58	56	70	51	56	44	55	72	70
Th (ppm)	171000	158300	183900	97700	46900	140000	137000	140600	96900	151200	144700	149000
U (ppm)	10980	20210	33700	11640	11810	18600	12300	26600	15270	17500	30400	40400
Ca (ppm)	11700	12590	12700	7170	4520	14400	12800	11890	7290	9600	12300	12300
Si (ppm)	3160	5800	2940	-	-	17100	5000	4700	1340	1300	7200	3650
Yb/Gd	0.004	0.005	0.005	0.004	0.004	0.004	0.004	0.005	0.004	0.005	0.004	0.005
Eu/Eu*	0.004	0.004	0.005	0.004	0.005	0.004	0.003	0.004	0.004	0.004	0.004	0.004

Values of - indicate elements are below detection limit of the instrument. Monazite trace elements calibrated against stoichiometric Ce fixed at 230526 ppm (Ce*)(Buick et al., 2010). C-core, R-Recrystallised zone

Table S4: LA-ICP-MS zircon REE and trace element analyses, Sample I11-004K Garnet-biotite gneiss (004), Sample I11-008C Charnockite (008)

	004G-1-1	004G-2-1	004G-5-1	004G-6-1	004G-7-1	004G-8-1	004G-9-1	004G-10-1	004G-11-1	008C-1-1	008C-2-1	008C-3-1	008C-5-1	008C-6-1	008C-8-1	008C-9-2	008C-10-1	008C-11-1
Position	C	R	R	R	C	C	R	R	C	SB	R	R	R	SB	R	R	R	R
Y	1414	130.6	98.6	113.5	1450	1029	113	108.1	816	166.7	149.5	163.8	216	178.1	116.5	170	980	331
Sm	34.2	12.4	7.9	3.9	113	21.4	13.8	4.2	32	1.22	2.51	2.43	3.7	2.5	1.18	1.04	8.6	3.18
Eu	9.2	1.92	0.73	0.11	30.1	5.6	1.79	0.09	7.3	-	-	-	0.089	-	-	0.058	2.32	-
Gd	34.2	19.3	12.4	12.6	66.5	24.4	19.5	16.8	30.3	10.6	8.4	8.4	13.4	11.3	7.5	10.1	29.1	20.9
Tb	9.42	3.47	2.21	3.09	12.5	7.43	2.55	2.51	6.3	3.29	2.52	2.82	3.46	3.3	2.08	2.35	9.1	5.45
Dy	116.4	20	15.8	16	125	85.9	19.1	16.2	71.8	22.3	22.2	21.2	29	24.9	14.5	22.9	101	45.4
Ho	45.3	4.23	3.13	3.68	45	32.7	3.68	3.59	25.2	5.19	4.32	5.33	6.3	5.47	3.25	5.4	31.4	10.64
Tm	223.7	12	8.8	11.1	237	168.2	11.1	9.5	114.1	16.5	13.9	17	20.4	16.4	8.9	21	135	33.8
Er	48.9	1.8	1.55	1.6	48.1	35.2	1.55	1.55	22.3	2.48	2.26	2.3	3.47	2.46	1.58	3.14	27.3	5.31
Yb	464	14.6	13.1	12.4	464	328	13.1	10.3	205.5	19.7	16.4	18	27.3	19.5	8.9	25.7	233	38.1
Lu	89.9	2.13	2.47	1.99	85.4	65.2	1.79	2.62	42.9	3.55	2.21	3.68	5.14	3.21	1.62	5.4	47.4	7.1
SmN	232.5	84.3	53.7	26.5	768.2	145.5	93.8	28.6	217.5	8.3	17.1	16.5	14.6	25.2	17.0	8.0	7.1	21.6
EuN	164.3	34.3	13.0	2.0	537.5	100.0	32.0	1.6	130.4	-	-	-	1.9	-	-	1.0	1.0	-
GdN	174.0	98.2	63.1	64.1	338.3	124.1	99.2	85.5	154.1	53.9	42.7	42.7	60.0	68.2	57.5	38.1	51.4	106.3
TbN	259.5	95.6	60.9	85.1	344.4	204.7	70.2	69.1	173.6	90.6	69.4	77.7	67.2	95.3	90.9	57.3	64.7	150.1
DyN	479.6	82.4	65.1	65.9	515.0	353.9	78.7	66.7	295.8	91.9	91.5	87.4	85.3	119.5	102.6	59.7	94.4	187.1
HoN	814.7	76.1	56.3	66.2	809.4	588.1	66.2	64.6	453.2	93.3	77.7	95.9	72.3	113.3	98.4	58.5	97.1	191.4
TmN	1407.8	75.5	55.4	69.9	1491.5	1058.5	69.9	59.8	718.1	103.8	87.5	107.0	80.6	128.4	103.2	56.0	132.2	212.7
ErN	2020.7	74.4	64.0	66.1	1987.6	1454.5	64.0	64.0	921.5	102.5	93.4	95.0	83.1	143.4	101.7	65.3	129.8	219.4
YbN	2855.4	89.8	80.6	76.3	2855.4	2018.5	80.6	63.4	1264.6	121.2	100.9	110.8	81.8	168.0	120.0	54.8	158.2	234.5
LuN	3699.6	87.7	101.6	81.9	3514.4	2683.1	73.7	107.8	1765.4	146.1	90.9	151.4	114.8	211.5	132.1	66.7	222.2	292.2
Th (ppm)	158.7	115.5	92.4	122.4	177.9	91.7	108.2	168	136	69.8	79.5	148.3	81.5	86.2	139.3	142	120	163.2
U (ppm)	6100	1010	1910	1370	4620	2580	1130	1300	1800	530	560	1700	670	730	1910	1510	3510	1060
YbN/GdN	16.41	0.92	1.28	1.19	8.44	16.26	0.81	0.74	8.21	2.25	2.36	2.59	2.46	2.09	1.44	3.08	9.69	2.21
Eu/Eu*	0.81	0.38	0.22	0.04	0.97	0.74	0.33	0.03	0.70	-	-	-	0.05	-	-	0.04	0.04	-

Values of - indicate trace elements are below detection limit of the instrument

R-Rim, C-Core, RE-Recrystallised

Table S4 continued: LA-ICP-MS zircon REE and trace element analyses, Sample I11-008C Charnockite (008)

	008C-12-1	008C-13-1	008C-14-1	008C-15-1	008C-16-1	008C-17-1	008C-18-1	008C-19-1	008C-20-1	008C-21-1	008C-22-1	008C-23-1	008C-24-1	008C-25.1	008C-26-1	008C-28-1	008C-29-1
Position	R	R	R	SB	R	SB	R	R	R	R	C	R	R	C	C	R	R
Y	135	115	313	142.5	175.8	124	165	216.6	228.5	145.3	1309	218	151.4	414	871	174.8	143.1
Sm	2.21	2.78	4.6	2.54	2.16	1.81	2.33	1.74	3.8	1.65	10.3	2.15	1.83	1.2	3.3	1.01	2.64
Eu	0.072	-	0.019	-	-	-	-	-	-	0.039	1.85	-	-	0.25	0.65	0.097	-
Gd	10.3	9.1	24.2	9.3	12.9	7.4	9.5	16.2	15.6	8.8	32.8	14.3	12.9	12.2	19.6	9.9	12
Tb	2.38	2.02	5.58	2.39	2.88	1.93	2.39	3.85	4.15	3.03	11.09	3.95	3.12	3.5	6.37	2.72	2.89
Dy	16.2	15.2	43.9	20.4	23.1	19	19.6	28.5	30.4	20	126.3	29.2	20.5	35.3	79.7	21.5	22
Ho	3.21	3.31	10.1	4.5	5.12	3.37	5.48	6.33	6.87	4.61	47.2	6.84	5.11	13.9	28.4	5.31	4.39
Tm	11.7	10.6	32.6	12.9	18.3	11.1	21.6	20.4	25.3	15.5	197.6	22.4	14.5	65.0	135	17.6	13.3
Er	1.56	1.38	4.29	1.95	2.83	1.69	3.66	2.9	3.54	2.11	38.6	3.8	2.31	12.8	26.6	2.67	2.02
Yb	12.5	10.5	31.9	16.2	21.5	16.1	36	24.1	28.2	13.7	349	27.9	18.2	118.0	231	24	19.2
Lu	3.02	1.85	5.44	2.65	3.74	2.13	5.9	3.51	4.57	2.97	66.9	4.65	2.87	23.2	50.2	4.03	3.68
SmN	15.0	18.9	31.3	17.3	14.7	12.3	15.8	11.8	25.8	11.2	70.0	14.6	12.4	7.8	22.4	6.9	17.9
EuN	1.3	-	0.3	-	-	-	-	-	-	0.7	33.0	-	-	4.5	11.6	1.7	-
GdN	52.4	46.3	123.1	47.3	65.6	37.6	48.3	82.4	79.3	44.8	166.8	72.7	65.6	62.1	99.7	50.4	61.0
TbN	65.6	55.6	153.7	65.8	79.3	53.2	65.8	106.1	114.3	83.5	305.5	108.8	86.0	95.9	175.5	74.9	79.6
DyN	66.7	62.6	180.9	84.1	95.2	78.3	80.8	117.4	125.3	82.4	520.4	120.3	84.5	145.4	328.4	88.6	90.6
HoN	57.7	59.5	181.7	80.9	92.1	60.6	98.6	113.8	123.6	82.9	848.9	123.0	91.9	250.0	510.8	95.5	79.0
TmN	73.6	66.7	205.2	81.2	115.2	69.9	135.9	128.4	159.2	97.5	1243.5	141.0	91.3	409.1	849.6	110.8	83.7
ErN	64.5	57.0	177.3	80.6	116.9	69.8	151.2	119.8	146.3	87.2	1595.0	157.0	95.5	528.9	1099.2	110.3	83.5
YbN	76.9	64.6	196.3	99.7	132.3	99.1	221.5	148.3	173.5	84.3	2147.7	171.7	112.0	726.2	1421.5	147.7	118.2
LuN	124.3	76.1	223.9	109.1	153.9	87.7	242.8	144.4	188.1	122.2	2753.1	191.4	118.1	954.7	2065.8	165.8	151.4
Th (ppm)	148.7	105	272	76.4	149.8	75.5	119	99.7	209.7	77.9	213.5	96.5	117.2	79.7	125.6	123	144.1
U (ppm)	1380	1030	1170	560	870	580	990	670	1090	640	3060	610	830	800	1730	930	1960
YbN/GdN	1.47	1.40	1.59	2.11	2.02	2.63	4.58	1.80	2.19	1.88	12.87	2.36	1.71	11.70	14.26	2.93	1.94
Eu/Eu*	0.04	-	0.004	-	-	-	-	-	-	0.02	0.28	-	-	0.13	0.19	0.06	-

Values of - indicate trace elements are below detection limit of the instrument

R-Rim, C-Core, RE-Recrystallised

Table S4 continued: LA-ICP-MS zircon REE and trace element analyses, Sample TB-14-025 Metapelitic gneiss (PA/PB)

	PA1-1.1	PB1-1.1	PB1-1.4	PB2-1.1	PB2-1.2													
Position	RE	R	RE	RE	RE													
Y	37.5	138.5	106.4	210.4	326													
Sm	5.02	43.6	7.5	5.02	3.13													
Eu	-	3.69	0.142	0.18	0.83													
Gd	14.6	30.6	16.7	21.8	19.4													
Tb	2.49	3.31	2.37	5.56	6.39													
Dy	9.76	19.6	14.2	35.3	50.2													
Ho	1.28	3.44	3.45	6.93	10.49													
Tm	1.58	10.77	10.79	16.4	25.2													
Er	0.136	1.59	1.68	2.25	3.15													
Yb	0.74	9.9	11.5	15	20.6													
Lu	0.046	1.38	1.81	2.04	2.89													
SmN	34.1	296.4	51.0	34.1	21.3													
EuN	-	65.9	2.5	3.2	14.8													
GdN	74.3	155.6	84.9	110.9	98.7													
TbN	68.6	91.2	65.3	153.2	176.0													
DyN	40.2	80.8	58.5	145.4	206.8													
HoN	23.0	61.9	62.1	124.6	188.7													
TmN	9.9	67.8	67.9	103.2	158.6													
ErN	5.6	65.7	69.4	93.0	130.2													
YbN	4.6	60.9	70.8	92.3	126.8													
LuN	1.9	56.8	74.5	84.0	118.9													
Th (ppm)	143.6	241.1	260.3	24.1	22													
U (ppm)	1514	1924	1088	1171	1842													
YbN/ GdN	0.06	0.39	0.83	0.83	1.28													
Eu/Eu*	-	0.29	0.04	0.04	0.25													

Values of - indicate trace elements are below detection limit of the instrument

R-Rim, C-Core, RE-Recrystallised

Table S5: LA-ICP-MS garnet REE and trace element analyses

	026 GRT CORE - 1	026 GRT CORE - 2	026 GRT CORE - 3	026 GRT CORE - 4	026 GRT CORE - 5	026 GRT RIM - 1	026 GRT RIM - 2	026 GRT RIM - 3	026 GRT RIM - 4	026 GRT RIM - 5
	Garnet-biotite gneiss – Type 1 (I11-004K)									
Y	130.2	130.8	126.1	132.9	121.4	124.3	121.7	117.6	128.8	129.4
Sm	5.06	5.6	4.4	6.08	5.29	6.01	6.21	5.47	6.5	5.43
Eu	-	-	-	0.009	-	0.017	-	-	-	-
Gd	19.1	17.6	19	18.5	17.7	18.2	18.8	18	19	18.1
Tb	3.55	3.64	3.74	3.73	3.72	3.87	3.78	3.69	3.95	3.7
Dy	24.59	23.5	23.59	25	23.2	23.29	23.8	22.87	24	24.9
Ho	4.73	4.3	4.81	4.52	4.31	4.45	4.57	4.16	4.75	4.44
Tm	12.38	12.69	13.15	13.54	12.02	11.62	10.85	11.7	13.21	12.94
Er	1.85	2.04	1.9	2	1.84	1.4	1.56	1.47	1.86	1.93
Yb	0.83	0.9	0.95	0.9	0.78	0.75	0.78	0.7	0.79	0.84
Lu	2.09	2.07	1.9	1.95	2.09	1.23	1.13	1.14	1.84	1.86
SmN	34.4	38.1	29.9	41.3	36.0	40.9	42.2	37.2	44.2	36.9
EuN	-	-	-	0.2	-	0.3	-	-	-	-
GdN	97.2	89.5	96.6	94.1	90.0	92.6	95.6	91.6	96.6	92.1
TbN	97.8	100.3	103.0	102.8	102.5	106.6	104.1	101.7	108.8	101.9
DyN	101.3	96.8	97.2	103.0	95.6	96.0	98.1	94.2	98.9	102.6
HoN	85.1	77.3	86.5	81.3	77.5	80.0	82.2	74.8	85.4	79.9
TmN	77.9	79.9	82.8	85.2	75.6	73.1	68.3	73.6	83.1	81.4
ErN	76.4	84.3	78.5	82.6	76.0	57.9	64.5	60.7	76.9	79.8
YbN	81.4	81.7	83.8	83.9	81.5	54.1	57.8	56.3	77.0	76.9
LuN	86.0	85.2	78.2	80.2	86.0	50.6	46.5	46.9	75.7	76.5
YbN/GdN	0.838	0.912	0.867	0.892	0.906	0.584	0.605	0.615	0.797	0.835
Eu/Eu*	-	-	-	0.002	-	0.005	-	-	-	-

Values of - indicate trace elements are below detection limit of the instrument

Table S5 continued: LA-ICP-MS garnet REE and trace element analyses

	026 GRT RIM - 6	026 GRT RIM - 7	026 GRT 2 CORE - 1	026 GRT 2 CORE - 2	026 GRT 2 CORE - 3	026 GRT 2 CORE - 4	026 GRT 2 RIM - 1	026 GRT 2 RIM - 2	026 GRT 2 RIM - 3	026 GRT 2 RIM - 4
	Garnet-biotite gneiss – Type 1 continued (I11-004K)									
Y	124.3	128.6	133.5	141.1	134.9	138.6	141.5	136.6	135.4	132.4
Sm	5.65	5.9	5.61	7.29	7.03	6.68	6.28	5.67	5.04	6.15
Eu	-	-	0.009	0.005	-	-	-	-	-	0.02
Gd	17.3	19.6	18.97	21.7	21.5	23.3	20.6	19.4	19.8	19.1
Tb	3.61	3.75	4.04	4.19	4.06	4.15	4.21	3.99	4.1	4.09
Dy	22.4	24.1	25.2	27.1	25.3	26.1	27.7	25.4	23.9	25.7
Ho	4.43	4.56	4.48	4.98	4.65	4.47	4.97	4.72	4.53	4.73
Tm	12.16	12.56	11.63	12.14	11.63	12.77	13.08	13.47	12.95	12.55
Er	1.82	1.98	1.53	1.77	1.53	1.71	1.68	1.76	1.68	1.74
Yb	0.76	0.94	0.82	0.77	0.74	0.59	0.68	0.68	0.72	0.7
Lu	1.75	1.8	1.21	1.33	1.14	1.18	1.37	1.51	1.35	1.35
SmN	38.4	40.1	38.1	49.6	47.8	45.4	42.7	38.5	34.3	41.8
EuN	-	-	0.2	0.1	-	-	-	-	-	0.4
GdN	88.0	99.7	96.5	110.4	109.4	118.5	104.8	98.7	100.7	97.2
TbN	99.4	103.3	111.3	115.4	111.8	114.3	116.0	109.9	112.9	112.7
DyN	92.3	99.3	103.8	111.7	104.2	107.5	114.1	104.7	98.5	105.9
HoN	79.7	82.0	80.6	89.6	83.6	80.4	89.4	84.9	81.5	85.1
TmN	76.5	79.0	73.2	76.4	73.2	80.4	82.3	84.8	81.5	79.0
ErN	75.2	81.8	63.2	73.1	63.2	70.7	69.4	72.7	69.4	71.9
YbN	74.6	78.4	56.3	66.6	59.1	63.6	62.2	62.0	64.9	67.6
LuN	72.0	74.1	49.8	54.7	46.9	48.6	56.4	62.1	55.6	55.6
YbN/GdN	0.848	0.786	0.584	0.603	0.541	0.536	0.593	0.629	0.644	0.696
Eu/Eu*	-	-	0.002	0.001	-	-	-	-	-	0.005

Values of - indicate trace elements are below detection limit of the instrument

Table S5 continued: LA-ICP-MS garnet REE and trace element analyses

	017 GRT CORE - 1	017 GRT CORE - 2	017 GRT CORE - 3	017 GRT CORE - 4	017 GRT CORE - 5	017 GRT CORE - 6	017 GRT CORE - 7	017 GRT CORE - 8	017 GRT CORE - 9	017 GRT CORE - 10
	Garnet-biotite gneiss - Type 2 (I11-004K)									
Y	99.8	109.9	113.2	91.1	90	83.8	110.3	79.4	117.4	107.7
Sm	10.77	10.71	11.4	11.7	10.89	12	9.73	12.13	11.14	12.42
Eu	0.035	0.081	0.022	0.023	0.03	0.021	0.047	0.017	0.004	0.043
Gd	35.3	40.1	39.6	33.1	32.4	34.5	36.2	31.4	35.5	38.6
Tb	6.18	7.05	7.17	5.71	5.49	5.26	6.88	4.93	6.72	6.85
Dy	28.5	32.1	31.7	25.8	25.1	23.1	33.5	22.29	33.51	32.07
Ho	3.66	4.31	4.29	3.45	3.19	2.98	4.52	2.74	4.38	4
Tm	6.3	7.77	8.07	6.19	5.28	4.82	7.56	4.84	8.63	6.7
Er	0.474	0.615	0.739	0.461	0.451	0.477	0.658	0.418	0.77	0.617
Yb	2.4	3.08	3.39	2.14	2.37	1.93	3.65	1.81	3.51	2.81
Lu	0.329	0.37	0.381	0.245	0.237	0.231	0.466	0.181	0.498	0.296
SmN	73.2	72.8	77.5	79.5	74.0	81.6	66.1	82.5	75.7	84.4
EuN	0.6	1.4	0.4	0.4	0.5	0.4	0.8	0.3	0.1	0.8
GdN	179.6	204.0	201.4	168.4	164.8	175.5	184.1	159.7	180.6	196.3
TbN	170.2	194.2	197.5	157.3	151.2	144.9	189.5	135.8	185.1	188.7
DyN	117.4	132.3	130.6	106.3	103.4	95.2	138.0	91.8	138.1	132.1
HoN	65.8	77.5	77.2	62.1	57.4	53.6	81.3	49.3	78.8	71.9
TmN	39.6	48.9	50.8	39.0	33.2	30.3	47.6	30.5	54.3	42.2
ErN	19.6	25.4	30.5	19.0	18.6	19.7	27.2	17.3	31.8	25.5
YbN	14.8	19.0	20.9	13.2	14.6	11.9	22.5	11.1	21.6	17.3
LuN	13.5	15.2	15.7	10.1	9.8	9.5	19.2	7.4	20.5	12.2
YbN/GdN	0.082	0.093	0.104	0.078	0.088	0.068	0.122	0.070	0.120	0.088
Eu/Eu*	0.005	0.010	0.003	0.003	0.004	0.003	0.007	0.003	0.001	0.005

Values of - indicate trace elements are below detection limit of the instrument

Table S5 continued: LA-ICP-MS garnet REE and trace element analyses

	017 GRT CORE - 11	017 GRT CORE - 12	017 GRT RIM - 1	017 GRT RIM - 2	017 GRT RIM - 3	017 GRT RIM - 4	017 GRT RIM - 5	017 GRT RIM - 6	017 GRT RIM - 7	017 GRT RIM - 8
	Garnet-biotite gneiss - Type 2 continued									
Y	100.4	102.4	111.2	118.4	118.2	119.3	121.8	118.8	121.7	116.4
Sm	12.08	12.2	9.51	7.21	7.25	8.19	8.34	9.46	7.58	8.36
Eu	0.02	0.031	0.008	0.004	-	-	0.009	0.008	0.007	-
Gd	36.5	37	31.3	29.8	30.3	29.1	31.2	28.8	31.9	29.5
Tb	6.35	6.18	5.74	6.17	6	5.82	6.02	6.28	6.26	6.13
Dy	28.5	29.4	31.4	30.7	31.68	32.4	33.11	32.1	33.1	30.2
Ho	3.63	4.1	4.31	4.47	4.56	4.51	4.58	4.61	5.06	4.61
Tm	6.38	6.62	8.79	9.48	9.05	10.03	9.37	9.03	9.94	9.04
Er	0.478	0.495	0.849	0.969	0.976	0.98	0.947	0.892	0.856	0.858
Yb	2.52	3.07	5.03	5.73	5.79	5.36	5.54	5.29	4.84	4.89
Lu	0.27	0.394	0.667	0.842	0.719	0.855	0.832	0.721	0.726	0.698
SmN	82.1	82.9	64.6	49.0	49.3	55.7	56.7	64.3	51.5	56.8
EuN	0.4	0.6	0.1	0.1	-	-	0.2	0.1	0.1	-
GdN	185.7	188.2	159.2	151.6	154.1	148.0	158.7	146.5	162.3	150.1
TbN	174.9	170.2	158.1	170.0	165.3	160.3	165.8	173.0	172.5	168.9
DyN	117.4	121.1	129.4	126.5	130.5	133.5	136.4	132.3	136.4	124.4
HoN	65.3	73.7	77.5	80.4	82.0	81.1	82.4	82.9	91.0	82.9
TmN	40.2	41.7	55.3	59.7	57.0	63.1	59.0	56.8	62.6	56.9
ErN	19.8	20.5	35.1	40.0	40.3	40.5	39.1	36.9	35.4	35.5
YbN	15.5	18.9	31.0	35.3	35.6	33.0	34.1	32.6	29.8	30.1
LuN	11.1	16.2	27.4	34.7	29.6	35.2	34.2	29.7	29.9	28.7
YbN/GdN	0.084	0.100	0.194	0.233	0.231	0.223	0.215	0.222	0.184	0.201
Eu/Eu*	0.003	0.004	0.001	0.001	-	-	0.001	0.001	0.001	-

Values of - indicate trace elements are below detection limit of the instrument

Table S5 continued: LA-ICP-MS garnet REE and trace element analyses

	017 GRT RIM - 9	017 GRT RIM - 10	017 GRT RIM - 11	017 GRT RIM - 12	017 GRT RIM BT - 1	017 GRT RIM BT - 2	017 GRT RIM BT - 3	017 GRT RIM BT - 4	017 GRT RIM BT - 5	017 GRT RIM BT - 6
	Garnet-biotite gneiss - Type 2 continued									
Y	119.1	119.4	126.6	123.1	122.1	120.5	119.8	121.9	116.9	103.7
Sm	8.21	8.22	9.18	8.77	8.96	8.48	9.15	8.96	7.55	8.05
Eu	0.003	0.021	-	0.009	0.008	-	0.029	0.009	0.015	0.008
Gd	32	31.8	33.9	33.2	32.7	33.1	33.6	32.9	31.9	30.3
Tb	5.93	6.47	6.53	6.24	6.5	6.29	6.13	6.25	6.02	5.76
Dy	32.7	31.5	33	32.8	33.3	31.2	33.6	32.43	30.11	28.2
Ho	4.63	4.8	5.05	4.67	4.62	4.71	4.88	4.75	4.5	3.9
Tm	9.52	9.51	9.9	9.8	9.64	9.02	10.03	10.3	9.1	8.27
Er	0.94	0.977	1.06	0.97	0.98	0.95	0.92	0.97	0.91	0.806
Yb	4.76	5.27	5.4	6.14	5.71	5.27	5.15	5.52	4.97	4.38
Lu	0.747	0.749	0.85	0.727	0.769	0.815	0.629	0.716	0.704	0.565
SmN	55.8	55.9	62.4	59.6	60.9	57.6	62.2	60.9	51.3	54.7
EuN	0.1	0.4	-	0.2	0.1	-	0.5	0.2	0.3	0.1
GdN	162.8	161.7	172.4	168.9	166.3	168.4	170.9	167.3	162.3	154.1
TbN	163.4	178.2	179.9	171.9	179.1	173.3	168.9	172.2	165.8	158.7
DyN	134.7	129.8	136.0	135.1	137.2	128.6	138.4	133.6	124.1	116.2
HoN	83.3	86.3	90.8	84.0	83.1	84.7	87.8	85.4	80.9	70.1
TmN	59.9	59.8	62.3	61.7	60.7	56.8	63.1	64.8	57.3	52.0
ErN	38.8	40.4	43.8	40.1	40.5	39.3	38.0	40.1	37.6	33.3
YbN	29.3	32.4	33.2	37.8	35.1	32.4	31.7	34.0	30.6	27.0
LuN	30.7	30.8	35.0	29.9	31.6	33.5	25.9	29.5	29.0	23.3
YbN/GdN	0.180	0.200	0.193	0.224	0.211	0.193	0.185	0.203	0.188	0.175
Eu/Eu*	0.001	0.003	-	0.001	0.001	-	0.004	0.001	0.003	0.001

Values of - indicate trace elements are below detection limit of the instrument

Table S5 continued: LA-ICP-MS garnet REE and trace element analyses

	019 GRT CORE - 1	019 GRT CORE - 2	019 GRT CORE - 3	019 GRT CORE - 4	019 GRT RIM - 1	019 GRT RIM - 3	019 GRT RIM - 4	019 GRT RIM - 5	019 GRT RIM - 6
	Transition zone (I11-004C)								
Y	94.1	120	133	150.5	5.31	3.94	8.11	13.92	9.23
Sm	3.71	4.45	6.83	5.48	1.87	1.5	1.88	2.38	2.29
Eu	-	0.01	0.029	-	-	-	-	0.009	-
Gd	18.3	22.2	30.3	26.6	5.63	4.5	5.77	9.32	7.17
Tb	3.62	4.91	6.2	5.72	0.747	0.606	0.678	1.36	1.09
Dy	22.4	29.4	36.7	36.4	2.02	1.57	2.57	4.92	3.67
Ho	3.56	4.93	5.8	6.12	0.179	0.09	0.284	0.419	0.291
Tm	7.92	11.64	12.91	14.08	0.164	0.071	0.267	0.68	0.39
Er	0.944	1.2	1.36	1.5	0.002	-	0.021	0.074	0.014
Yb	0.59	0.59	0.67	0.69	0.047	1	0.063	0.12	0.073
Lu	1.11	1.23	1.2	1.44	-	-	0.01	0.015	0.058
SmN	25.2	30.3	46.4	37.3	12.7	10.2	12.8	16.2	15.6
EuN	-	0.2	0.5	-	-	-	-	0.2	-
GdN	93.1	112.9	154.1	135.3	28.6	22.9	29.3	47.4	36.5
TbN	99.7	135.3	170.8	157.6	20.6	16.7	18.7	37.5	30.0
DyN	92.3	121.1	151.2	150.0	8.3	6.5	10.6	20.3	15.1
HoN	64.0	88.7	104.3	110.1	3.2	1.6	5.1	7.5	5.2
TmN	49.8	73.3	81.2	88.6	1.0	0.4	1.7	4.3	2.5
ErN	39.0	49.6	56.2	62.0	0.1	-	0.9	3.1	0.6
YbN	41.8	49.2	47.0	56.1	0.3	-	0.5	1.8	0.9
LuN	45.7	50.6	49.4	59.3	-	-	0.4	0.6	2.4
YbN/GdN	0.449	0.435	0.305	0.414	0.012	-	0.018	0.038	0.025
Eu/Eu*	-	0.002	0.005	-	-	-	-	0.005	-

Values of - indicate trace elements are below detection limit of the instrument

Table S5 continued: LA-ICP-MS garnet REE and trace element analyses

	022 GRT 1 CORE - 1	022 GRT 1 CORE - 2	022 GRT 1 CORE - 3	022 GRT 1 CORE - 4	022 GRT 1 CORE - 5	022 GRT 1 CORE - 6	022 GRT 1 CORE - 7	022 GRT 1 CORE - 8	022 GRT 1 CORE - 9
	Charnockite (I11-008C)								
Y	107.8	115.3	111.2	114.8	123.4	122.3	120.2	117.4	107.6
Sm	5.81	5.38	4.89	5.26	5.18	5.8	5.61	4.76	5.41
Eu	-	-	-	-	-	-	-	0.016	0.021
Gd	19.2	19.8	18	19.1	21.1	20.8	20.1	20.9	19
Tb	3.37	3.7	3.71	3.72	3.81	4.05	3.96	3.88	3.68
Dy	22.1	23.2	23.06	23.1	24.3	24.89	23.92	24.3	22.19
Ho	3.91	3.9	4.19	4.28	4.33	4.5	4.58	4.18	3.79
Tm	9.31	9.75	10.56	11.77	11.98	11.84	11.37	11.62	9.29
Er	1.305	1.145	1.39	1.54	1.81	1.64	1.61	1.45	1.1
Yb	7.44	7.11	10.24	9.62	10.06	10.01	9.98	9.78	8.66
Lu	1.016	0.883	1.44	1.45	1.56	1.51	1.5	1.45	1.07
SmN	39.5	36.6	33.2	35.8	35.2	39.4	38.1	32.4	36.8
EuN	-	-	-	-	-	-	-	0.3	0.4
GdN	97.7	100.7	91.6	97.2	107.3	105.8	102.2	106.3	96.6
TbN	92.8	101.9	102.2	102.5	105.0	111.6	109.1	106.9	101.4
DyN	91.1	95.6	95.0	95.2	100.1	102.6	98.6	100.1	91.4
HoN	70.3	70.1	75.4	77.0	77.9	80.9	82.4	75.2	68.2
TmN	58.6	61.4	66.5	74.1	75.4	74.5	71.6	73.1	58.5
ErN	53.9	47.3	57.4	63.6	74.8	67.8	66.5	59.9	45.5
YbN	45.8	43.8	63.0	59.2	61.9	61.6	61.4	60.2	53.3
LuN	41.8	36.3	59.3	59.7	64.2	62.1	61.7	59.7	44.0
YbN/GdN	0.469	0.434	0.688	0.609	0.577	0.582	0.601	0.566	0.551
Eu/Eu*	-	-	-	-	-	-	-	0.004	0.006

Values of - indicate trace elements are below detection limit of the instrument

Table S5 continued: LA-ICP-MS garnet REE and trace element analyses

	022 GRT 1 CORE - 10	022 GRT 1 CORE - 11	022 GRT 1 RIM - 1	022 GRT 1 RIM - 2	022 GRT 1 RIM - 3	022 GRT 1 RIM - 4	022 GRT 1 RIM - 5	022 GRT 1 RIM - 6	022 GRT 1 RIM - 7
	Charnockite continued (I11-008C)								
Y	108.4	118.7	107.9	110.6	118.7	112.7	122.5	121.4	122.1
Sm	5.15	6.02	4.93	5.07	4.7	4.84	5.12	5.39	5.5
Eu	0.008	-	0.012	-	-	0.004	0.004	-	-
Gd	19.7	19.8	20.2	19.4	18.9	19.7	20.6	20.7	19.94
Tb	3.84	4.09	3.71	3.65	4.01	3.54	4.04	3.95	3.99
Dy	21.96	23.4	20.9	21.46	22.8	21.63	24.06	23.92	24.9
Ho	3.86	4.19	4.16	4.07	4.4	4.13	4.43	4.52	4.67
Tm	9.89	10.46	9.76	10.32	11.35	11.25	12.56	11.53	11.81
Er	1.12	1.3	1.264	1.38	1.4	1.5	1.69	1.52	1.61
Yb	7.36	8.54	7.45	8.19	9.99	9.85	10.25	9.47	9.71
Lu	1.2	1.33	1.12	1.2	1.5	1.5	1.63	1.41	1.4
SmN	35.0	40.9	33.5	34.5	32.0	32.9	34.8	36.6	37.4
EuN	0.1	-	0.2	-	-	0.1	0.1	-	-
GdN	100.2	100.7	102.7	98.7	96.1	100.2	104.8	105.3	101.4
TbN	105.8	112.7	102.2	100.6	110.5	97.5	111.3	108.8	109.9
DyN	90.5	96.4	86.1	88.4	93.9	89.1	99.1	98.6	102.6
HoN	69.4	75.4	74.8	73.2	79.1	74.3	79.7	81.3	84.0
TmN	62.2	65.8	61.4	64.9	71.4	70.8	79.0	72.6	74.3
ErN	46.3	53.7	52.2	57.0	57.9	62.0	69.8	62.8	66.5
YbN	45.3	52.6	45.8	50.4	61.5	60.6	63.1	58.3	59.8
LuN	49.4	54.7	46.1	49.4	61.7	61.7	67.1	58.0	57.6
YbN/GdN	0.452	0.522	0.446	0.511	0.639	0.605	0.602	0.553	0.589
Eu/Eu*	0.002	-	0.003	-	-	0.001	0.001	-	-

Values of - indicate trace elements are below detection limit of the instrument

Table S5 continued: LA-ICP-MS garnet REE and trace element analyses

	022 GRT 1 RIM - 8	022 GRT 1 RIM - 9	022 GRT 1 RIM - 10	022 GRT 1 RIM - 11	022 GRT 1 RIM - 12	022 GRT 1 RIM - 13	022 GRT 1 RIM - 14	022 GRT 1 RIM - 15	022 GRT 2 CORE - 1
	Charnockite continued (I11-008C)								
Y	119.1	102.9	104.7	110.5	120.5	113	118.1	110.8	107.8
Sm	5.24	5.37	5.91	5.87	6.15	5.07	5.8	5.51	4.71
Eu	-	0.008	-	-	-	-	0.017	0.005	-
Gd	20.3	18.8	19.72	19.7	21.2	19.1	19.4	18.2	13.2
Tb	3.73	3.66	3.64	3.54	4.17	3.65	3.82	3.53	2.91
Dy	22.91	21.03	22.16	21.9	24.69	22.31	23.2	22.6	19.73
Ho	4.53	4	3.93	3.88	4.53	4.13	4.2	4.2	4.12
Tm	11.78	9.61	9.97	10.55	11.94	10.63	11.06	10.85	9.99
Er	1.48	1.27	1.27	1.274	1.43	1.46	1.33	1.42	1.19
Yb	10.09	7.87	7.68	8.07	9.6	9.09	9.52	8.96	6.76
Lu	1.43	1.11	1.09	1.12	1.36	1.49	1.36	1.32	1.028
SmN	35.6	36.5	40.2	39.9	41.8	34.5	39.4	37.5	32.0
EuN	-	0.1	-	-	-	-	0.3	0.1	-
GdN	103.3	95.6	100.3	100.2	107.8	97.2	98.7	92.6	67.1
TbN	102.8	100.8	100.3	97.5	114.9	100.6	105.2	97.2	80.2
DyN	94.4	86.7	91.3	90.2	101.7	91.9	95.6	93.1	81.3
HoN	81.5	71.9	70.7	69.8	81.5	74.3	75.5	75.5	74.1
TmN	74.1	60.5	62.7	66.4	75.1	66.9	69.6	68.3	62.9
ErN	61.2	52.5	52.5	52.6	59.1	60.3	55.0	58.7	49.2
YbN	62.1	48.4	47.3	49.7	59.1	55.9	58.6	55.1	41.6
LuN	58.8	45.7	44.9	46.1	56.0	61.3	56.0	54.3	42.3
YbN/GdN	0.601	0.506	0.471	0.496	0.548	0.576	0.594	0.596	0.620
Eu/Eu*	-	0.002	-	-	-	-	0.004	0.001	-

Values of - indicate trace elements are below detection limit of the instrument

Table S5 continued: LA-ICP-MS garnet REE and trace element analyses

	022 GRT 2 CORE - 2	022 GRT 2 CORE - 3	022 GRT 2 CORE - 4	022 GRT 2 CORE - 5	022 GRT 2 RIM - 1	022 GRT 2 RIM - 2	022 GRT 2 RIM - 3	022 GRT 2 RIM - 4	022 GRT 2 RIM - 5
	Charnockite continued (I11-008C)								
Y	108.7	110.3	106.2	108.7	102.1	101.9	101.7	105.8	97.2
Sm	3.83	3.92	4.1	4.19	4.02	4.15	3.63	4.54	3.4
Eu	0.013	-	0.013	-	-	0.012	-	-	0.004
Gd	14.4	14.7	13.5	14.55	13.97	12.68	13.73	13.6	12.83
Tb	2.98	2.94	2.97	3.14	2.88	3.17	2.88	2.89	2.95
Dy	19.32	20.8	20.49	21.1	19.83	20.48	20.38	21.47	19.74
Ho	3.97	3.93	3.77	4.17	3.74	3.73	3.58	3.78	3.46
Tm	9.57	10.24	9.61	9.64	9	9.13	8.87	9.31	8.51
Er	1.21	1.31	1.028	1.19	1.19	1.02	1.21	1.24	1.01
Yb	7.18	6.9	5.45	6.57	6.57	6.21	6.44	7.18	5.78
Lu	1.03	0.89	0.812	0.91	1.01	0.837	0.88	0.976	0.745
SmN	26.0	26.6	27.9	28.5	27.3	28.2	24.7	30.9	23.1
EuN	0.2	-	0.2	-	-	0.2	-	-	0.1
GdN	73.2	74.8	68.7	74.0	71.1	64.5	69.8	69.2	65.3
TbN	82.1	81.0	81.8	86.5	79.3	87.3	79.3	79.6	81.3
DyN	79.6	85.7	84.4	86.9	81.7	84.4	84.0	88.5	81.3
HoN	71.4	70.7	67.8	75.0	67.3	67.1	64.4	68.0	62.2
TmN	60.2	64.4	60.5	60.7	56.6	57.5	55.8	58.6	53.6
ErN	50.0	54.1	42.5	49.2	49.2	42.1	50.0	51.2	41.7
YbN	44.2	42.5	33.5	40.4	40.4	38.2	39.6	44.2	35.6
LuN	42.4	36.6	33.4	37.4	41.6	34.4	36.2	40.2	30.7
YbN/GdN	0.603	0.568	0.488	0.546	0.569	0.593	0.567	0.639	0.545
Eu/Eu*	0.005	-	0.005	-	-	0.005	-	-	0.002

Values of - indicate trace elements are below detection limit of the instrument

Table S5 continued: LA-ICP-MS garnet REE and trace element analyses

	022 GRT 2 RIM - 6	022 GRT 2 RIM - 7	022 GRT 3 CORE - 1	022 GRT 3 CORE - 2	022 GRT 3 CORE - 3	022 GRT 3 RIM - 1	022 GRT 3 RIM - 2	022 GRT 3 RIM - 3
	Charnockite continued (I11-008C)							
Y	96.9	94.5	107	107	114.1	110.9	107.3	109.1
Sm	3.2	3.53	3.53	2.82	2.82	2.78	2.47	2.08
Eu	0.008	-	-	-	0.007	0.004	-	-
Gd	13.6	13.87	10.89	10.33	10.78	10.35	9.77	9.97
Tb	3	2.78	2.85	2.61	2.74	2.46	2.46	2.51
Dy	18.89	18.53	19.16	18.25	19.03	19.08	18.35	18.27
Ho	3.39	3.35	3.84	3.68	3.7	3.9	3.91	4
Tm	8.31	8.59	10.3	10.31	11.23	10.58	10.7	11.1
Er	0.98	0.95	1.42	1.38	1.65	1.44	1.55	1.62
Yb	6.19	5.82	9.36	9.32	10.66	10.12	10.93	10.1
Lu	0.834	0.721	1.36	1.22	1.32	1.59	1.47	1.6
SmN	21.8	24.0	24.0	19.2	19.2	18.9	16.8	14.1
EuN	0.1	-	-	-	0.1	0.1	-	-
GdN	69.2	70.5	55.4	52.5	54.8	52.6	49.7	50.7
TbN	82.6	76.6	78.5	71.9	75.5	67.8	67.8	69.1
DyN	77.8	76.3	78.9	75.2	78.4	78.6	75.6	75.3
HoN	61.0	60.3	69.1	66.2	66.5	70.1	70.3	71.9
TmN	52.3	54.1	64.8	64.9	70.7	66.6	67.3	69.9
ErN	40.5	39.3	58.7	57.0	68.2	59.5	64.0	66.9
YbN	38.1	35.8	57.6	57.4	65.6	62.3	67.3	62.2
LuN	34.3	29.7	56.0	50.2	54.3	65.4	60.5	65.8
YbN/GdN	0.551	0.508	1.040	1.092	1.196	1.183	1.353	1.226
Eu/Eu*	0.003	-	-	-	0.003	0.002	-	-

Values of - indicate trace elements are below detection limit of the instrument

Table S5 continued: LA-ICP-MS garnet REE and trace element analyses

	PAGE - 1	PAGE - 2	PAGE - 3	PAGE - 4	PAGE - 5	PAGE - 6	PAGE - 7	PAGE - 8	PAGE - 9
	Metapelitic gneiss - Type 1 (TB-14-025)								
Position	R	R	R	C	C	C	C	C	C
Y	74.8	63	62.3	58.1	58.27	56.6	53.01	53.42	56.02
Sm	4.43	3.19	11.1	10.84	10.26	10.27	12.75	12.34	10.91
Eu	0.051	0.028	0.035	0.029	0.032	0.036	0.042	0.037	0.044
Gd	26.11	21.51	30.24	28.87	29.05	28.82	27.63	26.89	27.26
Tb	5.33	4.37	4.74	4.44	4.396	4.343	4.252	4.3	4.43
Dy	26.68	22.94	21.5	20.77	20.46	20.04	19.13	19.34	20.64
Ho	2.962	2.561	2.279	2.14	2.119	2.153	1.93	2.123	2.118
Tm	4.24	3.65	3.13	2.87	3	2.83	2.66	2.89	2.93
Er	0.328	0.281	0.28	0.236	0.232	0.245	0.194	0.192	0.224
Yb	1.449	1.27	1.22	1.106	1.23	1.179	1.006	1.082	1.107
Lu	0.179	0.144	0.144	0.14	0.139	0.125	0.108	0.119	0.143
SmN	30.1	21.7	75.5	73.7	69.7	69.8	86.7	83.9	74.2
EuN	0.9	0.5	0.6	0.5	0.6	0.6	0.8	0.7	0.8
GdN	132.8	109.4	153.8	146.8	147.8	146.6	140.5	136.8	138.7
TbN	146.8	120.4	130.6	122.3	121.1	119.6	117.1	118.5	122.0
DyN	109.9	94.5	88.6	85.6	84.3	82.6	78.8	79.7	85.0
HoN	53.3	46.1	41.0	38.5	38.1	38.7	34.7	38.2	38.1
TmN	26.7	23.0	19.7	18.1	18.9	17.8	16.7	18.2	18.4
ErN	13.6	11.6	11.6	9.8	9.6	10.1	8.0	7.9	9.3
YbN	8.9	7.8	7.5	6.8	7.6	7.3	6.2	6.7	6.8
LuN	7.4	5.9	5.9	5.8	5.7	5.1	4.4	4.9	5.9
YbN/GdN	0.067	0.071	0.049	0.046	0.051	0.049	0.044	0.049	0.049
Eu/Eu*	0.011	0.008	0.005	0.005	0.005	0.006	0.007	0.006	0.007

Values of - indicate trace elements are below detection limit of the instrument

Table S5 continued: LA-ICP-MS garnet REE and trace element analyses

	PAGE - 10	PAGE - 11	PAGE - 12	PAGE - 13	PAGE - 14	PAGE - 15	PAGE - 16	PAGE - 17	PAGE - 18
	Metapelitic gneiss - Type 1 continued (TB-14-025)								
Position	R	R	R	C	C	R	R	R	C
Y	66.49	74.16	64.9	59.15	53.69	71.7	57	56.7	53.93
Sm	9.49	6.71	8.88	8.03	11.65	2.4	13.49	11.87	13.73
Eu	0.052	0.051	0.041	0.042	0.048	0.028	0.032	0.042	0.035
Gd	29.33	29.67	30.43	28.86	27.94	18.88	28.66	29.42	24.38
Tb	4.804	5.24	4.9	4.59	4.274	4.71	4.185	4.36	4.487
Dy	22.76	26.01	23.64	20.97	19.39	25.62	18.73	20.18	21.42
Ho	2.52	2.909	2.478	2.239	1.968	2.812	1.957	2.019	2.139
Tm	3.57	4.08	3.64	2.99	2.655	4.18	2.83	2.72	2.62
Er	0.249	0.313	0.262	0.227	0.204	0.285	0.239	0.218	0.175
Yb	1.396	1.46	1.251	1.131	1.105	1.426	1.18	1.035	0.846
Lu	0.15	0.195	0.151	0.134	0.114	0.162	0.111	0.104	0.112
SmN	64.5	45.6	60.4	54.6	79.2	16.3	91.7	80.7	93.3
EuN	0.9	0.9	0.7	0.8	0.9	0.5	0.6	0.8	0.6
GdN	149.2	150.9	154.8	146.8	142.1	96.0	145.8	149.6	124.0
TbN	132.3	144.4	135.0	126.4	117.7	129.8	115.3	120.1	123.6
DyN	93.8	107.2	97.4	86.4	79.9	105.6	77.2	83.1	88.3
HoN	45.3	52.3	44.6	40.3	35.4	50.6	35.2	36.3	38.5
TmN	22.5	25.7	22.9	18.8	16.7	26.3	17.8	17.1	16.5
ErN	10.3	12.9	10.8	9.4	8.4	11.8	9.9	9.0	7.2
YbN	8.6	9.0	7.7	7.0	6.8	8.8	7.3	6.4	5.2
LuN	6.2	8.0	6.2	5.5	4.7	6.7	4.6	4.3	4.6
YbN/GdN	0.058	0.060	0.050	0.047	0.048	0.091	0.050	0.043	0.042
Eu/Eu*	0.009	0.009	0.007	0.007	0.008	0.009	0.005	0.007	0.006

Values of - indicate trace elements are below detection limit of the instrument

Table S5 continued: LA-ICP-MS garnet REE and trace element analyses

	PAGE - 19	PAGE - 20	PAGE - 21	PAGE - 22	PAGE - 23	PAGE - 24	PAGE - 25		
	Metapelitic gneiss - Type 1 continued (TB-14-025)								
Position	C	C	C	R	R	C	R		
Y	79.2	84.1	73.2	72.7	71.6	80	65.76		
Sm	12.16	12.51	13.35	8.35	7.93	13.51	9.21		
Eu	0.04	0.039	0.036	0.051	0.036	0.037	0.048		
Gd	23.41	25.27	24.9	29.49	28.61	25.21	29.29		
Tb	4.342	4.23	4.216	5.29	4.61	4.47	4.62		
Dy	24.1	24.64	23.83	25.84	22.65	25.12	22.95		
Ho	3.149	3.37	2.853	2.799	2.544	3.283	2.517		
Tm	4.83	5.74	4.34	3.81	3.98	4.94	3.74		
Er	0.417	0.514	0.365	0.308	0.346	0.449	0.311		
Yb	2.26	2.71	1.78	1.352	1.72	2.34	1.59		
Lu	0.254	0.366	0.193	0.147	0.197	0.316	0.171		
SmN	82.7	85.0	90.8	56.8	53.9	91.8	62.6		
EuN	0.7	0.7	0.6	0.9	0.6	0.7	0.9		
GdN	119.1	128.5	126.7	150.0	145.5	128.2	149.0		
TbN	119.6	116.5	116.1	145.7	127.0	123.1	127.3		
DyN	99.3	101.5	98.2	106.5	93.3	103.5	94.6		
HoN	56.6	60.6	51.3	50.3	45.8	59.0	45.3		
TmN	30.4	36.1	27.3	24.0	25.0	31.1	23.5		
ErN	17.2	21.2	15.1	12.7	14.3	18.6	12.9		
YbN	13.9	16.7	11.0	8.3	10.6	14.4	9.8		
LuN	10.5	15.1	7.9	6.0	8.1	13.0	7.0		
YbN/GdN	0.117	0.130	0.086	0.055	0.073	0.112	0.066		
Eu/Eu*	0.007	0.007	0.006	0.009	0.006	0.006	0.008		

Values of - indicate trace elements are below detection limit of the instrument

Table S5 continued: LA-ICP-MS garnet REE and trace element analyses

	PAG - 1	PAG - 2	PAG - 3	PAG - 4	PAG - 5	PAG - 6	PAG - 7	PAG - 8	PAG - 9
	Metapelitic gneiss - Type 2 (TB-14-025)								
Position	R	R	C	C	R	R	C	C	C
Y	94.1	95.1	91.9	88.8	85.3	85.8	73.6	79.9	77.9
Sm	14.14	14.61	14.81	15.31	14.14	14.16	11.33	12.84	12.9
Eu	0.032	0.035	0.034	0.038	0.029	0.033	0.039	0.043	0.044
Gd	27.61	28.1	27.7	25.96	26.95	28.25	24.98	27.29	27.57
Tb	3.99	3.83	3.88	3.85	3.87	4.01	3.526	3.841	3.938
Dy	21.32	21.27	20.88	20.93	20.82	21.09	18.55	20.12	19.86
Ho	3.354	3.43	3.295	3.257	3.122	3.171	2.784	2.977	2.816
Tm	8.18	7.8	7.53	7.53	6.87	6.95	5.99	6.27	5.9
Er	1.032	0.966	0.91	0.896	0.874	0.827	0.719	0.704	0.669
Yb	7	6.46	5.89	5.93	5.4	5.42	4.45	4.68	4.17
Lu	0.901	0.786	0.727	0.683	0.64	0.704	0.576	0.562	0.516
SmN	96.1	99.3	100.7	104.1	96.1	96.3	77.0	87.3	87.7
EuN	0.6	0.6	0.6	0.7	0.5	0.6	0.7	0.8	0.8
GdN	140.4	142.9	140.9	132.0	137.1	143.7	127.1	138.8	140.2
TbN	109.9	105.5	106.9	106.1	106.6	110.5	97.1	105.8	108.5
DyN	87.8	87.6	86.0	86.2	85.8	86.9	76.4	82.9	81.8
HoN	60.3	61.7	59.3	58.6	56.2	57.0	50.1	53.5	50.6
TmN	51.5	49.1	47.4	47.4	43.2	43.7	37.7	39.5	37.1
ErN	42.6	39.9	37.6	37.0	36.1	34.2	29.7	29.1	27.6
YbN	43.1	39.8	36.2	36.5	33.2	33.4	27.4	28.8	25.7
LuN	37.1	32.3	29.9	28.1	26.3	29.0	23.7	23.1	21.2
YbN/GdN	0.307	0.278	0.257	0.276	0.242	0.232	0.216	0.207	0.183
Eu/Eu*	0.005	0.005	0.005	0.006	0.004	0.005	0.007	0.007	0.007

Values of - indicate trace elements are below detection limit of the instrument

Table S5 continued: LA-ICP-MS garnet REE and trace element analyses

	PAG - 10	PAG - 11	PAG - 12	PAG - 13	PAG - 14	PAG - 15	PAG - 16	PAG - 17	PAG - 18
	Metapelitic gneiss - Type 2 continued (TB-14-025)								
Position	C	R	R	R	C	C	C	C	C
Y	72.2	79.9	78.45	114.2	96.8	91.3	94.2	99.6	99.6
Sm	11.97	13.56	13.14	14.55	14.88	14.43	14.22	14.98	14.19
Eu	0.039	0.039	0.036	0.029	0.042	0.041	0.029	0.04	0.029
Gd	25.6	29.1	27.77	26.44	25.77	26.04	26.11	26.9	25.67
Tb	3.633	3.995	3.943	3.831	3.579	3.62	3.6	3.627	3.634
Dy	18.56	20.33	20.25	21.93	19.83	19.26	20.2	20.85	20.54
Ho	2.7	2.898	2.908	3.85	3.037	2.995	3.2	3.487	3.568
Tm	5.49	5.97	6.05	9.86	7.08	6.62	7.59	8.2	8.78
Er	0.594	0.683	0.7	1.407	0.951	0.807	0.997	1.075	1.14
Yb	3.71	4.16	4.29	9.99	6.42	5.77	6.62	7.24	7.64
Lu	0.413	0.45	0.47	1.184	0.679	0.59	0.773	0.889	0.958
SmN	81.4	92.2	89.3	98.9	101.2	98.1	96.7	101.8	96.5
EuN	0.7	0.7	0.6	0.5	0.8	0.7	0.5	0.7	0.5
GdN	130.2	148.0	141.3	134.5	131.1	132.5	132.8	136.8	130.6
TbN	100.1	110.1	108.6	105.5	98.6	99.7	99.2	99.9	100.1
DyN	76.5	83.8	83.4	90.4	81.7	79.4	83.2	85.9	84.6
HoN	48.6	52.1	52.3	69.2	54.6	53.9	57.6	62.7	64.2
TmN	34.6	37.6	38.1	62.1	44.6	41.7	47.8	51.6	55.3
ErN	24.5	28.2	28.9	58.1	39.3	33.3	41.2	44.4	47.1
YbN	22.8	25.6	26.4	61.5	39.5	35.5	40.7	44.6	47.0
LuN	17.0	18.5	19.3	48.7	27.9	24.3	31.8	36.6	39.4
YbN/GdN	0.175	0.173	0.187	0.457	0.301	0.268	0.307	0.326	0.360
Eu/Eu*	0.007	0.006	0.006	0.004	0.006	0.006	0.005	0.006	0.005

Values of - indicate trace elements are below detection limit of the instrument

Table S5 continued: LA-ICP-MS garnet REE and trace element analyses

	PAG - 19	PAG - 20	PAG - 21						
	Metapelitic gneiss - Type 2 continued (TB-14-025)								
Position	C	R	R						
Y	100.2	106.3	121						
Sm	14.09	15.24	15.05						
Eu	0.034	0.033	0.038						
Gd	25.68	26.72	29.05						
Tb	3.624	3.78	4.066						
Dy	21.05	22.09	23.97						
Ho	3.513	3.762	4.22						
Tm	9.06	9.4	10.84						
Er	1.215	1.275	1.452						
Yb	7.71	8.72	10.08						
Lu	0.986	1.107	1.276						
SmN	95.8	103.6	102.3						
EuN	0.6	0.6	0.7						
GdN	130.6	135.9	147.8						
TbN	99.8	104.1	112.0						
DyN	86.7	91.0	98.8						
HoN	63.2	67.7	75.9						
TmN	57.0	59.2	68.2						
ErN	50.2	52.7	60.0						
YbN	47.4	53.7	62.0						
LuN	40.6	45.6	52.5						
YbN/GdN	0.363	0.395	0.420						
Eu/Eu*	0.005	0.005	0.005						

Values of - indicate trace elements are below detection limit of the instrument

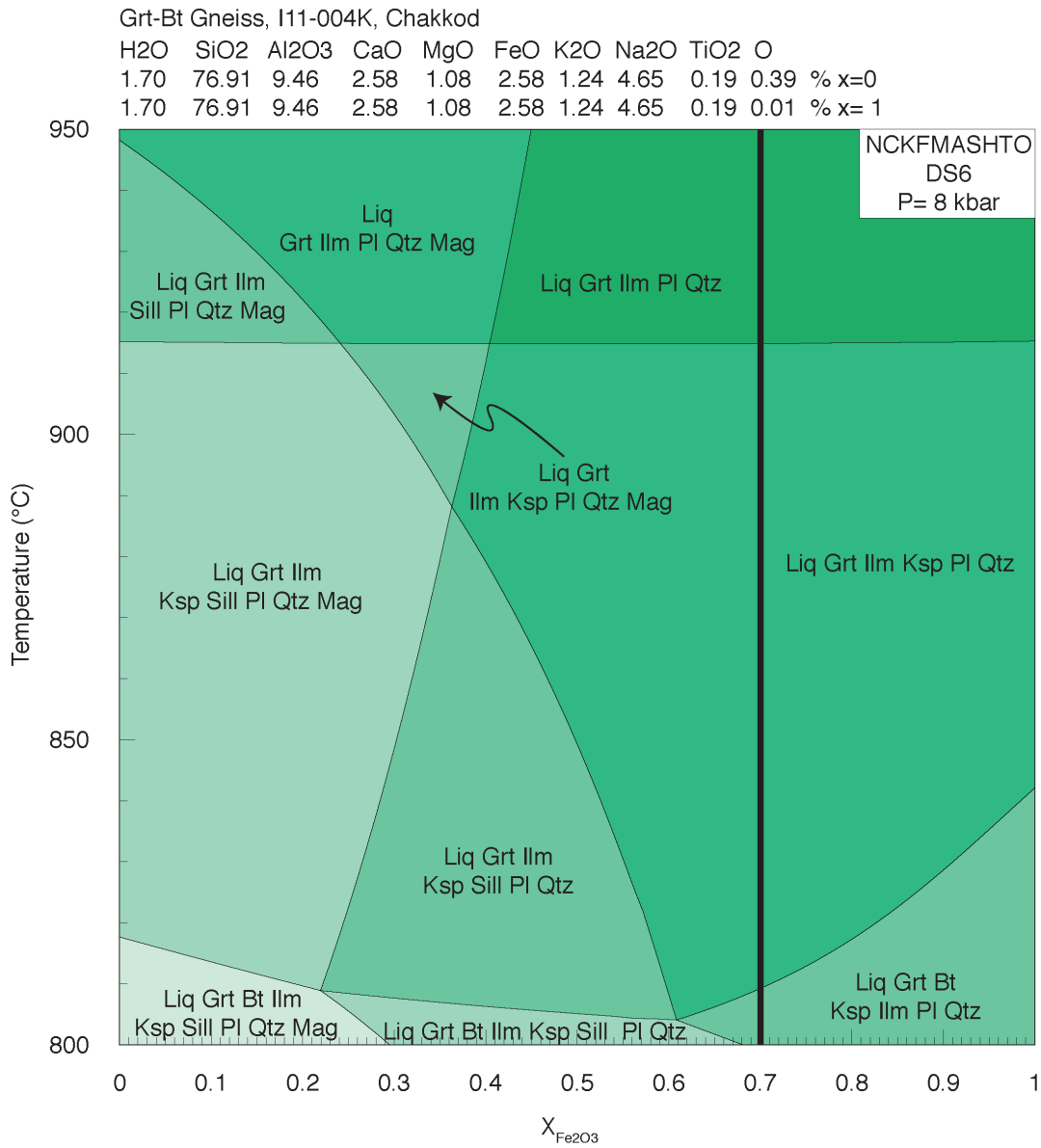

Fig. S1: Garnet-biotite gneiss *T–X* pseudosection with varying ferric iron content (O) from the XRF measured value of 0.39 (X=0) to 0.01 (X=1). Note that higher X values in this diagram actually correspond to lower X_{Fe2O3} in the rock. A mid value of X=0.7 (black line) was selected for the final *P–T* diagram.

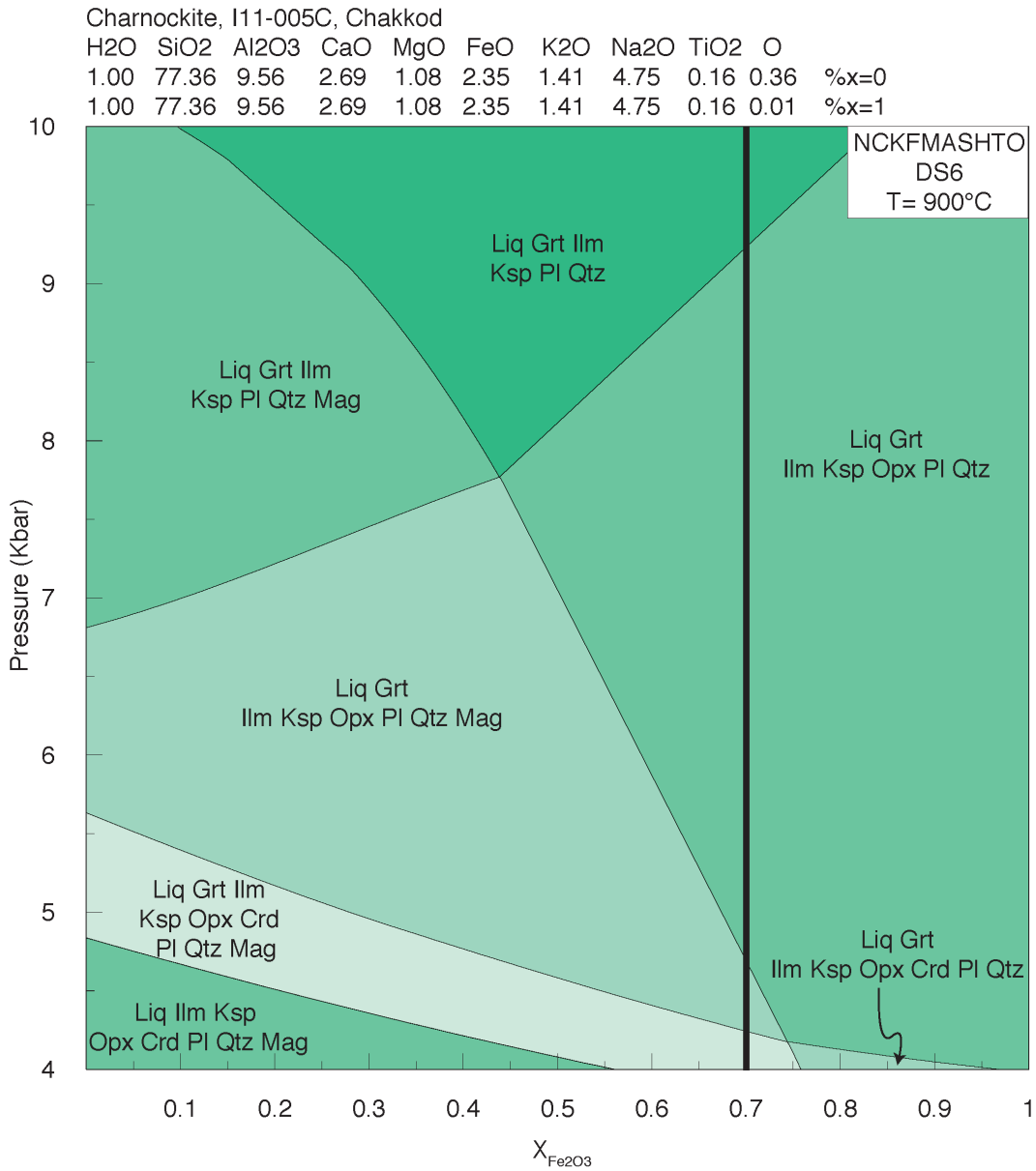

Fig. S2: Charnockite *P–X* pseudosection with varying ferric iron content (O) from the XRF measured value of 0.35 (X=0) to 0.01 (X=1). Note that higher X values in this diagram actually correspond to lower X_{Fe2O3} in the rock. A mid value of X=0.7 (black line) was selected for the final *P–T* diagram.

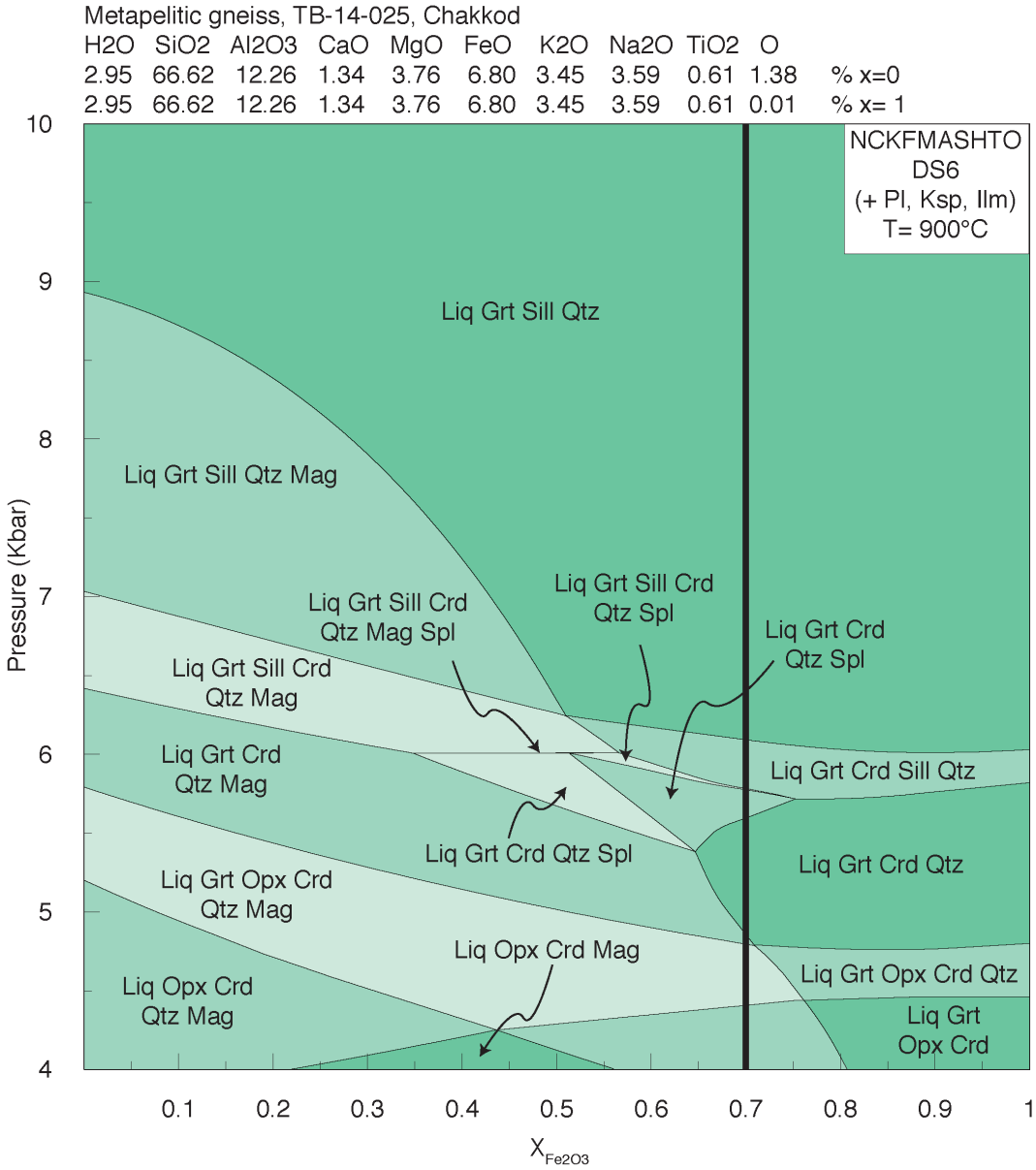

Fig. S3: Metapelitic gneiss *P–X* pseudosection with varying ferric iron content (O) from the XRF measured value of 1.34 (X=0) to 0.01 (X=1). Note that higher X values in this diagram actually correspond to lower X_{Fe2O3} in the rock. A mid value of X=0.7 (black line) was selected for the final *P–T* diagram.

Appendix C

This appendix contains the supplementary figures S1–S5 from 'Reappraising the *P–T* evolution of the Rogaland–Vest Agder Sector, southwestern Norway'.

Contents:

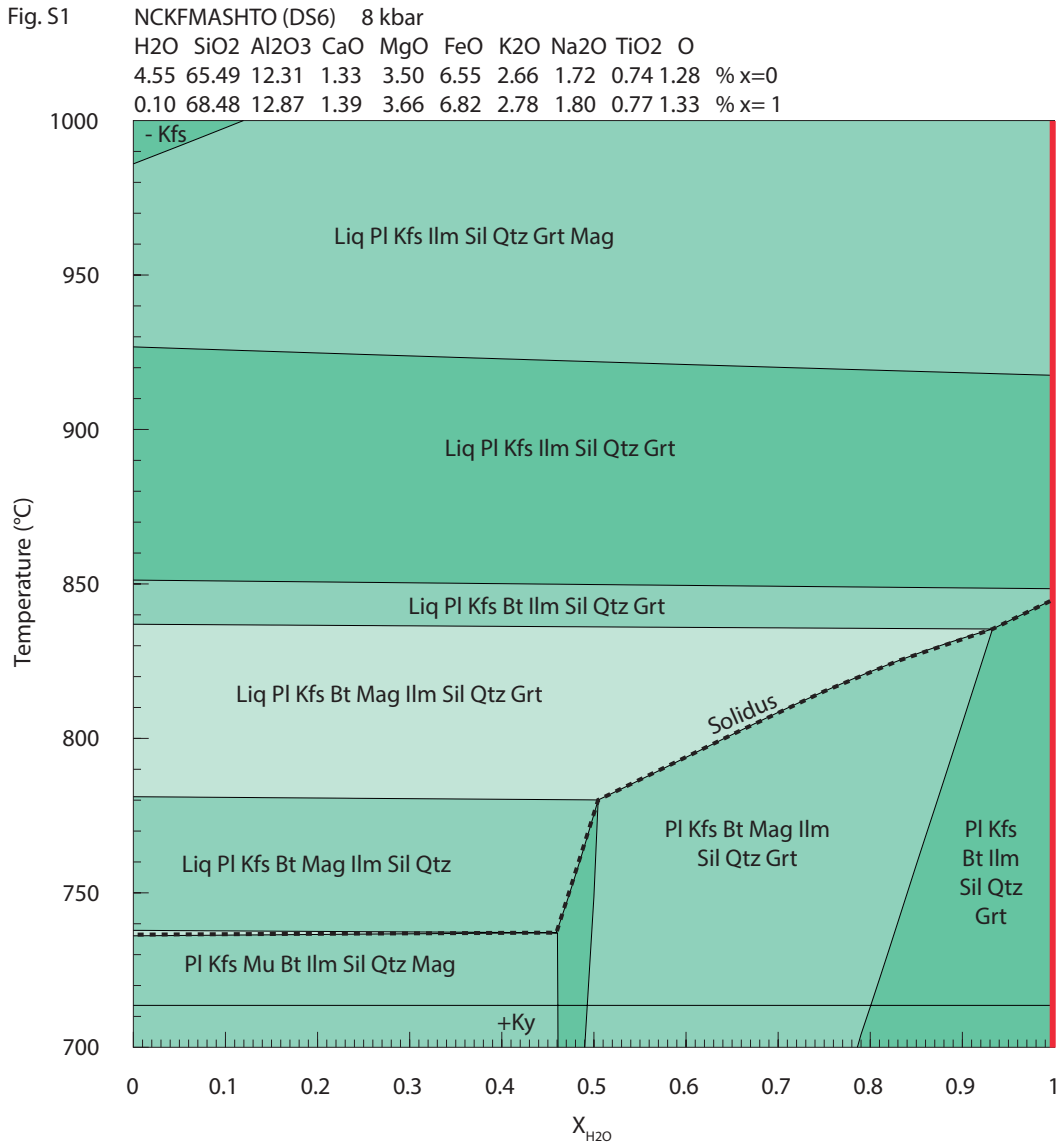

Fig. S1: T–X_{H2O} diagram for the distal sample (ROG13/11). The peak regional assemblage is in bold, the solidus is marked with a dashed line and the modelled X content is marked with a red line. X varies from the measured LOI (X = 0, 4.44 mol.%) to a lower value (X = 1, 0.10 mol.%). Note that higher X values in this diagram actually correspond to lower X_{H2O} in the rock. A value of X = 1 was chosen for the modelled water content as the sample has experienced retrogression (e.g. pinitisation of cordierite) and to bring the solidus as close as possible to the peak assemblage to represent peak conditions.

Fig. S2

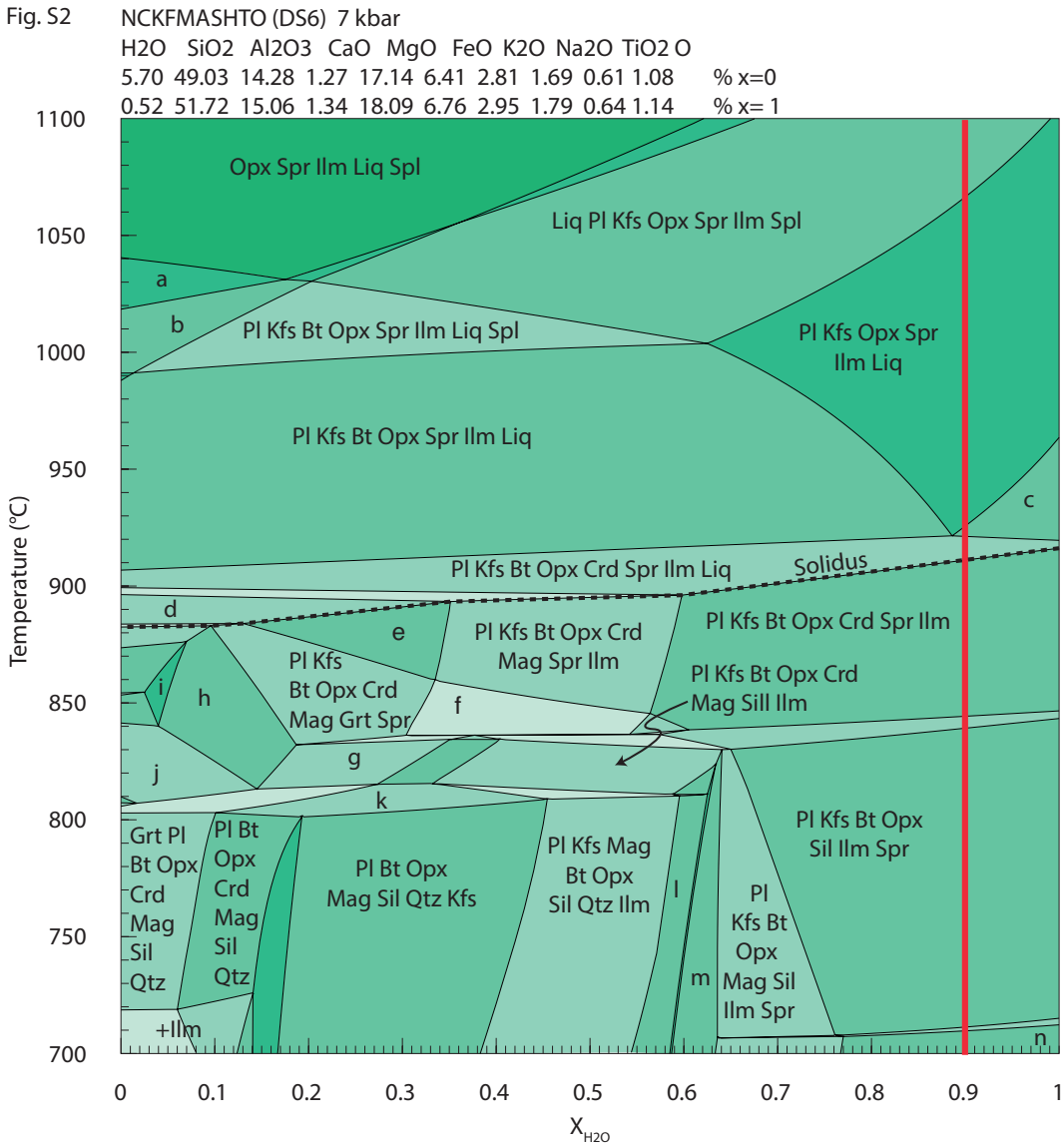

a - Bt Opx Spr Ilm Liq Spl
b - Pl Bt Opx Spr Ilm Liq Spl
c - Pl Kfs Opx Spr Ilm Liq Crd
d - Pl Kfs Bt Opx Crd Mag Spr Liq
e - Pl Kfs Bt Opx Crd Mag Spr
f - Pl Kfs Bt Opx Crd Mag Grt Spr Ilm
g - Bt Opx Crd Pl Kfs Sil Mag Grt Spr
h - Pl Kfs Bt Opx Crd Mag Grt
i - Pl Kfs Bt Opx Crd Mag
j - Pl Kfs Bt Opx Crd Mag Grt Qtz
k - Pl Kfs Bt Opx Crd Mag Sil Qtz
l - Pl Kfs Opx Bt Sil Ilm Qtz
m - Pl Kfs Bt Opx Mag Sil Ilm
n - Pl Kfs Bt Opx Sil Ilm Cor

Fig. S2: T–X_{H2O} diagram for the intermediate sample (ROG13/10). The peak regional assemblage is in bold, the solidus is marked with a dashed line and the modelled X content is marked with a red line. X varies from the measured LOI (X = 0, 5.70 mol.%) to a lower value (X = 1, 0.52 mol.%). Note that higher X values in this diagram actually correspond to lower X_{H2O} in the rock. A value of X = 0.9 was chosen for the modelled water content as the sample has experienced retrogression (e.g. abundant late biotite), but to also account for prograde/peak regional cordierite.

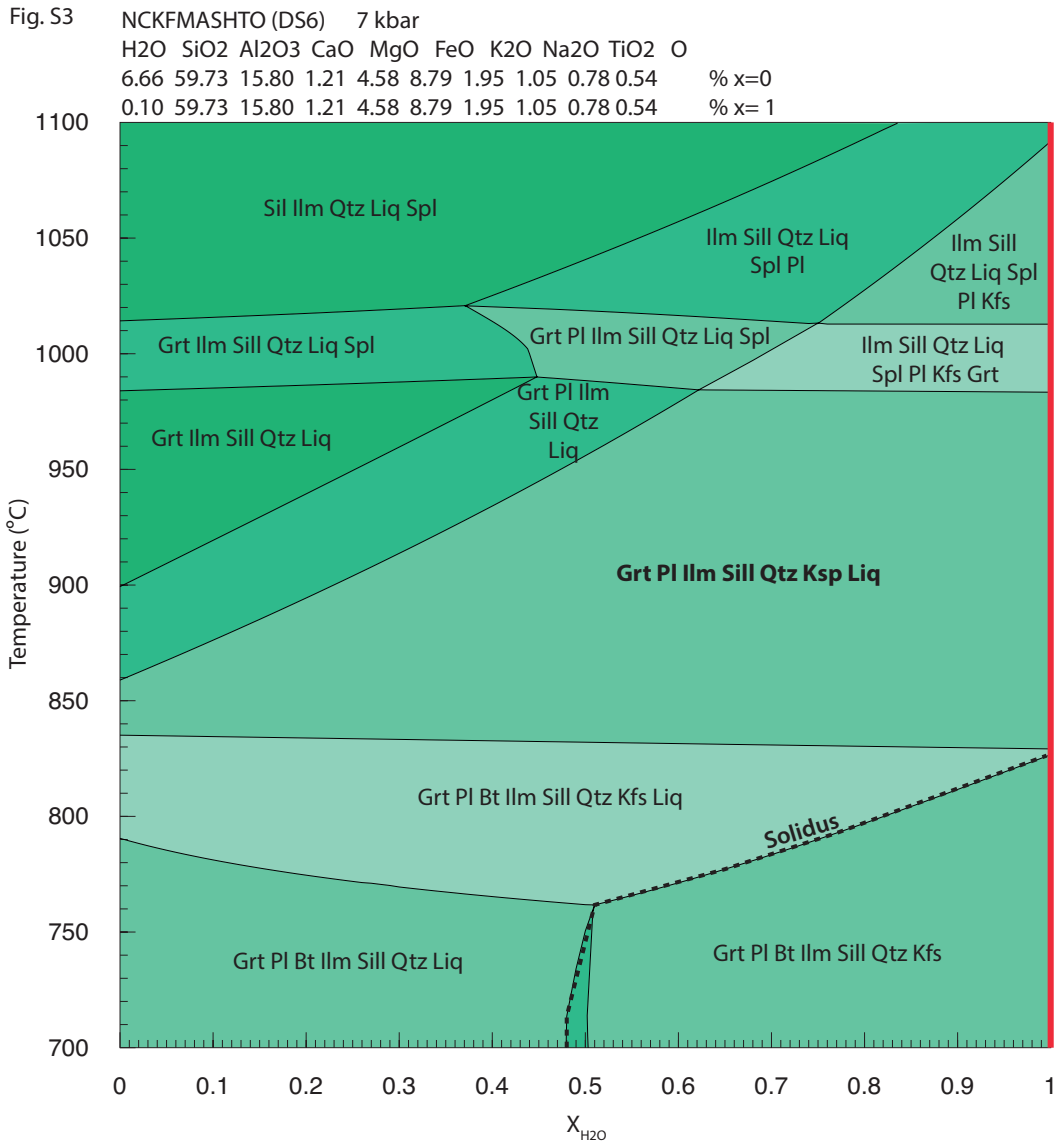

Fig. S3: T–X_{H2O} diagram for the proximal sample (ROG14/5). The peak regional assemblage is in bold, the solidus is marked with a dashed line and the modelled X content is marked with a red line. X varies from the measured LOI (X = 0, 6.66 mol.%) to a lower value (X = 1, 0.10 mol.%). Note that higher X values in this diagram actually correspond to lower X_{H2O} in the rock. A value of X = 1 was chosen for the modelled water content as the sample has experienced retrogression (e.g. pinitisation of cordierite) and to bring the solidus as close as possible to the peak assemblage to represent peak conditions.

Fig. S4

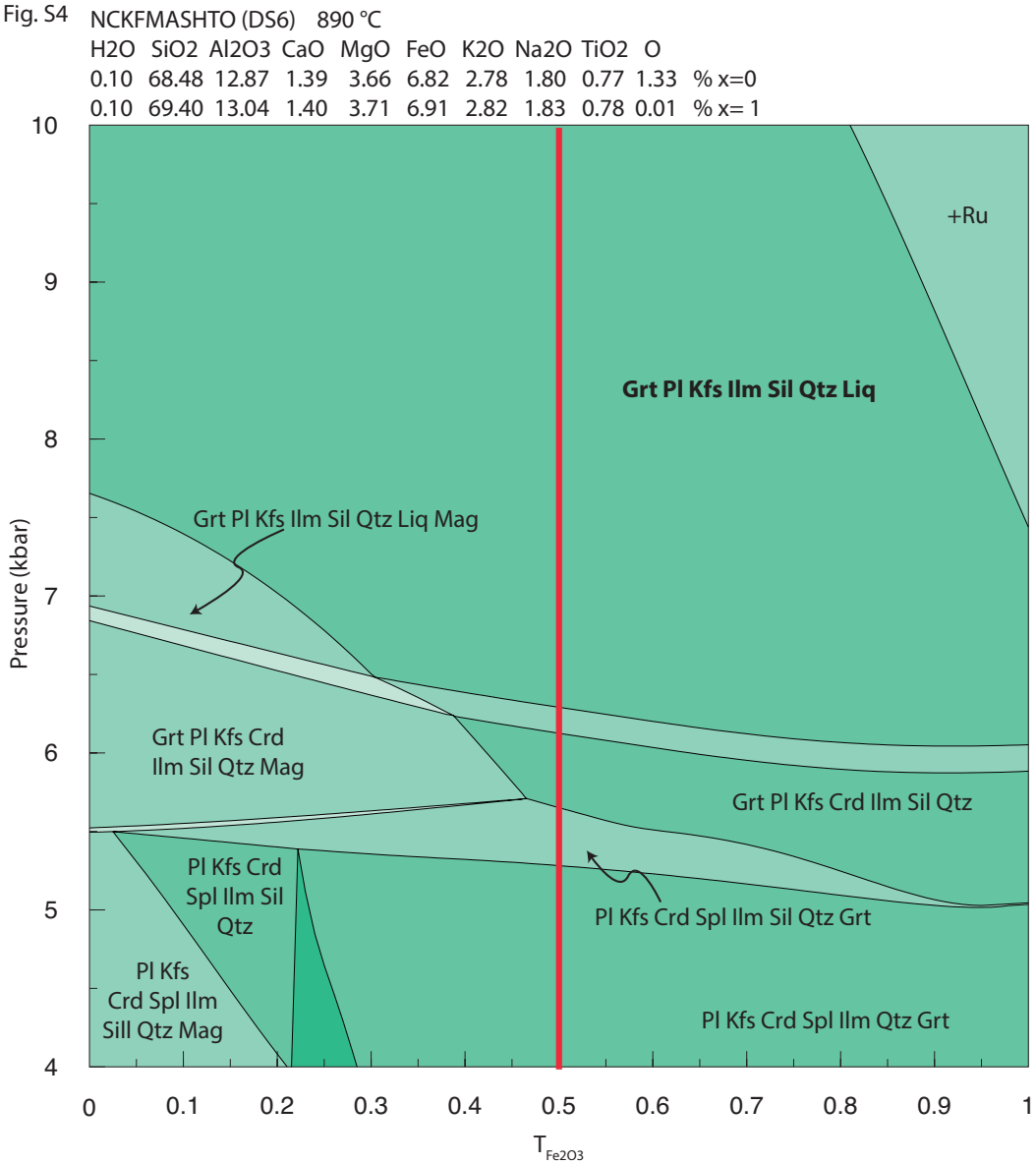

Fig. S4: P–X_{Fe2O3} diagram for the distal sample (ROG13/11). The peak regional assemblage is in bold, the solidus is marked with a dashed line and the modelled X content is marked with a red line. X varies from the measured ferric iron (X = 0, 4.44 mol.%) to a lower value (X = 1, 0.10 mol.%). Note that higher X values in this diagram actually correspond to lower X_{Fe2O3} in the rock. A value of X = 0.5 was chosen for the modelled ferric iron content as the sample has experienced oxidation since peak metamorphism and because this was the lowest value required to remove magnetite from the modelled evolution of the sample.

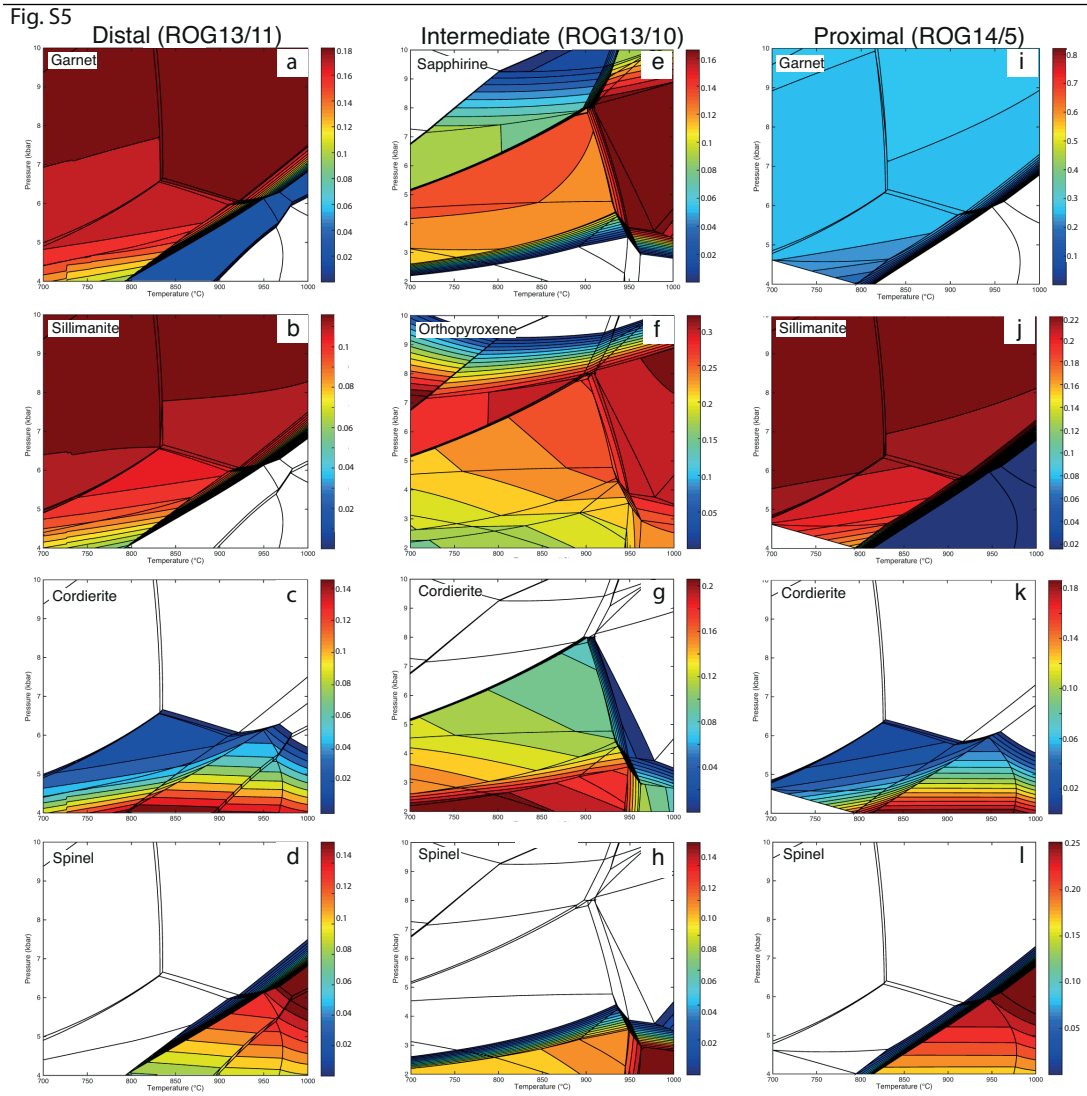

Fig. S5: Contoured pseudosections for key minerals using TCInvestigator (Pearce et al., 2015). Distal sample (ROG13/11): a – Modal proportion of garnet. b – Modal proportion of sillimanite. c – Modal proportion of cordierite. d – Modal proportion of spinel. Intermediate (ROG13/10): e – Modal proportion of sapphirine. f – Modal proportion of orthopyroxene. g – Modal proportion of cordierite. h – Modal proportion of spinel. Proximal (ROG14/5): i – Modal proportion of garnet. j – Modal proportion of sillimanite. k – Modal proportion of cordierite. l – Modal proportion of spinel.

Appendix D

This appendix contains Appendix 1 and 2 from the paper 'Constraining the timing of prograde metamorphism in long-lived hot orogens' as well as the two full TIMA maps used within this paper.

Contents:

Appendix 1

Methodology:

Phase equilibria modelling:

P–T conditions for ROG13/2 were constrained by a combination of *P–T* and *P–X* pseudosections modelled within the $Na_2O-CaO-K_2O-FeO-MgO-Al_2O_3-SiO_2-H_2O-TiO_2-O$ system (NCKFMASHTO) using THERMOCALC 3.33i. As no compatible osumilite model for DS6 is available, modelling was conducted using DS5 (tc–ds55s, sapphirine update of Holland and Powell (1998), generated on 22/11/2003, as used by Kelsey et al. (2004) and Korhonen et al. (2013)). The modelled bulk rock composition was determined using X-ray fluorescence (XRF) analysis with this composition taken from an essentially garnet-free portion of osumilite migmatite. Modelled H_2O content was constrained using a *P–X* at 900°C (average peak temperature for regional metamorphism from Blereau et al., 2017) with H_2O concentrations ranging from low (0.1 mol%) to a maximum concentration (2.59 mol%) with all loss of ignition from XRF assumed to be H_2O. A H_2O content of ~50% (1.295, normalised to 1.28) was chosen as the minimum value to achieve the desired assemblage.

Calculations considered the phases: garnet, orthopyroxene, silicate melt, quartz, K-feldspar, plagioclase, sillimanite/kyanite, osumilite, ilmenite, rutile, magnetite-spinel, cordierite and biotite.

Activity composition models used were as follows:

- Silicate melt, biotite, garnet: White et al., (2007).
- Cordierite: Holland and Powell (1998).
- Orthopyroxene and spinel-magnetite: White et al., (2002).
- Plagioclase and K-feldspar: Holland and Powell (2003).
- Osumilite: modified from Holland et al., (1996) by T. J. B Holland, pers. comm. via R. W. White, April 2012; used in Korhonen et al., (2013). a–X models available on request.
- Ilmenite: White et al., (2000).
- Pure end member phases: Sillimanite, rutile, quartz.

Modelled bulk composition normalised by THERMOCALC is as follows:

H_2O	SiO_2	Al_2O_3	CaO	MgO	FeO	K_2O	Na_2O	TiO_2	O
1.28	67.91	8.41	1.05	7.48	6.63	2.15	2.83	1.04	1.22

Mineral abbreviations follow Kretz (1983) and Whitney and Evans (2010).

Phase maps were created using the Tescan Integrated Mineral Analysis (TIMA) instrument located in the John de Laeter Centre at Curtin University and were used to locate the textural positions of osumilite (e.g. Fig. 2, S1) and interpret the mineralogical evolution.

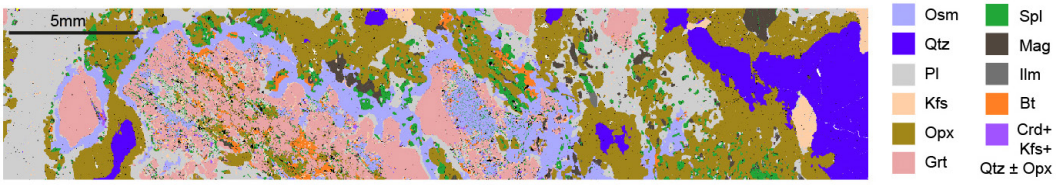

Figure S1: Part of a TIMA map of a rare garnet-bearing domain within the melanosome with osumilite rims around garnet. Minerals after Kretz (1983).

^{40}Ar/^{39}Ar analysis:

Fifty-five unaltered, inclusion free, optically transparent osumilite fragments were selected from the Rogaland sample (ROG13/2) for ^{40}Ar/^{39}Ar dating, with size ranging from 355–450 µm. The sample was disaggregated using the SELFRAG Lab electrical pulse disaggregation (EPD) system housed in the John de Laeter Centre at Curtin University. The minerals were separated by careful hand-picking under a binocular microscope. The selected osumilite grains were thoroughly rinsed with distilled water in an ultrasonic cleaner. The osumilite came from predominantly, garnet-absent migmatite but a small amount of garnet was recovered from the disaggregated sample, indicating the disaggregation of a rare garnet-bearing domain within the bulk sample.

The disc into which the osumilite fragments were placed for irradiation contains smaller pits into which muscovite standard WA1ms was placed as a neutron fluence monitor, for which an age of 2613.0 Ma (± 0.09%) was used (Jourdan et al., 2014).

Mean J-values computed from the WA1ms grains in each disc ranged from 0.01033000 ± 0.00000600 (0.058%) to 0.01033250 ± 0.00001860 (0.18%). Mass discrimination was monitored using an automated air pipette, This indicated mean fractionation ranging from 1.00419 ± 0.08 to 1.00432 ± 0.05 per dalton (atomic mass unit). The correction factors for interfering isotopes were (^{39}Ar/^{37}Ar)Ca = 7.60x10-4 (± 1.2%), (^{36}Ar/^{37}Ar)Ca = 2.70x10-4 (± 1%) and (^{40}Ar/^{39}Ar)K = 7.3x10-4 (± 12.4%).

Following irradiation, ^{40}Ar/^{39}Ar analyses were performed at the Western Australian Argon Isotope Facility (WAAIF) at Curtin University following three different approaches.

Six single-fragment aliquots were step-heated for age determination using a 110 W Spectron Laser Systems continuous Nd-YAG (IR; 1064 nm) laser, rastered for approximately 1 min to ensure a homogenously distributed temperature. Three five-fragment aliquots were wrapped in copper foil and step-heated in a double vacuum high frequency Pond Engineering furnace (for diffusion modelling). Extraction temperatures were measured using a Pond Engineering thermocouple. Each extraction step last 10 minutes including 2 minutes for ramping up the temperature and 8 minutes in a steady state at the desired temperature. Each step was followed by a drop of temperature of 150°C during mass spectrometer analysis. The gas was purified in a stainless steel extraction line using two AP10 and one GP50 SAES getter. For these aliquots, Ar isotopes were measured in static mode using a MAP 215-50 mass spectrometer (resolution of ~500; sensitivity of 4x10^{-14} mol/V) with a Balzers SEV 217 electron

multiplier using 9 to 10 cycles of peak-hopping. Blanks were monitored every 3 to 4 steps. Typical ^{40}Ar blanks ranged from 1 x 10^{-16} to 2 x 10^{-16} mol. The data acquisition was performed using the Argus program written by M.O. McWilliams, in a LabView environment.

Two additional single-fragment aliquots were analysed on a low volume (600 cc) Thermofisher© ARGUS VI mass spectrometer, also at the Western Australian Argon Isotope Facility at Curtin University. Step-heating was undertaken using a continuous 100 W PhotoMachine© CO_2 (IR, 10.4 µm) laser fired for a duration of 60 seconds. The gas was purified in an extra low-volume stainless steel extraction line of 240cc using one SAES AP10 and one GP50 getter. Ar isotopes were measured in static mode using a mass resolution of ~200. Measurements were carried out in multi-collection mode using four Faraday cups to measure masses 40 to 37 and a zero-background compact discrete-dynode ion counter to measure mass 36. The relative abundance of each mass was measured simultaneously using 10 cycles of peak-hopping and 33 seconds of integration time for each mass. Detectors were calibrated to each other electronically and using Air shot beam signals.

The raw data were processed using the ArArCALC software (Koppers, 2002). Ages were calculated using the decay constants of Renne et al. (2011).

Ar isotopic data corrected for blanks, mass discrimination and radioactive decay are given in Appendix 2. Individual errors in Appendix 2 are given at the 1σ level. Our criteria for the determination of plateaux are that plateaux must include at least 70% of the ^{39}Ar released, that plateaux must be composed of a minimum of 3 consecutive steps agreeing at 95% confidence level and satisfying a probability of fit (P) of at least 0.05. Plateau ages (Fig. 3) are given at the 2σ level and were calculated using the mean of all the plateau steps, each weighted by the inverse of their individual variances. The uncertainties on the $^{40}Ar^*/^{39}Ar$ ratios of the monitor are included in the calculation of the integrated and plateau age uncertainties, but the uncertainties on the age of the monitor and on the decay constant are not (internal errors only). Fully propagated uncertainties including uncertainty on the R-value of the monitor WA1ms against FCs (Jourdan et al., 2014) and uncertainty of the decay constants using a Monte Carlo error propagation approach (Renne et al., 2010) are given with the age results in the main text. The two ARGUS analyses failed to yield acceptable plateau ages (Fig. S2), although the age spectra converge toward apparent ages of ~919 Ma and ~1066 Ma, in agreement with the plateau ages obtained with the MAP 215-50 instrument. Single fragment analysis from a mineral separate was used as the true grain size was difficult to discern until the TIMA mapping was implemented (due to the difficult nature of identifying osumilite in thin section) and there was no initial expectation that osumilite would have yielded more than one age. Future studies on large grains of osumilite should implement micro drilling or other techniques to spatially quantify the $^{40}Ar/^{39}Ar$ dates.

Diffusion modelling:

Argon temperature-controlled diffusion experiments were performed on three aliquots of five

osumilite grains fragments taken from the same sample as those used for $^{40}Ar/^{39}Ar$ dating (Fig. S3). For the diffusion calculation, ^{39}Ar was selected as diffusant. Osumilite does not contain calcium so no correction for calcium interference using ^{37}Ar was required.

The fraction of ^{39}Ar and the duration of each step were used to calculate *D* values using the classic equation of Dodson (1973) for a spherical volume (Equation 1). For each sample, -log*D* vs. 1000/*T* values are displayed on an Arrhenius plot (Fig. S4). The two diffusion parameters, activation energy E_a and frequency factor D_0, were calculated from the arrays defined on the Arrhenius plots, up to the temperatures at which the crystals broke down and started to melt. We used a crystal radius of 175 µm and a spherical geometry for the calculation. A spherical volume is appropriate for all grain shapes, other than platy minerals, with little effect on the diffusion results. Errors on the y-axis intercept D_0 and slope E_a were calculated using a robust regression (Isoplot v3.7; (Ludwig, 2003)) since the scatter on the regression line is much larger than the uncertainties on the individual measurements.

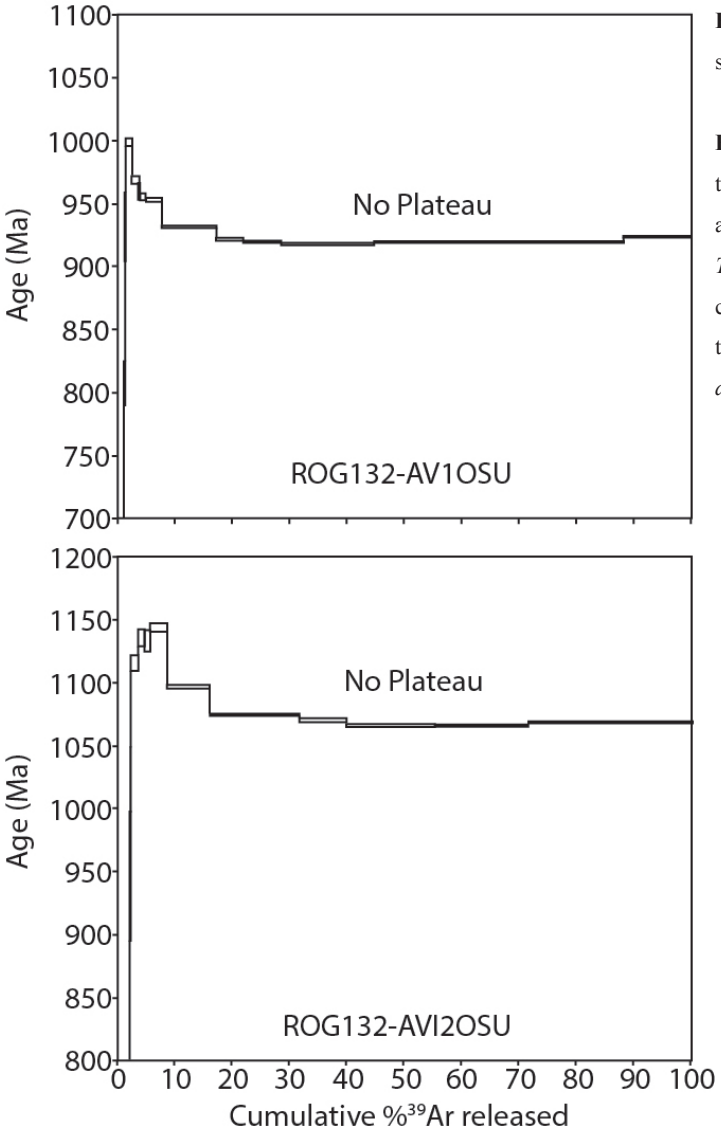

Figure S2: Osumilite $^{40}Ar/^{39}Ar$ age spectra from ARGUS laser analyses

Equation 1: Mineral specific closure temperature for argon diffusion. *E*- activation energy (or E_a), *R*- gas constant, T_c- closure temperature, *A*- volume constant, T_{c0}- intial estimate of closure temperature, D_0- diffusion coefficient, *dT/dt*- cooling rate, *a*- grain size.

$$\frac{E}{R \times T_c} = \ln\left(-\frac{A \times R \times T_{c0}^2 \times D_0}{E \times (dT/dt) \times a^2}\right)$$

Figure S3: 355–450 µm osumilite fragments from migmatite ROG13/2. Fragments to the left and right contain numerous fractures and inclusions respectively and so weren't picked into the final sample. Fragments in the centre are representative of those sent for irradiation.

The Arrhenius plots (Fig. S4) show that the ^{39}Ar gas release from the osumilite grains occurred in three distinct stages. The low-*T* stage involved rapid release of only a few percent of the total gas, forming a shallow slope on the plot and indicating fast diffusivity at low temperature (i.e. corresponding to closure temperatures of ca. 220°C (1% ^{39}Ar), 77°C (1.6% ^{39}Ar) and 69°C (4% ^{39}Ar). We interpret these data as indicating very fast release of argon via cracks and defects and coming from any potassium located in low retentive cation sites. The second stage, at higher-*T* involved slower release of most of the gas, forming a much steeper slope (Fig. S3). The third stage, whilst also steep and at even higher-*T* would correspond to an unreasonably high closure temperature (~900°C) and is interpreted as a change in the nature of osumilite when melting. The second stage was used for the determination of closure temperature. Age spectra from the diffusion experiments failed to form plateaux, which is not surprising for multigrain aliquots. Whilst these experiments potentially show evidence for domain-based diffusion, each grain fragment yielded a statistically acceptable plateau. It is unlikely therefore, that a single fragment contains multiple domains as they would not likely yield a consistent plateau.

The second part of the arrays described above yielded a range of E_a (activation energy) values and D_0 (pre-exponential diffusion factor) average values, calculated for fragments with an average radius of 175 µm (summarised in Table 1, Fig S4). Based on these D_0 and E_a values, the closure temperature of each aliquot was calculated using a Monte Carlo simulation run on Quantum XL™ software. This approach allows for the complete propagation of uncertainties on each value and minimizes error correlations. The simulation consisted of 10,000 random trials using a triangular distribution for the E_a and D_0 values to account for the uncertainties derived for those values (Fig. S4) and a uniform distribution of radii between 175 and 250 µm to account for the true variation in size of the osumilite crystals analysed. Closure temperatures in the main text and Fig. S4 were calculated for a cooling rate of 10 °C/Ma with uncertainties at the 2σ level. In each case, more than 90% of the uncertainty of the closure temperature values is controlled by the uncertainty on the E_a value (Fig. S5). The values calculated using Monte Carlo simulations take into account the range of possible values and distribution of each parameter rather than simply averaging each parameter, providing good estimates of the true closure temperature (Scibiorski et al., 2015).

Two alternative modelled diffusion profiles were calculated for the Rogaland osumilite using the ArArDiff algorithm (Jourdan and Eroglu, 2017). Diffusion parameters from experiment 1 were

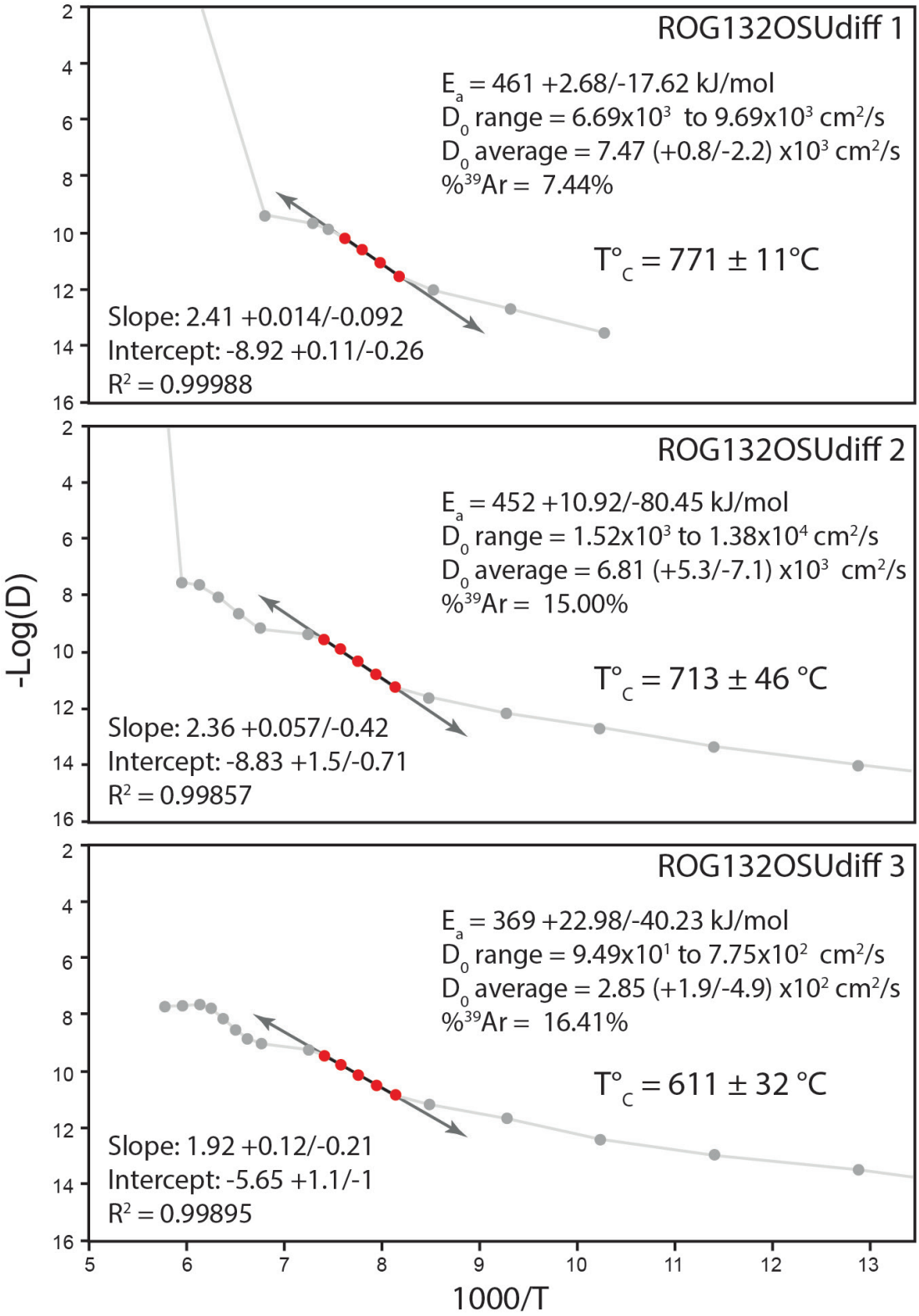

Figure S4: Arrhenius plots for three furnace diffusion experiments on multigrain osumilite aliquots. The red dots are those steps from which the regression line was drawn, from which the listed values of E_a, D_0, *Tc* were calculated.

Diffusion Parameters

	D_0 (cm²/s)	E_a (kJ/mol)	Radius (µm)
Osumilite	7.47 x10³	461	5000

Crystallisation age = 1070 Ma

	Start (Ma)	End (Ma)	Duration (Ma)	Starting temp. (°C)	Ending temp. (°C)	Cooling rate (°C)/Ma
Thermal History 1 (Hot)						
Period 1	1070	1000	70	800	950	-2
Period 2	1000	930	70	950	900	1
Period 3	930	870	60	950	700	4
Period 4	870	0	870	700	0	1
Thermal History 2 (Cold)						
Period 1	1070	1000	70	800	850	-1
Period 2	1000	930	70	850	800	1
Period 3	930	870	60	860	700	3
Period 4	870	0	870	700	0	1

Table S1: Temperature, time and diffusion parameters used in the generation of the diffusion models.

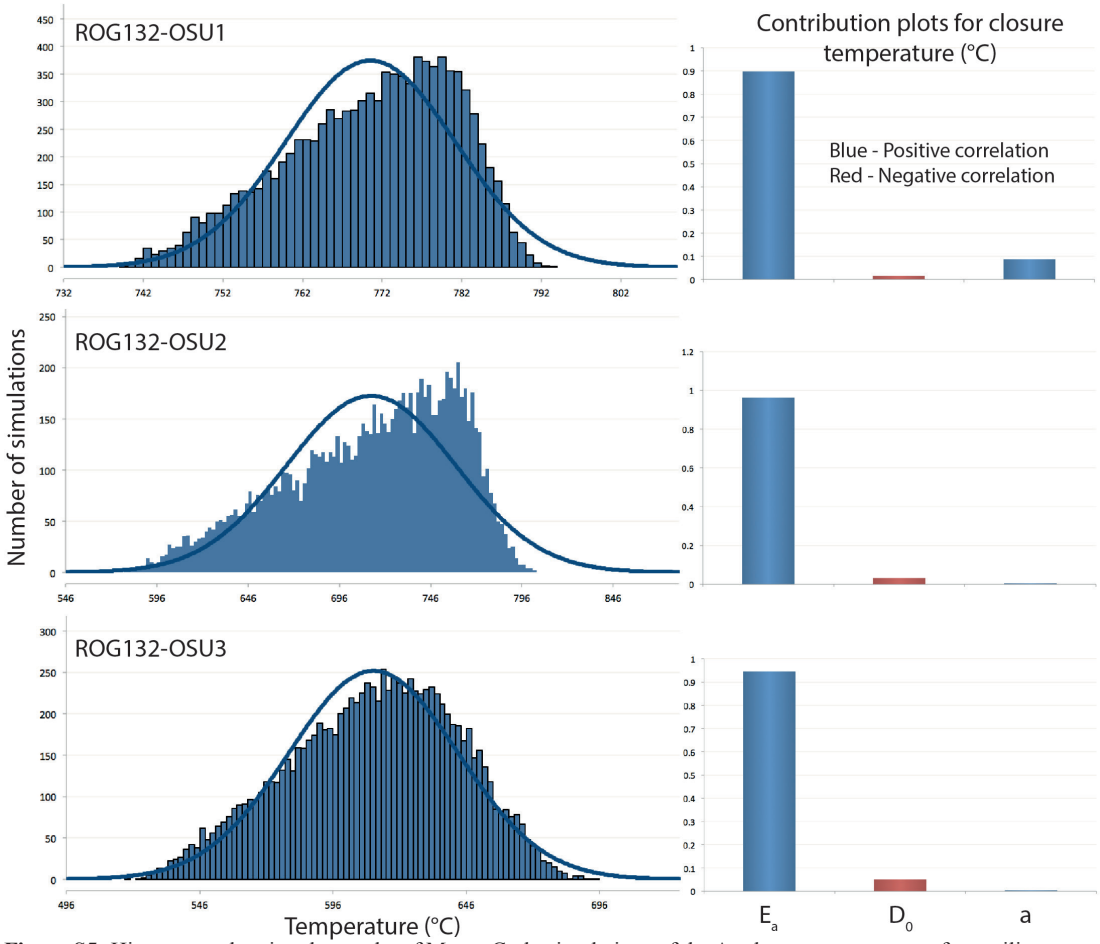

Figure S5: Histograms showing the results of Monte Carlo simulations of the Ar closure temperature of osumilite. Accompanying contribution plots show which parameter out of E_a, D_0 and a (radius of grain) has the most control over the distribution.

used with the radius of the largest grain size of 5000 µm used. Temperature-time conditions were based on the coldest and hottest possible peak temperatures indicated for the two metamorphic events estimated by Blereau et al., (2017) and the ages of monazite from Laurent et al., (2016) (summarised in Table S1). The ArArDiff algorithm is capable of modelling up to four *T–t* periods, which required some simplification of the Rogaland metamorphic evolution. Periods 1–2 were set to represent heating and cooling during the regional metamorphism. Period 3 was set to represent the abrupt heating due to contact metamorphism. Period 4 was set to represent subsequent cooling. Due to the limitations of the ArArDiff algorithm, only typical analytical uncertainties on the $^{40}Ar/^{39}Ar$ analyses could be propagated. The grain size used within the model only causes major variations in the outcome of the

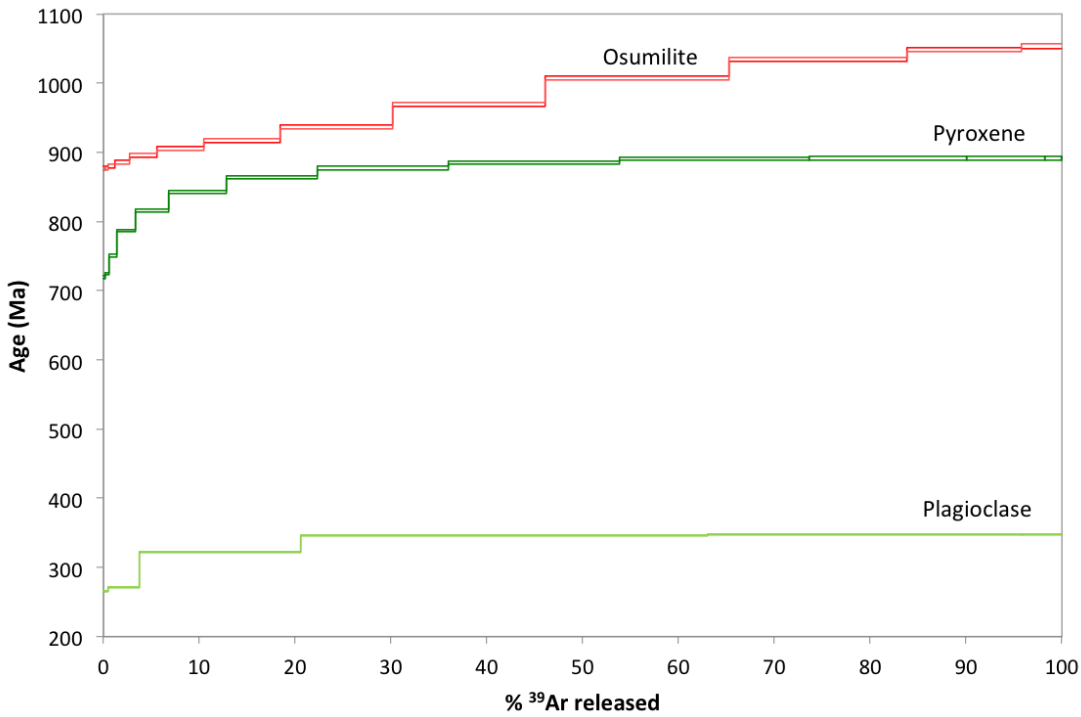

Figure S6: Theoretical Ar/Ar age spectra, for the modelled Rogaland cold thermal history for osumilite, pyroxene and plagioclase.

References:

Blereau, E., Johnson, T. E., Clark, C., Taylor, R. J. M., Kinny, P. D. & Hand, M., 2017. Reappraising the P–T evolution of the Rogaland–Vest Agder Sector, southwestern Norway. Geoscience Frontiers, 8, 1–14.

Dodson, M. H., 1973, Closure temperature in cooling geochronological and petrological systems: Contributions to Mineralogy and Petrology, v. 40, no. 3, p. 259-274.

Holland, T.J.B., Babu, E.V.S.S.K, & Waters, D.J., 1996. Phase relations of Osumilite and dehydration melting in pelitic rocks: a simple thermodynamic model for the KFMASH system. Contributions to Mineralogy and Petrology, 124, 383-394.

Holland, T.J.B., & Powell, R., 1998. An internally consistent thermodynamic dataset for phases of petrological interest. Journal of Metamorphic Geology, 16, 309-343.

Holland, T.J.B. & Powell, R., 2003. Activity-composition relations for phases in petrological calculations: an asymmetric multicomponent formulation. Contributions to Mineralogy and Petrology, 145, 492-501.

Jourdan, F. Eroglu, E., 2017. 40Ar/39Ar and (U-Th)/He model age signatures of elusive mercurian and venusian meteorites. Meteoritics and Planetary Science, In Press.

Jourdan, F., Frew, A., Joly, A., Mayers, C., Evans, N. J., 2014. WA1ms: A ~2.61 Ga muscovite standard for 40Ar/39Ar dating. Geochimica et Cosmochimica Acta, 141, 113–126.

Kelsey, D. E., White, R. W., Holland, T. H., and Powell, R., 2004, Calculated phase equilibria in K_2O–FeO–MgO–Al_2O_3–Si_2O–H_2O for sapphrine-quartz-bearing mineral assemblages: Journal of Metamorphic Geology, 22, 559-578.

Kelsey, D. E., and Hand, M., 2015, On ultrahigh temperature crustal metamorphism: Phase equilibria, trace element thermometry, bulk composition, heat sources, timescales and tectonic settings: Geoscience Frontiers, 6, 311–356.

Koppers, A.A.P., 2002. ArArCALC-software for $^{40}Ar/^{39}Ar$ age calculations. Computers & Geosciences, 28, 605–619.

Korhonen, F. J., Brown, M., Clark, C., and Bhattacharya, S., 2013, Osumilite-melt interactions in the ultrahigh temperatures granulites: phase equilibria modelling and implications for the P-T-t evolution of the Eastern Ghats Provincee, India: Journal of Metamorphic Geology, 31, 881-907.

Kretz, R., 1983. Symbols for rock-forming minerals. American Mineralogist, 68, 277-279.

Laurent, A. T., Seydoux-Guillaume, A.-M., Duchene, S., Bingen, B., Bosse, V., and Datas, L., 2016, Sulphate incorporation in monazite lattice and dating the cycle of sulphur in metamorphic belts: Contributions to Mineralogy and Petrology, v. 171, no. 11, p. 94.

Ludwig, K. R., 2003. Isoplot 3.00: a geochronological toolkit for Microsoft Excel: Berkeley Geochronological Centre Special Publication, v. 4.

McDougall, I. and Harrison, M., 1999. Geochronology and Thermochronology by the 40Ar/39Ar Method: Oxford University Press on Demand.

Olierook, H.K.H., Jourdan, F., Merle, R.E., Timms, N.E., Kusznir, N., Muhling, J.R., 2016. Bunbury Basalt: Gondwana breakup products or earliest vestiges of the Kerguelen mantle plume? Earth and Planetary Science Letters, v. 440, 1–14.

Renne, P.R., Balco, G., Ludwig, K.R., Mundil, R., Min, K., 2011. Response to the comment by W.H. Schwarz et al. on “Joint determination of K-40 decay constants and Ar-40*/K-40 for the Fish Canyon sanidine standard, and improved accuracy for Ar-40/Ar-39 geochronology” by PR Renne et al. (2010). Geochimica et Cosmochimica Acta, 75, 5097-5100.

Scibiorski, E., Tohver, E., and Jourdan, F., 2015, Rapid cooling and exhumation in the western part of the Mesoproterozoic Albany-Fraser Orogen, Western Australia: Precambrian Research, v. 265, p. 232-248.

White, R.W., Powell, R., Holland, T.J.B. & Worley, B.A., 2000. The effect of TiO2 and Fe2O3 on metapelitic assemblages at greenschist and amphibolite facies conditions: mineral equilibria calculations in the system K2O-FeO-MgO-Al2O3-SiO2-H2O-TiO2-Fe2O3. Journal of Metamorphic Geology, 18, 497-511.

White R.W., Powell R., Clarke G.L., 2002. The interpretation of reaction textures in Fe-rich metapelitic granulites of the Musgrave Block, central Australia: constraints from mineral equilibria calculations in the system K2O-FeO-MgO-Al2O3-SiO2-H2O-TiO2-Fe2O3. Journal of Metamorphic Geology, 20, 41-55.

White, R.W., Powell, R. & Holland, T.J.B., 2007. Progress relating to calculation of partial melting equilibria for metapelites. Journal of Metamorphic Geology, 25, 511-527.

Whitney, D. L., & Evans, B. W., 2010. Abbreviations for names of rock-forming minerals. American Mineralogist, 95, 185-187.

Appendix 2

Relative Abundances			36Ar [V]	%1σ	37Ar [V]	%1σ	38Ar [V]	%1σ	39Ar [V]	%1σ	40Ar [V]	%1σ	40(r)/39(k) ± 2σ	Age ± 2σ (Ma)	40Ar(r) (%)	39Ar(k) (%)	K/Ca ± 2σ
6M40998D	62 °C		0.0000006	999.146	0.0000346	453.523	0.0000042	143.130	0.0003590	2.700	0.017129	0.973	47.21409 ± 10.42034	718.43 ± 130.85	98.96	0.14	4 ± 41
6M41000D	63 °C		0.0000019	342.709	0.0000269	583.485	0.0000970	8.286	0.0076109	0.355	0.592473	0.083	77.91865 ± 0.76154	1067.92 ± 7.88	100.09	3.00	122 ± 1420
6M41001D	64 °C	✓	0.0000080	73.047	0.0000681	226.622	0.0000464	17.307	0.0041130	0.806	0.318832	0.077	76.93173 ± 1.50927	1057.68 ± 15.71	99.25	1.62	26 ± 118
6M41002D	64 °C	✓	0.0000074	80.897	0.0000146	1103.005	0.0000970	10.080	0.0079761	0.436	0.612213	0.055	76.47763 ± 0.80872	1052.94 ± 8.44	99.64	3.15	234 ± 5165
6M41003D	65 °C	✓	0.0000019	323.963	0.0001242	125.743	0.0001442	7.748	0.0124657	0.609	0.964742	0.121	77.34426 ± 1.00467	1061.96 ± 10.43	99.94	4.92	43 ± 109
6M41005D	65 °C	✓	0.0000018	323.807	0.0000415	377.766	0.0000559	14.835	0.0060232	0.648	0.461851	0.055	76.58619 ± 1.15610	1054.08 ± 12.06	99.88	2.38	62 ± 472
6M41006D	66 °C	✓	0.0000060	129.420	0.0000310	499.289	0.0002692	3.760	0.0235718	0.315	1.812691	0.110	76.82402 ± 0.54923	1056.55 ± 5.72	99.90	9.30	327 ± 3269
6M41007D	67 °C	✓	0.0000062	131.169	0.0000326	483.752	0.0004919	2.610	0.0405386	0.237	3.113395	0.045	76.75463 ± 0.38882	1055.83 ± 4.05	99.94	15.99	535 ± 5174
6M41008D	68 °C	✓	0.0000136	49.586	0.0000754	208.355	0.0006096	1.828	0.0519169	0.119	3.980474	0.051	76.59134 ± 0.21306	1054.13 ± 2.22	99.90	20.48	296 ± 1234
6M41271D	70 °C	✓	0.0000033	223.580	0.0000093	831.341	0.0010878	1.901	0.0895890	0.178	6.892991	0.029	76.95033 ± 0.28109	1057.87 ± 2.93	100.01	35.34	4123 ± 68551
6M41272D	72 °C	✓	0.0000083	70.877	0.0000793	120.285	0.0001084	8.964	0.0093563	0.682	0.717857	0.073	76.98748 ± 1.12079	1058.26 ± 11.66	100.34	3.69	51 ± 122
		Σ	0.0000321	68.325	0.0002044	237.992	0.0030116	1.228	0.2535205	0.095	19.484650	0.021					

Information on Analysis and Constants Used in Calculations

Sample = ROG132-1
Material = osu
Location = Laser
Analyst = Fred Jourdan
Project = OSUMILTE_EB2016
Mass Discrimination Law = POW
Irradiation = I21t40h
J = 0.01033250 ± 0.00001860
WA1ms = 2613.000 ± 2.352 Ma
IGSN = Undefined
Preferred Age = Undefined
Classification = Undefined
Experiment Type = Undefined
Extraction Method = Undefined
Heating = 60 sec
Isolation = 5.00 min
Instrument = MAP215-50
Lithology = Undefined
Lat-Lon = Undefined - Undefined
Feature = Undefined

Age Equations = Min et al. (2000)
Negative Intensities = Allowed
Decay Constant 40K = 5.531 ± 0.013 E-10 1/a
Decay Constant 39Ar = 2.940 ± 0.029 E-07 1/h
Decay Constant 37Ar = 8.230 ± 0.082 E-04 1/h
Decay Constant 36Cl = 2.303 ± 0.046 E-06 1/a
Decay Constant 40K(EC,β⁺) = 0.576 ± 0.002 E-10 1/a
Decay Constant 40K(β⁻) = 4.955 ± 0.013 E-10 1/a
Atmospheric Ratio 40/36(a) = 298.56 ± 0.30
Atmospheric Ratio 38/36(a) = 0.1869 ± 0.0002
Production Ratio 39/37(ca) = 0.000760 ± 0.000009
Production Ratio 38/37(ca) = 0.000023 ± 0.000002
Production Ratio 36/37(ca) = 0.000270 ± 0.000002
Production Ratio 40/39(k) = 0.000730 ± 0.000091
Production Ratio 38/39(k) = 0.012400 ± 0.003968
Production Ratio 36/38(cl) = 263.00 ± 13.15
Scaling Ratio K/Ca = 0.430
Abundance Ratio 40K/K = 1.1700 ± 0.0100 E-04
Atomic Weight K = 39.0983 ± 0.0001 g

Results	40(a)/36(a) ± 2σ	40(r)/39(k) ± 2σ	Age ± 2σ (Ma)	MSWD	39Ar(k) (%,n)	K/Ca ± 2σ
Age Plateau		76.74257 ± 0.14268 ± 0.19%	1055.71 ± 3.24 ± 0.31%	0.81	96.86	39 ± 66
			Full External Error ± 9.93	59%	9	
			Analytical Error ± 1.49	2.00	2σ Confidence Limit	
				1.0000	Error Magnification	
Total Fusion Age		76.81765 ± 0.15844 ± 0.21%	1056.49 ± 3.32 ± 0.31%		11	533 ± 2539
			Full External Error ± 9.96			
			Analytical Error ± 1.65			
Normal Isochron	86.20 ± 497.36 ± 577.00%	76.94530 ± 0.19349 ± 0.25%	1057.82 ± 3.52 ± 0.33%	0.57	96.86	
			Full External Error ± 10.04	78%	9	
			Analytical Error ± 2.01	2.07	2σ Confidence Limit	
				1.0000	Error Magnification	
				1	Number of Iterations	
				0.0000000691	Convergence	
Inverse Isochron	60.88 ± 50.55 ± 83.03%	76.78335 ± 0.16199 ± 0.21%	1056.13 ± 3.34 ± 0.32%	0.83	96.86	
Clustered Points				56%	9	
			Full External Error ± 9.97	2.07	2σ Confidence Limit	
			Analytical Error ± 1.69	1.0000	Error Magnification	
				14	Number of Iterations	
				0.0000059313	Convergence	
				1%	Spreading Factor	

Relative Abundances			36Ar [V]	%1σ	37Ar [V]	%1σ	38Ar [V]	%1σ	39Ar [V]	%1σ	40Ar [V]	%1σ	40(r)/39(k) ± 2σ	Age ± 2σ (Ma)	40Ar(r) (%)	39Ar(k) (%)	K/Ca ± 2σ
6M41290D	61 °C		0.0000051	113.539	0.0000660	136.232	0.0000071	62.114	0.0003208	4.139	0.015399	0.729	52.73886 ± 11.58838	786.50 ± 140.14	109.86	0.11	2 ± 6
6M41293D	63 °C		0.0000000	15003.917	0.0000114	804.385	0.0000004	1240.122	0.0005381	2.429	0.033402	0.545	62.08835 ± 6.87088	896.17 ± 78.20	100.03	0.19	20 ± 326
6M41294D	64 °C		0.0000008	741.571	0.0000911	89.887	0.0000634	8.918	0.0054961	0.648	0.355531	0.071	64.64314 ± 1.05114	925.02 ± 11.77	99.93	1.95	26 ± 47
6M41295D	64 °C		0.0000040	168.502	0.0000857	97.549	0.0000955	5.701	0.0086064	0.464	0.549240	0.092	63.67581 ± 0.76579	914.15 ± 8.63	99.78	3.05	43 ± 84
6M41296D	65 °C	✓	0.0000016	329.184	0.0000932	89.589	0.0001410	7.175	0.0110508	0.313	0.694300	0.036	62.87193 ± 0.49027	905.07 ± 5.55	100.07	3.92	51 ± 91
6M41298D	65 °C	✓	0.0000061	86.065	0.0000346	247.172	0.0001559	8.630	0.0116518	0.221	0.727561	0.042	62.28447 ± 0.38857	898.40 ± 4.42	99.75	4.13	145 ± 716
6M41299D	66 °C	✓	0.0000024	267.504	0.0000631	148.976	0.0001785	2.547	0.0165506	0.303	1.035300	0.073	62.50989 ± 0.45345	900.96 ± 5.15	99.93	5.87	113 ± 336
6M41300D	67 °C	✓	0.0000016	421.232	0.0000549	219.287	0.0004175	3.134	0.0365288	0.301	2.278506	0.044	62.36166 ± 0.39519	899.28 ± 4.49	99.98	12.96	286 ± 1254
6M41301D	68 °C	✓	0.0000015	564.061	0.0001523	58.676	0.0004668	3.813	0.0398931	0.257	2.505596	0.041	62.79654 ± 0.34966	904.21 ± 3.96	99.98	14.15	113 ± 132
6M41303D	70 °C	✓	0.0000067	131.703	0.0003092	25.751	0.0016701	1.426	0.1375187	0.196	8.628913	0.044	62.73223 ± 0.25496	903.48 ± 2.89	99.98	48.78	191 ± 99
6M41304D	72 °C	✓	0.0000046	120.624	0.0000910	101.894	0.0001585	6.885	0.0132544	0.309	0.833114	0.060	62.96035 ± 0.46936	906.07 ± 5.31	100.17	4.70	63 ± 128
6M41305D	75 °C	✓	0.0000023	231.990	0.0000258	286.937	0.0000110	50.468	0.0004859	2.096	0.028321	0.454	59.72407 ± 7.09328	869.06 ± 81.95	102.45	0.17	8 ± 47
		Σ	0.0000094	236.557	0.0005228	59.336	0.0033648	1.193	0.2818955	0.115	17.685183	0.024					

Information on Analysis and Constants Used in Calculations

Sample = ROG132-2
Material = osu
Location = Laser
Analyst = Fred Jourdan
Project = OSUMILTE_EB2016
Mass Discrimination Law = POW
Irradiation = I21t40h
J = 0.01033250 ± 0.00001860
WA1ms = 2613.000 ± 2.352 Ma
IGSN = Undefined
Preferred Age = Undefined
Classification = Undefined
Experiment Type = Undefined
Extraction Method = Undefined
Heating = 60 sec
Isolation = 5.00 min
Instrument = MAP215-50
Lithology = Undefined
Lat-Lon = Undefined - Undefined
Feature = Undefined

Age Equations = Min et al. (2000)
Negative Intensities = Allowed
Decay Constant 40K = 5.531 ± 0.013 E-10 1/a
Decay Constant 39Ar = 2.940 ± 0.029 E-07 1/h
Decay Constant 37Ar = 8.230 ± 0.082 E-04 1/h
Decay Constant 36Cl = 2.303 ± 0.046 E-06 1/a
Decay Constant 40K(EC,β^+) = 0.576 ± 0.002 E-10 1/a
Decay Constant 40K(β^-) = 4.955 ± 0.013 E-10 1/a
Atmospheric Ratio 40/36(a) = 298.56 ± 0.30
Atmospheric Ratio 38/36(a) = 0.1869 ± 0.0002
Production Ratio 39/37(ca) = 0.000760 ± 0.000009
Production Ratio 38/37(ca) = 0.000023 ± 0.000002
Production Ratio 36/37(ca) = 0.000270 ± 0.000002
Production Ratio 40/39(k) = 0.000730 ± 0.000091
Production Ratio 38/39(k) = 0.012400 ± 0.003968
Production Ratio 36/38(cl) = 263.00 ± 13.15
Scaling Ratio K/Ca = 0.430
Abundance Ratio 40K/K = 1.1700 ± 0.0100 E-04
Atomic Weight K = 39.0983 ± 0.0001 g

Results	40(a)/36(a) ± 2σ	40(r)/39(k) ± 2σ	Age ± 2σ (Ma)	MSWD	39Ar(k) (%,n)	K/Ca ± 2σ
Age Plateau		62.64579 ± 0.17221 ± 0.27%	902.50 ± 3.22 ± 0.36%	1.49 17%	94.69 8	50 ± 48
			Full External Error ± 8.85	2.07	2σ Confidence Limit	
			Analytical Error ± 1.95	1.2198	Error Magnification	
Total Fusion Age		62.72623 ± 0.15439 ± 0.25%	903.42 ± 3.10 ± 0.34%		12	232 ± 275
			Full External Error ± 8.82			
			Analytical Error ± 1.75			
Normal Isochron	409.80 ± 823.39	62.68424 ± 0.22618	902.94 ± 3.62	0.14	94.69	
Overestimated Error	± 200.93%	± 0.36%	± 0.40%	99%	8	
			Full External Error ± 9.01	2.15	2σ Confidence Limit	
			Analytical Error ± 2.56	1.0000	Error Magnification	
				1	Number of Iterations	
				0.0000001221	Convergence	
Inverse Isochron	4036.38 ± 15456.08	62.89228 ± 0.54974	905.30 ± 6.73	0.37	94.69	
	± 382.92%	± 0.87%	± 0.74%	90%	8	
			Full External Error ± 10.66	2.15	2σ Confidence Limit	
			Analytical Error ± 6.23	1.0000	Error Magnification	
				11	Number of Iterations	
				0.0002189486	Convergence	
				8%	Spreading Factor	

Relative Abundances			36Ar [V]	%1σ	37Ar [V]	%1σ	38Ar [V]	%1σ	39Ar [V]	%1σ	40Ar [V]	%1σ	40(r)/39(k) ± 2σ	Age ± 2σ (Ma)	40Ar(r) (%)	39Ar(k) (%)	K/Ca ± 2σ
6M41307D	62 °C		0.0000026	209.343	0.0000188	598.570	0.0000063	80.622	0.0006164	1.838	0.031198	0.411	51.87381 ± 5.64381	776.01 ± 68.65	102.49	0.30	14 ± 169
6M41309D	63 °C		0.0000102	51.784	0.0000791	134.550	0.0000323	18.067	0.0031243	0.639	0.197302	0.142	64.11788 ± 1.30991	919.12 ± 14.72	101.53	1.50	17 ± 46
6M41310D	64 °C		0.0000126	39.691	0.0000546	216.275	0.0001592	4.917	0.0127980	0.423	0.811137	0.075	63.67266 ± 0.59513	914.11 ± 6.71	100.46	6.16	101 ± 436
6M41311D	64 °C	✓	0.0000045	122.861	0.0000216	552.225	0.0001035	8.043	0.0082909	0.505	0.517018	0.106	62.51951 ± 0.75645	901.07 ± 8.59	100.26	3.99	165 ± 1820
6M41312D	65 °C	✓	0.0000071	62.504	0.0000197	604.054	0.0000929	5.833	0.0088410	0.445	0.546914	0.081	62.09888 ± 0.63602	896.29 ± 7.24	100.38	4.25	193 ± 2330
6M41314D	65 °C	✓	0.0000094	47.582	0.0000441	271.640	0.0000874	11.544	0.0069313	0.474	0.432405	0.066	62.78957 ± 0.71350	904.13 ± 8.08	100.65	3.34	68 ± 367
6M41315D	66 °C	✓	0.0000071	75.836	0.0001249	91.783	0.0002196	4.792	0.0183661	0.274	1.140922	0.047	62.23651 ± 0.38755	897.86 ± 4.41	100.19	8.84	63 ± 116
6M41316D	67 °C	✓	0.0000017	368.029	0.0000461	266.477	0.0003886	2.597	0.0328173	0.281	2.049572	0.028	62.43762 ± 0.37123	900.14 ± 4.22	99.97	15.79	306 ± 1631
6M41317D	68 °C	✓	0.0000081	76.257	0.0001624	71.825	0.0005311	3.140	0.0449718	0.126	2.810668	0.040	62.55197 ± 0.18515	901.44 ± 2.10	100.09	21.64	119 ± 171
6M41319D	70 °C	✓	0.0000027	255.509	0.0001477	76.270	0.0007593	2.105	0.0622880	0.264	3.905047	0.032	62.70580 ± 0.34046	903.18 ± 3.86	100.02	29.98	181 ± 277
6M41320D	72 °C	✓	0.0000065	108.952	0.0000339	342.359	0.0000881	6.927	0.0084505	0.330	0.527352	0.055	62.63432 ± 0.65328	902.37 ± 7.41	100.37	4.07	107 ± 733
6M41321D	75 °C	✓	0.0000103	53.468	0.0000211	515.250	0.0000022	273.900	0.0002970	3.789	0.018358	0.689	72.17052 ± 12.38540	1007.43 ± 132.55	116.75	0.14	6 ± 62
		Σ	0.0000792	24.830	0.0003442	116.382	0.0024705	1.367	0.2077925	0.108	12.987893	0.017					

Information on Analysis and Constants Used in Calculations

Sample = ROG132-3
Material = osu
Location = Laser
Analyst = Fred Jourdan
Project = OSUMILTE_EB2016
Mass Discrimination Law = POW
Irradiation = I21t40h
J = 0.01033250 ± 0.00001860
WA1ms = 2613.000 ± 2.352 Ma
IGSN = Undefined
Preferred Age = Undefined
Classification = Undefined
Experiment Type = Undefined
Extraction Method = Undefined
Heating = 60 sec
Isolation = 5.00 min
Instrument = MAP215-50
Lithology = Undefined
Lat-Lon = Undefined - Undefined
Feature = Undefined

Age Equations = Min et al. (2000)
Negative Intensities = Allowed
Decay Constant 40K = 5.531 ± 0.013 E-10 1/a
Decay Constant 39Ar = 2.940 ± 0.029 E-07 1/h
Decay Constant 37Ar = 8.230 ± 0.082 E-04 1/h
Decay Constant 36Cl = 2.303 ± 0.046 E-06 1/a
Decay Constant 40K(EC,β+) = 0.576 ± 0.002 E-10 1/a
Decay Constant 40K(β-) = 4.955 ± 0.013 E-10 1/a
Atmospheric Ratio 40/36(a) = 298.56 ± 0.30
Atmospheric Ratio 38/36(a) = 0.1869 ± 0.0002
Production Ratio 39/37(ca) = 0.000760 ± 0.000009
Production Ratio 38/37(ca) = 0.000023 ± 0.000002
Production Ratio 36/37(ca) = 0.000270 ± 0.000002
Production Ratio 40/39(k) = 0.000730 ± 0.000091
Production Ratio 38/39(k) = 0.012400 ± 0.003968
Production Ratio 36/38(cl) = 263.00 ± 13.15
Scaling Ratio K/Ca = 0.430
Abundance Ratio 40K/K = 1.1700 ± 0.0100 E-04
Atomic Weight K = 39.0983 ± 0.0001 g

Results	40(a)/36(a) ± 2σ	40(r)/39(k) ± 2σ	Age ± 2σ (Ma)	MSWD	39Ar(k) (%,n)	K/Ca ± 2σ
Age Plateau		62.51782 ± 0.13297 ± 0.21%	901.05 ± 2.97 ± 0.33%	1.07	92.04	27 ± 51
			Full External Error ± 8.76	38%	9	
			Analytical Error ± 1.51	2.00	2σ Confidence Limit	
				1.0321	Error Magnification	
Total Fusion Age		62.61748 ± 0.14779 ± 0.24%	902.18 ± 3.06 ± 0.34%		12	260 ± 604
			Full External Error ± 8.79			
			Analytical Error ± 1.68			
Normal Isochron	59.88 ± 136.47 ± 227.92%	62.58301 ± 0.17566 ± 0.28%	901.79 ± 3.24 ± 0.36%	0.63	92.04	
				73%	9	
			Full External Error ± 8.86	2.07	2σ Confidence Limit	
			Analytical Error ± 1.99	1.0000	Error Magnification	
				1	Number of Iterations	
				0.0000004054	Convergence	
Inverse Isochron	781.84 ± 741.49 ± 94.84%	62.62895 ± 0.21244 ± 0.34%	902.31 ± 3.51 ± 0.39%	1.03	92.04	
Clustered Points				41%	9	
			Full External Error ± 8.96	2.07	2σ Confidence Limit	
			Analytical Error ± 2.41	1.0165	Error Magnification	
				27	Number of Iterations	
				0.0001149398	Convergence	
				4%	Spreading Factor	

Relative Abundances			36Ar [V]	%1σ	37Ar [V]	%1σ	38Ar [V]	%1σ	39Ar [V]	%1σ	40Ar [V]	%1σ	40(r)/39(k) ± 2σ	Age ± 2σ (Ma)	40Ar(r) (%)	39Ar(k) (%)	K/Ca ± 2σ
6M42165D	62 °C		0.0000088	58.309	0.0009009	35.888	0.0000108	45.507	0.0002953	3.060	0.015835	0.701	45.02310 ± 10.82640	690.56 ± 138.02	83.79	0.12	0.1 ± 0.1
6M42167D	63 °C		0.0000054	99.481	0.0004020	91.974	0.0000265	22.127	0.0013064	1.338	0.097706	0.178	73.59168 ± 3.16314	1022.38 ± 33.57	98.38	0.54	1.4 ± 2.6
6M42168D	64 °C		0.0000084	75.764	0.0004419	73.903	0.0000813	7.510	0.0061696	0.409	0.489426	0.085	78.93157 ± 0.90181	1078.18 ± 9.28	99.49	2.56	6.0 ± 8.9
6M42169D	64 °C		0.0000023	256.507	0.0006190	64.909	0.0000715	6.938	0.0054290	0.488	0.426973	0.282	78.53420 ± 1.10235	1074.08 ± 11.37	99.85	2.25	3.8 ± 4.9
6M42170D	65 °C		0.0000078	90.505	0.0005555	58.961	0.0000927	8.316	0.0074497	0.546	0.649044	0.047	86.82152 ± 1.10562	1157.59 ± 10.89	99.65	3.09	5.8 ± 6.8
6M42172D	65 °C	✓	0.0000043	137.964	0.0000228	1459.753	0.0000848	6.283	0.0063514	0.672	0.497840	0.049	78.58664 ± 1.19982	1074.62 ± 12.37	100.26	2.64	119.9 ± 3500.8
6M42173D	66 °C	✓	0.0000050	112.345	0.0003031	106.942	0.0000969	8.477	0.0076520	0.443	0.603716	0.065	78.70433 ± 0.83186	1075.84 ± 8.57	99.75	3.18	10.9 ± 23.2
6M42174D	67 °C	✓	0.0000031	181.619	0.0002088	148.294	0.0001347	4.587	0.0107287	0.343	0.839777	0.062	78.18836 ± 0.63026	1070.51 ± 6.51	99.89	4.46	22.1 ± 65.5
6M42175D	68 °C	✓	0.0000078	84.327	0.0000819	393.063	0.0001630	6.069	0.0139220	0.510	1.083947	0.040	77.68897 ± 0.84407	1065.35 ± 8.75	99.78	5.78	73.1 ± 574.4
6M42177D	70 °C	✓	0.0000064	103.470	0.0000563	589.489	0.0006494	2.460	0.0531096	0.201	4.158839	0.034	78.27009 ± 0.32793	1071.36 ± 3.39	99.95	22.06	405.3 ± 4778.3
6M42178D	72 °C	✓	0.0000131	89.227	0.0003718	94.896	0.0014683	1.986	0.1225392	0.137	9.563554	0.091	78.01262 ± 0.26204	1068.70 ± 2.71	99.96	50.90	141.7 ± 269.0
6M42179D	75 °C	✓	0.0000002	3641.272	0.0000437	830.785	0.0000607	12.746	0.0046791	0.528	0.365112	0.070	78.03916 ± 1.13838	1068.97 ± 11.77	100.01	1.94	46.0 ± 764.3
6M42180D	88 °C		0.0000185	40.660	0.0003868	87.563	0.0000075	69.204	0.0001951	3.814	0.016175	0.842	54.84486 ± 23.46354	811.63 ± 279.76	66.06	0.08	0.2 ± 0.4
6M42182D	62 °C		0.0000080	70.833	0.0000804	404.589	0.0000134	33.883	0.0009112	1.382	0.095477	0.431	102.17583 ± 4.75454	1302.79 ± 43.20	97.50	0.38	4.9 ± 39.4
		Σ	0.0000902	27.842	0.0042236	30.127	0.0029613	1.361	0.2407383	0.096	18.903422	0.047					

Information on Analysis and Constants Used in Calculations

Sample = ROG132-4
Material = osu
Location = Laser
Analyst = Fred Jourdan
Project = OSUMILTE_EB2016
Mass Discrimination Law = POW
Irradiation = I21t40h
J = 0.01033000 ± 0.00000600
WA1ms = 28.294 ± 0.037 Ma
IGSN = Undefined
Preferred Age = Undefined
Classification = Undefined
Experiment Type = Undefined
Extraction Method = Undefined
Heating = 60 sec
Isolation = 5.00 min
Instrument = MAP215-50
Lithology = Undefined
Lat-Lon = Undefined - Undefined
Feature = Undefined

Age Equations = Min et al. (2000)
Negative Intensities = Allowed
Decay Constant 40K = 5.531 ± 0.013 E-10 1/a
Decay Constant 39Ar = 2.940 ± 0.029 E-07 1/h
Decay Constant 37Ar = 8.230 ± 0.082 E-04 1/h
Decay Constant 36Cl = 2.303 ± 0.046 E-06 1/a
Decay Constant 40K(EC,β^+) = 0.576 ± 0.002 E-10 1/a
Decay Constant 40K(β^-) = 4.955 ± 0.013 E-10 1/a
Atmospheric Ratio 40/36(a) = 298.56 ± 0.30
Atmospheric Ratio 38/36(a) = 0.1869 ± 0.0002
Production Ratio 39/37(ca) = 0.000702 ± 0.000008
Production Ratio 38/37(ca) = 0.000023 ± 0.000002
Production Ratio 36/37(ca) = 0.000263 ± 0.000002
Production Ratio 40/39(k) = 0.000730 ± 0.000091
Production Ratio 38/39(k) = 0.012400 ± 0.003968
Production Ratio 36/38(cl) = 263.00 ± 13.15
Scaling Ratio K/Ca = 0.430
Abundance Ratio 40K/K = 1.1700 ± 0.0100 E-04
Atomic Weight K = 39.0983 ± 0.0001 g

Results	40(a)/36(a) ± 2σ	40(r)/39(k) ± 2σ	Age ± 2σ (Ma)	MSWD	39Ar(k) (%,n)	K/Ca ± 2σ
Age Plateau		78.13645 ± 0.18050 ± 0.23%	1069.98 ± 2.09 ± 0.20%	0.86	90.96	12.8 ± 21.8
				52%	7	
			Full External Error ± 7.19	2.15	2σ Confidence Limit	
			Analytical Error ± 1.87	1.0000	Error Magnification	
Total Fusion Age		78.41241 ± 0.17855 ± 0.23%	1072.83 ± 2.07 ± 0.19%		14	24.5 ± 14.8
			Full External Error ± 7.20			
			Analytical Error ± 1.84			
Normal Isochron	7.44 ± 1192.25 ##########	78.05678 ± 0.26757 ± 0.34%	1069.15 ± 2.92 ± 0.27%	0.40	90.96	
				85%	7	
			Full External Error ± 7.47	2.26	2σ Confidence Limit	
			Analytical Error ± 2.77	1.0000	Error Magnification	
				1	Number of Iterations	
				0.0000000048	Convergence	
Inverse Isochron	17056.35 ########## ± 1646.77%	76.00350 ± 3.70279 ± 4.87%	1047.80 ± 38.75 ± 3.70%	0.45	90.96	
Clustered Points				82%	7	
			Full External Error ± 39.34	2.26	2σ Confidence Limit	
			Analytical Error ± 38.74	1.0000	Error Magnification	
				15	Number of Iterations	
				0.0007607133	Convergence	
				1%	Spreading Factor	

Relative Abundances			36Ar [V]	%1σ	37Ar [V]	%1σ	38Ar [V]	%1σ	39Ar [V]	%1σ	40Ar [V]	%1σ	40(r)/39(k) ± 2σ	Age ± 2σ (Ma)	40Ar(r) (%)	39Ar(k) (%)	K/Ca ± 2σ
6M42184D	63 °C		0.0000007	1248.070	0.0001828	196.131	0.0000260	26.116	0.0012390	1.059	0.072582	0.207	58.42140 ± 4.56459	853.78 ± 53.17	99.72	0.53	3 ± 11
6M42185D	64 °C		0.0000048	201.471	0.0002831	130.981	0.0000674	10.749	0.0058872	0.696	0.370333	0.037	62.66483 ± 1.31775	902.55 ± 14.94	99.62	2.54	9 ± 23
6M42186D	64 °C		0.0000043	231.382	0.0002519	130.496	0.0000701	9.136	0.0050876	0.465	0.318130	0.089	62.77594 ± 1.31043	903.81 ± 14.85	100.40	2.20	9 ± 23
6M42187D	65 °C		0.0000067	145.683	0.0000370	882.334	0.0000837	11.255	0.0069607	0.314	0.433046	0.104	61.92487 ± 0.93288	894.14 ± 10.63	99.54	3.00	81 ± 1429
6M42189D	65 °C		0.0000045	216.807	0.0001081	334.765	0.0000876	8.181	0.0065905	0.459	0.407739	0.054	62.07201 ± 1.05043	895.81 ± 11.95	100.33	2.84	26 ± 175
6M42190D	66 °C		0.0000074	135.369	0.0004635	72.090	0.0000827	9.294	0.0065872	0.315	0.408914	0.031	61.73169 ± 0.99045	891.94 ± 11.30	99.45	2.84	6 ± 9
6M42191D	67 °C		0.0000009	1073.071	0.0000800	527.881	0.0000695	10.021	0.0067973	0.312	0.416525	0.072	61.23634 ± 0.94283	886.28 ± 10.79	99.93	2.93	37 ± 386
6M42192D	68 °C		0.0000029	356.438	0.0003296	109.533	0.0002915	3.846	0.0232688	0.193	1.431138	0.061	61.46501 ± 0.36303	888.89 ± 4.15	99.94	10.04	30 ± 66
6M42194D	70 °C	✓	0.0000128	98.151	0.0000737	508.568	0.0011324	1.461	0.0917882	0.162	5.563180	0.123	60.56645 ± 0.25976	878.60 ± 2.98	99.93	39.62	535 ± 5446
6M42195D	72 °C	✓	0.0000071	140.514	0.0002459	153.303	0.0009164	2.939	0.0760652	0.132	4.625968	0.024	60.78674 ± 0.18128	881.13 ± 2.08	99.95	32.84	133 ± 408
6M42196D	75 °C	✓	0.0000085	117.301	0.0000072	5347.397	0.0000224	27.953	0.0013823	0.909	0.082463	0.182	57.81256 ± 4.45490	846.68 ± 52.10	96.91	0.60	82 ± 8808
		Σ	0.0000431	77.797	0.0008264	146.381	0.0028498	1.382	0.2316541	0.085	14.130017	0.050					

Information on Analysis and Constants Used in Calculations

Sample = ROG132-5
Material = osu
Location = Laser
Analyst = Fred Jourdan
Project = OSUMILTE_EB2016
Mass Discrimination Law = POW
Irradiation = I21t40h
J = 0.01033000 ± 0.00000600
WA1ms = 28.294 ± 0.037 Ma
IGSN = Undefined
Preferred Age = Undefined
Classification = Undefined
Experiment Type = Undefined
Extraction Method = Undefined
Heating = 60 sec
Isolation = 5.00 min
Instrument = MAP215-50
Lithology = Undefined
Lat-Lon = Undefined - Undefined
Feature = Undefined

Age Equations = Min et al. (2000)
Negative Intensities = Allowed
Decay Constant 40K = 5.531 ± 0.013 E-10 1/a
Decay Constant 39Ar = 2.940 ± 0.029 E-07 1/h
Decay Constant 37Ar = 8.230 ± 0.082 E-04 1/h
Decay Constant 36Cl = 2.303 ± 0.046 E-06 1/a
Decay Constant 40K(EC,β^+) = 0.576 ± 0.002 E-10 1/a
Decay Constant 40K(β^-) = 4.955 ± 0.013 E-10 1/a
Atmospheric Ratio 40/36(a) = 298.56 ± 0.30
Atmospheric Ratio 38/36(a) = 0.1869 ± 0.0002
Production Ratio 39/37(ca) = 0.000702 ± 0.000008
Production Ratio 38/37(ca) = 0.000023 ± 0.000002
Production Ratio 36/37(ca) = 0.000263 ± 0.000002
Production Ratio 40/39(k) = 0.000730 ± 0.000091
Production Ratio 38/39(k) = 0.012400 ± 0.003968
Production Ratio 36/38(cl) = 263.00 ± 13.15
Scaling Ratio K/Ca = 0.430
Abundance Ratio 40K/K = 1.1700 ± 0.0100 E-04
Atomic Weight K = 39.0983 ± 0.0001 g

Results	40(a)/36(a) ± 2σ	40(r)/39(k) ± 2σ	Age ± 2σ (Ma)	MSWD	39Ar(k) (%,n)	K/Ca ± 2σ
Age Plateau		60.71137 ± 0.20016 ± 0.33%	880.26 ± 2.44 ± 0.28%	1.82	73.06	135 ± 406
			Full External Error ± 6.28	16%	3	
			Analytical Error ± 2.30	3.00	2σ Confidence Limit	
				1.3472	Error Magnification	
Total Fusion Age		60.93943 ± 0.14829 ± 0.24%	882.88 ± 1.88 ± 0.21%		11	121 ± 353
			Full External Error ± 6.10			
			Analytical Error ± 1.70			
Normal Isochron	188.58 ± 481.19 ± 255.17%	60.80272 ± 0.16632 ± 0.27%	881.31 ± 2.07 ± 0.24%	0.68	73.06	
			Full External Error ± 6.15	41%	3	
			Analytical Error ± 1.91	3.83	2σ Confidence Limit	
				1.0000	Error Magnification	
				1	Number of Iterations	
				0.0000000213	Convergence	
Inverse Isochron	3086.72 ± 17865.81 ± 578.80%	61.07795 ± 1.03289 ± 1.69%	884.47 ± 11.86 ± 1.34%	0.63	73.06	
Clustered Points			Full External Error ± 13.20	43%	3	
			Analytical Error ± 11.83	3.83	2σ Confidence Limit	
				1.0000	Error Magnification	
				12	Number of Iterations	
				0.0000649291	Convergence	
				2%	Spreading Factor	

Relative Abundances			36Ar [V]	%1σ	37Ar [V]	%1σ	38Ar [V]	%1σ	39Ar [V]	%1σ	40Ar [V]	%1σ	40(r)/39(k) ± 2σ	Age ± 2σ (Ma)	40Ar(r) (%)	39Ar(k) (%)	K/Ca ± 2σ
6M42198D	61 °C		0.0000065	158.758	0.0000740	641.476	0.0000020	335.519	0.0000512	15.505	0.015177	0.434	333.93865 ± 159.04514	2699.23 ± 667.63	112.80	0.02	0 ± 4
6M42199D	62 °C		0.0000089	122.792	0.0002565	185.840	0.0000059	127.160	0.0008041	1.478	0.067175	0.510	86.81038 ± 8.58468	1157.48 ± 84.54	103.94	0.29	1 ± 5
6M42201D	63 °C		0.0000072	152.452	0.0000021	21917.307	0.0000236	27.973	0.0016163	0.735	0.114318	0.187	69.40764 ± 4.16590	977.43 ± 45.32	98.13	0.59	326 ± 143034
6M42202D	64 °C		0.0000010	1084.136	0.0000861	581.305	0.0000944	8.300	0.0080486	0.461	0.532041	0.043	66.06519 ± 0.99642	940.70 ± 11.06	99.94	2.94	40 ± 468
6M42203D	64 °C	✓	0.0000109	102.597	0.0002659	175.475	0.0000795	11.589	0.0067039	0.513	0.435512	0.063	64.47087 ± 1.20230	922.91 ± 13.48	99.24	2.45	11 ± 38
6M42204D	65 °C	✓	0.0000008	1363.931	0.0001124	414.973	0.0000527	16.494	0.0052021	0.410	0.336537	0.087	64.73839 ± 1.31224	925.91 ± 14.69	100.07	1.90	20 ± 165
6M42206D	65 °C	✓	0.0000050	215.014	0.0001545	325.390	0.0000720	11.430	0.0061183	0.695	0.401000	0.083	65.29180 ± 1.39729	932.09 ± 15.59	99.62	2.24	17 ± 111
6M42207D	66 °C	✓	0.0000010	1042.270	0.0001399	338.861	0.0000887	11.562	0.0076486	0.404	0.489997	0.064	64.10052 ± 0.98418	918.75 ± 11.06	100.06	2.80	24 ± 159
6M42208D	67 °C	✓	0.0000106	103.496	0.0002976	162.173	0.0001953	5.595	0.0164571	0.297	1.055382	0.073	64.31798 ± 0.55868	921.20 ± 6.27	100.30	6.02	24 ± 77
6M42209D	68 °C	✓	0.0000026	403.439	0.0002141	220.843	0.0002041	5.311	0.0174513	0.138	1.113484	0.056	63.84719 ± 0.40459	915.91 ± 4.55	100.07	6.38	35 ± 155
6M42211D	70 °C	✓	0.0000073	157.671	0.0001608	300.164	0.0010170	2.100	0.0850541	0.146	5.457567	0.043	64.19104 ± 0.21169	919.77 ± 2.38	100.04	31.11	227 ± 1365
6M42212D	72 °C	✓	0.0000053	219.427	0.0003219	141.760	0.0014151	1.593	0.1150539	0.195	7.422475	0.037	64.49882 ± 0.26380	923.22 ± 2.96	99.98	42.09	154 ± 436
6M42213D	75 °C	✓	0.0000058	196.659	0.0000906	506.892	0.0000309	22.535	0.0031704	0.525	0.202409	0.094	64.38678 ± 2.26274	921.97 ± 25.38	100.85	1.16	15 ± 153
		Σ	0.0000141	279.847	0.0009819	174.683	0.0032774	1.291	0.2733798	0.100	17.643074	0.022					

Information on Analysis and Constants Used in Calculations

Sample = ROG1312-6
Material = osu
Location = Laser
Analyst = Fred Jourdan
Project = OSUMILTE_EB2016
Mass Discrimination Law = POW
Irradiation = I21t40h
J = 0.01033000 ± 0.00000600
WA1ms = 28.294 ± 0.037 Ma
IGSN = Undefined
Preferred Age = Undefined
Classification = Undefined
Experiment Type = Undefined
Extraction Method = Undefined
Heating = 60 sec
Isolation = 5.00 min
Instrument = MAP215-50
Lithology = Undefined
Lat-Lon = Undefined - Undefined
Feature = Undefined

Age Equations = Min et al. (2000)
Negative Intensities = Allowed
Decay Constant 40K = 5.531 ± 0.013 E-10 1/a
Decay Constant 39Ar = 2.940 ± 0.029 E-07 1/h
Decay Constant 37Ar = 8.230 ± 0.082 E-04 1/h
Decay Constant 36Cl = 2.303 ± 0.046 E-06 1/a
Decay Constant 40K(EC,β+) = 0.576 ± 0.002 E-10 1/a
Decay Constant 40K(β-) = 4.955 ± 0.013 E-10 1/a
Atmospheric Ratio 40/36(a) = 298.56 ± 0.30
Atmospheric Ratio 38/36(a) = 0.1869 ± 0.0002
Production Ratio 39/37(ca) = 0.000702 ± 0.000008
Production Ratio 38/37(ca) = 0.000023 ± 0.000002
Production Ratio 36/37(ca) = 0.000263 ± 0.000002
Production Ratio 40/39(k) = 0.000730 ± 0.000091
Production Ratio 38/39(k) = 0.012400 ± 0.003968
Production Ratio 36/38(cl) = 263.00 ± 13.15
Scaling Ratio K/Ca = 0.430
Abundance Ratio 40K/K = 1.1700 ± 0.0100 E-04
Atomic Weight K = 39.0983 ± 0.0001 g

Results	40(a)/36(a) ± 2σ	40(r)/39(k) ± 2σ	Age ± 2σ (Ma)	MSWD	39Ar(k) (%,n)	K/Ca ± 2σ
Age Plateau		64.26753 ± 0.16637 ± 0.26%	920.63 ± 2.05 ± 0.22%	1.36	96.15	13 ± 30
			Full External Error ± 6.36	21%	9	
			Analytical Error ± 1.87	2.00	2σ Confidence Limit	
				1.1647	Error Magnification	
Total Fusion Age		64.55106 ± 0.15819 ± 0.25%	923.81 ± 1.96 ± 0.21%		13	120 ± 418
			Full External Error ± 6.35			
			Analytical Error ± 1.77			
Normal Isochron Overestimated Error	383.76 ± 577.42 ± 150.46%	64.40404 ± 0.35821 ± 0.56%	922.16 ± 4.10 ± 0.45%	0.09	96.15	
				100%	9	
			Full External Error ± 7.29	2.07	2σ Confidence Limit	
			Analytical Error ± 4.02	1.0000	Error Magnification	
				1	Number of Iterations	
				0.0000000272	Convergence	
Inverse Isochron Overestimated Error	1917.20 ± 3285.95 ± 171.39%	64.39092 ± 0.35046 ± 0.54%	922.01 ± 4.02 ± 0.44%	0.22	96.15	
				98%	9	
			Full External Error ± 7.25	2.07	2σ Confidence Limit	
			Analytical Error ± 3.93	1.0000	Error Magnification	
				8	Number of Iterations	
				0.0000346943	Convergence	
				3%	Spreading Factor	

Relative Abundances		36Ar [V]	%1σ	37Ar [V]	%1σ	38Ar [V]	%1σ	39Ar [V]	%1σ	40Ar [V]	%1σ	40(r)/39(k) ± 2σ	Age ± 2σ (Ma)	40Ar(r) (%)	39Ar(k) (%)	K/Ca ± 2σ
6M20764	1 °C	0.0000012	43.390	0.0001088	89.867	0.0000746	34.620	0.0010154	0.545	0.018405	0.109	17.78559 ± 0.36485	305.04 ± 5.76	98.11	0.31	4 ± 7
6M20765	1 °C	0.0000016	33.165	0.0001862	54.010	0.0000606	32.062	0.0003662	1.585	0.003078	0.664	9.70118 ± 0.94385	172.73 ± 16.03	115.47	0.11	1 ± 1
6M20767	2 °C	0.0000015	29.610	0.0001108	87.322	0.0000552	39.839	0.0020132	0.325	0.060742	0.025	30.38315 ± 0.23628	493.67 ± 3.36	100.70	0.61	8 ± 14
6M20768	2 °C	0.0000022	20.598	0.0000562	180.854	0.0000562	39.163	0.0005550	1.234	0.029562	0.082	54.47753 ± 1.43519	807.41 ± 17.16	102.27	0.17	4 ± 15
6M20770	2 °C	0.0000026	19.457	0.0001003	92.901	0.0000581	41.605	0.0002996	1.927	0.017875	0.133	62.18377 ± 2.60012	897.26 ± 29.58	104.26	0.09	1 ± 2
6M20771	2 °C	0.0000030	12.411	0.0000477	230.924	0.0000069	260.180	0.0003198	1.754	0.019984	0.110	65.27713 ± 2.39611	932.10 ± 26.73	104.44	0.10	3 ± 13
6M20773	3 °C	0.0000016	32.358	0.0001006	128.067	0.0000678	37.534	0.0035626	0.174	0.253808	0.014	71.37430 ± 0.26401	998.88 ± 2.84	100.19	1.08	15 ± 39
6M20774	3 °C	0.0000019	25.644	0.0000875	125.544	0.0001474	15.229	0.0039616	0.191	0.271223	0.012	68.60082 ± 0.27278	968.81 ± 2.98	100.20	1.20	19 ± 49
6M20776	3 °C	0.0000030	16.298	0.0000438	251.036	0.0000629	31.297	0.0037607	0.139	0.252479	0.012	67.37242 ± 0.20307	955.33 ± 2.24	100.35	1.14	37 ± 186
6M20777	4 °C	0.0000006	97.705	0.0000330	332.877	0.0001574	13.239	0.0095309	0.104	0.640103	0.008	67.17838 ± 0.14432	953.19 ± 1.59	100.03	2.89	124 ± 828
6M20779	5 °C	0.0000196	2.191	0.0000613	201.937	0.0003876	6.479	0.0312479	0.045	2.043645	0.003	65.21258 ± 0.05962	931.38 ± 0.67	99.71	9.46	219 ± 885
6M20780	6 °C	0.0000016	26.312	0.0000329	364.746	0.0001797	13.617	0.0155974	0.047	1.003872	0.007	64.33120 ± 0.06334	921.52 ± 0.71	99.95	4.72	204 ± 1488
6M20782	7 °C	0.0000029	18.001	0.0000163	705.073	0.0002916	7.845	0.0218875	0.044	1.404452	0.006	64.12737 ± 0.05815	919.23 ± 0.65	99.94	6.63	578 ± 8152
6M20783	10 °C	0.0000161	3.666	0.0001876	51.124	0.0007182	3.066	0.0533495	0.038	3.418439	0.002	63.98582 ± 0.04928	917.64 ± 0.55	99.86	16.15	122 ± 125
6M20785	15 °C	0.0000947	0.833	0.0005398	18.424	0.0017871	1.144	0.1436510	0.033	9.237778	0.002	64.11007 ± 0.04274	919.04 ± 0.48	99.69	43.49	114 ± 42
6M20786	25 °C	0.0000251	2.172	0.0002217	58.970	0.0005037	4.343	0.0392225	0.044	2.537548	0.004	64.50503 ± 0.05823	923.47 ± 0.65	99.70	11.87	76 ± 90
	Σ	0.0001432	1.452	0.0004876	89.859	0.0046149	1.941	0.3303409	0.019	21.212994	0.001					

Information on Analysis and Constants Used in Calculations

Sample = ROG132-AVI1OSU
Material = osu
Location = Laser
Analyst = Fred Jourdan
Project = OSUMILTE_EB2016
Mass Discrimination Law = POW
Irradiation = I21t40h
J = 0.01033250 ± 0.00001860
WA1ms = 2613.000 ± 2.352 Ma
IGSN = Undefined
Preferred Age = Undefined
Classification = Undefined
Experiment Type = Undefined
Extraction Method = Undefined
Heating = 60 sec
Isolation = 5.00 min
Instrument = ARGUS VI
Lithology = Undefined
Lat-Lon = Undefined - Undefined
Feature = Undefined

Age Equations = Min et al. (2000)
Negative Intensities = Allowed
Decay Constant 40K = 5.531 ± 0.013 E-10 1/a
Decay Constant 39Ar = 2.940 ± 0.029 E-07 1/h
Decay Constant 37Ar = 8.230 ± 0.082 E-04 1/h
Decay Constant 36Cl = 2.303 ± 0.046 E-06 1/a
Decay Constant 40K(EC,β^+) = 0.576 ± 0.002 E-10 1/a
Decay Constant 40K(β^-) = 4.955 ± 0.013 E-10 1/a
Atmospheric Ratio 40/36(a) = 298.56 ± 0.30
Atmospheric Ratio 38/36(a) = 0.1869 ± 0.0002
Production Ratio 39/37(ca) = 0.000702 ± 0.000008
Production Ratio 38/37(ca) = 0.000023 ± 0.000002
Production Ratio 36/37(ca) = 0.000263 ± 0.000002
Production Ratio 40/39(k) = 0.000730 ± 0.000091
Production Ratio 38/39(k) = 0.012400 ± 0.003968
Production Ratio 36/38(cl) = 263.00 ± 13.15
Scaling Ratio K/Ca = 0.430
Abundance Ratio 40K/K = 1.1700 ± 0.0100 E-04
Atomic Weight K = 39.0983 ± 0.0001 g

Results	40(a)/36(a) ± 2σ	40(r)/39(k) ± 2σ	Age ± 2σ (Ma)	MSWD	39Ar(k) (%,n)	K/Ca ± 2σ
Age Plateau Cannot Calculate						
Total Fusion Age		64.08557 ± 0.02418 ± 0.04%	918.76 ± 2.61 ± 0.28%		16	291 ± 524
			Full External Error ± 8.77			
			Analytical Error ± 0.27			
Normal Isochron Cannot Calculate						
Inverse Isochron Cannot Calculate						

Relative Abundances		36Ar [V]	%1σ	37Ar [V]	%1σ	38Ar [V]	%1σ	39Ar [V]	%1σ	40Ar [V]	%1σ	40(r)/39(k) ± 2σ	Age ± 2σ (Ma)	40Ar(r) (%)	39Ar(k) (%)	K/Ca ± 2σ
6M20796	1 °C	0.0000007	91.490	0.0000150	948.030	0.0000392	98.305	0.0005510	1.148	0.006535	0.618	11.48922 ± 0.75000	202.84 ± 12.53	96.88	0.37	16 ± 299
6M20797	1 °C	0.0000006	79.314	0.0000282	495.925	0.0000120	303.922	0.0002499	2.785	0.002717	1.395	10.19972 ± 1.23189	181.17 ± 20.82	93.84	0.17	4 ± 38
6M20798	2 °C	0.0000007	66.333	0.0002039	65.335	0.0000088	437.525	0.0015162	0.502	0.032064	0.121	21.00209 ± 0.27938	355.11 ± 4.29	99.32	1.02	3 ± 4
6M20799	2 °C	0.0000002	269.147	0.0001122	129.519	0.0000055	713.611	0.0003696	2.068	0.019104	0.218	51.48460 ± 2.31997	771.27 ± 28.29	99.63	0.25	1 ± 4
6M20801	2 °C	0.0000008	69.576	0.0000029	4713.276	0.0000201	197.993	0.0002052	3.304	0.013872	0.283	66.47907 ± 4.68080	945.47 ± 51.84	98.34	0.14	30 ± 2875
6M20802	2 °C	0.0000003	140.759	0.0000717	212.887	0.0000126	332.967	0.0001498	4.925	0.010412	0.380	68.88234 ± 7.00120	971.89 ± 76.42	99.11	0.10	1 ± 4
6M20803	3 °C	0.0000018	30.597	0.0000409	322.686	0.0000271	140.066	0.0019752	0.348	0.163709	0.024	82.61800 ± 0.59963	1115.92 ± 6.04	99.68	1.33	21 ± 134
6M20804	3 °C	0.0000015	31.044	0.0000101	1519.229	0.0000320	115.828	0.0015869	0.384	0.134698	0.029	84.59537 ± 0.67563	1135.74 ± 6.74	99.67	1.07	68 ± 2055
6M20806	3 °C	0.0000011	41.133	0.0001116	116.232	0.0000045	869.490	0.0014167	0.484	0.119837	0.034	84.37179 ± 0.83886	1133.51 ± 8.37	99.74	0.95	5 ± 13
6M20807	4 °C	0.0000018	29.711	0.0000380	373.767	0.0000652	57.413	0.0044390	0.178	0.379830	0.011	85.44604 ± 0.31286	1144.20 ± 3.10	99.86	2.99	50 ± 375
6M20808	5 °C	0.0000042	9.534	0.0000887	155.162	0.0001314	30.282	0.0110571	0.065	0.894002	0.005	80.73997 ± 0.10706	1096.89 ± 1.09	99.86	7.45	54 ± 166
6M20809	6 °C	0.0000073	7.348	0.0001021	129.502	0.0002680	14.883	0.0230827	0.049	1.815810	0.003	78.57060 ± 0.07889	1074.65 ± 0.81	99.88	15.56	97 ± 252
6M20811	7 °C	0.0000038	12.425	0.0000840	141.222	0.0001317	28.661	0.0120959	0.079	0.946295	0.005	78.13754 ± 0.12589	1070.18 ± 1.30	99.88	8.15	62 ± 175
6M20812	10 °C	0.0000072	6.224	0.0001801	67.920	0.0002906	14.183	0.0228928	0.046	1.781935	0.006	77.74452 ± 0.07276	1066.12 ± 0.75	99.88	15.43	55 ± 74
6M20813	15 °C	0.0000077	7.551	0.0002024	74.219	0.0002808	13.251	0.0242005	0.041	1.883959	0.003	77.75305 ± 0.06578	1066.20 ± 0.68	99.88	16.31	51 ± 76
6M20814	25 °C	0.0000158	3.240	0.0000859	176.175	0.0004916	7.761	0.0425752	0.038	3.324481	0.004	77.97369 ± 0.05959	1068.49 ± 0.62	99.86	28.70	213 ± 751
	Σ	0.0000553	3.621	0.0003575	155.584	0.0017723	8.753	0.1483640	0.024	11.529260	0.002					

Information on Analysis and Constants Used in Calculations

Sample = ROG132-AVI2OSU
Material = osu
Location = Laser
Analyst = Fred Jourdan
Project = OSUMILTE_EB2016
Mass Discrimination Law = POW
Irradiation = I21t40h
J = 0.01033250 ± 0.00001860
WA1ms = 2613.000 ± 2.352 Ma
IGSN = Undefined
Preferred Age = Undefined
Classification = Undefined
Experiment Type = Undefined
Extraction Method = Undefined
Heating = 60 sec
Isolation = 5.00 min
Instrument = ARGUS VI
Lithology = Undefined
Lat-Lon = Undefined - Undefined
Feature = Undefined

Age Equations = Min et al. (2000)
Negative Intensities = Allowed
Decay Constant 40K = 5.531 ± 0.013 E-10 1/a
Decay Constant 39Ar = 2.940 ± 0.029 E-07 1/h
Decay Constant 37Ar = 8.230 ± 0.082 E-04 1/h
Decay Constant 36Cl = 2.303 ± 0.046 E-06 1/a
Decay Constant 40K(EC,β^+) = 0.576 ± 0.002 E-10 1/a
Decay Constant 40K(β^-) = 4.955 ± 0.013 E-10 1/a
Atmospheric Ratio 40/36(a) = 298.56 ± 0.30
Atmospheric Ratio 38/36(a) = 0.1869 ± 0.0002
Production Ratio 39/37(ca) = 0.000702 ± 0.000008
Production Ratio 38/37(ca) = 0.000023 ± 0.000002
Production Ratio 36/37(ca) = 0.000263 ± 0.000002
Production Ratio 40/39(k) = 0.000730 ± 0.000091
Production Ratio 38/39(k) = 0.012400 ± 0.003968
Production Ratio 36/38(cl) = 263.00 ± 13.15
Scaling Ratio K/Ca = 0.430
Abundance Ratio 40K/K = 1.1700 ± 0.0100 E-04
Atomic Weight K = 39.0983 ± 0.0001 g

Results	40(a)/36(a) ± 2σ	40(r)/39(k) ± 2σ	Age ± 2σ (Ma)	MSWD	39Ar(k) (%,n)	K/Ca ± 2σ
Age Plateau Cannot Calculate						
Total Fusion Age		77.59760 ± 0.03782 ± 0.05%	1064.59 ± 2.92 ± 0.27%		16	178 ± 555
			Full External Error ± 9.89			
			Analytical Error ± 0.39			
Normal Isochron Cannot Calculate						
Inverse Isochron Cannot Calculate						

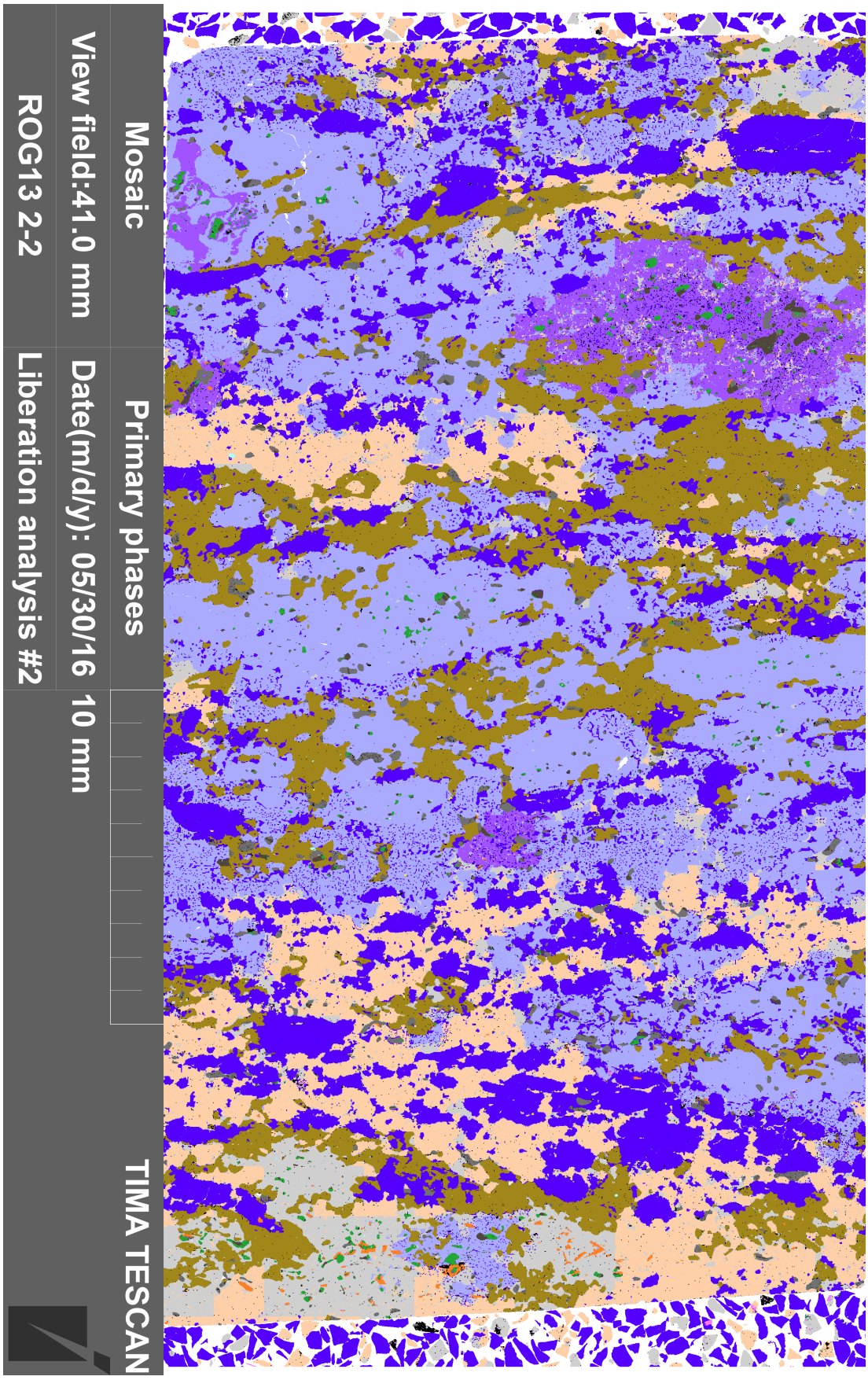
Mosaic
Primary phases
TIMA TESCAN
View field:41.0 mm
Date(m/d/y): 05/30/16
10 mm
ROG13 2-2
Liberation analysis #2

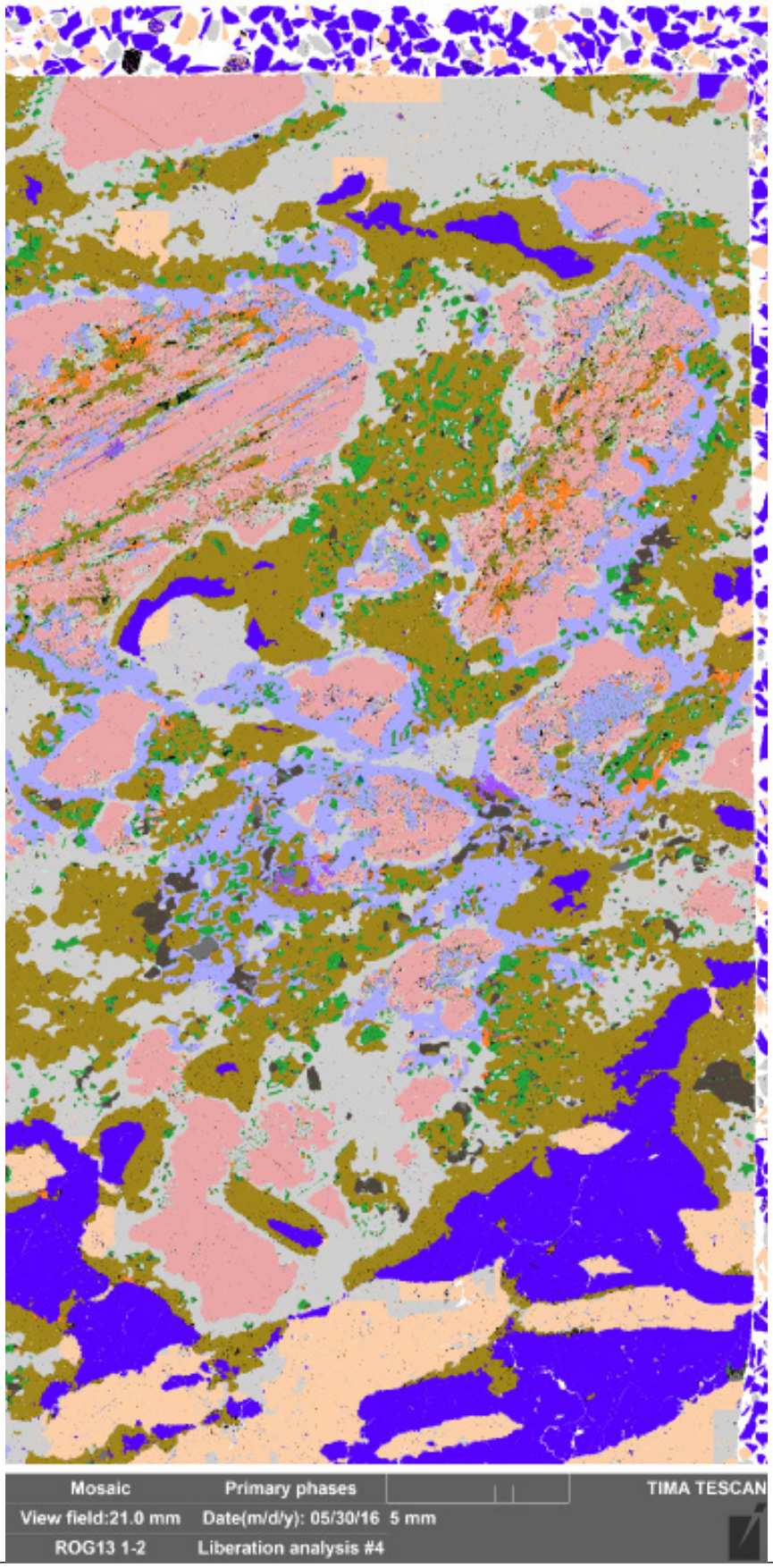
Mosaic
Primary phases
TIMA TESCAN
View field:21.0 mm
Date(m/d/y): 05/30/16
5 mm
ROG13 1-2
Liberation analysis #4

Appendix E

This appendix contains the supplementary tables S1–7 from the paper 'Using accessory minerals to unravel thermal histories in polymetamorphic terranes: an example from Rogaland, SW Norway'.

Contents:

Using accessory minerals to unravel thermal histories in polymetamorphic terranes: an example from Rogaland, SW Norway

E. BLEREAU, C. CLARK, R. J. M. TAYLOR, P. D. KINNY, T. E. JOHNSON, E. SANSOM, M. HAND

Table S1: All data for zircon SHRIMP U–Pb analyses

Table S1: SHRIMP analytical results for zircons from sample ROG13/11

Texture	Spot	238U	232Th	232Th	f204	206Pb*/238U		207Pb*/206Pb*		207Pb*/235U		238U/206Pb*		207Pb*/206Pb*		207Pb*/235U		Disc.
ID	no.	(ppm)	(ppm)	238U	(%)	date (Ma) ± 1σ		date (Ma) ± 1σ		date (Ma) ± 1σ		± %		± %		± %		(%)
R	R1135-1.2	1048	75	0.07	0.06	951	±14	970	±12	957	±16	6.29	1.6	0.071	0.6	1.57	1.7	+2
R	R1137-1.4	785	88	0.11	0.14	957	±10	960	±14	958	±12	6.25	1.1	0.071	0.7	1.57	1.3	+0
R	R113-1.2	894	23	0.03	0.46	988	±30	1014	±40	996	±38	6.04	3.3	0.073	2.0	1.67	3.9	+3
RE	R1131-1.2	938	28	0.03	0.05	1009	±15	1061	±31	1025	±23	5.90	1.6	0.075	1.5	1.74	2.2	+5
RE	R1114-1.1	720	131	0.18	3.66	1046	±14	1062	±46	1051	±28	5.67	1.4	0.075	2.3	1.82	2.7	+2
RE	R1131-1.1	1060	160	0.15	0.94	1055	±11	1196	±66	1101	±39	5.62	1.1	0.080	3.3	1.96	3.5	+13
RE	R1118-1.1	684	39	0.06	0.05	1098	±14	1128	±11	1108	±17	5.39	1.4	0.077	0.6	1.98	1.5	+3
RE *	R1118-1.2	1602	717	0.45	2.22	1126	±11	1300	±52	1187	±34	5.24	1.1	0.084	2.7	2.22	2.9	+15
C	R1135-1.1	132	30	0.23	0.24	1140	±43	1158	±99	1146	±74	5.17	4.2	0.078	5.0	2.09	6.5	+2
C	R1112-1.1	182	128	0.70	0.25	1207	±18	1290	±57	1237	±41	4.86	1.7	0.084	2.9	2.38	3.4	+7
RE *	R1137-1.1	819	152	0.19	0.06	1292	±14	1473	±8	1362	±17	4.51	1.2	0.092	0.4	2.82	1.3	+14
C *	R113-1.1	291	141	0.48	0.17	1449	±21	1550	±27	1491	±32	3.97	1.6	0.096	1.5	3.34	2.2	+7
C	R1136-1.1	330	233	0.71	0.10	1738	±26	1757	±10	1746	±32	3.23	1.7	0.107	0.5	4.58	1.8	+1
C *	R1137-1.2	506	245	0.48	0.09	1741	±26	1840	±9	1786	±31	3.23	1.7	0.112	0.5	4.81	1.8	+6
C *	R1112-1.2	706	541	0.77	0.03	1795	±21	1917	±6	1852	±25	3.11	1.3	0.117	0.4	5.20	1.4	+7

Table S1: SHRIMP analytical results for zircons from sample ROG13/10

Texture	Spot	238U	232Th	232Th	f204	206Pb*/238U		207Pb*/206Pb*		207Pb*/235U		238U/206Pb*		207Pb*/206Pb*		207Pb*/235U		Disc.
ID	no.	(ppm)	(ppm)	238U	(%)	date (Ma) ± 1σ		date (Ma) ± 1σ		date (Ma) ± 1σ		± %		± %		± %		(%)
RE	13-10_r4	1478	132	0.09	0.47	1055	±13	1015	±19	1042	±17	5.62	1.3	0.073	0.9	1.79	1.6	-4
RE	13-10_r2	714	131	0.18	--	1076	±12	1070	±12	1074	±15	5.51	1.2	0.075	0.6	1.88	1.4	-1

RE	13-10_r7	1208	119	0.10	0.03	1133	±14	1147	±9	1138	±16	5.21	1.3	0.078	0.5	2.07	1.4	+1

Errors are 1-sigma (abs) or % where indicated. Pb* indicate radiogenic proportions. All ages are common Pb corrected using measured 204Pb. f204 is % of common 206Pb. R-Rim, C-Core, RE-Recrystallised, S-Sector zoned, DR-Dark rim, LR- Light rim, * excluded from probability plots

Table S1: SHRIMP analytical results for zircons from sample ROG13/10 continued

Texture	Spot	238U	232Th	232Th	f204	206Pb*/238U		207Pb*/206Pb*		207Pb*/235U		238U/206Pb*		207Pb*/206Pb*		207Pb*/235U		Disc.
ID	no.	(ppm)	(ppm)	238U	(%)	date (Ma) ± 1σ		date (Ma) ± 1σ		date (Ma) ± 1σ		± %		± %		± %		(%)
RE *	13-10_r3	653	170	0.26	0.22	1201	±17	1351	±27	1256	±26	4.88	1.5	0.087	1.4	2.44	2.1	+12
RE *	R101-6-1.2	1519	291	0.19	0.03	1202	±11	1280	±9	1230	±14	4.88	1.0	0.083	0.5	2.36	1.1	+7
RE *	R102-2-1.1	642	158	0.25	0.21	1237	±12	1387	±20	1293	±19	4.73	1.0	0.088	1.0	2.57	1.5	+12
RE	R101-2.3-1.3	1186	384	0.32	0.10	1285	±35	1372	±45	1318	±50	4.53	3.0	0.088	2.3	2.66	3.8	+7
RE	R101-2.3-1.2	1384	262	0.19	0.05	1288	±37	1212	±29	1259	±44	4.52	3.2	0.081	1.5	2.46	3.5	-7
C *	R102-4.5-1.2	862	278	0.32	0.08	1304	±25	1376	±7	1332	±28	4.46	2.1	0.088	0.3	2.71	2.1	+6
C	R102-12-1.2	462	118	0.26	0.25	1340	±27	1392	±33	1360	±38	4.33	2.2	0.088	1.7	2.82	2.8	+4
C *	R102-1-1.2	662	187	0.28	0.07	1379	±13	1476	±7	1417	±16	4.19	1.1	0.092	0.4	3.04	1.1	+7
C	R102-7-1.1	454	136	0.30	0.09	1384	±17	1427	±9	1401	±21	4.18	1.4	0.090	0.5	2.97	1.5	+3
RE *	R102-7-1.2	641	177	0.28	0.08	1400	±13	1498	±7	1439	±16	4.12	1.0	0.093	0.4	3.13	1.1	+7
RE	R101-2.3-1.1	398	115	0.29	0.15	1447	±21	1491	±10	1465	±25	3.97	1.6	0.093	0.5	3.23	1.7	+3
C	R101-1-1.1	454	97	0.21	0.13	1450	±17	1487	±18	1465	±23	3.97	1.3	0.093	0.9	3.23	1.6	+3
C	R102-1-1.1	641	187	0.29	0.13	1466	±20	1514	±19	1486	±27	3.92	1.5	0.094	1.0	3.32	1.8	+3
C	R101-6-1.1	848	337	0.40	0.02	1470	±16	1488	±15	1477	±21	3.90	1.2	0.093	0.8	3.29	1.4	+1
RE	R101-4-1.1	610	172	0.28	0.06	1496	±18	1498	±24	1486	±27	3.83	1.3	0.093	1.3	3.37	1.8	+0
C	R101-8-1.3	457	141	0.31	0.06	1496	±15	1492	±8	1495	±18	3.83	1.1	0.093	0.4	3.36	1.2	-0
RE	R101-8-1.1	584	169	0.29	0.04	1502	±19	1518	±7	1508	±23	3.81	1.4	0.094	0.4	3.42	1.5	+1
C	R101-5-1.1	635	213	0.33	0.06	1508	±14	1543	±13	1522	±19	3.80	1.1	0.096	0.7	3.48	1.3	+3
C	R102-10-1.1	638	203	0.32	0.04	1527	±27	1505	±17	1517	±33	3.74	2.0	0.094	0.9	3.46	2.2	-2
C	R101-1-1.2	463	116	0.25	0.07	1530	±17	1528	±18	1529	±24	3.73	1.2	0.095	0.9	3.51	1.6	-0
C	R102-10-1.2	479	137	0.29	0.24	1538	±20	1515	±28	1528	±32	3.71	1.5	0.094	1.5	3.50	2.1	-2
C	R101-4-1.2	634	185	0.29	0.04	1542	±17	1519	±12	1532	±21	3.70	1.2	0.095	0.6	3.52	1.4	-2
C	R102-3-1.1	578	168	0.29	0.08	1551	±22	1517	±14	1536	±27	3.68	1.6	0.094	0.7	3.54	1.8	-2
C	R101-8-1.2	496	135	0.27	0.12	1592	±24	1549	±19	1574	±32	3.57	1.7	0.096	1.0	3.71	2.0	-3

Errors are 1-sigma (abs) or % where indicated. Pb* indicate radiogenic proportions. All ages are common Pb corrected using measured 204Pb. f204 is % of common 206Pb. R-Rim, C-Core, RE-Recrystallised, S-Sector zoned, DR-Dark rim, LR- Light rim, * excluded from probability plots

Table S1: SHRIMP analytical results for zircons from sample ROG13/2

Texture	Spot	238U	232Th	232Th	f204	206Pb*/238U		207Pb*/206Pb*		207Pb*/235U		238U/206Pb*		207Pb*/206Pb*		207Pb*/235U		Disc.
ID	no.	(ppm)	(ppm)	238U	(%)	date (Ma) ± 1σ		date (Ma) ± 1σ		date (Ma) ± 1σ		± %		± %		± %		(%)
S	13-2_8	42	116	2.79	--	899	±15	924	±79	906	±38	6.69	1.7	0.070	3.8	1.44	4.2	+3
DR	13-2_4	182	196	1.08	0.30	921	±10	901	±53	915	±26	6.51	1.2	0.069	2.6	1.46	2.9	-2
DR	13-2_10	482	218	0.45	0.25	932	±11	962	±21	941	±15	6.43	1.2	0.071	1.0	1.53	1.6	+3
LR	13-2_7	189	103	0.54	0.00	950	±15	1006	±44	967	±27	6.30	1.7	0.073	2.2	1.59	2.8	+6
RE	13-2_3	222	40	0.18	0.13	1011	±18	988	±35	1004	±26	5.89	2.0	0.072	1.7	1.69	2.6	-2
C	13-2_2	185	21	0.12	--	1113	±13	1198	±43	1142	±29	5.31	1.2	0.080	2.2	2.08	2.5	+8
C	13-2_5	332	92	0.28	0.05	1113	±25	1194	±65	1141	±47	5.30	2.5	0.080	3.3	2.08	4.1	+7
RE	13-2_9	78	80	1.02	--	1114	±24	1051	±92	1092	±56	5.30	2.3	0.074	4.6	1.93	5.1	-7
C	13-2_11	174	69	0.40	0.15	1420	±16	1339	±76	1388	±58	4.06	1.3	0.086	4.0	2.92	4.2	-7
RE	13-2_6	392	136	0.35	0.10	1476	±19	1490	±11	1482	±23	3.89	1.4	0.093	0.6	3.30	1.6	+1
C	13-2_12	209	91	0.43	--	1574	±27	1556	±14	1566	±32	3.62	1.9	0.096	0.7	3.68	2.0	-1

Table S1: SHRIMP analytical results for zircons from sample ROG14/5

Texture	Spot	238U	232Th	232Th	f204	206Pb*/238U		207Pb*/206Pb*		207Pb*/235U		238U/206Pb*		207Pb*/206Pb*		207Pb*/235U		Disc.
ID	no.	(ppm)	(ppm)	238U	(%)	date (Ma) ± 1σ		date (Ma) ± 1σ		date (Ma) ± 1σ		± %		± %		± %		(%)
RE	14-5_1	805	116	0.14	--	919	±18	941	±11	925	±20	6.53	2.1	0.070	0.6	1.49	2.2	+3
RE	14-5_8	595	17	0.03	0.00	928	±9	949	±13	934	±12	6.46	1.1	0.071	0.6	1.51	1.2	+2
S	14-5_3	662	60	0.09	--	950	±15	932	±38	945	±23	6.30	1.6	0.070	1.9	1.54	2.5	-2
RE	14-5_9	629	23	0.04	--	964	±16	980	±17	969	±19	6.20	1.7	0.072	0.8	1.60	1.9	+2
RE *	14-5_7	654	23	0.04	0.13	975	±11	872	±22	943	±15	6.13	1.2	0.068	1.1	1.53	1.6	-13
RE *	14-5_4	890	18	0.02	0.06	985	±20	1055	±12	1007	±23	6.06	2.2	0.074	0.6	1.70	2.3	+7
RE	14-5_2	756	11	0.02	--	996	±12	986	±44	993	±25	5.98	1.3	0.072	2.2	1.66	2.5	-1
S	14-5_6	543	17	0.03	0.04	1007	±13	1036	±29	1016	±21	5.91	1.4	0.074	1.5	1.72	2.1	+3

Errors are 1-sigma (abs) or % where indicated. Pb* indicate radiogenic proportions. All ages are common Pb corrected using measured 204Pb. f204 is % of common 206Pb. R-Rim, C-Core, RE-Recrystallised, S-Sector zoned, DR-Dark rim, LR- Light rim, * excluded from probability plots

Table S1: SHRIMP analytical results for zircons from sample ROG14/5 continued

Texture	Spot	238U	232Th	232Th	f204	206Pb*/238U		207Pb*/206Pb*		207Pb*/235U		238U/206Pb*		207Pb*/206Pb*		207Pb*/235U		Disc.
ID	no.	(ppm)	(ppm)	238U	(%)	date (Ma) ± 1σ		date (Ma) ± 1σ		date (Ma) ± 1σ		± %		± %		± %		(%)
S	14-5_5	526	18	0.03	0.04	1025	±15	988	±14	1013	±18	5.80	1.6	0.072	0.7	1.71	1.8	-4

Table S1: SHRIMP analytical results for zircons from sample ROG14/8

Texture	Spot	238U	232Th	232Th	f204	206Pb*/238U		207Pb*/206Pb*		207Pb*/235U		238U/206Pb*		207Pb*/206Pb*		207Pb*/235U		Disc.
ID	no.	(ppm)	(ppm)	238U	(%)	date (Ma) ± 1σ		date (Ma) ± 1σ		date (Ma) ± 1σ		± %		± %		± %		(%)
R	R14-8-22.2	215	143	0.66	--	913	±10	875	±30	902	±17	6.57	1.2	0.068	1.4	1.43	1.9	-5
R	R14-8-23.2	253	148	0.59	--	916	±12	957	±21	928	±17	6.55	1.4	0.071	1.0	1.49	1.8	+5
R	R14-8-2.2	351	254	0.72	--	922	±10	921	±19	922	±14	6.50	1.1	0.070	0.9	1.48	1.5	-0
RE	R14-8-26.2	108	33	0.30	--	926	±12	925	±41	926	±22	6.47	1.3	0.070	2.0	1.49	2.4	-0
RE	R14-8-2.1	132	34	0.26	0.02	930	±11	996	±61	950	±31	6.44	1.3	0.072	3.0	1.55	3.3	+7
RE	R14-8-10.2	108	30	0.28	0.06	931	±12	956	±51	938	±27	6.44	1.4	0.071	2.5	1.52	2.8	+3
RE	R14-8-14.1	138	44	0.32	0.05	938	±11	1021	±32	963	±20	6.39	1.3	0.073	1.6	1.58	2.0	+9
RE	R14-8-1.2	202	89	0.44	0.29	940	±11	889	±33	925	±19	6.37	1.2	0.069	1.6	1.49	2.0	-6
RE	R14-8-6.1	188	57	0.30	--	941	±11	939	±24	940	±16	6.36	1.2	0.070	1.2	1.52	1.7	-0
RE	R14-8-20.1	331	149	0.45	0.12	942	±10	983	±18	954	±14	6.36	1.1	0.072	0.9	1.56	1.5	+5
RE	R14-8-26.1	137	39	0.29	0.18	946	±11	1008	±44	964	±24	6.33	1.3	0.073	2.2	1.59	2.5	+7
RE	R14-8-7.2	145	43	0.29	0.15	952	±11	1012	±42	970	±23	6.28	1.3	0.073	2.1	1.60	2.4	+6
RE	R14-8-21.1	472	41	0.09	0.32	954	±14	980	±26	962	±20	6.27	1.6	0.072	1.3	1.58	2.1	+3
RE	R14-8-1.1	161	53	0.33	0.09	955	±11	961	±28	957	±18	6.26	1.2	0.071	1.3	1.57	1.8	+1
RE	R14-8-3.1	107	31	0.29	0.11	960	±20	1002	±47	973	±32	6.23	2.3	0.073	2.3	1.61	3.3	+5
RE	R14-8-24.2	157	49	0.31	--	965	±15	1013	±26	980	±21	6.19	1.7	0.073	1.3	1.62	2.1	+5
RE	R14-8-12.2	297	124	0.42	--	965	±10	961	±21	964	±15	6.19	1.2	0.071	1.0	1.58	1.6	-0
RE	R14-8-7.1	115	31	0.27	0.20	966	±12	936	±45	957	±25	6.19	1.4	0.070	2.2	1.57	2.6	-3
RE	R14-8-13.1	136	41	0.30	0.03	977	±12	956	±40	970	±23	6.11	1.3	0.071	2.0	1.60	2.4	-2

Errors are 1-sigma (abs) or % where indicated. Pb* indicate radiogenic proportions. All ages are common Pb corrected using measured 204Pb. f204 is % of common 206Pb. R-Rim, C-Core, RE-Recrystallised, S-Sector zoned, DR-Dark rim, LR- Light rim, * excluded from probability plots

Table S1: SHRIMP analytical results for zircons from sample ROG14/8 continued

Texture	Spot	238U	232Th	232Th	f204	206Pb*/238U		207Pb*/206Pb*		207Pb*/235U		238U/206Pb*		207Pb*/206Pb*		207Pb*/235U		Disc.
ID	no.	(ppm)	(ppm)	238U	(%)	date (Ma) ± 1σ		date (Ma) ± 1σ		date (Ma) ± 1σ		± %		± %		± %		(%)
RE	R14-8-4.2	192	68	0.35	--	981	±16	1044	±23	1000	±21	6.09	1.8	0.074	1.1	1.68	2.1	+7
RE	R14-8-23.1	147	42	0.28	--	981	±22	992	±30	984	±28	6.08	2.4	0.072	1.5	1.64	2.8	+1
RE	R14-8-25.1	113	32	0.28	0.04	988	±16	1050	±32	1007	±24	6.04	1.8	0.074	1.6	1.70	2.4	+6
C (S)	R14-8-5.1	679	135	0.20	--	991	±16	960	±38	981	±25	6.02	1.7	0.071	1.9	1.63	2.6	-3
RE *	R14-8-27.2	143	45	0.31	0.03	1007	±12	922	±32	980	±20	5.92	1.3	0.070	1.6	1.63	2.1	-10
RE	R14-8-18.2	200	75	0.37	0.36	1007	±19	1041	±42	1018	±30	5.91	2.0	0.074	2.1	1.73	2.9	+4
RE	R14-8-10.1	277	138	0.50	0.10	1010	±11	1019	±18	1013	±15	5.89	1.2	0.073	0.9	1.71	1.5	+1
RE	R14-8-18.1	312	161	0.51	0.07	1017	±11	1012	±27	1016	±18	5.85	1.2	0.073	1.4	1.72	1.8	-1
RE	R14-8-25.2	276	137	0.50	0.00	1036	±11	1035	±17	1036	±15	5.73	1.2	0.074	0.8	1.77	1.4	-0
RE	R14-8-19.1	173	44	0.25	--	1045	±17	990	±75	1027	±42	5.68	1.8	0.072	3.7	1.75	4.1	-6

Errors are 1-sigma (abs) or % where indicated. Pb* indicate radiogenic proportions. All ages are common Pb corrected using measured 204Pb. f204 is % of common 206Pb. R-Rim, C-Core, RE-Recrystallised, S-Sector zoned, DR-Dark rim, LR- Light rim, * excluded from probability plots

Using accessory minerals to unravel thermal histories in polymetamorphic terranes: an example from Rogaland, SW Norway

E. BLEREAU, C. CLARK, R. J. M. TAYLOR, P. D. KINNY, T. E. JOHNSON, E. SANSOM, M. HAND

Table S2: All data for monazite SHRIMP U−Pb analyses

Table S2: SHRIMP analytical results for monazite from sample ROG13/11

Texture ID	Spot no.	238U (ppm)	232Th (ppm)	232Th/238U	206Pb (c/sec)	206Pb*/238U date (Ma) ± 1σ		207Pb*/206Pb* date (Ma) ± 1σ		207Pb*/235U date (Ma) ± 1σ		238U/206Pb* ± %		207Pb*/206Pb* ± %		207Pb*/235U ± %		Disc. Pb-Pb %	Disc. U-Pb %
C	R11-1-15.1	9027	172241	19.08	2092	960	±11	943	±40	955	±11	6.23	1.2	0.071	2.0	1.561	2.3	-2	+1
E	R11-1-11.2	4451	138669	31.16	4778	987	±10	988	±35	987	±10	6.04	1.1	0.072	1.7	1.644	2.0	+0	-0
C	R31-4.1	1599	15966	9.98	1475	988	±12	984	±21	987	±16	6.04	1.3	0.072	1.0	1.643	1.7	-0	+0
E	R11-3-3.2	4385	176549	40.26	5206	991	±10	967	±13	984	±10	6.02	1.1	0.071	0.6	1.635	1.2	-3	+1
C	R11-1-4.1	10222	111823	10.94	12659	999	±10	1025	±7	1007	±10	5.97	1.0	0.073	0.3	1.696	1.1	+3	-1
C	R11-3-4.1	5296	213132	40.24	5659	1002	±10	995	±9	1000	±10	5.95	1.1	0.072	0.4	1.676	1.2	-1	+0
C	R11-3-6.1	4208	154191	36.64	4991	1013	±10	1045	±9	1023	±11	5.88	1.1	0.074	0.4	1.738	1.2	+3	-1
C	R11-1-16.1	7582	103481	13.65	9227	1019	±10	1019	±11	1019	±10	5.84	1.0	0.073	0.5	1.729	1.2	-0	+0
C	R31-3.1	3581	11503	3.21	3508	1021	±11	1035	±19	1026	±16	5.82	1.2	0.074	1.0	1.746	1.5	+1	-0
C	R11-1-11.1	8908	128676	14.45	10323	1022	±10	1024	±8	1023	±10	5.82	1.0	0.073	0.4	1.739	1.1	+0	-0
C	R31-1.1	6655	11760	1.77	6075	1023	±11	1029	±9	1025	±13	5.81	1.2	0.074	0.4	1.745	1.3	+1	-0
C	R31-3.2	5918	12349	2.09	5768	1027	±11	1032	±9	1028	±13	5.79	1.2	0.074	0.5	1.753	1.3	+1	-0
C	R11-1-8.1	4172	122856	29.45	5074	1027	±10	1003	±16	1020	±11	5.79	1.1	0.073	0.8	1.729	1.4	-3	+1
C	R31-2.1	4754	11262	2.37	4483	1029	±11	1033	±10	1030	±13	5.78	1.2	0.074	0.5	1.759	1.3	+0	-0
C	R11-1-7.1	7474	106220	14.21	8755	1032	±10	1034	±7	1033	±10	5.76	1.1	0.074	0.4	1.765	1.1	+0	-0
C	R31-5.1	2079	19378	9.32	1993	1034	±12	1036	±18	1034	±16	5.75	1.3	0.074	0.9	1.770	1.6	+0	-0
C	R31-4.2	7057	11242	1.59	6999	1038	±11	1015	±9	1030	±13	5.72	1.2	0.073	0.5	1.759	1.2	-3	+1
C	R31-6.1	6758	14806	2.19	6287	1038	±11	1030	±9	1036	±13	5.72	1.2	0.074	0.4	1.774	1.2	-1	+0

Table S2: SHRIMP analytical results for monazite from sample ROG13/2

Texture	Spot	238U	232Th	232Th	206Pb	206Pb*/238U		207Pb*/206Pb*		207Pb*/235U		238U/206Pb*		207Pb*/206Pb*		207Pb*/235U		Disc.	Disc.
ID	no.	(ppm)	(ppm)	238U	(c/sec)	date (Ma) ± 1σ		date (Ma) ± 1σ		date (Ma) ± 1σ		± %		± %		± %		Pb-Pb %	U-Pb %
E	R132-5.2	1382	55406	40.09	1115	983	±12	985	±21	984	±17	6.07	1.4	0.072	1.0	1.634	1.7	+0	+0
C	R132-5.1	2153	43481	20.19	1774	985	±12	1004	±19	991	±16	6.06	1.3	0.073	1.0	1.654	1.6	+2	+1
E	R132-2.2	2245	58728	26.16	2100	991	±15	1038	±28	1006	±21	6.02	1.6	0.074	1.4	1.693	2.1	+5	+1
C	R132-4.2	3104	57887	18.65	2478	1015	±12	1008	±24	1013	±18	5.86	1.2	0.073	1.2	1.712	1.7	-1	-0
C	R132-1.1	15563	35056	2.25	15096	1037	±11	988	±47	1021	±26	5.73	1.2	0.072	2.3	1.733	2.6	-5	-2

Errors are 1-sigma (abs) or % where indicated. Pb* indicate radiogenic proportions. All ages are common Pb corrected using measured 204Pb. RE-Recrystallised zone, C-Core, L- Light BSE, E, Edge of grain, Inc- Sillimanite inclusions

Table S2: SHRIMP analytical results for monazite from sample ROG13/2 continued

Texture	Spot	238U	232Th	232Th	206Pb	206Pb*/238U		207Pb*/206Pb*		207Pb*/235U		238U/206Pb*		207Pb*/206Pb*		207Pb*/235U		Disc.	Disc.
ID	no.	(ppm)	(ppm)	238U	(c/sec)	date (Ma) ± 1σ		date (Ma) ± 1σ		date (Ma) ± 1σ		± %		± %		± %		Pb-Pb %	U-Pb %
C	R132-2.1	2309	68604	29.72	2128	1027	±12	1033	±14	1029	±15	5.79	1.3	0.074	0.7	1.755	1.4	+1	+0
RE	R132-1.2	2368	91066	38.45	2017	1023	±12	1047	±16	1030	±15	5.82	1.3	0.074	0.8	1.759	1.5	+2	+1

Table S2: SHRIMP analytical results for monazite from sample ROG14/5

Texture	Spot	238U	232Th	232Th	206Pb	206Pb*/238U		207Pb*/206Pb*		207Pb*/235U		238U/206Pb*		207Pb*/206Pb*		207Pb*/235U		Disc.	Disc.
ID	no.	(ppm)	(ppm)	238U	(c/sec)	date (Ma) ± 1σ		date (Ma) ± 1σ		date (Ma) ± 1σ		± %		± %		± %		Pb-Pb %	U-Pb %
RE (Inc)	R145-8.1	1317	115645	87.80	912	886	±11	923	±105	896	±47	6.79	1.4	0.070	5.1	1.418	5.3	+4	+1
RE	R145-7.2	4338	80577	18.57	3467	895	±10	895	±21	895	±14	6.71	1.2	0.069	1.0	1.414	1.6	-0	-0
RE	R145-6.1	3714	74116	19.96	2997	902	±10	897	±19	900	±14	6.66	1.2	0.069	0.9	1.427	1.5	-1	-0
RE (Inc)	R145-10.2	4486	120491	26.86	3425	914	±10	943	±14	923	±13	6.56	1.2	0.071	0.7	1.481	1.4	+3	+1
C	R145-6.2	2114	112182	53.06	1548	915	±11	945	±32	924	±19	6.55	1.3	0.071	1.6	1.484	2.0	+3	+1
RE	R145-5.3	3012	125868	41.79	2392	916	±10	894	±83	910	±38	6.55	1.2	0.069	4.0	1.450	4.2	-3	-1
RE	R145-5.1	2818	92413	32.80	2269	921	±11	930	±14	924	±13	6.51	1.2	0.070	0.7	1.484	1.4	+1	+0

C	R145-9.1	2658	58985	22.19	2177	931	±11	902	±33	922	±19	6.44	1.2	0.069	1.6	1.481	2.0	-3	-1
C (inc)	R145-8.2	3580	74178	20.72	2905	931	±11	959	±18	940	±14	6.43	1.2	0.071	0.9	1.523	1.5	+3	+1
C	R145-5.2	4583	43692	9.53	4136	943	±10	922	±45	937	±23	6.35	1.2	0.070	2.2	1.516	2.5	-2	-1
C (inc)	R145-10.1	3979	49432	12.42	3315	950	±11	960	±17	953	±14	6.29	1.2	0.071	0.8	1.557	1.5	+1	+0
RE (Inc)	R145-3.2	4238	77188	18.21	3680	954	±11	991	±12	965	±13	6.27	1.2	0.072	0.6	1.587	1.3	+4	+1
C	R145-1.1	3953	59039	14.94	3331	966	±11	922	±67	953	±33	6.18	1.2	0.070	3.3	1.556	3.5	-5	-1
RE	R145-2.2	2856	137698	48.21	2191	968	±11	945	±14	961	±14	6.17	1.3	0.071	0.7	1.576	1.4	-3	-1
C	R145-7.1	5152	51301	9.96	4625	969	±11	944	±27	962	±17	6.16	1.2	0.071	1.3	1.578	1.8	-3	-1
C (inc)	R145-3.1	2933	73064	24.91	2526	977	±11	956	±20	971	±15	6.11	1.2	0.071	1.0	1.601	1.6	-2	-1
C (inc)	R145-4.1	3556	86992	24.46	3152	983	±11	984	±13	983	±14	6.07	1.2	0.072	0.6	1.634	1.4	+0	+0
C	R145-2.1	3735	61996	16.60	3397	990	±11	926	±46	970	±25	6.03	1.2	0.070	2.2	1.599	2.6	-7	-2

Errors are 1-sigma (abs) or % where indicated. Pb* indicate radiogenic proportions. All ages are common Pb corrected using measured 204Pb. RE-Recrystallised zone, C-Core, L- Light BSE, E, Edge of grain, Inc- Sillimanite inclusions

Using accessory minerals to unravel thermal histories in polymetamorphic terranes: an example from Rogaland, SW Norway

E. BLEREAU, C. CLARK, R. J. M. TAYLOR, P. D. KINNY, T. E. JOHNSON, E. SANSOM, M. HAND

Table S3: All data for zircon LA-ICP-MS REE and trace element analyses

Table S3: LA-ICP-MS zircon REE and trace element analyses

	R1118-1.1	R1114-1.1	R1112-1.1	R1136-1.1	R1131-1.1	R1131-1.2	R113-1.2	R13-2-2	R13-2-3	R13-2-4	R13-2-5	R13-2-6
	Garnet–Sillimanite–Cordierite migmatite (ROG13/11, 30 km)							Osumilite–Orthopyroxene–Spinel migmatite (ROG13/2, 2 km)				
Position	RE	RE	C	C	RE	RE	R	C	RE	DR	C	RE
Y	455.0	992.0	450.0	564.0	823.0	395.0	1216.0	502.0	340.0	249.2	701.0	1163.0
Sm	3.6	10.7	5.2	13.7	24.3	2.2	0.5	1.0	4.8	6.8	5.6	7.1
Eu	0.5	2.2	0.2	2.0	1.8	0.2	0.3	0.2	0.2	0.2	0.8	0.2
Gd	26.4	32.2	19.1	31.7	24.4	15.1	7.5	6.4	25.1	32.4	30.9	28.6
Tb	6.4	9.3	4.6	8.2	6.7	5.9	5.2	2.7	6.6	5.9	9.3	9.2
Dy	53.5	109.2	50.6	71.0	77.8	49.3	98.9	40.5	52.5	46.6	88.0	105.1
Ho	16.9	37.2	16.3	17.8	26.2	11.0	40.3	18.3	13.2	9.8	28.5	46.2
Er	68.0	161.6	63.0	71.7	113.4	38.8	203.3	88.0	33.3	23.6	109.3	185.6
Tm	14.8	30.6	10.5	17.7	26.0	6.8	60.8	25.0	4.5	4.1	22.5	39.3
Yb	146.0	310.0	113.0	221.1	249.0	63.1	756.0	273.0	32.1	19.7	254.0	397.0
Lu	26.7	57.2	20.4	41.5	48.4	11.8	164.7	60.2	4.0	3.1	39.6	69.4

	R13-2-12	R13-2-8	R13-2-7	R13-2-10	R13-2-11	R114-5-1	R114-5-2	R114-5-3	R114-5-5	R114-5-6	R114-5-8	R114-5-9
	Osumilite–Orthopyroxene–Spinel migmatite (ROG13/2, 2 km) continued					Garnet–Sillimanite–Cordierite–Spinel migmatite (ROG14/5, at the contact)						
Position	C	S	LR	DR	C	RE	RE	S	S	S	S	RE
Y	1706.0	1223.0	1052.0	576.0	1363.0	183.5	124.9	111.5	155.1	154.7	116.7	140.2
Sm	60.0	5.8	5.4	7.4	11.5	13.1	9.0	2.1	3.1	1.3	1.2	3.4
Eu	2.4	0.0	0.4	-	0.2	19.2	9.0	-	0.1	0.1	-	0.02
Gd	82.0	43.1	35.3	26.3	36.7	45.3	17.2	15.7	20.9	25.9	15.7	17.6
Tb	18.2	15.0	12.9	7.9	12.1	6.0	2.7	2.5	4.0	3.9	3.5	3.7
Dy	180.0	145.1	123.0	76.3	127.1	27.1	19.1	14.9	24.5	26.4	19.9	21.0
Ho	69.4	45.5	40.9	21.5	52.2	5.1	4.0	3.5	4.6	5.3	3.8	5.1

Er	262.0	133.4	120.0	63.4	208.4	9.9	8.3	8.7	10.2	11.5	8.3	12.7
Tm	53.0	20.6	19.3	9.7	42.4	1.3	0.9	1.3	1.4	1.3	1.0	2.1
Yb	467.0	150.2	159.0	74.7	414.0	8.2	7.9	10.5	9.3	8.2	6.4	12.0
Lu	87.2	22.8	21.1	12.7	75.1	1.1	1.1	1.5	1.3	1.3	1.0	1.5
Values of - indicate trace elements are below detection limit of the instrument					R-Rim, C-Core, RE-Recrystallised, DR-Dark rim, LR-Light rim, S-Sector zoned; Only concordant data was analysed							
Table S3 continued: LA-ICP-MS zircon REE and trace element analyses												
	R148-6.1	R148-7.1	R148-7.2	R148-5.1	R148-4.2	R148-2.1	R148-2.2	R148-1.1	R148-1.2	R148-23.2	R148-23.1	R148-22.2
	Garnet bearing anorthosite (ROG14/8, at the contact)											
Position	RE	RE	RE	S	RE	RE	R	C	RE	R	RE	R
Y	897.0	607.0	1440.0	185.2	1101.0	627.0	1701.0	669.0	892.0	872.0	994.0	728.0
Sm	2.5	1.3	3.4	4.5	3.2	2.1	0.2	1.8	1.7	3.4	4.9	3.7
Eu	0.2	0.05	0.2	0.1	0.3	0.04	0.1	0.2	0.1	0.1	0.1	-
Gd	18.4	9.7	28.9	27.4	17.5	9.2	10.6	12.7	8.1	14.2	18.3	16.5
Tb	7.7	4.2	12.0	6.0	7.1	4.8	6.6	4.0	4.8	5.2	6.0	5.1
Dy	88.1	51.8	130.1	34.1	98.6	57.5	114.2	61.8	63.3	71.3	81.0	62.3
Ho	32.2	21.3	48.1	5.4	40.0	23.4	58.4	24.2	30.9	27.3	30.7	25.7
Er	137.1	96.8	214.1	13.5	179.1	107.4	313.0	110.4	153.4	150.2	141.3	115.9
Tm	22.5	20.3	41.8	1.5	36.3	21.1	66.0	23.3	36.1	31.4	27.6	23.7
Yb	195.8	203.7	356.0	11.8	368.0	226.0	669.0	227.0	351.0	308.2	253.0	235.0
Lu	33.3	40.4	61.2	1.5	64.0	42.8	123.1	43.6	72.7	62.1	46.8	48.2
	R148-21.1	R148-20.1	R148-19.1	R148-18.1	R148-18.2	R148-14.1	R148-13.1	R148-12.2	R148-10.2	R148-10.1	R148-26.1	R148-26.2
	Garnet bearing anorthosite (ROG14/8, at the contact) continued											
Position	RE	RE	RE#	RE	RE	RE	RE	RE	RE	RE	RE	RE
Y	830.0	1719.0	536.0	2057.0	1350.0	955.0	956.0	2289.0	636.0	2356.0	978.0	730.0
Sm	4.3	19.7	3.8	20.8	5.4	3.0	1.9	16.8	1.3	11.7	2.8	2.0
Eu	0.2	0.2	0.2	0.8	0.2	-	0.2	0.6	0.1	1.0	0.1	0.2
Gd	16.2	53.2	11.5	60.7	25.1	17.6	18.0	59.7	9.3	53.3	20.8	11.3
Tb	5.2	16.3	3.6	15.9	7.8	6.1	5.0	19.1	3.5	17.8	7.0	4.9
Dy	65.5	189.5	48.0	198.7	110.7	76.5	74.4	209.7	47.1	210.5	91.8	60.3

Ho	23.9	58.6	16.4	68.5	44.3	29.9	30.1	76.9	20.3	81.4	32.6	24.6
Er	114.0	207.3	80.5	273.2	214.3	149.7	151.4	339.4	95.7	353.0	136.7	124.5
Tm	20.2	33.3	15.0	49.5	44.8	31.8	32.6	64.4	19.6	68.3	26.0	26.8
Yb	221.0	245.9	148.1	424.0	434.0	310.4	325.6	583.0	180.4	638.0	225.0	273.3
Lu	43.4	39.3	31.5	76.7	93.0	67.1	69.8	113.8	36.4	120.7	38.3	55.2

Using accessory minerals to unravel thermal histories in polymetamorphic terranes: an example from Rogaland, SW Norway

E. BLEREAU, C. CLARK, R. J. M. TAYLOR, P. D. KINNY, T. E. JOHNSON, E. SANSOM, M. HAND

Table S4: All data for monazite LA-ICP-MS REE and trace element analyses

Table S4: LA-ICP-MS monazite REE and trace element analyses

	R113-6.1	R111-11.1	R111-11.2	R111-4.1	R111-7.1	R113-3.2	R113-4.1	R111-15.1	R31-4.1	R31-4.2	R31-3.1	R31-3.2
	Garnet–Sillimanite–Cordierite migmatite (ROG13/11, 30 km)											
Position	C	C	E	C	C	E	C	C	C	C	C	C
Y	4380	2380	6240	9320	20730	4570	18200	15000	12990	4280	22210	10100
La	105000	75600	83200	105400	112500	95200	102900	107000	104800	93800	106700	107600
Ce	230526	230526	230526	230526	230526	230526	230526	230526	230526	230526	230526	230526
Pr	28230	34160	32430	27900	27840	29960	28420	27480	27380	30490	28580	28130
Nd	112300	144800	131200	110100	103300	119400	109200	106400	104800	117400	107300	105900
Sm	14340	18000	22450	18160	16420	14640	14650	16000	16730	14440	15970	17180
Eu	101	86	236	309	490	77	528	416	389	137	389	351
Gd	9570	6980	14710	15550	14490	7160	10780	12470	13760	6900	12520	14010
Tb	771	360	1035	1401	1698	507	1136	1310	1359	488	1467	1443
Dy	1862	753	2181	3570	6000	1318	4260	3868	3260	1039	4020	2853
Ho	118	53	141	223	504	115	494	362	329	115	530	247
Er	89	52	122	154	349	118	597	330	373	152	760	261
Tm	5	4	9	8	16	8	50	20	24	10	47	13
Yb	18	15	33	30	48	33	207	70	71	28	143	47
Lu	2	1	2	2	2	2	14	6	6	2	12	6

	R31-2.1	R31-1.1	R31-5.1	R31-6.1	R132-1.2	R132-1.1	R132-2.1	R132-2.2	R132-4.2	R132-5.1	R132-5.2	R145-10.1
	Garnet–Sillimanite–Cordierite migmatite (ROG13/11, 30 km) continued				Osumilite–Orthopyroxene–Spinel migmatite (ROG13/2, 2 km)							
Position	C	C	C	C	RE	C	C	E	C	C	E	C inc
Y	4790	13700	833	19980	25540	48400	13660	16340	24430	27800	12280	2150
La	102900	109600	95700	109000	100100	114000	103500	100700	96400	108000	101500	109400
Ce	230526	230526	230526	230526	230526	230526	230526	230526	230526	230526	230526	230526

Pr	29140	27720	29860	27530	33060	30670	31060	30940	32610	30020	31230	27870
Nd	113300	106400	117000	108800	138500	121400	129000	127800	139000	120800	127400	103300
Sm	16750	16620	14450	17360	21270	19860	20290	19140	23950	19210	18660	13270
Eu	223	360	71	391	1422	4430	1272	1091	943	1626	715	174
Gd	9680	13420	6090	14720	13870	15980	13410	12820	18040	15020	11560	6610
Tb	728	1349	277	1646	1278	1831	1003	1010	1519	1461	869	353
Dy	1346	3130	336	4550	4667	8000	3047	3400	5090	5590	2700	703
Ho	120	306	19	484	692	1368	373	446	651	796	325	57
Er	114	330	26	528	1276	3013	584	776	1131	1550	522	73
Tm	5	18	1	30	126	380	49	73	103	155	40	5
Yb	21	51	7	95	516	2052	207	374	450	740	177	22
Lu	3	8	1	13	71	299	24	39	44	70	11	1
Monazite trace elements calibrated against stoichiometric Ce fixed at 230526 ppm (Ce*)(Buick et al., 2010). C-Core, RE-Recrystallise zone, E-Edge of grain, Inc-inclusion												
Table S4 continued: LA-ICP-MS monazite REE and trace element analyses												
	R145-10.2	R145-9.1	R145-7.1	R145-7.2	R145-8.1	R145-8.2	R145-5.1	R145-5.2	R145-5.3	R145-6.1	R145-6.2	R145-4.1
	Garnet–Sillimanite–Cordierite–Spinel migmatite (ROG14/5, at the contact)											
Position	RE inc	C	C	RE	RE inc	C inc	RE	C	RE	RE	C	C inc
Y	1953	1874	3800	1624	1404	1850	3930	2418	4780	4610	1709	2428
La	90000	108000	108900	79600	94100	107400	96800	110900	113500	93100	82100	109700
Ce	230526	230526	230526	230526	230526	230526	230526	230526	230526	230526	230526	230526
Pr	32430	27830	28290	34400	31730	28770	29040	28320	28070	30860	33560	29410
Nd	125500	104500	101900	137300	124900	105000	109200	102100	103100	121100	138900	110300
Sm	12250	12450	15000	14150	14060	13770	11730	13530	15730	14690	13500	15450
Eu	51	147	237	37	46	108	47	125	252	74	55	131
Gd	4450	5640	10400	5690	5240	6860	5490	6850	10570	6240	4363	8710
Tb	226	299	700	284	241	383	379	396	724	426	223	510
Dy	517	584	1316	519	421	655	911	703	1327	1025	425	808
Ho	50	47	91	41	34	43	96	55	109	106	38	57
Er	78	59	85	52	42	41	126	55	103	133	45	50
Tm	6	3	4	2	2	2	8	3	5	8	2	2

Yb	28	15	13	9	6	5	27	8	15	25	7	9
Lu	2	1	1	1	1	0.5	3	1	1	2	0.4	1
	R145-3.2	R145-2.2	R145-2.1	R145-1.1								
	Garnet–Sillimanite–Cordierite–Spinel migmatite (ROG14/5, at the contact) continued											
Position	RE inc	RE	C	C								
Y	3011	3159	4550	5610								
La	114600	93000	105200	108600								
Ce	230526	230526	230526	230526								
Pr	27910	32440	28800	28550								
Nd	106800	129300	111200	111000								
Sm	14610	14950	14620	13950								
Eu	147	85	206	165								
Gd	6860	5950	8350	6400								
Tb	389	342	539	412								
Dy	743	700	1010	970								
Ho	70	74	104	137								
Er	90	90	147	257								
Tm	6	6	10	22								
Yb	16	21	44	112								
Lu	1	2	3	6								
Monazite trace elements calibrated against stoichiometric Ce fixed at 230526 ppm (Ce*)(Buick et al., 2010). C-Core, RE-Recrystallise zone, E-Edge of grain, Inc-inclusion												

Using accessory minerals to unravel thermal histories in polymetamorphic terranes: an example from Rogaland, SW Norway

E. BLEREAU, C. CLARK, R. J. M. TAYLOR, P. D. KINNY, T. E. JOHNSON, E. SANSOM, M. HAND

Table S5: All data for garnet LA-ICP-MS REE and trace element analyses

Table S5: LA-ICP-MS garnet REE and trace element analyses

	R1311G-1 - 1	R1311G-1 - 2	R1311G-1 - 3	R1311G-1 - 4	R1311G-2 - 1	R1311G-2 - 2	R1311G-2 - 3	R1311G-2 - 4	R1311G-2 - 5	R1311G-3 - 1
	Garnet–sillimanite–cordierite migmatite (ROG13/11, 30 km)									
Texture	Grt 1 Rim	Grt 1 Rim	Grt 1 Rim	Grt 1 Rim	Grt 1 Core	Resorbed Grt 1	Grt 1 Core	Grt 1 Core	Resorbed Grt 1	Grt 2 Core
Y	781.0	450.0	1000.0	651.0	511.0	1037.0	539.0	250.3	958.0	452.0
Sm	4.3	2.5	6.0	7.0	7.8	7.5	6.7	8.7	5.6	10.4
Eu	0.1	0.1	0.1	0.1	0.1	0.1	0.1	0.1	0.1	0.1
Gd	48.8	29.6	55.6	55.4	74.1	74.0	69.1	65.8	53.2	25.2
Tb	19.0	11.9	22.8	17.4	23.1	28.0	22.9	14.0	20.4	6.2
Dy	147.4	94.9	198.0	129.2	140.1	221.0	145.0	74.2	176.7	64.9
Ho	23.9	15.5	38.8	20.8	19.5	41.9	19.1	9.4	38.7	18.7
Er	44.9	32.2	85.4	44.5	30.7	92.0	31.1	16.0	101.2	70.3
Tm	5.6	3.9	10.3	5.4	3.0	10.4	3.0	1.6	14.1	12.3
Yb	32.8	23.0	61.2	32.1	15.6	60.5	14.2	6.5	92.9	95.4
Lu	3.6	2.8	8.1	4.0	1.6	8.5	1.7	0.9	14.4	16.5
SmN	29.0	17.0	40.6	47.6	53.0	51.0	45.5	59.3	38.3	70.7
EuN	1.7	1.8	2.2	1.5	1.0	1.2	2.6	2.2	2.5	2.4
GdN	248.2	150.6	282.8	281.8	376.9	376.4	351.5	334.7	270.6	128.2
TbN	523.4	326.7	628.1	480.2	636.4	771.3	630.9	384.8	562.0	171.6
DyN	607.3	391.0	815.8	532.3	577.3	910.6	597.4	305.7	728.1	267.4
HoN	429.3	279.3	697.8	374.5	350.7	753.6	343.5	168.5	696.0	336.3
ErN	282.6	202.6	537.4	280.1	193.2	579.0	195.7	100.7	636.9	442.4
TmN	229.3	162.4	426.4	221.5	123.1	431.4	122.3	65.3	584.3	508.3
YbN	201.8	141.5	376.6	197.5	96.0	372.3	87.4	39.9	571.7	587.1

LuN	146.5	114.0	333.7	166.3	66.7	347.7	68.7	35.8	590.5	679.0
YbN/GdN	0.81	0.94	1.33	0.70	0.25	0.99	0.25	0.12	2.11	4.58
Eu/Eu*	0.012	0.021	0.013	0.009	0.005	0.006	0.013	0.011	0.016	0.024
Textures- 13/11- Grt1 Sillimanite rich, Melanosome, Grt2 Peritectic garnet; 13/2– Grt1- mineral separate, Grt2 - small relic grain; 14/5- Grt1- Primary garnet, Grt2(Grt1) - Secondary Grt on Grt 1, Grt2(Spl) -Grt2 on Spinel, Grt2(Ilm)- Grt2 on Ilmenite; 14/8- Grt 1- Large garnet, Grt 2- Small garnet grains										
Table S5: LA-ICP-MS garnet REE and trace element analyses										
	R1311G-3 - 2	R1311G-3 - 3	R1311G-3 - 4	R1311G-3 - 5	R1311G-3 - 6	R1311G-3 - 7	R1311G-3 - 8	R132G-1 - 1	R132G-1 - 2	R132G-1 - 3
	Garnet–sillimanite–cordierite migmatite (ROG13/11, 30 km) continued							Osumilite–orthopyroxene–spinel migmatite(ROG13/2, 2 km)		
Texture	Grt 2 Core	Grt 2 Core	Grt 2 Core	Grt 2 Rim	Grt 2 Rim	Grt 2 Rim	Grt 2 Rim	TS	TS	TS
Y	299.2	355.0	290.3	280.9	309.5	275.9	267.0	12100.0	11790.0	11640.0
Sm	7.6	8.3	6.8	7.7	9.2	6.7	7.8	18.2	17.6	20.3
Eu	0.1	0.1	0.1	0.2	0.1	0.1	0.1	0.4	0.4	0.3
Gd	17.6	20.0	15.4	22.3	24.8	23.8	25.3	164.6	160.9	155.3
Tb	4.2	4.9	3.8	5.8	6.0	5.6	5.7	70.0	67.3	66.0
Dy	40.7	45.3	37.0	45.9	48.3	46.1	44.1	1190.0	1122.0	1110.0
Ho	12.3	14.4	11.3	9.5	10.7	9.3	9.1	641.0	620.0	610.0
Er	43.0	51.2	40.4	24.4	28.0	22.4	23.4	3060.0	2880.0	2850.0
Tm	7.3	8.9	7.2	3.2	4.0	3.1	2.8	546.0	520.0	518.0
Yb	57.2	68.6	54.8	20.2	24.8	19.6	18.6	3230.0	3070.0	3010.0
Lu	9.2	12.6	9.3	2.4	3.0	2.4	2.1	686.0	656.0	639.0
SmN	51.5	56.4	46.2	52.1	62.3	45.8	53.3	123.7	119.6	138.0
EuN	1.1	1.6	1.0	2.7	2.3	2.0	2.3	7.3	6.6	4.9
GdN	89.5	101.7	78.3	113.4	126.1	121.1	128.7	837.2	818.4	789.9
TbN	116.3	133.9	105.2	158.7	165.6	153.4	156.7	1928.4	1854.0	1818.2
DyN	167.7	186.7	152.5	189.1	199.0	189.9	181.7	4903.2	4623.0	4573.5
HoN	220.7	259.7	202.5	171.6	192.3	166.9	163.5	11528.8	11151.1	10971.2
ErN	270.6	322.2	254.2	153.6	176.2	140.9	147.3	19257.4	18124.6	17935.8
TmN	300.0	366.9	296.7	131.0	165.3	126.9	116.9	22562.0	21487.6	21405.0
YbN	352.0	422.2	337.2	124.5	152.6	120.6	114.5	19876.9	18892.3	18523.1
LuN	376.5	517.7	384.0	97.1	122.6	99.2	86.4	28230.5	26995.9	26296.3

YbN/GdN	3.93	4.15	4.31	1.10	1.21	1.00	0.89	23.74	23.08	23.45
Eu/Eu*	0.016	0.020	0.016	0.033	0.024	0.024	0.026	0.015	0.014	0.011
Textures- 13/11- Grt1 Sillimanite rich, Melanosome, Grt2 Peritectic garnet; 13/2– Grt1- mineral separate, Grt2 - small relic grain; 14/5- Grt1- Primary garnet, Grt2(Grt1) - Secondary Grt on Grt 1, Grt2(Spl) -Grt2 on Spinel, Grt2(Ilm)- Grt2 on Ilmenite; 14/8- Grt 1- Large garnet, Grt 2- Small garnet grains										
Table S5 continued: LA-ICP-MS garnet REE and trace element analyses										
	R132G-2 - 1	R132G-2 - 2	R132G-2 - 3	R132G-2 - 4	R145G-1 - 1	R145G-1 - 2	R145G-1 - 3	R145G-1 - 4	R145G-2 - 1	R145G-2 - 2
	Osumilite–orthopyroxene–spinel migmatite (ROG13/2, 2 km) continude				Garnet–Sillimanite–Cordierite–Spinel migmatite (ROG14/5, at the contact)					
Texture	Euhedral Grt Core	Euhedral Grt Core	Euhedral Grt Core	Euhedral Grt Rim	Grt 1	Grt 1	Grt 1	Grt 1	Grt 2	Grt 2
Y	4280.0	4380.0	4210.0	7100.0	366.0	391.0	301.0	353.0	248.7	207.0
Sm	4.4	5.6	3.9	6.3	10.4	11.7	11.7	7.2	7.2	4.6
Eu	0.1	0.1	0.1	0.1	0.1	0.1	0.1	0.2	0.2	0.2
Gd	75.7	75.0	75.0	118.5	37.4	41.8	27.0	23.3	19.5	18.8
Tb	40.3	41.5	40.7	67.5	8.3	8.6	6.8	6.4	4.5	4.3
Dy	522.0	531.0	513.0	850.0	56.3	57.3	49.0	52.0	33.8	30.4
Ho	158.3	165.7	159.4	269.4	12.6	13.7	9.1	12.2	8.7	7.4
Er	517.0	533.0	512.0	868.0	42.1	46.1	22.2	31.5	31.5	26.0
Tm	79.0	81.4	78.4	133.8	7.1	8.0	3.2	4.4	5.9	4.5
Yb	526.0	540.0	526.0	892.0	54.8	64.6	20.5	29.0	43.6	36.5
Lu	73.1	73.7	70.8	124.8	8.2	10.8	2.3	3.6	7.2	5.7
SmN	29.8	38.2	26.5	43.0	70.4	79.5	79.5	48.7	48.6	31.5
EuN	1.0	1.4	1.8	2.3	2.0	1.9	2.2	3.0	2.7	3.4
GdN	385.0	381.5	381.5	602.7	190.2	212.6	137.3	118.5	99.2	95.6
TbN	1110.2	1143.3	1121.2	1859.5	227.8	237.7	186.8	177.4	123.4	118.5
DyN	2150.8	2187.9	2113.7	3502.3	232.0	236.1	201.9	214.3	139.3	125.3
HoN	2847.1	2980.2	2866.9	4845.3	225.9	246.6	162.8	220.1	156.7	132.9
ErN	3253.6	3354.3	3222.2	5462.6	264.9	290.1	139.7	198.2	198.2	163.6
TmN	3264.5	3363.6	3239.7	5528.9	291.7	331.8	133.9	183.1	245.5	184.3
YbN	3236.9	3323.1	3236.9	5489.2	337.2	397.5	126.2	178.5	268.3	224.6
LuN	3008.2	3032.9	2913.6	5135.8	338.3	444.9	96.3	148.6	295.9	235.4

YbN/GdN	8.41	8.71	8.49	9.11	1.77	1.87	0.92	1.51	2.71	2.35
Eu/Eu*	0.005	0.007	0.009	0.007	0.015	0.013	0.021	0.036	0.036	0.054
Textures- 13/11- Grt1 Sillimanite rich, Melanosome, Grt2 Peritectic garnet; 13/2– Grt1- mineral separate, Grt2 - small relic grain; 14/5- Grt1- Primary garnet, Grt2(Grt1) - Secondary Grt on Grt 1, Grt2(Spl) -Grt2 on Spinel, Grt2(Ilm)- Grt2 on Ilmenite; 14/8- Grt 1- Large garnet, Grt 2- Small garnet grains										
Table S5 continued: LA-ICP-MS garnet REE and trace element analyses										
	R145G-2 - 3	R145G-2 - 4	R145G-3 - 1	R145G-3 - 2	R145G-3 - 3	R145G-4 - 1	R145G-4 - 2	R145G-4 - 3	R148G-1 - 1	R148G-1 - 2
	Garnet–Sillimanite–Cordierite–Spinel migmatite (ROG14/5, at the contact) continued							Garnet-bearing anorthosite (ROG14/8, at the contact)		
Texture	Grt 2	Grt 2	Grt 2 Spl	Grt 2 Spl	Grt 2 Spl	Grt 2 Ilm	Grt 2 Ilm	Grt 2 Ilm	Grt 1 Core	Grt 1 Core
Y	275.0	222.0	98.1	161.0	76.2	205.0	199.0	95.0	899.0	888.0
Sm	5.4	4.5	4.6	4.4	3.5	4.9	4.1	4.0	15.1	14.3
Eu	0.2	0.2	0.2	0.2	0.2	0.3	0.3	0.3	0.5	0.4
Gd	24.2	21.7	13.8	14.6	9.1	17.7	17.0	10.5	58.2	55.0
Tb	5.8	4.9	3.0	4.0	2.1	4.5	4.2	2.3	15.9	15.8
Dy	45.2	40.7	20.5	26.9	13.0	32.1	30.7	16.0	133.8	128.2
Ho	9.2	7.6	3.6	5.3	2.5	7.1	6.5	3.2	30.1	30.7
Er	23.4	18.8	7.9	12.7	6.0	18.9	18.6	8.9	87.6	84.1
Tm	3.3	2.6	1.0	1.8	0.9	3.3	3.0	1.3	13.0	12.7
Yb	22.7	17.6	6.7	12.9	5.5	21.9	21.5	9.6	87.7	86.2
Lu	2.8	1.9	0.8	1.6	0.9	3.0	2.9	1.3	10.6	10.0
SmN	36.4	30.7	31.0	29.9	24.1	33.0	28.1	26.9	102.7	97.2
EuN	4.1	3.8	4.2	3.4	3.1	5.2	4.6	4.8	8.3	7.3
GdN	123.1	110.4	70.2	74.3	46.3	90.0	86.5	53.4	296.0	279.8
TbN	160.9	135.5	82.1	109.6	59.0	123.1	116.3	63.6	436.6	435.5
DyN	186.2	167.7	84.5	110.8	53.6	132.3	126.5	65.9	551.3	528.2
HoN	166.2	136.2	64.2	95.0	44.4	127.0	117.6	57.4	541.4	552.2
ErN	147.3	118.3	49.7	79.9	38.0	118.9	117.1	56.3	551.3	529.3
TmN	137.2	106.6	40.9	75.6	35.5	138.0	122.7	52.9	538.8	525.2
YbN	139.7	108.3	41.0	79.4	33.7	134.8	132.3	59.1	539.7	530.5
LuN	114.4	77.0	32.5	64.2	36.6	125.1	121.0	54.7	435.0	410.3

YbN/GdN	1.13	0.98	0.58	1.07	0.73	1.50	1.53	1.11	1.82	1.90
Eu/Eu*	0.051	0.053	0.083	0.066	0.088	0.084	0.080	0.119	0.042	0.039
Textures- 13/11- Grt1 Sillimanite rich, Melanosome, Grt2 Peritectic garnet; 13/2– Grt1- mineral separate, Grt2 - small relic grain; 14/5- Grt1- Primary garnet, Grt2(Grt1) - Secondary Grt on Grt 1, Grt2(Spl) -Grt2 on Spinel, Grt2(Ilm)- Grt2 on Ilmenite; 14/8- Grt 1- Large garnet, Grt 2- Small garnet grains										
Table S5 continued: LA-ICP-MS garnet REE and trace element analyses										
	R148G-1 - 3	R148G-1 - 4	R148G-2 - 1	R148G-2 - 2	R148G-2 - 3	R148G-2 - 4	R148G-3 - 1	R148G-3 - 2	R148G-3 - 3	R148G-3 - 4
	Garnet-bearing anorthosite (ROG14/8, at the contact) continued									
Texture	Grt 1 Core	Grt 1 Core	Grt 1 Rim	Grt 1 Rim	Grt 1 Rim	Grt 1 Rim	Grt 2	Grt 2	Grt 2	Grt 2
Y	791.0	821.0	913.0	1134.0	918.0	769.0	2160.0	1940.0	2360.0	2400.0
Sm	13.8	14.1	13.0	18.2	14.1	12.4	9.6	8.5	11.5	9.7
Eu	0.5	0.4	0.5	0.6	0.5	0.4	0.4	0.3	0.3	0.4
Gd	50.7	48.0	44.4	56.7	45.1	41.0	37.3	33.3	41.5	40.8
Tb	12.9	13.0	13.0	16.8	12.7	11.5	14.2	13.0	16.6	16.2
Dy	110.9	110.9	123.0	154.0	118.8	101.8	203.0	185.0	220.0	227.0
Ho	26.9	28.4	34.0	41.5	33.2	27.2	82.0	73.3	92.1	92.0
Er	80.2	85.0	107.0	138.0	110.4	86.6	346.0	314.0	407.0	385.0
Tm	12.7	13.6	16.8	21.1	17.9	13.5	64.1	59.6	78.6	71.5
Yb	86.2	98.9	116.0	159.0	132.4	98.2	508.0	487.0	635.0	559.0
Lu	11.4	13.1	16.0	22.0	20.4	12.9	78.1	76.2	100.8	85.0
SmN	93.8	95.9	88.4	123.7	96.1	84.3	65.2	57.8	78.2	65.9
EuN	8.3	7.8	8.1	9.8	8.2	7.4	7.3	5.8	6.1	7.5
GdN	257.9	244.2	225.8	288.4	229.4	208.5	189.7	169.4	211.1	207.5
TbN	354.5	358.1	358.1	462.8	351.0	317.1	391.2	357.3	457.6	446.3
DyN	456.9	456.9	506.8	634.5	489.5	419.4	836.4	762.3	906.5	935.3
HoN	483.8	510.8	611.5	746.4	597.1	489.2	1474.8	1318.3	1656.5	1654.7
ErN	504.7	534.9	673.4	868.5	694.8	545.0	2177.5	1976.1	2561.4	2422.9
TmN	525.6	562.4	694.2	871.9	738.4	556.6	2648.8	2462.8	3247.9	2954.5
YbN	530.5	608.6	713.8	978.5	814.8	604.3	3126.2	2996.9	3907.7	3440.0
LuN	467.5	539.9	658.4	905.3	838.3	531.7	3214.0	3135.8	4148.1	3497.9

YbN/GdN	2.06	2.49	3.16	3.39	3.55	2.90	16.48	17.69	18.51	16.58
Eu/Eu*	0.047	0.046	0.051	0.048	0.050	0.051	0.057	0.051	0.042	0.055
Textures- 13/11- Grt1 Sillimanite rich, Melanosome, Grt2 Peritectic garnet; 13/2– Grt1- mineral separate, Grt2 - small relic grain; 14/5- Grt1- Primary garnet, Grt2(Grt1) - Secondary Grt on Grt 1, Grt2(Spl) -Grt2 on Spinel, Grt2(Ilm)- Grt2 on Ilmenite; 14/8- Grt 1- Large garnet, Grt 2- Small garnet grains										

Using accessory minerals to unravel thermal histories in polymetamorphic terranes: an example from Rogaland, SW Norway

E. BLEREAU, C. CLARK, R. J. M. TAYLOR, P. D. KINNY, T. E. JOHNSON, E. SANSOM, M. HAND

Table S6: SHRIMP U–Pb with respective REE data

Table S6: SIMS U-Pb ages and normalised LA-ICP-MS REE values: Zircon

Tex-ture	Spot	206Pb*/238U		232Th															
ID	no.	date (Ma) ± 1σ		238U	Y	SmN	EuN	GdN	TbN	DyN	HoN	ErN	TmN	YbN	LuN	Th (ppm)	U (ppm)	YbN/ GdN	Eu/Eu*
R	R113-1.2	988	±30	0.03	1216.0	3.5	6.1	38.1	144.1	407.5	724.8	1279.4	2512.4	4652.3	6777.8	24.4	840.0	121.95	0.29
RE	R1131-1.2	1009	±15	0.03	395.0	15.0	3.2	76.8	161.2	203.1	197.8	244.2	281.0	388.3	485.6	35.1	666.0	5.06	0.07
RE	R1114-1.1	1046	±14	0.18	992.0	72.7	39.3	163.8	256.2	449.9	669.1	1017.0	1264.5	1907.7	2353.9	200.7	347.0	11.65	0.33
RE	R1131-1.1	1055	±11	0.15	823.0	165.2	32.7	124.1	184.6	320.6	471.2	713.7	1074.4	1532.3	1991.8	229.2	523.0	12.35	0.23
RE	R1118-1.1	1098	±14	0.06	455.0	24.5	8.2	134.3	176.3	220.4	304.0	427.9	611.6	898.5	1098.8	76.1	478.0	6.69	0.10
C	R1112-1.1	1207	±18	0.70	450.0	35.4	3.9	97.2	127.0	208.5	293.2	396.5	433.9	695.4	839.5	129.2	439.0	7.16	0.06
C	R1136-1.1	1738	±26	0.71	564.0	93.1	36.1	161.2	225.9	292.5	320.1	451.2	731.4	1360.6	1707.8	71.2	1222.0	8.44	0.28
S	13-2_8	899	±15	2.79	1223.0	39.4	0.3	219.2	411.8	597.9	818.3	839.5	849.6	924.3	938.3	132.4	30.1	4.22	0.002
DR	13-2_4	921	±10	1.08	249.2	46.2	3.8	164.8	162.3	192.0	176.1	148.5	169.0	121.2	127.6	160.3	78.1	0.74	0.04
DR	13-2_10	932	±11	0.45	576.0	50.3	-	133.8	217.9	314.4	386.7	399.0	400.8	459.7	522.2	246.7	408.0	3.44	-
LR	13-2_7	950	±15	0.54	1052.0	36.7	6.2	179.6	355.4	506.8	735.6	755.2	797.5	978.5	868.3	94.8	45.1	5.45	0.06
RE	13-2_3	1011	±18	0.18	340.0	32.6	3.2	127.7	181.3	216.3	237.8	209.6	186.8	197.5	165.8	116.8	92.9	1.55	0.04
C	13-2_2	1113	±13	0.12	502.0	6.7	4.3	32.6	73.3	166.9	329.1	553.8	1033.1	1680.0	2477.4	25.7	153.5	16.41	0.22
C	13-2_5	1113	±25	0.28	701.0	38.1	14.6	157.2	256.2	362.6	512.6	687.9	929.8	1563.1	1629.6	48.0	242.1	9.95	0.15
C	13-2_11	1420	±16	0.40	1363.0	78.2	3.4	186.7	332.8	523.7	938.8	1311.5	1752.1	2547.7	3090.5	68.5	134.7	13.65	0.03
RE	13-2_6	1476	±19	0.35	1163.0	48.3	2.7	145.5	253.7	433.0	830.9	1168.0	1624.0	2443.1	2856.0	159.4	357.0	16.79	0.03
C	13-2_12	1574	±27	0.43	1706.0	407.9	43.6	417.1	501.4	741.7	1248.2	1648.8	2190.1	2873.8	3588.5	204.0	186.2	6.89	0.11
RE	14-5_1	919	±18	0.14	183.5	89.1	342.9	230.4	166.4	111.7	92.4	62.3	54.5	50.5	46.5	134.3	1205.0	0.22	2.15
RE	14-5_8	928	±9	0.03	116.7	8.2	-	79.9	96.7	82.0	69.1	52.2	40.9	39.4	41.6	16.0	368.5	0.49	-
S	14-5_3	950	±15	0.09	111.5	14.4	-	79.9	69.4	61.4	63.1	54.8	51.7	64.6	63.0	50.6	366.0	0.81	-
RE	14-5_9	964	±16	0.04	140.2	23.1	0.4	89.5	101.1	86.5	91.7	79.9	86.4	73.8	61.3	37.1	361.0	0.82	0.01

RE	14-5_2	996	±12	0.02	124.9	61.2	160.7	87.5	75.5	78.7	71.2	52.2	35.5	48.6	45.3	12.1	551.0	0.56	2.16
S	14-5_6	1007	±13	0.03	154.7	8.7	1.1	131.7	106.3	108.8	94.8	72.4	52.5	50.5	52.3	21.0	458.0	0.38	0.02
S	14-5_5	1025	±15	0.03	155.1	21.1	1.1	106.3	108.8	100.9	82.7	64.2	59.5	57.2	53.1	22.9	429.0	0.54	0.02
R	R14-8-22.2	913	±10	0.66	728.0	25.2	-	83.9	140.5	256.7	462.2	729.4	979.3	1446.2	1983.5	98.5	100.6	17.23	-
R	R14-8-23.2	916	±12	0.59	872.0	23.1	1.2	72.2	144.1	293.8	491.0	945.2	1297.5	1896.6	2555.6	156.5	178.7	26.26	0.03
R	R14-8-2.2	922	±10	0.72	1701.0	1.2	1.1	53.9	182.4	470.5	1050.4	1969.8	2727.3	4116.9	5065.8	261.4	273.2	76.36	0.04
RE	R14-8-26.2	926	±12	0.30	730.0	13.6	3.0	57.5	133.6	248.5	442.4	783.5	1107.4	1681.8	2271.6	40.7	80.1	29.26	0.09
RE	R14-8-2.1	930	±11	0.26	627.0	14.3	0.7	46.8	132.8	236.9	420.9	675.9	871.9	1390.8	1761.3	41.9	110.7	29.72	0.02
RE	R14-8-10.2	931	±12	0.28	636.0	8.9	1.0	47.3	95.0	194.1	365.1	602.3	809.9	1110.2	1497.9	35.8	75.8	23.47	0.03
RE	R14-8-14.1	938	±11	0.32	955.0	20.4	-	89.5	166.7	315.2	537.8	942.1	1314.0	1910.2	2761.3	51.0	112.0	21.34	-
RE	R14-8-1.2	940	±11	0.44	892.0	11.6	1.3	41.2	131.1	260.8	555.8	965.4	1491.7	2160.0	2991.8	79.8	126.3	52.43	0.05
RE	R14-8-6.1	941	±11	0.30	897.0	16.7	2.9	93.6	211.6	363.0	579.1	862.8	929.8	1204.9	1370.4	75.8	162.8	12.87	0.05
RE	R14-8-20.1	942	±10	0.45	1719.0	133.9	3.9	270.6	449.0	780.8	1054.0	1304.6	1376.0	1513.2	1617.3	141.7	227.5	5.59	0.02
RE	R14-8-26.1	946	±11	0.29	978.0	19.0	1.7	105.8	192.8	378.2	586.3	860.3	1074.4	1384.6	1576.1	65.4	135.6	13.09	0.03
RE	R14-8-7.2	952	±11	0.29	1440.0	23.1	3.9	147.0	330.0	536.1	865.1	1347.4	1727.3	2190.8	2518.5	107.8	183.4	14.90	0.05
RE	R14-8-21.1	954	±14	0.09	830.0	29.2	3.0	82.4	143.0	269.9	429.9	717.4	834.7	1360.0	1786.0	49.5	320.0	16.50	0.05
RE	R14-8-1.1	955	±11	0.33	669.0	12.2	3.0	64.6	109.9	254.6	435.3	694.8	962.8	1396.9	1794.2	45.8	118.6	21.62	0.08
RE	R14-8-24.2	965	±15	0.31	915.0	23.8	-	106.3	191.5	384.0	568.3	738.8	843.0	1046.2	971.2	77.1	181.2	9.84	-
RE	R14-8-12.2	965	±10	0.42	2289.0	114.2	10.5	303.7	526.2	864.0	1383.1	2135.9	2661.2	3587.7	4683.1	174.5	235.0	11.81	0.05
RE	R14-8-7.1	966	±12	0.27	607.0	8.6	0.8	49.3	116.0	213.4	383.1	609.2	838.8	1253.5	1662.6	32.8	81.5	25.41	0.03
RE	R14-8-13.1	977	±12	0.30	956.0	12.9	3.6	91.6	138.8	306.6	541.4	952.8	1347.1	2003.7	2872.4	45.6	95.0	21.88	0.07
RE	R14-8-4.2	981	±16	0.35	1101.0	21.8	5.2	89.0	196.7	406.3	719.4	1127.1	1500.0	2264.6	2633.7	79.4	168.4	25.44	0.09
RE	R14-8-23.1	981	±22	0.28	994.0	33.3	2.5	93.1	164.5	333.7	552.2	889.2	1140.5	1556.9	1925.9	53.2	128.0	16.73	0.040
RE	R14-8-25.1	988	±16	0.28	654.0	15.0	-	53.9	97.8	220.8	402.9	679.0	929.8	1415.4	1868.3	39.4	90.4	26.25	-
C (S)	R14-8-5.1	991	±16	0.20	185.2	30.6	2.1	139.4	166.1	140.5	96.9	85.0	60.3	72.6	60.1	138.6	511.0	0.52	0.03
RE	R14-8-18.2	1007	±19	0.37	1350.0	36.7	3.8	127.7	215.2	456.1	796.8	1348.6	1851.2	2670.8	3827.2	80.7	152.3	20.92	0.05
RE	R14-8-10.1	1010	±11	0.50	2356.0	79.5	18.0	271.1	490.4	867.3	1464.0	2221.5	2822.3	3926.2	4967.1	158.3	214.5	14.48	0.10
RE	R14-8-18.1	1017	±11	0.51	2057.0	141.4	14.8	308.7	438.0	818.7	1232.0	1719.3	2045.5	2609.2	3156.4	151.2	204.3	8.45	0.07
RE	R14-8-25.2	1036	±11	0.50	1570.0	25.8	3.9	162.3	327.8	613.9	991.0	1453.7	1785.1	2406.2	2633.7	122.0	204.0	14.83	0.04
RE	R14-8-19.1	1045	±17	0.25	536.0	25.8	3.2	58.5	99.2	197.8	295.0	506.6	621.5	911.4	1296.3	40.8	106.2	15.58	0.08

Table S6: SIMS U-Pb ages and normalised LA-ICP-MS REE values: Monazite

Texture	Spot	206Pb/238U		232Th															
ID	no.	date (Ma) ± 1σ		238U	Y	LaN	PrN	NdN	SmN	EuN	GdN	TbN	DyN	HoN	ErN	TmN	YbN	LuN	Th (ppm)
C	R11-1-15.1	960	±11	19.08	15000	455901	308418	235190	108770	7429	63428	36088	15937	6511	2077	835	430	248	69200
E	R11-1-11.2	987	±10	31.16	6240	354495	363973	290009	152617	4220	74822	28512	8986	2536	767	352	204	95	70300
C	R31-4.1	988	±12	9.98	12990	446527	307295	231653	113732	6946	69990	37438	13432	5917	2347	979	439	247	51900
E	R11-3-3.2	991	±10	40.26	4570	405624	336251	263926	99524	1382	36419	13967	5431	2068	743	321	204	93	128300
C	R11-1-4.1	999	±10	10.94	9320	449084	313131	243369	123453	5518	79095	38595	14710	4011	966	350	185	98	65000
C	R11-3-4.1	1002	±10	40.24	18200	438432	318967	241379	99592	9429	54832	31295	17553	8885	3757	2074	1274	580	88800
C	R11-3-6.1	1013	±10	36.64	4380	447380	316835	248232	97485	1795	48678	21240	7672	2129	560	219	111	70	98900
C	R31-3.1	1021	±11	3.21	22210	454623	320763	237179	108566	6946	63683	40413	16564	9532	4783	1938	877	473	59100
C	R11-1-11.1	1022	±10	14.45	2380	322113	383389	320071	122366	1532	35504	9917	3103	955	326	153	93	47	81600
C	R31-1.1	1023	±11	1.77	13700	466979	311111	235190	112984	6429	68260	37163	12897	5504	2077	740	314	337	57000
C	R31-3.2	1027	±11	2.09	10100	458458	315713	234085	116791	6268	71261	39752	11755	4444	1643	545	288	239	60400
C	R31-2.1	1029	±11	2.37	4790	438432	327048	250442	113868	3975	49237	20055	5546	2149	714	217	127	113	62200
C	R11-1-7.1	1032	±10	14.21	20730	479335	312458	228338	111625	8750	73703	46777	24722	9065	2196	674	296	95	53000
C	R31-5.1	1034	±12	9.32	833	407755	335129	258621	98232	1268	30977	7636	1384	337	162	38	42	36	103400
C	R31-4.2	1038	±11	1.59	4280	399659	342200	259505	98165	2446	35097	13444	4281	2072	957	417	170	97	83900
C	R31-6.1	1038	±11	2.19	19980	464423	308979	240495	118015	6982	74873	45344	18747	8705	3323	1231	585	527	89100
E	R132-5.2	983	±12	40.09	12280	432467	350505	281609	126852	12768	58800	23939	11125	5845	3285	1653	1089	453	63300
C	R132-5.1	985	±12	20.19	27800	460162	336925	267020	130591	29036	76399	40248	23033	14317	9755	6405	4554	2881	49320
E	R132-2.2	991	±15	26.16	16340	429058	347250	282493	130116	19482	65209	27824	14009	8022	4884	3021	2302	1588	75400
C	R132-4.2	1015	±12	18.65	24430	410737	365993	307250	162814	16839	91760	41846	20972	11709	7118	4260	2769	1815	71300
C	R132-1.1	1037	±11	2.25	48400	485726	344220	268347	135010	79107	81282	50441	32963	24604	18962	15702	12628	12305	38200
C	R132-2.1	1027	±12	29.72	13660	440988	348597	285146	137933	22714	68210	27631	12555	6709	3675	2017	1274	984	71500
RE	R132-1.2	1023	±12	38.45	25540	426502	371044	306145	144596	25393	70549	35207	19230	12446	8030	5215	3175	2901	81300
RE (Inc)	R145-8.1	886	±11	87.80	1404	400937	356117	276083	95581	829	26653	6645	1735	619	266	86	39	23	167800
RE	R145-7.2	895	±10	18.57	1624	339156	386083	303492	96193	664	28942	7818	2138	741	329	89	54	26	133900
RE	R145-6.1	902	±10	19.96	4610	396677	346352	267683	99864	1320	31740	11736	4223	1912	838	319	153	74	97700
RE (Inc)	R145-10.2	914	±10	26.86	1953	383468	363973	277409	83277	916	22635	6218	2130	897	493	230	171	84	141300
C	R145-6.2	915	±11	53.06	1709	349808	376655	307029	91774	982	22192	6140	1751	674	283	95	42	18	150000

RE	R145-5.3	916	±10	41.79	4780	483596	315039	227896	106934	4500	53764	19945	5468	1964	650	210	95	49	67800
RE	R145-5.1	921	±11	32.80	3930	412441	325926	241379	79742	839	27925	10438	3754	1728	790	327	167	103	99640
C	R145-9.1	931	±11	22.19	1874	460162	312346	230990	84636	2627	28688	8231	2406	853	369	144	91	35	79600
C (inc)	R145-8.2	931	±11	20.72	1850	457605	322896	232095	93610	1927	34893	10543	2699	777	256	67	33	20	98800
C	R145-5.2	943	±10	9.53	2418	472518	317845	225685	91978	2227	34842	10901	2897	986	344	118	49	32	60900
C (inc)	R145-10.1	950	±11	12.42	2150	466127	312795	228338	90211	3100	33622	9711	2897	1016	456	189	134	53	77400
RE (Inc)	R145-3.2	954	±11	18.21	3011	488283	313244	236074	99320	2618	34893	10705	3061	1264	564	232	97	58	78100
C	R145-1.1	966	±11	14.94	5610	462718	320426	245358	94833	2950	32553	11353	3997	2455	1617	897	689	253	77600
RE	R145-2.2	968	±11	48.21	3159	396251	364085	285809	101632	1523	30264	9419	2884	1338	568	260	127	68	125000
C	R145-7.1	969	±11	9.96	3800	463997	317508	225243	101971	4232	52899	19284	5422	1640	537	171	79	49	70000
C (inc)	R145-4.1	983	±11	24.46	2428	467405	330079	243811	105031	2343	44303	14050	3329	1016	317	83	58	28	108300
C	R145-2.1	990	±11	16.60	4550	448232	323232	245800	99388	3679	42472	14848	4162	1862	922	428	268	124	63300

Using accessory minerals to unravel thermal histories in polymetamorphic terranes: an example from Rogaland, SW Norway

E. BLEREAU, C. CLARK, R. J. M. TAYLOR, T. E. JOHNSON, P. KINNY, E. SANSOM, M. HAND

Table S7: Raw, normalised and buffered modified REE compositions from diffusion modelling and multi-spot senarios

Table S7: Raw, normalised and buffered modified REE compositions from diffusion modelling and multi-spot senarios

	Gd	Tb	Dy	Ho	Er	Tm	Yb	Lu
C0	21.626	5.082	50.967	17.792	69.916	14.52	126.75	24.3
CEq	19.66	3.63	24.27	5.56	15.89	2.42	16.25	2.43
C0 N	110	140	210	320	440	600	780	1000
CEq N	110	110	110	110	110	110	110	110
850 °C for x Myr								
0.5	21.61	5.07	50.72	17.68	69.41	14.41	125.72	24.10
1	21.61	5.07	50.72	17.68	69.41	14.41	125.72	24.10
5	21.61	5.07	50.72	17.68	69.41	14.41	125.71	24.09
10	21.61	5.07	50.72	17.68	69.41	14.41	125.68	24.07
30	21.61	5.07	50.72	17.68	69.40	14.39	125.38	23.98
100	21.61	5.07	50.72	17.67	69.25	14.33	124.45	23.72
200	21.61	5.07	50.71	17.64	69.04	14.25	123.41	23.44
0.5 N	109.93	139.57	208.98	317.91	436.84	595.32	773.63	991.57
1 N	109.93	139.57	208.98	317.91	436.84	595.32	773.63	991.57
5 N	109.93	139.57	208.98	317.90	436.84	595.31	773.61	991.44
10 N	109.93	139.57	208.98	317.90	436.84	595.29	773.41	990.67
30 N	109.93	139.57	208.98	317.90	436.76	594.72	771.55	986.76
100 N	109.93	139.57	208.97	317.73	435.81	592.03	765.85	976.25
200 N	109.93	139.57	208.92	317.29	434.49	588.89	759.42	964.48
0.5 B	110.00	139.57	208.98	317.91	436.84	595.32	773.63	991.57
1 B	110.00	139.57	208.98	317.91	436.84	595.32	773.63	991.57
5 B	110.00	139.57	208.98	317.90	436.84	595.31	773.61	991.44
10 B	110.00	139.57	208.98	317.90	436.84	595.29	773.41	990.67
30 B	110.00	139.57	208.98	317.90	436.76	594.72	771.55	986.76
100 B	110.00	139.57	208.97	317.73	435.81	592.03	765.85	976.25
200 B	110.00	139.57	208.92	317.29	434.49	588.89	759.42	964.48
900 °C for x Myr								
0.5	21.61	5.07	50.72	17.68	69.41	14.41	125.66	24.07
1	21.61	5.07	50.72	17.68	69.41	14.41	125.48	24.01
5	21.61	5.07	50.71	17.66	69.19	14.41	124.26	23.68
10	21.61	5.07	50.69	17.63	68.94	14.41	123.08	23.36

30	21.61	5.06	50.56	17.52	68.17	13.96	119.48	22.39
100	21.61	5.05	50.23	17.25	66.22	13.28	110.52	20.04
200	21.60	5.04	49.85	16.95	64.05	12.55	101.47	17.90
0.5 N	109.93	139.57	208.98	317.90	436.83	595.32	773.29	990.36
1 N	109.93	139.57	208.98	317.90	436.80	595.32	772.19	988.06
5 N	109.93	139.57	208.96	317.59	435.45	595.31	764.65	974.29
10 N	109.93	139.57	208.85	317.01	433.88	595.29	757.44	961.25
30 N	109.92	139.50	208.33	315.11	429.02	576.69	735.28	921.22
100 N	109.90	139.25	206.95	310.29	416.74	548.81	680.11	824.73
200 N	109.86	138.96	205.41	304.90	403.06	518.59	624.44	736.52
0.5 B	110.00	139.57	208.98	317.90	436.83	595.32	773.29	990.36
1 B	110.00	139.57	208.98	317.90	436.80	595.32	772.19	988.06
5 B	110.00	139.57	208.96	317.59	435.45	595.31	764.65	974.29
10 B	110.00	139.57	208.85	317.01	433.88	595.29	757.44	961.25
30 B	110.00	139.50	208.33	315.11	429.02	576.69	735.28	921.22
100 B	110.00	139.25	206.95	310.29	416.74	548.81	680.11	824.73
200 B	110.00	138.96	205.41	304.90	403.06	518.59	624.44	736.52
950 °C for x Myr								
0.5	21.61	5.07	50.68	17.62	68.96	14.23	123.29	23.42
1	21.61	5.06	50.61	17.57	68.56	14.10	121.49	22.94
5	21.60	5.05	50.19	17.25	66.31	13.34	111.56	20.34
10	21.60	5.04	49.79	16.94	64.19	12.64	102.95	18.29
30	21.57	5.00	48.58	16.03	58.15	10.87	83.98	14.20
100	21.50	4.91	45.65	14.12	47.83	8.31	58.86	8.99
200	21.42	4.81	43.00	12.68	40.88	6.64	43.29	6.14
0.5 N	109.93	139.56	208.82	316.99	433.99	588.22	758.70	963.88
1 N	109.93	139.53	208.53	315.97	431.45	582.59	747.63	944.09
5 N	109.89	139.19	206.81	310.20	417.30	551.29	686.51	837.11
10 N	109.84	138.86	205.17	304.76	403.98	522.46	633.54	752.50
30 N	109.70	137.85	200.15	288.28	365.94	449.31	516.79	584.30
100 N	109.35	135.32	188.10	253.87	300.99	343.34	362.22	370.04
200 N	108.96	132.62	177.19	228.02	257.27	274.31	266.43	252.48
0.5 B	110.00	139.56	208.82	316.99	433.99	588.22	758.70	963.88
1 B	110.00	139.53	208.53	315.97	431.45	582.59	747.63	944.09
5 B	110.00	139.19	206.81	310.20	417.30	551.29	686.51	837.11
10 B	110.00	138.86	205.17	304.76	403.98	522.46	633.54	752.50
30 B	110.00	137.85	200.15	288.28	365.94	449.31	516.79	584.30
100 B	110.00	135.32	188.10	253.87	300.99	343.34	362.22	370.04
200 B	110.00	132.62	177.19	228.02	257.27	274.31	266.43	252.48
1000 °C for x Myr								
0.5	21.59	5.04	49.91	17.06	65.14	12.99	107.40	19.37
1	21.58	5.02	49.32	16.63	62.31	12.11	97.21	17.06

5	21.50	4.92	46.17	14.54	50.36	9.00	66.07	10.52
10	21.42	4.83	43.67	13.16	43.66	7.39	50.55	7.46
30	21.20	4.60	38.69	10.65	31.83	4.75	29.24	4.04
100	20.82	4.29	32.34	7.75	21.07	3.03	19.15	2.76
200	20.57	4.08	28.84	6.61	18.09	2.66	17.35	2.55
0.5 N	109.84	138.91	205.62	306.82	409.95	536.68	660.90	796.93
1 N	109.77	138.40	203.22	299.19	392.11	500.21	598.22	702.01
5 N	109.35	135.56	190.23	261.46	316.95	371.71	406.56	433.06
10 N	108.95	132.98	179.93	236.65	274.75	305.18	311.09	307.06
30 N	107.82	126.75	159.41	191.62	200.29	196.09	179.92	166.46
100 N	105.91	118.06	133.24	139.45	132.62	125.03	117.83	113.52
200 N	104.62	112.46	118.82	118.84	113.85	109.91	106.77	105.01
0.5 B	110.00	138.91	205.62	306.82	409.95	536.68	660.90	796.93
1 B	110.00	138.40	203.22	299.19	392.11	500.21	598.22	702.01
5 B	110.00	135.56	190.23	261.46	316.95	371.71	406.56	433.06
10 B	110.00	132.98	179.93	236.65	274.75	305.18	311.09	307.06
30 B	110.00	126.75	159.41	191.62	200.29	196.09	179.92	166.46
100 B	110.00	118.06	133.24	139.45	132.62	125.03	117.83	113.52
200 B	110.00	112.46	118.82	118.84	113.85	110.00	110.00	110.00
1050 °C for x Myr								
0.5	21.45	4.87	45.11	14.04	48.33	8.58	62.47	9.84
1	21.34	4.76	42.32	12.60	41.43	6.93	46.85	6.85
5	20.89	4.37	34.39	8.73	24.52	3.55	22.07	3.12
10	20.65	4.17	30.64	7.25	19.90	2.90	18.56	2.70
30	20.21	3.86	26.35	6.01	16.84	2.52	16.73	2.48
100	19.83	3.69	24.70	5.64	16.06	2.44	16.33	2.44
200	19.73	3.65	24.43	5.59	15.95	2.43	16.28	2.43
0.5 N	109.09	134.23	185.85	252.55	304.13	354.41	384.42	405.06
1 N	108.54	131.02	174.39	226.54	260.71	286.30	288.28	281.79
5 N	106.27	120.35	141.70	157.08	154.33	146.49	135.80	128.46
10 N	105.02	114.91	126.24	130.46	125.25	119.65	114.23	110.91
30 N	102.81	106.45	108.57	108.16	105.95	104.30	102.97	102.22
100 N	100.89	101.58	101.76	101.53	101.06	100.74	100.50	100.37
200 N	100.37	100.61	100.65	100.55	100.38	100.26	100.18	100.13
0.5 B	110.00	134.23	185.85	252.55	304.13	354.41	384.42	405.06
1 B	110.00	131.02	174.39	226.54	260.71	286.30	288.28	281.79
5 B	110.00	120.35	141.70	157.08	154.33	146.49	135.80	128.46
10 B	110.00	114.91	126.24	130.46	125.25	119.65	114.23	110.91
30 B	110.00	110.00	110.00	110.00	110.00	110.00	110.00	110.00
100 B	110.00	110.00	110.00	110.00	110.00	110.00	110.00	110.00
200 B	110.00	110.00	110.00	110.00	110.00	110.00	110.00	110.00
1100 °C for x Myr								

0.5	20.80	4.31	33.70	8.56	24.24	3.54	22.18	3.15
1	20.54	4.11	30.00	7.13	19.74	2.89	18.61	2.71
5	19.94	3.74	25.19	5.76	16.33	2.47	16.48	2.46
10	19.78	3.67	24.63	5.64	16.05	2.44	16.33	2.44
30	19.69	3.64	24.34	5.58	15.92	2.42	16.27	2.43
100	19.67	3.63	24.28	5.56	15.90	2.42	16.25	2.43
200	19.66	3.63	24.27	5.56	15.89	2.42	16.25	2.43
0.5 N	105.78	118.84	138.84	153.88	152.53	146.22	136.48	129.51
1 N	104.48	113.29	123.59	128.18	124.23	119.52	114.52	111.34
5 N	101.40	102.95	103.81	103.68	102.75	102.03	101.43	101.09
10 N	100.63	101.21	101.47	101.37	101.00	100.73	100.51	100.39
30 N	100.15	100.26	100.30	100.27	100.20	100.14	100.10	100.08
100 N	100.03	100.04	100.05	100.05	100.03	100.02	100.02	100.01
200 N	100.01	100.02	100.02	100.02	100.01	100.01	100.01	100.00
0.5 B	110.00	118.84	138.84	153.88	152.53	146.22	136.48	129.51
1 B	110.00	113.29	123.59	128.18	124.23	119.52	114.52	111.34
5 B	110.00	110.00	110.00	110.00	110.00	110.00	110.00	110.00
10 B	110.00	110.00	110.00	110.00	110.00	110.00	110.00	110.00
30 B	110.00	110.00	110.00	110.00	110.00	110.00	110.00	110.00
100 B	110.00	110.00	110.00	110.00	110.00	110.00	110.00	110.00
200 B	110.00	110.00	110.00	110.00	110.00	110.00	110.00	110.00
0.5 Myr for x °C	Gd	Tb	Dy	Ho	Er	Tm	Yb	Lu
850	21.61	5.07	50.72	17.68	69.41	14.41	125.72	24.10
900	21.61	5.07	50.72	17.68	69.41	14.41	125.66	24.07
950	21.61	5.07	50.68	17.62	68.96	14.23	123.29	23.42
1000	21.59	5.04	49.91	17.06	65.14	12.99	107.40	19.37
1050	21.45	4.87	45.11	14.04	48.33	8.58	62.47	9.84
1100	20.80	4.31	33.70	8.56	24.24	3.54	22.18	3.15
850 N	109.93	139.57	208.98	317.91	436.84	595.32	773.63	991.57
900 N	109.93	139.57	208.98	317.90	436.83	595.27	773.29	990.36
950 N	109.93	139.56	208.82	316.99	433.99	588.22	758.70	963.88
1000 N	109.84	138.91	205.62	306.82	409.95	536.68	660.90	796.93
1050 N	109.09	134.23	185.85	252.55	304.13	354.41	384.42	405.06
1100 N	105.78	118.84	138.84	153.88	152.53	146.22	136.48	129.51
850 B	110.00	139.57	208.98	317.91	436.84	595.32	773.63	991.57
900 B	110.00	139.57	208.98	317.90	436.83	595.27	773.29	990.36
950 B	110.00	139.56	208.82	316.99	433.99	588.22	758.70	963.88
1000 B	110.00	138.91	205.62	306.82	409.95	536.68	660.90	796.93
1050 B	110.00	134.23	185.85	252.55	304.13	354.41	384.42	405.06
1100 B	110.00	118.84	138.84	153.88	152.53	146.22	136.48	129.51

1 Myr for x °C								
850	21.61	5.07	50.72	17.68	69.41	14.41	125.72	24.10
900	21.61	5.07	50.72	17.68	69.41	14.40	125.48	24.01
950	21.61	5.06	50.61	17.57	68.56	14.10	121.49	22.94
1000	21.58	5.02	49.32	16.63	62.31	12.11	97.21	17.06
1050	21.34	4.76	42.32	12.60	41.43	6.93	46.85	6.85
1100	20.54	4.11	30.00	7.13	19.74	2.89	18.61	2.71
850 N	109.93	139.57	208.98	317.91	436.84	595.32	773.63	991.57
900 N	109.93	139.57	208.98	317.90	436.80	594.95	772.19	988.06
950 N	109.93	139.53	208.53	315.97	431.45	582.59	747.63	944.09
1000 N	109.77	138.40	203.22	299.19	392.11	500.21	598.22	702.01
1050 N	108.54	131.02	174.39	226.54	260.71	286.30	288.28	281.79
1100 N	104.48	113.29	123.59	128.18	124.23	119.52	114.52	111.34
850 B	110.00	139.57	208.98	317.91	436.84	595.32	773.63	991.57
900 B	110.00	139.57	208.98	317.90	436.80	594.95	772.19	988.06
950 B	110.00	139.53	208.53	315.97	431.45	582.59	747.63	944.09
1000 B	110.00	138.40	203.22	299.19	392.11	500.21	598.22	702.01
1050 B	110.00	131.02	174.39	226.54	260.71	286.30	288.28	281.79
1100 B	110.00	113.29	123.59	128.18	124.23	119.52	114.52	111.34
5 Myr for x °C								
850	21.61	5.07	50.72	17.68	69.41	14.41	125.71	24.09
900	21.61	5.07	50.71	17.66	69.19	14.31	124.26	23.68
950	21.60	5.05	50.19	17.25	66.31	13.34	111.56	20.34
1000	21.50	4.92	46.17	14.54	50.36	9.00	66.07	10.52
1050	20.89	4.37	34.39	8.73	24.52	3.55	22.07	3.12
1100	19.94	3.74	25.19	5.76	16.33	2.47	16.48	2.46
850 N	109.93	139.57	208.98	317.90	436.84	595.31	773.61	991.44
900 N	109.93	139.57	208.96	317.59	435.45	591.34	764.65	974.29
950 N	109.89	139.19	206.81	310.20	417.30	551.29	686.51	837.11
1000 N	109.35	135.56	190.23	261.46	316.95	371.71	406.56	433.06
1050 N	106.27	120.35	141.70	157.08	154.33	146.49	135.80	128.46
1100 N	101.40	102.95	103.81	103.68	102.75	102.03	101.43	101.09
850 B	110.00	139.57	208.98	317.90	436.84	595.31	773.61	991.44
900 B	110.00	139.57	208.96	317.59	435.45	591.34	764.65	974.29
950 B	110.00	139.19	206.81	310.20	417.30	551.29	686.51	837.11
1000 B	110.00	135.56	190.23	261.46	316.95	371.71	406.56	433.06
1050 B	110.00	120.35	141.70	157.08	154.33	146.49	135.80	128.46
1100 B	110.00	110.00	110.00	110.00	110.00	110.00	110.00	110.00
10 Myr for x °C								
850	21.61	5.07	50.72	17.68	69.41	14.41	125.68	24.07
900	21.61	5.07	50.69	17.63	68.94	14.22	123.08	23.36
950	21.60	5.04	49.79	16.94	64.19	12.64	102.95	18.29

1000	21.42	4.83	43.67	13.16	43.66	7.39	50.55	7.46
1050	20.65	4.17	30.64	7.25	19.90	2.90	18.56	2.70
1100	19.78	3.67	24.63	5.64	16.05	2.44	16.33	2.44
850 N	109.93	139.57	208.98	317.90	436.84	595.29	773.41	990.67
900 N	109.93	139.57	208.85	317.01	433.88	587.74	757.44	961.25
950 N	109.84	138.86	205.17	304.76	403.98	522.46	633.54	752.50
1000 N	108.95	132.98	179.93	236.65	274.75	305.18	311.09	307.06
1050 N	105.02	114.91	126.24	130.46	125.25	119.65	114.23	110.91
1100 N	100.63	101.21	101.47	101.37	101.00	100.73	100.51	100.39
850 B	110.00	139.57	208.98	317.90	436.84	595.29	773.41	990.67
900 B	110.00	139.57	208.85	317.01	433.88	587.74	757.44	961.25
950 B	110.00	138.86	205.17	304.76	403.98	522.46	633.54	752.50
1000 B	110.00	132.98	179.93	236.65	274.75	305.18	311.09	307.06
1050 B	110.00	114.91	126.24	130.46	125.25	119.65	114.23	110.91
1100 B	110.00	110.00	110.00	110.00	110.00	110.00	110.00	110.00
30 Myr for x °C								
850	21.61	5.07	50.72	17.68	69.40	14.39	125.38	23.98
900	21.61	5.06	50.56	17.52	68.17	13.96	119.48	22.39
950	21.57	5.00	48.58	16.03	58.15	10.87	83.98	14.20
1000	21.20	4.60	38.69	10.65	31.83	4.75	29.24	4.04
1050	20.21	3.86	26.35	6.01	16.84	2.52	16.73	2.48
1100	19.69	3.64	24.34	5.58	15.92	2.42	16.27	2.43
850 N	109.93	139.57	208.98	317.90	436.76	594.72	771.55	986.76
900 N	109.92	139.50	208.33	315.11	429.02	576.69	735.28	921.22
950 N	109.70	137.85	200.15	288.28	365.94	449.31	516.79	584.30
1000 N	107.82	126.75	159.41	191.62	200.29	196.09	179.92	166.46
1050 N	102.81	106.45	108.57	108.16	105.95	104.30	102.97	102.22
1100 N	100.15	100.26	100.30	100.27	100.20	100.14	100.10	100.08
850 B	110.00	139.57	208.98	317.90	436.76	594.72	771.55	986.76
900 B	110.00	139.50	208.33	315.11	429.02	576.69	735.28	921.22
950 B	110.00	137.85	200.15	288.28	365.94	449.31	516.79	584.30
1000 B	110.00	126.75	159.41	191.62	200.29	196.09	179.92	166.46
1050 B	110.00	110.00	110.00	110.00	110.00	110.00	110.00	110.00
1100 B	110.00	110.00	110.00	110.00	110.00	110.00	110.00	110.00
100 Myr for x °C								
850	21.61	5.07	50.72	17.67	69.25	14.33	124.45	23.72
900	21.61	5.05	50.23	17.25	66.22	13.28	110.52	20.04
950	21.50	4.91	45.65	14.12	47.83	8.31	58.86	8.99
1000	20.82	4.29	32.34	7.75	21.07	3.03	19.15	2.76
1050	19.83	3.69	24.70	5.64	16.06	2.44	16.33	2.44
1100	19.67	3.63	24.28	5.56	15.90	2.42	16.25	2.43
850 N	109.93	139.57	208.97	317.73	435.81	592.03	765.85	976.25

900 N	109.90	139.25	206.95	310.29	416.74	548.81	680.11	824.73
950 N	109.35	135.32	188.10	253.87	300.99	343.34	362.22	370.04
1000 N	105.91	118.06	133.24	139.45	132.62	125.03	117.83	113.52
1050 N	100.89	101.58	101.76	101.53	101.06	100.74	100.50	100.37
1100 N	100.03	100.04	100.05	100.05	100.03	100.02	100.02	100.01
850 B	110.00	139.57	208.97	317.73	435.81	592.03	765.85	976.25
900 B	110.00	139.25	206.95	310.29	416.74	548.81	680.11	824.73
950 B	110.00	135.32	188.10	253.87	300.99	343.34	362.22	370.04
1000 B	110.00	118.06	133.24	139.45	132.62	125.03	117.83	113.52
1050 B	110.00	110.00	110.00	110.00	110.00	110.00	110.00	110.00
1100 B	110.00	110.00	110.00	110.00	110.00	110.00	110.00	110.00
200 Myr for x °C								
850	21.61	5.07	50.71	17.64	69.04	14.25	123.41	23.44
900	21.60	5.04	49.85	16.95	64.05	12.55	101.47	17.90
950	21.42	4.81	43.00	12.68	40.88	6.64	43.29	6.14
1000	20.57	4.08	28.84	6.61	18.09	2.66	17.35	2.55
1050	19.73	3.65	24.43	5.59	15.95	2.43	16.28	2.43
1100	19.66	3.63	24.27	5.56	15.89	2.42	16.25	2.43
850 N	109.93	139.57	208.92	317.29	434.49	588.89	759.42	964.48
900 N	109.86	138.96	205.41	304.90	403.06	518.59	624.44	736.52
950 N	108.96	132.62	177.19	228.02	257.27	274.31	266.43	252.48
1000 N	104.62	112.46	118.82	118.84	113.85	109.91	106.77	105.01
1050 N	100.37	100.61	100.65	100.55	100.38	100.26	100.18	100.13
1100 N	100.01	100.02	100.02	100.02	100.01	100.01	100.01	100.00
850 B	110.00	139.57	208.92	317.29	434.49	588.89	759.42	964.48
900 B	110.00	138.96	205.41	304.90	403.06	518.59	624.44	736.52
950 B	110.00	132.62	177.19	228.02	257.27	274.31	266.43	252.48
1000 B	110.00	112.46	118.82	118.84	113.85	110.00	110.00	110.00
1050 B	110.00	110.00	110.00	110.00	110.00	110.00	110.00	110.00
1100 B	110.00	110.00	110.00	110.00	110.00	110.00	110.00	110.00
N= Normalised, B= Buffered to equilibrium composition								
Multi-spot senarios								
1100 1 Myr	Gd	Tb	Dy	Ho	Er	Tm	Yb	Lu
5-3.1	20.54	4.11	30.00	7.13	19.74	2.89	18.61	2.71
4.5-2.6	20.68	4.17	30.48	7.21	19.88	2.90	18.65	2.71
4-2.1	20.81	4.23	30.93	7.29	20.00	2.91	18.68	2.71
3.5-1.6	20.92	4.28	31.33	7.36	20.10	2.92	18.70	2.71
3.1-1.1	21.02	4.32	31.68	7.42	20.19	2.93	18.72	2.71
2.5-0.6	21.11	4.36	31.97	7.47	20.27	2.93	18.74	2.72
2.0-0.1	21.17	4.39	32.19	7.51	20.32	2.94	18.75	2.72
1.5-0.5	21.20	4.41	32.32	7.53	20.35	2.94	18.76	2.72

1–1	21.22	4.41	32.36	7.53	20.36	2.94	18.76	2.72
0.5-1.5	21.20	4.41	32.32	7.53	20.35	2.94	18.76	2.72
0.1–2	21.17	4.39	32.19	7.51	20.32	2.94	18.75	2.72
0.6-2.5	21.11	4.36	31.97	7.47	20.27	2.93	18.74	2.72
1.1-3.0	21.02	4.32	31.68	7.42	20.19	2.93	18.72	2.71
1.6-3.5	20.92	4.28	31.33	7.36	20.10	2.92	18.70	2.71
2–4	20.81	4.23	30.93	7.29	20.00	2.91	18.68	2.71
2.6-4.5	20.68	4.17	30.48	7.21	19.88	2.90	18.65	2.71
3.1-5	20.54	4.11	30.00	7.13	19.74	2.89	18.61	2.71
5-3.1 N	104.48	113.29	123.59	128.18	124.23	119.52	114.52	111.34
4.5-2.6 N	105.17	114.91	125.58	129.73	125.09	119.97	114.74	111.46
4-2.1 N	105.83	116.46	127.43	131.16	125.85	120.36	114.93	111.56
3.5-1.6 N	106.42	117.89	129.10	132.42	126.52	120.70	115.09	111.65
3.1-1.1 N	106.94	119.15	130.55	133.49	127.08	120.99	115.23	111.72
2.5-0.6 N	107.36	120.18	131.73	134.35	127.53	121.21	115.33	111.78
2.0-0.1 N	107.66	120.96	132.61	134.99	127.86	121.38	115.41	111.82
1.5-0.5 N	107.85	121.44	133.16	135.38	128.06	121.48	115.46	111.84
1–1 N	107.92	121.61	133.35	135.51	128.13	121.51	115.48	111.85
0.5-1.5 N	107.85	121.44	133.16	135.38	128.06	121.48	115.46	111.84
0.1–2 N	107.66	120.96	132.61	134.99	127.86	121.38	115.41	111.82
0.6-2.5 N	107.36	120.18	131.73	134.35	127.53	121.21	115.33	111.78
1.1-3.0 N	106.94	119.15	130.55	133.49	127.08	120.99	115.23	111.72
1.6-3.5 N	106.42	117.89	129.10	132.42	126.52	120.70	115.09	111.65
2–4 N	105.83	116.46	127.43	131.16	125.85	120.36	114.93	111.56
2.6-4.5 N	105.17	114.91	125.58	129.73	125.09	119.97	114.74	111.46
3.1-5 N	104.48	113.29	123.59	128.18	124.23	119.52	114.52	111.34
5-3.1 B	110.00	113.29	123.59	128.18	124.23	119.52	114.52	111.34
4.5-2.6 B	110.00	114.91	125.58	129.73	125.09	119.97	114.74	111.46
4-2.1 B	110.00	116.46	127.43	131.16	125.85	120.36	114.93	111.56
3.5-1.6 B	110.00	117.89	129.10	132.42	126.52	120.70	115.09	111.65
3.1-1.1 B	110.00	119.15	130.55	133.49	127.08	120.99	115.23	111.72
2.5-0.6 B	110.00	120.18	131.73	134.35	127.53	121.21	115.33	111.78
2.0-0.1 B	110.00	120.96	132.61	134.99	127.86	121.38	115.41	111.82
1.5-0.5 B	110.00	121.44	133.16	135.38	128.06	121.48	115.46	111.84
1–1 B	110.00	121.61	133.35	135.51	128.13	121.51	115.48	111.85
0.5-1.5 B	110.00	121.44	133.16	135.38	128.06	121.48	115.46	111.84
0.1–2 B	110.00	120.96	132.61	134.99	127.86	121.38	115.41	111.82
0.6-2.5 B	110.00	120.18	131.73	134.35	127.53	121.21	115.33	111.78
1.1-3.0 B	110.00	119.15	130.55	133.49	127.08	120.99	115.23	111.72
1.6-3.5 B	110.00	117.89	129.10	132.42	126.52	120.70	115.09	111.65
2–4 B	110.00	116.46	127.43	131.16	125.85	120.36	114.93	111.56
2.6-4.5 B	110.00	114.91	125.58	129.73	125.09	119.97	114.74	111.46

3.1-5 B	110.00	113.29	123.59	128.18	124.23	119.52	114.52	111.34
1050 5 Myr								
5-3.1	20.89	4.37	34.39	8.73	24.52	3.55	22.07	3.12
4.5-2.6	21.11	4.49	35.77	9.05	25.09	3.59	22.23	3.14
4-2.1	21.29	4.61	37.09	9.34	25.62	3.64	22.38	3.15
3.5-1.6	21.42	4.71	38.31	9.61	26.08	3.68	22.50	3.16
3.1-1.1	21.51	4.79	39.38	9.85	26.48	3.71	22.61	3.17
2.5-0.6	21.56	4.85	40.26	10.04	26.81	3.73	22.69	3.17
2.0-0.1	21.59	4.90	40.92	10.19	27.05	3.75	22.76	3.18
1.5-0.5	21.61	4.92	41.33	10.28	27.20	3.77	22.79	3.18
1–1	21.61	4.93	41.47	10.31	27.25	3.77	22.81	3.18
0.5-1.5	21.61	4.92	41.33	10.28	27.20	3.77	22.79	3.18
0.1–2	21.59	4.90	40.92	10.19	27.05	3.75	22.76	3.18
0.6-2.5	21.56	4.85	40.26	10.04	26.81	3.73	22.69	3.17
1.1-3.0	21.51	4.79	39.38	9.85	26.48	3.71	22.61	3.17
1.6-3.5	21.42	4.71	38.31	9.61	26.08	3.68	22.50	3.16
2–4	21.29	4.61	37.09	9.34	25.62	3.64	22.38	3.15
2.6-4.5	21.11	4.49	35.77	9.05	25.09	3.59	22.23	3.14
3.1-5	20.89	4.37	34.39	8.73	24.52	3.55	22.07	3.12
5-3.1 N	106.27	120.35	141.70	157.08	154.33	146.49	135.80	128.46
4.5-2.6 N	107.38	123.75	147.39	162.72	157.91	148.50	136.81	129.02
4-2.1 N	108.28	126.89	152.84	168.04	161.21	150.31	137.71	129.51
3.5-1.6 N	108.95	129.64	157.85	172.89	164.15	151.90	138.49	129.93
3.1-1.1 N	109.40	131.91	162.25	177.12	166.67	153.24	139.14	130.29
2.5-0.6 N	109.68	133.67	165.87	180.59	168.72	154.31	139.66	130.56
2.0-0.1 N	109.83	134.91	168.59	183.19	170.23	155.10	140.04	130.77
1.5-0.5 N	109.91	135.66	170.28	184.81	171.17	155.59	140.27	130.89
1–1 N	109.93	135.90	170.86	185.36	171.48	155.76	140.35	130.93
0.5-1.5 N	109.91	135.66	170.28	184.81	171.17	155.59	140.27	130.89
0.1–2 N	109.83	134.91	168.59	183.19	170.23	155.10	140.04	130.77
0.6-2.5 N	109.68	133.67	165.87	180.59	168.72	154.31	139.66	130.56
1.1-3.0 N	109.40	131.91	162.25	177.12	166.67	153.24	139.14	130.29
1.6-3.5 N	108.95	129.64	157.85	172.89	164.15	151.90	138.49	129.93
2–4 N	108.28	126.89	152.84	168.04	161.21	150.31	137.71	129.51
2.6-4.5 N	107.38	123.75	147.39	162.72	157.91	148.50	136.81	129.02
3.1-5 N	106.27	120.35	141.70	157.08	154.33	146.49	135.80	128.46
5-3.1 B	110.00	120.35	141.70	157.08	154.33	146.49	135.80	128.46
4.5-2.6 B	110.00	123.75	147.39	162.72	157.91	148.50	136.81	129.02
4-2.1 B	110.00	126.89	152.84	168.04	161.21	150.31	137.71	129.51
3.5-1.6 B	110.00	129.64	157.85	172.89	164.15	151.90	138.49	129.93
3.1-1.1 B	110.00	131.91	162.25	177.12	166.67	153.24	139.14	130.29
2.5-0.6 B	110.00	133.67	165.87	180.59	168.72	154.31	139.66	130.56

2.0-0.1 B	110.00	134.91	168.59	183.19	170.23	155.10	140.04	130.77
1.5-0.5 B	110.00	135.66	170.28	184.81	171.17	155.59	140.27	130.89
1–1 B	110.00	135.90	170.86	185.36	171.48	155.76	140.35	130.93
0.5-1.5 B	110.00	135.66	170.28	184.81	171.17	155.59	140.27	130.89
0.1–2 B	110.00	134.91	168.59	183.19	170.23	155.10	140.04	130.77
0.6-2.5 B	110.00	133.67	165.87	180.59	168.72	154.31	139.66	130.56
1.1-3.0 B	110.00	131.91	162.25	177.12	166.67	153.24	139.14	130.29
1.6-3.5 B	110.00	129.64	157.85	172.89	164.15	151.90	138.49	129.93
2–4 B	110.00	126.89	152.84	168.04	161.21	150.31	137.71	129.51
2.6-4.5 B	110.00	123.75	147.39	162.72	157.91	148.50	136.81	129.02
3.1-5 B	110.00	120.35	141.70	157.08	154.33	146.49	135.80	128.46
900 100 Myr								
5-3.1	21.61	5.05	50.23	17.25	66.22	13.28	110.52	20.04
4.5-2.6	21.63	5.08	50.97	17.78	69.57	14.27	121.60	22.50
4-2.1	21.63	5.08	50.97	17.79	69.91	14.50	125.65	23.71
3.5-1.6	21.63	5.08	50.97	17.79	69.92	14.52	126.60	24.15
3.1-1.1	21.63	5.08	50.97	17.79	69.92	14.52	126.74	24.27
2.5-0.6	21.63	5.08	50.97	17.79	69.92	14.52	126.75	24.30
2.0-0.1	21.63	5.08	50.97	17.79	69.92	14.52	126.75	24.30
1.5-0.5	21.63	5.08	50.97	17.79	69.92	14.52	126.75	24.30
1–1	21.63	5.08	50.97	17.79	69.92	14.52	126.75	24.30
0.5-1.5	21.63	5.08	50.97	17.79	69.92	14.52	126.75	24.30
0.1–2	21.63	5.08	50.97	17.79	69.92	14.52	126.75	24.30
0.6-2.5	21.63	5.08	50.97	17.79	69.92	14.52	126.75	24.30
1.1-3.0	21.63	5.08	50.97	17.79	69.92	14.52	126.74	24.27
1.6-3.5	21.63	5.08	50.97	17.79	69.92	14.52	126.60	24.15
2–4	21.63	5.08	50.97	17.79	69.91	14.50	125.65	23.71
2.6-4.5	21.63	5.08	50.97	17.78	69.57	14.27	121.60	22.50
3.1-5	21.61	5.05	50.23	17.25	66.22	13.28	110.52	20.04
5-3.1 N	109.90	139.25	206.95	310.29	416.74	548.81	680.11	824.73
4.5-2.6 N	110.02	139.94	210.01	319.72	437.81	589.77	748.28	926.05
4-2.1 N	110.02	139.94	210.01	319.96	439.97	599.00	773.24	975.79
3.5-1.6 N	110.02	139.94	210.01	319.96	440.02	599.96	779.08	993.99
3.1-1.1 N	110.02	139.94	210.01	319.96	440.03	600.00	779.92	998.88
2.5-0.6 N	110.02	139.94	210.01	319.96	440.03	600.00	780.00	999.85
2.0-0.1 N	110.02	139.94	210.01	319.96	440.03	600.00	780.00	999.98
1.5-0.5 N	110.02	139.94	210.01	319.96	440.03	600.00	780.00	1000.00
1–1 N	110.02	139.94	210.01	319.96	440.03	600.00	780.00	1000.00
0.5-1.5 N	110.02	139.94	210.01	319.96	440.03	600.00	780.00	1000.00
0.1–2 N	110.02	139.94	210.01	319.96	440.03	600.00	780.00	999.98
0.6-2.5 N	110.02	139.94	210.01	319.96	440.03	600.00	780.00	999.85
1.1-3.0 N	110.02	139.94	210.01	319.96	440.03	600.00	779.92	998.88

1.6-3.5 N	110.02	139.94	210.01	319.96	440.02	599.96	779.08	993.99
2–4 N	110.02	139.94	210.01	319.96	439.97	599.00	773.24	975.79
2.6-4.5 N	110.02	139.94	210.01	319.72	437.81	589.77	748.28	926.05
3.1-5 N	109.90	139.25	206.95	310.29	416.74	548.81	680.11	824.73
5-3.1 B	110.00	139.25	206.95	310.29	416.74	548.81	680.11	824.73
4.5-2.6 B	110.00	139.94	210.01	319.72	437.81	589.77	748.28	926.05
4-2.1 B	110.00	139.94	210.01	319.96	439.97	599.00	773.24	975.79
3.5-1.6 B	110.00	139.94	210.01	319.96	440.02	599.96	779.08	993.99
3.1-1.1 B	110.00	139.94	210.01	319.96	440.03	600.00	779.92	998.88
2.5-0.6 B	110.00	139.94	210.01	319.96	440.03	600.00	780.00	999.85
2.0-0.1 B	110.00	139.94	210.01	319.96	440.03	600.00	780.00	999.98
1.5-0.5 B	110.00	139.94	210.01	319.96	440.03	600.00	780.00	1000.00
1–1 B	110.00	139.94	210.01	319.96	440.03	600.00	780.00	1000.00
0.5-1.5 B	110.00	139.94	210.01	319.96	440.03	600.00	780.00	1000.00
0.1–2 B	110.00	139.94	210.01	319.96	440.03	600.00	780.00	999.98
0.6-2.5 B	110.00	139.94	210.01	319.96	440.03	600.00	780.00	999.85
1.1-3.0 B	110.00	139.94	210.01	319.96	440.03	600.00	779.92	998.88
1.6-3.5 B	110.00	139.94	210.01	319.96	440.02	599.96	779.08	993.99
2–4 B	110.00	139.94	210.01	319.96	439.97	599.00	773.24	975.79
2.6-4.5 B	110.00	139.94	210.01	319.72	437.81	589.77	748.28	926.05
3.1-5 B	110.00	139.25	206.95	310.29	416.74	548.81	680.11	824.73
850 100 Myr								
5-3.1	21.61	5.07	50.72	17.67	69.25	14.33	124.45	23.72
4-2.1	21.63	5.08	50.97	17.79	69.92	14.52	126.75	24.30
3.1-5	21.61	5.07	50.72	17.67	69.25	14.33	124.45	23.72
5-3.1 N	109.93	139.57	208.97	317.73	435.81	592.03	765.85	976.25
4-2.1 N	110.02	139.94	210.01	319.96	440.03	600.00	780.00	1000.00
3.1-5 N	109.93	139.57	208.97	317.73	435.81	592.03	765.85	976.25
5-3.1 B	110.00	139.57	208.97	317.73	435.81	592.03	765.85	976.25
4-2.1 B	110.02	139.94	210.01	319.96	440.03	600.00	780.00	1000.00
3.1-5 B	110.00	139.57	208.97	317.73	435.81	592.03	765.85	976.25
N= Normalised, B= Buffered to equilibrium composition								